Springer ThesesRecognizing Outstanding Ph.D. Research

Christopher Race

The Modelling of Radiation Damage in Metals Using Ehrenfest Dynamics



Springer Theses

Recognizing Outstanding Ph.D. Research

For further volumes: http://www.springer.com/series/8790

Aims and Scope

The series "Springer Theses" brings together a selection of the very best Ph.D. theses from around the world and across the physical sciences. Nominated and endorsed by two recognized specialists, each published volume has been selected for its scientific excellence and the high impact of its contents for the pertinent field of research. For greater accessibility to non-specialists, the published versions include an extended introduction, as well as a foreword by the student's supervisor explaining the special relevance of the work for the field. As a whole, the series will provide a valuable resource both for newcomers to the research fields described, and for other scientists seeking detailed background information on special questions. Finally, it provides an accredited documentation of the valuable contributions made by today's younger generation of scientists.

Theses are accepted into the series by invited nomination only and must fulfill all of the following criteria.

- They must be written in good English.
- The topic of should fall within the confines of Chemistry, Physics and related interdisciplinary fields such as Materials, Nanoscience, Chemical Engineering, Complex Systems and Biophysics.
- The work reported in the thesis must represent a significant scientific advance.
- If the thesis includes previously published material, permission to reproduce this must be gained from the respective copyright holder.
- They must have been examined and passed during the 12 months prior to nomination.
- Each thesis should include a foreword by the supervisor outlining the significance of its content.
- The theses should have a clearly defined structure including an introduction accessible to scientists not expert in that particular field.

Christopher Race

The Modelling of Radiation Damage in Metals Using Ehrenfest Dynamics

Doctoral Thesis accepted by Imperial College, London, UK



Author
Dr. Christopher Race
Department of Physics
Imperial College
London
UK

e-mail: chris.race06@imperial.ac.uk

Supervisor
Prof. Adrian Sutton
Head of Condensed Matter Theory
Physics Department
Imperial College
SW7 2AZ London
UK

ISSN 2190-5053

e-ISSN 2190-5061

ISBN 978-3-642-15438-6

e-ISBN 978-3-642-15439-3

DOI 10.1007/978-3-642-15439-3

Springer Heidelberg Dordrecht London New York

© Springer-Verlag Berlin Heidelberg 2010

This work is subject to copyright. All rights are reserved, whether the whole or part of the material is concerned, specifically the rights of translation, reprinting, reuse of illustrations, recitation, broadcasting, reproduction on microfilm or in any other way, and storage in data banks. Duplication of this publication or parts thereof is permitted only under the provisions of the German Copyright Law of September 9, 1965, in its current version, and permission for use must always be obtained from Springer. Violations are liable to prosecution under the German Copyright Law.

The use of general descriptive names, registered names, trademarks, etc. in this publication does not imply, even in the absence of a specific statement, that such names are exempt from the relevant protective laws and regulations and therefore free for general use.

Cover design: eStudio Calamar, Berlin/Figueres

Printed on acid-free paper

Springer is part of Springer Science+Business Media (www.springer.com)



Supervisor's Foreword

Over the past 50 years atomistic simulations of metals have progressed from empirical pair potentials to solving the Schrödinger equation, at least for the electrons, within the usual approximations of practical implementations of density functional theory. Throughout this time the overwhelming majority of these simulations have made use of the Born-Oppenheimer approximation. This assumes that the electrons remain in their ground state whatever the configuration of the metal ions. For many phenomena in metals this is an excellent approximation, but there are some very significant cases where it breaks down with farreaching consequences. For example, electrons become excited when a particle travels at very high speeds inside the metal, and this becomes the principal means by which the particle loses energy. In addition to conducting heat away from the region disturbed by the particle, excited electrons may also alter the forces acting between atoms in ways that cannot be described by the Born-Oppenheimer approximation. Electronic excitation also plays a key role in laser treatments of metals, and in the passage of high electron current densities along metallic nanowires, and there are many other examples.

How does one allow for electronic excitation in a simulation of a metal? It is clear that this is a quantum mechanical problem involving the time-dependent Schrodinger equation for the electrons. The electronic wave functions have to be coupled to the positions of the ions: this is electron-phonon coupling. Electronic screening has to be treated dynamically as well. The instantaneous forces acting on ions are still determined by the Hellmann–Feynman theorem, but the electronic charge density that appears in the theorem is now dependent on the history of the ionic motion since it is no longer determined by the instantaneous positions of the ions as it is in the Born–Oppenheimer approximation. The simplest approach is semi-classical, with the ions treated as classical objects and the electronic degrees of freedom solved through the quantum Liouville equation coupled to the positions of the ions. This is the Ehrenfest approach and it describes well the transfer of energy from hot ions to cold electrons, but interestingly not the reverse process from hot electrons to cold ions. It is thus well suited to describing electronic

excitations in irradiation damage, ion implantation and channeling in metals but not current-induced Joule heating or laser treatments of metals.

In this thesis Chris Race describes a number of Ehrenfest simulations of metals in which highly excited ions transfer energy to electrons. The models used to describe metals are significantly better than the "jellium" models of early work on irradiation damage of metals in that the ions are not smeared out into a uniform positive background charge density, and the atomic structure is allowed to evolve dynamically under the influence of excited electrons. Although the electrons are treated quantum mechanically the models are much simpler than current implementations of time-dependent density functional theory (TDDFT), and this has allowed tens of thousands of metallic atoms to be treated dynamically for up to 1 ps. Unlike TDDFT simulations the results are not chemically specific but they reveal new generic physics, which more accurate TDDFT methods will eventually be able to treat with chemical specificity.

It will probably be quite some time before TDDFT simulations will be able to treat billions of metal atoms dynamically for up to 1 ns, but this is now quite routinely done with classical interatomic potentials. In these classical molecular dynamics simulations excited electrons are assumed to provide only a frictional force opposed to the atom velocity and proportional to its speed. The work described here by Chris Race has tested this assumption. It turns out that while this provides a reasonably accurate description of the average energy transfer from ions to electrons, the additional forces caused by excited electrons have directions and magnitudes that depend on the local atomic environment, the local electronic temperature and the crystallographic direction in which the particle is moving. A simple model, suitable for very large scale (billion atom) classical molecular dynamics simulations of irradiation damage in metals, which captures this much richer physics, is developed and validated using the Ehrenfest simulations. This is an example of the power of the approach taken here of using simple models to explore the generic physics of the problem. There are further examples, including the discovery of a resonance in the charge transferred to a channeling ion, and an anti-resonance in the stopping power it experiences. The time-periodic potential experienced by the channeling ion, which is perforce absent in the earlier jellium models, excites electrons into states localized on the channeling ion and its immediate transitory neighbours.

The simple tight binding models described by Chris Race in this thesis have opened up a new chapter in the simulation of irradiation damage of metals. They have shown that electronic excitations have a much more interesting and significant role than has hitherto been assumed. It is hoped that this work will stimulate more accurate studies in future using TDDFT methods.

Acknowledgements

I would like to thank the radiation damage team at Imperial College for all their help and support over a very fun four years. In particular, I am extremely grateful to my supervisor Adrian Sutton and to Daniel Mason.

And I wouldn't have got anywhere at all without the love and encouragement of my wife, Rachel, whom I cannot possibly thank enough.

I am grateful to the following authors for permission to reproduce figures and tables from their papers: D.R. Olander (figure 1.1); L.K. Mansur (figure 1.2); U. Fischer (table 1.1); R.M. Nieminen (figures 3.7 and 3.8); N.R. Arista (figure 3.9); M.W. Finnis (figure 3.10); D.J. Bacon and P.E.J. Flewitt (figures 3.11 and 3.12); D.M. Duffy (figures 3.13 and 3.14); D. Sanchez-Portal (figure 3.15); and R.E. Allen (figure 8.10).

Contents

Part I Introductory Material

1	Intro	oduction		3
	1.1	Why S	imulate Radiation Damage?	3
	1.2	Semi-C	Classical Simulation as a Link in the	
		Multi-S	Scale Chain	6
	1.3	How to	Read this Thesis	7
	Refe	rences .		8
2	A R	adiation	Damage Cascade	ç
	2.1	The Ea	rly Stages	ç
		2.1.1	Ion Channelling	Ģ
		2.1.2	Sub-Cascade Branching	11
	2.2	The Di	splacement Phase	12
	2.3	The Th	nermal Spike	12
	Refe	rences .		13
3	The	Treatme	ent of Electronic Excitations in Atomistic Simulations	
	of R	adiation	Damage—A Brief Review	15
	3.1		neoretical Treatment of Radiation Damage	17
	3.2	The Ele	ectronic Stopping Regime	18
		3.2.1	General Concepts	18
		3.2.2	Models of Fast, Light Particle Stopping	21
		3.2.3	Expanding the Realm of Stopping	
			Power Theory	23
		3.2.4	Models of Fast, Heavy Particle Stopping	27
		3.2.5	Models of Slow, Heavy Particle Stopping	35
		3.2.6	The Gaps in Stopping Power Theory	39
	3.3	The Ele	ectron–Phonon Coupling Regime	42
		3.3.1	The Importance of Electron–Phonon Coupling in	
			Radiation Damage	42

xii Contents

		3.3.2	Two-Temperature Models	44
		3.3.3	Representing the Electron–Phonon Coupling	45
		3.3.4	Models of Electron–Phonon Coupling	46
	3.4	Electro	nic Effects in Atomistic Models of	
			on Damage	49
		3.4.1	The Binary Collision Approximation	49
		3.4.2	Molecular Dynamics Models	51
	3.5	Improv	ing the Models: Incorporating Electrons Explicitly	57
	Refe			61
4	Theo	retical E	Background	67
	4.1		ew	67
	4.2		mi-Classical Approximation	69
		4.2.1	The Ehrenfest Approximation	70
		4.2.2	The Approximations in Ehrenfest Dynamics	74
	4.3	The Inc	dependent Electron Approximation	75
		4.3.1	Density Functional Theory	76
		4.3.2	Time-Dependent Density Functional Theory	80
	4.4	Tight-E	Binding Models	81
		4.4.1	Ab-Initio Tight-Binding	82
		4.4.2	Semi-Empirical Tight-Binding	83
		4.4.3	The Harris-Foulkes Functional	83
		4.4.4	Towards Semi-Empirical Tight-Binding	85
		4.4.5	Self-Consistent Tight-Binding	89
	4.5	Time-D	Dependent Tight-Binding	91
		4.5.1	The Description of the System	91
		4.5.2	The Evolution of our System	92
	4.6	Ehrenfe	est Dynamics	95
		4.6.1	Ehrenfest Dynamics versus Surface Hopping	95
		4.6.2	Energy Transfer in Ehrenfest Dynamics	98
	4.7	Conclu	sions	99
	Refe	rences .		99
Par	t II	Simulati	ng Radiation Damage in Metals	
5	A Fr	amewor	k for Simulating Radiation Damage in Metals	103
-			ble Model Metal	103
		5.1.1	The Parameters of the Model	105
		5.1.2	The Electronic Structure of the Model	106
		5.1.3	A Note on the Truncation of the	
			Hopping Integrals	108
	5.2	Ehrenfe	est Dynamics	109
	5.3		D: Our Simulation Software	110
		rences		111

Contents xiii

6	The	Single O	Oscillating Ion	113
	6.1	Simula	tions of a Single Oscillating Ion	114
	6.2	Simula	tion Results	116
		6.2.1	Frequency and Temperature Dependence of	
			Energy Transfer	117
		6.2.2	Position and Direction Dependence	117
	6.3	Theore	tical Analysis of the System	119
	6.4		ning the Results	123
		6.4.1	High Frequency Cut-Off	124
		6.4.2	Isotropic Damping about Equilibrium	
			Lattice Site	124
		6.4.3	Absence of Energy Transfer at	
			Some Frequencies	124
		6.4.4	Frequency Independence of β at	
			High Temperature	128
	6.5	Conclu	isions	131
	Refe			131
7	Semi	i-classica	d Simulations of Collision Cascades	133
	7.1	The Ev	volution of a Cascade	133
		7.1.1	Thermalization of the Initial Distribution	133
		7.1.2	The Evolution of the Ions	135
	7.2	The El	ectronic Subsystem	136
		7.2.1	The Evolving Electronic System	139
		7.2.2	Adiabaticity, Non-Adiabaticity and	
			Electronic Excitations	142
		7.2.3	Achieving Adiabatic Evolution by Altering	
			the Electron-Ion Mass Ratio	145
		7.2.4	The Irreversible Energy Transfer	151
	7.3		isions	152
				152
	11010	ichees .		152
8	The	Nature o	of the Electronic Excitations	153
•	8.1		s of Excitation in Collision Cascades	153
	0.1	8.1.1	Fitting a Pseudo-Temperature	155
		8.1.2	Why do we Obtain Hot Electrons?	158
		8.1.3	The Importance of the Result	161
		8.1.4	Thermalization or Thermal Excitation?	163
	8.2		onic Entropy in Ehrenfest Simulations	166
	0.2	8.2.1	Two Definitions of Electronic Entropy	167
		8.2.1	Reconciling the Two Entropies	168
		8.2.3	A Thought Experiment	168
	8.3		isions	169
		rences .		170
	I/CIG	ICHCES .		1/0

xiv Contents

9	The 1	Electroni	c Forces	171
	9.1	Underst	anding the Electronic Force	172
	9.2	The Eff	ect of Electronic Excitations on	
		the 'Co	nservative' Force	175
		9.2.1	The Importance of the Reduction in the	
			Attractive Electronic Force	179
		9.2.2	Replacement Collision Sequences	181
	9.3	Conclus	sions	186
	Refer			187
40	61			100
10			ons	189
	10.1		lassical Simulations of Ion Channelling	190
		10.1.1	The Simulation Set-Up	190
		10.1.2	The Evolution of a Channelling Simulation	191
		10.1.3	Challenges in Simulating Ion Channelling	192
	10.2		State Charge	193
		10.2.1	Results for a Non-Self-Consistent Model	193
		10.2.2	A Perturbation Theory Analysis	198
		10.2.3	The Effect of Channelling Direction	206
		10.2.4	The Effect of Charge Self-Consistency	
			Parameters U and V	207
	10.3	Electror	nic Stopping Power for a Channelling Ion	210
		10.3.1	Results	210
		10.3.2	The Origin of the Stopping Power:	
			A Tight-Binding Perspective	212
		10.3.3	The 'Knee' in the Stopping Power	
			for $U = V = 0$	214
		10.3.4	Effect of Onsite Charge Self-Consistency	217
	10.4	Conclus	sions	221
	Refer			222
11	The 1		c Drag Force	223
	11.1	Is a Sin	nple Drag Model Good Enough?	224
		11.1.1	An Investigation of Damping Models for	
			Total Energy Loss in Collision Cascades	224
	11.2	The Mic	croscopic Behaviour of the Non-Adiabatic Force	227
		11.2.1	The Non-Adiabatic Force in Ehrenfest Dynamics	227
		11.2.2	The Character of the Non-Adiabatic Force	229
	11.3	An Imp	roved Model of the Non-Adiabatic Force	230
		11.3.1	A "Non-Adiabatic Bond Model"	231
		11.3.2	The Performance of Our Proposed Model	235
	11.4		sions	241
		ences		244

Contents xv

12	Conc	luding Re	emarks	247
	12.1		ns	247
	12.2		ults	248
		12.2.1	The Nature of the Electronic Excitations	248
		12.2.2	The Effect of Electronic Excitations on the	
			Conservative Forces	249
		12.2.3	Non-Adiabatic Effects on Channelling Ions	250
		12.2.4	The Non-Adiabatic Force in Collision Cascades	25
	12.3	Possible	Directions for Further Research	25
	Refer	rences		25
13	Anno	ndiose		25.
13	13.1		ix A: Selected Proofs	25. 25.
	13.1	13.1.1		25. 25:
			Proof of Equation (4.10)-(i)	
		13.1.2	Proof of Equation (4.10)-(ii)	25
		13.1.3	Proof of Equation (4.12)	25
		13.1.4	Proof of Equation (4.28)	25
		13.1.5	Proof of Equation (4.85)	25
		13.1.6	Proof of Equation (4.86)	25
		13.1.7	Proof of Equation (4.102)	26
		13.1.8	Proof of Equation (4.131)	26
		13.1.9	Proof of Equation (4.135)	26
		13.1.10	Proof of Equation (4.137)	26
		13.1.11	Proof of Equation (4.141): The conservation	
			of total energy	26
		13.1.12	Proof of Increase of Pseudo-Entropy (8.16)	26
		13.1.13	Proof of Equation (9.4)	26
		13.1.14	Proof that $Im\{\mathbf{f}_4\} = 0 \dots$	26
		13.1.15	Proof of Equation (11.9)	26
		13.1.16	Proof of Equation (11.12)	27
		13.1.17	Proof of Equation (11.18)	27
	13.2	Appendi	ix B: Perturbation Theory	27
		13.2.1	A Periodic Perturbation	27
		13.2.2	The Effect of a Sinusoidal Perturbation	
			on an Electronic System	27
		13.2.3	A Quantum Mechanical Oscillator	28
	13.3	Appendi	ix C: The Coupling Matrix for a Single	
			ng Ion	28
	13.4		x D: Some Features of the Electronic Excitation	
			m in Collision Cascades	28
		13.4.1	Anomalous Excitations Early in the Cascade	28
		13.4.2	The Width of the Temperature Fitting Window	29
		13.4.3	The Sommerfeld Expression for the Heat Capacity	
		13.7.3	of Our Model	29
			Of Our Mouch	47

xvi Contents

	13.4.4 Behaviour of the Fitted Temperature Early	
	in the Cascade	294
13.5	Appendix E: The Strain on an Inclusion due to	
	Electronic Heating	294
Refer	ences	297
Index		299

Part I Introductory Material

Chapter 1 Introduction

1.1 Why Simulate Radiation Damage?

We will begin with a current and major challenge to materials science, raised by a current and major challenge to society. The need for low carbon sources of energy has created new interest in nuclear power, both fission and fusion, and reinvigorated research into materials for application under irradiation. Each square metre of the first wall of any functioning future fusion reactor will be bombarded every second by over 15 × 10¹⁸ 14 MeV [1] neutrons. This radiation causes significant damage to the materials—the order of the lattice will be disrupted by the creation of vacancies and interstitial defects, the distribution of alloying components and microstructural inclusions will be disturbed and the transmutation of the very nuclei that make up the materials will change alloy compositions and may give rise to helium filled voids (see Figs. 1.1 and 1.2). All these types of damage will, over time, change the mechanical properties of the materials and potentially lead to their catastrophic failure. Our motivation here is to gain a better understanding of the long term behaviour of materials under irradiation.

To gain a feeling for the size of the materials science challenge at hand we might consider one of the current best candidate materials for use in a future fusion reactor. Table 1.1 shows the alloy composition for Eurofer steel. In addition to this complex composition, carefully designed microstructures are necessary to obtain the desired mechanical properties in the harsh operating environment of a fusion reactor. And yet, we can see from the transmutation rates given in Table 1.1 that the neutron irradiation will have a huge effect on the initial composition.

The practical need for a better understanding of radiation damage processes is intimately bound up with the economics of nuclear power. If cost were not an issue, the brute force solution to the problem of material degradation might be simply to replace components with precautionary frequency. However, fusion power and next generation fission reactors may be of only borderline economic

4 1 Introduction

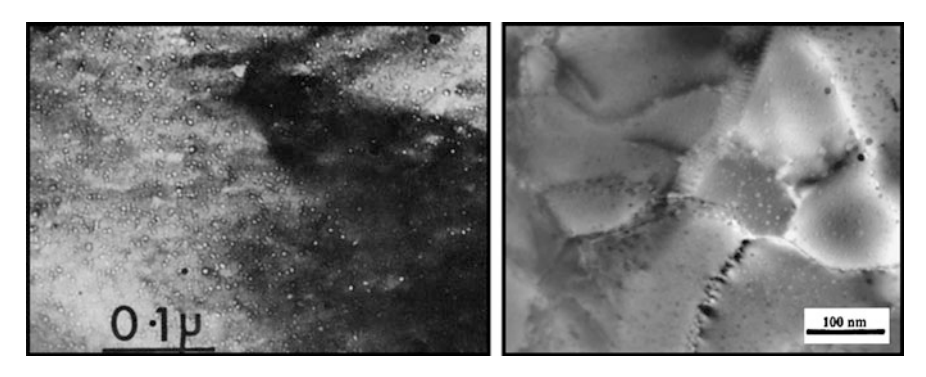


Fig. 1.1 TEM images of intragranular fission gas bubbles. (Reprinted from Olander, D.R., Wongsawaeng, D.: Re-solution of fission gas—a review: part I. Intragranular bubbles. J. Nucl. Mater., **354**(1–3), 94–109 (2006), Copyright (2006), with permission from Elsevier)

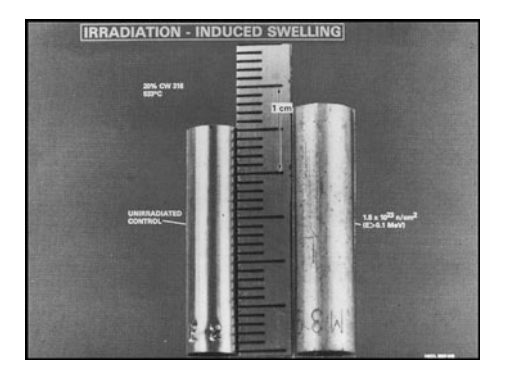


Fig. 1.2 Photograph of 316 stainless steel rods before and after irradiation at 533°C to a fluence of 1.5×10^{23} n m⁻². Swelling is caused by the accumulation of fission gas or by the formation of less dense phases. (Reprinted from Mansur, L.K.: Theory and experimental background on dimensional changes in irradiated alloys. J. Nucl. Mater., 216, 97–123 (1994), Copyright (1994), with permission from Elsevier)

viability and so the confidence to eke out another year of safe life from a given component is of huge significance.

The sceptical reader might raise several objections to the above discussion. First, they might question the viability (or even possibility) of efficient fusion power. They would be far from alone in doing so. We will not consider this question here, but simply point out that *should* nuclear fusion power become a reality it will do so only after the materials science challenges outlined above have been addressed.

Second, they might point out that nuclear fission power is a proven technology and presents no major new challenges. For an answer to this objection we can look to the projected 60% decline in output of fission power generation in the United Kingdom (UK) over the next decade [4]. Given that many people believe that

Table 1.1 Elemental composition in atomic parts per million (appm) of Eurofer steel and transmutation rates in appm per full power year (fpy) for irradiation simulations in the high flux test module (HFTM) of the International Fusion Material Irradiation Facility neutron source and the first wall of a typical fusion power reactor (FPR) employing helium cooled lithium lead (HCLL) and pebble bed (HCPB) blankets

Element	Content (appm)	HFTM (appm/fpy)	HCLL (appm/fpy)	HCPB (appm/fpy)
Н	_	1408	+1051	+951
He	_	+299	+249	+230
Li	_	+0.3	+0.9	+5.3
Be	_	+2.3	+2.3	+2.2
B	51	+3.6	+0.5	-2.9
C	4860	-7.2	-4.6	-4.4
N	1191	-4.4	-3.5	-2.9
O	347	-0.20	-0.8	-0.7
Mg	_	+1.6	+1.4	+1.2
Al	206	+0.54	+0.2	+0.1
Si	990	-2.3	-1.2	-1.1
P	90	-0.01	-0.01	-0.02
S	87	-0.42	-0.3	-0.3
Ti	116	+32	+19	+17
V	2183	+216	+164	+155
Cr	96 240	+211	+74	+55
Mn	4048	+1111	+601	+502
Fe	885 880	-1956	-752	-738
Co	47	-0.02	-0.02	+3.1
Ni	47	-0.13	-0.3	+0.3
Си	44	+0.02	-0.3	-0.4
Nb	6	< 0.01	< 0.01	< 0.01
Mo	29	-0.06	-0.07	-0.1
Hf	_	+1.5	+1.1	+0.8
Ta	215	+6	+1.3	-46
W	3327	-16	-19	-191
Re	_	+7.0	+17	+206
Os	_	+0.01	+0.2	+32

The steel alloying elements are italicized. Reprinted from Fischer, U., Simakov, S.P., Wilson, P.P.H.: Transmutation behaviour of Eurofer under irradiation in the IFMIF test facility and fusion power reactors. J. Nucl. Mater., **329–333**(Part 1), 228–232 (2004), Copyright (2004), with permission from Elsevier.

nuclear power must play a significant role in the UK's power generation if we are to meet our CO₂ reduction targets then extending the life of existing nuclear power plants acquires a high importance. Any arguments to push reactor components beyond their currently defined safe operating windows will have to rely on a sound scientific understanding of the behaviour under irradiation of the materials of which they are composed.

A third objection that the sceptic might raise would question the role of the theorist in solving the above problems. Can we not simply test candidate materials 6 1 Introduction

by exposing them to the radiation that they must endure? Unfortunately we cannot determine the effect of 20 years exposure to a high fluence of 14 MeV neutrons on, say, a sample of Eurofer without having a functioning fusion reactor to provide the correct radiation source and 20 years to wait. Exposing a sample to a higher energy, more intense source for a shorter period might produce a degree of damage that is equivalent in some way—in terms of the number of displacements per atom, for instance, but the differences in the detail of damage produced by different radiation spectra are subtle and understanding them will require a concerted effort by theorists and experimentalists. In addition, even if a perfect experimental testing methodology existed, a combinatorial problem would remain: we would need to test a daunting number of samples of many different materials at different temperatures, pressures and radiation doses.

In the above discussion we have focussed on the example of nuclear power generation. Radiation damage is of much wider technological and theoretical interest, however. Further motivation for the study of radiation damage is provided by fields such as materials modification by ion implantation, medical imaging, medical treatments, and cosmic ray damage.

1.2 Semi-classical Simulation as a Link in the Multi-scale Chain

The study of radiation damage is inherently a multiscale endeavour. The processes at work span time- and length-scales from the electronic to the geological and their full treatment requires the consideration of quantum mechanical electrons, of individual atomic motion, of dislocation dynamics and of macroscopic mechanical properties. We must consider processes that are intrinsically non-adiabatic, such as the excitation of electrons on attosecond timescales, through to quasi-static behaviour over the course of many years.

In the work described in this thesis we have focussed on one particular aspect of modelling radiation damage: we consider the role played by electrons in determining the initial damage caused by the impact of high energy particles on metallic materials. To do this we have employed a semi-classical simulation method that couples the evolution of a set of classical ions and a system of quantum mechanical electrons. By choosing a simple tight-binding representation of our electronic system we can achieve simulations on sufficiently large time- and length-scales to directly investigate the evolution of a variety of radiation damage phenomena. However, we also recognise that the relative complexity of our method (compared, say, with classical molecular dynamics) is restrictive and so the approach we take emphasises the fact that our model is a first link in a

¹ The term "semi-classical" is taken to mean different things in different fields. Throughout this thesis we use it to describe a combined system of quantum mechanical electrons and classical ions

multiscale modelling chain. We explicitly discuss how our findings can help to evaluate and improve other models on longer time- and length-scales.

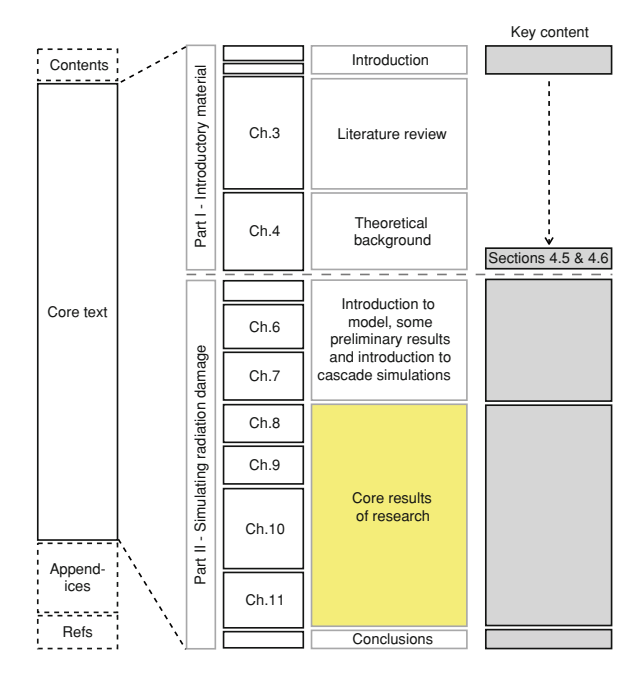
1.3 How to Read this Thesis

The work presented in this thesis formed part of a project at Imperial college involving another doctoral student (J. le Page), in addition to the present author, a post-doctoral researcher (D. R. Mason) and a number of academic staff (A. P. Sutton, W. M. C. Foulkes, A. P. Horsfield and M. W. Finnis). Most of our activities were undertaken collaboratively and so I have indicated the different roles played by each of the three primary researchers (the present author, J. le Page and D. R. Mason) in each piece of work presented. At the beginning of each chapter I have noted the contribution of researchers other than the present author in the following form:

Attribution: In the following the simulations...

The thesis is divided into two parts. The rest of the present part (part I) contains background information useful in understanding the new work that will be presented in part II. Chapter 2 will introduce the context of our research by telling the story of a radiation damage *collision cascade*. In doing so we will raise the questions that our research seeks to answer and understand the limits of our approach and how it must therefore work in concert with other techniques.

Fig. 1.3 A 'schematic map' of the thesis, summarising the type of content in each chapter and indicating the location of the key new results



8 1 Introduction

In Chap. 3 we will review those parts of the vast body of radiation damage literature relevant to our work. Chapter 4 introduces some important theoretical concepts that form the basis for our model. Much of this material may be familiar to the reader and so we emphasise that Sects. 4.5 and 4.6 are intended to form a relatively self-contained theoretical introduction to our model and its dynamics.

In part II, the bulk of this thesis, we describe the new work that has been undertaken by the present author, and the results achieved. Each chapter begins with a brief summary and ends (where appropriate) with a summary of the conclusions.

Because this thesis is long, and contains much background material, some readers may wish to skip large sections (see Fig. 1.3). The review in Chap. 3 can be omitted by the reader familiar with radiation damage theory. Readers familiar with electronic structure theory might safely ignore most of the theoretical background in Chap. 4, though Sects. 4.5 and 4.6 provide direct context for our work. In part II, the most important results are presented in Chaps. 8–11. Of the other chapters, 5 introduces our model, 6 presents some preliminary results that help to establish its capabilities and 7 discusses the evolution of a cascade simulation within our model.

References

- Fischer, U., Simakov, S.P., Wilson, P.P.H.: Transmutation behaviour of Eurofer under irradiation in the IFMIF test facility and fusion power reactors. J. Nucl. Mater., 329–333(Part 1), 228–232 (2004)
- Olander, D.R., Wongsawaeng, D.: Re-solution of fission gas—a review: part I. Intragranular bubbles. J. Nucl. Mater., 354(1–3), 94–109 (2006)
- Mansur, L.K.: Theory and experimental background on dimensional changes in irradiated alloys. J. Nucl. Mater., 216, 97–123 (1994)
- 4. UK Department of Energy and Climate Change. Electricity generation projections

Chapter 2 A Radiation Damage Cascade

To help us understand the nature of the problems that the work in this thesis will address, we now consider the evolution of a typical radiation damage event. This will allow us to highlight where the electrons are expected to play a major role in the evolution of damage and introduce some of the commonly used terminology in the radiation damage field. We will focus our discussion on the concept of a radiation damage *collision cascade* and the various stages in its development. In Fig. 2.1 we give schematic illustrations of these different stages.

2.1 The Early Stages

Our story begins when an energetic particle impinges on some target material (see Fig. 2.1a). This particle, depending on its mass and on its charge, can penetrate a significant distance into the target material before undergoing a collision with an atom of the target. This collision will set the target atom (known as the *primary knock-on atom* or PKA) in motion often with a very high velocity (see Fig. 2.1b). The statistical distribution of the energy of the PKA (its *spectrum*) will vary depending on the target material and on the type of irradiation [1]: a 14 MeV fusion neutron can produce PKAs of up to 1 MeV in iron with half being above 10 keV; the slower neutrons from fission reactors produce PKA energies of up to several hundreds of keV; and the recoiling ²³⁴U nucleus from the decay of ²³⁸Pu will have an energy of around 100 keV.

2.1.1 Ion Channelling

When a PKA has a kinetic energy $\sim 100 \text{ keV}$ it will have a very low cross-section for interaction with other nuclei of the target material and so is able to travel large

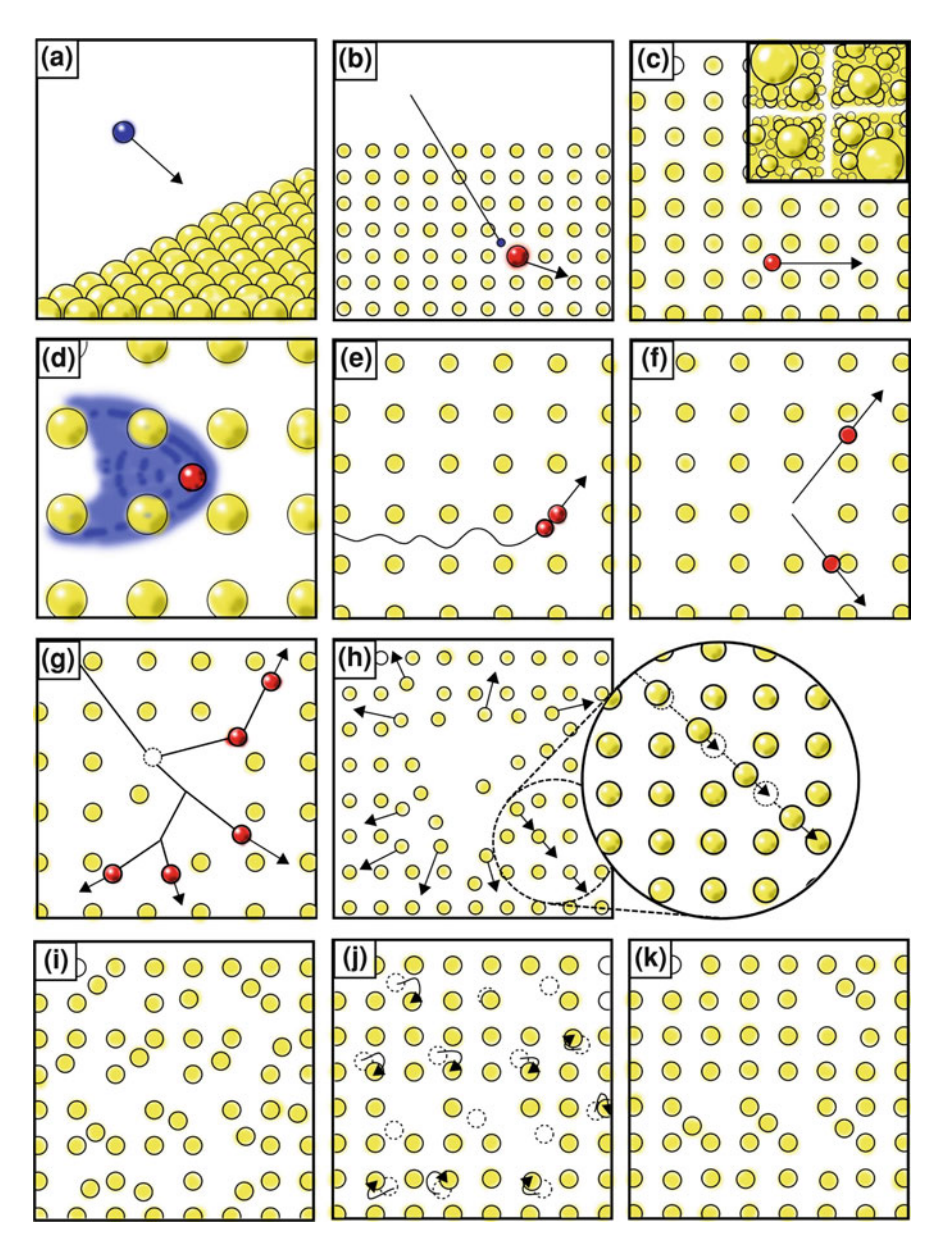


Fig. 2.1 Schematic representations of the stages of evolution of a collision cascade

distances without undergoing a significant collision. This process is known as *channelling* after the open channels in the crystal structure down which such ions move (see Fig. 2.1c) and can be responsible for dramatically changing the damage distribution in crystalline materials. Experiments involving the implantation of

40 keV radioactive 125 Xe ions into crystalline tungsten revealed penetration to depths of up to 10^{-6} m for particle beams directed along crystalline axes, compared with a maximum depth in amorphous tungsten of 0.1×10^{-6} m [2].

Because the rapidly moving channelling ion interacts only fleetingly with the surrounding ions it loses energy predominantly to the electrons of the target material (see Fig. 2.1d) and so the rate of energy transfer into the electrons is a significant issue. We investigate the influence of electrons on ion channelling in Chap. 10. Experimental analysis of irradiated samples, particularly of insulators, often reveals tracks of damage surrounding the paths traversed by channelling ions. This damage to the lattice must be mediated by the electrons and several mechanisms have been proposed. One possibility is that some electrons in the channelling ion's path become so excited that they are ballistically ejected from the track region, which then experiences a build up of spatial charge. The coulombic repulsion between the charged ions is then thought to be responsible for the damage and this model is referred to as the coulomb explosion model. Alternatively, the passage of the channelling ion might serve to rapidly heat the electrons. The transfer of this heat energy into the ions in the track region would then be responsible for generating the damage. This is the thermal spike model. A third possibility is suggested by some of our work (see Chap. 9): the excitation of the electrons implies a weakening of the bonding forces in the track region such that the surrounding material is placed under an implied strain and the resulting outward pressure may be directly responsible for the damage.

2.1.2 Sub-cascade Branching

Eventually our channelling ion will either slow to the point that its cross-section for inter-ionic interaction becomes significant or it will encounter a defect in the channel. At this point it will undergo a collision with another ion (see Fig. 2.1e). Depending on the energies of the two ions emerging from the collision it may be possible for them both to continue to penetrate a significant distance into the target material, in which case we have sub-cascade branching (see Fig. 2.1f) or no further channelling will occur and the next stage of cascade evolution will begin.

The phenomenon of sub-cascade branching is important for anyone engaged in simulating collision cascades. Any ion moving with a kinetic energy greater than ~ 10 keV will tend to impart enough energy to its collision partner to form a sub-cascade. Hence, the behaviour of a collision cascade arising from a high energy PKA will look very much like a set of several lower energy cascades. Provided a simulator can reach length-scales large enough to contain cascades of up to 10 keV, they can claim to be able to capture much of the physics of collision cascades up to much higher energies. (Though not all: phenomena arising from the overlap of the effects of several sub-cascades will not be captured, of course.)

2.2 The Displacement Phase

Once the kinetic energies of our moving ions (either a PKA or an ion in a subcascade) get below ~ 10 keV then their interactions with surrounding ions will be strong, collisions will be frequent and the *displacement phase* of the cascade begins. Over the course of 1–10 ps the majority of ions in a region of 10–100 nm in size will be displaced from their equilibrium lattice sites by a series of collisions forming a *displacement spike* (see Fig. 2.1g).

The predominant mode of energy loss from a given moving ion during the displacement phase will be to other ions, but the electrons will still have an important role to play in the dynamics. At this stage of the cascade the initial excess of energy imparted by the incoming radiation is still predominantly contained within the ionic system and so there is a net energy flow from ions to electrons. Thus the electronic system tends to damp the ionic motion and if this damping is strong the evolution of a cascade can be curtailed and the damage produced can be reduced. Understanding the precise nature of the damping is an open problem, which we address in Chap. 11. As the cascade progresses the electrons become increasingly excited. In Chap. 8 we investigate what form these excitations might take and in Chap. 9 we consider how their accumulation might affect the motion of the ions.

During the displacement phase we often see the formation of *replacement collision sequences* (RCS) in which a series of collisions takes place along a close-packed line of ions (see Fig. 2.1h). Each ion replaces the next along the close-packed line until sufficient energy has been lost (to the surrounding atoms and to the electrons) that the sequence is terminated and an interstitial defect atom results. The RCS is an important mechanism for carrying defects large distances from the centre of a cascade and we consider the possibility that their formation might be affected by electronic excitations in Chap. 9.

2.3 The Thermal Spike

After the displacement phase there follows a brief *relaxation phase* during which the cascade energy is rapidly shared amongst all the ions in the cascade region forming a hot (and potentially molten) region sometimes referred to as a *thermal spike*. At this stage an initial defect distribution will be evident, with many interstitial atoms and vacancies (see Fig. 2.1i).

There is then a *cooling* phase, lasting several hundred picoseconds, during which the thermal spike gradually grows and cools and many of the interstitial and vacancy defects recombine (see Fig. 2.1j) and a final damage distribution is established (see Fig. 2.1k). This process of *recovery* takes place in a region of the target material in which the ions will be interacting with excited electrons. The rate at which energy exchange between the ionic and electronic subsystems takes place

can have a significant impact on the final damage distribution. The presence of a hot electronic system, acting as a heat bath in contact with the ionic system, can help to anneal defects and reduce the amount of residual damage. Conversely, a rapid transfer of energy from the ions to the electrons might quench in a higher defect population. There is still much to discover about the role played by electrons during the cooling phase and there are many open questions about the so-called *electron-phonon coupling* (discussed in Sect. 3.3). However, the time-scale of the cooling phase lies beyond the reach of our semi-classical simulations and so we will have little to say about such matters here.

References

- Greenwood, L.R.: Neutron interactions and atomic recoil spectra. J. Nucl. Mater. 216, 29–44 (1994)
- Domeij, B., Brown, F., Davies, J.A., Piercy, G.R., Kornelsen, E.V.: Anomalous penetration of heavy ions of kev energies in monocrystalline tungsten. Phys. Rev. Lett. 12(13), 363–366 (1964)

Chapter 3 The Treatment of Electronic Excitations in Atomistic Simulations of Radiation Damage—A Brief Review

Attribution: The material of this chapter closely follows the contents of a review article [1] written by the present author and submitted for publication in the Institute of Physics journal Reports on Progress in Physics.

Having made the case for studying radiation damage phenomena via simulation, and having drawn attention (in Chap. 2) to the variety of ways in which the electrons of a target material are expected to exert an influence on the dynamics of the ions, we are faced with the task of finding a robust scheme for incorporating electronic effects in our simulations. Broadly speaking, there are two ways in which we might approach this problem. The most straightforward way would be to incorporate a description of the electrons within the dynamics of our model system. We will refer to such a scheme as including the electrons *explicitly*. In formulating such models we will have to choose some more or less approximate description of the electrons, of their dynamics, and of their coupling to the ions. In doing so we hope to retain as much of the relevant physics as possible in the usual trade-off between physical accuracy and tractability (which we will discuss in detail in Chap. 4).

Alternatively, we can throw out the electrons and focus on evolving a dynamical model of the ions only. We do, however, represent the electrons *implicitly* via their effect on the ion dynamics. In this case, we hope to find a simple, economical model, which though it places the physics of the electrons in something of a "black box" nevertheless captures the effect of that physics to a satisfactory degree.

In this chapter we present a brief review of the vast body of theory pertaining to the problem in hand. To preempt our discussion a little we will say this: models that incorporate an explicit description of the electronic system are computationally expensive, too expensive, with present resources, to be applicable to the direct simulation to conclusion of collision cascades. We would assert that in the short to medium term the most productive approach to investigating radiation damage phenomena via direct simulation will employ what we will term augmented classical

molecular dynamics (MD) models incorporating electronic effects implicitly. So why study, as we have, the use of more complex models in radiation damage? To help us answer that question, and to provide a focal point for this review, let us consider a putative augmented MD model. The form of this model is typical of such models described in the literature (and later in this chapter).

Assume that we are concerned with a set of N_a classical ions of masses $\{M_I\}_{I=1}^{N_a}$ with positions $\{\mathbf{R}_I\}_{I=1}^{N_a}$ evolving according to Newtonian equations,

$$M_I \frac{\mathrm{d}^2 \mathbf{R}_{\mathrm{I}}}{\mathrm{d}t^2} = \mathbf{F}_{\mathrm{Cl},I} - \beta_I \frac{\mathrm{d}\mathbf{R}_{\mathrm{I}}}{\mathrm{d}t} + \boldsymbol{\eta}_I(t). \tag{3.1}$$

Here $\mathbf{F}_{\text{Cl,I}}$ is the force on the *I*th ion derived within some classical force model (a pairwise potential, perhaps). β_I gives rise to a drag like force. $\eta_I(t)$ is some other ion specific force, whose inclusion makes (3.1) completely general.

Now, in the models found in the literature, the $\eta_I(t)$ are typically stochastic forces designed to yield a physically reasonable approach to the long term steady state. The bulk of the effect of electrons, at least early in a cascade, will be modelled by the drag term β_I d \mathbf{R}_I /dt. This is the nub of the matter: the augmented MD models in the literature assume that the primary effect of the electrons on the dynamics of high energy ions is to reduce their kinetic energy via the action of forces directly opposed to their motion. Most models go further than this and adopt a β_I that is a simple constant. The resulting picture is beguilingly simple: the effect of $\eta_I(t)$ notwithstanding, our ions now move as if immersed in a viscous soup of electrons.

So, again, why study more complex, more expensive models? Practitioners in the radiation damage field sometimes assert that it is "well-established" that the effect of electrons on ion dynamics is to provide a viscous drag; in other words, that there exists some constant β that can be used in a model dynamics like that in (3.1) to capture the effect of electrons. Such statements are subjective. A parallel, objectively true statement would be that "there exists a large body of theoretical literature, concerning so-called *electron stopping theory*, pointing almost unanimously toward a viscous drag model of electronic effects".

How might we get from the latter objective statement to the former subjective one, given that the theories in question are derived only within certain (well-defined) approximations? First, we might argue directly for the validity of the approximations employed: that they throw out no physics of significance. Below we will discuss the various theories and their approximations. Second, we might appeal to experiment: do the empirical data validate the hypothesis of a simple drag force? Do they refute alternative hypotheses? We will also consider such questions later in this chapter. Third, we might look for some sort of "physical convergence", investigating a level of theory in which the approximations that yield a viscous damping are relaxed to see if any new behaviour of significance emerges.

Effectively, it is this last approach that we have taken in the work described in this thesis. A model that treats the dynamics of a set of classical ions coupled to an explicit model of the electronic system can go beyond the approximations made in the theories that predict a viscous drag: it need neither treat the electrons as a

homogeneous medium, nor need it reduce the ionic dynamics to a series of independently occurring binary encounters.

3.1 The Theoretical Treatment of Radiation Damage

The body of literature on the subject of the theoretical treatment of radiation damage is vast. The field stretches back over a century and has attracted the attention of a wide range of researchers. An understanding of radiation damage processes has variously been important across the spectrum from fundamental physics research to application on an industrial scale. We cannot come close to a comprehensive treatment, and so our aim in this brief review will be to consider only the larger themes. Most importantly we will focus only on those parts of the theory that have something to say about the role of electrons. We will examine the types of theoretical model that have been proposed to describe the process of energy exchange between ions and electrons. We will discuss how they work, what questions they address and how well they are able to answer them. We will also focus our discussion on providing a context for the new work described in part II of this thesis.

Broadly speaking we will split the field of radiation damage theory into two convenient segments. The first contains *analytical models*, which attempt to provide a concise description of particular radiation damage phenomena and either offer insight into them or provide a means of making quantitative predictions about them. The second contains *simulation models*, which begin with some description of a system in which a radiation damage event is to occur and then provide insight or predictions via dynamic evolution of that system.

Radiation damage theorists also typically divide the role of electrons into two regimes, the *electronic stopping regime* and the *electron-phonon coupling regime*. The distinction is most often drawn in terms of the mode of ionic evolution characteristic of each regime. In the electron stopping regime the ions are assumed to have relatively high kinetic energies and to move ballistically through the host material, with the interaction with other ions being well described by a series of binary collisions. In terms of the interaction of the ions with the electrons, energy transfer from the excited ions to the relatively cool electrons will be the dominant process. The earliest stages of collision cascade evolution, such as channelling and sub-cascade branching, are those that lie most obviously in this regime. By contrast, in the electron-phonon coupling regime the ions have lower energies and oscillate around their equilibrium positions, and a many-body description of the ionic system becomes necessary. Also, the exchange of energy between ions and electrons in both directions will be important. The system is then well described as a collection of phonons and electrons exchanging energy with one another. The later stages of cascade evolution, such as the recovery phase, seem most susceptible to such a description.

¹ See references [2–8] for details of various aspects of radiation damage.

It is important to note that the boundary between the two regimes is both ill-defined (theoretically) and indistinct (in reality). For example, once many ions are in motion in the displacement phase of cascade evolution then a treatment in the mode of electronic stopping is inadequate: the ions certainly don't spend much time in free flight and their interactions are often many-body in nature. Equally, however, it is clear that the ions are excited way beyond oscillation about some equilibrium positions and so a description in electron—phonon coupling terms is neither appropriate. In fact the distinction is largely one of practical convenience, allowing the development of different treatments at each extreme of cascade evolution. This may be partly responsible for the unfortunate tendency of the literature to focus on those problems that most firmly lie within the scope of one approximation or the other, to the relative neglect of some of the more complex phenomena in between; much of the evolution of a cascade, after all, clearly involves physics which falls between the two regimes.

We also emphasise that the underlying physics of the energy exchange between ions and electrons is the same in both regimes [9]: it is fully described by the time-dependent Schrödinger equation acting on a state vector describing a set of quantum mechanical ions and electrons. This somewhat obvious point can become obscured by the convenience of the artificial and conventional distinction between the electron stopping and electron–phonon coupling regimes.

3.2 The Electronic Stopping Regime

We will begin our review of radiation damage theory by considering the electronic stopping regime. The subject of how a fast particle is slowed down, or *stopped*, by its interaction with some *stopping medium* is one of broad interest. Particulate radiation can play the role of an experimental probe of fundamental physical laws, can form the basis of manufacturing processes in which materials are modified by ion implantation and can function as a diagnostic and therapeutic tool in medical applications. And damage to functional materials exposed to radiation in power generation demands a sound understanding of the particle stopping process.

3.2.1 General Concepts

If we consider the case of some particle, our *projectile*, penetrating a stopping medium that is a solid made up of ions and electrons (either bound to the ions or part of an electron gas), then the processes by which the projectile might lose energy can be classified into five basic types:

- 1. Changes in the internal state of the target ions, such as electronic excitation and ionization, or excitations of the electron gas;
- 2. Changes in the internal state of the projectile such as electronic excitation, ionization and electron capture;

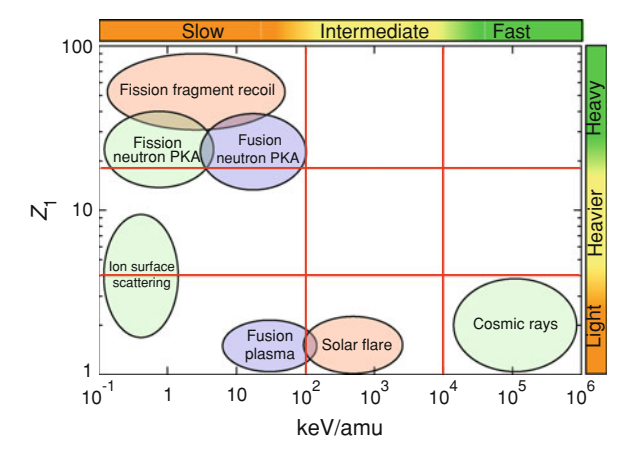


Fig. 3.1 The classification of electronic stopping behaviour into various regimes based on projectile atomic number and kinetic energy per atomic mass unit. A sample of applications is indicated on the chart according to their corresponding regimes. (Reprinted figure 1 with permission from Race, C.P., Mason, D.R., Finnis, M.W., Foulkes, W.M.C., Horsfield, A.P., Sutton, A.P.: The treatment of electronic excitations in atomistic models of radiation damage in metals. Rep. Prog. Phys. **73**, 116501 (2010). Copyright (2010) by the Institute of Physics Publishing Ltd.)

- 3. Transfer of energy to the motion of the target ions in collisions or in the generation of phonons;
- 4. Emission of radiation (e.g. Bremstrahlung and Cerenkov radiation); and,
- 5. Chemical or nuclear reactions.

The physics of these processes is varied and complex and which of them are significant depends most strongly on the velocity and on the charge of the projectile. So, to help simplify the process of modelling electronic stopping, practitioners conventionally classify the variety of projectile species by atomic number, Z_1 , into light ($Z_1 \leq 2$), heavier or intermediate ($3 \leq Z_1 \leq 18$) and heavy ($Z_1 \gtrsim 19$) ions, and by kinetic energy per atomic mass unit, into fast ($E/W \gtrsim 10 \, \text{MeV}$), intermediate ($100 \, \text{keV} \lesssim E/W \lesssim 10 \, \text{MeV}$) and slow ($1 \, \text{keV} \lesssim E/W \lesssim 100 \, \text{keV}$) ions. Figure 3.1 illustrates this classification scheme and shows how different applications of stopping theory fall into the different categories.

From our point of view, concerning ourselves with how the theoretical literature might inform simulation work, the key concept is that of a *stopping power*. A stopping power, which we shall denote S, is defined as the rate of loss of projectile kinetic energy E_K per unit length x along its path, ²

$$S \equiv \frac{dE_{K}}{dx}.$$
 (3.2)

² Such quantities have the dimensions of a force, and, indeed, the term 'stopping force' is gaining currency. But historically 'stopping power' has been prevalent and we shall use it here.

The energy lost by the projectile to the stopping medium is transferred to both the centre of mass motion of the ions of the target medium and to electronic excitations of its electrons. It is conventional to divide the total stopping power into a sum of nuclear (n) and electronic (e) contributions,

$$S = S_{\rm n} + S_{\rm e},\tag{3.3}$$

a separation which relies on the two types of loss mechanism being uncorrelated (and which becomes increasingly invalid with reducing projectile velocity).

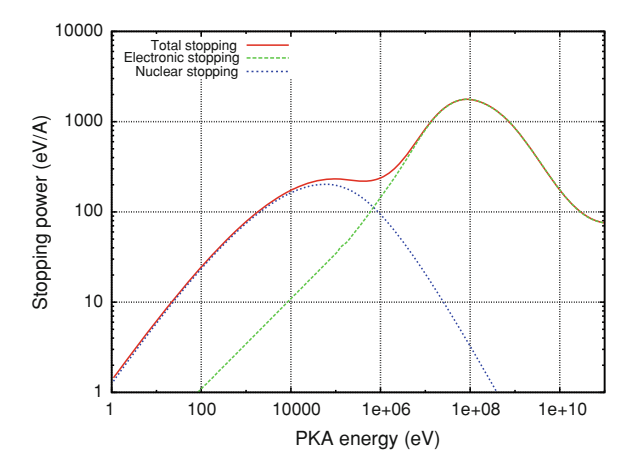
We need not concern ourselves with the nuclear stopping power, because in our work, and in closely related classical molecular dynamics (MD) simulations, the transfer of energy between ions is handled explicitly. However, we will note a useful general property of the two terms. Figure 3.2 shows the predicted stopping powers of an iron target for intruding iron projectiles (the results are derived from the *SRIM* code [10], which we shall discuss later in Sect. 3.2.4.3) and we can see that at low velocities, nuclear stopping is the dominant effect, with electronic stopping coming to the fore at higher speeds.

We can understand the origin of this different behaviour of the two terms if we consider a collision between a projectile particle of mass m_1 and charge q_1 moving with speed v and a stationary target particle of mass m_2 and charge q_2 . If the collision takes place such that the initial distance between the projectile and target perpendicular to the projectile path, the *impact parameter*, is b, then the Rutherford formula predicts an energy transfer to the target of,

$$T = \frac{2q_1^2q_2^2}{(4\pi\epsilon_0)^2 m_2 v^2 b^2} \left(\frac{1}{1 + (q_1 q_2 / 4\pi\epsilon_0 \mu v^2 b)^2} \right), \tag{3.4}$$

where the reduced mass $\mu \equiv m_1 m_2 / (m_1 + m_2)$. Assuming that the target particle remains stationary and that the projectile path is unchanged by the collision allows us to simplify the above result:

Fig. 3.2 Predicted nuclear and electronic stopping powers of an iron target for an iron atom projectile as a function of its kinetic energy. Data taken from the *SRIM* code [10]



$$T \approx \frac{2q_1^2q_2^2}{(4\pi\epsilon_0)^2 m_2 v^2 b^2}. (3.5)$$

If the number of particles per unit volume in the stopping medium is n, then integrating over a range of valid impact parameters yields a stopping power,

$$S(q_1, q_2, v) = 2\pi n \int_{b_{\min}}^{b_{\max}} db \, b \, T(b)$$

$$= \frac{4\pi q_1^2 q_2^2}{(4\pi \epsilon_0)^2 m_2 v^2} n \ln \frac{b_{\max}}{b_{\min}}.$$
(3.6)

Because this stopping power is dominated at high velocities by the prefactor to the logarithm, the factor of $1/m_2$ will determine the relative magnitude of the stopping powers due to electrons and to ions. Electronic losses thus dominate at high projectile speed.

The basic aim of electronic stopping theory is to provide predictions of the electronic stopping power of an arbitrary target for an arbitrary projectile across the full range of kinetic energies. The theories of electronic stopping given in the literature take many and varied forms. Some formalisms are classical, others quantum mechanical; some consider the interaction of the projectile with the target as a series of binary collisions, others treat the target electrons as a continuum; some start from first principles, whilst others attempt a completely empirical fitting.

Different approaches are appropriate to the different ranges of projectile energy and atomic number, depending on what simplifying assumptions may be made. The easiest case to treat (and the one that has attracted most attention) is that of fast, light particles. Such projectiles are likely to be stripped of all electrons and so may be treated as simple point charges. The dominant energy loss mechanism will be via excitations of the target electrons, or via radiative processes at relativistic velocities. The higher nuclear charges of heavier particles mean that we must consider the possibility of bound electronic states on the projectile and the additional energy loss mechanisms that thus become available. For slower particles, screening of the projectile charge by the target electrons becomes significant and few of the simplifying assumptions used for fast, light particles can be made. We will discuss each of these different levels of complexity in turn.

3.2.2 Models of Fast, Light Particle Stopping

3.2.2.1 Early Models

The earliest theories of electronic stopping, due to Thomson [11] and Darwin [12] and dating from the 1910s, consider a point charge projectile losing energy to the electrons of a target medium made up of atoms of atomic number Z_2 and atomic

density n_a . The electrons are assumed to be free and the collisions are treated within the approximation of (3.5) and so the resulting stopping powers take the form,

$$S(Z_1, \nu) = \frac{4\pi Z_1^2 e^4}{(4\pi \varepsilon_0)^2 m_e \nu^2} Z_2 n_a L_{\text{free}}, \qquad L_{\text{free}} = \frac{1}{2} \ln \frac{T_{\text{max}}}{T_{\text{min}}}.$$
 (3.7)

 $L_{\rm free}$ is known as a *stopping number* and many of the theories of fast particle stopping take the form of (3.7), but with different expressions for the stopping number. The use of (3.7) requires values for the maximum and minimum kinetic energy transfers. $T_{\rm max}$ is determined by considering a head-on collision with b=0,

$$T_{\text{max}} = \frac{4m_1 m_{\text{e}}}{(m_1 + m_{\text{e}})^2} \frac{1}{2} m_1 v^2, \tag{3.8}$$

but T_{\min} must be set artificially to a non-zero value to prevent divergence of the stopping power. This divergence is essentially due to the long range nature of the Coulomb interaction and can be overcome by choosing a maximum impact parameter, such as the atomic radius in the case of Darwin's theory.

3.2.2.2 The Bohr Formula

In reality the divergence in S is prevented by the fact that the electrons of the target medium are not free, but are bound to the target ions. Bohr undertook a treatment of electronic stopping [13] that considers the collision between a charged projectile and classical electrons bound harmonically to the target ion with angular frequencies ω_j . Like those of Thomson and Darwin, Bohr's theory is classical and perturbative, in that it assumes that the projectile trajectory is unaffected and that the target electron remains stationary for the purposes of calculating the energy transfer. Bohr's result is then,

$$S(Z_1, \nu) = \frac{4\pi Z_1^2 e^4}{(4\pi \varepsilon_0)^2 m_e \nu^2} n_a L_{\text{Bohr}},$$

$$L_{\text{Bohr}} = \sum_j f_j \ln \left(\frac{C m_e \nu^3}{Z_1 e^2 \omega_j} \right),$$
(3.9)

in which C is a constant (C = 1.1229) and the relative contributions of different frequencies ω_i are given by the values of f_i , subject to $\sum_i f_i = 1$.

An important new feature appears in Bohr's theory: the binding of the electrons sets a natural upper limit to the impact parameter. If *b* becomes too large, the collision takes place so slowly that the electron moves appreciably over the course of the interaction and no energy is transferred. Alternatively, we can say that at too large an impact parameter, the Coulomb interaction of the electron with the

projectile becomes insignificant when compared with the binding forces. We thus have,

$$b_{\text{max}} \sim \frac{v}{\omega_i}. \tag{3.10}$$

The quantity b/v is known as the *collision time*.

3.2.2.3 The Bethe Formula

Another much quoted theory of electronic stopping is due to Bethe³ and yields a stopping number,

$$L_{\text{Bethe}} = \sum_{j} f_{j} \ln \left(\frac{2m_{\text{e}}v^{2}}{\hbar \omega_{j}} \right). \tag{3.11}$$

We will not have much to say about Bethe's formula, since it applies only to very fast particles. It is similar in spirit to Bohr's treatment, in that it is fundamentally perturbative, but it is quantum mechanical, rather than classical. The frequencies ω_j are those associated with excitations of the electrons of the target ion and the f_j are generalized oscillator strengths [15], again giving the relative contributions of the different excitations.

Figure 3.3 shows the behaviour of the Bohr and Bethe stopping powers along with some experimental stopping data. At high energies the stopping power drops away as $1/v^2$ as a consequence of the physics embodied in the Rutherford scattering formula. The impulse imparted to a target electron is proportional to the duration of its interaction with the projectile, measured by the collision time b/v. The energy transfer will vary as the square of this. Both the Bohr and Bethe formulae exhibit a strong peak at approximately the correct energy. This is known as the Bragg peak and being able to predict its location is important experimentally because the depth resolution of experimental probes is maximized at the peak.

3.2.3 Expanding the Realm of Stopping Power Theory

The treatments of stopping power in Bohr's and Bethe's theories make some fairly restrictive simplifying assumptions. In this section we will discuss the implications of those assumptions and detail some corrections that can be made to relax the assumptions somewhat. Later we will go on to consider alternative theories with complementary realms of applicability.

³ The original derivation is in German [14]. Sigmund [5] has provided a thorough English language treatment.

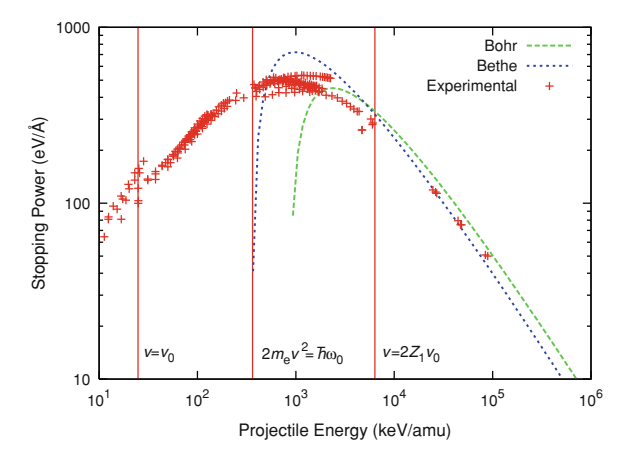


Fig. 3.3 Sample electronic stopping power data for oxygen projectiles in a gold target. Experimental data (red crosses) from the database of Paul [16] are shown, along with stopping powers calculated via the Bohr (green long dashed line) and Bethe (blue short dashed line) theories. Various velocity thresholds discussed in the main text are indicated. The average excitation energy in the theoretical expressions, $\ln I \equiv \sum_j f_j \ln(\hbar \omega_j)$, is calculated using a commonly used scaling relation $I \approx Z_2 \times (10\,\text{eV})$ [17]. (Reprinted figure 2 with permission from Race, C.P., Mason, D.R., Finnis, M.W., Foulkes, W.M.C., Horsfield, A.P., Sutton, A.P.: The treatment of electronic excitations in atomistic models of radiation damage in metals. Rep. Prog. Phys. 73, 116501 (2010). Copyright (2010) by the Institute of Physics Publishing Ltd.)

In Bohr's theory, the perturbative treatment means that the energy transfer to a bound electron diverges for small impact parameters. This divergence is eliminated by treating close collisions, with impact parameter below some threshold value b^* as being between free particles. This treatment is valid because at small enough b the collision time is much shorter than the period of the electron's oscillatory motion and so the binding can be ignored. Hence we have,

$$\frac{b^*}{v} \ll \frac{1}{\omega_j}.\tag{3.12}$$

We also recall that the treatment of more distant collisions is perturbative and this implies a further restriction on b^* . The full Rutherford formula predicts an energy transfer,

$$T(b) = \frac{2Z_1^2 e^4}{(4\pi\epsilon_0)^2 m_e v^2 b^2} \left(\frac{1}{1 + (Z_1 e^2 / 4\pi\epsilon_0 m_e v^2 b)^2} \right), \tag{3.13}$$

in this case, and so for the approximate form to be valid we require that the correction term (for the effect of the deviation of the projectile path and the particle position) in the denominator of the second factor be small. This must still be true at the lower limit of the impact parameters treated in this perturbative limit and so we arrive at a second condition.

$$\frac{Z_1 e^2}{4\pi\varepsilon_0 m_e v^2 b^*} \ll 1. \tag{3.14}$$

Since both conditions on b^* must be satisfied, we arrive at a validity condition for the Bohr formula of.

$$\frac{4\pi\varepsilon_0 m_{\rm e} v^3}{Z_1 e^2 \omega_i} \gg 1. \tag{3.15}$$

Bohr's treatment is classical and so we must be able to describe the projectile as a well-confined wave packet throughout the collision. For a projectile beam with a spread in transverse momentum δp_1 there will be a corresponding uncertainty in impact parameter $\Delta b \sim \hbar/2\delta p_1$. This gives rise to a spread in the transverse component of the momentum transferred in the collision of $\delta p_2 \sim (2|Z_1e^2|/b^2v)\delta b$ [from (3.5)]. If we minimize $((\delta p_1)^2 + (\delta p_2)^2)^{1/2}$ as a function of δb and assume that this uncertainty in the transverse momentum must be much smaller than the total momentum transfer if the classical approximation is to be valid, then we obtain the condition.

$$\frac{2|Z_1e^2|}{4\pi\varepsilon_0\hbar\nu}\gg 1. \tag{3.16}$$

Though this criterion seems to imply that Bohr's formula becomes more valid with decreasing projectile velocity (below some high threshold), we must remember that we have also assumed that the target electron remains at rest during the collision, so that,

$$v \gg v_0, \tag{3.17}$$

where our measure of a typical electron velocity is the Bohr velocity $v_0 = e^2/4\pi\epsilon_0\hbar = c/137$. Hence the formula is only valid over a small range of high velocities,

$$v_0 \ll v \ll 2Z_1v_0.$$
 (3.18)

These validity criteria, along with others to be discussed below, are illustrated in Fig. 3.4.

The assumptions made in Bethe's stopping power theory imply similar restrictions on its applicability. Once again, we will not go into detail and refer the interested reader to Sigmund's book [5] for more information. Essentially, Bethe applies the same trick as Bohr and separates the collisions for different treatment in close and distant cases. In the case of the Bethe formula, this separation is made at a threshold momentum transfer q^* , rather than at some particular impact parameter. For consistency between energy and momentum transfer in close collisions we must ensure,

$$q^*v > \omega_0, \tag{3.19}$$

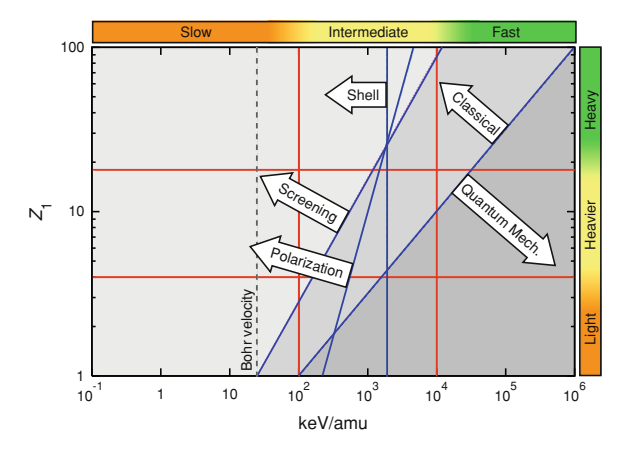


Fig. 3.4 The projectile kinetic energy and atomic number regimes of electronic stopping theory in an iron target $(Z_2=26)$ showing order of magnitude thresholds for various effects and corrections. Bohr's classical threshold $v \lesssim 2Z_1v_0$ is shown, along with the thresholds for screening $(v \lesssim Z_1^{2/3}v_0)$ and Barkas (polarization) effects $(v \lesssim (Z_1Z_2)^{1/3}v_0)$. The velocity at which shell effects become important $(v \lesssim Z_2^{2/3}v_0)$ and the Bohr velocity, v_0 , below which the projectile ion will have very low charge with many bound states, are also indicated. (After Sigmund [3].) (Reprinted figure 3 with permission from Race, C.P., Mason, D.R., Finnis, M.W., Foulkes, W.M.C., Horsfield, A.P., Sutton, A.P.: The treatment of electronic excitations in atomistic models of radiation damage in metals. Rep. Prog. Phys. 73, 116501 (2010). Copyright (2010) by the Institute of Physics Publishing Ltd.)

where ω_0 is a typical excitation frequency. For Bethe's approximate perturbative treatment of distant collisions to hold, the kinetic energy transferred to the electron must be small compared with a typical excitation frequency. Hence, a second condition emerges,

$$\frac{\hbar^2(q^*)^2}{2m_e} \ll \hbar\omega_0. \tag{3.20}$$

Combining the above conditions, we arrive at a validity criterion,

$$v \gg \sqrt{\frac{\hbar\omega_0}{2m_e}},\tag{3.21}$$

restricting the use of the Bethe theory to high velocity projectiles. This criterion is once again illustrated in Fig. 3.4.

There are refinements and corrections corresponding to the key simplifying assumptions in the Bohr and Bethe theories. Ziegler [18] provides a detailed review, but here we will simply list them along with brief explanations of the underlying physics.

The Bloch formula: A revised stopping formula was proposed by Bloch to correct for the most glaring defects in the theories of Bohr and Bethe (see [19] for a derivation). For distant collisions, the errors in Bohr's classical model of electron binding become significant, whereas Bethe's quantum mechanical treatment is

more realistic. At the other extreme of impact parameter, the perturbative quantum mechanical treatment applied by Bethe (the Born approximation) does not give a good account of close collisions. In contrast, with fair justification, Bohr explicitly treats such collisions as being between free particles. Because the Rutherford formula is equally correct for both classical and quantum mechanical particles, the classical nature of the Bohr model is not an issue for small *b*. The formula proposed by Bloch converges to the Bohr model for close collisions and the Bethe model for distant ones.

Shell corrections: So-called shell corrections have been given for the Bohr [13] and Bethe [14] models and account for the motion of electrons during collisions, in violation of the assumptions in the basic models. If we use a Thomas–Fermi model [20] of typical electron velocities $(Z_2^{2/3}v_0)$ then the threshold for the importance of shell effects will be $v \lesssim Z_2^{2/3}v_0$

Barkas effect: The Barkas or Barkas-Andersen effect refers to a difference in the stopping powers of positive and negatively charged particles. The effect was first observed in the differing ranges of positive and negative pions by Smith et al. [21] with further investigation by Barkas et al. [22] and Andersen et al. [23]. The underlying cause of the effect is the polarization of the electron density of the target by the charge on the projectile particle, which leads to positively and negatively charged projectiles experiencing a different electron density. For this reason the Barkas effect is sometimes also referred to as the *polarization* effect. The impact of polarization is assessed for the Bohr and Bethe models in references [24] and [25] respectively. The necessary corrections vary as Z_1^3 and can be viewed as higher order terms in a perturbative expansion in the projectile atomic number.

Screening: Use of the Thomas–Fermi model for typical electron velocities suggests that the effect of screening of the projectile charge by electrons in the target medium should become important for $v \le Z_1^{2/3} v_0$.

The thresholds for each of these effects are illustrated in 3.4.

3.2.4 Models of Fast, Heavy Particle Stopping

In the previous section we considered some of the corrections that can be made to the Bohr and Bethe theories; relaxation of the underlying assumptions resulted in considerable extra complexity. In fact, such complexity arises even in the simplest case of a projectile with very low charge $(Z_1 \leq 2)$. If we wish to consider projectiles with higher atomic numbers then a perturbative treatment will no longer be valid: the interaction of the highly charged projectile with the target electrons is simply too strong. In other words, the unperturbed evolution of the system (e.g. the straight projectile path or the initial quantum state of the projectile-target system) is not a good approximation for the correct evolution under the perturbation.

In this section we will consider some more recent models designed to capture the physics of fast, heavy particle stopping using non-perturbative treatments. The new physics emerging in this regime is a result of the attraction of electrons of the target medium to the intruding projectile. These electrons will act to screen the projectile charge and may occupy bound states on the projectile, which will become a complex compound object, whose internal excitations will open new channels for energy exchange. In addition, the charge on the projectile will no longer be Z_1e and will generally change along the ion path due to various charge changing processes, which also may contribute to energy exchange.

3.2.4.1 The Effective Charge of the Projectile

The fact that the charge on an intruding particle can change as its bound states are ionized by or capture electrons from the target medium gives rise to the concept of the *effective charge* of the projectile, which we will denote Z_1^*e . Rather than formulate new models of stopping power for heavy ions, we might then be tempted simply to replace Z_1 with Z_1^*e in the perturbative models for light ions. Quite apart from objections based on the new physics associated with the possibility of bound projectile states and screening, we cannot assume that the charge on a projectile ion will be constant during its flight. Even if it achieves some steady state with a well-defined mean value, this will be the result of repeated charge-changing processes. Writing the fluctuating number of bound electrons as N_{bound} , the varying effective charge will be $Z_1^*e = (Z_1 - N_{\text{bound}})e$ whose mean value we will denote $\langle Z_1^* \rangle e$.

Remarkably, effective charge based models of electronic stopping have achieved some success (the empirical model in the *SRIM* code discussed in Sect. 3.2.4.3 is partly based on effective charge concepts), but there are limits to their usefulness, as we shall see.

If we assume that the idea of introducing an effective charge into a simple stopping theory is valid, then, writing a stopping power $S(Z_1, Z_2, v)$ dependent on the projectile and target atomic numbers and on the projectile velocity, we can define an empirical effective charge $\langle Z_1^* \rangle_{\text{emp}}$ [26, 27],

$$\left[\langle Z_1^* \rangle_{\text{emp}}\right]^2 \equiv \mathcal{S}(Z_1, Z_2, \nu) / \mathcal{S}(1, Z_2, \nu), \tag{3.22}$$

relative to the proton stopping power in the same target. This definition makes sense in the light of the Z_1^2 dependence in the stopping equation (3.6). Experimental stopping data for protons compared with carbon and iodine projectiles in a range of targets up to $Z_2 = 79$ (Au) suggest that $\langle Z_1^* \rangle_{\text{emp}}/Z_1$ is independent of Z_2 to within 10% [28]. This points towards some validity for the use of effective charge and suggests the possibility of treating the projectile and target as separable variables of the stopping problem.

Effective charge can also be defined theoretically, most commonly via so-called *stripping models*. These arrive at an equilibrium charge by assuming that electrons whose orbital velocities are lower than the velocity of the projectile ion are

stripped away by collisions with electrons of the target medium. With a Thomas–Fermi model of the atom, the electron orbital velocities are $v_e \sim Z_1^{2/3} v_0$ and we can write a much used stripping criterion [3],

$$\langle Z_1^* \rangle_{\text{strip}} = (1 - \exp(-\nu/Z_1^{2/3}\nu_0))Z_1.$$
 (3.23)

Clearly the effective charge concept is overly simple. One possible complication, analysed by Brandt and Kitagawa [29], is that the charge felt by an electron of the target interacting with a projectile carrying with it a distribution of bound charge will depend on its impact parameter with the nucleus. This leads us to expect that, even for a given net charge $(Z_1 - N_{\text{bound}})e$, the stopping power will still have a Z_1 dependence: it should increase with increasing atomic number. Experimental data for ions of boron through to fluorine of fixed charge in $\langle 111 \rangle$ channels in gold reveal the expected effect [29]: for example, $S(N^{5+}) > S(C^{5+}) > S(B^{5+})$. The variations in these data are also well captured by a theoretical model proposed by Brandt and Kitagawa and incorporating the effect of a spatial distribution to the effective charge [29].

A valid effective charge theory would be able to provide estimates of heavy ion stopping powers. This would be done by multiplying some reference stopping power (normally taken to be that of a proton or alpha particle in the same target medium, for which comprehensive data are available) by the velocity dependent effective charge predicted by the model. Alternatively the effective charge could be used as an input to a theoretical model of stopping power. Both these approaches will be complicated by the fact that the stopping power as a mean over the fluctuating charge state of a projectile ion, $\langle \mathcal{S}(Q) \rangle$, will not in general be equal to the stopping power at the mean charge, $\mathcal{S}(\langle Q \rangle)$.

A more important point is highlighted by Sigmund [30]: the utility of an effective charge theory is dependent on the stopping of heavy ions and the stopping of the projectile in the reference data-set being governed by the same physics. Yet we have no reason to expect that a singly ionized gold ion will behave in the same way as a proton. Where effective charge theories have been validated by experiment [28, 29] attention tends to have been focused on the high velocity regime. In this case the projectile particles will be highly ionized and poorly screened and the problem of almost bare particle stopping is most susceptible to an effective charge treatment. At lower velocities, where the effects of screening and bound states become significant, any attempt to incorporate these effects in an effective charge model is likely to result in a model so clumsy that a direct calculation of heavy ion stopping powers, ignoring any reference data-set, will be at least as straightforward [3].

3.2.4.2 Non-Perturbative Models of Heavy Ion Stopping

As discussed previously, the key differences in moving from light to heavy particle stopping arise because of the much stronger interaction between the projectile

particle and the electrons of the target medium. Models attempting to capture these effects must move beyond the perturbative treatments of the Bohr and Bethe theories. Much work has been done over the last decade on models of fast, heavy ions, with the result that there now exists a varied class of models that have the ability to make predictions of stopping powers in good agreement with experimental data. Once again, we will not attempt a comprehensive survey of these models, but rather discuss their general nature, the information that they require to function and the results that they predict. More information can be found in the discussion and references in Sigmund's book [5].

Broadly speaking, the aim of all the models considered in this section is to take data derived from experiment or from other theoretical calculations and to use these to predict stopping powers as a function of projectile energy for a given combination of projectile and target species. The aspiration is that this should be achieved without the use of any adjustable parameters. The approaches taken by different researchers are diverse: both classical and quantum mechanical models exist; some rely on straight analytical calculations and others incorporate an element of dynamical simulation.

Sigmund and Schinner [31, 32] have developed what they call the *Binary Theory*, which uses Bohr's classical approach to calculate energy transfer in collisions between the projectile and electrons bound to the target ions. The approach is extended beyond the perturbative regime by using a screened interaction potential to mimic the effect of the electronic binding. There is intuitive sense to this approach; the principal effect of the binding of electrons is to reduce the energy transfer at larger impact parameters and similar behaviour occurs when the interaction potential itself is screened. Information concerning the binding frequencies $\{\omega_i\}$ of the electrons is thus encoded in screened potentials,

$$V(r) = -\frac{Z_1 e^2}{r} e^{-r\omega_j/\nu},$$
 (3.24)

and the stopping cross-section due to each electron is calculated independently. In the above expression we can identify the adiabatic radius v/ω_j acting as a decay length in the potential. Various of the corrections discussed in Sect. 3.2.3 can be included in the Binary Theory. The Barkas correction is automatically included, because the scheme is non-perturbative. Screening of the projectile charge with a radius a_{scr} (not to be confused with the screening in (3.24), used to represent the effect of binding) can be added to the interaction potentials,

$$V(r) = -\frac{N_{\text{bound}}e^{2}}{r}e^{-r\omega_{j}/\nu} - \frac{(Z_{1} - N_{\text{bound}})e^{2}}{r}e^{-r/a},$$

$$\frac{1}{a^{2}} = \left(\frac{\omega_{j}}{\nu}\right)^{2} + \frac{1}{a_{\text{scr}}^{2}}.$$
(3.25)

Sigmund and Schinner have also implemented quantum mechanical corrections at higher velocities and shell corrections and they give an approximate treatment of projectile excitations by repeating calculations with the roles of projectile and target exchanged.

To produce predictions of stopping power, the basic Binary Theory requires data on the atomic binding frequencies ω_j of the target electrons and their relative strengths (occupations) f_j . Significantly it also requires knowledge of the effective charge $(Z_1 - N_{\text{bound}})e$.

With all the corrections included, the model compares well with experimental data (from the database of Paul [16], discussed in Sect. 3.2.4.3, below) for a range of projectiles ($3 < Z_1 < 18$) in N, Al, Ni and C targets over a range of energies from 1 keV/amu to 100 MeV/amu.

Grüner et al. [33] present a second classical scheme in which the classical trajectory Monte Carlo method is used to model the interaction of a small number of target nuclei, a projectile nucleus, and their associated electrons. Classical equations of motion are used to calculate the evolution of the system of electrons and nuclei for a statistical sample of starting conditions. This model requires knowledge of the binding energies and occupations of the electronic orbitals, but unlike the Binary Theory it provides information about the charge state of the projectile as an output rather than needing it as an input. Another feature of the model is that, because all the constituent particles are treated explicitly, information about the relative contribution of various energy exchange processes to the stopping power is available. In a simulation of a 1 MeV/amu Ni ion in a gaseous Ar target [33], 80% of the energy loss is attributable to target ionization, 12% to target excitation and 20% to electron capture by the projectile. Projectile excitation is found to have a contribution of -13% (an accelerating effect) due to polarization of the projectile electrons by the ionized target. Like the Binary Theory, the model of Grüner et al. gives good predictions. Simulations of a 1 MeV/amu Ni projectile in solid carbon agree with experiment to within 2.8% and 3.7% for the steady state charge and steady state stopping power respectively.

Some other stopping models have a quantum mechanical foundation. Grande and Schiwietz [34] developed the Pertubative Convolution Approximation (PCA) in an effort to obtain stopping power predictions with the accuracy of full quantum mechanical calculations, but with much less computational effort. The PCA takes the form of an integration over the electron density ρ of the target to give the energy transfer ΔE from the projectile to the target electrons as a function of impact parameter,

$$\Delta E(b, v) = \int dz \int d^2 r_{\perp} K(b - r_{\perp}, v) \rho(r_{\perp}, z).$$
 (3.26)

The integral is carried out in cylindrical polar coordinates about a z-axis through the target nucleus and parallel to the projectile velocity. The function K(b, v) gives the energy transfer to an electron at impact parameter b from a projectile with velocity v. The form of K(b, v) is given in [34] and treats close collisions as free and distant collisions within the perturbative approximation (as for the Bethe theory). To make predictions, the model requires the projectile screening function,

the electron density of the target and the oscillator frequencies and oscillator strengths of the target as inputs.

The original method is perturbative, but Schiwietz and Grande [35] have also developed an extension to the PCA called the Unitary Convolution Approximation (UCA), which extends the applicability of the scheme to high Z_1 . Comparisons of ΔE as a function of b and of Z_1 with intensive quantum mechanical calculations [36] show good and very good agreement respectively. Data for the stopping of oxygen in Al and Si across an energy range from 0.1 MeV/amu to 100 MeV/amu show good agreement with experiment [37].

The above models stand or fall on their ability to make accurate predictions of stopping powers, that being the reason for their construction. Two important experimental studies by Blazevic et al. [38, 39] have provided data for testing the predictions of the models. Blazevic et al. separated out the initial charge states of Ne ions before firing them through thin carbon films and measuring their final charge state and energy. They were then able to determine the charge-dependent stopping power of carbon for neon and the cross-sections for charge changing processes. In reference [38] Blazevic et al. compared their results for charge-dependent stopping against predictions from the Binary Theory of Sigmund and Schinner and the UCA method of Schiwietz and Grande amongst others. The UCA agrees almost to within experimental error. The Binary Theory performs less well, because it shows too weak a scaling with projectile charge when compared with the experimental results.

In this section we have discussed a selection of the sort of models currently being used to calculate stopping powers for fast, heavy ions. All of these models require input concerning the excitation spectrum of the target and focus their efforts on processing this information through some model of the collision dynamics to work out how these excitations will be stimulated. As such, none of the models can be considered as ab-initio in character. A more damning charge, perhaps, is that most modern stopping models (that of Grüner et al. being a notable exception) also require specification of the effective charge of the projectile. As we discussed in Sect. 3.2.4.1, this concept is ill-defined and represents at best some sort of average of the real fluctuating charge. Moreover, at least in principle, much physics could be hidden within a carefully chosen velocity- and target-dependent effective charge. In that case it would be hard to determine just how much of the job of predicting the detailed variation of the electronic stopping power was falling to the model and how much was already embodied in the input parameters.

If we are to evaluate these stopping models on their ability to make predictions alone (and the inherent complexity of many of them makes it difficult to see how they could be used as tools to obtain much insight into the physics of the stopping process) then they should perhaps be considered to be in competition with empirical fitting and interpolation methods to be discussed in the next section.

One final point about stopping models for fast particles is worth making. Data on their performance against experimental results shows that they can routinely calculate electronic stopping powers across an energy range from tens of keV/amu up to tens of MeV/amu for projectile ions in the "light" and "heavier" ranges

(see Fig. 3.1 for the classification) in a wide variety of targets to within experimental error (which can be as good as 2% at 50 MeV/amu, but as bad as 20% at 5 keV/amu [40]). Given this fact, and given that the stopping models' primary role is as predictive, rather than exploratory, tools, then we can perhaps regard the problem of predicting the stopping powers of fast and intermediate velocity ions as solved, at least for the time being. The practical justification for further refining stopping power predictions for fast ions is not immediately clear and the applications shown in Fig. 3.1 suggest that more work on the stopping of slower and heavier projectiles is needed. In this regime the physics is more complicated and the theoretical and experimental literature much more sparse.

3.2.4.3 Empirical Models of Stopping Power

If all we desire is predictions of stopping powers for arbitrary projectile speeds and projectile and target species, then, rather than develop analytical models of the stopping process, a more direct approach is to take the range of experimental data and develop a robust scheme to interpolate and extrapolate from them. Such an approach sacrifices much opportunity for physical insight, but is not significantly worse off in this respect than some of the more complex and obscure analytical models considered above. Empirical fitting schemes are still much used to provide parameters for other calculations or for molecular dynamics simulations.

We can see how an empirical fitting scheme might be plausible if we examine some useful scaling relations in experimental stopping power data. Figure 3.5 illustrates how data-sets for different targets and projectiles can be superimposed via some simple transformations. The fitting process then needs only to capture the underlying shape of the stopping power curve as a function of projectile energy and any structure in the data not dealt with by the scaling relations.

We will briefly consider two of the most widely cited fitting schemes. First, that of Ziegler et al. [2], implemented in the SRIM code⁴ [10]. Their approach begins with proton stopping powers, $S(Z_1 = 1, Z_2, \nu)$, and scales them by an effective charge fraction γ such that,

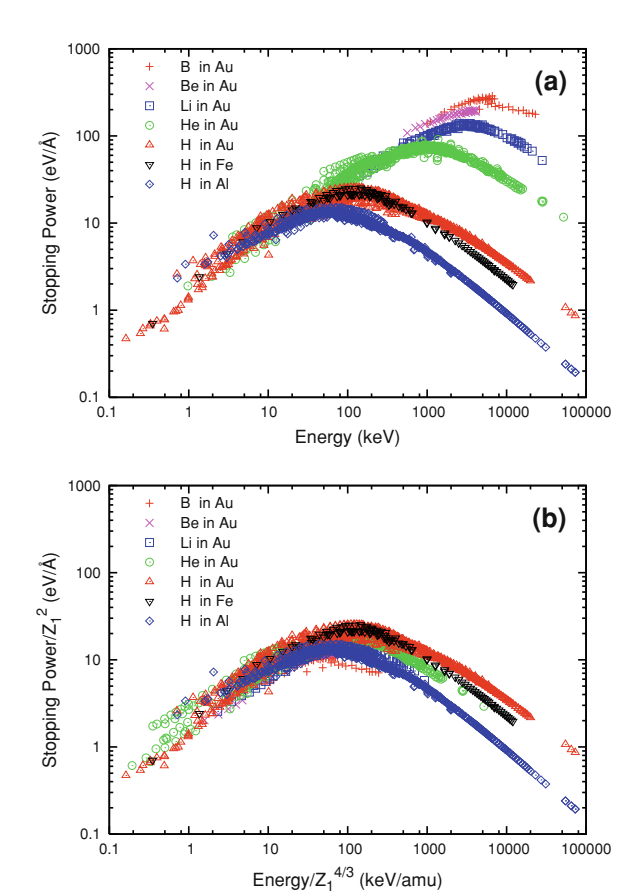
$$S(Z_1, Z_2, \nu) = Z_1^2 \gamma^2 S(Z_1 = 1, Z_2, \nu). \tag{3.27}$$

The proton stopping powers are calculated using the local density approximation of Lindhard and Scharff [41], in which the stopping power of a target medium is written as an integral over the electron density of the medium, $n_e(\mathbf{x})$,

$$S(Z_1 = 1, Z_2, \nu) = \int d\mathbf{x} \, n_e(\mathbf{x}) S(Z_1 = 1, n_e),$$
 (3.28)

⁴ SRIM stands for 'the stopping and range of ions in matter'.

Fig. 3.5 A demonstration of how simple scaling relationships (b) can capture much of the behaviour of the electronic stopping power (a) for a variety of projectile and target combinations. The scaling of stopping power by $1/Z_1^2$ is informed by the prefactor in the fast particle stopping theories (3.7), (Sect. 3.2.2.2) and (3.11) and the normalisation of the particle velocity by $1/Z_1^{2/3}$ is suggested by the Thomas-Fermi scaling of electronic velocities. (Data are from the database of Paul [16].) (Reprinted figure 8 with permission from Race, C.P., Mason, D.R., Finnis, M.W., Foulkes, W.M.C., Horsfield, A.P., Sutton, A.P.: The treatment of electronic excitations in atomistic models of radiation damage in metals. Rep. Prog. Phys. 73, 116501 (2010). Copyright (2010) by the Institute of Physics Publishing Ltd.)



where $S(Z_1 = 1, n_e)$, the stopping power for a proton of a free-electron gas of constant density n_e , is calculated using dielectric stopping theory (see Sect. 3.2.5.2). To achieve good agreement with experimental proton stopping powers, an empirically fitted multiplicative factor varying between 1.0 and 1.2 is included in the model. A second empirical function is used to provide the ionization state of the projectile as an input to a calculation of the effective charge.

The second scheme that we will consider is due to Paul and Schinner [42, 43] and is implemented in the MSTAR code [16]. The model uses stopping data for helium as the experimental reference and fits the quantity,

$$S_{\text{rel}} = \frac{S(Z_1, Z_2, \nu)/Z_1^2}{S(Z_1 = 2, Z_2, \nu)/(2)^2},$$
(3.29)

as a function of Z_1 and v. A three parameter fitting function is used to fit data at each value of Z_1 and then the parameters are themselves fitted as functions of Z_1 . This results in a universal fitting scheme.

Paul and Schinner [44] have compared experimental data for the stopping of carbon projectiles in amorphous carbon targets with the predictions of several empirical fitting and theoretical models. The fitting models of Ziegler et al. and Paul and Schinner give an understandably good match. Sigmund and Schinner's Binary Theory [31, 32] shows a similarly good performance for projectile energies from 1 keV/amu to 100 MeV/amu. The UCA (Unitary Convolution Approximation), of Grande and Schiwietz [37], though performing well at higher energies, significantly underestimates the stopping power for projectiles with energies below 1 MeV/amu.

3.2.5 Models of Slow, Heavy Particle Stopping

When we considered the subject of effective ion charge, we remarked that stripping models of the degree of ionization of the projectile work reasonably well at high velocity, lending support to the concept of an effective charge. However, when projectile velocities fall below the Bohr velocity, $v_0 = e^2/4\pi\epsilon_0\hbar$, we start to see the effects of atomic structure in experimentally measured stopping powers. The observed oscillation in the stopping power as a function of projectile atomic number is referred to as Z_1 -structure and predicting its behaviour requires a different class of analytical models

We will now turn our attention to just such models: designed to predict the stopping powers of slow, heavy ions (i.e. those with kinetic energies significantly below 1 MeV/amu). First we will consider three of the earliest models to tackle this problem, two of which treat the stopping problem within the framework of binary collisions and the third of which considers the electrons as a continuous stopping medium. Later, we will go on to consider more recent efforts in this area.

3.2.5.1 Binary Models of Slow Particle Stopping

Two models that calculate the electronic stopping power by considering the excitation of electrons during binary collisions between the projectile and a target ion are those due to Firsov [45] and Lindhard and Scharff [46]. Both models continue to be much cited up to the present day.

Firsov's model considers the target and projectile ions to form a quasi-molecule during the period of their interaction. The inelasticity of the collision is then attributed to the exchange of electrons between the two ions. An electron swapping association from the (initially stationary) target atom to the (moving) projectile atom must receive an impulse to increase its momentum. The associated increase in kinetic energy is assumed to come from the colliding ions. Firsov [45] used a Thomas–Fermi model of the ions to predict an energy loss during a collision of

$$\Delta E = 0.35 \frac{\hbar v}{a_0} \frac{(Z_1 + Z_2)^{5/3}}{1 + 0.16(Z_1 + Z_2)^{1/3} r_{\min}/a_0},$$
(3.30)

where $r_{\rm min}$ is the distance of closest approach and a_0 is the Bohr radius $\hbar^2/m_{\rm e}e^2$. The energy loss is proportional to the relative velocity of the two ions, v, because the momentum change associated with electron exchange is proportional to v.

Lindhard and Scharff [46] published an alternative formula, once again based on a Thomas–Fermi model of two colliding ions, but never gave a derivation. A similar, more general result, derived by considering the scattering of the electrons of the target atom by the screened field of the projectile, has been given by Tilinin [47]. If a Thomas–Fermi model is used then Tilinin's model predicts an electronic stopping power,

$$S = \frac{8\pi n_{\rm e} e^2 a_0 Z_1 Z_2}{\left(Z_1^{2/3} + Z_2^{2/3}\right)^{-3/2}} \tau(E, Z_1/Z_2) \frac{\nu}{\nu_0},\tag{3.31}$$

where the function τ is the result of an integral over the electronic densities experienced during the collision. Lindhard and Scharff's original formula [46] is equivalent, except that τ is replaced by an empirical constant $\xi_e \sim 1-2$. As long as ν is not too small, then $\tau \sim 1$ and Tilinin's formula (3.31) approaches that of Lindhard and Scharff. The most important feature of (3.31) (and the one most often made reference to in recent literature) is the proportionality of the stopping power to projectile velocity. This feature is shared with the stopping power implied by Firsov's formula (3.30).

Neither Firsov's model nor that of Lindhard and Scharff predicts any Z_1 -structure, because they make use of a simple model for atomic structure. They also fail to take account of a similar fluctuation in stopping power with the atomic number of the target, known as Z_2 -structure, though in principle, with a suitable atomic model, both effects could be accounted for.

3.2.5.2 Electron Gas models of Slow Particle Stopping

An alternative approach to the modelling of slow particle stopping, and one that seems particularly well suited to handle metallic targets, treats the electrons of the stopping medium as a continuous system through which the projectile moves. An early discussion of such models by Fermi and Teller [48] pointed out that since the maximum energy transfer to an electron will correspond to the case of a head-on collsion with the projectile, only those electrons with velocities within ν of the Fermi velocity ν_F will be permitted by exclusion to take part in the stopping process. The final result of their analysis is a stopping power

$$S = \frac{2m_e e^4 v}{3\pi\hbar^3} \ln\left(\frac{\hbar v_F}{e^2}\right),\tag{3.32}$$

once again proportional to the projectile velocity.

A little later, Lindhard [49] gave a more general treatment. His model attributes the stopping power to the electrostatic force exerted on the projectile by the shift in the target electron density caused by the electric field of the projectile charge. The

total electric potential $\phi(\mathbf{x}, t)$ at any point \mathbf{x} and time t is allowed to depend on the potential due to the projectile $\phi_{\text{Proj}}(\mathbf{x}', t')$ at points \mathbf{x}' and times t' in the past via,

$$\phi(\mathbf{x},t) = \int_{-\infty}^{t} dt' \int d\mathbf{x}' \epsilon^{-1}(\mathbf{x} - \mathbf{x}', t - t') \phi_{\text{Proj}}(\mathbf{x}', t'), \qquad (3.33)$$

where ϵ^{-1} is a linear operator. In Fourier space, this relationship is,

$$\phi(\mathbf{q},\omega) = \frac{1}{\epsilon(\mathbf{q},\omega)} \phi_{\text{Proj}}(\mathbf{q},\omega). \tag{3.34}$$

and the response of the electron system to the intruding projectile is characterized by a frequency- and wavevector-dependent dielectric constant $\epsilon(\mathbf{q}, \omega)$. Such a dielectric constant introduces a history dependence into the system that allows for a finite response time of the electron gas to the potential due to the projectile. The model predicts that the centre of the screening cloud around an intruding charge will tend to lag behind, giving rise to a retarding force on the charge. Lindhard's [49] expression for this retarding force is

$$\frac{\mathrm{dE}}{\mathrm{d}x} = -\frac{2Z_1^2 e^2}{\pi v^2} \int_0^{qv} \omega \mathrm{d}\omega \int_0^\infty \frac{\mathrm{dq}}{q} \, \mathfrak{F} \left\{ \frac{1}{\epsilon(\mathbf{q}, \omega)} \right\}, \tag{3.35}$$

in which $\mathfrak{F}\{\cdot\}$ indicates the taking of the imaginary part. Ritchie [50] has published an alternative derivation of (3.35) in which he treats the problem of finding the induced charge density directly within first order perturbation theory, without introducing a classical electric field. Lindhard [49, 51] has given results for limiting cases of low and high projectile velocities. At high (but non-relativistic velocities) the stopping power reduces to the Bethe formula (3.11) and at low velocities to the Fermi–Teller formula (3.32).

3.2.5.3 Non-Linear Calculations of Electron Gas Stopping

Lindhard's stopping power formula (3.35) arises from a perturbative treatment of the effect of the charged particle on the electron gas of the target. Unfortunately, at typical metallic densities, and particularly at lower projectile velocities a non-perturbative treatment is necessary. We will consider this issue only briefly; a detailed account of electron gas stopping theories is to be found in the review by Echenique et al. [7]

Calculations of the screening of a stationary proton in a free-electron gas carried out by Almbladh et al. [52] using Kohn–Sham density functional theory (DFT) [53] highlight the deficiencies of a linear (perturbative) treatment. When the DFT calculations are compared to linear response calculations using the Kohn–Sham DFT form of the dielectric function the latter are found to underestimate the

⁵ At higher velocities $v > v_0$, this simple picture of a retarded screening response becomes much more complicated. For instance, strong oscillations appear in the induced charge density. A full discussion of these so-called *wake effects* is included in the review by Echenique et al. [7].

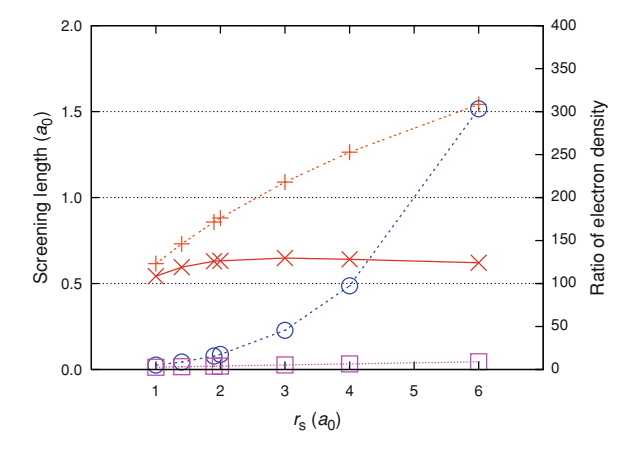


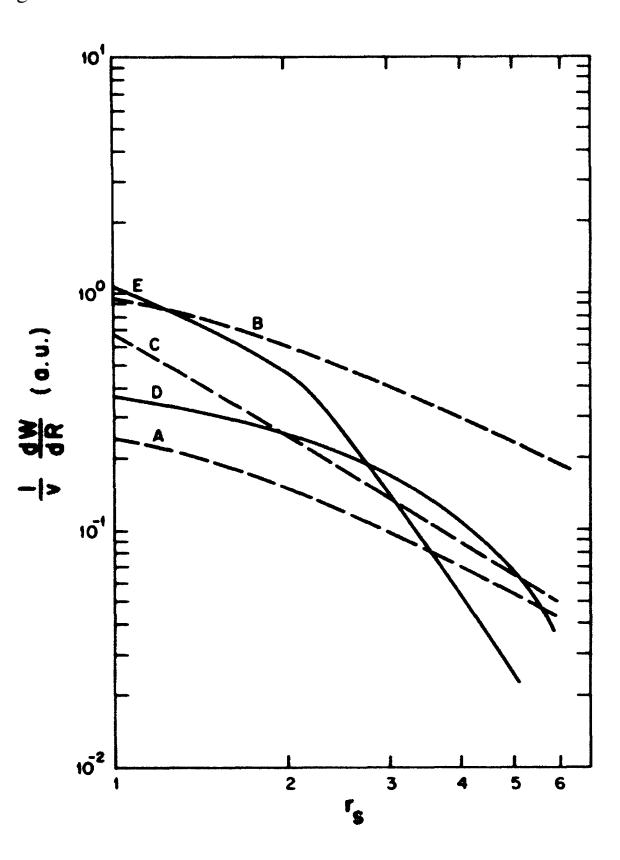
Fig. 3.6 Results of calculations for a proton in a free-electron gas of varying density, indicated by the one electron radius $r_s = (3/4\pi n_e)^{1/3}$. The screening length is indicated for linear response (*orange vertical crosses*) and non-linear DFT calculations (*red diagonal crosses*). Distances are given in atomic units, $a_0 = 0.529$ Å. Also plotted, on the right-hand axis, are the ratio of the charge density at the proton position to the background density for linear response (*purple squares*) and non-linear DFT calculations (*blue circles*). (Data from Almbladh et al. [52].) (Reprinted figure 4 with permission from Race, C.P., Mason, D.R., Finnis, M.W., Foulkes, W.M.C., Horsfield, A.P., Sutton, A.P.: The treatment of electronic excitations in atomistic models of radiation damage in metals. Rep. Prog. Phys. 73, 116501 (2010). Copyright (2010) by the Institute of Physics Publishing Ltd.)

extent to which charge piles up around the proton and overestimate the variation in the screening length (see Fig. 3.6).

Time-dependent DFT calculations (see [54] for a review of the relevant theory) of the stopping power for slow ($\nu < \nu_F$) hydrogen and helium nuclei in an electron gas [55] reveal the difference between a linear and a non-linear treatment. The results are shown in Fig. 3.7: the non-linear calculations show a more rapid decrease in stopping power as the electron density is reduced, due to the formation of bound states that screen the nuclear charge. At high densities, the electron gas screens the nuclear charges so efficiently that no bound states may form and the results of the linear and non-linear calculations converge. At lower electron gas densities the stopping power for helium is predicted by the non-linear calculations to be lower than that for hydrogen. This feature would never be predicted by a linear theory and arises because the higher nuclear charge of a helium atom is more effective at producing bound states.

Similar non-linear calculations for higher atomic number projectiles by Echenique et al. [55] reveal Z_1 -structure. Figure 3.8 shows the effective charge, defined here as the ratio of the calculated stopping power for a particular value of Z_1 to the calculated stopping power of a proton, as a function of projectile atomic number. The results show strong oscillations with troughs at $Z_1 = 2$, 10, 18, corresponding to stable filled shells of bound states. Higher density electron gases

Fig. 3.7 Stopping powers as a function of the one electron radius $r_{\rm s} = (3/4\pi n_{\rm e})^{1/3}$ for linear response theory are (dashed lines) and for nonlinear DFT (solid lines). Results for helium (B and E) and hydrogen (A and D) are shown as labelled. (Reprinted figure 3 with permission from Echenique, P.M., Nieminen, R.M., Ashley, J.C., Ritchie, R.H.: Phys. Rev. A 33(2), 897-904 (1986). Copyright (1986) by the American Physical Society.)

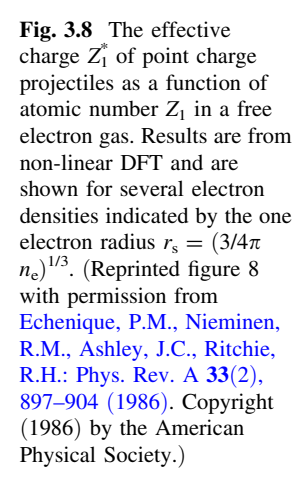


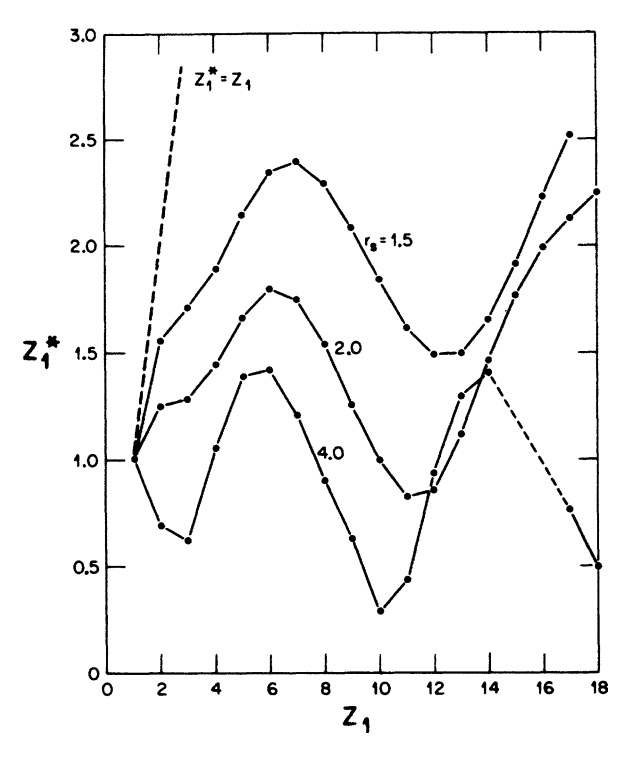
screen the nuclear charges more effectively, making it harder for bound states to form, and the pattern shifts upwards in atomic number.

As a final demonstration of the importance of a non-perturbative treatment, Fig. 3.9 shows results of calculations by Arista [56] of the Z_1 dependence of the stopping power for bare ions of a free electron gas with a density equivalent to that in carbon. These results show strong oscillations with atomic number for $v < v_0$, but they are all but gone by the time $v \approx 2v_0$, as the increasing velocity makes it harder for bound states to form. A comparison of Arista's results with those from the linear dielectric theory shows good agreement in the case $Z_1 = 1$. For $Z_1 = 7$, however, the non-linear theory overestimates the stopping power by 60%. This tendency to overestimate stopping is typical of perturbative theories.

3.2.6 The Gaps in Stopping Power Theory

From the point of view of informing classical models of electronic effects on the evolution of radiation damage phenomena, stopping power theory, as reviewed above, has several major gaps. We list them here to provide context for our own work, described in part II of this thesis.





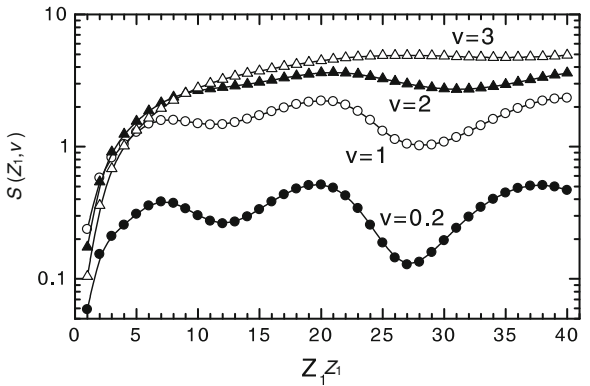


Fig. 3.9 The Z_1 -structure in the stopping power for bare ions in a free electron gas of density equivalent to that in carbon at several projectile velocities (given in units of v_0). (Reprinted from Arista, N.R.: Energy loss of ions in solids: non-linear calculations for slow and swift ions. Nucl. Instrum. Methods Phys. Res. Sect. B Beam Interact. Mater. Atoms **195**(1–2), 91–105 (2002), Copyright (2002), with permission from Elsevier.)

The concept of effective charge: Almost all the stopping models require some sort of effective charge as an input. This is highly unsatisfactory for the reasons discussed in Sect. 3.2.4.1. The charge on a projectile, to the extent even that it is well-defined, given

the nature of screening and bound states, will tend to fluctuate constantly. Attempting to capture all of this complexity in a single quantity might obscure some important behaviour. It would be far more satisfactory if the charge were an *output* of a stopping model or simulation (as it is in the model of Grüner et al. [33], discussed on page 49).

All the models predict a drag force: All of the stopping models examined above predict that the electrons will remove energy from the ions through the action of a drag force, directly opposed to the ion velocity. Such a drag is predicted directly by those models that treat the electrons as a continuum. In the case of models that examine binary collisions, a drag force emerges from a statistical treatment of a series of collisions (particularly when one allows the inelastic nature of the collisions to affect only the energies of the participating ions and not their directions as in the binary collision approximation to be discussed in Sect. 3.4.1).

At lower velocities, the commonly applied stopping models also predict that the drag effect will be proportional to the speed of the projectile. This proportionality can be seen to arise fairly directly out of the form of the models, particularly in the case of the collision based models of Firsov [45] and Lindhard and Scharff [46].

Certainly the drag force (possibly proportional to ion speed) emerges naturally out of the models themselves, rather than being deliberately imposed and so whether or not we believe the form of the force comes down to whether we accept the validity of the approximations made in the various models. Experimental validation of the predictions is difficult because they can only really be compared against ion range distributions and stopping measurements in thin films. Such validation thus involves comparison with average quantities and with statistical distributions and we can perhaps imagine that a fairly broad class of stopping models could, if appropriately parameterized, prove valid in such tests. A model of electronic stopping that relaxed those assumptions that lead to the prediction of a simple drag force would allow us to determine the size of the errors in the simpler models. Whilst the plausibility of the assumptions in those simpler models suggests that such errors will be small, we cannot be sure. Nor can we be sure of the effects they will have on, for example, cascade dynamics, unless we look.

The models lack an environmental dependence: All of the stopping models that we have examined treat the stopping medium as basically homogeneous. This is explicit within the electron gas models and emerges in the case of the collisional models when we consider their application in a simulation of a radiation damage process. Importantly, many-body effects (here *classical* many-body effects) are ignored, because atoms are either entirely absent from the description or are treated only two at a time as they take part in collisions. Such an approximation might well be valid for fast moving ions (for example in the case of ion channelling), but seems unrealistic in the case of a collision cascade displacement spike.⁶

⁶ Note that some more recent work with time-dependent DFT (Campillo et al. [57] and Pitarke and Campillo [58]) and a linear combination of atomic orbitals approach (Dorado and Flores [59]) is capable of predicting the stopping force on a channelling ion as a function of the distance of the ion from the central axis of the path. Such models fall short of incorporating a full dependence on the surrounding atomic environment, though.

Overall, from the point of view of anyone attempting to incorporate electronic effects into atomistic simulations of radiation damage events, stopping power theory provides only a small part of the information required and leaves open most questions about the more subtle effects.

3.3 The Electron-Phonon Coupling Regime

In the later stages of a collision cascade, when the initial PKA energy is shared amongst many ions, the target system might resemble something between a molten region and a system of phonons in a near perfect lattice, depending on the energy distribution. A system in such a state seems inappropriate for a description in terms of stopping powers and the radiation damage community has traditionally separated out these lower energy problems into the so-called *electron-phonon coupling* regime.

Much of the vast literature on the subject of electron-phonon coupling is concerned with the concept of the electron-phonon coupling in general (see for example [60] or [61] for excellent accounts). In a radiation damage context, the notion of electron-phonon coupling is best considered to refer to the interaction of electrons and ions below some particular energy threshold. The electron-phonon coupling regime seems to be defined more as that set of circumstances in which electronic stopping theory *does not* apply than as that set of circumstances in which the ionic system is well modelled by a set of phonons. Hence, here we will focus on the work that directly addresses or informs atomistic simulations of radiation damage and has been heavily cited in the radiation damage literature.

A further problem with applying results from the electron–phonon coupling literature to radiation damage studies is that it is not at all clear how to incorporate the electronic effects into an atomistic simulation. A representation in terms of a drag force has been argued for (see Sect. 3.3.3) and has been incorporated into simulations within a Langevin framework (see Sect. 3.3.4), but such matters are far from settled.

Finally, even if it were clear how to implement the effects of electron–phonon coupling within an atomistic simulation, extraction of data from the literature to parameterize the model would remain fraught with ambiguity. Theoretical estimates using different models and experimental measures of electron–phonon coupling range across several orders of magnitude in a given material (as we shall see in Sect. 3.4.2.2). Most radiation damage simulators therefore tend to consider a broad range of parameterizations to cover the ambiguity.

3.3.1 The Importance of Electron-Phonon Coupling in Radiation Damage

Despite the complexities discussed above, a sound understanding of the process of energy exchange between ions and electrons in the electron–phonon coupling regime is very important if we wish to capture the evolution of a radiation damage process correctly. Once a thermal spike has formed and most atoms over a large region ($\sim 1,000~\text{Å}$) are significantly excited but few are moving ballistically, it is reasonable to model the system as an excited ionic subsystem interacting with a, likely initially much cooler, electronic subsystem. In such a model, the electrons will act as a heat sink for the ions and, because of their relatively high thermal conductivity, will provide an efficient means of removing energy from the cascade region. The strength of the interaction between the ions and electrons can thus have a significant effect on the cascade dynamics: rapid removal of energy from the ions might inhibit production of defects in the displacement phase or it might quench in defects in the relaxation phase. Alternatively, return of energy from the electrons (acting as a heat reservoir) during the relaxation phase might serve to anneal out defects and reduce the residual defect population.

The extent to which the role played by the electronic system might vary in real materials was investigated by Flynn and Averback [62] in a simple model. Consider a thermal spike formed by depositing an energy Q into a spherical region of the target of radius r. The energy per ion will be $Q(r_0/r)^3$, where r_0 is the Wigner–Seitz radius. In terms of an ionic temperature T_a the energy per ion can be written as $3k_BT_a$. The evolution of the thermal spike as it grows and cools will then be described by,

$$r(t) \propto \left(\frac{Q}{3k_{\rm B}T_{\rm a}(t)}\right)^{1/3} r_0.$$
 (3.36)

Turning to the process of energy exchange between ions and electrons, Flynn and Averback consider the scattering of electrons from state to state by imperfections in the crystal lattice, with the emission or absorption of phonons. The electron *mean free path*, λ_{mfp} (the distance travelled by an electron between scattering events) is a measure of the rate of this scattering, and, when the ions are not much displaced from their equilibrium lattice sites, this can be written

$$\lambda_{\rm mfp} = \frac{r_0 T_0}{T_{\rm a}(t)}, \quad \text{where} \quad \lambda_{\rm mfp} \le r_0,$$
(3.37)

where T_0 is the ionic temperature at which $\lambda_{\rm mfp} = r_0$. In effect, the parameter T_0 measures the strength of the electron-phonon coupling: a low value corresponds to a strong coupling (a high rate of energy exchange).

If we compare the mean free path to the size of the thermal spike we have,

$$\frac{\lambda_{\text{mfp}}}{r(t)} = \left(\frac{3k_{\text{B}}}{Q}\right)^{1/3} \frac{T_0}{T_a^{2/3}(t)},\tag{3.38}$$

⁷ The Wigner-Seitz radius is defined as the radius of a spherical volume equivalent to the volume per atom in the solid, i.e. $\frac{4}{3}\pi r_0^3 = 1/n_a$ for a number density of atoms n_a .

we can see that beyond some point in the evolution the cascade will have cooled sufficiently that $\lambda_{\rm mfp} > r$. The electrons will then be heated only very ineffectively by their interaction with the cascade.

Exactly when this qualitative change in the behaviour of the electrons takes place will depend on the value of T_0 . We can obtain values for this parameter from the electrical resistivity using the formula [63] $\lambda_{\rm mfp} = (92 \times 10^{-18} \ {\rm Ohm} \ {\rm m}^2)(r_0^2/\rho_{\rm e}(T_{\rm ref}) \ a_0^2)$, where $\rho_{\rm e}(T_{\rm ref})$ is the electrical resistivity at a reference temperature $T_{\rm ref}$ and a_0 is the Bohr radius. If T_0 is low (a high coupling), the electrons will tend to heat into equilibrium with the ions throughout the evolution of a thermal spike.

Flynn and Averback consider the case of electrons diffusing out of a thermal spike via a random walk involving $(r/\lambda_{\rm mfp})^2$ scattering events at each of which the electrons acquire an energy $k_{\rm B}\Theta_{\rm D}$, where $\Theta_{\rm D}$ is the Debye temperature. These electrons acquire a temperature $T_{\rm e}=\Theta_{\rm D}(r/\lambda_{\rm mfp})^2$. We can then define a critical thermal spike temperature,

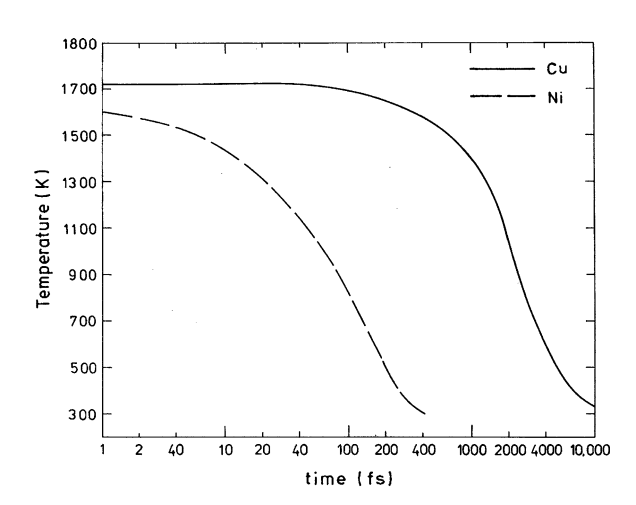
$$T_{\text{crit}} = \frac{9k_{\text{B}}^2}{Q^2 \Theta_{\text{D}}^3} T_0^6, \tag{3.39}$$

above which the electrons will remain in equilibrium with the ions. Quoted values for T_0 of 4.5×10^4 and 1.5×10^4 K for copper and nickel respectively [62] imply values for $T_{\rm crit}$ of 2×10^5 and 300 K, suggesting very different behaviours for the two metals.

3.3.2 Two-Temperature Models

Another view of the potential importance of electron phonon-coupling can be obtained if we consider a simple picture of interacting electron and ionic

Fig. 3.10 The evolution of the ionic temperature given by the coupled equations (3.40) and (3.41) for values of g_p , the electron–phonon coupling constant, for Cu and Ni. (Reprinted figure 1 with permission from Finnis, M.W., Agnew, P., Foreman, A.J.E.: Phys. Rev. B 44(2), 567–574 (1991). Copyright (1991) by the American Physical Society.)



subsystems, each independently in equilibrium at their own temperatures, $T_{\rm e}$ and $T_{\rm a}$ respectively, but out of equilibrium with one another. Such models are called *two-temperature models* and form the basis of several atomistic simulation schemes to be discussed in Sect. 3.3.4.

In a radiation damage thermal spike, the ionic subsystem will be initially hot and we would expect our two-temperature picture of the evolution to have validity as long as the rate of thermalization of the electronic subsystem is sufficiently high when compared with the rate of energy transfer into the electrons. Often the relevant time-scales are such that the picture should not remain valid (see the data quoted in Sect. 8.1.3), but some of the work presented in this thesis (see Sect. 8.1.3) suggests that the very nature of the electronic excitations can be such that the validity condition can be considerably relaxed.

The evolution of a two-temperature model can be represented by heat diffusion equations for the evolving spatial temperature distributions $T_{\rm e}({\bf x},\,t)$ and $T_{\rm a}({\bf x},\,t)$ in the two subsystems,

$$c_{\mathbf{e}}(T_{\mathbf{e}})\frac{\partial}{\partial t}T_{\mathbf{e}}(\mathbf{x},t) = \nabla_{\mathbf{x}}[\kappa_{\mathbf{e}}(T_{\mathbf{e}},T_{\mathbf{a}})\nabla_{\mathbf{x}}T_{\mathbf{e}}] - g_{\mathbf{p}}(T_{\mathbf{e}},T_{\mathbf{a}})[T_{\mathbf{e}}-T_{\mathbf{a}}], \tag{3.40}$$

$$c_{\mathbf{a}}(T_{\mathbf{a}})\frac{\partial}{\partial t}T_{\mathbf{a}}(\mathbf{x},t) = \nabla_{\mathbf{x}}[\kappa_{\mathbf{a}}(T_{\mathbf{a}})\nabla_{\mathbf{x}}T_{\mathbf{a}}] + g_{\mathbf{p}}(T_{\mathbf{e}},T_{\mathbf{a}})[T_{\mathbf{e}}-T_{\mathbf{a}}], \tag{3.41}$$

where $c_{\rm e}$ and $c_{\rm a}$ are the electronic and ionic heat capacities per unit volume and $\kappa_{\rm e}$ and $\kappa_{\rm a}$ are the electronic and ionic thermal conductivities, respectively. $g_{\rm p}(T_{\rm e},\,T_{\rm a})$ is the electron-phonon coupling (measured in W m⁻³ K⁻¹ or dimensionally equivalent units).

Finnis et al. [64] extended the arguments of Flynn and Averback [62] to develop a formula to estimate the value of g_p in different metals (which will be discussed in Sect. 3.3.4). They used such estimates to derive numerical solutions of (3.40) and (3.41). These are shown in Fig. 3.10 and show a much more rapid cooling of the ionic subsystem in nickel than in copper, again suggesting that the strength of the electron–phonon coupling has a significant influence on cascade dynamics.

3.3.3 Representing the Electron-Phonon Coupling

We now turn our attention to how the effects of electron-phonon coupling might be incorporated within an atomistic simulation. Finnis et al. [64] simplified the two-temperature model, by noting that the ionic thermal conductivity will generally be small, to write,

$$\frac{\mathrm{dT_a}}{\mathrm{d}t} = \frac{g_\mathrm{p}}{c_\mathrm{a}} (T_\mathrm{e} - T_\mathrm{a}). \tag{3.42}$$

This equation then tells us how quickly we need to remove energy from (or inject energy into) the ions in an atomistic simulation to account for energy exchange with the electrons. Exactly how that energy should best be removed (or injected) is still an open question, but approximate methods, such as uniformly scaling down (or up) the ionic velocities or applying a force parallel to the velocity, are generally used. In addition, a stochastic force is often used to represent energy transfer *from* electrons to *ions* as part of a Langevin model.

If we follow Finnis et al. and elect to use a damping force, defined for the *I*th ion, with velocity \mathbf{v}_I as,

$$\mathbf{F}_{I} = -\beta_{I} \mathbf{v}_{I},\tag{3.43}$$

them this force will do work on the ion at a rate of $-\beta_I v_I^2$. If we introduce a temperature *per ion*, T_I , then this can be equated with the rate of energy transfer due to the electron–phonon coupling $3 k_{\rm B} dT_I/dt = (g_{\rm p}/c_{\rm a})(T_{\rm e}-T_{\rm I})$. Identifying the thermal energy due to the temperature T_I with the ionic kinetic energy, $3 k_{\rm B} T_I = M_I v_I^2$ for ions of mass M_I , allows us to write the drag coefficient

$$\beta_I = \frac{g_{\rm p} M_I}{c_{\rm a}} \left(\frac{T_I - T_{\rm e}}{T_I} \right). \tag{3.44}$$

When the ions are hotter than the electrons, a positive value for β_I will provide a drag force, removing energy from the ions. In the opposite case of $T_e > T_I$, β_I will be negative and the ions will be accelerated.

3.3.4 Models of Electron-Phonon Coupling

Once we have arrived at a model for incorporating the effects of electron–phonon coupling within a simulation scheme we will require data to help parameterize the model. Many analytical frameworks exist for calculating the electron–phonon coupling g_p . We will begin this section by considering the example due to Finnis et al. [64], developed as an extension to the analysis by Flynn and Averback [62], which is particularly physically transparent.

Finnis et al. [64] begin with an electron with mean free path $\lambda_{\rm mfp} = r_0 T_0 / T_{\rm a}$ scattering from lattice distortions and acquiring energy $k_{\rm B}\Theta_{\rm D}$ in each event. If the electronic velocity is assumed to be the Fermi velocity $v_{\rm F}$, then the scattering rate will be $v_{\rm F}/\lambda_{\rm mfp}$. Quantum mechanical exclusion means that only electrons close to the Fermi level will be able to participate in scattering: $\sim k_{\rm B} T_{\rm e} D(\epsilon_{\rm F})$ electrons will take part if $D(\epsilon_{\rm F})$ is the electronic density of states at the Fermi level. We thus arrive at a rate for energy acquisition by the electrons of,

$$\frac{dE_e}{dt} = \frac{k_B^2 \Theta_D D(\varepsilon_F) \nu_F T_a T_e}{r_0 T_0}.$$
(3.45)

Finnis et al. let $T_a \rightarrow (T_e - T_a)$ in order to turn this into a net rate of energy transfer. There is no physical argument for this substitution; it is simply an ad-hoc change designed to give an energy transfer that vanishes when $T_a = T_e$. We can now write for the electron-phonon coupling,

$$g_{\rm p} = \frac{k_{\rm B}^2 \Theta_{\rm D} D(\varepsilon_{\rm F}) \nu_{\rm F} T_{\rm e}}{r_{\rm o} T_{\rm o}},\tag{3.46}$$

and a damping coefficient,

$$\beta_{I} = \frac{3\Theta_{\rm D}c_{\rm e}\nu_{\rm F}M_{I}}{\pi^{2}r_{0}T_{0}c_{a}} \left(\frac{T_{I} - T_{\rm e}}{T_{I}}\right),\tag{3.47}$$

where, again, $c_{\rm e}$ and $c_{\rm a}$ are the electronic and ionic heat capacities per unit volume and the density of states $D(\varepsilon_{\rm F})$ has been subsumed into $c_{\rm e}=(\pi^2/3)k_{\rm B}^2D(\varepsilon_{\rm F})T_{\rm e}$.

Though the literature contains other, more formal, treatments of the electronphonon coupling [9, 65, 66], they all reduce to a form similar to (3.46), with different numerical prefactors depending on how well they capture details of the true electronic and lattice structures. They generally begin by considering a quantum mechanical ionic subsystem with phonons of energy $\hbar\Omega_{\rm s}({\bf q})$ and momentum $\hbar \mathbf{q}$. These phonons are populated according to occupation numbers $\mathcal{N}(\mathbf{q}, s)$, in which s indexes the phonon branch, and coupled to a quantum mechanical electronic subsystem. The electronic states have energy $\varepsilon_{v}(\mathbf{k})$, momentum $\hbar \mathbf{k}$ and occupations $f(\varepsilon_{\nu}(\mathbf{k}))$, where ν is a band-index. At equilibrium $f(\varepsilon(\mathbf{k}, v))$ will be a Fermi-Dirac distribution and $\mathcal{N}(\mathbf{q}, s)$ a Bose-Einstein distribution. The electron-ion interaction will cause electrons to scatter from states (\mathbf{k}, v) to states (\mathbf{k}', v') with the emission or absorption of phonons (\mathbf{q}, s) . These processes must conserve energy $\varepsilon_{v'}(\mathbf{k}') - \varepsilon_{v}(\mathbf{k}) = \hbar\Omega_{s}(\mathbf{q})$ and momentum \mathbf{k}' – $\mathbf{k} = \mathbf{q}$. If we treat the lattice distortion due to the phonons as a perturbation then a Fermi's Golden Rule (FGR) analysis [67] gives, for the rate of scattering with energy transfer $\hbar\omega$ and momentum transfer q from ions to electrons [9],

$$\Gamma(\mathbf{q},\omega) \propto \sum_{s} \sum_{\mathbf{k},\nu} \sum_{\mathbf{k}',\nu'} \delta_{\Omega_{s}(\mathbf{q}),\omega} \delta_{\mathbf{k}'-\mathbf{k},\mathbf{q}}$$

$$\times \delta(\varepsilon_{\nu'}(\mathbf{k}') - \varepsilon_{\nu}(\mathbf{k}) - \hbar\Omega_{s}(\mathbf{q})) |V_{\mathbf{k}\nu\mathbf{k}'\nu'}(\mathbf{q},s)|^{2}$$

$$\times \{f(\varepsilon_{\nu}(\mathbf{k})[1 - f(\varepsilon_{\nu'}(\mathbf{k}')] \mathcal{N}(\mathbf{q},s) - f(\varepsilon_{\nu'}(\mathbf{k}')[1 - f(\varepsilon_{\nu}(\mathbf{k})][\mathcal{N}(\mathbf{q},s) + 1]\},$$
(3.48)

where $V_{\mathbf{k}} v \mathbf{k'} v'(\mathbf{q}, s)$ is the coupling between electronic states (\mathbf{k}, v) and $(\mathbf{k'}, v')$ by the lattice distortion due to the phonon mode (\mathbf{q}, s) . Of the terms in braces, the first corresponds to the stimulated absorption of a phonon and the second to stimulated and spontaneous emission of a phonon. The rate of energy absorption by the electrons is thus given by,

$$\frac{\mathrm{dE_e}}{\mathrm{d}t} = \int \mathrm{d}\omega \,\hbar\omega \sum_{\mathbf{q}} \Gamma(\mathbf{q}, \omega). \tag{3.49}$$

The various models of electron–phonon coupling basically differ in how they approximate the formulae (3.48) and (3.49). As an example, Kaganov et al. [66] treat the case of a free electron gas and find, if the electrons and ions are not too far out of equilibrium $(T_a \gg \Theta_D, |T_a - T_e| \ll T_a)$ an electron–phonon coupling constant,

$$g_{\rm p} = \frac{\pi m_{\rm e} n_{\rm e} v_{\rm s}^2}{6\tau_{\rm e} T_{\rm e}},\tag{3.50}$$

where $\tau_e = \lambda_{mfp}/\nu_F$ is the electron–phonon scattering time and ν_s is the speed of sound in the lattice. This has the same form as the result (3.46) due to Finnis et al. [64]. In fact the two formulae are equivalent under the transformation,

$$\frac{\pi^2}{6} \to \left(\frac{108\pi^2}{z^2}\right)^{1/3} \frac{T_{\rm e}^2}{T_{\rm a}\Theta_{\rm D}},$$
 (3.51)

where z is the number of valence electrons per atom in the free-electron gas of Kaganov et al. [66].

We remarked earlier about the considerable uncertainty involved in selecting a numerical value of the electron–phonon coupling from the literature. To highlight this, table 3.1 presents a selection of literature estimates of g_p . It includes values calculated by Finnis et al. [64] using (3.46) and values calculated using the same formula by Gao et al. [68]. These differ by approximately a factor of 2 due to the choice of values for T_0 .

Theoretical values calculated by Wang et al. [69] and Qiu and Tien [71] using the formula (3.50) due to Kaganov et al. [66] are also included. The large differences in the values for chromium and vanadium are due to differing assumptions about the number of valence electrons contributing to the free electron gas density: Wang et al. assume $n_e = n_a$; Qiu and Tien assume a variable ratio 0.5 $\leq n_e/n_a \leq 2.0$.

The large difference between the values for nickel calculated using (3.46) and (3.50) is due to the presence of the electronic density of states at the Fermi level in the former. This is particularly high in nickel (compared, say, to copper) and thus implies a large electron–phonon coupling. This band structure dependent effect is absent from the free-electron based formula (3.50).

Table 3.1 also shows examples of experimental values for the electron phonon-coupling. These values are selected from those collected by Qiu and Tien [71]. They are derived from short pulse laser heating experiments (see [72, 73] for examples, [74] for a review) in which the relaxation to equilibrium of an electronic system is monitored following excitation by a laser pulse of ~ 100 fs duration. These experimental values show better agreement with calculations using (3.50) than with those using (3.46), despite the presence of more band structure dependent effects in the latter formula.

For each method individually, the values of electron-phonon coupling vary by several orders of magnitude between weakly coupled gold and strongly coupled vanadium. We might thus expect any effects of electron-phonon coupling on

OF	Theoretical				Experimental
	Equation (3.46)		Equation (3.50)		
	Finnis et al. [64]	Gao et al. [68]	Wang et al. [69]	Qiu and Tien [70]	Qiu and Tien [70]
V		4,803 ^a	183	648	523 ± 37
Cr			179	45	42 ± 5
Fe		1815.0	119		
Ni	3,164.1	1714.5	107		
Cu	81.9	40.1 (36.4 ^a)	12.7	14	4.8 ± 0.7
Ag		9.4 ^a	3.34	3.1	2.8
Au		14.2 ^a	2.3	2.6	2.8 ± 0.5
W			27.6	27	26 ± 3

Table 3.1 A sample of experimental and theoretical estimates of the electron–phonon coupling g_p from the literature

All data given in units of $10^{16}~W~m^{-3}~K^{-1}$. See main text for a discussion of the trends and variation in the values. (This table was prepared by the present author for inclusion in reference [1].)

cascade development to be strongly material dependent. Equally importantly, for any given material, the estimated values of g_p vary by over an order of magnitude. This fact makes it difficult to choose the values of the coupling parameters in a simulation scheme.

3.4 Electronic Effects in Atomistic Models of Radiation Damage

In the previous two Sects. 3.2 and 3.3, we discussed various models for the effect of electrons on ion dynamics in two distinct regimes of the evolution of radiation damage events. In this section of our review we will introduce the various approaches that have been taken to directly simulating such events and discuss the ways that electronic effects have been incorporated. These methods of incorporation are most frequently informed by and parameterized using the models of electronic stopping and electron–phonon coupling that we have considered.

3.4.1 The Binary Collision Approximation

The earliest computer simulations of radiation damage events were carried out in the so-called *binary collision approximation* (BCA) (see Yoshida [75] for an example). These treat a radiation damage cascade as a series of binary interactions between ions in a target material. A typical BCA simulation begins with a PKA

^a Calculated by the present authors using the approach of Gao et al.

with some initial kinetic energy \mathcal{T}_0 moving through a simulation cell containing other ions. This PKA moves with constant velocity until it comes within range of another ion. At this point the two ions are assumed to collide and the resulting velocities of the projectile and the target are calculated using simple scattering theory under an assumed potential. After each collision the projectile and target atom are treated differently depending on their kinetic energies. If \mathcal{T}_t is the kinetic energy transferred to the target and \mathcal{T}_p is the remaining projectile kinetic energy then there are four possible outcomes:

- 1. $T_t > E_d$, $T_p > E_{cut}$: The target atom joins the cascade and both atoms go on to undergo further collisions.
- 2. $T_t > E_d$, $T_p < E_{cut}$: The target atom joins the cascade and the projectile replaces the target at its lattice site.
- 3. $T_t < E_d$, $T_p > E_{cut}$: The target atom remains on its lattice site and the projectile proceeds on a modified trajectory to undergo further collisions
- 4. $T_t < E_d$, $T_p < E_{cut}$: The target atom remains on its lattice site and the projectile becomes an interstitial atom.

The cut-off energy $E_{\rm cut}$ is an additional simulation parameter whose value is selected in order to improve the results. It does not necessarily have the same value as the displacement threshold energy $E_{\rm d}$.

Beyond the basic form of the approximation, different BCA schemes show considerable variety. Some treat amorphous materials (see the early work of Oen et al. [76, 77]), in which case target ions for collisions can be efficiently generated at random around the mean free-flight path. Others treat crystalline materials; a more demanding task given that target ions must be found by searching the lattice around the projectile path.

BCA simulations provided much early insight into the dynamics of collision cascades; it was early BCA simulations in crystalline lattices [78, 79, 80] that provided a means of exploring anomalies in experimental range data in crystalline targets [81] and confirmed the role of ion channelling. What is more, the relatively low computational cost of BCA simulations (because the target material is generated 'on the fly') has ensured that they remain in common use up to the present day. Though molecular dynamics provides a more realistic description of cascade dynamics, with BCA codes it is possible to simulate large numbers of damage events up to very high PKA energies, and thereby gather good cascade statistics. Two much used codes are the SRIM code [10] for simulations of amorphous targets and Marlowe [82] for the treatment of crystalline targets.

However, the BCA contains some major deficiencies. First, the model of the ion dynamics is highly prescriptive and so does not allow for processes such as the recombination of interstitial defects and vacancies. If the initial and final positions of the ions are recorded [83, 84] then an initial defect population can be determined. It is then possible to *add in* a recombination phase, either by simply assuming some interaction radius within which recombination will take place, or by implementing a period of diffusive defect motion [85].

A second, and much more significant, deficiency of the BCA is its representation of the cascade dynamics. There is ambiguity in how the evolution of a series of binary collisions is to be followed; the question of which collision should be considered next is tackled in various ways in the literature. Because the 'true' chronology of the cascade is uncertain, there is also no obvious way of determining how the developing cascade should be allowed to interact with existing defects.

Third, there is the matter of how electronic effects are incorporated. The earliest simulations took no account of energy loss to electrons, but later codes use models like those of Firsov [45] and Lindhard and Scharff [46] (see Sect. 3.2.5.1) to calculate an inelastic energy loss during the collisions. It is not immediately obvious that this approach would be valid, particularly when the evolution is dominated by glancing collisions (e.g. in channelling) or by head-on collisions (e.g. in replacement collision sequences). The fact that ion range distributions predicted by BCA simulations agree well with experimental data does not necessarily confirm the validity of the electronic loss model, for similar reasons to those given on page 61.

3.4.2 Molecular Dynamics Models

Classical molecular dynamics (MD) simulations achieve an improvement over the BCA in terms of the realism of their modelling of cascade dynamics by including an explicit representation of the ions. They represent a system undergoing radiation damage as a set of point particles moving under some force model. Since the 1960s, computational power has been sufficient to allow the simulation of collision cascades with MD (Gibson et al. [86] present an early example). We will not discuss the use of standard MD to investigate radiation damage (various reviews, such as references [87] and [88] provide details), but consider, rather, how the effects of energy exchange between electrons and ions have been incorporated within MD simulation schemes.

3.4.2.1 Molecular Dynamics with Electronic Drag

The form of the electronic stopping power predicted by various models in the slow particle regime (Sect. 3.2.5) suggests an obvious way of incorporating the energy loss from ballistic ions. Various MD models have explored the effects of a viscous drag on cascade dynamics, and such a force has been used to represent not just the electronic stopping power, but also the effect of the electron–phonon coupling, consistent with the approach suggested by Finnis et al. [64] (see Sect. 3.3.3). Such models consider ions moving under an equation of motion,

$$M_I \ddot{\mathbf{R}}_I = \mathbf{F}_I - \beta_I \dot{\mathbf{R}}_I, \tag{3.52}$$

where \mathbf{F}_I is the force on ion I of mass M_I due to the other ions under the chosen interatomic potential. \mathbf{R}_I , $\dot{\mathbf{R}}_I$ and $\ddot{\mathbf{R}}_I$ indicate the ion position and its time derivatives and β_I is the drag coefficient. In the simplest models β_I is chosen to be a constant for all ions.

Extensive studies by Nordlund et al. [89–92] using a constant drag coefficient investigated the effect of electronic stopping power on the initial damage in collision cascade simulations. The value of the drag coefficient was drawn from the SRIM code [2] and assumed to act only on ions whose kinetic energy \mathcal{T}_I exceeded 10 eV:

$$\beta_I = \beta T_I \ge 10 \text{ eV}$$

= $0T_I < 10 \text{ eV}$. (3.53)

We will have more to say about such cut-offs in the electronic damping in Sect. 11.1.1.

Based on their simulation results Nordlund et al. conclude that the electron-phonon coupling has little effect on the initial damage distribution caused by a collision cascade [89, 90]. This conclusion is based on comparisons between their simulations and experimental data of the value of the *mixing parameter*, a high level cascade statistic measuring the extent to which the original ionic configuration has been disturbed. Nordlund et al. find that the variation between different materials with very different predicted electron–phonon coupling strengths is well reproduced by their model despite the fact that no effort is made to incorporate the effects of electron–phonon coupling. Instead they attribute the variations in mixing to differences in the inter-ionic potentials, leading to different elastic properties and melting points and so to different cascade behaviour. The effects of such material properties on cascade dynamics in MD simulations have been extensively studied [89].

Zhong et al. [92] draw similar conclusions to Nordlund et al. They compare defect yields in the self-bombardment of tungsten between simulation and experiment, claiming agreement within $\sim 30\%$ for a model omitting electron-phonon coupling effects.

The conclusions described above are, perhaps, too bold. Even if an MD model without electron–phonon coupling were to replicate the experimental results perfectly, this would not necessarily indicate the unimportance of electron–phonon coupling. For one thing, we would have to be careful about what aspects of the cascade we were comparing; most cascade statistics are extremely high level and represent the results of statistical averaging, and so it is plausible that they could be accurately reproduced by a broad range of different models. Also, where models contain free parameters, whose values are chosen with reference to experimental data, it is possible for the fitting to compensate for the lack of a model of electron–phonon coupling as far as the high level features of the cascade are concerned, whilst perhaps giving very poor reproduction of the finer detail of cascade evolution.

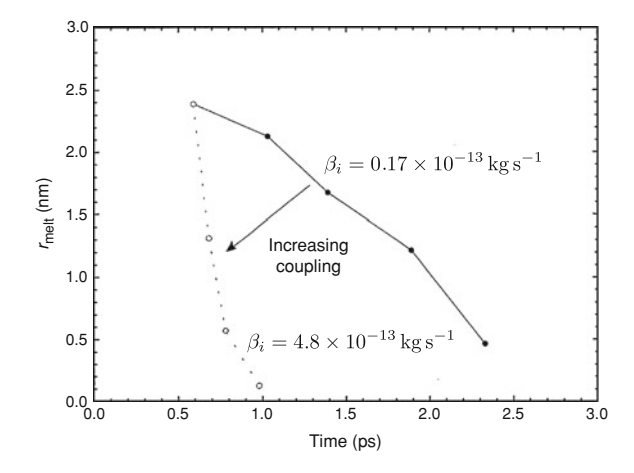


Fig. 3.11 The evolution of the radius of the molten zone in cascade simulations in α -Fe. Increasing the electron–phonon coupling strength dramatically increases the rate of cooling of the cascade. (Reprinted figure 2 with permission from Gao, F., Bacon, D.J., Flewitt, P.E.J., Lewis, T.A.: The effects of electron–phonon coupling on defect production by displacement cascades in α -iron. Model. Simul. Mater. Sci. Eng. **6**(5), 543–556 (1998). Copyright (1998) by the Institute of Physics Publishing Ltd.)

Finally, the uncertainty in experimental results can be quite high (many tens of percent) and so, given that the agreement with experiment claimed by Nordlund et al. is in any case only to within 50%, there is ample room for electron–phonon coupling to play a significant role even without quibbling with the logic behind the conclusion.

Lending support to the potential importance of electron phonon-coupling is work by Bacon et al. [68, 93]. In [68] they augment an MD model of α -iron with a frictional force to represent the effect of electron–phonon coupling and examine the differences in the later stages of cascade evolution (once a molten region has formed) as the value of the drag coefficient is varied. They observe a dramatic effect on the rate at which the molten zone shrinks (see Fig. 3.11) and a significant, though less strong, effect on the number of Frenkel pairs produced (Fig. 3.12).

There is still considerable uncertainty about how electron-phonon coupling should be treated in MD simulations. Given the scarcity of experimental data against which to validate coupling models and the uncertainties in those data, more realistic treatments of the interaction between electrons and ions could help to resolve the issue.

3.4.2.2 Electrons as a Heat Bath

The electrons in a radiation damage process will do more than simply provide a mechanism of ionic energy loss; we have already discussed how they will function as a heat bath and how they can enhance energy transport out of the cascade

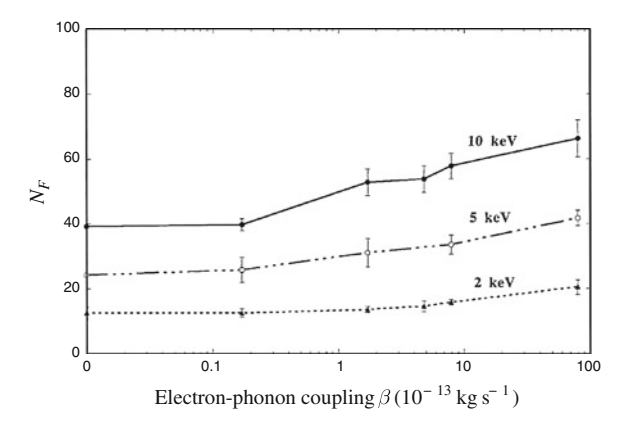


Fig. 3.12 The number of Frenkel pairs produced in cascades with various PKA energies as a function of electron–phonon coupling strength. (Reprinted figure 4 with permission from Gao, F., Bacon, D.J., Flewitt, P.E.J., Lewis, T.A.: The effects of electron–phonon coupling on defect production by displacement cascades in α -iron. Model. Simul. Mater. Sci. Eng. **6**(5), 543–556 (1998). Copyright (1998) by the Institute of Physics Publishing Ltd.)

region. In order to improve the modelling of electron–phonon coupling Caro and Victoria [94] proposed modelling the electrons as a Langevin heat bath, in which case the ions obey a new equation of motion,

$$M_I \ddot{\mathbf{R}}_I = \mathbf{F}_I + \boldsymbol{\eta}_I(t) - \beta_I \dot{\mathbf{R}}_I, \tag{3.54}$$

where β_I is a drag coefficient and $\eta_I(t)$ is a stochastic force, distributed with probability $P(\eta)$

$$\langle \boldsymbol{\eta} \rangle = 0, \quad \langle \boldsymbol{\eta}(t) \cdot \boldsymbol{\eta}(t') \rangle = 2\beta_I k_{\rm B} T_{\rm e} \delta(t - t'),$$

$$P(\eta) = (2\pi \langle \eta^2 \rangle)^{-1/2} \exp(-\eta^2 / 2 \langle \eta^2 \rangle).$$
(3.55)

Since many of the models for electronic stopping power also predict a force proportional to and opposed to the ion velocity, Caro and Victoria propose that (3.54) could, in principle, capture the effects of electronic stopping *and* electronic phonon coupling, provided that the differences in their magnitudes could be accounted for. To achieve this aim they make the drag coefficient acting on a given ion dependent on the local electronic density at its location. Since an ion undergoing an energetic collision will experience a much higher average electronic density than an ion oscillating about its equilibrium position, such a model is plausible. It can also be implemented efficiently, since information about the local electronic density will be readily available in a simulation that makes use of embedded atom model (EAM) potentials [95]. Caro and Victoria choose the form of their β so that it matches the linear response theory of Kitagawa and Ohtsuki [96] at high density and results derived from density functional theory by Echenique et al. [97] at low density:

$$\beta_I = A \log_{10}(\alpha \rho_I^{1/3} + b), \tag{3.56}$$

where ρ_I is the electron density experienced by an ion at \mathbf{R}_I and A, α and b are constants whose values are given in reference [94]. This fitting is entirely empirical.

The model has been implemented by Prönnecke et al [98] and used to study collision cascades in copper. Adding even a weak coupling is found to significantly reduce the duration of 2.5 keV and 5.0 keV collision cascades.

A key deficiency of Caro and Victoria's original model (and one acknowledged in reference [94]) is the handling of the temperature dependence of the stochastic force $\eta(t)$. In Langevin dynamics at equilibrium we should have $\eta \propto \sqrt{T_{\rm e}}$, according to the fluctuation dissipation theorem. For completeness, therefore, we need some model for the evolution of the electronic temperature distribution. Caro and Victoria avoid this requirement by assuming that the rate of heat transport by the electrons is sufficiently high in comparison with the strength of the electron–phonon coupling that the electronic system can function as a perfect heat sink, remaining at some target temperature. However, excluding electronic heating means the electrons cannot act to anneal out defects. Such an assumption also makes it unlikely that the model will correctly describe cascades in metals with strong electron–phonon coupling.

Duffy and Rutherford [99–101] have extended the model of Caro and Victoria by representing the electrons as an inhomogeneous heat bath. Once again the ions obey a Langevin equation of motion as in (3.54),

$$M_I \ddot{\mathbf{R}}_I = \mathbf{F}_I + \boldsymbol{\eta}_I(t) - \beta_I \dot{\mathbf{R}}_I,$$

but now the magnitude of the stochastic force $\eta_I(t)$ is a function of a varying local electronic temperature.

Duffy and Rutherford also adopt a different form for the damping coefficient β_I . They represent the effects of electron–phonon coupling by a constant damping β_p applied to all ions and the electronic stopping power by a second constant β_s applied only to fast moving ions, $\dot{R}_I > v_t$, for some threshold velocity v_t . Hence,

$$\beta_{I} = \beta_{p} + \beta_{s} \quad \dot{R}_{I} \ge v_{t},$$

$$= \beta_{p} \qquad \dot{R}_{I} < v_{t}.$$
(3.57)

 $\beta_{\rm s}$ is derived from the SRIM code [2] $(\beta_{\rm s}/M_I=1~{\rm ps}^{-1}~{\rm for~bcc~iron})$ and a variety of values for $\beta_{\rm p}$ is explored (0.05 ${\rm ps}^{-1} \le \beta_{\rm p}/M_I \le 30~{\rm ps}^{-1}$). $v_{\rm t}$ is set such that $\frac{1}{2}M_Iv_{\rm t}^2$ is twice the cohesive energy.

Duffy and Rutherford coarse-grain the electronic temperature distribution into cells of around 340 ions and evolve it according to a heat diffusion equation,

⁸ Similar models have been used by Ivanov and Zhigilei [102, 103] and Duvenbeck et al. [104–106], but they include a less full description of the physics of energy exchange and so we will not discuss them here.

$$c_{\rm e} \frac{\partial T_{\rm e}}{\partial t} = \nabla (\kappa_{\rm e} \nabla T_{\rm e}) - g_{\rm p} (T_{\rm e} - T_{\rm a}) + g_{\rm s} T_{\rm a}', \tag{3.58}$$

where $c_{\rm e}$ and $\kappa_{\rm e}$ are the electronic heat capacity and thermal conductivity. $T_{\rm a}$ is an average ion temperature over the $N_{\rm cell}$ atoms of the coarse-graining cell,

$$\frac{3}{2}k_{\rm B}T_{\rm a} = \frac{1}{N_{\rm cell}} \sum_{I} \frac{1}{2} M_{\rm I} \dot{R}_{i}^{2}, \tag{3.59}$$

and T_a is the equivalent average over only those N_{cell}' atoms with $\dot{R}_I \ge v_t$. The terms in g_p and g_s in (3.58) are source terms. The former corresponds to the work done by the forces $-\beta_p \dot{\mathbf{R}}_I$ and η_I and the latter arises because of the electronic stopping force $-\beta_s \dot{\mathbf{R}}_I$. The values of g_p and g_s are dictated by energy conservation.

Rutherford and Duffy have explored the effect of electron–phonon coupling on the development of 10 keV cascades in iron by varying β_p across the range of literature values (see Sect. 3.3.4). Increasing the electron–phonon coupling initially increases the number of stable defect pairs formed (which can be attributed to the freezing in of defects by more rapid quenching of the thermal spike), but at higher values of β_p causes a decrease in the number of stable defects (which is due to the reduction in the size of the cascade by the rapid removal of energy).

Duffy and Rutherford's model also allows the effect of allowing the electronic temperature to vary (in space and time) to be compared with the perfect heat sink of Caro and Victoria. Use of the inhomogeneous heat bath tends to reduce the stable defect yield at all values of β_p (see Fig. 3.13), but increase the maximum number of defects formed at higher values of β_p (see Fig. 3.14). Both the above effects could be due to the return of energy from hot electrons to the ions in the cascade. Such feedback would prolong the thermal spike, and so increase the maximum number of defects formed, but also give prolonged annealing and so reduce the final stable defect yield.

The model due to Duffy and Rutherford and described above is a significant improvement over earlier MD schemes with an electronic damping term. However, the effect of the electrons on the ion dynamics is still modelled only by a simple damping force and the usual ad hoc distinction between the electron stopping and the electron–phonon coupling regimes is still made. This distinction is commonly drawn in terms of the character of the ionic motion: generally ballistic in the former regime and highly correlated and confined around the equilibrium positions in the latter regime. However, molecular dynamics simulations contain an explicit representation of the ionic system and so, at least in principle, it should be possible to find some single framework that can account for the effect of

⁹ Note that figures 3.14 and 3.13 cannot be properly interpreted at lower values of the coupling $(\beta_p/M_I \lesssim 1 \, \mathrm{ps^{-1}})$. The electronic stopping power was not included in simulations using a homogeneous thermostat $(\beta_s = 0)$ and so the impact of allowing the electrons to heat up is entangled with that of a higher average damping unless $\beta_p \gg \beta_s$.

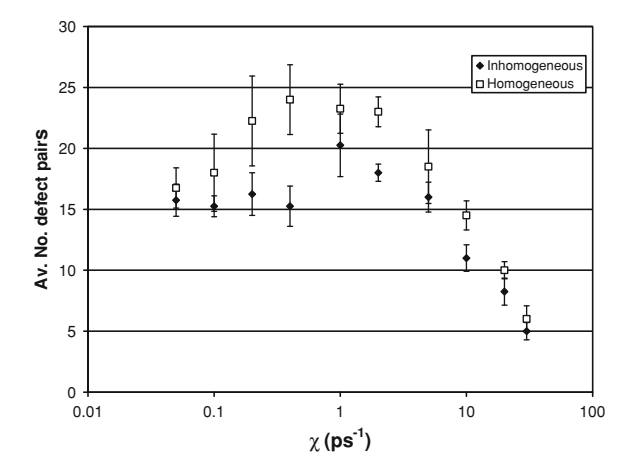


Fig. 3.13 The number of stable defect pairs at the conclusion of the cascade simulations as a function of electron–phonon coupling. The plotted measure is related to the damping coefficient by $\chi = \beta_p/M_I$. The inhomogeneous thermostat, which allows for feedback of energy from the heated electron to the ions, results in prolonged annealing and a reduced defect yield. Note that the electronic stopping power $(\beta_s/M_I = 1 \text{ ps}^{-1})$ is only applied in the inhomogeneous case. (Reprinted figure 6 with permission from Rutherford, A.M., Duffy, D.M.: The effect of electronion interactions on radiation damage simulations. J. Phys. Condens. Matter **19**(49), 496201 (2007). Copyright (2007) by the Institute of Physics Publishing Ltd.)

electrons across the whole range of ionic energies. The fact that a simple damping force is used is a likely consequence of the fact that electronic stopping theory has nothing to say about any additional subtleties that might exist.

One way that we might move forward, to develop a better model of electronic effects going beyond a simple damping and no longer relying on an artificial separation into "regimes", might be to find a way to incorporate an explicit model of the electronic system into radiation damage simulations. Part II of this thesis describes work that begins this task. But first, the final section of this review will consider some other, similar, attempts to move beyond simple augmented MD models.

3.5 Improving the Models: Incorporating Electrons Explicitly

Although theoretical tools have recently been developed that allow for the simulation of systems of *quantum mechanical* ions coupled to quantum mechanical electrons (see references [107–111] for a discussion of *correlated electron–ion dynamics* (CEID)), they are restricted by their computational complexity to the treatment of only a few quantum mechanical ions. For the meantime they will therefore be of only very indirect use to the study of radiation damage and we will not consider them further here.

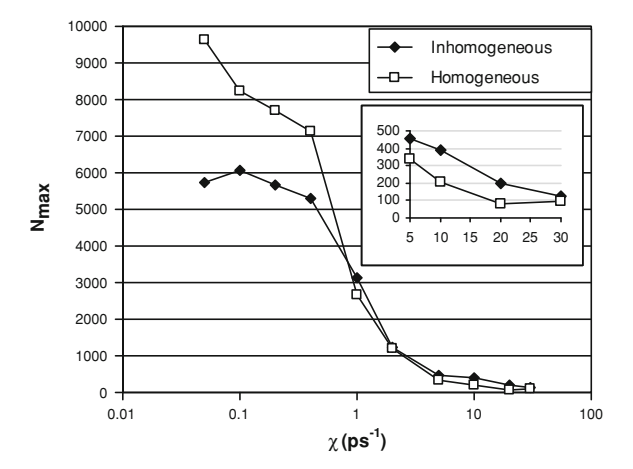


Fig. 3.14 The peak number of (mostly unstable) defects measured during the cascade evolution as a function of electron–phonon coupling ($\chi = \beta_p/M_I$). At high coupling, the use of an inhomogeneous evolving electronic temperature distribution is seen to enhance the degree of ionic mixing. The cascade is prolonged by the feedback of energy from electrons to ions. As in Fig. 3.13 above, no simple interpretation of the data for $\chi \lesssim 1\,\mathrm{ps^{-1}}$ is possible. (Reprinted figure 5 with permission from Rutherford, A.M., Duffy, D.M.: The effect of electron–ion interactions on radiation damage simulations. J. Phys. Condens. Matter **19**(49), 496201 (2007). Copyright (2007) by the Institute of Physics Publishing Ltd.)

In contrast, currently available computational resources allow simulations of quantum mechanical electrons coupled to *classical* ions in systems of hundreds of atoms upwards, depending on the complexity of the model employed for the electrons. Our own work, described in this thesis, is of this kind and we will complete the current review by describing another piece of work in a similar vein. A discussion of the differences between this and our own work will provide useful context for later chapters.

Pruneda et al. [112] have undertaken time-dependent density functional theory (TD-DFT) 10 simulations of the channelling of protons and antiprotons in the insulator lithium fluoride. Their aim is to investigate a threshold effect in the electronic stopping power evident in experimental data [114–116]. The stopping power is found to drop to zero below a certain velocity (0.1 ν_0 for protons in LiF), an effect attributed to the presence of a band gap, which imposes a minimum energy on electronic excitations in the target.

Pruneda et al. [112] have run a series of simulations in a $4 \times 4 \times 4$ unit cell lattice of LiF (128 ions) using the Siesta TD-DFT code [117] with the adiabatic local density approximation (ALDA) to the exchange-correlation energy. The ions are held frozen at their perfect lattice sites and a proton or anti-proton is constrained to move down the centre of a [110] channel at a fixed velocity. Figure 3.15

¹⁰ See, for example, references [54] and [113] for details of the theory.

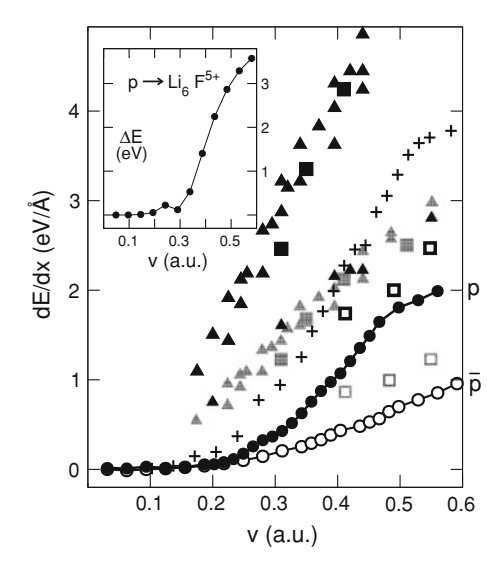


Fig. 3.15 Electronic stopping power dE/dx as a function of particle velocity from time-dependent DFT simulations of channelling in LiF. The results for protons are shown as filled circles, anti-protons as empty circles. The crosses show results for protons when extra basis states are added along the channelling particle's path. (Reprinted figure 2 with permission from Pruneda, J.M., Sanchez-Portal, D., Arnau, A., Juaristi, J.I., Artacho, E.: Phys. Rev. Lett. **99**(23), 235501 (2007). Copyright (2007) by the American Physical Society.)

shows the results of the simulations for projectile velocities up to $0.6 v_0$ and a threshold effect is clearly evident at around the velocity suggested by experiment.

If the channelling particle is regarded as a periodic perturbation to the electronic system of the target, then its frequency will be determined by the rate at which the projectile passes from one cell to the equivalent point in the next [118]. The threshold velocity can then be understood as corresponding to the minimum possible excitation in the electronic system, in this case the band gap.

One potential problem with using TD-DFT to simulate radiation damage events is that the high computational burden of the method restricts its application to small systems of no more than a few hundred atoms. This high burden arises because the calculation of the electronic forces on the nuclei requires that time-dependent one-electron orbitals be calculated to high precision, which in turn demands many basis states per atom. Also, calculation of the electronic Hamiltonian is inherently time consuming, requiring many three-dimensional spatial integrals over the basis states.

The effect of finite system size effects on quantitative output from dynamical simulations can be particularly severe (as we will discuss in the context of our own work in chapter 6). Whilst Pruneda et al. state that their 128 atom super-cell (with calculations at a single k-point) was chosen after "convergence tests" they also make it clear that the values found for the stopping power were not converged. Their results for the stopping power above the threshold are a factor of two smaller

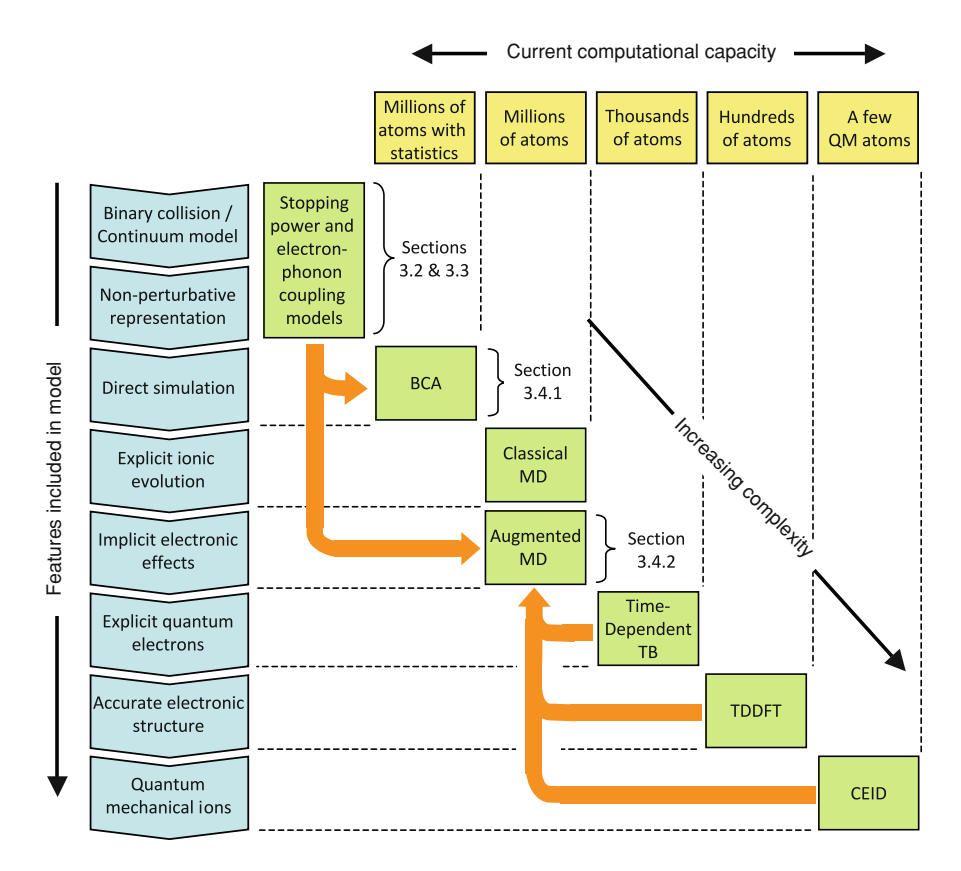


Fig. 3.16 An overview of the theories and models covered in this review. The types of model are represented in terms of their incremental physical content along with an indication of the size of system that can be modelled with current computational resources. Augmented classical molecular dynamics models represent a current "best compromise", able to handle simulations of millions of atoms, but having the potential to include much of the key physics of energy exchange between ions and electrons. Such models are informed by analytical stopping power and electron–phonon coupling theories and by the the results of simulations with more complex models. (Reprinted figure 21 with permission from Race, C.P., Mason, D.R., Finnis, M.W., Foulkes, W.M.C., Horsfield, A.P., Sutton, A.P.: The treatment of electronic excitations in atomistic models of radiation damage in metals. Rep. Prog. Phys. **73**, 116501 (2010). Copyright (2010) by the Institute of Physics Publishing Ltd.)

than those found by experiment and the discrepancy is likely to be a finite size effect. Indeed they find that adding extra hydrogenic basis states every 0.5 Å along the projectile's path gives a \sim 75% enhancement in the stopping power.

This helps to illustrate that when simulating dynamical processes that depend upon excitations of a quantum mechanical electronic system we must be especially conscious of possible adverse effects of small system size. One great benefit of Kohn–Sham DFT is its ability to provide *quantitatively* accurate predictions, but we should remember that the small system sizes used in DFT calculations are

themselves an approximation. Convergence of the ground-state energy at a given system size can in no way be taken as confirmation that predictions of dynamical properties will be well-converged.

The fact that the effect of the approximation of small system size can easily negate the accuracy of the electronic model in TD-DFT leads us to consider making a different trade-off. In our work we adopt a more approximate model of the electronic structure, thereby being explicit about our inability to produce quantitative predictions. But this allows us to simulate much larger systems, giving us greater confidence that we will have achieved true system size convergence and that the conclusions of our *qualitative* investigations of radiation damage phenomena will be sound. As a parallel and complementary endeavour to work such as that of Pruneda et al. this has great appeal.

References

- 1. Race, C.P., Mason, D.R., Finnis, M.W., Foulkes, W.M.C., Horsfield, A.P., Sutton, A.P.: The treatment of electronic excitations in atomistic models of radiation damage in metals. Rep. Prog. Phys. **73**, 116501 (2010)
- Ziegler, J.F., Biersack, J.P., Littmark, U.: The Stopping and Range of Ions in Solids. Pergamon, New York (1985)
- 3. Sigmund, P.: Stopping of Heavy Ions—A Theoretical Approach. Springer, Berlin (2004)
- 4. Seitz, F., Koehler, J.S.: Displacement of atoms during irradiation. Solid State Phys. Adv. Res. Appl. **2**, 305–448 (1956)
- Sigmund, P.: Particle Penetration and Radiation Effects—General Aspects and Stopping of Swift Point Charges. Springer, Berlin (2006)
- Bohr, N.: The penetration of atomic particles through matter. Matematisk Fysiske Meddelelser—Kongelige Danske Videnskabernes Selskab 18(8) (1948)
- 7. Echenique, P.M., Flores, F., Ritchie, R.H.: Dynamic screening of ions in condensed matter. Solid State Phys. Adv. Res. Appl. **43**, 229–308 (1990)
- 8. Averback, R.S., Diaz de la Rubia, T.: Displacement damage in irradiated metals and semiconductors. Solid State Phys. Adv. Res. Appl. **51**, 281–402 (1997)
- Koponen, I.: Energy transfer between electrons and ions in dense displacement cascades. Phys. Rev. B 47(21), 14011–14019 (1993)
- 10. URL http://www.srim.org
- 11. Thomson, J.J.: Ionization by moving electrified particles. Philos. Mag. 23(136), 449–457 (1912)
- 12. Darwin, C.G.: A theory of the absorption and scattering of the α rays. Philos. Mag. 13, 901–920 (1912)
- 13. Bohr, N.: On the theory of the decrease of velocity of moving electrified particles on passing through matter. Philos. Mag. 23(2), 10–31 (1912)
- 14. Bethe, H.: Zur theorie des durchgangs schneller korpuskularstrahlen durch materie. Ann. Phys. **397**(3), 325–400 (in German)
- 15. Schiff, L.I.: Quantum Mechanics. McGraw-Hill, New York (1955)
- 16. URL http://www.exphys.uni-linz.ac.at/stopping/
- 17. Bloch, F.: Bremsvermögen von atomen mit mehreren elektronen. Zeitschrift für Physik A: Hadrons and Nuclei **81**(5), 363–376 (1933)
- Ziegler, J.F.: Stopping of energetic light ions in elemental matter. J. Appl. Phys. 85(3), 1249–1272

- 19. Lindhard, J., Sorensen, A.H.: Relativistic theory of stopping for heavy ions. Phys. Rev. A 53(4), 2443–2456 (1996)
- 20. Ashcroft, N.W., Mermin, N.D.: Solid State Physics. Thomson, Toronto (1976)
- 21. Smith, F.M., Birnbaum, W., Barkas, W.H.: Measurements of meson masses and related quantities. Phys. Rev. **91**(3), 765–766
- 22. Barkas, W.H., Dyer, J.N., Heckman, H.H.: Resolution of the Σ-mass anomaly. Phys. Rev. Lett. 11(1), 26–28 (1963)
- Andersen, H.H., Simonsen, H., Srensen, H.: An experimental investigation of chargedependent deviations from the Bethe stopping power formula. Nucl. Phys. A 125(1), 171– 175 (1969)
- 24. Ashley, J.C., Ritchie, R.H., Brandt, W.: z^3_1 effect in the stopping power of matter for charged particles. Phys. Rev. B 5(7), 2393–2397 (1972)
- 25. Lindhard, J.: The Barkas effect—or z_1^3 , z_1^4 -corrections to stopping of swift charged particles. Nucl. Instrum. Methods 132,1–5 (1976)
- Northcliffe, L.C.: Passage of heavy ions through matter. Ann. Rev. Nucl. Sci. 13(1), 67–102 (1963)
- Northcliffe, L.C.: Energy loss and effective charge of heavy ions in aluminum. Phys. Rev. 120(5), 1744–1757 (1960)
- 28. Yarlagadda, B.S., Robinson, J.E., Brandt, W.: Effective-charge theory and the electronic stopping power of solids. Phys. Rev. B 17(9), 3473–3483 (1978)
- 29. Brandt, W., Kitagawa, M.: Effective stopping-power charges of swift ions in condensed matter. Phys. Rev. B **25**(9), 5631–5637 (1982)
- Sigmund, P.: Charge-dependent electronic stopping of swift nonrelativistic heavy ions. Phys. Rev. A 56(5), 3781–3793 (1997)
- 31. Sigmund, P., Schinner, A.: Binary stopping theory for swift heavy ions. Eur. Phys. J. D At. Mol. Opt. Plasma Phys. **12**(3), 425–434
- 32. Sigmund, P., Schinner, A.: Binary theory of electronic stopping. Nucl. Instrum. Methods Phys. Res. Sect. B Beam Interact. Mater. Atoms **195**(1–2), 64–90 (2002)
- Grüner, F., Bell, F., Assmann, W., Schubert, M.: Integrated approach to the electronic interaction of swift heavy ions with solids and gases. Phys. Rev. Lett. 93(21), 213201 (2004)
- Grande, P.L., Schiwietz, G.: Impact-parameter dependence of the electronic energy loss of fast ions. Phys. Rev. A 58(5), 3796–3801 (1998)
- Schiwietz, G., Grande, P.L.: A unitary convolution approximation for the impact-parameter dependent electronic energy loss. Nucl. Instrum. Methods Phys. Res. Sect. B Beam Interact. Mater. Atoms 153(1–4), 1–9 (1999)
- 36. Schiwietz, G.: Coupled-channel calculation of stopping powers for intermediate energy light ions penetrating atomic H and He targets. Phys. Rev. A **42**(1), 296–306 (1990)
- Grande, P.L., Schiwietz, G.: The unitary convolution approximation for heavy ions. Nucl. Instrum. Methods Phys. Res. Sect. B Beam Interact. Mater. Atoms 195(1–2), 55–63 (2002)
- 38. Blazevic, A., Bohlen, H.G., von Oertzen, W.: Charge-state changing processes for Ne ions passing through thin carbon foils. Phys. Rev. A **61**(3), 32901 (2000)
- 39. Blazevic, A., Bohlen, H.G., von Oertzen, W.: Stopping power of swift neon ions in dependence on the charge state in the non-equilibrium regime. Nucl. Instrum. Methods Phys. Res. Sect. B Beam Interact. Mater. Atoms 190(1–4), 64–68 (2002)
- Baurichter, A., Sigmund, P., Srensen, A.H.: Panel discussion on stopping of heavy ions. Nucl. Instrum. Methods Phys. Res. Sect. B Beam Interact. Mater. Atoms 195(1–2), 224–231 (2002)
- 41. Lindhard, J., Scharff, M.: Energy loss in matter by fast particles of low charge. Matematisk Fysiske Meddelelser—Kongelige Danske Videnskabernes Selskab **27**(15), 1–31 (1953)
- Paul, H., Schinner, A.: An empirical approach to the stopping power of solids and gases for ions from ₃Li to ₁₈Ar. Nucl. Instrum. Methods Phys. Res. Sect. B Beam Interact. Mater. Atoms 179(3), 299–315 (2001)

References 63

 Paul, H., Schinner, A.: An empirical approach to the stopping power of solids and gases for ions from 3Li to 18Ar—Part II. Nucl. Instrum. Methods Phys. Res. Sect. B Beam Interact. Mater. Atoms 195(1–2), 166–174 (2002)

- Paul, H., Schinner, A.: Judging the reliability of stopping power tables and programs for heavy ions. Nucl. Instrum. Methods Phys. Res. Sect. B Beam Interact. Mater. Atoms 209, 252–258 (2003)
- 45. Firsov, O.B.: A quantitative interpretation of the mean electronic excitation energy in atomic collisions. Soviet Physics JETP **36**,1076 (1959)
- Lindhard, J., Scharff, M.: Energy dissipation by ions in the keV region. Phys. Rev. 124(1), 128–130 (1961)
- 47. Tilinin, I.S.: Quasiclassical expression for inelastic energy losses in atomic particle collisions below the bohr velocity. Phys. Rev. A **51**(4), 3058–3065 (1995)
- 48. Fermi, E., Teller, E.: The capture of negative mesotrons in matter. Phys. Rev. **72**(5), 399–408 (1947)
- 49. Lindhard, J.: On the properties of a gas of charged particles. Matematisk Fysiske Meddelelser—Kongelige Danske Videnskabernes Selskab 28(8), (1954)
- 50. Ritchie, R.H.: Interaction of charged particles with a degenerate Fermi–Dirac electron gas. Phys. Rev. 114(3),644–654 (1959)
- 51. Lindhard, J., Winther, A.: Stopping power of electron gas and equipartition rule. Matematisk Fysiske Meddelelser—Kongelige Danske Videnskabernes Selskab **34**(4),1–21 (1964)
- 52. Almbladh C.O., von Barth U., Popovic Z.D., Stott M.J. (1976) Screening of a proton in an electron gas. Phys. Rev. B **14**(6), 2250–2254 (1976)
- 53. Kohanoff, J.: Electronic Structure Calculations for Solids and Molecules: Theory and Computational Methods. Cambridge University Press, Cambridge, UK (2006)
- 54. Gross, E.K.U., Dobson, J.F., Petersilka, M.: Density Functional Theory of Time-Dependent Phenomena, volume 181 of Topics in Current Chemistry. Springer, Berlin (1996)
- Echenique, P.M., Nieminen, R.M., Ashley, J.C., Ritchie, R.H.: Nonlinear stopping power of an electron gas for slow ions. Phys. Rev. A 33(2), 897–904 (1986)
- Arista, N.R.: Energy loss of ions in solids: non-linear calculations for slow and swift ions. Nucl. Instrum. Methods Phys. Res. Sect. B Beam Interact. Mater. Atoms 195(1–2), 91–105 (2002)
- Campillo, I., Pitarke, J.M., Eguiluz, A.G.: Electronic stopping power of aluminum crystal. Phys. Rev. B 58(16), 10307–10314 (1998)
- Pitarke, J.M., Campillo, I.: Band structure effects on the interaction of charged particles with solids. Nucl. Instrum. Methods Phys. Res. Sect. B Beam Interact. Mater. Atoms 164– 165, 147–160 (2000)
- 59. Dorado, J.J., Flores, F.: Molecular-orbital theory for the stopping power of atoms in the low-velocity regime: the case of helium in alkali metals. Phys. Rev. A 47(4), 3062–3072 (1993)
- Grimvall, G.: The Electron-Phonon Interaction in Metals. North-Holland Publishing Company, Oxford, UK (1981)
- 61. Ziman, J.M.: Electrons and Phonons. Oxford University Press, Oxford, UK (2001)
- 62. Flynn, C.P., Averback, R.S.: Electron-phonon interactions in energetic displacement cascades. Phys. Rev. B **38**(10), 7118–7120 (1988)
- 63. Ashcroft, N.W., Mermin, N.D.: Solid State Physics, pp. 52. Thomson, Toronto (1976)
- 64. Finnis, M.W., Agnew, P., Foreman, A.J.E.: Thermal excitation of electrons in energetic displacement cascades. Phys. Rev. B **44**(2), 567–574 (1991)
- Allen, P.B.: Theory of thermal relaxation of electrons in metals. Phys. Rev. Lett. 59 (13), 1460–1463 (1987)
- 66. Kaganov, M.I., Lifshitz, I.M., Tanatorov, L.V.: Relaxation between electrons and the crystalline lattice. J. Exp. Theor. Phys. 4(2), 173–178 (1956)
- 67. Messiah, A.: Quantum Mechanics. Dover Publications, Mineola, NY (1999)
- 68. Gao, F., Bacon, D.J., Flewitt, P.E.J., Lewis, T.A.: The effects of electron–phonon coupling on defect production by displacement cascades in α -iron. Model. Simul. Mater. Sci. Eng. 6(5), 543–556 (1998)

- Wang, Z.G., Dufour, C., Paumier, E., Toulemonde, M.: The Se sensitivity of metals under swift-heavy-ion irradiation: a transient thermal process. J. Phys. Condens. Matter 6(34), 6733–6750 (1994)
- Race, C.P., Mason, D.R., Sutton, A.P.: Electronic excitations and their effect on the interionic forces in simulations of radiation damage in metals. J. Phys. Condens. Matter 21(11), 115702
- Qiu, T.Q., Tien, C.L.: Short-pulse laser heating on metals. Int. J. Heat Mass Transf. 35(3), 719–726 (1992)
- Brorson, S.D., Kazeroonian, A., Moodera, J.S., Face, D.W., Cheng, T.K., Ippen, E.P., Dresselhaus, M.S., Dresselhaus, G.: Femtosecond room-temperature measurement of the electron-phonon coupling constant λ in metallic superconductors. Phys. Rev. Lett. 64(18), 2172–2175 (1990)
- Elsayed-Ali, H.E., Norris, T.B., Pessot, M.A., Mourou, G.A.: Time-resolved observation of electron-phonon relaxation in copper. Phys. Rev. Lett. 58(12),1212–1215 (1987)
- Bennemann, K.H.: Ultrafast dynamics in solids. J. Phys. Condens. Matter 16(30), R995– R1056 (2004)
- 75. Yoshida M.: Distribution of interstitials and vacancies produced by an incident and fast neutron. J. Phys. Soc. Jpn. **16**(1), 44–50 (1961)
- Oen, O.S., Holmes, D.K., Robinson, M.T.: Ranges of energetic atoms in solids. J. Appl. Phys. 34(2), 302–312 (1963)
- Oen, O.S., Robinson, M.T.: Monte carlo range calculations for a Thomas–Fermi potential.
 J. Appl. Phys. 35(8), 2515–2521 (1964)
- 78. Beeler, J.R., Besco, D.G.: Range and damage effects of tunnel trajectories in a wurtzite structure. J. Appl. Phys. **34**(9), 2873–2878 (1963)
- Robinson, M.T., Oen, O.S.: The channeling of energetic atoms in crystal lattices. Appl. Phys. Lett. 2(2), 30–32 (1963)
- 80. Robinson, M.T., Ordean, S.O.: Computer studies of the slowing down of energetic atoms in crystals. Phys. Rev. **132**(6), 2385–2398 (1963)
- 81. Piercy, G.R., Brown, F., Davies, J.A., McCargo, M.: Experimental evidence for the increase of heavy ion ranges by channeling in crystalline structure. Phys. Rev. Lett. **10**(9), 399–400 (1963)
- 82. Robinson, M.T., Torrens, I.M.: Computer simulation of atomic-displacement cascades in solids in the binary-collision approximation. Phys. Rev. B **9**(12), 5008–5024 (1974)
- 83. Beeler, J.R.: Vacancy and interstitial cluster production in neutron-irradiated α-iron. J. Appl. Phys. **37**(8), 3000–3009 (1966)
- Beeler, J.R.: Primary damage state in neutron-irradiated iron. J. Appl. Phys. 35(7), 2226– 2236 (1964)
- 85. Beeler, J.R.: Displacement spikes in cubic metals. I. α-Iron, copper, and tungsten. Phys. Rev. **150**(2), 470–487 (1966)
- Gibson, J.B., Goland, A.N., Milgram, M., Vineyard, G.H.: Dynamics of radiation damage. Phys. Rev. 120(4), 1229–1253 (1960)
- 87. Malerba, L.: Molecular dynamics simulation of displacement cascades in Fe: a critical review. J. Nucl. Mater. **351**(1–3), 28–38 (2006)
- 88. Diaz de la Rubia, T.: Irradiation-induced defect production in elemental metals and semiconductors: a review of recent molecular dynamics studies. Ann. Rev. Mater. Sci. 26, 613–649 (1996)
- 89. Nordlund, K., Ghaly, M., Averback, R.S., Caturla, M., Diaz de la Rubia, T., Tarus, J.: Defect production in collision cascades in elemental semiconductors and fcc metals. Phys. Rev. B *57*(13), 7556–7570 (1998)
- 90. Nordlund, K., Ghaly, M., Averback, R.S.: Mechanisms of ion beam mixing in metals and semiconductors. J. Appl. Phys. 83(3), 1238–1246 (1998)
- 91. Nordlund, K., Wei, L., Zhong, Y., Averback, R.S.: Role of electron-phonon coupling on collision cascade development in Ni, Pd, and Pt. Phys. Rev. B **57**(22), R13965–R3968 (1998)

References 65

 Zhong, Y., Nordlund, K., Ghaly, M., Averback, R.S.: Defect production in tungsten: a comparison between field-ion microscopy and molecular-dynamics simulations. Phys. Rev. B 58(5), 2361–2364 (1998)

- Kapinos, V.G., Bacon, D.J.: Influence of ion-electron interaction on the formation mechanism of depleted zones in displacement cascades in metals. Phys. Rev. B 50(18), 13194–13203 (1994)
- Caro, A., Victoria, M.: Ion–electron interaction in molecular-dynamics cascades. Phys. Rev. A 40(5), 2287–2291 (1989)
- 95. Finnis, M.W.: Interatomic Forces in Condensed Matter. Oxford Materials. Oxford University Press, Oxford (2003)
- 96. Kitagawa, M., Ohtsuki, Y.H.: Inelastic scattering of slow ions in channeling. Phys. Rev. B **9**(11), 4719–4723 (1974)
- 97. Echenique, P.M., Nieminen, R.M., Ritchie, R.H.: Density functional calculation of stopping power of an electron gas for slow ions. Solid State Commun. 37(10), 779–781 (1981)
- Prönnecke, S., Caro, A., Victoria, M., Diaz de la Rubia, T., Guinan, M.W.: The effect of electronic energy loss on the dynamics of thermal spikes in Cu. J. Mater. Res. 6(3), 483–491 (1991)
- Duffy, D.M., Rutherford, A.M.: Including the effects of electronic stopping and electronic in interactions in radiation damage simulations. J. Phys. Condens. Matter 19(1), 016207 (2007)
- 100. Duffy, D.M., Itoh, N., Rutherford, A.M., Stoneham, A.M.: Making tracks in metals. J. Phys. Condens. Matter 20(8), 082201 (2008)
- Rutherford, A.M., Duffy, D.M.: The effect of electron-ion interactions on radiation damage simulations. J. Phys. Condens. Matter 19(49), 496201 (2007)
- 102. Ivanov, D.S., Zhigilei, L.V.: Combined atomistic-continuum modeling of shortpulse laser melting and disintegration of metal films. Phys. Rev. B 68(6), 64114 (2003)
- Ivanov, D.S., Zhigilei, L.V.: Kinetic limit of heterogeneous melting in metals. Phy. Rev. Lett. 98(19), 195701 (2007)
- Duvenbeck, A., Sroubek, Z., Wucher, A.: Electronic excitation in atomic collision cascades.
 Nucl. Instrum. Methods Phys. Res. Sect. B Beam Interact. Mater. Atoms 228(1–4), 325–329 (2005)
- 105. Duvenbeck, A., Sroubek, F., Sroubek, Z., Wucher, A.: Computer simulation of low-energy electronic excitations in atomic collision cascades. Nucl. Instrum. Methods Phys. Res. Sect. B Beam Interact. Mater. Atoms 225(4), 464–477 (2004)
- Duvenbeck, A., Wucher, A.: Low-energy electronic excitation in atomic collision cascades: a nonlinear transport model. Phys. Rev. B (Condens. Matter Mater. Phys.) 72(16), 165408, 2005
- 107. Horsfield, A.P., Bowler, D.R., Fisher, A.J., Todorov, T.N., Sanchez, C.G.: Correlated electron–ion dynamics: the excitation of atomic motion by energetic electrons. J. Phys. Condens. Matter 17, 4793–4812 (2005)
- Horsfield, A.P., Bowler, D.R., Fisher, A.J., Todorov, T.N., Sanchez, C.: Beyond Ehrenfest: correlated non-adiabatic molecular dynamics. J. Phys. Condens. Matter 16(46), 8251–8266 (2004)
- 109. McEniry, E.J., Bowler, D.R., Dundas, D., Horsfield, A.P., Sánchez, C.G., Todorov, T.N.: Dynamical simulation of inelastic quantum transport. J. Phys. Condens. Matter 19, 196201 (2007)
- 110. McEniry, E.J., Frederiksen, T., Todorov, T.N., Dundas, D., Horsfield, A.P.: Inelastic quantum transport in nanostructures: the self-consistent born approximation and correlated electron-ion dynamics. Phys. Rev. B 78, 35446 (2008)
- 111. Stella, L., Meister, M., Fisher, A.J., Horsfield, A.P.: Robust non-adiabatic molecular dynamics for metals and insulator. J. Phys. Chem. 127, 214104 (2007)
- 112. Pruneda, J.M., Sanchez-Portal, D., Arnau, A., Juaristi, J.I., Artacho, E.: Electronic stopping power in LiF from first principles. Phys. Rev. Lett. **99**(23), 235501 (2007)
- 113. Joubert, D. (ed.): Density Functionals: Theory and Applications. Springer, Berlin (1997)

- 114. Auth, C., Mertens, A., Winter, H., Borisov, A. (1998) Threshold in the stopping of slow protons scattered from the surface of a wide-band-gap insulator. Phys. Rev. Lett. **81**(22), 4831–1834 (1998)
- 115. Draxler, M., Chenakin, S.P., Markin, S.N., Bauer, P.: Apparent velocity threshold in the electronic stopping of slow hydrogen ions in LiF. Phys. Rev. Lett. **95**(11), 113201 (2005)
- 116. Markin, S.N., Primetzhofer, D., Bauer, P.: Vanishing electronic energy loss of very slow light ions in insulators with large band gaps. Phys. Rev. Lett. **103**(11), 113201 (2009)
- 117. Tsolakidis, A., Sánchez-Portal, D., Martin, R.M.: Calculation of the optical response of atomic clusters using time-dependent density functional theory and local orbitals. Phys. Rev. B **66**(23), 235416 (2002)
- 118. Artacho, E.: Electronic stopping in insulators: a simple model. J. Phys. Condens. Matter 19(27), 275211 (2007)

Chapter 4 Theoretical Background

4.1 Overview

Our brief survey in Chap. 3 lays out the current state of the art in atomistic simulations of radiation damage. The best models available for large-scale simulations, where by "best" we mean "having thrown away the least physics", are augmented classical molecular dynamics models. In classical MD only the nuclei are treated dynamically, with positions and momenta evolved according to Newton's equations. The electrons are thrown away completely and their influence on the ionic motion is added back in piecemeal to account for various effects of the true electron—ion interaction.

Ordinary classical MD takes account of the largest of these effects: the action of the electrons to provide bonding interactions between the nuclei is included in the classical potentials in which the ions move. Models such as those of Bacon et al. [1, 2, 3] and Nordlund et al. [4] include the additional effect of energy loss from the ions to the electrons by adding a dissipative drag force to the ionic equations of motion. Caro and Victoria [5] and Duffy et al. [6–8] go further still by allowing for the reverse transfer of energy with a stochastic force term, thereby treating the electrons as a heat bath, influencing ionic motion via the Langevin equations.

The alternative to throwing away the electrons and then imposing their effects as some set of external influences on the ion dynamics is to leave them in the dynamical system in the first place. Whether or not we can achieve superior results with such an approach depends, of course, on the details of any proposed model. But the potential for improvement is clear for four reasons:

- 1. The electrons are quantum mechanical;
- 2. The electronic subsystem has a detailed structure—the *electronic structure*;
- 3. This electronic structure depends in detail on the state of the ionic subsystem; and.

4. The state of the electronic system depends on its own history and on that of the ionic subsystem.

In accounting for the bonding effect of electrons, ordinary MD, in not too extreme a circumstance, can do quite a good job. Potentials such as the Finnis—Sinclair potential take account of the electronic structure in the second-moment approximation and incorporate a dependence of the electronic structure on the nearest-neighbour environment of each ion. Attempts to capture the exchange of energy between ions and electrons do less well in addressing the above four issues. In fact, only the local electron density dependent model of Caro and Victoria [5] takes any account of electronic structure and its dependence on the atomic environment in determining the strength of the drag force.

The first point, that the electrons are quantum mechanical, is the hardest to interpret. There is no doubt that at typical metallic electron densities a 'correct' description of the electronic subsystem must be quantum mechanical, whereas a classical description of the ionic subsystem will have broad validity. But ultimately our interest in studying radiation damage is in the state of the ionic system, specifically in the residual defect populations. We have no reason to expect in advance that the full effect of the electrons on ionic motion cannot be adequately represented via some set of classical degrees of freedom. Equally, however, we have no reason to expect that it can.

Our intention in developing a more sophisticated model of coupled electronic and ionic dynamics is therefore to explore the phenomena that arise due to energy exchange processes in radiation damage simulations. Our results will allow us to test the validity of the simpler classical models, to propose improved ways of capturing electronic effects with classical degrees of freedom in an MD simulation and maybe to predict new features in the system dynamics. In the rest of this chapter we will describe the theory that underpins our chosen model. We will explain what physics is thrown away at each point in the chain of approximations that gives rise to the final form of the model. Only by understanding what is and what is not accounted for in the dynamics of our system can we hope to correctly interpret our simulation results.

We will begin by looking ahead with a brief description of our model system, which we will define via a 'recipe', starting with a full quantum mechanical description of the combined system of ions and electrons and gradually paring it back via a series of approximations. Each stage in the process will be discussed in full later in the chapter, whereupon the various approximations will be motivated pragmatically (we need to arrive at a tractable set of equations for our chosen application) and justified physically (we must not throw out the baby with the bathwater):

- 1. We begin with a set of non-relativistic quantum mechanical nuclei and electrons evolving via the time-dependent Schrödinger equation under a fully interacting Hamiltonian.
- 2. We make the semi-classical approximation, choosing to treat the nuclei as classical particles, interacting with quantum mechanical electrons.

4.1 Overview 69

We make the single-particle approximation, treating a set of non-interacting electrons.

- 4. We adopt a particularly simple tight-binding description of the electronic system.
- 5. We adopt Ehrenfest dynamics as the description of the evolution of our semiclassical system.

We will now discuss the above process in detail, and at the end of the chapter we will consider what we are left with and what we might legitimately be able to do with it.

4.2 The Semi-Classical Approximation

Let us begin by considering the participants in a radiation damage event: a set of N_n nuclei of masses $\{M_I\}_{I=1}^{N_n}$ and atomic numbers $\{Z_I\}_{I=1}^{N_n}$ and a set of N_e electrons of masses m_e . The positions and momenta of the nuclei will be described by position and momentum operators $\{\hat{\mathbf{R}}_I\}_{I=1}^{N_n}$ and $\{\hat{\mathbf{P}}_I\}_{I=1}^{N_n}$ respectively and those of the electrons by $\{\hat{\mathbf{r}}_i\}_{I=1}^{N_e}$ and $\{\hat{\mathbf{p}}_i\}_{I=1}^{N_e}$ respectively. Within non-relavistic quantum mechanics, such a system is fully described by a many-body state vector $|\Phi(t)\rangle$ evolving under a Hamiltonian \hat{H} via the time-dependent Schrödinger equation (TDSE),

$$i\hbar \frac{\partial}{\partial t} |\Phi(t)\rangle = \hat{H} |\Phi(t)\rangle,$$
 (4.1)

where we define \hat{H} :

$$\hat{H} \equiv \hat{T}_{n}(\{\hat{\mathbf{p}}_{I}\}) + \hat{T}_{e}(\{\hat{\mathbf{p}}_{i}\}) + \hat{V}_{nn}(\{\hat{\mathbf{R}}_{I}\}) + \hat{V}_{ee}(\{\hat{\mathbf{r}}_{i}\}) + \hat{V}_{ne}(\{\hat{\mathbf{R}}_{I}\}, \{\hat{\mathbf{r}}_{i}\}).$$
(4.2)

The various operators are the nuclear kinetic energy,

$$\hat{T}_{\rm n} \equiv \sum_{I}^{N_{\rm n}} \frac{\hat{\mathbf{P}}_{I}^{2}}{2M_{I}},\tag{4.3}$$

the electronic kinetic energy,

$$\hat{T}_{\rm e} \equiv \sum_{i}^{N_{\rm e}} \frac{\hat{\mathbf{p}}_{i}^{2}}{2m_{\rm e}},\tag{4.4}$$

the nuclear-nuclear interaction, 1

$$\hat{V}_{\rm nn} \equiv \frac{1}{2} \sum_{I,J \neq I}^{N_{\rm n}} \frac{Z_I Z_J}{|\hat{\mathbf{R}}_I - \hat{\mathbf{R}}_J|},\tag{4.5}$$

the electron-electron interaction,

$$\hat{V}_{\text{ee}} \equiv \frac{1}{2} \sum_{i \neq j}^{N_{\text{e}}} \frac{1}{|\hat{\mathbf{r}}_i - \hat{\mathbf{r}}_j|},\tag{4.6}$$

and the electron-nuclear interaction,

$$\hat{V}_{\text{ne}} \equiv -\sum_{I}^{N_{\text{n}}} \sum_{i}^{N_{\text{e}}} \frac{Z_{I}}{|\hat{\mathbf{r}}_{i} - \hat{\mathbf{R}}_{I}|}.$$

$$(4.7)$$

The subscripts n and e indicate that an operator acts on the nuclear subspace \mathcal{W}_n or electronic subspace \mathcal{W}_e of the Hilbert space $\mathcal{W}=\mathcal{W}_n\otimes\mathcal{W}_e$ of the combined system, respectively.

Numerical solution of (4.1) for more than a few interacting particles is utterly intractable and we must make approximations to proceed. It would be helpful if we could reduce the size of the quantum mechanical problem that we need to solve. The nuclei are relatively massive and so we might hope that we can treat them as classical particles. We will follow the approach of Todorov [9] to derive the equations of motion of a set of classical nuclei and quantum mechanical electrons. The assumptions that we have to make along the way will quantify the validity of this so-called *semi-classical approximation*.

4.2.1 The Ehrenfest Approximation

We will begin by considering the behaviour of the expectation of the nuclear positions and momenta,

$$\langle \hat{\mathbf{R}}_I \rangle \equiv \langle \Phi(t) | \hat{\mathbf{R}}_I | \Phi(t) \rangle,$$
 (4.8)

$$\langle \hat{\mathbf{P}}_I \rangle \equiv \langle \Phi(t) | \hat{\mathbf{P}}_I | \Phi(t) \rangle,$$
 (4.9)

in anticipation of being able to identify these with the positions $\{\mathbf{R}_I\}_{I=1}^{N_n}$ and momenta $\{\mathbf{P}_I\}_{I=1}^{N_n}$ of a set of classical nuclei. The time derivative of the expectation of a nuclear position is given by

¹ Throughout this chapter, we will leave factors of $e^2/4\pi\varepsilon_0$ implicit in electrostatic terms.

$$\frac{\mathrm{d}}{\mathrm{d}t}\langle\hat{\mathbf{R}}_{I}\rangle = \frac{1}{i\hbar}\langle[\hat{\mathbf{R}}_{I},\hat{H}]\rangle = \langle\nabla_{\hat{\mathbf{P}}_{I}}\hat{H}\rangle,\tag{4.10}$$

where the first equality is proved in Sect. 13.1.1 and the second in Sect. 13.1.2. Here $\nabla_{\hat{\mathbf{P}}_I}$ represents $\sum_{\eta=1}^3 (\partial/\partial \hat{P}_{I,\eta}) \eta$ where $\hat{P}_{I,\eta}$ is the η th cartesian component of the momentum operator of the Ith nucleus and η is the unit vector in the η th direction. The only term in \hat{H} to depend explicitly on the nuclear momenta is \hat{T}_n and so the evolution of the expectation of the nuclear positions is given by,

$$\frac{\mathrm{d}}{\mathrm{d}t}\langle\hat{\mathbf{R}}_{I}\rangle = \frac{1}{M_{I}}\langle\hat{\mathbf{P}}_{I}\rangle. \tag{4.11}$$

Similarly, the time derivative of the expectation of a nuclear momentum is given by (see Sects. 13.1.1 and 13.1.3 for proofs),

$$\frac{\mathrm{d}}{\mathrm{d}t}\langle\hat{\mathbf{P}}_{I}\rangle = \frac{1}{\mathrm{i}\hbar}\langle[\hat{\mathbf{P}}_{I},\hat{H}]\rangle = -\langle\nabla_{\hat{\mathbf{R}}_{I}}\hat{H}\rangle,\tag{4.12}$$

with $\nabla_{\hat{\mathbf{R}}_I} = \sum_{\eta=1}^3 (\partial/\partial \hat{R}_{I,i}) \boldsymbol{\eta}$. Whereas (4.11) admits an immediate classical interpretation if we identify $\langle \hat{\mathbf{R}}_I \rangle$ and $\langle \hat{\mathbf{P}}_I \rangle$ with classical coordinates \mathbf{R}_I and \mathbf{P}_I respectively, the more complicated dependence of \hat{H} on $\langle \hat{\mathbf{R}}_I \rangle$ obscures any such correspondence in (4.12).

Taken together the exact equations (4.11) and (4.12) represent the *Ehrenfest theorem*. To go further we must now make the *Ehrenfest approximation*. The idea is as follows: we assume that the wavefunction $|\Phi(t)\rangle$ is of such a form that the spread in the positions of the nuclei is small enough that the approximation,

$$\langle F(\{\langle \hat{\mathbf{R}}_I \rangle\}, \{\hat{\mathbf{r}}_i\}) \rangle = \langle F(\{\langle \hat{\mathbf{R}}_I \}, \{\hat{\mathbf{r}}_i\}) \rangle$$
(4.13)

is valid for a function F of the nuclear and electronic position operators. In that case we can write

$$\frac{\mathrm{d}}{\mathrm{d}t}\langle \hat{\mathbf{P}}_I \rangle = -\langle \nabla_{\langle \hat{\mathbf{R}}_I \rangle} \hat{H}(\{\langle \hat{\mathbf{R}}_J \rangle\}) \rangle. \tag{4.14}$$

Only the operators $\hat{V}_{nn}(\{\hat{\mathbf{R}}_I\})$ and $\hat{V}_{ne}(\{\hat{\mathbf{R}}_I\}, \{\hat{\mathbf{r}}_i\})$ depend explicitly on $\hat{\mathbf{R}}_I$. Using (4.14) we can clearly replace the expectation of the term in \hat{V}_{nn} with the gradient of a classical potential,

$$\langle \nabla_{\hat{\mathbf{R}}_{J}} \hat{V}_{nn}(\{\langle \hat{\mathbf{R}}_{J} \rangle\}) \rangle = \nabla_{\mathbf{R}_{J}} V_{nn}(\{\mathbf{R}_{J}\}), \tag{4.15}$$

where,

$$V_{\rm nn} \equiv \frac{1}{2} \sum_{I \neq J}^{N_{\rm n}} \frac{Z_I Z_J}{|\mathbf{R}_I - \mathbf{R}_J|}.$$
 (4.16)

It is not possible to directly replace the term in $\hat{V}_{ne}(\{\hat{\mathbf{R}}_I\}, \{\hat{\mathbf{r}}_i\})$ with a potential $V_{ne}(\{\mathbf{R}_I\}, \{\hat{\mathbf{r}}_i\})$ because of the dependence on the electronic position operators. However, if we rewrite (4.7) as,

$$\hat{V}_{\text{ne}}(\{\hat{\mathbf{R}}_I\}, \{\hat{\mathbf{r}}_i\}) \equiv \sum_{I}^{N_n} \sum_{i}^{N_e} \int d\mathbf{r} \, \delta(\mathbf{r} - \hat{\mathbf{r}}_i) \hat{\mathcal{V}}_I(\mathbf{r}, \hat{\mathbf{R}}_I), \tag{4.17}$$

where we have defined,

$$\hat{\mathcal{V}}_I(\mathbf{r}, \hat{\mathbf{R}}_I) \equiv -\frac{Z_I}{|\mathbf{r} - \hat{\mathbf{R}}_I|},\tag{4.18}$$

then,

$$\langle \hat{V}_{\text{ne}} \rangle = \sum_{I=1}^{N_n} \int d\mathbf{r} \langle \hat{\rho}(\mathbf{r}) \hat{\mathcal{V}}(\mathbf{r}, \hat{\mathbf{R}}_I) \rangle,$$
 (4.19)

where $\hat{\rho}(\mathbf{r})$ is the electronic number density operator,

$$\hat{\rho}(\mathbf{r}) = \sum_{i} \delta(\mathbf{r} - \hat{\mathbf{r}}_{i}). \tag{4.20}$$

Using (4.14) we then have,

$$\langle \nabla_{\langle \hat{\mathbf{R}}_I \rangle} \hat{V}_{\text{ne}}(\{\langle \hat{\mathbf{R}}_J \rangle\}, \{\hat{\mathbf{r}}_i\}) \rangle = \int d\mathbf{r} \rho(\mathbf{r}) \nabla_{\mathbf{R}_I} \mathcal{V}_I(\mathbf{r}, \mathbf{R}_I), \tag{4.21}$$

where $\rho(\mathbf{r}) = \langle \hat{\rho}(\mathbf{r}) \rangle$ and we have written $\mathcal{V}_I(\mathbf{r}, \mathbf{R}_I) = -Z_I/|\mathbf{r} - \mathbf{R}_I|$ to make clear that $\mathcal{V}_I(\mathbf{r}, \mathbf{R}_I)$ is a simple function rather than an operator on the nuclear subspace.

If we identify the expectation of the nuclear position and momentum operators with the coordinates of a classical particle, we can now write, from (4.12), (4.15) and (4.21),

$$\frac{\mathrm{d}}{\mathrm{d}t}\mathbf{P}_{I} = -\nabla_{\mathbf{R}_{I}}V_{\mathrm{nn}}(\{\mathbf{R}_{J}\}) - \int \mathrm{d}\mathbf{r}\rho(\mathbf{r})\nabla_{\mathbf{R}_{I}}V_{I}(\mathbf{r},\mathbf{R}_{I})$$
(4.22)

and from (4.11)

$$\frac{\mathrm{d}}{\mathrm{d}t}\mathbf{R}_{I} = \frac{1}{M_{I}}\mathbf{P}_{I}.\tag{4.23}$$

These equations represent the Ehrenfest approximation for the motion of a set of classical particles coupled to a set of quantum mechanical electrons via the potentials $V_I(\mathbf{r}, \mathbf{R}_I)$.

To complete our definition of the dynamics of a semi-classical system we need an equation for the evolution of the quantum mechanical electrons. In the fully quantum system this is obtained from the full state vector evolved under the full Hamiltonian,

$$i\hbar \frac{\partial}{\partial t} |\Phi(t)\rangle = \hat{H} |\Phi(t)\rangle.$$
 (4.24)

For the semi-classical system, we might hope that the evolution of an electronic state vector $|\Psi^{\rm I}(t)\rangle$, defined on the sub-space $\mathcal{W}_{\rm e}$ and where 'I' indicates we are dealing with a many-body state for interacting electrons, under an electronic Hamiltonian $\hat{H}_{\rm e}(\{\hat{\mathbf{r}}_i\}, \{\hat{\mathbf{p}}_i\}, \{\mathbf{R}_I\})$,

$$i\hbar \frac{\partial}{\partial t} |\Psi^{I}(t)\rangle = \hat{H}_{e} |\Psi^{I}(t)\rangle,$$
 (4.25)

would do the job. The most obvious choice for the form of \hat{H}_e is,

$$\hat{H}_{e}(\{\hat{\mathbf{r}}_{i}\}, \{\hat{\mathbf{p}}_{i}\}, \{\mathbf{R}_{I}(t)\}) = \hat{T}_{e}(\{\hat{\mathbf{p}}_{i}\}) + \hat{V}_{ee}(\{\hat{\mathbf{r}}_{i}\}) + \hat{V}_{ne}'(\{\hat{\mathbf{r}}_{i}\}, \{\mathbf{R}_{I}(t)\}), \quad (4.26)$$

where we have introduced an operator for the electron-nuclear interaction,

$$\hat{V}'_{\text{ne}}(\{\hat{\mathbf{r}}_i\}, \{\mathbf{R}_I(t)\}) \equiv -\sum_{I}^{N_n} \sum_{i}^{N_e} \frac{Z_I}{|\hat{\mathbf{r}}_i - \mathbf{R}_I|}$$

$$= \sum_{I}^{N_n} \sum_{i}^{N_e} \int d\mathbf{r} \delta(\mathbf{r} - \hat{\mathbf{r}}_i) \mathcal{V}_I(\mathbf{r}, \mathbf{R}_I)$$

$$= \sum_{i}^{N_e} \int d\mathbf{r} \delta(\mathbf{r} - \hat{\mathbf{r}}_i) V_{\text{ne}}(\mathbf{r}, \mathbf{R}),$$
(4.27)

which operates only on the electronic subspace W_e and we have defined $V_{\rm ne}({\bf r},{\bf R}) \equiv \sum_I \mathcal{V}_I({\bf r},{\bf R}_I)$. The desired property of $|\Psi^I(t)\rangle$ is that for any electronic operator $\hat{A}_e(\{\hat{\bf r}_i\},\{\hat{\bf p}_i\})$, the expectation obeys,

$$\langle \Psi^{I}(t)|\hat{A}_{e}|\Psi^{I}(t)\rangle = \langle \Phi(t)|\hat{A}_{e}|\Phi(t)\rangle,$$
 (4.28)

where we are necessarily assuming that at some initial time t_0 , $|\Phi(t_0)\rangle$ can be written as a direct product of an electronic state $|\Psi^{\rm T}(t_0)\rangle$ and a nuclear state $|\chi(t_0)\rangle$,

$$|\Phi(t_0)\rangle = |\chi(t_0)\rangle \otimes |\Psi'^{\mathrm{I}}(t_0)\rangle,$$
 (4.29)

and,

$$|\Psi^{\prime I}(t_0) = |\Psi^{I}(t_0)\rangle. \tag{4.30}$$

That (4.28) holds is proved in Sect. 13.1.4 following Todorov [9].

We now have a closed set of equations for the evolution of a set of classical ions and quantum mechanical electrons:

$$\frac{\mathrm{d}}{\mathrm{d}t}\mathbf{R}_{I} = \frac{1}{M_{I}}\mathbf{P}_{I},\tag{4.23}$$

$$\frac{\mathrm{d}}{\mathrm{d}t}\mathbf{P}_{I} = -\nabla_{\mathbf{R}_{I}}V_{\mathrm{nn}}(\{\mathbf{R}_{J}\}) - \int \mathrm{d}\mathbf{r}\rho(\mathbf{r})\nabla_{\mathbf{R}_{I}}\mathcal{V}_{I}(\mathbf{r},\mathbf{R}_{I}), \tag{4.22}$$

$$i\hbar \frac{\partial}{\partial t} |\Psi^{I}(t)\rangle = \hat{H}_{e} |\Psi^{I}(t)\rangle,$$
 (4.25)

$$\hat{H}_{e}(\{\hat{\mathbf{r}}_{i}\}, \{\hat{\mathbf{p}}_{i}\}, \{\mathbf{R}_{I}(t)\}) = \hat{T}_{e}(\{\hat{\mathbf{p}}_{i}\}) + \hat{V}_{ee}(\{\hat{\mathbf{r}}_{i}\}) + \hat{V}'_{ne}(\{\hat{\mathbf{r}}_{i}\}, \{\mathbf{R}_{I}(t)\}). \tag{4.26}$$

We will refer to the dynamics defined by the above equations as *Ehrenfest dynamics*.

4.2.2 The Approximations in Ehrenfest Dynamics

In deriving the equations of Ehrenfest dynamics we made the Ehrenfest approximation for the expectation of a function $F(\{\hat{\mathbf{R}}_I\}, \{\hat{\mathbf{r}}_i\})$:

$$\langle F(\{\hat{\mathbf{R}}_I\}, \{\hat{\mathbf{r}}_i)\} = \langle F(\{\langle \hat{\mathbf{R}}_I \rangle\}, \{\hat{\mathbf{r}}_i\}) \rangle. \tag{4.13}$$

If we make a parallel assumption about a function $G(\{\hat{\mathbf{P}}_I\})$ of the nuclear momenta,

$$\langle G(\{\hat{\mathbf{P}}_I\})\rangle = \langle G(\{\langle \hat{\mathbf{P}}_I \rangle\}\rangle,$$
 (4.31)

then we can write down a semi-classical expression for the total energy of the system,

$$E_{SC}(t) \equiv \langle \Psi^{I}(t)|\hat{H}_{e}|\Psi^{I}(t)\rangle + T_{n}(\{\mathbf{P}_{I}\}) + V_{nn}(\{\mathbf{R}_{I}\}), \tag{4.32}$$

where,

$$T_{\rm n}(\{\mathbf{P}_I\}) = \sum_{I}^{N_{\rm n}} \frac{1}{2M_I} (\mathbf{P}_I(t))^2.$$
 (4.33)

We hope that this will remain a good approximation to the energy of the true fully quantum system throughout a simulation,

$$E_{\rm SC} \approx \langle \Phi(t)|\hat{H}|\Phi(t)\rangle.$$
 (4.34)

Differentiating E_{SC} with respect to time shows that the nuclear forces (4.22) in Ehrenfest dynamics give energy conservation, $dE_{SC}/dt = 0$. We consider the conservation of the semi-classical energy further in Sect. 4.5.

So in order to arrive at our semi-classical dynamics we have assumed:

- 1. $\langle F(\{\hat{\mathbf{R}}_I\}, \{\hat{\mathbf{r}}_i\}) \rangle = \langle F(\{\langle \hat{\mathbf{R}}_I \rangle\}, \{\hat{\mathbf{r}}_i\}) \rangle$, for $F = V_{\rm nn}, \mathcal{V}_I$, essentially that the nuclear wavefunctions are narrow on the scale of the variation of $V_{\rm nn}$ and \mathcal{V}_I , and,
- 2. $\langle G(\{\hat{\mathbf{P}}_I\}) \rangle = \langle G(\{\langle \hat{\mathbf{P}}_I \rangle \}) \rangle$, that the relative spread (the uncertainty) in the momentum is small.

Since the spatial variation of the electron–nuclear interaction will be on the scale of the atomic spacing, a, the first condition requires a spread in the nuclear wavefunctions $\Delta R_I = [\langle \hat{\mathbf{R}}_I^2 \rangle - \langle \hat{\mathbf{R}}_I \rangle^2]^{1/2}$ of

$$\Delta R_I \ll a. \tag{4.35}$$

The second condition demands an uncertainty in the momentum, ΔP_I , that is small compared to $\langle \hat{\mathbf{P}}_I \rangle$. For an atom with kinetic energy \mathcal{T} , this implies

$$\left(\Delta P_I = \frac{\hbar}{\Delta R_I}\right) \ll \left(P_I = \sqrt{2M_I T}\right). \tag{4.36}$$

Hence,

$$\frac{\hbar}{\sqrt{2M_IT}} \ll \Delta R_I \ll a. \tag{4.37}$$

Since a will typically be of the order of angstroms and a thermal estimate of the kinetic energy, $T \sim k_{\rm B}T_{\rm I}$, where $T_{\rm I}$ is the temperature of the nuclei, gives a lower bound of 3.6×10^{-12} m at $T_{\rm I} = 300$ K for copper, a value of $\Delta R \sim 10^{-11}$ m satisfies both conditions. Todorov [9] notes that Mittleman [10] gives an expression for the growth in the spread of a nuclear wave-packet in time,

$$\Delta R(t) = \left[(\Delta R(t_0))^2 + \frac{\hbar^2}{4M_I^2} \frac{t^2}{(\Delta R(t_0))^2} \right]^{1/2}.$$
 (4.38)

This predicts that the nuclear wave-functions will retain an initial spread $\sim 10^{-11}$ m on picosecond time-scales.

4.3 The Independent Electron Approximation

In Sect. 4.2 we demonstrated how a system of interacting quantum mechanical electrons and nuclei could be approximated by a system of quantum mechanical electrons interacting with classical ions. The ionic dynamics is now easy to handle, but solving for the electronic dynamics is still a formidable task. In any case, we must solve the electronic problem in order to calculate the electronic forces on the ions. The electrons are still represented by a many-body state, $|\Psi^{I}(t)\rangle$, evolving under the electronic Hamiltonian \hat{H}_{e} , defined in (4.26),

$$i\hbar \frac{\partial}{\partial t} |\Psi^{I}(t)\rangle = \hat{H}_{e}(\{\mathbf{R}_{I}(t)\}) |\Psi^{I}(t)\rangle.$$
 (4.39)

We would like some way of approximating $|\Psi^{I}(t)\rangle$ and its evolution that doesn't involve solving for the dynamics of the interacting electron system. Ideally, we would like to solve the considerably simpler non-interacting electron problem for a set of independent electrons evolving under a suitable Hamiltonian. We will adopt the approach of Kohn–Sham density functional theory (DFT) to argue for the plausibility of such an approximation.

It is not our intention to provide an explanation of DFT, but to outline those parts of the theory that will help us to understand the nature of the approximations made in working with non-interacting electrons. To assist in that understanding we will temporarily take a step back from the time-dependent problem of an evolving electronic state $|\Psi^{\rm I}(t)\rangle$ and consider the time-independent problem. Much of the physical content of the necessary approximations is the same. Another reason for treating the time-independent case is that we will later use Kohn–Sham DFT as a reference point for our discussion of the tight-binding approximation in Sect. 4.4. At the end of this section we will briefly discuss the transferability to the more complicated time-dependent case of what we learn. Much of the material in this section is drawn from the book by Finnis [11].

4.3.1 Density Functional Theory

Consider again our system of interacting electrons in an external potential $V_{\rm ext}(\mathbf{r})$, so that the electronic Hamiltonian is,

$$\hat{H}_{e}(\{\hat{\mathbf{r}}_{i}\}) = \hat{T}_{e}(\{\hat{\mathbf{p}}_{i}\}) + \hat{V}_{ee}(\{\hat{\mathbf{r}}_{i}\}) + \hat{V}_{ext}(\{\hat{\mathbf{r}}_{i}\}), \tag{4.40}$$

where,

$$\hat{V}_{\text{ext}}(\{\hat{\mathbf{r}}_i\}) = \sum_{i}^{N_{\text{e}}} V_{\text{ext}}(\hat{\mathbf{r}}_i). \tag{4.41}$$

In our system the external potential is provided by the classical nuclei,

$$\hat{V}_{\text{ext}}(\{\hat{\mathbf{r}}_i\}) = \hat{V}_{\text{ne}}(\{\hat{\mathbf{r}}_i\}, \{\mathbf{R}_I\}), \tag{4.42}$$

but for now we will retain the more general notation. The aim of DFT is to express the energy of the system (and other properties) as functionals of the electron density. The central proposition, a generalization of the Hohenberg–Kohn theorem [12], is that "for any reasonable density $\rho(\mathbf{r})$ there is an antisymmetric [electronic state] $|\Psi^I\rangle$ describing N_e electrons with density $\rho(\mathbf{r})$ " [11] where we recall that,

$$\rho(\mathbf{r}) \equiv \left\langle \Psi^{\mathrm{I}} | \sum_{i} \delta(\mathbf{r} - \hat{\mathbf{r}}_{i}) | \Psi^{\mathrm{I}} \right\rangle. \tag{4.43}$$

The energy of the electrons in state $|\Psi^{I}\rangle$ is given by

$$E_{\rm e} = \langle \Psi^{\rm I} | \hat{T}_{\rm e} + \hat{V}_{\rm ee} + \hat{V}_{\rm ext} | \Psi^{\rm I} \rangle, \tag{4.44}$$

which we would like to write as a functional $E_e[\rho(\mathbf{r})]$. Considering first the energy due to the external potential, we can define

$$V_{\text{ext}}[\rho(\mathbf{r})] = \langle \boldsymbol{\Psi}^{\text{I}} \hat{V}_{\text{ext}} | \boldsymbol{\Psi}^{\text{I}} \rangle$$

$$= \left\langle \boldsymbol{\Psi}^{\text{I}} | \left(\sum_{i} \int d\mathbf{r} \delta(\mathbf{r} - \hat{\mathbf{r}}_{i}) V_{\text{ext}}(\mathbf{r}) \right) | \boldsymbol{\Psi}^{\text{I}} \right\rangle$$

$$= \int d\mathbf{r} \rho(\mathbf{r}) V_{\text{ext}}(\mathbf{r}),$$
(4.45)

because $|\Psi^{I}\rangle$ is defined as corresponding to $\rho(\mathbf{r})$.

No such definitions of functionals of the electronic kinetic energy and the electron-electron interaction are possible because different states corresponding to the same density can give different values of these energies. We can remove this ambiguity by specifying that for a given $\rho(\mathbf{r})$, $|\Psi^{\rm I}[\rho]\rangle$ is that state vector corresponding to $\rho(\mathbf{r})$ that minimises the sum of the electronic kinetic and electron-electron interaction energies. We can then unambiguously define

$$T_{\rm e}[\rho] \equiv \langle \Psi^{\rm I}[\rho] | \hat{T}_{\rm e} | \Psi^{\rm I}[\rho] \rangle,$$
 (4.46)

and,

$$V_{\rm ee}[\rho] \equiv \langle \Psi^{\rm I}[\rho] | \hat{V}_{\rm ee} | \Psi^{\rm I}[\rho] \rangle. \tag{4.47}$$

To establish our ability to write a general property of the system as a functional of the density, we must consider the ground state $|\Psi^I_0\rangle$. Hohenberg and Kohn [12] show that in this case the density unambiguously (up to an irrelevant constant) determines the external potential $V_{\rm ext}({\bf r})$. Once $V_{\rm ext}({\bf r})$ is fixed then we have a full description of the system via the Hamiltonian and hence *all* its properties, including excited states, can in principle be written as functionals of $\rho_0({\bf r}) \equiv \langle \Psi^I_0 | \sum_i \delta({\bf r} - \hat{\bf r}_i) | \Psi^I_0 \rangle$. What is possible in practice is a different matter.

So far we have established the usefulness of the density as a description of the system and this insight will be valuable later. Now, however, we come to the key point of our discussion of DFT. Kohn and Sham [13] found a clever way to sidestep the difficulty in determining $T_{\rm e}[\rho]$ and $V_{\rm ee}[\rho]$, which essentially involves solving the interacting many-electron problem by considering a fictitious system of $N_{\rm e}$ non-interacting electrons. This is just the sort of system that we would prefer to work with. We define a new electronic Hamiltonian,

$$\hat{H}'_{e}(\{\hat{\mathbf{r}}_{i}\}) \equiv \hat{T}_{e}(\{\hat{\mathbf{p}}_{i}\}) + \hat{V}'_{ext}(\{\hat{\mathbf{r}}_{i}\}), \tag{4.48}$$

$$\hat{V}'_{\text{ext}}(\{\hat{\mathbf{r}}_i\}) \equiv \sum_i V'_{\text{ext}}(\hat{\mathbf{r}}_i), \tag{4.49}$$

and assume that there exists a form of $V_{\rm ext}'(\mathbf{r})$ such that the ground state $|\Psi_0^{\rm SD}\rangle$ of $\hat{H}_{\rm e}'$ has the same density as the ground state $|\Psi_0^{\rm I}\rangle$ of the interacting system Hamiltonian $\hat{H}_{\rm e}$,

$$\left\langle \Psi_0^{\text{SD}} | \sum_i \delta(\mathbf{r} - \hat{\mathbf{r}}_i) | \Psi_0^{\text{SD}} \right\rangle = \rho_0(\mathbf{r}). \tag{4.50}$$

We know how to solve the non-interacting problem via a set of one-electron Schrödinger equations. The solution will be a Slater determinant (SD) of single-particle states $\{|\psi_i\rangle\}_{i=1}^{N_c}$ satisfying

$$\hat{H}_{e}'|\psi_{i}\rangle = \varepsilon_{i}|\psi_{i}\rangle \tag{4.51}$$

for energy eigenvalues $\{\varepsilon_i\}_{i=1}^{N_e}$. The equations (4.51) are the *Kohn–Sham equations*. For our non-interacting system, we can easily calculate the kinetic energy in a general Slater determinant state $|\Psi^{\text{SD}}\rangle$ and if we make the additional stipulation that for some density $\rho(\mathbf{r})$, $|\Psi^{\text{SD}}[\rho]\rangle$ is that state consistent with $\rho(\mathbf{r})$ that minimises the electronic kinetic energy $\langle \Psi^{\text{SD}}[\rho]|\hat{T}_{\text{e}}|\Psi^{\text{SD}}[\rho]\rangle$ we can define the kinetic energy functional

$$T'_{e}[\rho] = \langle \Psi^{\text{SD}}[\rho] | \hat{T}_{e} | \Psi^{\text{SD}}[\rho] \rangle. \tag{4.52}$$

As before, we can also write,

$$V'_{\text{ext}}[\rho] = \int d\mathbf{r} \rho(\mathbf{r}) V'_{\text{ext}}(\mathbf{r}). \tag{4.53}$$

Since the calculation of $T_e[\rho]$ is relatively easy we now attempt to write the energy of the *interacting* system as

$$E_{\rm e}[\rho] = T'_{\rm e}[\rho] + V_{\rm ee}[\rho] + V_{\rm ne}[\rho] + (T_{\rm e}[\rho] - T'_{\rm e}[\rho]).$$
 (4.54)

We don't know the form of $V_{\rm ee}[\rho]$, but we expect that the greater portion of it will be accounted for by the Hartree energy,

$$E_{\rm H}[\rho] = \frac{1}{2} \iint d\mathbf{r} d\mathbf{r}' \frac{\rho(\mathbf{r})\rho(\mathbf{r}')}{|\mathbf{r} - \mathbf{r}'|},\tag{4.55}$$

and so we rewrite the energy,

$$E_{\rm e}[\rho] = T_{\rm e}'[\rho] + E_{\rm H}[\rho] + V_{\rm ne}[\rho] + \left\{ \left(T_{\rm e}[\rho] - T_{\rm e}'[\rho] \right) + \left(V_{\rm ee}[\rho] - E_{\rm H}[\rho] \right) \right\}. \quad (4.56)$$

The term in braces is usually called the *exchange-correlation energy*, which we will write $E_{\rm XC}[\rho]$,

$$E_{\rm e}[\rho] = T_{\rm e}'[\rho] + E_{\rm H}[\rho] + V_{\rm ne}[\rho] + E_{\rm XC}[\rho].$$
 (4.57)

 $E_{\rm XC}$ includes a correction to the kinetic energy (note that $T_{\rm e}[\rho]$ is defined over a restricted set of states $|\Psi^{\rm SD}\rangle$ of Slater determinant form, whereas the set of $|\Psi^{\rm I}\rangle$ over which $T_{\rm e}[\rho]$ is defined is not thus restricted) and a correction for the bits of the electron–electron interaction not included in the Hartree energy. We hope that these corrections will be small and amenable to simple approximations.

The final part of the jigsaw is to find the form of \hat{V}'_{ext} so that we can solve the independent electron problem. To do this we recall that V'_{ext} is defined to be that potential which makes the ground state density of the non-interacting problem the same as the ground state density for the interacting electrons, $\rho_0(\mathbf{r})$. In each case we can find the ground state density by functional differentiation (see Ref. [11] for details). In the case of the non-interacting system, the ground state is found by solving

$$\frac{\delta}{\delta\rho} \left\{ T_{\rm e}'[\rho] + V_{\rm ext}'[\rho] - \mu' \left(\int d\mathbf{r} \rho(\mathbf{r}) - N_{\rm e} \right) \right\} \bigg|_{\rho_0} = 0, \tag{4.58}$$

where the chemical potential μ' is a Lagrange multiplier enforcing conservation of the number of electrons. For the interacting system we have

$$\frac{\delta}{\delta\rho} \left\{ T_{\rm e}[\rho] + V_{\rm ee}[\rho] + V_{\rm ne}[\rho] - \mu \left(\int d\mathbf{r} \rho(\mathbf{r}) - N_{\rm e} \right) \right\} \bigg|_{\rho_0} = 0. \tag{4.59}$$

Our stipulation that the ground state density is the same in both cases ensures that $\mu' = \mu$, otherwise bringing the two systems notionally into contact would result in a flow of charge from one to the other contradicting the stipulation. Subtracting (4.58) from (4.59), we can then write

$$\frac{\delta}{\delta\rho} \left\{ (T_{e}[\rho] + V_{ee}[\rho] + V_{ne}[\rho]) - \left(T'_{e}[\rho] + V'_{ext}[\rho] \right) \right\} \bigg|_{\rho_{0}} = 0, \tag{4.60}$$

$$\frac{\delta}{\delta\rho} \left\{ V_{\text{ne}}[\rho] - V'_{\text{ext}}[\rho] + E_{\text{H}}[\rho] + E_{\text{XC}}[\rho] \right\} \bigg|_{\rho_0} = 0.$$
 (4.61)

Now,

$$\frac{\delta}{\delta \rho} V_{\text{ne}}[\rho] = V_{\text{ne}}(\mathbf{r}), \tag{4.62}$$

and

$$\frac{\delta}{\delta\rho}E_{\rm H}[\rho] = \int d\mathbf{r}' \frac{\rho(\mathbf{r})}{|\mathbf{r} - \mathbf{r}'|} \equiv V_{\rm H}[\rho](\mathbf{r}), \tag{4.63}$$

where we have defined the Hartree potential $V_{\rm H}[\rho](\mathbf{R})$ and we define an exchange-correlation potential,

$$V_{\rm XC}[\rho](\mathbf{r}) \equiv \frac{\delta E_{\rm XC}[\rho]}{\delta \rho},\tag{4.64}$$

to write

$$V_{\text{ext}}'[\rho_0](\mathbf{r}) = V_{\text{ne}}(\mathbf{r}) + V_{\text{H}}[\rho_0](\mathbf{r}) + V_{\text{XC}}[\rho_0](\mathbf{r}). \tag{4.65}$$

Provided we have the correct form for the exchange-correlation potential we have found a formal way of calculating properties of our interacting electron system by solving an independent electron problem. The process is formally exact and the errors in any practical scheme have been helpfully collected together in the approximation that will have to be made to $V_{\rm XC}[\rho]({\bf r})$. Note that the equality only holds for $\rho=\rho_0$, the exact ground state density. This gives rise to the need for a self-consistent solution of the Kohn–Sham equations (4.51), in which we make use of a potential

$$V_{\text{ext}}^{\text{KS}}[\rho](\mathbf{r}) \equiv V_{\text{ne}}(\mathbf{r}) + V_{\text{H}}[\rho](\mathbf{r}) + V_{\text{XC}}[\rho](\mathbf{r}), \tag{4.66}$$

defined for an arbitrary density $\rho(\mathbf{r})$. We will return to this point in Sect. 4.4.3. Since our aim in this chapter is to justify our chosen approach to the dynamic simulation of radiation damage we should consider the implications of the above discussion of DFT for time-dependent problems.

4.3.2 Time-Dependent Density Functional Theory

The Runge–Gross theroem [14] is the time-dependent equivalent of the Hohenberg–Kohn theorem and states that for interacting electrons evolving under a time-dependent external potential $V_{\rm ext}({\bf r},t)$ there is a one-to-one mapping between the evolving electron density $\rho({\bf r},t)$ and the external potential (up to a purely time-dependent constant) *provided* that we specify an initial electronic state $|\Psi(t_0)\rangle$ at some time t_0 . It is then possible to write down a set of time-dependent Kohn–Sham equations for the evolution of a set of single particle eigenstates $\{|\psi_i(t)\rangle\}_{i=1}^{N_c}$ evolving under an external potential $V_{\rm ext}({\bf r},t)$,

$$i\hbar \frac{\partial}{\partial t} |\psi_i(t)\rangle = (\hat{T}_e + \hat{V}'_{ext}) |\psi_i(t)\rangle, \tag{4.67}$$

where

$$\hat{V}'_{\text{ext}} = \int d\mathbf{r} \rho(\mathbf{r}, t) V'_{\text{ext}}(\mathbf{r}, t). \tag{4.68}$$

We assume that a form of $V'_{\text{ext}}(\mathbf{r}, t)$ exists such that

$$\sum_{i=1}^{N_{\rm c}} o_i \langle \psi_i(t) | \delta(\mathbf{r} - \hat{\mathbf{r}}_i) | \psi_i(t) \rangle = \rho(\mathbf{r}, t), \tag{4.69}$$

where $\{o_i\}$ are the occupations of the single particle eigenstates and we recall that $\rho(\mathbf{r}, t)$ is the electron density in the time-dependent *interacting* electronic problem. In this case the solution of the single particle problem will give us information about the time-dependent interacting electron system. As before, we introduce an exchange-correlation potential. This time, however, it is time-dependent and is defined via,

$$V'_{\text{ext}}(\mathbf{r},t) = V_{\text{ne}}(\mathbf{r},t) + V_{\text{H}}[\rho](\mathbf{r},t) + V_{\text{XC}}[\rho](\mathbf{r},t), \tag{4.70}$$

where

$$V_{\rm H}[\rho](\mathbf{r},t) \equiv \int d\mathbf{r}' \frac{\rho(\mathbf{r}',t)}{|\mathbf{r}-\mathbf{r}'|}.$$
 (4.71)

Approximation of $V_{\rm XC}$ is a much tougher task in the time dependent problem, because the correct form is dependent on the entire history of the electronic density. In practice a time-local form depending only on the instantaneous density is used, most frequently the adiabatic local density approximation (ALDA).

4.4 Tight-Binding Models

Kohn–Sham density functional theory, as discussed in Sect. 4.3.1, presents the very general possibility of solving an interacting electron problem via the solution of the Kohn–Sham equations (4.51) for a suitably chosen electronic Hamiltonian \hat{H}'_{c} . The approach is in principle exact, although at least some degree of approximation must be employed in practice in the form chosen for $\hat{V}_{XC}[\rho]$. In order to speed up our calculations of electronic structure we will make further approximations by representing the electronic system within a semi-empirical tight-binding (SETB) model.

We will discuss our specific model later, and argue for the validity of the approximations that it employs. For now, we note that the central feature of any tight-binding model is the choice of a basis set for the electronic system of local orbitals, centred on the atoms. We will write such a basis as $\{|\phi_{I\mu}\rangle\}_{I,\mu}$, where $|\phi_{I\mu}\rangle$ is the orbital of the μ th type, centred on the Ith atom at R_I . The wavefunctions associated with these orbitals are

$$\phi_{I\mu}(\mathbf{r}, \mathbf{R}_I) = \langle \mathbf{r} | \phi_{I\mu} \rangle = \phi_{\mu}(\mathbf{r} - \mathbf{R}_I), \tag{4.72}$$

where $\{\phi_{\mu}(\mathbf{r})\}_{\mu}$ is the set of orbital wavefuctions, which may, for example, be the atomic orbitals of isolated atoms.

4.4.1 Ab-Initio Tight-Binding

There is nothing to stop us working in such a local basis to solve the Kohn–Sham equations (4.51).

$$\hat{H}_{e}^{\prime}|\psi_{i}\rangle = \varepsilon_{i}|\psi_{i}\rangle,\tag{4.51}$$

in which case we retain the exactness-in-principle of DFT. This approach is called *ab-initio tight-binding*.² If we consider the ground-state density³ $\rho_0(\mathbf{r})$ then we can write the kinetic energy of the non-interacting electrons,

$$\hat{T}'_{e}[\rho_{0}] = \sum_{i} o_{i} \langle \psi_{i} | (\hat{H}'_{e}[\rho_{0}] - \hat{V}'_{ext}[\rho_{0}]) | \psi_{i} \rangle$$

$$= \sum_{i} o_{i} \varepsilon_{i} - \int d\mathbf{r} \, \rho_{0}(\mathbf{r}) V'_{ext}[\rho_{0}](\mathbf{r}), \qquad (4.73)$$

where $\{|\psi_i\rangle\}$ are the Kohn–Sham orbitals corresponding to ρ_0 and $\{o_i\}$ are their occupations. Given that we have assumed $\rho(\mathbf{r}) = \rho_0(\mathbf{r})$ we can use (4.65)

$$V_{\text{ext}}'[\rho_0](\mathbf{r}) = V_{\text{ne}}(\mathbf{r}) + V_{\text{H}}[\rho_0](\mathbf{r}) + V_{\text{XC}}[\rho_0](\mathbf{r}), \tag{4.65}$$

and so (4.57) can be rewritten

$$E_{e}[\rho_{0}] = \sum_{i} o_{i} \varepsilon_{i} - E_{H}[\rho_{0}] + E_{XC}[\rho_{0}] - \int d\mathbf{r} \rho_{0}(\mathbf{r}) V_{XC}[\rho_{0}](\mathbf{r}), \qquad (4.74)$$

since,

$$-\int d\mathbf{r}\rho_0(\mathbf{r})V_{\rm H}[\rho_0](\mathbf{r}) = -2E_{\rm H}[\rho_0], \tag{4.75}$$

i.e. the Hartree energy is "double-counted" in the energy of the non-interacting electron system. The key to solving the Kohn–Sham equations then lies in calculating the matrix elements of the single particle Hamiltonian in the local orbital basis,

$$\langle \phi_{I\mu} \hat{H}'_{\rm e} | \phi_{J\nu} \rangle,$$
 (4.76)

and solving the resulting matrix eigenvalue equation.

 $^{^2}$ Local basis sets are often exploited in so-called linear-scaling or order-*N* DFT codes to obtain efficient computations for large (\sim 1,000 atom) system sizes.

³ Here we are again side-stepping the issue of how to find $\rho_0(\mathbf{r})$. We will return to it in Sect. 4.4.5, but for now we will simply assume that it is known.

4.4.2 Semi-Empirical Tight-Binding

Ab-initio tight-binding is too computationally taxing to be useful (at the present time) for large-scale radiation damage simulations. This is mainly because the calculation of the matrix elements (4.76) involves integrals over real space, which must be carried out with very high precision, especially if calculations of forces (involving derivatives of the matrix elements) are required. Additionally, for satisfactory precision, large basis sets are required, increasing the number of matrix elements that must be calculated. Instead, in our work, we choose to adopt a semi-empirical tight-binding (SETB) model in which various approximations are made in a trade-off between computational efficiency and the accuracy of the calculated electronic structure. In this section we will consider how we can arrive at a simpler model for the electronic energy $E_{\rm e}[\rho]$.

4.4.3 The Harris-Foulkes Functional

In Sect. 4.3.1 we showed how the Kohn–Sham approach to DFT allows us to find the ground state electron density of a set of interacting electrons by solving an appropriate non-interacting electron problem. In order to formulate the non-interacting problem correctly, we had to assume fore-knowledge of the ground state density, i.e. we wrote (4.65),

$$V_{\text{ext}}'[\rho_0](\mathbf{r}) = V_{\text{ne}}(\mathbf{r}) + V_{\text{H}}[\rho_0](\mathbf{r}) + V_{\text{XC}}[\rho_0](\mathbf{r}). \tag{4.65}$$

This need to know ρ_0 in order to find ρ_0 means that Kohn–Sham DFT requires a self-consistent solution.

To exemplify this, let us construct the more general external potential (4.66) for the single particle problem from some assumed charge density $\rho^{\rm in}(\mathbf{r})$ (our input density),

$$V_{\rm ext}^{\rm KS}[\rho^{\rm in}](\mathbf{r}) \equiv V_{\rm ne}(\mathbf{r}) + V_{\rm H}[\rho^{\rm in}](\mathbf{r}) + V_{\rm XC}[\rho^{\rm in}](\mathbf{r}).$$
 (4.77)

We then solve,

$$\hat{H}_{\rm e}^{\rm KS}|\psi_i\rangle = \varepsilon_i|\psi_i\rangle, \quad \hat{H}_{\rm e}^{\rm KS} \equiv \hat{T}_{\rm e} + \hat{V}_{\rm ext}^{\rm KS}, \quad \hat{V}_{\rm ext}^{\rm KS} \equiv \sum_i V_{\rm ext}^{\rm KS}[\rho^{\rm in}](\hat{\mathbf{r}}_i), \qquad (4.78)$$

for the single particle eigenstates $\{|\psi_i\rangle\}$ and their energy eigenvalues $\{\varepsilon_i\}$. If these eigenstates are occupied according to occupations $\{o_i\}$, then we can now construct a new density,

$$\rho(\mathbf{r}) = \sum_{i} o_i \langle \psi_i | \mathbf{r} \rangle \langle \mathbf{r} | \psi_i \rangle. \tag{4.79}$$

We will have found the ground state density if $\rho = \rho^{\rm in}$. Solving the Kohn–Sham DFT problem then reduces to finding a successful algorithm for searching the space of possible densities for the correct ρ_0 . Most often this is done by starting with a reasonable guess for $\rho^{\rm in}$, solving for ρ and then generating a new input density $\rho^{\rm in'}$ from a mixture of ρ and the old $\rho^{\rm in}$.

We are not concerned here with particular solutions to Kohn-Sham DFT. Instead we note that we can write the energy of the non-interacting system as⁴

$$E_{e}^{NI}[\rho^{in}] \equiv \sum_{i} o_{i} \varepsilon_{i} = \sum_{i} o_{i} \langle \psi_{i} | \hat{H}_{e}^{KS} | \psi_{i} \rangle$$

$$= T_{e}'[\rho] + \int d\mathbf{r} \rho(\mathbf{r}) V_{\text{ext}}^{KS}[\rho^{\text{in}}](\mathbf{r}),$$
(4.80)

a functional of only ρ^{in} , because ρ^{in} determines ρ via the Kohn–Sham equations (4.78). We can now define a new functional of the interacting system,

$$E'_{e}[\rho, \rho^{in}] = E_{e}^{NI}[\rho^{in}] - \int d\mathbf{r} \rho(\mathbf{r}) V_{ext}^{KS}[\rho^{in}](\mathbf{r}) + E_{H}[\rho] + V_{ne}[\rho] + E_{XC}[\rho]. \quad (4.81)$$

Given the definition of $V_{\rm ext}^{\rm KS}[\rho](\mathbf{r})$,

$$\int d\mathbf{r} \rho(\mathbf{r}) V_{\text{ext}}^{\text{KS}}[\rho^{\text{in}}](\mathbf{r}) = \int d\mathbf{r} \rho(\mathbf{r}) V_{\text{ne}}(\mathbf{r}) + \int d\mathbf{r} \rho(\mathbf{r}) V_{\text{H}}[\rho^{\text{in}}](\mathbf{r}) + \int d\mathbf{r} \rho(\mathbf{r}) V_{\text{XC}}[\rho^{\text{in}}](\mathbf{r}), \qquad (4.82)$$

and we have,

$$E_{e}'[\rho, \rho^{in}] = E_{e}^{NI}[\rho^{in}] + E_{H}[\rho] - \int d\mathbf{r}\rho(\mathbf{r})V_{H}[\rho^{in}](\mathbf{r}) + E_{XC}[\rho]$$
$$- \int d\mathbf{r}\rho(\mathbf{r})V_{XC}[\rho^{in}](\mathbf{r}). \tag{4.83}$$

Now if $\rho(\mathbf{r})$ is not too different from $\rho^{\text{in}}(\mathbf{r})$, which will be the case if $\rho^{\text{in}}(\mathbf{r})$ is close to the ground state density $\rho_0(\mathbf{r})$, then we can consider writing,

$$\rho(\mathbf{r}) = \rho^{\text{in}}(\mathbf{r}) + \delta\rho(\mathbf{r}), \tag{4.84}$$

where $\delta \rho({\bf r})$ is some small variation in the density. Then we can show (see Sect. 13.1.5) that

$$E_{\rm H}[\rho] - \int d\mathbf{r} \rho(\mathbf{r}) V_{\rm H}[\rho^{\rm in}](\mathbf{r}) = -E_{\rm H}[\rho^{\rm in}] + \frac{1}{2} \iint d\mathbf{r} d\mathbf{r}' \frac{\delta \rho(\mathbf{r}') \delta \rho(\mathbf{r})}{|\mathbf{r} - \mathbf{r}'|}, \quad (4.85)$$

⁴ The remainder of Sect. 4.4.3 is based on material in Ref. [11].

exact to second order in $\delta \rho(\mathbf{r})$ and (see Sect. 13.1.6) that

$$E_{\rm XC}[\rho] - \int d\mathbf{r} \rho(\mathbf{r}) V_{\rm XC}[\rho^{\rm in}] \approx E_{\rm XC}[\rho^{\rm in}] - \int d\mathbf{r} \rho^{\rm in}(\mathbf{r}) V_{\rm XC}[\rho^{\rm in}] + \frac{1}{2} \iint d\mathbf{r} d\mathbf{r}' \frac{\delta^2 E_{\rm XC}[\rho]}{\delta \rho(\mathbf{r}') \delta \rho(\mathbf{r})} |_{\rho^{\rm in}} \delta \rho(\mathbf{r}') \delta \rho(\mathbf{r}),$$

$$(4.86)$$

again to second order in $\delta \rho(\mathbf{r})$. Our new functional thus becomes, to second order

$$\begin{split} E_{\mathrm{e}}^{\prime(2)}[\rho,\rho^{\mathrm{in}}] &= \hat{T}_{\mathrm{e}}^{\prime}[\rho] + \int \mathrm{d}\mathbf{r}\rho(\mathbf{r})V_{\mathrm{ext}}^{\mathrm{KS}}[\rho^{\mathrm{in}}](\mathbf{r}) \\ &- E_{\mathrm{H}}[\rho^{\mathrm{in}}] + \frac{1}{2} \! \int \!\! \int \mathrm{d}\mathbf{r} \mathrm{d}\mathbf{r}^{\prime} \frac{\delta\rho(\mathbf{r}^{\prime})\delta\rho(\mathbf{r})}{|\mathbf{r} - \mathbf{r}^{\prime}|} \\ &+ E_{\mathrm{XC}}[\rho^{\mathrm{in}}] - \! \int \! \mathrm{d}\mathbf{r}\rho^{\mathrm{in}}(\mathbf{r})V_{\mathrm{XC}}[\rho^{\mathrm{in}}] + \frac{1}{2} \! \int \!\!\! \int \mathrm{d}\mathbf{r} \mathrm{d}\mathbf{r}^{\prime} \frac{\delta^{2}E_{\mathrm{XC}}[\rho]}{\delta\rho(\mathbf{r}^{\prime})\delta\rho(\mathbf{r})} \bigg|_{\rho^{\mathrm{in}}} \delta\rho(\mathbf{r}^{\prime})\delta\rho(\mathbf{r}) \end{split}$$

$$(4.87)$$

Hence to *first* order in $\delta \rho(\mathbf{r})$ we can define a new functional, the *Harris–Foulkes* functional [15],

$$E_{\rm e}^{\rm HF}[\rho^{\rm in}] \equiv E_{\rm e}^{'(1)}[\rho^{\rm in}] = E_{\rm e}^{\rm NI}[\rho^{\rm in}] - E_{\rm H}[\rho^{\rm in}] + E_{\rm XC}[\rho^{\rm in}] - \int d\mathbf{r} \rho^{\rm in}(\mathbf{r}) V_{\rm XC}[\rho^{\rm in}]. \tag{4.88}$$

The utility of this functional lies in the fact that it is a functional of one density only, but is stationary at the correct ground state density $\rho_0(\mathbf{r})$. Evaluated at this density, the Harris–Foulkes functional gives the exact ground state energy. Finding a stationary point of $E_{\rm e}^{\rm HF}$ does not require a self-consistent solution and so in this respect it presents a density functional view of the energy that is compatible with a SETB model of electronic structure.

4.4.4 Towards Semi-Empirical Tight-Binding

We will now consider how a SETB model can approximate the value of the energy of a combined system of classical nuclei and quantum mechanical electrons. We will begin by adding in the classical nuclear-nuclear repulsion term $V_{\rm nn}$ to the Harris–Foulkes functional (4.88) to write,

$$E^{\rm HF}[\rho](\{\mathbf{R}_I\}) = E_{\rm e}^{\rm NI}[\rho] - E_{\rm H}[\rho] + E_{\rm XC}[\rho] - \int d\mathbf{r} \, \rho(\mathbf{r}) V_{\rm XC}[\rho] + V_{\rm nn}(\{\mathbf{R}_I\}),$$
(4.89)

where we have dropped the unnecessary superscript 'in' from the electronic density. Our hope is that this energy can be well approximated by an expression of the form

$$E^{\text{TB}}[\rho](\{\mathbf{R}_I\}) = \sum_{i} o_i \varepsilon_i + V_{\text{rep}}(\{\mathbf{R}_I\}), \tag{4.60}$$

where $\{\varepsilon_i\}$ are the eigenvalues resulting from solution of a non-interacting electron problem with a tight-binding Hamiltonian \hat{H}^{TB} dependent only on the nuclear coordinates,

$$\hat{H}^{\text{TB}}(\{\mathbf{R}_I\})|\psi_i\rangle = \varepsilon_i|\psi_i\rangle,\tag{4.91}$$

and $\{o_i\}$ are their occupations. V_{rep} is a repulsive potential that is a function of the nuclear coordinates only. The two key approximations in writing this tight-binding energy functional are as follows:

1. The sum over the eigenvalues is intended to represent the energy of the non-interacting electron system,

$$\sum_{i} o_{i} \varepsilon_{i} \approx E_{\rm e}^{\rm NI}[\rho]. \tag{4.92}$$

Hence our tight-binding Hamiltonian $\hat{H}^{TB}(\{\mathbf{R}_I\})$ is an approximation to the non-interacting electronic Hamiltonian \hat{H}'_e and we choose to write its matrix elements in the local orbital basis as pairwise functions of the inter-nuclear separations.,

$$\langle \phi_{I\mu} | \hat{H}_{e}^{TB} | \phi_{J\nu} \rangle \approx \langle \phi_{I\mu} | \hat{H}_{e}' | \phi_{J\nu} \rangle \equiv \gamma (\mathbf{R}_I - \mathbf{R}_J).$$
 (4.93)

The repulsive term is intended to represent the remaining terms in the Harris– Foulkes functional,

$$V_{\rm rep}(\{\mathbf{R}_I\}) \approx V_{\rm nn}(\{\mathbf{R}_I\}) - E_{\rm H}[\rho] + E_{\rm XC}[\rho] - \int \mathrm{d}\mathbf{r} \rho(\mathbf{r}) V_{\rm XC}[\rho](\mathbf{r}). \tag{4.94}$$

Again, we choose a form that is a sum of pairwise functions of the nuclear coordinates,

$$V_{\text{rep}}(\{\mathbf{R}_I\}) = \frac{1}{2} \sum_{I,I=I}^{N_n} u(|\mathbf{R}_I - \mathbf{R}_J|). \tag{4.95}$$

To argue for the plausibility of our SETB model functional $E^{TB}[\hat{\rho}](\{\mathbf{R}_I\})$, we must essentially demonstrate that all the terms in $E^{HF}[\rho](\{\mathbf{R}_I\})$ can be approximated by a sum of pairwise contributions. The following arguments for such a representation follow Foulkes and Haydock [16]

To begin, we choose to write $\rho(\mathbf{r})$ as a sum of spherically symmetric atomcentered densities corresponding to the occupied orbitals of some local basis. Let $\rho_I(\mathbf{r})$ be the density due to the atom at \mathbf{R}_I , then,

$$\rho(\mathbf{r}) = \sum_{I} \rho_{I}(\mathbf{r}). \tag{4.96}$$

Taking each term in (4.89) in turn, we can see that the nuclear–nuclear interaction energy (4.16) is pairwise by definition:

$$V_{\rm nn} \equiv \frac{1}{2} \sum_{I=I}^{N_{\rm n}} \frac{Z_I Z_J}{|\mathbf{R}_I - \mathbf{R}_J|}.$$
 (4.16)

The contribution from the Hartree energy, negative because it is compensating for a double-counting in the non-interacting electron system, is,

$$-E_{H} = -\frac{1}{2} \iint d\mathbf{r} d\mathbf{r}' \frac{\rho(\mathbf{r})\rho(\mathbf{r}')}{|\mathbf{r} - \mathbf{r}'|}$$

$$= -\frac{1}{2} \iint d\mathbf{r} d\mathbf{r}' \sum_{I,J} \frac{\rho_{I}(\mathbf{r})\rho_{J}(\mathbf{r}')}{|\mathbf{r} - \mathbf{r}'|}$$

$$= -\frac{1}{2} \iint d\mathbf{r} d\mathbf{r}' \sum_{I,J\neq I} \frac{\rho_{I}(\mathbf{r})\rho_{J}(\mathbf{r}')}{|\mathbf{r} - \mathbf{r}'|} - \frac{1}{2} \iint d\mathbf{r} d\mathbf{r}' \sum_{I} \frac{\rho_{I}(\mathbf{r})\rho_{I}(\mathbf{r}')}{|\mathbf{r} - \mathbf{r}'|}.$$

$$(4.97)$$

The first term in the last line has a pairwise representation and the second term will be a constant. If we further assume that no charge transfer occurs, such that each atom remains strictly neutral then the pairwise representation of the sum $V_{\rm nn}-E_{\rm H}$ will be short-ranged.

The exchange-correlation terms are more difficult to deal with, but we can start by assuming that the exchange-correlation energy can be written in the *local density approximation* (LDA). We introduce the funtional $V_{\text{LDA}}[\rho](\mathbf{r})$ to write,

$$E_{\rm XC}[\rho] \approx \int d\mathbf{r} \, \rho(\mathbf{r}) V_{\rm LDA}[\rho](\mathbf{r}).$$
 (4.98)

The energy of interest in the Harris–Foulkes functional (4.89) then becomes,

$$\int d\mathbf{r} \rho(\mathbf{r}) \{ V_{\text{LDA}}[\rho](\mathbf{r}) - V_{\text{XC}}[\rho] \}. \tag{4.99}$$

Whilst this term cannot be exactly represented by a sum of pairwise contributions, the approximation will be good provided that the overlap of three or more atom-centered densities is insignificant [16]. This is often the case.

Having argued for the representation (4.95) in terms of pairwise functions of the inter-nuclear separation, we must now consider the similar representation (4.93) of the matrix elements of the non-interacting Hamiltonian \hat{H}'_e . We have,

$$\langle \phi_{I\mu} | \hat{H}'_{e} | \phi_{J\nu} \rangle = \langle \phi_{I\mu} | \hat{T}_{e} + \hat{V}^{KS}_{ext} | \phi_{J\nu} \rangle$$

$$= \langle \phi_{I\mu} | \hat{T}_{e} | \phi_{J\nu} \rangle + \langle \phi_{I\mu} | \hat{V}^{KS}_{ext} | \phi_{J\nu} \rangle.$$
(4.100)

Considering the first term, we have,

$$\langle \phi_{I\mu} | \hat{T}_{e} | \phi_{J\nu} \rangle = \int d\mathbf{r} \langle \phi_{I\mu} | \mathbf{r} \rangle \frac{-\hbar^{2}}{2m_{e}} \nabla_{\mathbf{r}}^{2} \langle \mathbf{r} | \phi_{J\nu} \rangle$$

$$= \frac{-\hbar^{2}}{2m_{e}} \int d\mathbf{r} \phi_{\mu} (\mathbf{r} - \mathbf{R}_{I}) \nabla_{\mathbf{r}}^{2} \phi_{\nu} (\mathbf{r} - \mathbf{R}_{J}),$$
(4.101)

which depends only on $\mathbf{R}_I - \mathbf{R}_J$ (or on $|\mathbf{R}_I - \mathbf{R}_J|$ for our choice of spherically symmetric orbitals) and on μ and ν as required. The potential term is more difficult to handle, but if we make the local density approximation (LDA) and assume that $V_{\text{LDA}}[\rho](\mathbf{r})$ is linear in $\rho(\mathbf{r})$ then our choice of ρ as a sum of atom-centred densities allows us to write $V_{\text{ext}}^{\text{KS}}[\rho]$ as a sum of atom-centred contributions (see Sect. 13.1.7),

$$V_{\text{ext}}^{\text{KS}}[\rho] = \sum_{I} V_{\text{ext},I}^{\text{KS}}[\rho_I(\mathbf{r})]. \tag{4.102}$$

We can now write our matrix elements as

$$\langle \phi_{I\mu} | \hat{V}_{\text{ext}}^{\text{KS}} | \phi_{J\nu} \rangle = \sum_{K} \int d\mathbf{r} \, \phi_{\mu}(\mathbf{r} - \mathbf{R}_{I}) V_{\text{ext},K}^{\text{KS}} \phi_{\nu}(\mathbf{r} \mathbf{R}_{J}). \tag{4.103}$$

For the case $I \neq J$ the above expression can be reduced to a pairwise form provided we neglect the so-called three-centre integrals, which are those terms in which neither K = I nor K = J. This gives us the approximation,

$$\langle \phi_{I\mu} | \hat{V}_{\text{ext}}^{\text{KS}} | \phi_{J\nu} \rangle \approx \langle \phi_{I\mu} | V_{\text{ext},J}^{\text{KS}} | \phi_{J\nu} \rangle + \langle \phi_{I\mu} | V_{\text{ext},I}^{\text{KS}} | \phi_{J\nu} \rangle, \tag{4.104}$$

and we can write our Hamiltonian in the form (4.93) of pairwise contributions. It is worth recapping the approximations that were necessary to reach our form of SETB model:

- 1. We assume that the electron density can be decomposed into spherically symmetric atom-centred contributions (4.96),
- 2. We neglect the simultaneous overlap of three or more orbitals,
- 3. We assume that the Kohn–Sham potential $V_{\rm ext}^{\rm KS}$ can be written as a sum of atom-centred contributions. To show this we must assume that the exchange-correlation energy can be written not only in the LDA, but also with an LDA functional linear in the density, and,
- 4. We ignore three-centre integrals in the calculation of the Hamiltonian matrix elements.

Foulkes and Haydock [16] demonstrate that the errors in the form of SETB model that we have examined are dominated by the neglect of the three-centre integrals. Such integrals are not negligible and this final approximation is poorly justified. To mitigate the severity of this neglect we can make an appeal to the empiricism inherent in an SETB model. That is to say that in fitting the functions

 $\gamma(|\mathbf{R}_I - \mathbf{R}_J|)$ and $u(|\mathbf{R}_I - \mathbf{R}_J|)$ (see (4.93) and (4.95), respectively) in order to match various properties of our model with some target values, we hope that some of our errors will be compensated for. So whilst we have argued for the physical reasonableness of a simple SETB model, the final demonstration of its validity lies in its success in application.

4.4.5 Self-Consistent Tight-Binding

In Sect. 4.4.3 we derived the Harris–Foulkes functional, which is a functional of a single electron density and is stationary at the correct ground state density. Because this functional does not require a self-consistent solution it was a useful starting point for discussing SETB. However, the corresponding approach to SETB, namely parameterizing the Hamiltonian matrix elements and the other terms in the total energy, is not always appropriate. It works well in cases where we expect strict charge neutrality, for example when we wish to find a model for a perfect crystal, but not so well in situations where significant charge transfer might occur.

We could imagine taking the case of a perfect crystal with a self-intersitial defect. We might expect some deviation from perfect neutrality in the region of the defect, but the question is how to ensure our SETB model gets the charge on the defect correct. If we are using a model that was parameterized to reproduce various physical properties of a perfect lattice then we cannot expect it to reproduce the correct defect charge. There is nothing in the derivation of the Harris–Foulkes functional that precludes a parameterization that gets the correct defect charge (we made no assumption of local charge neutrality) and indeed we could imagine making such adjustments to our pairwise functions at short range that the charge on our defect state was correctly reproduced. But this approach is not physically persuasive and certainly does not produce a model that is transferable to say another type of defect or a general lattice distortion.

Instead, we will bite the bullet of self-consistency and introduce terms into our functional that account for the energy associated with charge transfer. If we consider the functional $E_{\rm e}^{'(2)}[\rho,\rho^{\rm in}]$ (4.87), the Harris–Foulkes functional plus second-order terms in $\delta\rho$, and consider minimizing with respect to $\rho({\bf r})$ we obtain the equation

$$\frac{\delta T_{\rm e}'[\rho]}{\delta \rho}\bigg|_{\rho_0} + V_{\rm ext}^{\rm KS}[\rho^{\rm in}] + \frac{1}{2} \int d\mathbf{r}' \bigg\{ \frac{1}{|\mathbf{r} - \mathbf{r}'|} + \frac{\delta^2 E_{\rm XC}[\rho]}{\delta \rho(\mathbf{r}) \delta \rho(\mathbf{r}')} \bigg|_{\rho^{\rm in}} \bigg\} \delta \rho(\mathbf{r}') = 0, \quad (4.105)$$

which corresponds to the solution of a new set of Kohn-Sham equations

$$\left(\hat{T}_{e} + V_{ext}^{KS}[\rho^{in}] + \frac{1}{2} \int d\mathbf{r}' \left\{ \frac{1}{|\mathbf{r} - \mathbf{r}'|} + \frac{\delta^{2} E_{XC}[\rho]}{\delta \rho(\mathbf{r}) \delta \rho(\mathbf{r}')} \Big|_{\rho^{in}} \right\} \delta \rho(\mathbf{r}') \right) |\psi_{i}\rangle = \varepsilon_{i} |\psi_{i}\rangle.$$
(4.106)

From an SETB perspective we can then imagine that we are adding in corrections to our basic model that make it applicable in situations other than the ones for which it was parameterized. Specifically, in our case, we assume we are starting with a model parameterized for a perfect crystal with charge neutral atoms and introduce terms to account for the energy of deviations from that neutrality.

We augment our original tight-binding model functional $E^{\text{TB}}[\rho](\{\mathbf{R}_I\})$:

$$E^{\text{TB}'}[\rho](\{\mathbf{R}_I\}) = E^{\text{TB}}[\rho](\{\mathbf{R}_I\}) + \mathcal{E}[\rho](\{\mathbf{R}_I\}). \tag{4.107}$$

The new term $\mathcal{E}[\rho](\{\mathbf{R}_I\})$, dependent on the state of the electronic system and the ionic coordinates is intended to represent the second-order correction to the Harris–Foulkes energy, $E''[\rho]$, defined via,

$$E'_{\rm e}[\rho, \rho^{\rm in}] = E^{\rm HF}[\rho^{\rm in}] + E''[\rho],$$
 (4.108)

$$E''[\rho = \rho^{\text{in}} + \delta \rho] \equiv \frac{1}{2} \int d\mathbf{r}' \left\{ \frac{1}{|\mathbf{r} - \mathbf{r}'|} + \frac{\delta^2 E_{\text{XC}}[\rho]}{\delta \rho(\mathbf{r}) \delta \rho(\mathbf{r}')} \Big|_{\rho^{\text{in}}} \right\}.$$
(4.109)

The simplest approximation to this energy, the *self-consistent charge transfer model*, can be written [11],

$$\mathcal{E}[\rho](\{\mathbf{R}_I\}) = \frac{1}{2} \sum_{I} U_I \Delta q_I^2 + \frac{1}{2} \sum_{I,J \neq I} U_{IJ} \Delta q_I \Delta q_J, \tag{4.110}$$

where Δq_I is the deviation in the number of electrons on atom I from that implied by the density $\rho^{\rm in}$. The first term can be interpreted as an energy penalty associated with localising charge on a single atom. The second term is an inter-site Coulombic interaction energy between charges on different atoms and U_{IJ} most commonly takes a form like $1/|\mathbf{R}_I - \mathbf{R}_J|$ or similar.

Just as the inclusion of the second order energy shift $E''[\rho]$ in the functional implied a change to the effective external potential in the Kohn–Sham equations, so we must also augment our tight-binding expression for the Hamiltonian operator to account for $\mathcal{E}[\rho](\{\mathbf{R}_I\})$. In fact, the Hamiltonian must become,

$$\hat{H}_{e}^{TB'} = \hat{H}_{e}^{TB} + \hat{V}^{SC}, \tag{4.111}$$

where,

$$\hat{V}^{\text{SC}} = \int d\mathbf{r} |\mathbf{r}\rangle \frac{\delta \mathcal{E}[\rho]}{\delta \rho} \langle \mathbf{r}|, \qquad (4.112)$$

but we will postpone further discussion of this adjustment until the next section when we discuss the dynamical evolution of a simple tight-binding model.

4.5 Time-Dependent Tight-Binding

So far, our theoretical discussion has focussed mainly on the case of time-independent electronic structure. In this section we will derive the dynamical equations that govern the evolution of a set of classical ions coupled to a quantum mechanical electronic system described by a tight-binding model.

The tight-binding model that we use in our simulations is exceedingly simple. It consists of a single spherically symmetric (*s*-like) atomic orbital centred on each atom. In addition, these orbitals are assumed to be orthogonal to one another. In the rest of our theoretical discussion we will specialize to consider a model of just such a simple form. We do this because we require no further complexity and because the simple model will help us illuminate and pull together some of the preceding theory in the most readily comprehensible way. We intend, therefore, that this section should provide a fairly self-contained description of our dynamical semi-classical system. Inevitably this will involve some repetition of material discussed above, but we hope that this repetition will be useful in clarifying the nature of the model that we use in our work.

4.5.1 The Description of the System

Our simulation system consists of a set of N_n classical ions of masses $\{M_I\}_{I=1}^{N_n}$ (all of which will be the same) with positions $\{\mathbf{R}_I(t)\}_{I=1}^{N_n}$, which we denote collectively by the $3N_n$ dimensional vector $\mathbf{R}(t)$. We will denote the velocity of ion I by $\dot{\mathbf{R}}_I(t) = \frac{\partial}{\partial t}\mathbf{R}_I(t)$. Each ion is assumed to carry with it a positive charge of eq_0 such that the overall system of ions and electrons is charge neutral.

The electronic system will be described by a density matrix $\hat{\rho}(t)$ evolving in time under the influence of our tight-binding Hamiltonian, $\hat{H}_{\rm e}^{\rm TB}$, or $\hat{H}_{\rm e}^{\rm TB'}$ in the case of a self-consistent charge transfer (SCCT) model. We can write $\hat{\rho}(t)$ in terms of a set of time-dependent state-vectors $\{|\psi_i(t)\rangle\}_{i=1}^{N_{\rm n}}$ with occupations $\{o_i\}_{i=1}^{N_{\rm n}}$, which are permitted to take any value in the range $0 \le o_i \le 1$, but which remain fixed at their initial values in our dynamical evolution. Hence,

$$\hat{\rho}(t) = \sum_{i}^{N_{\rm n}} o_i |\psi_i(t)\rangle \langle \psi_i(t)|. \tag{4.113}$$

We will account for spin degeneracy (i.e. up to double occupation of each state) with explicit factors of 2 where required.

Our tight-binding Hamiltonian is defined in the basis of atomic orbitals $\{|\mathbf{R}_I\rangle\}_{i=1}^{N_n}$, where $|\mathbf{R}_I\rangle$ is the orbital associated with the *I*th atom, at position \mathbf{R}_I . These orbitals are assumed to be orthonormal,

$$\langle \mathbf{R}_I | \mathbf{R}_J \rangle = \delta_{IJ}. \tag{4.114}$$

The basic, non-self-consistent, Hamiltonian is defined in this local basis as,

$$\hat{H}^{\text{TB}} = \sum_{II} |\mathbf{R}_I\rangle \gamma(|\mathbf{R}_I - \mathbf{R}_J|) \langle \mathbf{R}_J|, \qquad (4.115)$$

where the function $\gamma(R)$ gives the *hopping integrals* as a function of inter-ionic separation. The on-site terms $\langle \mathbf{R}_I | \hat{H}^{\mathrm{TB}} | \mathbf{R}_I \rangle$ of this Hamiltonian are zero in our model. In the SCCT model, the Hamiltonian includes additional terms,

$$\hat{H}^{TB'} = \hat{H}^{TB} + \hat{V}^{SC}, \tag{4.116}$$

which we will derive later.

4.5.2 The Evolution of our System

The state of our semi-classical system, then, is characterised by the classical coordinates $\mathbf{R}(t)$ and $\dot{\mathbf{R}}(t)$ and by the density matrix $\hat{\rho}(t)$. We now need to derive expressions for how these entities evolve under the influence of the tight-binding Hamiltonian. Our starting point will be the total energy of the system, which we write,

$$E^{\text{TB}'}[\rho](\mathbf{R},t) = 2\text{Tr}\{(\hat{\rho}(t) - \hat{\rho}^0)\hat{H}^{\text{TB}}(\mathbf{R})\} + \mathcal{E}[\hat{\rho} - \hat{\rho}^0](\mathbf{R}) + V_{\text{rep}}(\mathbf{R}), \quad (4.117)$$

where we have included the repulsive classical potential $V_{\rm rep}({\bf R})$ and the factor of 2 accounts for spin degeneracy. ${\cal E}[\hat{\rho}-\hat{\rho}^0]({\bf R})$ is a self-consistency energy dependent on the state of the electronic system and the ionic positions.

In contrast to our previous discussions, the above energy is defined relative to a reference density matrix $\hat{\rho}^0$, which is diagonal in the local orbital basis. This definition of the energy is consistent with the tight-binding bond model (TBBM) of Sutton et al. [17]. It does not materially alter any aspect of the behaviour of the model, but it does make a difference to what the repulsive potential is implied to represent (and can strengthen the arguments for the SETB approximation). Following the TBBM approach, $\hat{\rho}^0$ is taken to represent the density matrix of the free atoms at infinite separation. As such it can be written,

$$\hat{\rho}^0 = \sum_{I} |\mathbf{R}_I\rangle \frac{q_0}{2} \langle \mathbf{R}_I| \tag{4.118}$$

and so

$$2\text{Tr}\{(\hat{\rho}(t) - \hat{\rho}^{0})\hat{H}^{\text{TB}}(\mathbf{R})\} = 2\text{Tr}\{\hat{\rho}(t)\hat{H}^{\text{TB}}(\mathbf{R})\},\tag{4.119}$$

since the onsite terms in \hat{H}^{TB} are zero.

To obtain the equations of motion for **R**, $\dot{\mathbf{R}}$ and $\hat{\rho}$ we will adopt a Lagrangian formalism (the following derivation follows that given by Todorov [9]). The Lagrangian for our system will be [18],

$$L = 2i\hbar \sum_{i} o_{i} \langle \psi_{i} | \dot{\psi}_{i} \rangle - E^{TB'}[\rho](\mathbf{R}) + T_{n}(\dot{\mathbf{R}}). \tag{4.120}$$

To proceed, we expand the state-vectors $|\psi_i(t)\rangle$ in the local orbital basis,

$$|\psi_i(t)\rangle = \sum_I a_{iI}(t)|\mathbf{R}_I\rangle,$$
 (4.121)

(which defines the expansion coefficients $\{a_{iI}\}$) so that the Lagrangian becomes

$$L(\{a_{iI}\}, \{a_{iI}^*\}, \{\dot{a}_{iI}\}, \{\dot{a}_{iI}^*\}, \mathbf{R}, \dot{\mathbf{R}}) = 2i\hbar \sum_{i} \sum_{I} o_{i} a_{iI}^* \dot{a}_{iI}$$
$$-2 \sum_{i} \sum_{II} o_{i} a_{iI}^* a_{iJ} \langle \mathbf{R}_{I} | \hat{H}^{TB} | \mathbf{R}_{J} \rangle - \mathcal{E}[\rho - \rho^{0}](\mathbf{R}) + \sum_{I} \frac{1}{2} M_{I} (\dot{\mathbf{R}})^{2}.$$
(4.122)

Lagrange's equations [19] are then

$$\frac{\partial L}{\partial a_{iI}} - \frac{\mathrm{d}}{\mathrm{d}t} \frac{\partial L}{\partial \dot{a}_{iI}} = 0 \tag{4.123}$$

$$\frac{\partial L}{\partial a_{iI}^*} - \frac{\mathrm{d}}{\mathrm{d}t} \frac{\partial L}{\partial \dot{a}_{iI}} = 0 \tag{4.124}$$

$$\nabla_{\mathbf{R}_{I}}L - \frac{\mathrm{d}}{\mathrm{d}t}\nabla_{\dot{\mathbf{R}}_{I}}L = 0. \tag{4.125}$$

The gradient operator is defined in cartesian coordinates as

$$\nabla_{\mathbf{R}_{I}} = \left(\frac{\partial}{\partial \mathbf{R}_{x}}, \frac{\partial}{\partial \mathbf{R}_{y}}, \frac{\partial}{\partial \mathbf{R}_{z}}\right) \tag{4.126}$$

with a similar definition for $\nabla_{\dot{\mathbf{R}}_{i}}$.

From (4.123) we obtain

$$2i\hbar o_{i}\frac{\mathrm{d}}{\mathrm{d}t}a_{iI}^{*} = -2o_{i}\sum_{I}a_{iJ}^{*}\langle\mathbf{R}_{J}|\hat{H}^{\mathrm{TB}}|\mathbf{R}_{I}\rangle - \frac{\partial}{\partial a_{iI}}\mathcal{E}[\rho - \rho^{0}](\mathbf{R}). \tag{4.127}$$

From (4.124),

$$2i\hbar o_i \frac{\mathrm{d}}{\mathrm{d}t} a_{iI} = 2o_i \sum_J a_{iJ} \langle \mathbf{R}_J | \hat{H}^{\mathrm{TB}} | \mathbf{R}_I \rangle | + \frac{\hat{o}}{\hat{o} a_{iI}^*} \mathcal{E}[\rho - \rho^0](\mathbf{R}). \tag{4.128}$$

And from (4.125),

$$M_{I}\ddot{\mathbf{R}}_{I} = -2o_{i}\sum_{IJ}a_{iJ}^{*}a_{iI}\langle\mathbf{R}_{I}|\nabla_{\mathbf{R}_{I}}\hat{H}^{\mathrm{TB}}|\mathbf{R}_{J}\rangle - \nabla_{\mathbf{R}_{I}}\mathcal{E}[\rho - \rho^{0}](\mathbf{R}) - \nabla_{\mathbf{R}_{I}}V_{\mathrm{rep}}(\mathbf{R}).$$
(4.129)

4.5.2.1 The Evolution of the Density Matrix

We can write the evolution of a state-vector $|\psi_i(t)\rangle$ as

$$i\hbar \frac{\mathrm{d}}{\mathrm{d}t} |\psi_i(t)\rangle = i\hbar \frac{\mathrm{d}}{\mathrm{d}t} \left(\sum_I a_{iI} |\mathbf{R}_I\rangle \right)$$

$$= i\hbar \sum_I \dot{a}_{iI} |\mathbf{R}_I\rangle,$$
(4.130)

since the local orbital basis is fixed in time. Using (4.128) this becomes (see Sect. 13.1.8)

$$i\hbar \frac{\mathrm{d}}{\mathrm{d}t}|\psi_i(t)\rangle = \hat{H}^{\mathrm{TB}}|\psi_i\rangle + \frac{1}{2o_i}\sum_{I}\frac{\partial}{\partial a_{iI}^*}\mathcal{E}[\rho - \rho^0]|\mathbf{R}_I\rangle. \tag{4.131}$$

The effect of the charge self-consistency energy $\mathcal{E}[\rho](\mathbf{R})$ in the second term is to introduce additional terms into the tight-binding Hamiltonian

$$\hat{H}^{TB}(\mathbf{R}) \to \hat{H}^{TB'}[\rho](\mathbf{R}) = \hat{H}^{TB}(\mathbf{R}) + \hat{V}^{SC}[\rho](\mathbf{R}).$$
 (4.132)

We adopt a form of the self-consistent charge transfer model, so that,

$$\mathcal{E}[\rho - \rho^0](\mathbf{R}) = \frac{1}{2} \sum_{I} U_I \Delta q_I^2 + \frac{1}{2} \sum_{I,I \neq I} U_{IJ}(\mathbf{R}) \Delta q_I \Delta q_J, \tag{4.133}$$

where U_I is a constant and $U_{IJ}(\mathbf{R})$ is a function of the ionic coordinates. The quantity Δq_I is the excess number of electrons on the *I*th ion and is given by,

$$\Delta q_I = 2\langle \mathbf{R}_I | \hat{\rho} | \mathbf{R}_I \rangle - q_0
= 2 \sum_i o_i a_{iI}^* a_{iI} - q_0.$$
(4.134)

The corresponding form for \hat{V}^{SC} is,

$$\hat{V}^{\text{SC}} = \sum_{IK} |\mathbf{R}_I\rangle \left(U_I \Delta q_I + \sum_{J \neq I} U_{IJ}(\mathbf{R}) \Delta q_J \right) \delta_{IK} \langle \mathbf{R}_K |, \tag{4.135}$$

such that equation (4.131), for the evolution of a state-vector, becomes (see Sect. 13.1.9),

$$i\hbar \frac{d}{dt}|\psi_i\rangle = (\hat{H}^{TB} + \hat{V}^{SC})|\psi_i\rangle = \hat{H}^{TB'}|\psi_i\rangle,$$
 (4.136)

i.e. the time-dependent Schrödinger equation.

The equivalent equation for the evolution of the density matrix is the quantum Liouville equation (see Sect. 13.1.10)

$$i\hbar \frac{d}{dt}\hat{\rho} = [\hat{H}^{TB'}, \hat{\rho}]. \tag{4.137}$$

4.5.2.2 The Evolution of the Ionic System

The third of the Lagrangian equations (4.125) gave us (4.129)

$$M_{I}\ddot{\mathbf{R}}_{I} = -2o_{i}\sum_{IJ}a_{iJ}^{*}a_{iI}\langle\mathbf{R}_{I}|\nabla_{\mathbf{R}_{I}}\hat{H}^{\mathrm{TB}}|\mathbf{R}_{J}\rangle - \nabla_{\mathbf{R}_{I}}\mathcal{E}[\rho - \rho^{0}](\mathbf{R}) - \nabla_{\mathbf{R}_{I}}V_{\mathrm{rep}}(\mathbf{R}),$$

$$(4.129)$$

which defines the forces acting on the ions. The first term in this equation is simply

$$-2\operatorname{Tr}(\hat{\rho}\nabla_{\mathbf{R}_{l}}\hat{H}^{\mathrm{TB}}) = -2\operatorname{Tr}((\hat{\rho} - \hat{\rho}^{0})\nabla_{\mathbf{R}_{l}}\hat{H}^{\mathrm{TB}}). \tag{4.138}$$

We have thus arrived at a set of coupled equations for the evolution of our ions at positions $\{\mathbf{R}_I(t)\}$ and our electronic system described by $\hat{\rho}(t)$,

$$M_I \ddot{\mathbf{R}}_I = -2 \text{Tr}(\hat{\rho} \nabla_{\mathbf{R}_I} \hat{H}^{\text{TB}}) - \nabla_{\mathbf{R}_I} \mathcal{E}[\rho - \rho^0](\mathbf{R}) - \nabla_{\mathbf{R}_I} V_{\text{rep}}(\mathbf{R}), \tag{4.139}$$

$$i\hbar \frac{\mathrm{d}}{\mathrm{d}t}\hat{\rho} = \left[(\hat{H}^{\mathrm{TB}} + \hat{V}^{\mathrm{SC}}), \hat{\rho} \right]. \tag{4.140}$$

The coupling exists because the Hamiltonian \hat{H}^{TB} is parameterized by the ionic coordinates **R** and because the force on the ions is dependent on $\hat{\rho}(t)$. In Sect. 13.1.11 we show that the above equations conserve the total energy of the system,

$$\frac{\mathrm{d}}{\mathrm{d}t} \left(E^{\mathrm{TB'}} + \sum_{I} \frac{1}{2} M_{I} \dot{\mathbf{R}}^{2} \right) = 0. \tag{4.141}$$

4.6 Ehrenfest Dynamics

4.6.1 Ehrenfest Dynamics versus Surface Hopping

Having derived a set of equations for the evolution of coupled quantum mechanical electrons (4.140) and classical ions (4.139) we will now give some

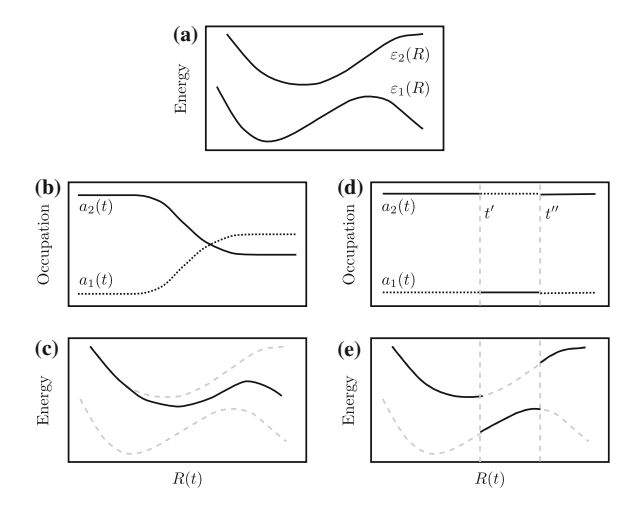


Fig. 4.1 A schematic representation of the difference between Ehrenfest dynamics and surface hopping for a simple two level system. **a** The eigenvalues as a function of the ionic coordinate under study. **b** The variation of the occupations of the eigenstates in the Ehrenfest evolution of the system. **c** The weighted average electronic potential energy surface on which the system evolves in Ehrenfest dynamics. **d** and **e** correspond to **b** and **c** respectively, but for a sample system evolving under a surface hopping algorithm in which hops are implemented at times t' and t'' as indicated. See the main text for discussion

thought to how realistic a dynamics they give rise to. To help draw out some of the possible difficulties with Ehrenfest dynamics we will compare it to another widely used implementation of semi-classical dynamics known as (*trajectory*) surface hopping [20].

Let us begin by considering the evolution of a simple system with two electronic eigenstates $|\phi_1(R)\rangle$ and $|\phi_2(R)\rangle$ varying as a function of a single ionic coordinate R. The energies of these eigenstates $\varepsilon_1(R)$ and $\varepsilon_2(R)$ define two potential energy surfaces on which R will evolve. Let us assume that our system is initialized such that the upper eigenstate is fully occupied $(a_2(t_0)=1)$ and the lower state initially unoccupied $(a_1(t_0)=0)$. We then allow the system to evolve from t_0 to t_1 . Figure 4.1a shows the evolution of the eigenstate energies as a function of R(t), which we will assume varies monotonically from $R(t_0)$ to $R(t_1)$. Importantly, we have chosen to consider a case in which the shapes of the two potential energy surfaces $\varepsilon_1(R)$ and $\varepsilon_2(R)$ are significantly different.

Figure 4.1b shows the evolution of the occupations of the eigenstates under Ehrenfest dynamics. The occupations vary continuously as the density matrix evolves,

$$a_{1,2}(t) = \langle \phi_{1,2}(R) | \hat{\rho}(t) | \phi_{1,2}(R) \rangle.$$
 (4.142)

In Fig. 4.1c we show the effective potential energy surface on which the ionic system evolves. The important thing to note is that the shape of this surface is an

average of the individual eigenstate surfaces, weighted by their occupations, and it is representative of neither surface individually. This can be a significant source of error in Ehrenfest dynamics.

The (trajectory) surface hopping method of Tully and Preston [20] solves the above problem by forcing the ionic system to always evolve on a potential energy surface due to a single eigenstate (or more generally on a set of fully occupied eigenstates). The details of the implementation of the method vary, but we can understand the underlying aim by considering a large number of equivalent copies of our semi-classical system all with the same initial conditions. The ionic coordinate R(t) is evolved on the occupied electronic potential energy surface up to some time t'. Meanwhile, the electronic system is evolved under the electronic Hamiltonian according to the Liouville equation. Now, at time t', the occupations of the eigenstates are reset probabilistically based on the transition probabilities implied by the evolved density matrix, but such that each eigenstate remains either completely occupied or completely unoccupied. The evolving eigenstate occupations for a single copy of the system are illustrated schematically in Fig. 4.1d. In Fig. 4.1e we show the effective electronic potential on which the ionic system evolves for this sample system and we see that, in contrast with the Ehrenfest system, it is always representative of a single eigenstate surface.

Clearly there is some considerable latitude in the precise specification of a surface hopping implementation. Any implementation must ensure that across a sample of trajectories the average occupation of the eigenstates agrees with the density matrix

$$\langle a_i(t) \rangle_{\text{sample}} = \langle \phi_i(R(t)) | \hat{\rho}(t) | \phi_i(R(t)) \rangle.$$
 (4.143)

The frequency with which the occupations are resampled (i.e. the frequency at which *hops* between potential energy surfaces are made) is a significant variable. Often the chosen approach is to implement the minimum number of switches across an ensemble of trajectories that maintains the correct average occupations (the *fewest switches* approach [21]).

The key difference between Ehrenfest dynamics and the surface hopping method is in the implied treatment of *coherence* in the evolution of the electronic system. This difference is highlighted in our example in which the two eigenstate energies imply very different ionic evolutions. In the Ehrenfest case, the evolution of the electrons is fully coherent, with interference between the quantum mechanical amplitudes persisting over infinite time-scales. In our semi-classical system this manifests itself in a trajectory for the ionic system evolving on a weighted average potential energy surface. In "reality", we would expect that a fully quantum mechanical electron-ion system would evolve so that the ions end up on one or the other of the divergent ionic trajectories, because we would expect the superposition of the two possible evolutions to undergo decoherence as the overlap between the ionic wavefunctions for the trajectories decayed [22]. The surface hopping method attempts to account for this decoherence process within a semi-classical framework. In effect we can regard the classical ionic system as

enforcing a "measurement" of the quantum mechanical electrons on a time-scale set by the hopping frequency. The evolution of the electronic system is then coherent on the short term, but is forced to be consistent with a single ionic trajectory representative of one of a set of possible outcomes on the longer term.

Given the above discussion, why have we chosen to adopt Ehrenfest dynamics rather than a surface hopping approach? First, there are a number of somewhat arbitrary choices to be made in the implementation of surface hopping. As already mentioned, we must choose how to implement the hops. Also, in order to conserve the total energy of the semi-classical system we must adjust the ionic kinetic energy whenever a hop is made. There is considerable ambiguity in how to achieve this, particularly in the case of large hops when there may be insufficient kinetic energy in the modes selected by our method of choice (i.e. in so-called *classically forbidden* transitions). Ambiguities such as these do not appear in Ehrenfest dynamics.

Second, the surface hopping method is defined in the space of instantaneous eigenstates of the Hamiltonian and the electronic forces on the ions in terms of the gradients of the eigenvalues. Such quantities are expensive to obtain for large systems and so our Ehrenfest dynamics in a local orbital basis (in which the Hamiltonian is sparse) is considerably more efficient.

Third, in a metallic system we would not expect to see large differences in the shape of potential energy surfaces corresponding to eigenstates close in energy and so the ionic trajectory on the average potential energy surface might remain representative of the "true" dynamics.

4.6.2 Energy Transfer in Ehrenfest Dynamics

Having arrived at a set of equations for evolving a set of classical ions coupled to a tight-binding model of quantum mechanical electrons we will now consider a key feature of the dynamics of our system. Our aim in simulating radiation damage with our semi-classical system is to understand the effects of non-adiabaticity on the ionic evolution: that is to say the effects of energy exchange between the ions and electrons.

It is well known that Ehrenfest dynamics does not correctly reproduce the full physics of electron-ion energy exchange. The ions in our semi-classical system are explicitly represented at the individual level and so the electronic system is able to identify the ionic temperature. However, the ions experience the electrons only as a structureless fluid and so cannot correctly determine the electronic temperature [23, 24]. This flaw in Ehrenfest dynamics, a result of the mean-field approximation, means that our semi-classical system will never achieve thermal equilibrium between the ions and the electrons.

The failure to equilibrate is due to the fact that Ehrenfest dynamics does not reproduce the effect of spontaneous phonon emission. However, a typical radiation

damage event will begin with an initially unexcited electronic system and an ionic system with a large excess of energy, and so we can safely neglect the effects of spontaneous phonon emission in our simulations. Because of the computational complexity of our semi-classical method our simulations never reach time-scales at which we would need to be concerned about the failure of Ehrenfest dynamics to achieve electron-ion equilibrium. J le Page has explored these issues thoroughly in the context of radiation damage [25, 26]. In Sect. 13.2.3 a simple treatment of a quantum mechanical oscillator is presented in an attempt to illuminate the nature of the failure of Ehrenfest dynamics.

4.7 Conclusions

In this introductory chapter we began by considering a fully quantum mechanical system of ions and electrons. We applied various approximating assumptions to arrive at a description of a semi-classical system of classical ions and quantum mechanical electrons, in which the electrons are described by a simple tight-binding model. We derived a set of energy conserving equations for the evolution of this semi-classical system, which will form the basis of our simulations of radiation damage phenomena. We considered the dynamics described by those equations, highlighting their key physical failings, but explaining why they should prove adequate for our purposes.

References

- 1. Elsayed-Ali, H.E., Norris, T.B., Pessot, M.A., Mourou, G.A.: Time-resolved observation of electron–phonon relaxation in copper. Phys. Rev. Lett. **58**(12), 1212–1215 (1987)
- Kapinos, V.G., Bacon, D.J.: Influence of ion-electron interaction on the formation mechanism of depleted zones in displacement cascades in metals. Phys. Rev. B 50(18), 13194–13203 (1994)
- 3. Kapinos, V.G., Bacon, D.J.: Effect of melting and electron–phonon coupling on the collapse of depleted zones in copper, nickel, and α-iron. Phys. Rev. B, **53**(13), 8287–8295 (1996)
- Nordlund, K., Wei, L., Zhong, Y., Averback, R.S.: Role of electron-phonon coupling on collision cascade development in ni, pd, and pt. Phys. Rev. B, 57(22), R13965–R13968 (1998)
- Caro, A., Victoria, M.: Ion–electron interaction in molecular-dynamics cascades. Phys. Rev. A 40(5), 2287–2291 (1989)
- Duffy, D.M., Rutherford, A.M.: Including the effects of electronic stopping and electron—ion interactions in radiation damage simulations. J. Phys. Condens. Matter 19(1), 016207 (2007)
- 7. Duffy, D.M., Itoh, N., Rutherford, A.M., Stoneham, A.M.: Making tracks in metals. J. Phys. Condens. Matter **20**(8), 082201 (2008)
- Rutherford, A.M., Duffy, D.M.: The effect of electron-ion interactions on radiation damage simulations. J. Phys. Condens. Matter 19(49), 496201 (2007)
- Todorov, T.N.: Time-dependent tight binding. J. Phys. Condens. Matter 13(45), 10125–10148 (2001)

- 10. Mittleman, M.H.: Proton-hydrogen scattering system. Phys. Rev. 122(2), 499–506 (1961)
- 11. Finnis, M.W.: Interatomic Forces in Condensed Matter. Oxford Materials. Oxford University Press, Oxford (2003)
- 12. Hohenberg, P., Kohn, W.: Inhomogeneous electron gas. Phys. Rev. 136(3B), B864–B871 (1964)
- 13. Kohn, W., Sham, L.J.: Self-consistent equations including exchange and correlation effects. Phys. Rev. **140**(4A), A1133–A1138 (1965)
- Runge, E., Gross, E.K.U.: Density-functional theory for time-dependent systems. Phys. Rev. Lett. 52(12), 997 (1984)
- 15. Foulkes, W.M.C.: PhD Thesis. Cambridge (1987)
- Matthew, W., Foulkes, C., Haydock, R: Tight-binding models and density functional theory. Phys. Rev. B 39(17), 12520–12536 (1989)
- 17. Sutton, A.P., Finnis, M.W., Pettifor, D.G., Ohta, Y.: The tight-binding bond model. J. Phys. C Solid State Phys. 21(1), 35–66 (1988)
- Schiff, L.I.: Quantum Mechanics, page 348. McGraw-Hill Book Company Inc., New York (1955)
- 19. Landau, L.D., Lifshitz, E.M.: Mechanics, page 3. Elsevier (2005)
- 20. Tully, J.C., Preston, R.K.: Trajectory surface hopping approach to nonadiabatic molecular collisions: The reaction of h⁺ with d₂. J. Chem. Phys. **55**(2), 562–572 (1971)
- Tully, J.C.: Molecular dynamics with electronic transitions. J. Chem. Phys. 93(2), 1061–1071 (1990)
- Bittner, E.R., Rossky, P.J.: Decoherent histories and nonadiabatic quantum molecular dynamics simulations. J. Chem. Phys. 107(20), 8611–8618 (1997)
- Horsfield, A.P., Bowler, D.R., Ness, H., Sanchez, C.G., Todorov, T.N., Fisher, A.J.: The transfer of energy between electrons and ions in solids. Rep. Prog. Phys. 69, 1195–1234 (2006)
- Horsfield, A.P., Bowler, D.R., Fisher, A.J., Todorov, T.N., Montgomery, M.J.: Power dissipation in nanoscale conductors: classical, semi-classical and quantum dynamics. J. Phys. Condens. Matter, 16(21), 3609–3622 (2004)
- 25. le Page, J., Mason, D.R., Foulkes, W.M.C.: The ehrenfest approximation for electrons coupled to a phonon system. J. Phys. Condens. Matter **20**(12), 125212 (2008)
- 26. le Page, J.: The transfer of energy between electrons and ions in solids. PhD thesis, University of London (2008)

Part II Simulating Radiation Damage in Metals

In Part I of this thesis we reviewed past efforts to include the effect of electronic excitations in simulations of radiation damage and gave the theoretical background to the approach that we have taken to the problem. In Part II, we will now examine the simulations that we have undertaken and the results of those simulations. We will begin by describing the software that we have used for our simulations (Chap. 5) and then consider the results of an investigation into the response of our model system to a simple periodic perturbation (Chap. 6). These results establish the applicability (and the limits of applicability) of our model to radiation damage phenomena. We will then move on to consider simulations of radiation damage events, focussing mostly on the behaviour of collision cascades. Chapter 7 presents the results of a single cascade simulation with the aim of introducing the types of information that are accessible in our Ehrenfest simulations.

Chapters 8 to 11 present the key results of this thesis. Chapters 8, 9 and 11 contain a detailed analysis of the nature of the electronic excitations and electronic forces in collision casades. Chapter 10 considers simulations of an entirely different radiation damage phenomenon—that of ion channelling.

Chapter 5

A Framework for Simulating Radiation Damage in Metals

Summary: In this chapter we introduce the simple tight-binding model and the simulation software that we have used for our simulations of radiation damage.

5.1 A Simple Model Metal

When compared with classical molecular dynamics (MD), simulations with Ehrenfest dynamics, incorporating an explicit model of quantum mechanical electrons, are computationally expensive. So that we can still simulate radiation damage events on realistic time and length scales despite this extra expense we have chosen to use a particularly simple model of a metallic system.

We have adopted the single *s*-band tight-binding model of Sutton et al. [1], in which the electrons are represented by a set of *s*-like atomic orbitals anchored, one each, at the positions of N_a ions. We denote the basis state on the ion at position \mathbf{R}_I by $|\mathbf{R}_I\rangle$. The set of these atomic orbitals $\{|\mathbf{R}_I\rangle\}$ is assumed to be orthonormal.

The basic non-self-consistent electronic Hamiltonian for the model is defined as ¹

$$\hat{H} = \sum_{II} |\mathbf{R}_I\rangle \gamma(|\mathbf{R}_{IJ}|)\langle \mathbf{R}_J|, \qquad (5.1)$$

where $\mathbf{R}_{IJ} = \mathbf{R}_J - \mathbf{R}_I$ and $\gamma(R)$ gives the *hopping integrals* as a simple function of the inter-ionic separation. The hopping integral function is defined as

¹ From now on, since we will only be discussing the case of classical ions and quantum mechanical electrons, we will write a Hamiltonian for a system of non-interacting electrons simply as \hat{H} rather than \hat{H}^{TB} . We will write the Hamiltonian for the self-consistent charge transfer model as \hat{H}^{SC} rather than \hat{H}^{TB} .

$$\gamma(|\mathbf{R}_{IJ}|) = -\frac{\epsilon c}{2} \left(\frac{a}{|\mathbf{R}_{IJ}|}\right)^{q}.$$
 (5.2)

It is a specification of the model that the hopping integrals are truncated between the second- and third-nearest-neighbour distances in the perfect crystal. ϵ , c, a and a are parameters of the model: a is a length scale, ϵ an energy scale, a is a measure of the spatial extent of the a-orbitals and a is a constant determined by the desired equilibrium. These parameters are set using conditions defined below. Note that the on-site (diagonal) terms in the Hamiltonian defined above are zero.

The electronic system is represented by a single-particle density matrix $\hat{\rho}$. If we also define a density matrix $\hat{\rho}^0$ for the corresponding free atoms (i.e. $\mathbf{R}_{IJ} \to \infty$ for all I, J) then we can define a binding energy for our model metal²:

$$E_{\rm B} = 2\text{Tr}\left[(\hat{\rho} - \hat{\rho}^0)\hat{H}\right] + E_{\rm rep},\tag{5.3}$$

where

$$E_{\text{rep}} = \frac{\epsilon}{2} \sum_{I,I \neq I} \left(\frac{a}{|\mathbf{R}_{IJ}|} \right)^p \tag{5.4}$$

is a repulsive energy due to repulsive pair potentials between the classical ions. Again, p is a parameter of the model. The factor of 2 in (5.3) accounts for spin degeneracy: we have chosen a form for the density matrix such that its eigenvalues are in the range 0–1.

An important parameter of the model is the *band-filling*, denoted v. This is allowed to take a fractional value in order to best fit certain desired properties of real metals. The number of electrons associated with each of the N_a ions is 2v and since the free atoms (and the whole system) are assumed neutral, each ion is assumed to carry a positive charge of +2ve. The excess of electrons on the *I*th ion we will denote Δq_I and write

$$\Delta q_I = 2(\rho_{II} - \rho_{II}^0) = 2\rho_{II} - 2\nu, \tag{5.5}$$

where

$$\rho_{II} = \langle \mathbf{R}_I | \hat{\rho} | \mathbf{R}_I \rangle. \tag{5.6}$$

As we defined it in (5.1), \hat{H} has zero onsite elements so that even non-zero charges will not affect the binding energy. In most of our simulations, the charges on our ions will remain close to zero and we will not have to worry about how to capture the energy associated with charge localization. However in some simulations (see Chap. 10) charge transfer is significant and we must introduce charge self-consistent terms to our Hamiltonian as discussed in Sect. 4.5.2.1. The charge self-consistent version of our model takes the form

² This approach conforms to the tight-binding bond model. See Sutton et al. [2] for details.

$$\hat{H}^{SC} = \hat{H} + \sum_{I} |\mathbf{R}_{I}\rangle \left(U\Delta q_{I} + \sum_{J} z_{IJ}\Delta q_{J}\right) \langle \mathbf{R}_{I}|, \tag{5.7}$$

where,

$$z_{IJ} = \frac{e^2}{4\pi\epsilon_0} \left(|\mathbf{R}_{IJ}|^2 + \left[\frac{e^2}{4\pi\epsilon_0 V} \right]^2 \right)^{-1/2}, \tag{5.8}$$

and U and V are parameters controlling the strength of the charge interactions on a single site and between sites respectively. The most physically realistic choice for these parameters³ is U = V = 7 eV. The onsite elements of \hat{H}^{SC} are such that they give a self-consistent binding energy

$$E_{\rm B} = 2\text{Tr}\left[\left(\hat{\rho} - \hat{\rho}^0\right)\hat{H}\right] + \frac{1}{2}U\sum_{I}\Delta q_I^2 + \frac{1}{2}\sum_{I,J\neq I}z_{IJ}\Delta q_I\Delta q_J + E_{\rm rep}.$$
 (5.9)

5.1.1 The Parameters of the Model

The six parameters of our non-self-consistent tight-binding model are ϵ , a, p, q, c and v, and are chosen to reproduce certain properties of a real metal. In our case, we use the parameterization for copper given in reference [1]. The length scale a is chosen freely to be equal to the lattice parameter a_f of face-centred cubic (fcc) copper at room temperature. For a given choice of the powers p and q, we can then determine c by stipulating that the binding energy per atom,

$$\frac{E_{\rm B}}{N_{\rm a}} = \frac{\epsilon}{2} \sum_{J \neq I} \left(\frac{a_{\rm f}}{|\mathbf{R}_{IJ}|} \right)^p - \epsilon c \sum_{J \neq I} \rho_{IJ} \left(\frac{a_{\rm f}}{|\mathbf{R}_{IJ}|} \right)^q, \tag{5.10}$$

must be minimized when the lattice parameter is equal to $a_{\rm f}$. This condition implies,

$$c = \frac{p}{2q} \left(\sum_{J \neq I} \left(\frac{a_{\rm f}}{|\mathbf{R}_{IJ}|} \right)^p \middle/ \sum_{J \neq I} \rho_{IJ} \left(\frac{a_{\rm f}}{|\mathbf{R}_{IJ}|} \right)^q \right). \tag{5.11}$$

The energy scale for a given choice of p and q is chosen to give the correct value of the binding energy per atom,

 $^{^{3}}$ From now on we will leave the units of U and V implicit.

Table 5.1 The values of the parameters of our tight-binding model, chosen to reproduce certain properties of fcc copper metal. Values taken from reference [1]

Parameter		Fitting constraint
а	3.6 Å	Chosen to equal $a_{\rm f}$
c	112.35	Ensures equilibrium at $a_{\rm f}$
ϵ	0.012611 eV	Fixed by binding energy $E_{\rm B}$
p	9 }{	Product pq set by bulk modulus
q	3	p, q chosen as integers
v	0.24304	To fit elastic constants

$$\frac{E_{\rm B}}{N_{\rm a}} = \frac{\epsilon}{2} \left(\frac{p}{q} - 1 \right) \sum_{I \neq I} \left(\frac{a_{\rm f}}{|\mathbf{R}_{IJ}|} \right)^p, \tag{5.12}$$

and the values of p and q, restricted to be integers for numerical convenience, are chosen to fit the bulk modulus,

$$B = \frac{E_{\rm B}pq}{9N_{\rm a}V_{\rm cell}} \tag{5.13}$$

where V_{cell} is the volume of a *primitive* unit cell. Finally, the band-filling v is chosen to give the best possible fit to the elastic constants of copper. Table 5.1 gives a summary of the fitting constraints for the model parameters and their values (as given in reference [1]).

5.1.2 The Electronic Structure of the Model

Because our tight-binding model takes such a simple form, we can easily calculate the band structure. In a perfect crystal the energy eigenstates will be Bloch states with wave-vectors \mathbf{k} . Writing these states as $|\mathbf{k}\rangle$ we have

$$|\mathbf{k}\rangle = \frac{1}{\sqrt{N_a}} \sum_{I} e^{i\mathbf{k}\cdot\mathbf{R}_I} |\mathbf{R}_I\rangle.$$
 (5.14)

The band structure is given by,

$$E(\mathbf{k}) = \langle \mathbf{k} | \hat{H} | \mathbf{k} \rangle, \tag{5.15}$$

where we do not need to consider the charge self-consistent terms because all the ions in the perfect crystal will be neutral. Hence,

$$E(\mathbf{k}) = \frac{1}{N_{a}} \sum_{IJ} e^{i\mathbf{k} \cdot (\mathbf{R}_{J} - \mathbf{R}_{I})} \gamma(|\mathbf{R}_{IJ}|)$$

$$= \frac{1}{N_{a}} \sum_{I} e^{i\mathbf{k} \cdot (\mathbf{R}_{0} - \mathbf{R}_{I})} \gamma(|\mathbf{R}_{I0}|),$$
(5.16)

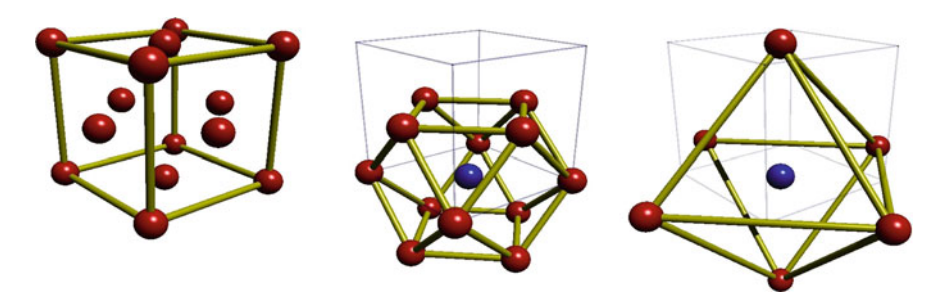
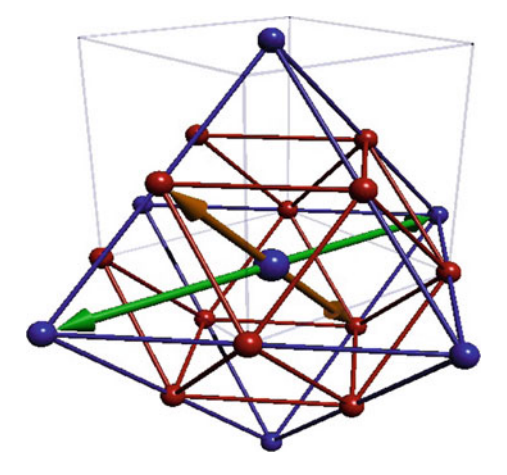


Fig. 5.1 Schematic diagrams of (*left*) the face-centred cubic (fcc) unit cell and the shells of (*centre*) nearest- and (*right*) next-nearest-neighbours about a sample ion (shown in *blue*)

Fig. 5.2 A schematic diagram showing an example of a pair of nearest-neighbours (shorter (orange) arrows) and a pair of next-nearest-neighbours (longer (green) arrows) about an atom of interest



where \mathbf{R}_0 is the position of any atom, chosen as a reference. We then divide the atoms around the one at \mathbf{R}_0 into two shells of neighbours and next-nearest neighbours (no other atoms contribute because of the truncated hopping integrals in our model). We index the shells by b and then further divide the atoms in each shell into pairs such that the reference atom lies exactly between each pair (see Figs. 5.1 and 5.2). If we write the positions of the ath pair of atoms in the bth shell of neighbours in terms of a displacement $\pm \mathbf{d}_a^b$ from the reference atom, then the band structure can be written

$$E(\mathbf{k}) = \sum_{b} \sum_{a} \left(e^{i\mathbf{k}\cdot\mathbf{d}_{a}^{b}} + e^{-i\mathbf{k}\cdot\mathbf{d}_{a}^{b}} \right) \gamma(|\mathbf{d}_{a}^{b}|)$$

$$= 2 \sum_{b} \sum_{a} \cos(\mathbf{k}\cdot\mathbf{d}_{a}^{b}) \gamma(|\mathbf{d}_{a}^{b}|).$$
(5.17)

If we write **k** in terms of its cartesian components $\mathbf{k} = (k_x, k_y, k_z)$ then the six second-nearest neighbours lying at $a\langle 100\rangle$ and the twelve nearest neighbours lying at $(a/2)\langle 110\rangle$ give a band energy

Fig. 5.3 The band structure and density of states (DOS) of our simple model metal

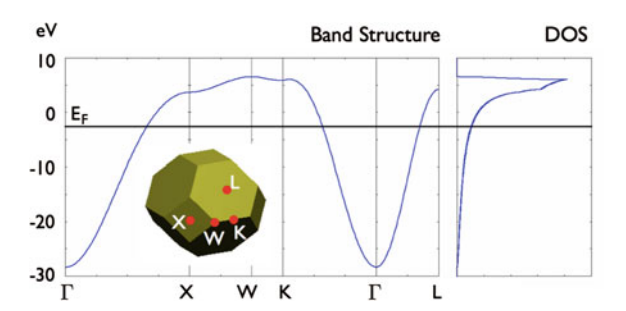
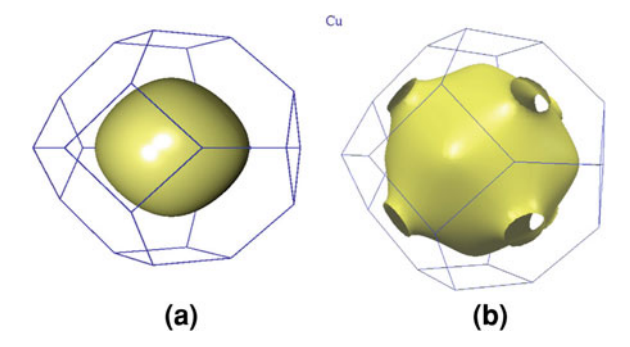


Fig. 5.4 The Fermi surfaces of (a) our model metal, and (b) real copper (from http://www.phys.ufl.edu/fermisurface/)



$$E(k_x, k_y, k_z) = -4\gamma(a/2) \left[\cos(\frac{1}{2}k_x a) \cos(\frac{1}{2}k_y a) + \cos(\frac{1}{2}k_y a) \cos(\frac{1}{2}k_z a) + \cos(\frac{1}{2}k_z a) \cos(\frac{1}{2}k_z a) \cos(\frac{1}{2}k_x a) \right]$$

$$-2\gamma(a) \left[\cos(k_x a) + \cos(k_y a) + \cos(k_z a) \right].$$
(5.18)

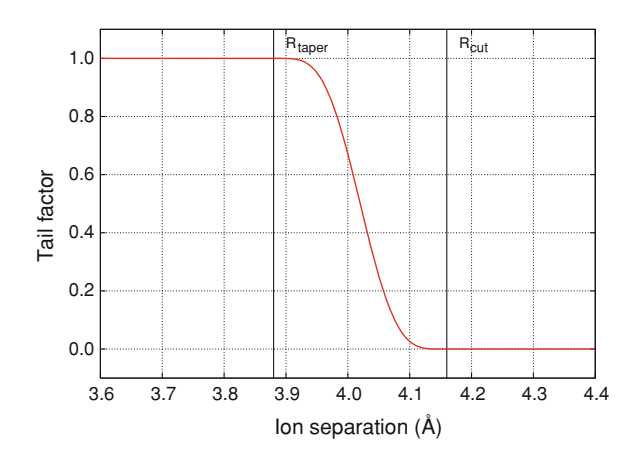
This expression and the above notation will be useful in the next chapter when we examine some preliminary simulation results.

The band structure and density of states of our model metal are illustrated in Fig. 5.3. Figure 5.4a and b compare the model Fermi surface and that of real copper.

5.1.3 A Note on the Truncation of the Hopping Integrals

The truncation of the hopping integrals in the original model of reference [1] is accomplished with a fourth-order polynomial tail. Because our simulations use a fourth order integrator for the system dynamics we have found it necessary to use a smoother tail matching the function and first four derivatives to the hopping

Fig. 5.5 The 10th order polynomial tail used to truncate the hopping integrals in our tight-binding model



integral at the inside of the smoothing region and to zero at the outside. This requires the 10th order polynomial tail⁴ illustrated in Fig. 5.5.

5.2 Ehrenfest Dynamics

Our simulations proceed under Ehrenfest dynamics as described in Sect. 4.5.2. The electrons are represented by a single particle density matrix of dimension $N_a \times N_a$, where N_a is the number of ions and also the number of atomic orbitals. This density matrix is evolved under the tight-binding Hamiltonian (with or without the charge self-consistent terms) described above, using the quantum Liouville equation,

$$i\hbar \frac{d}{dt}\hat{\rho} = [\hat{H}, \hat{\rho}]. \tag{5.19}$$

The ions are represented as a set of classical particles of mass M whose positions $\{\mathbf{R}_I\}$ evolve under Hellmann–Feynman forces due to the electrons and repulsive forces corresponding to the repulsive term in the binding energy (5.4)

$$M\frac{\mathrm{d}^2}{\mathrm{d}t^2}\mathbf{R}_I = -2\mathrm{Tr}(\hat{\rho}\nabla_{\mathbf{R}_I}\hat{H}) - \nabla_{\mathbf{R}_I}E_{\mathrm{rep}}.$$
 (5.20)

Because the hopping integrals and repulsive potential take simple power law forms, these forces can be written down analytically and calculated very efficiently,

⁴ Details of this tail were worked out by D. R. Mason.

$$M\frac{\mathrm{d}^2}{\mathrm{d}t^2}\mathbf{R}_I = \sum_J 2\Re\{\rho_{IJ}\} \frac{q\epsilon c}{a} \frac{\mathbf{R}_{IJ}}{|\mathbf{R}_{IJ}|} \left(\frac{a}{|\mathbf{R}_{IJ}|}\right)^{q+1} - \sum_J \frac{p\epsilon}{a} \frac{\mathbf{R}_{IJ}}{|\mathbf{R}_{IJ}|} \left(\frac{a}{|\mathbf{R}_{IJ}|}\right)^{p+1}. \quad (5.21)$$

Because of the way we define our density matrix, with eigenvalues between 0 and 1 and not accounting for spin degeneracy, the quantity

$$\rho_{IJ} + \rho_{JI} = 2\Re\{\rho_{IJ}\}\tag{5.22}$$

is the *bond-order* between orbitals $|\mathbf{R}_I\rangle$ and $|\mathbf{R}_I\rangle$. Similarly,

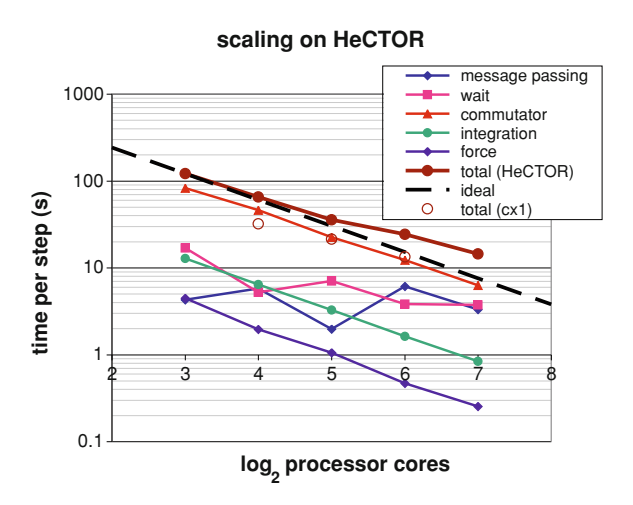
$$-i(\rho_{IJ} - \rho_{JI}) = 2\Im\{\rho_{IJ}\}\tag{5.23}$$

will be the *bond-current* from $|\mathbf{R}_I\rangle$ to $|\mathbf{R}_J\rangle$ and $2\rho_II$ and $-2(\rho_{II}-v)e$ will be the number of electrons in orbital $|\mathbf{R}_I\rangle$ and the net charge on the *I*th ion respectively.

5.3 *spICED*: Our Simulation Software

All of the simulations of radiation damage cascades and ion channelling documented in the remainder of this thesis were performed using the *sparse parallel Imperial College Ehrenfest Dynamics* code, or *spICED*. This software was specially written for the project by D. R. Mason and comprises some eighty thousand lines of Fortran 95 code. *spICED* is parallelized with MPI with good scaling up to 128 cores on HeCTOR (see Fig. 5.6). Though the code has been designed specifically for flexibility and robustness, it is fast enough that simulations of ten thousand atoms over picosecond time-scales can be routinely performed. These time- and length-scales make possible the direct simulation of radiation damage events.

Fig. 5.6 The scaling of processing time on HeCTOR. Timings are broken down by process (Figure produced by D. R. Mason.)



The parameters for simulations are specified via flexible xml input files that allow the control of all the model parameters and output data. A wide range of raw and processed output data is made available by *spICED*, including raw density matrix output, force histogram output, densities and local densities of states, eigenspectra and full atom-by-atom details of positions, velocities, energies, charges and forces. We will introduce various features of *spICED* throughout the remainder of this thesis as they are made use of.

References

- Sutton, A.P.M., Todorov, T.N., Cawkwell, M.J., Hoekstra, J.: A simple model of atomic interactions in noble metals based explicitly on electronic structure. Phil. Mag. A 81(7), 1833–1848 (2001)
- Sutton, A.P., Finnis, M.W., Pettifor, D.G., Ohta, Y.: The tight-binding bond model. J. Phys. C Solid State Phys. 21(1), 35–66 (1988)

Chapter 6 The Single Oscillating Ion

Summary: In this chapter we describe the results of simulations of a single oscillating ion in a perfect lattice designed to probe the response of our system to various perturbations and determine its suitability for simulations of radiation damage phenomena. We find that the rate of energy transfer from the oscillating ion to the electrons of our system is dependent on the frequency of oscillation, on the local atomic environment and on the electronic temperature. We explain this behaviour using time-dependent perturbation theory.

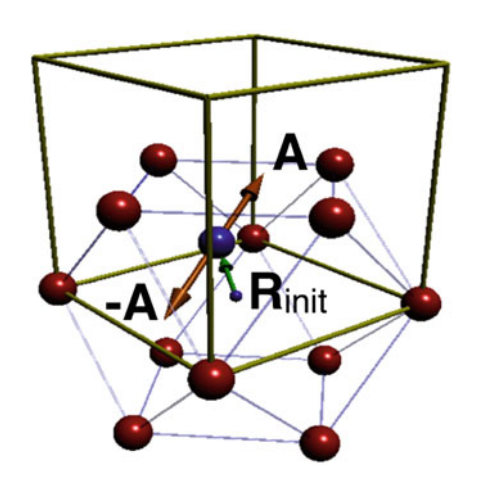
Attribution: The Ehrenfest simulations of a single oscillating ion discussed in this chapter we carried out by D. R. Mason. Much of the general perturbation theory analysis was worked out by J. le Page, as indicated in the relevant sections. The detailed perturbation analysis of the transition spectrum within our tight-binding model was conducted by the present author.

The underlying aim of our work is to study the effect of energy exchange between electrons and ions on the outcome of radiation damage events. Before we undertake simulations of complex damage processes we need to be confident that our model can capture the physics of that energy exchange. This is about more than just the physics included in our model: we must also be sure that the system sizes that we are able to simulate are adequate for our purposes.

To help build confidence in our approach we will begin by examining the results of simulations of a highly idealized scenario: we will take a block of perfect crystal and force a single ion to undergo sinusoidal oscillations. With this simple set-up we can probe the response of our system to ionic motion across a range of simulation parameters. The simplicity of this scenario also means that it can be treated analytically within time-dependent perturbation theory.

Fig. 6.1 A schematic illustration of the set-up for our oscillator simulations. The (blue) oscillating atom is shown within a shell of its (red) nearest neighbours.

R_{init} is its initial displacement from its perfect lattice site and A gives the direction and amplitude of its oscillation. The (yellow) cube indicates the face centred cubic unit cell



6.1 Simulations of a Single Oscillating Ion

Our oscillator simulations begin with a block of around 1,000 atoms of our tight-binding copper model with periodic boundary conditions. Because charge transfers in these simulations are negligible we use the simpler version of the Hamiltonian, omitting the charge self-consistent terms. All the ions of the simulation cell are held fixed at their perfect lattice sites except for one ion, which is forced to undergo sinusoidal oscillations at angular frequency Ω such that its position is given by

$$\mathbf{R}_{\rm osc}(t) = \mathbf{R}_{\rm init} + \mathbf{A}\sin(\Omega t). \tag{6.1}$$

 \mathbf{R}_{init} gives an initial fixed displacement of the ion from its perfect lattice site (and may be zero) and \mathbf{A} gives the direction and amplitude of the oscillation (see Fig. 6.1). The electronic density matrix is initialised at a temperature $T_{\rm e}$ so that if $\{|\phi_i\rangle\}$ are the eigenvalues of the initial electronic Hamiltonian $\hat{H}(t=0)$ with eigenvalues $\{\varepsilon_i\}$ then

$$\hat{\rho}(t=0) = \sum_{i} |\phi_{i}\rangle f(\varepsilon_{i}; T_{e}, \mu)\langle\phi_{i}|. \tag{6.2}$$

 $f(\varepsilon; T_e, \mu)$ is the Fermi-Dirac distribution

$$f(\varepsilon; T_{\rm e}, \mu) = \frac{1}{1 + {\rm e}^{(\varepsilon - \mu)/k_{\rm B}T_{\rm e}}}$$
(6.3)

at temperature $T_{\rm e}$ and with chemical potential μ . We shall have more to say about this initialization in Sect. 7.2.

Our simulations are designed to test the response of the electronic system to the oscillating ion as we vary the following simulation parameters:

- Angular frequency of oscillation, Ω ;
- Initial electronic temperature, $T_{\rm e}$;
- Direction of oscillation, A/|A|; and,
- Initial position of oscillator, R_{init}.

To measure the response of our system we will keep track of the irreversible energy transfer to the electrons $\Delta E(t)$. In Sect. 7.2.4, we will discuss the definition of this variable in more general circumstances, but in this present case, because the electronic Hamiltonian is strictly periodic in time, we can easily determine the energy transfer whenever the ion returns to the centre of its oscillation. The electronic energy is

$$E_{\rm e}(t) = \text{Tr}(\hat{\rho}(t)\hat{H}(t)), \tag{6.4}$$

and so the irreversible energy transfer will be given by

$$\Delta E(t = m\tau) = E_{\rm e}(t = m\tau) - E_{\rm e}(t = 0),$$
 (6.5)

For integer m and

$$\tau = \frac{2\pi}{\Omega} \tag{6.6}$$

the period of the oscillator.

In our review of the radiation damage literature in Chap. 3, one prominent feature stood out: the concept of a viscous damping force on the ions due to the electrons. Our oscillator simulations can provide a first test of the validity of this concept within Ehrenfest simulations of radiation damage. We begin by assuming that the irreversible energy transfer to the electrons can be represented by a viscous force on the oscillating ion

$$\mathbf{F}(t) = -\tilde{\beta}(m)\dot{\mathbf{R}}_{\rm osc}(t). \tag{6.7}$$

For generality, we have allowed the damping constant β to vary from cycle to cycle. We now expect the energy transfer over the *m*th cycle to be

$$\widetilde{\Delta E}(m) = \int_{m\tau}^{(m+1)\tau} dt \, \mathbf{F}(t) \cdot \dot{\mathbf{R}}_{\rm osc}(t) = -\int_{m\tau}^{(m+1)\tau} dt \, \tilde{\beta}(m) \dot{\mathbf{R}}_{\rm osc}^{2}(t)$$
(6.8)

where we assume that $\tilde{\beta}$ varies slowly enough that it can be treated as constant over a cycle. So for our oscillator we have

$$\widetilde{\Delta E}(m) = \int_{m\tau}^{(m+1)\tau} dt \, \widetilde{\beta}(m) |\mathbf{A}|^2 \Omega^2 \cos^2(\Omega t) = \frac{1}{2} \widetilde{\beta}(m) |\mathbf{A}|^2 \Omega^2 \tau. \tag{6.9}$$

In fact, as our results will show, the energy transfer varies little from cycle to cycle while ever the response of our finite system is valid, and so we can define an effective damping constant

$$\beta(\Omega, T_{\rm e}) = \frac{2\Delta E(m\tau)}{|\mathbf{A}|^2 \Omega^2 m\tau} \tag{6.10}$$

where we have indicated a possible dependence on the oscillator frequency and the initial electronic temperature.

Now, the theories of slow particle stopping (Sect. 3.2.5) predict that the damping force on a particle (the electronic stopping force) should be proportional to its velocity,

$$\frac{dE}{dr} \propto -\nu,$$
 (6.11)

i.e. they suggest a rate of energy loss

$$\frac{\mathrm{dE}}{\mathrm{d}t} \propto v^2. \tag{6.12}$$

For our oscillator, the velocity is proportional to $A\Omega$ and since we have

$$\frac{\Delta E(m\tau)}{m\tau} = \frac{1}{2} |\mathbf{A}|^2 \beta(\Omega, T_{\rm e}) \Omega^2, \tag{6.13}$$

the theories of slow particle stopping correspond to a damping coefficient β independent of frequency.

6.2 Simulation Results

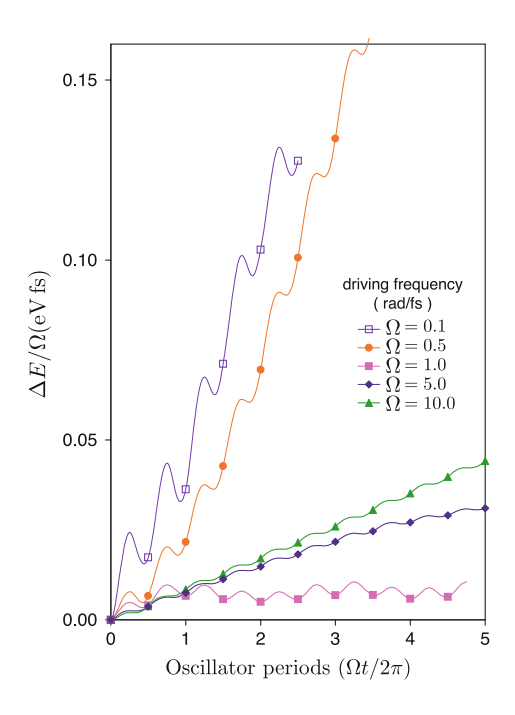
Figure 6.2 shows the function $\Delta E(t)/\Omega$ as a function of time expressed in oscillator periods $\Omega t/2\pi$ for a range of frequencies for low amplitude oscillations around a perfect lattice site (i.e. $\mathbf{R}_{\text{init}}=0$). Our expression (6.13) suggests that for a frequency independent damping all the plots in Fig. 6.2 should coincide. They clearly do not. Also, if β were unchanged from cycle to cycle, all the plots would be linear in time. Only the case of $\Omega=10$ rad fs⁻¹ appears to conform to this expectation. In the case of $\Omega=1$ rad fs⁻¹, there is very little energy transfer to the electrons at all and $\Delta E(t)$ oscillates around a fixed average.

Finally, Fig. 6.2 actually shows $\Delta E(t)$ calculated at many points within each cycle (using the approach detailed in Sect. 7.2.4 rather than equation (6.5) and we can see that at some points during each cycle energy is returned *from* the ions *to* the electrons. This is inconsistent with the existence of a simple damping force and so we should be clear that our effective damping constant is defined as an average over an oscillator period.

Compared with the simple damping model, then, our results contain three features that require explanation:

6.2 Simulation Results 117

Fig. 6.2 Sample results for the heating of the electronic subsystem as a function of time, at several oscillator frequencies. (results from simulations by D. R. Mason.) (Reprinted figure 4 with permission from Mason, D.R., le Page, J., Race, C.P., Foulkes, W.M.C., Finnis, M.W., Sutton, A.P.: Electronic damping of atomic dynamics in irradiation damage of metals. J. Phys. Condens Matter 19(43), 436209 (2007). Copyright (2007) by the Institute of Physics Publishing Ltd.)



- 1. The frequency dependence of β
- 2. The failure of the expected relationship $\Delta E \propto t$
- 3. The absence of long term energy transfer at some frequencies

6.2.1 Frequency and Temperature Dependence of Energy Transfer

Before we undertake a theoretical analysis of the system we will examine the results in more detail. Figure 6.3 shows the dependence of the effective damping coefficient on the frequency of the oscillator and on the initial temperature of the electronic subsystem. We note the following features for later explanation:

- 1. There is significant variation in β with frequency at low temperature.
- 2. β is frequency independent at very high temperature.
- 3. The effective damping decreases with increasing temperature.
- 4. The effective damping decreases rapidly at high frequency.

6.2.2 Position and Direction Dependence

Figure 6.4 shows the effective damping for a series of simulations at a fixed frequency of $\Omega = 1$ rad fs⁻¹, but for different directions of oscillation A/|A| and

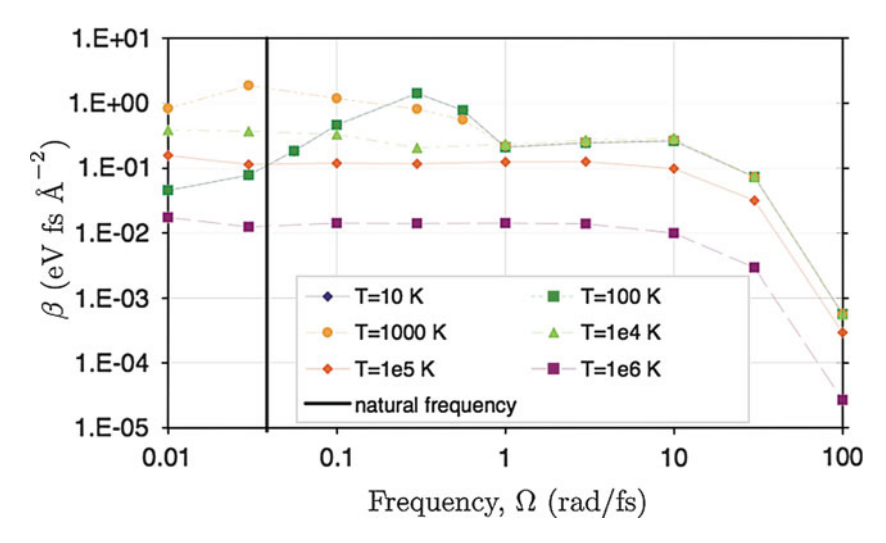


Fig. 6.3 The variation of the effective damping coefficient with oscillator frequency and initial electronic temperature. (results from simulations by D. R. Mason.) (Reprinted figure 1 with permission from Mason, D.R., le Page, J., Race, C.P., Foulkes, W.M.C., Finnis, M.W., Sutton, A.P.: Electronic damping of atomic dynamics in irradiation damage of metals. J. Phys. Condens Matter **19**(43), 436209 (2007). Copyright (2007) by the Institute of Physics Publishing Ltd.)

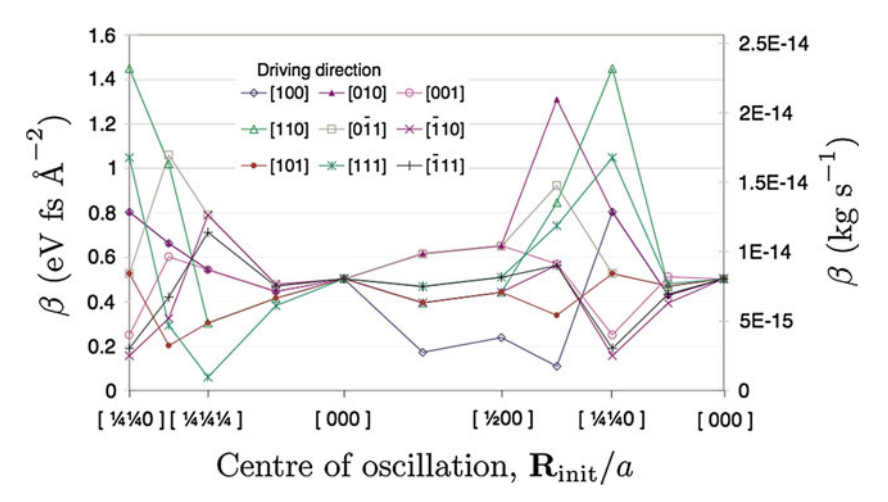


Fig. 6.4 The variation of the effective damping coefficient for $\Omega=1$ rad fs $^{-1}$ with oscillator position \mathbf{R}_{init} and direction $\mathbf{A}/|\mathbf{A}|$. (results from simulations by D. R. Mason.) (Reprinted figure 3 with permission from Mason, D.R., le Page, J., Race, C.P., Foulkes, W.M.C., Finnis, M.W., Sutton, A.P.: Electronic damping of atomic dynamics in irradiation damage of metals. J. Phys. Condens Matter $\mathbf{19}(43)$, 436209 (2007). Copyright (2007) by the Institute of Physics Publishing Ltd.)

for different mean positions of the oscillating ion $R_{\rm init}$. The lattice vectors on the horizontal axis show the values of $R_{\rm init}$ and in general these are not points of stable equilibrium. We note the following features of the results for consideration:

6.2 Simulation Results 119

The effective damping is strictly isotropic for oscillations about the equilibrium lattice site.

- 6. For oscillations about other points there is significant directional dependence.
- There is a significant dependence of the effective damping on the mean position of the oscillator within the unit cell.

The seven features of the results listed above suggest that an effective damping model that aimed to capture all the features of the energy transfer from ions to electrons would have to go well beyond a simple constant.

6.3 Theoretical Analysis of the System

Because the phenomena in our oscillator simulations are so simple, involving a single moving ion in a perfect lattice, we can undertake a perturbation theory analysis of our results. In Sect. 13.2, we derive the result for the energy transfer due to a sinusoidally varying perturbation $\hat{V}(t) = \hat{V}^0 \sin \Omega t$. This expression is, to first order and neglecting oscillatory contributions [see equation (B.54) in Sect. 13.2.2.3],

$$\Delta E(t) = \frac{1}{2\hbar^2} \sum_{ij} o_i (1 - o_j) (\varepsilon_j - \varepsilon_i) |V_{ij}^0|^2 s(\varepsilon_i - \varepsilon_j, \Omega; t). \tag{6.14}$$

$$s(\varepsilon, \Omega; t) = t^2(\operatorname{sinc}^2[(\varepsilon/\hbar - \Omega)t/2] + \operatorname{sinc}^2[(\varepsilon/\hbar + \Omega)t/2]), \tag{6.15}$$

where $\{|\phi_i\rangle\}$ are the eigenstates of the unperturbed Hamiltonian \hat{H}^0 , with energies $\{\varepsilon_i\}$, $\{o_i\}$ are their initial occupations and $\omega_{ji} = (\varepsilon_i - \varepsilon_j)/\hbar$.

Because our unperturbed system is a perfect lattice, the eigenstates of the unperturbed Hamiltonian will be Bloch states,

$$|\mathbf{k}\rangle = \frac{1}{\sqrt{N_a}} \sum_{I} e^{i\mathbf{k}\cdot\mathbf{R}_I} |\mathbf{R}_I\rangle,$$
 (6.16)

for wave-vector **k**. If we initially occupy these eigenstates according to a Fermi-Dirac distribution at temperature T_e , chemical potential μ then we can write,

$$o_i = f(E_{\mathbf{k}_i}; T_{\mathbf{e}}, \mu), \tag{6.17}$$

where $E_{\mathbf{k}} = \langle \mathbf{k} \hat{H}^0 | \mathbf{k} \rangle$. Our expression for the irreversible energy transfer is then

$$\Delta E(t) = \frac{1}{2\hbar^2} \sum_{\mathbf{k}\mathbf{k}'} f(E_{\mathbf{k}}) [1 - f(E_{\mathbf{k}'})] [E_{\mathbf{k}'} - E_{\mathbf{k}}] |V_{\mathbf{k}\mathbf{k}'}^0|^2 s(\omega_{\mathbf{k}\mathbf{k}'}, \Omega; t).$$
 (6.18)

where we have adopted the notation $V^0_{\mathbf{k}\mathbf{k}'} = \langle \mathbf{k}\hat{V}^0|\mathbf{k}'\rangle$ and $\omega_{\mathbf{k}\mathbf{k}'} = (E_{\mathbf{k}'} - E_{\mathbf{k}})/\hbar$.

This form of the energy transfer expression has an intuitive interpretation in terms of transitions from occupied states of energy $E_{\bf k}$ to unoccupied states with energy $E_{\bf k'}$. The Fermi factors account for exclusion, the factor $[E_{\bf k'}-E_{\bf k}]$ gives the energy change of the transition and $|V^0_{\bf kk'}|^2$ gives the strength of coupling between the two states. The function $s(E({\bf k'})-E({\bf k}),\Omega;t)$ then gives the relative rates at which transitions of different energies are stimulated by the oscillator perturbation: it determines the sampling of the *transition spectrum*. The concept of the transition spectrum, the set of all possible energy changes $E({\bf k'})-E({\bf k})$ for all ${\bf k},{\bf k'}$, will be important in understanding the oscillator results.

Before we return to discuss our simulation results, a few more analytical expressions will be useful. If we consider the case of an infinite sample of our tight-binding model $(N_a \rightarrow \infty)$ then the sums over Bloch states will become integrals over k-space,

$$\Delta E(t) = \frac{1}{2\hbar^2} \left(\frac{N_a a^3}{8\pi^3} \right)^2 \int d^3k \int d^3k' f(E_{\mathbf{k}}) [1 - f(E_{\mathbf{k}'})] [E_{\mathbf{k}'} - E_{\mathbf{k}}]$$

$$\times |V_{\mathbf{k}\mathbf{k}'}^0|^2 s(E_{\mathbf{k}'} - E_{\mathbf{k}}, \Omega; t).$$
(6.19)

We will then transform each of the three-dimensional k-space integrals into a product of an energy integral and an integral over a two-dimensional isoenergetic surface in k-space. Indicating the surface of energy ε by $S(\varepsilon)$, writing E_k as e and the transition energy $E_{\mathbf{k}'} - E_{\mathbf{k}}$ as ε gives,

$$\begin{split} \Delta E(t) &= \frac{1}{2\hbar^2} \left(\frac{N_{\mathrm{a}} a^3}{8\pi^3} \right)^2 \int\limits_{\mathrm{band}} \mathrm{d}e \int\limits_{-\infty}^{\infty} \mathrm{d}\varepsilon \int\limits_{S(e)} \mathrm{d}^2k \int\limits_{S(e+\varepsilon)} \mathrm{d}^2k' \frac{\left|V_{\mathbf{k}\mathbf{k}'}^0\right|^2}{\left|\nabla_{\mathbf{k}} E_{\mathbf{k}}\right| \left|\nabla_{\mathbf{k}'} E_{\mathbf{k}'}\right|} \left(6.20\right) \\ &\times f(e) [1 - f(e+\varepsilon)] \varepsilon \, s(\varepsilon, \Omega; t). \end{split}$$

We can now define a new (dimensionless) function

$$|\tilde{V}(e, e + \varepsilon)|^2 = \left(\frac{N_a a^3}{8\pi^3}\right)^2 \int_{S(e)} d^2k \int_{S(e+\varepsilon)} d^2k' \frac{\left|V_{\mathbf{k}\mathbf{k'}}^0\right|^2}{\left|\nabla_{\mathbf{k}}E_{\mathbf{k}}\right|\left|\nabla_{\mathbf{k'}}E_{\mathbf{k'}}\right|}$$
(6.21)

that determines the transition spectrum density of the infinite system where terms like

$$\frac{N_{\rm a}a^3}{8\pi^3} \frac{1}{|\nabla_{\mathbf{k}} E_{\mathbf{k}}|},\tag{6.22}$$

are the densities of states in k-space. We then write the energy transfer as a sampling from this function governed by s,

¹ The details of this transformation were originally worked out by J. le Page and are discussed in reference [1].

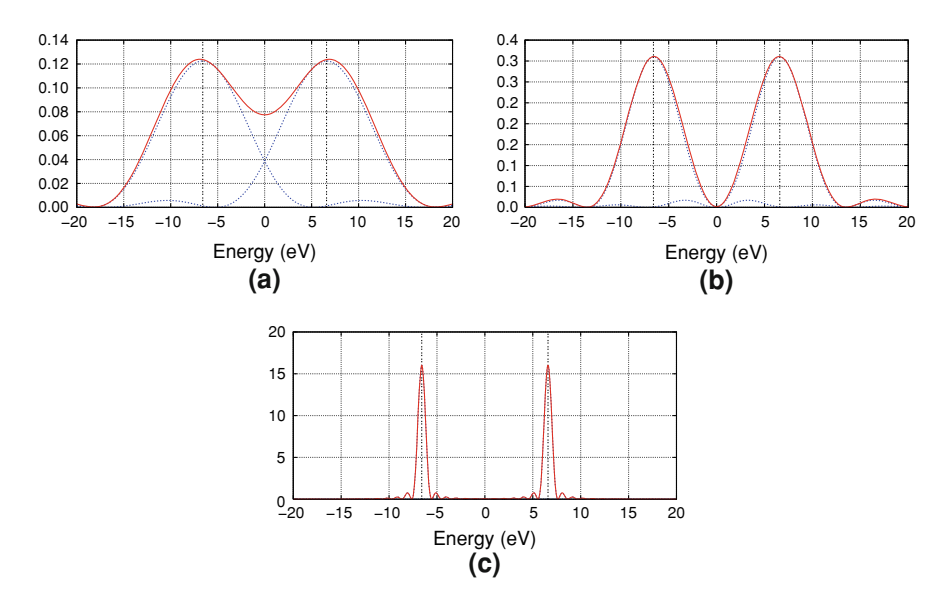


Fig. 6.5 Examples of the form of s (ε , Ω ; t) (solid red lines) for $\Omega=1$ rad fs⁻¹ at **a** 0.35 fs, **b** 0.6 fs and **c** 4.0 fs. The pair of functions in the form $t^2 \text{sinc}^2[(\varepsilon/\hbar \pm \Omega)t/2]$ (dashed blue lines) each increases in height as $\sim t^2$ and narrows as $\sim 1/t$

$$\Delta E(t) = \frac{1}{2\hbar^2} \int_{\text{band}} de \int_{-\infty}^{\infty} d\varepsilon |\tilde{V}(e, e + \varepsilon)|^2 f(e) [1 - f(e + \varepsilon)] \, \varepsilon \, s(\varepsilon, \Omega; t). \quad (6.23)$$

We must also consider the time dependence embodied in the function $s(\varepsilon, \Omega; t)$,

$$s(\varepsilon, \Omega; t) = t^{2} \left\{ \operatorname{sinc}^{2} \left[(\varepsilon/\hbar - \Omega)t/2 \right] + \operatorname{sinc}^{2} \left[(\varepsilon/\hbar + \Omega)t/2 \right] \right\}. \tag{6.24}$$

Each term in $t^2 \mathrm{sinc}^2[(\varepsilon/\hbar \pm \Omega)t/2]$ represents a sampling function in the space of the energies of possible electronic transitions, one centred on $\hbar\Omega$ and one on $-\hbar\Omega$. Fig. 6.5a illustrates the form of s for a frequency of 1 rad fs⁻¹ at time of 0.35 fs after the beginning of the oscillation. As time passes the height of the terms in $t^2 \mathrm{sinc}^2$ grows as t^2 and their width narrows as 1/t such that the area under each function is proportional to t (see Fig. 6.5b). Broadly speaking, then, the energy transfer should be proportional to t.

Figure 6.5c illustrates the situation in which Ω and t are such that there is very little overlap between the two $t^2 \mathrm{sinc}^2$ functions. Now, for a given pair of eigenstates $|\phi_i\rangle$ and $|\phi_j\rangle$ such that $|\varepsilon_j - \varepsilon_i| \approx \hbar\Omega$ only one of the $t^2 \mathrm{sinc}^2$ will contribute significantly to the energy transfer. If $\varepsilon_j < \varepsilon_i(\omega_{ji} > 0)$ then only the term in $t^2 \mathrm{sinc}^2[(\varepsilon/\hbar - \Omega)t/2]$ will contribute and we can view this as representing excitations into state $|\phi_i\rangle$ from states $|\phi_j|$ lower in energy. Conversely, for $\varepsilon_j > \varepsilon_i$ $(\omega_{ji} < 0)$, only the term in $t^2 \mathrm{sinc}^2[(\varepsilon/\hbar + \Omega)t/2]$ contributes and we can view it as representing the decay into state $|\phi_i\rangle$ from states $|\phi_j\rangle$ higher in energy.

This is made even clearer if we consider the long term limit of $s(\varepsilon, \Omega; t)$ by making use of the result [2],

$$\lim_{t \to \infty} [t \operatorname{sinc}^2(ut)] = \pi \delta(u), \tag{6.25}$$

to obtain,

$$\lim_{t \to \infty} s(\varepsilon, \Omega; t) = 2\pi t [\delta(\varepsilon/\hbar - \Omega) + \delta(\varepsilon/\hbar + \Omega)]. \tag{6.26}$$

Then the energy transfer will be

$$\lim_{t \to \infty} \Delta E(t) = \frac{\pi t}{\hbar^2} \int_{\text{band}} de \int_{-\infty}^{\infty} d\epsilon \, |\tilde{V}(e, e)|^2 f(e) [1 - f(e + \epsilon)] \, \epsilon \, [\delta(\epsilon/\hbar - \Omega) + \delta(\epsilon/\hbar + \Omega)]. \tag{6.27}$$

We can go one step further by incorporating the integration over the band within a new function

$$q(\varepsilon; T_{\rm e}) = \frac{1}{\hbar} \int_{\rm bod} de \, |\tilde{V}(e, e + \varepsilon)|^2 f(e) [1 - f(e + \varepsilon)]. \tag{6.28}$$

 $q(\varepsilon; T_{\rm e})$ now determines the rate at which transitions of energy ε can occur in our system given the crystal structure, the oscillator direction and the electronic temperature (which determines the occupations). With this new notation, the energy transfer is written

$$\Delta E(t) = \frac{1}{2\hbar} \int_{-\infty}^{\infty} d\varepsilon \, q(\varepsilon; T_{\rm e}) \, \varepsilon \, s(\varepsilon, \Omega; T_{\rm e}), \tag{6.29}$$

which in the long time limit becomes,

$$\lim_{t \to \infty} \Delta E(t) = \frac{\pi t}{\hbar} \int_{-\infty}^{\infty} d\varepsilon \, q(\varepsilon; T_{\rm e}) \, \varepsilon \left[\delta(\varepsilon/\hbar - \Omega) + \delta(\varepsilon/\hbar + \Omega) \right],$$

$$= \pi \hbar \Omega t \left[q(\hbar \Omega; T_{\rm e}) - q(-\hbar \Omega; T_{\rm e}) \right].$$
(6.30)

Because our simulations make use of a particularly simple tight-binding model, we can also develop analytical expressions for the energy transfer for the system we are studying. In Sect. 5.1.2, we introduced a notation that allows us to write the electronic Hamiltonian of our perfect crystal as a sum over pairs of atoms in nearest and next-nearest neighbour shells about each ion,

$$\hat{H} = -\frac{1}{2} \sum_{I} \sum_{b} \sum_{a} \gamma(|\mathbf{d}_{a}^{b}|) \{ |\mathbf{R}_{I}\rangle \langle \mathbf{R}_{I} + \mathbf{d}_{a}^{b}| + |\mathbf{R}_{I} + \mathbf{d}_{a}^{b}\rangle \langle \mathbf{R}_{I}| + |\mathbf{R}_{I}\rangle \langle \mathbf{R}_{I} - \mathbf{d}_{a}^{b}| + |\mathbf{R}_{I} - \mathbf{d}_{a}^{b}\rangle \langle \mathbf{R}_{I}| \},$$
(6.31)

where $\pm \mathbf{d}_a^b$ is the position of the ions in the *a*th pair in the *b*th neighbour shell relative to the *I*th ion at \mathbf{R}_I . $\gamma(|\mathbf{d}_a^b|)$ is the value of the hopping integral at the neighbour separation and the factor of $\frac{1}{2}$ accounts for the double counting of each atom pair.

We will restrict our analysis to the case of a single ion oscillating about its perfect lattice site. Without loss of generality we will specify this to be the ion indexed by I = 0 and initially at the position $\mathbf{R}_0(t = 0) = (0, 0, 0)$. In the notation of (6.1), then, $\mathbf{R}_{\text{init}} = 0$ and the oscillator position will be,

$$\mathbf{R}_{\text{osc}} = \mathbf{R}_0 = \mathbf{A}\sin(\Omega t). \tag{6.32}$$

For this simple system, the operator for the perturbation due to the oscillator will be

$$\hat{V}(t) = \hat{V}^0 \sin(\Omega t), \qquad \hat{V}^0 = \nabla_{\mathbf{R}_0} \hat{H} \cdot \mathbf{A}$$
 (6.33)

to first order in the displacement. In the notation used for \hat{H} , above, this is

$$\hat{V}(t) = -\sin(\Omega t) \sum_{b} \sum_{a} \left(\frac{\mathbf{A} \cdot \mathbf{d}_{a}^{b}}{|\mathbf{d}_{a}^{b}|} \frac{\mathrm{d}\gamma(\mathbf{R})}{\mathrm{d}R} \Big|_{R = |\mathbf{d}_{a}^{b}|} \right) \left\{ |\mathbf{R}_{0}\rangle \langle \mathbf{R}_{0} + \mathbf{d}_{a}^{b}| + |\mathbf{R}_{0} + \mathbf{d}_{a}^{b}\rangle \langle \mathbf{R}_{0}| - |\mathbf{R}_{0}\rangle \langle \mathbf{R}_{0} - \mathbf{d}_{a}^{b}| - |\mathbf{R}_{0} - \mathbf{d}_{a}^{b}\rangle \langle \mathbf{R}_{0}| \right\}.$$

$$(6.34)$$

To calculate the energy transfer we will require the matrix elements $V_{\mathbf{k}\mathbf{t}'}^0$

$$V_{\mathbf{k}\mathbf{k}'}^{0} = -\frac{1}{N_{a}}\sin(\Omega t)\sum_{b}\sum_{a}\left(\frac{\mathbf{A}\cdot\mathbf{d}_{a}^{b}}{\left|\mathbf{d}_{a}^{b}\right|}\frac{\mathrm{d}\gamma(\mathbf{R})}{\mathrm{d}R}\Big|_{R=\left|\mathbf{d}_{a}^{b}\right|}\right)\left\{e^{-i\mathbf{k}\cdot\mathbf{R}_{0}}e^{i\mathbf{k}'\cdot(\mathbf{R}_{0}+\mathbf{d}_{a}^{b})}\right.$$

$$\left.+e^{-i\mathbf{k}\cdot(\mathbf{R}_{0}+\mathbf{d}_{a}^{b})}e^{i\mathbf{k}'\cdot\mathbf{R}_{0}}-e^{-i\mathbf{k}\cdot\mathbf{R}_{0}}e^{i\mathbf{k}'\cdot(\mathbf{R}_{0}-\mathbf{d}_{a}^{b})}-e^{-i\mathbf{k}\cdot(\mathbf{R}_{0}-\mathbf{d}_{a}^{b})}e^{i\mathbf{k}'\cdot\mathbf{R}_{0}}\right\}$$

$$(6.35)$$

$$V_{\mathbf{k}\mathbf{k}'}^{0} = -\frac{1}{N_{a}}\sin(\Omega t)e^{i(\mathbf{k}'-\mathbf{k})\cdot\mathbf{R}_{0}}\sum_{b}\sum_{a}\left(\frac{\mathbf{A}\cdot\mathbf{d}_{a}^{b}}{\left|\mathbf{d}_{a}^{b}\right|}\frac{d\gamma(\mathbf{R})}{dR}\right|_{R=|\mathbf{d}_{a}^{b}|}$$

$$\times\left\{e^{i\mathbf{k}'\cdot\mathbf{d}_{a}^{b}}-e^{-i\mathbf{k}'\cdot\mathbf{d}_{a}^{b}}-e^{i\mathbf{k}\cdot\mathbf{d}_{a}^{b}}+e^{-i\mathbf{k}\cdot\mathbf{d}_{a}^{b}}\right\}$$
(6.36)

$$V_{\mathbf{k}\mathbf{k}'}^{0} = \frac{2\mathrm{i}}{N_{a}}\sin(\Omega t)\mathrm{e}^{\mathrm{i}(\mathbf{k}'-\mathbf{k})\cdot\mathbf{R}_{0}}\sum_{b}\sum_{a}\left(\frac{\mathbf{A}\cdot\mathbf{d}_{a}^{b}}{\left|\mathbf{d}_{a}^{b}\right|}\frac{\mathrm{d}\gamma(\mathbf{R})}{\mathrm{d}R}\Big|_{R=\left|\mathbf{d}_{a}^{b}\right|}\right)$$

$$\times\left\{\sin(\mathbf{k}\cdot\mathbf{d}_{a}^{b})-\sin(\mathbf{k}'\cdot\mathbf{d}_{a}^{b})\right\}.$$
(6.37)

6.4 Explaining the Results

We now have all the analytical tools required for an explanation of the features of the results of Figs. 6.2, 6.3 and 6.4 listed above.

6.4.1 High Frequency Cut-off

Figure 6.3 shows a rapid fall off in the damping coefficient at high frequency. This is easily explained in terms of the finite band-width of the tight-binding model that we are using. The maximum possible energy change in any transition in the electronic system will be that corresponding to a transition from the bottom of the band to the top of the band or vice versa. No higher energy transitions exist and so we can see that $q(\varepsilon; T_{\rm el})$ will be zero for $|\varepsilon| >$ band-width. Since for all reasonable times $s(\varepsilon, \hbar\Omega; t)$ will be significant only for $\varepsilon \approx \pm \hbar\Omega$ we can see the origin of the cut-off.

The existence of a finite band-width is an anomaly in a model of a metal, but will not necessarily cause problems in our work. If our simulations involve only ionic motions with characteristic frequencies such that $\hbar\Omega$ < band-width then the finite band-width will not have any effect. If we needed to deal with higher frequencies (i.e. we needed to accommodate higher energy electronic transitions) then we would need to consider augmenting the model, most obviously perhaps by adding further orbitals to each lattice site. For a 10 keV copper atom passing at a distance b=0.5 Å from a second atom, the maximum frequency characteristic of the motion will be $2\pi v/b=21$ rad fs⁻¹. This is within our model bandwidth.

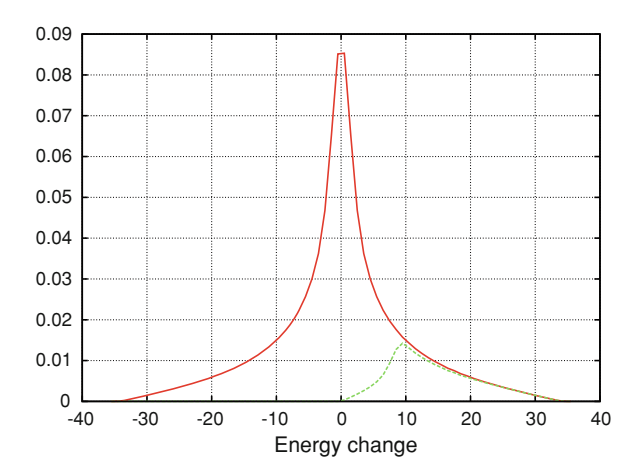
6.4.2 Isotropic Damping About Equilibrium Lattice Site

We found that the effective damping for oscillations about the equilibrium lattice site was isotropic. This is consistent with our perturbation theory result in which all the crystal structure dependence is within the squared coupling matrix elements $\left|V_{\mathbf{k}\mathbf{k}'}^0\right|^2$ and from (6.37) we can see that these are isotropic. However, we should note that $\left|V_{\mathbf{k}\mathbf{k}'}^0\right|^2$ is only isotropic because we have evaluated it to first order in the oscillator displacement. For higher amplitude oscillations this approximation is invalid and we would expect anisotropic coupling even about the equilibrium lattice site.

6.4.3 Absence of Energy Transfer at Some Frequencies

First-order time-dependent perturbation theory suggests that in an infinite system in the long-time limit we should see an energy transfer that is linear in time. Figure 6.2 clearly shows that at some oscillator frequencies this behaviour is not observed. We must ask ourselves when we expect our single oscillator simulation results, taken over only a short time and for a finite system, to reproduce the linear transfer result. Because of the simplicity of the system under study we can write down an exact expression for the squared coupling matrix elements,

Fig. 6.6 The density of transitions within our simple tight-binding model (*solid line*) and density of available transitions at $T_{\rm el} = 0$ K (*dashed line*) as defined in the main text



$$\begin{split} \left| V_{\mathbf{k}\mathbf{k}'}^{0} \right|^{2} &= \sum_{\eta} \left(\frac{2(R_{0})_{\eta}}{N_{a}} \right)^{2} \left\{ \sqrt{2} \left| \gamma_{1}' \right| \left[\sin \left(\frac{1}{2} k_{\eta} a \right) \left(\cos \left(\frac{1}{2} k_{\eta+1} a \right) + \cos \left(\frac{1}{2} k_{\eta+2} a \right) \right) \right. \\ &\left. - \sin \left(\frac{1}{2} k_{\eta}' a \right) \left(\cos \left(\frac{1}{2} k_{\eta+1}' a \right) + \cos \left(\frac{1}{2} k_{\eta+2}' a \right) \right) \right] + \left| \gamma_{2}' \right| \left[\sin \left(k_{\eta}' a \right) - \sin (k_{\eta} a) \right] \right\}^{2}. \end{split}$$

$$(6.38)$$

where the index η labels the cartesian components and is modulo 3. γ_1' and γ_2' give the gradients of the hopping integral function at the nearest- and second-nearest-neighbour separations respectively. Armed with this expression for the coupling matrix we can compute the energy transfer from an oscillating ion as a double sum over Bloch-like states $|\mathbf{k}\rangle$ sampled with a density corresponding to an arbitrarily large crystal. We can determine the energy transfer as a function of time, oscillator direction, oscillator frequency and electronic temperature and probe the behaviour of $|\langle \mathbf{k}|\hat{V}^0|\mathbf{k}'\rangle|^2$ in detail.

Given that the perturbation theory result for the energy transfer involves a sampling of the spectrum of possible transitions within a pair of $t^2 \mathrm{sinc}^2$ functions narrowing with time, we might guess that the failure of our simulations to show linear energy transfer at certain frequencies could be due to the finite size of our system. We can test this conjecture by considering the density of possible transitions within the electronic subsystem. A good approximation to this transition density, obtained by producing a histogram from calculations on a system of large size, is shown in Fig. 6.6. The strongly peaked line is the density of all transitions within the system. This function is simply the convolution of the density of states with itself and so we can see that the sharp peak is made up mostly of low energy transitions between states in the peak of the density of states (see Fig. 5.3). The second line shows the density of transitions permitted by Fermi statistics at $T_e = 0$ K, i.e. it includes only those transitions $|\mathbf{k}\rangle \rightarrow |\mathbf{k}'\rangle$ for which $f(E_\mathbf{k})[1 - f(E_\mathbf{k})] > 0$. We refer to this as the density of available transitions and we can see that, because the Fermi energy is some way below the peak in the density of states,

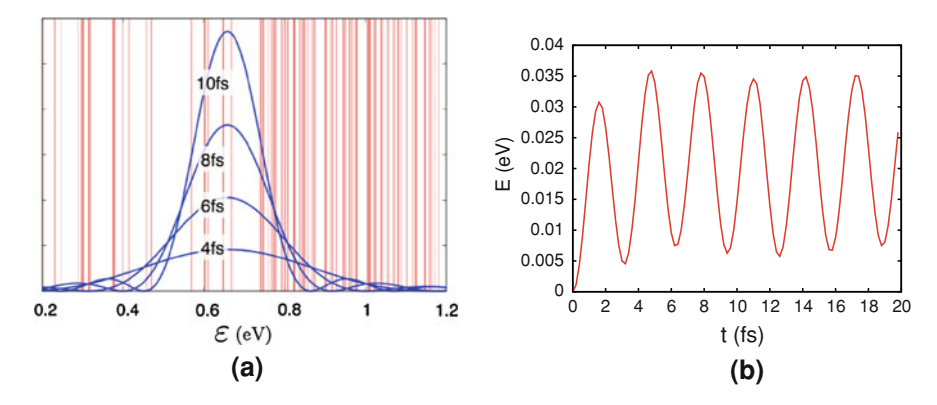


Fig. 6.7 a The spectrum of available transitions in a $8 \times 7 \times 5$ unit cell block of our tight-binding model at an electronic temperature of 0 K. Superimposed is that part of $s(\varepsilon, \Omega; t)$ corresponding to electronic excitations at various times and for $\Omega = 1.0$ rad fs⁻¹. b The heating function $\Delta E(t)$ calculated via first order time-dependent pertubation theory for the same system

the effect of Fermi statistics at low temperature is to exclude most of the low energy transitions in addition to the negative energy transitions.

In the case of a finite system the density of available transitions will become a discrete spectrum of transitions. The relative contribution of each of these transitions to the energy transfer $\Delta E(t)$ will be partly determined by the Fermi occupancy functions and by the coupling matrix element, but the strongest effect will be that of the function $s(\varepsilon,\hbar\Omega;t)$, which samples from this spectrum. Figure 6.7a shows part of the spectrum of available transitions for a system of the same size as the one used in the simulations, at a temperature of 0 K. Also shown is the term of $s(\varepsilon,\hbar\Omega;t)$ corresponding to upward energy transitions for an oscillator at $\Omega=1.0$ rad fs⁻¹, $\hbar\Omega=0.659$ eV at various times. Clearly the spectrum of available transitions is very sparse within the sampling functions at this oscillator frequency and we should not expect well-behaved heating. Figure 6.7b shows the calculated heating function (which should be compared with the actual simulation output in Fig. 6.2).

It is interesting to compare the results at zero temperature with those at 10^5 K. At high temperatures the large number of low energy transitions between states at the top of the band is no longer excluded and so the discrete spectrum around $\Omega=1.0$ rad fs⁻¹ is much denser. Figure 6.8a shows the large number of available transitions over even a narrow energy range and we can see from Fig. 6.8b that we obtain good heating results at this higher temperature.

It is clear that we must take care that the results of any simulations are not spuriously affected by finite size effects. For any given system size there will be some time beyond which the sinc functions of s are too narrow to sample a

 $^{^2}$ The downward term plays no part at low temperature and the oscillatory cross term is insignificant at longer times.

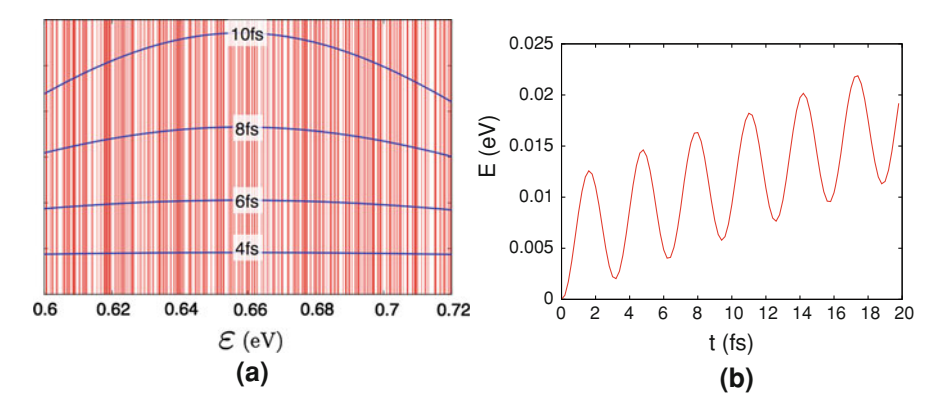


Fig. 6.8 The spectrum of available transitions in a $8 \times 7 \times 5$ unit cell block of our tight-binding model at an electronic temperature of 10^5 K. Superimposed is that part of $s(\varepsilon, \Omega; t)$ corresponding to electronic excitations at various times and for $\Omega = 1.0$ rad fs⁻¹. The heating function $\Delta E(t)$ calculated via first order time-dependent pertubation theory for the same system

significant number of transitions. This sets a maximum time constraint for our oscillator simulations and we can obtain an estimate of this upper limit via the following argument: If we assume an even distribution of transitions in two-dimensional energy space then the number of energy transitions sampled at time t will be

$$n_{\rm trans} \approx \left(\frac{N_{\rm a}}{E_{\rm band}}\right)^2 (\text{Energy range of available transitions}) (\text{width of s})$$
 (6.39)

where $E_{\rm band}$ is the band width and $N_{\rm a}$ is the number of atomic orbitals. In the case where $\hbar\Omega\gg k_{\rm B}T_{\rm e}$ (i.e. low temperature) only *excitations* of the electronic system will be significant and the energy range of available transitions will be $2k_{\rm B}T_{\rm e}+\hbar\Omega$ up to a maximum of $E_{\rm band}-\hbar\Omega$. The width of the sinc² function will be $4\pi\hbar/t$ and so the number of transitions sampled will be

$$n_{\rm trans} \approx \left(\frac{N_{\rm a}}{E_{\rm band}}\right)^2 \min(2k_{\rm B}T_{\rm e} + \hbar\Omega, E_{\rm band} - \hbar\Omega) \frac{4\pi\hbar}{t}.$$
 (6.40)

The upper time limit will then be determined by some minimum number of transitions n_{trans} , which must be sampled in order to obtain a valid estimate of energy transfer.

Our results suggest that a system size of 1,000 atoms would be a minimum required to obtain results free of finite size effects. Our chosen simulation method will certainly allow us to model systems significantly larger than 1,000 atoms, but this lower bound on system size would prove problematic for techniques such as time-dependent density functional theory.

At first sight it might seem that the finite system size problem could be circumvented via k-point sampling of the eigenstates of the system. However the

energy transfer depends on the system size not via the density of states but via the density of transitions. Sampling at multiple k-points would merely produce multiple equally sparse transition spectra unless there was some way of coupling together eigenstates from different k-points. It seems unlikely that any method of achieving this would scale better computationally than N_a^2 , which is the scaling achieved via the most obvious means of increasing the density of the transition spectrum, namely increasing the system size.

The minimum system size and maximum simulation time constraints derived by considering our simple oscillator simulations are probably harsher than necessary. In a "real" simulation of a radiation damage process the ionic motion will include components at all frequencies over a wide range and so the effect of any particularly sparse regions of the transition spectrum will be reduced. Also, since all the ions will be in motion, the transition spectrum will change with time, weakening any constraints on system size.

6.4.4 Frequency Independence of β at High Temperature

An explanation of why the effective damping becomes independent of frequency at high temperature will require a detailed look at the coupling matrix, but we should first ask what condition must be satisfied to obtain frequency independence. Recall that in the long time limit and for an infinite system we have an expression for the heating,

$$\lim_{t \to \infty} \Delta E(t) = \pi \hbar \Omega t [q(\hbar \Omega; T_{\rm e}) - q(-\hbar \Omega; T_{\rm e})]. \tag{6.30}$$

We also have our definition of β from (6.10),

$$\beta(\Omega, T_{\rm e}) = \frac{2\Delta E(\tau)}{|\mathbf{A}|^2 \Omega^2 \tau},\tag{6.41}$$

so we will have a frequency independent damping if,

$$[q(\hbar\omega; T_{\rm e}) - q(-\hbar\omega; T_{\rm e})] \propto \Omega. \tag{6.42}$$

Given the complexity of $q(\varepsilon; T_{\rm e})$ it might seem unlikely that this condition will be satisfied.

At high temperatures all possible transitions within the electronic system will be available as shown in Fig. 6.9a. We can also see from this figure that the function $q(\varepsilon; T_{\rm e})$ is much less strongly peaked than the density of available transitions. Figure 6.9b shows the ratio of the two functions in Fig. 6.9a and we can see that the effect of the coupling matrix factor $\left|V_{\rm kk'}^0\right|^2$ is to dramatically reduce the weight of low energy transitions in $q(\varepsilon; T_{\rm e})$. Figure 6.9c illustrates the function of interest $\left[q(\hbar\Omega; T_{\rm e}) - q(-\hbar\Omega; T_{\rm e})\right]$ and we see that it has the required linear behaviour up to $\varepsilon \approx 6$ eV. We should note that because of the logarithmic

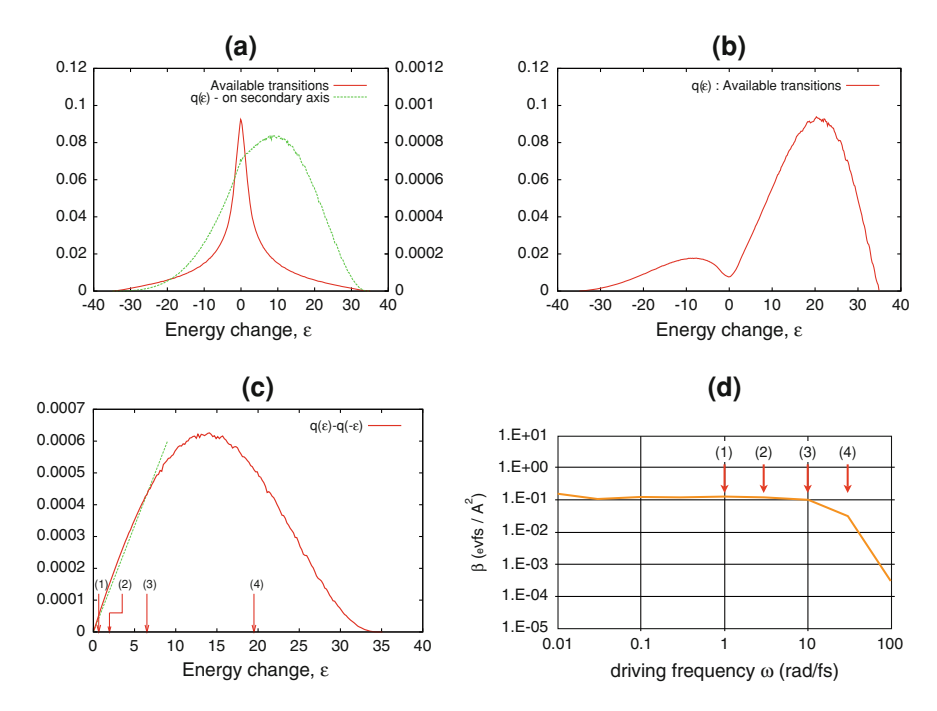


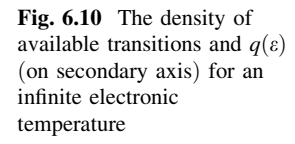
Fig. 6.9 Exploring the coupling matrix at high temperature. a The density of available transitions and $q(\varepsilon)$ at $T_{\rm e}=10^5$ K; b the ratio of the two functions in the previous chart, showing how the low energy transitions receive a low weight; c the function of interest, $q(\varepsilon)-q(-\varepsilon)$ displaying the required linearity with frequency at low Ω ; d the behaviour of the damping with frequency at $T_{\rm e}=10^5$ K showing where the samples in the previous chart occur

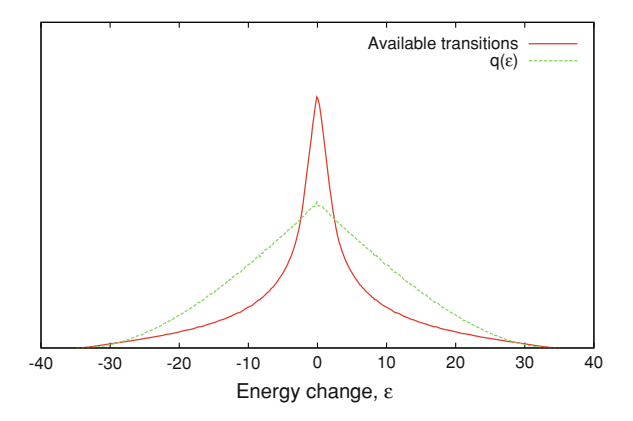
frequency scale in Fig. 6.3 the majority of the simulation results lie in this range 0–6 eV and so the range of linearity in $[q(\hbar\Omega;T_{\rm e})-q(-\hbar\Omega;T_{\rm e})]$ is sufficient to explain the observed behaviour. The points (1)–(4) in Fig. 6.9c are marked on the experimental plot in Fig. 6.9d to illuminate this fact. To understand why β is frequency independent up to $\hbar\Omega\approx 6\,{\rm eV}$ we will need insight into the coupling matrix $|V_{\rm kk'}^0|^2$.

We can eliminate the effect of the Fermi factors in $q(\varepsilon; T_{\rm e})$ by considering an infinite electronic temperature

$$\lim_{T_{\rm e}\to\infty} q(\varepsilon; T_{\rm e}) = \frac{\nu(1-\nu)}{\hbar} \int_{\rm band} d\epsilon \, \tilde{V}(e, e+\varepsilon)$$
 (6.43)

where v is the band-filling parameter of the tight-binding model. This function is plotted in Fig. 6.10 and it takes a simple, almost triangular form. If we consider only low energy transitions, $|\varepsilon| < 6 \text{ eV}$, we are confined to the peak of $q(\varepsilon; T_{\rm e} \to \infty)$ around which the relative variation is small and we can approximate





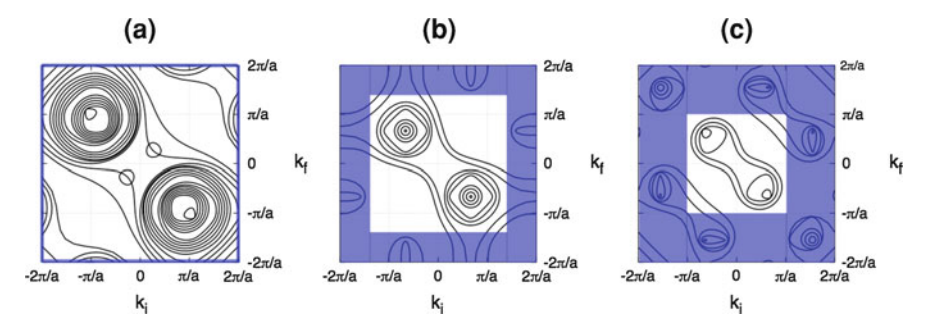


Fig. 6.11 The coupling matrix elements for transitions between states $|\mathbf{k}_i\rangle$ and $|\mathbf{k}_f\rangle$. Transitions along three paths in k-space are shown: $\mathbf{a} \ \Gamma \rightarrow X$, $(k_i, 0, 0) \rightarrow (k_f, 0, 0)$; $\mathbf{b} \ \Gamma \rightarrow K$, $(k_i, k_i, 0) \rightarrow (k_f, k_f, 0)$; $\mathbf{c} \ \Gamma \rightarrow L$, $(k_i, k_i, k_i) \rightarrow (k_f, k_f, k_f)$. The *unshaded areas* indicate the first Brillouin zone

$$q(\varepsilon; T_e \to \infty) \approx q(0; T_e \to \infty)$$
 (6.44)

i.e. as a constant. At a finite but high temperature the product of the Fermi occupancy factors will be

$$f(e)[1 - f(e + \varepsilon)] \approx \frac{1}{4} \left(1 + \frac{\varepsilon}{2k_{\rm B}T_{\rm e}} \right)$$
 (6.45)

so if the Fermi factors dominate the behaviour of $q(\varepsilon; T_{\rm e})$ for small ε we expect

$$q(\varepsilon; T_{\rm e}) - q(-\varepsilon; T_{\rm e}) \propto \frac{\varepsilon}{4k_{\rm B}T_{\rm e}}$$
 (6.46)

which, since $\varepsilon = \hbar \Omega$, is proportional to Ω as required for frequency independent damping.

The frequency independence is thus a consequence of the relatively flat peak in $q(\varepsilon; T_e)$, as shown in Fig. 6.10. If we contrast this with the sharply peaked density of available transitions in the same figure then we can see that the coupling matrix

 $V_{\mathbf{k}\mathbf{k}'}^0$ must be suppressing (weighting down) the low energy transitions in the sharp peak, which are predominantly those between pairs of states in the peak of the density of states at the top of the band. Figure 6.11 confirms this property of $V_{\mathbf{k}\mathbf{k}'}^0$ the figure shows the value of $V_{\mathbf{k}\mathbf{k}'}^0$ for transitions between states $|\mathbf{k}_i\rangle$ and $|\mathbf{k}_f\rangle$ along three paths in k-space and we can see that the effect of the coupling is to strongly enhance low energy transitions across the band whilst suppressing low energy transitions between states close together in k-space. Sect. 13.3 considers this behaviour in more detail. The effect of $V_{\mathbf{k}\mathbf{k}'}^0$ in weighting down certain transitions is critically important in obtaining a frequency independent damping at high electronic temperature.

6.5 Conclusions

Our simulations of a single oscillating ion have revealed the richness of the behaviour of the coupling between electrons and ions via the environment, frequency and temperature dependence of the effective damping of the oscillator. A time-dependent perturbation theory analysis has allowed us to explain these dependencies and establish the suitability of our simulation framework for the treatment of radiation damage events. In particular, we have found that finite system size effects can severely alter energy transfer behaviour, but that systems of $\gtrsim 1,000$ (achievable with our simple model) should be large enough to mitigate such effects.

References

- Mason, D.R., le Page, J., Race, C.P., Foulkes, W.M.C., Finnis, M.W., Sutton, A.P.: Electronic damping of atomic dynamics in irradiation damage of metals. J. Phys. Condens Matter 19(43), 436209 (2007)
- le Page, J.: The transfer of energy between electrons and ions in solids. PhD thesis, University of London (2008)

Chapter 7 Semi-classical Simulations of Collision Cascades

Summary: In this chapter we will describe in detail a simulation of a collision cascade using our time-dependent tight-binding model as implemented in the *spICED* software. We will consider how to determine the initial conditions of the ionic and electronic subsystems and look at a typical example of the ionic evolution. We will also take a detailed look at the electronic subsystem, how it evolves and how excitations occur. Finally, we propose a method by which the adiabatic evolution can be determined in our cascade simulations and define a measure of the non-adiabatic (irreversible) energy transfer from the ions to the electrons.

Most of the results presented in the remainder of this thesis are derived from Ehrenfest dynamics simulations of radiation damage collision cascades. We have already discussed the evolution of such cascades in detail (in Chap. 2), but in this chapter we will consider some examples of cascade simulations carried out with our simple tight-binding model metal using our Ehrenfest dynamics code, *spICED*. This will give us the opportunity to discuss some of the types of information available within semi-classical simulations. We will also consider some of the many subtleties that arise in undertaking such simulations, all of which must be borne in mind when interpreting our results.

We will first consider the ionic subsystem, its initialization and its evolution. The rest of the chapter will be devoted to a detailed discussion of the character and the evolution of the electronic subsystem, that being the aspect of our work which differs most from previous research in radiation damage simulation.

7.1 The Evolution of a Cascade

7.1.1 Thermalization of the Initial Distribution

Before we even begin a cascade simulation, typically by giving a primary knockon atom (PKA) some initial kinetic energy, we must consider the initial state of the ionic subsystem. In some of our simulations we start with a perfect lattice (see Sect. 11.1.1), sometimes even keeping the positions of all but one atom fixed (see Chap. 10), in which case the initial conditions are easily defined. More often, however, we would like to commence our simulations with the ions in a more realistic state, having a position and momentum distribution characteristic of some ionic temperature.

In classical molecular dynamics simulations, such a *thermalized* state is relatively easy to achieve. Prior to imparting kinetic energy to the PKA, the simulation cell can be evolved for a burn-in period to give the ions chance to equilibrate. Achieving a given temperature is then just a matter of ensuring the correct amount of internal energy is present in the ionic system at the start of the burn-in period. Implementation of an analogous process in our Ehrenfest dynamics simulations is complicated for two reasons:

- First, Ehrenfest dynamics is much more computationally expensive than classical MD and we would prefer not to expend precious simulation time in a long burn-in period. In fact, in the system sizes of several thousand atoms typical of our simulations, equilibration would take longer than the simulations themselves.
- 2. Even if we could equilibrate our ions in a burn-in period, the motion of the ions would stimulate excitations in the electronic system making it difficult to establish our choice of initial conditions for the electrons.

In our earliest simulations at finite ionic temperature we adopted a simple initialization scheme in which the ions were randomly assigned kinetic and potential energies according to a Maxwell–Boltmann distribution at the chosen temperature. Figure 7.1 shows the flaws in this scheme. We see a significant repartitioning of energy between ionic potential, ionic kinetic and electronic potential energy on a time-scale that is long compared to the several hundred femtosecond typical duration of our simulations. We thus require a way to properly burn-in an equilibrium temperature distribution, overcoming the computational problems listed above.

To mitigate the first problem we begin our simulations with a relatively long period (typically a picosecond) of classical molecular dynamics using a Sutton–Chen potential [1] fitted to the inter-ionic forces within our tight-binding model. This does a good job of partitioning the initial energy appropriately at a very low computational cost. However, if we immediately commence our Ehrenfest simulations after the classical MD phase, then we still see a slow repartitioning of energy when the Sutton–Chen interactions are exchanged for the tight-binding model. To correct for this, we also include a further short burn-in period, typically 100 fs long, using our tight-binding model. We must thus also address the second problem, that of irreversible energy transfer into the electronic subsystem, listed above.

Ideally we would like our second stage burn-in period to be conducted using Born-Oppenheimer dynamics within our tight-binding model. This is perfectly possible (we simply need to return the electrons to their ground state at every

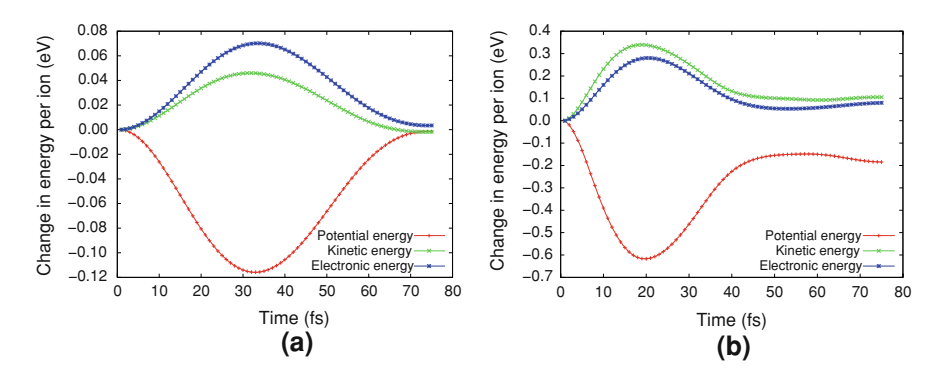


Fig. 7.1 The behaviour of the ionic kinetic, ionic potential and electronic energies in the early stages of the Ehrenfest evolution of a 2,016 atom block of our tight-binding model initialized to a given ionic temperature by allocating displacements and momenta according to a Maxwell–Boltzmann distribution. **a** Ionic temperature of 1,000 K. **b** Ionic temperature of 5,000 K

time-step), but not feasible in practice: to find the electronic ground state we must directly diagonalize the electronic Hamiltonian, a costly process that scales as the third power of the number of tight-binding orbitals. However, because the rate of transfer of energy to electrons is relatively slow, it is possible to implement a dynamics that is a compromise between the need to maintain the ground state and the requirement of computational tractability. We run Ehrenfest dynamics for the 100 fs burn-in period, but return the electrons to their ground state periodically (typically every 10 fs proves to be sufficiently frequent). The excess energy removed from the electronic system is disposed of. This does not significantly damage the integrity of our initial conditions and avoids the problem of how the energy should be returned to the ions that we would have if we aimed for perfect energy conservation.

Figure 7.2 shows sample data from a cascade simulation initialized using the above scheme. We still see a significant oscillation in the potential energy when the tight-binding model is introduced, but this is mainly due to a repartitioning of the potential energy between the classical potential energy in the repulsive ion—ion interaction and the potential energy in the newly introduced tight-binding bonds. The fluctuation in the kinetic energy is a better guide to the success of the scheme and this can be seen to be much reduced when compared with Fig. 7.1 (and it is reduced by several times more than the amount that we would expect simply because in Fig. 7.2 we are considering a lower temperature).

7.1.2 The Evolution of the Ions

Figures 7.3 and 7.4 show some snapshots of the evolution of the ionic coordinates from a sample cascade simulation. A PKA at the centre of a 3,840 atom simulation

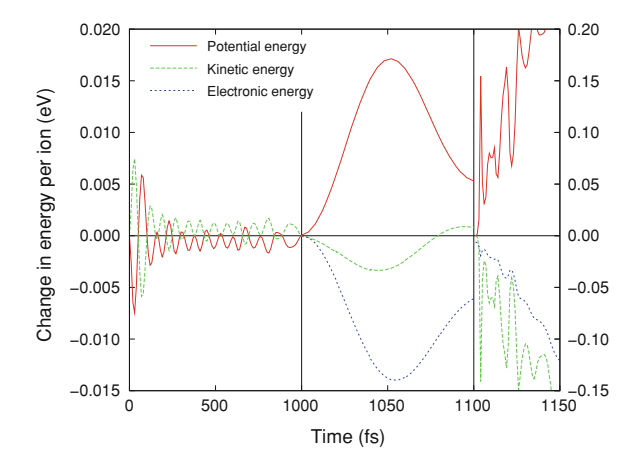


Fig. 7.2 The behaviour of the ionic kinetic, ionic potential and electronic energies in a cascade simulation initialized to an ionic temperature of 300 K using the simulation scheme described in the text. The data are divided by vertical lines into three stages. The first stage shows 1 ps of thermalization with classical MD with a matched Sutton–Chen potential. The second stage shows 100 fs of Ehrenfest dynamics in which the electrons are periodically returned to their ground state. Note the change in the time-scale on the plot axis. The final stage shows the beginning of a 1 keV cascade. The data for this stage are re-indexed to zero and shown on the right hand axis

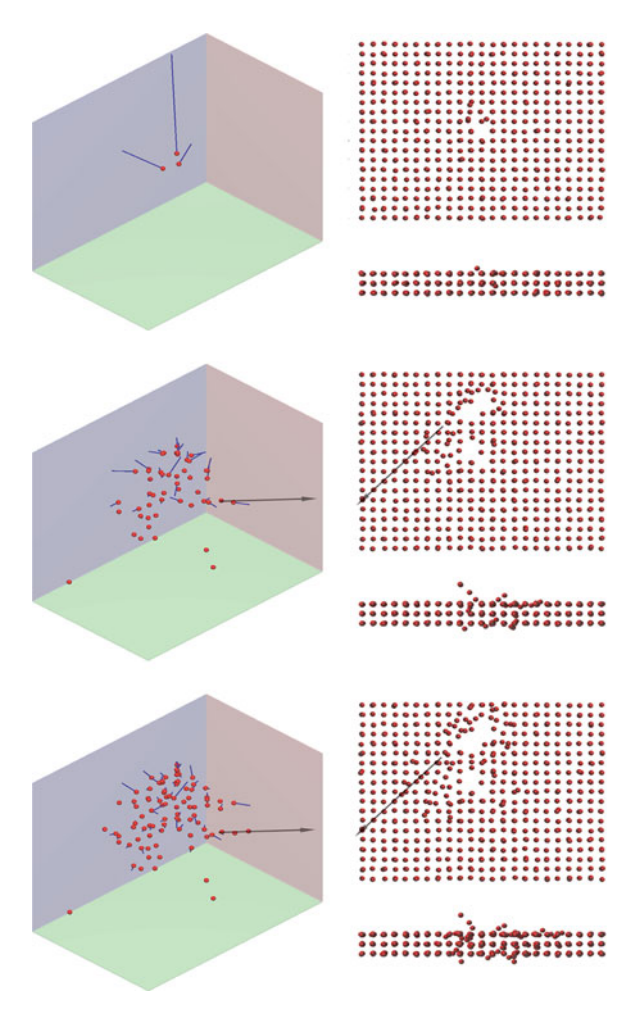
cell with periodic boundary conditions (thermalized at 300 K) is given 1 keV of kinetic energy in a low symmetry direction. Snapshots are shown at 10, 50, 70, 100, 160, and 260 fs into the cascade and in each case those ions that have been displaced by more than 1.0 Å from their perfect lattice site are shown on the left hand side along with a (blue) vector indicating their velocities. On the right hand side are shown all the ions that begin the simulation within a slice of material centred on the PKA.

The series of snapshots shows a typical cascade evolution. Damage rapidly spreads out in all directions from the location of the PKA. The apparent atomic density at the centre of the slice reduces as the ions tend to have velocities directed outwards from the PKA. We also see a clear example of a replacement collision sequence (shown by a grey vector) carrying energy out of the cascade centre relatively quickly.

7.2 The Electronic Subsystem

We will now give detailed consideration to the electronic system in our simulations, to how we initialize it and to how it evolves. As discussed in Chap. 5 and Sect. 4.5 we represent the electrons with a single-particle density matrix $\hat{\rho}$. Typically, we wish to initialize this density matrix so that it represents an

Fig. 7.3 Snapshots of a 3,840 atom cascade simulation at 10, 50 and 70 fs. Details are discussed in the main text of Sect. 7.1.2



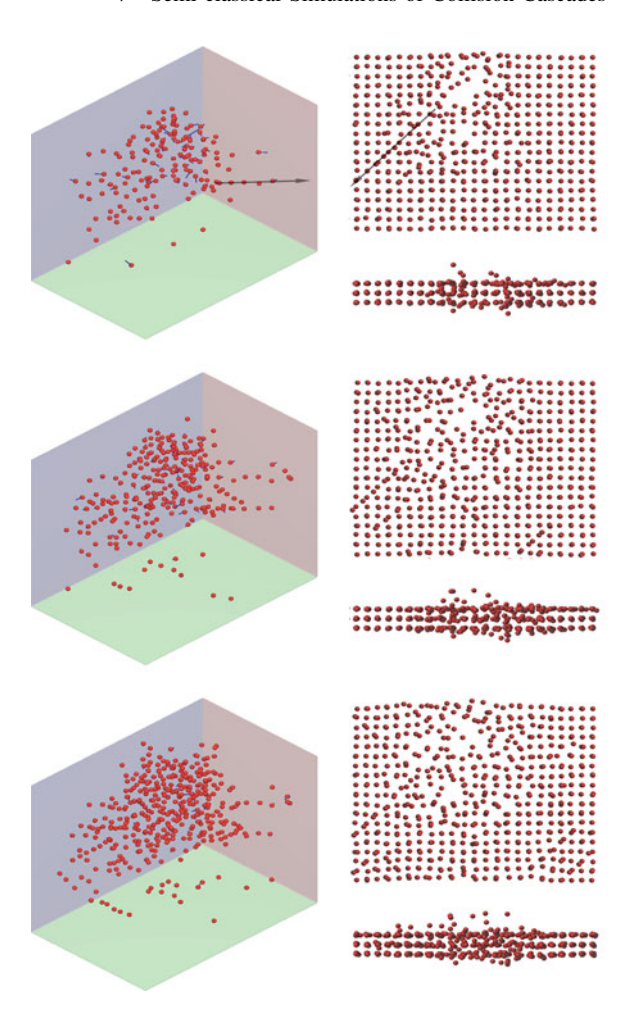
electronic system in equilibrium at some electronic temperature, often the same as the initial ionic temperature. We do this by setting the initial occupations $\{o_i\}$ of the instantaneous eigenstates $\{|\phi_i(\mathbf{R};t=0)\rangle, \varepsilon_i(\mathbf{R};t=0)\}$ of the electronic Hamiltonian at zero time according to a Fermi–Dirac distribution,

$$o_i = \frac{1}{1 + e^{(\varepsilon_i(\mathbf{R};t=0) - \mu)/k_{\rm B}T_{\rm e}}},$$
 (7.1)

at the chosen temperature $T_{\rm e}$, where μ is the chemical potential necessary to give the correct total number of electrons. The initial density matrix is then,

$$\hat{\rho}(t=0) = \sum_{i} |\phi_{i}(\mathbf{R}; t=0)\rangle o_{i}\langle \phi_{i}(\mathbf{R}; t=0)|.$$
 (7.2)

Fig. 7.4 Cascade evolution (cont.). As for figure 7.3 but with snapshots at 100, 160 and 230 fs



A density matrix of this form, at finite temperature, can be regarded as representing a statistical mixture of pure electronic states. An alternative approach to setting up the electronic system would be to use the probabilities given by the Fermi–Dirac distribution to construct a density matrix with eigenstate occupations that were all either 0 or 1. An average across an ensemble of such density matrices would give the same density matrix as our chosen method.

We might ask whether there is any material difference between adopting the statistical mixture versus a probabilistically constructed density matrix. By adopting

¹ Strictly it might also represent a coherent mixture of states or some combination of statistical and coherent mixing, but it seems overly pedantic to worry about this: we have already done more significant violence to our representation of the electrons by adopting the single-particle picture.

the mixed state we are evolving a single set of ionic positions under the influence of forces due to electrons in several states at the same time. This seems odd, but we must remember that as with all atomic simulations we are not interested in the fine detail of the ionic motion. We only require that the ionic motion be 'representative' in the sense that when we analyse it in order to answer carefully chosen questions we get 'valid' answers. So we need only worry about the difference between the two approaches to initialization if it were possible that the evolutions that would occur under the effects of the electronic systems in the mixture would somehow interfere with one another if they were to be treated separately.

An example, albeit a highly speculative one, will clarify this idea. Imagine that we form a density matrix as a statistical mixture of two density matrices, each with a different electron-hole excitation (we can also imagine that this mixture yields a set of occupations in accordance with some finite temperature Fermi–Dirac distribution, if we wish). Now imagine that the evolution under each of these density matrices treated separately gives rise in each case to a localized electronic charge, but on a different ion in the two cases. Next consider the evolution of the system with the mixed density matrix. It might be that in this case, interference between the two component matrices cancels out the charge localization effect. Or it might be that both localized charges form, in which case there will be an interaction energy between them that never arises in the separate treatments.

In the case of our simulations we do not expect that the difference between the two approaches will be significant. We are working with a metal, in which the eigenstates are all delocalized and charge localization phenomena are strongly screened. It therefore seems unlikely that different patterns of electron-hole pair excitation close to the Fermi level at low initial temperatures would give qualitatively different patterns of ionic evolution.

7.2.1 The Evolving Electronic System

Having thermalized our ions and then subsequently initialized our electrons we will commence a simulation. In the case of a collision cascade we will do this by imparting some kinetic energy to a PKA. The ions will then evolve under a set of classical repulsive forces and Hellmann–Feynman forces due to the electrons, whilst the electrons in turn evolve according to the Liouville equation under a Hamiltonian parameterized by the ionic positions.

We can consider the evolution of the electrons from several viewpoints. In the real-space picture of our tight-binding model, with local atomic orbitals $\{|\mathbf{R}_1\rangle, |\mathbf{R}_2\rangle, ...\}$ we will see bonds between atoms forming and breaking as the magnitudes of the bond-orders, $2\Re\{\langle\mathbf{R}_I|\hat{\rho}|\mathbf{R}_J\rangle\}$, in the density matrix vary in time due to the movement of the ions. We will see charge flowing on and off the different ions quantified by the bond-currents $2\Im\{\langle\mathbf{R}_I|\hat{\rho}|\mathbf{R}_J\rangle\}$. And as energy is irreversibly transferred into the electronic subsystem we will see a gradual weakening of the attractive bonding interactions.

Alternatively we can adopt the viewpoint of wavefunction Ehrenfest in which the initial eigenstates $\{|\phi_i(\mathbf{R};t=0)\rangle\}$ evolve according to the time-dependent Schrödinger equation under the electronic Hamiltonian. We refer to these evolving states as the *Ehrenfest wavefunctions*, $\{|\psi_i(t)\rangle\}$, where $|\psi_i(t=0)\rangle = |\phi_i(\mathbf{R};t=0)\rangle$. The occupations of these wavefunctions remain fixed throughout the simulation and so we can always represent the density matrix as,

$$\hat{\rho}(t) = \sum_{i} |\psi_{i}(t)\rangle o_{i}\langle \psi_{i}(t)|, \qquad o_{i} = \langle \phi_{i}(\mathbf{R}; t=0)|\hat{\rho}(t=0)|\phi_{i}(\mathbf{R}; t=0)\rangle.$$
 (7.3)

A third view of the evolution is afforded by examining the instantaneous eigenstates $\{|\phi_i(\mathbf{R};t)\rangle\}$ of the electronic Hamiltonian and monitoring their energies $\{\varepsilon_i(\mathbf{R};t=0)\}$ and occupations $\langle\phi_i(\mathbf{R};t)|\hat{\rho}(t)|\phi_i(\mathbf{R};t)\rangle$. This is only a partial representation of the electrons since a density matrix constructed out of the above information,

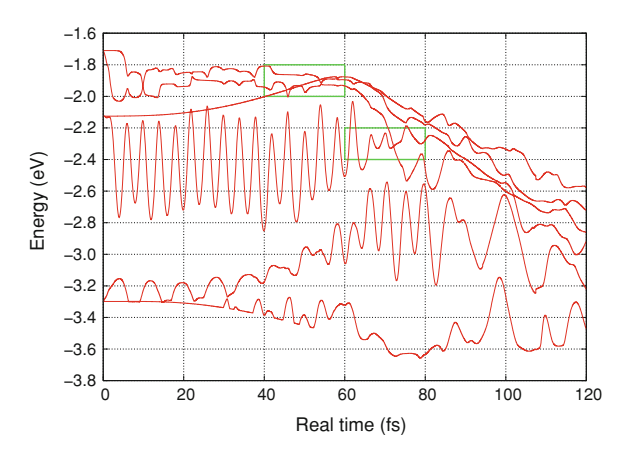
$$\hat{\varrho}(t) = \sum_{i} |\phi_{i}(\mathbf{R}; t)\rangle \langle \phi_{i}(\mathbf{R}; t)|\hat{\rho}(t)|\phi_{i}(\mathbf{R}; t)\rangle \langle \phi_{i}(\mathbf{R}; t)|, \tag{7.4}$$

omits the dynamical information contained in the full density matrix. Such a view is useful, however, because it allows us a clear view of excitations to the electronic system via the changing eigenstate occupations. We will return to this topic in Chap. 8.

7.2.1.1 The Non-crossing Theorem

Figure 7.5 shows the evolution of part of the eigenvalue spectrum in a typical simulation. The energy of the eigenvalues varies strongly with time and a curious feature of the plot is the apparent crossing of pairs of eigenvalues. Such crossings, or accidental degeneracies, should be ruled out by the so called *non-crossing theorem* [2]. Simply expressed, this theorem argues that the evolution of two

Fig. 7.5 Detail of the evolution of the energies of part of the eigenvalue spectrum in a cascade simulation. The *boxes* highlight several apparent crossings of pairs of eigenvalues. The data is from a small cascade of only 240 atoms to permit diagonalization of the electronic Hamiltonian every 0.01 fs



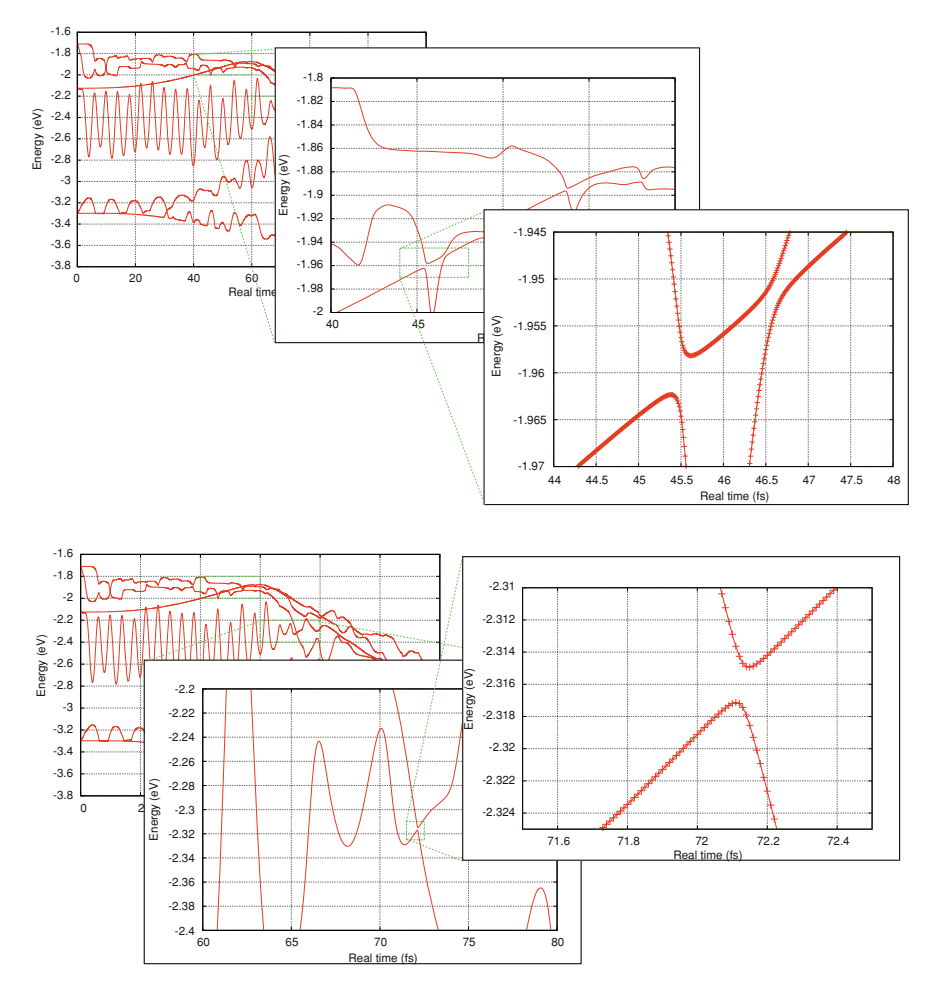


Fig. 7.6 Details of the highlighted apparent crossings in Fig. 7.5. When we examine the evolving eigenvalue spectrum more closely we see that the crossings are, in fact (narrowly), avoided, as predicted by the non-crossing theorem

eigenvalues through a putative crossing point can at best be reduced to the problem of the variation of those eigenvalues as a function of two collective coordinates of the system. A successful crossing then requires that the evolution of the system be such that the pair of collective variables passes *exactly* through a given point in their phase-space. If the system trajectory misses by any finite amount, as it almost certainly must, then the crossing does not occur: it is an *avoided crossing*. The concept of avoided crossings is important in analysing electronic excitations and we will return to it in Sect. 7.2.2.

Figure 7.6a, b show more detailed views of the eigenvalue data in Fig. 7.5 and if we extract information about the eigenstates with a high enough temporal

resolution we can see that the apparent crossings of eigenstates are actually narrowly avoided crossings.

Eigenvalue crossings certainly can occur in model systems, in situations of high symmetry, but the argument runs that this is normally a failure of the model to include all relevant effects in the Hamiltonian. Moving to the next better approximation to reality tends to break the accidental degeneracy and convert a crossing into an avoided crossing.

From the point of view of our simulations, we sometimes need to be careful to avoid the high degrees of symmetry that can give rise to accidental degeneracies and cause spurious effects. In our early studies of the single oscillating ion described in Chap. 6 we initially employed a cubic simulation cell with a perfect lattice. This generated high degeneracies in the system with the oscillating ion at its equilibrium site which were broken as soon as the oscillator was displaced. When the initial density matrix was set up such that only some of a group of degenerate states were occupied, the splitting of the degeneracy as a function of oscillator position produced a double well in the potential energy surface traversed by the oscillating ion.

7.2.2 Adiabaticity, Non-Adiabaticity and Electronic Excitations

Since the whole point of introducing into our simulations the considerable extra complexity of an explicit model of quantum mechanical electrons is to study *non-adiabatic* effects we will now take some time to define what would be meant by *adiabatic* evolution and to study some simple cases of non-adiabatic behaviour.

The *adiabatic theorem* of quantum mechanics (see references [3] and [4]) states that a stationary state $|\phi(t_0)\rangle$ of a time-dependent Hamiltonian $\hat{H}(t)$ will evolve into the corresponding stationary state $|\phi(t_1)\rangle$ at some later time t_1 if the changes to the Hamiltonian occur infinitely slowly.

In terms of the preceding discussion of our system, infinitely slow evolution of the electronic Hamiltonian (i.e. of the ion positions) would mean that the evolving Ehrenfest wavefunctions coincide with the instantaneous eigenstates at all times and the resulting *adiabatic* density matrix could be written,

$$\hat{\rho}^{\text{ad}}(t) = \sum_{i} |\phi_{i}(\mathbf{R}; t)\rangle o_{i}\langle \phi_{i}(\mathbf{R}; t)|.$$
 (7.5)

7.2.2.1 A Toy Model of an Avoided Crossing

To help make the above ideas more concrete we can examine the evolution of a simple toy model of an avoided crossing in a two level system. We begin by considering a pair of basis states $|1\rangle$ and $|2\rangle$, and an initial Hamiltonian in this basis,

$$H^{0}(R) = \begin{pmatrix} \alpha R & 0\\ 0 & -\alpha R \end{pmatrix}, \tag{7.6}$$

parameterized by a single system coordinate R which we will imagine to be an inter-ionic separation. The eigenvectors of our basis are then fixed, with eigenvalues varying linearly with R and crossing at the point R=0. We now introduce a small coupling δ between the basis states so that the Hamiltonian becomes,

$$H(R) = \begin{pmatrix} \alpha R & \delta(R) \\ \delta(R) & -\alpha R \end{pmatrix}, \tag{7.7}$$

where we define,

$$\delta(R) = \delta_0 \cos^2[(R - R_0)\pi/2], \quad -R_0 \le R \le R_0$$

= 0, otherwise. (7.8)

The elements of H are illustrated in Fig. 7.7 for values $\alpha = 1.0$ eV Å⁻¹ and δ_0 =0.01 Å, R_0 =1.0 Å.

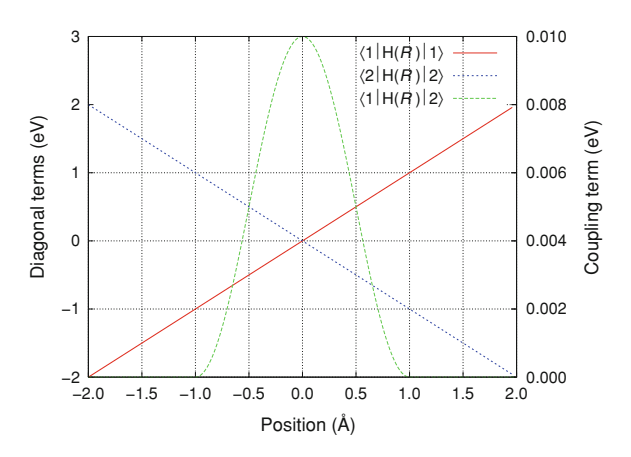
We will write the instantaneous eigenstates of this new Hamiltonian as, $|\phi_1(R)\rangle$ and $|\phi_2(R)\rangle$. In Fig. 7.8b we plot the projections of these eigenstates into the basis states and in Fig. 7.8a we plot their eigenvalues.

We see that, when $R \to -\infty, |\phi_1(R)\rangle \to |1\rangle$ and $|\phi_2(R)\rangle \to |2\rangle$. We now consider changing the variable R at a finite rate characterized by a velocity v so that R = vt for a time variable t and monitor the evolution of two time-dependent state vectors $|\psi_1(t)\rangle$ and $|\psi_2(t)\rangle$ whose initial values are specified as,

$$|\psi_1(t=-\infty)\rangle = |\phi_1(R=-\infty)\rangle, \qquad |\psi_2(t=-\infty)\rangle = |\phi_2(R=-\infty)\rangle.$$
 (7.9)

Imagine that at $t=-\infty$ we occupy only the state $|\psi_1(t=-\infty)\rangle = |\phi_1(R=-\infty)\rangle = |1\rangle$ and then evolve the system to $R=+\infty$ at a particular fixed velocity v. Figure 7.9 shows the results of such evolutions. When the coordinate R is changed very slowly (see Fig. 7.9a) the evolution of $|\psi_1(t)\rangle$ is

Fig. 7.7 The Hamiltonian matrix elements for a toy model of an avoided eigenvalue crossing



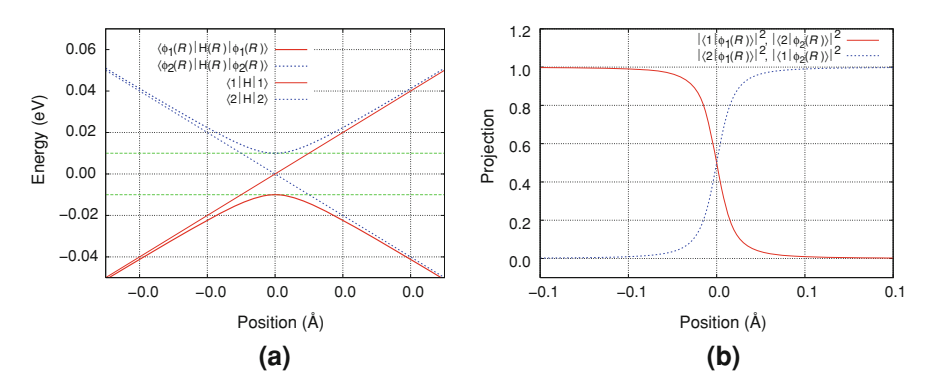


Fig. 7.8 The eigenvalue energies (a) and basis state projections (b) for the eigenstates of the Hamiltonian in a toy model of an avoided eigenstate crossing

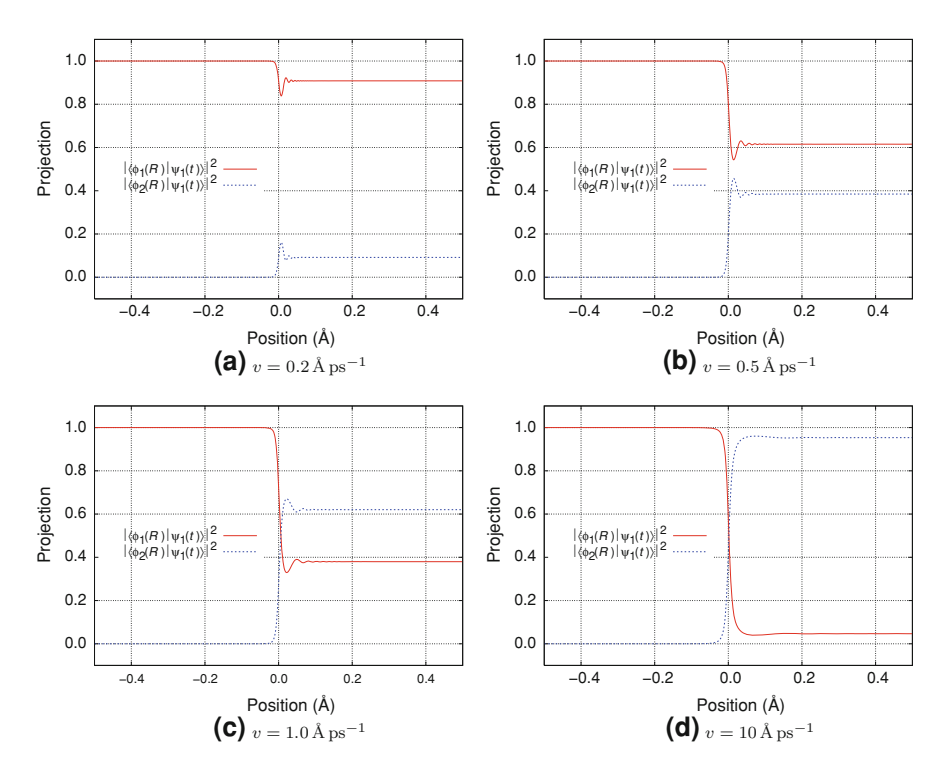
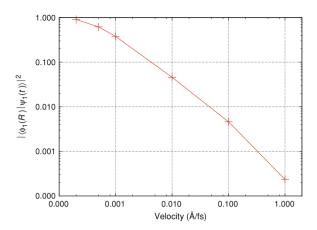


Fig. 7.9 The projection of the evolving state $|\psi_1(t)\rangle$ into the lowest eigenstate $|\phi_1(R)\rangle$ in simulations using a toy model of an avoided eigenvalue crossing. The results for several velocities (indicated in the captions) are shown

almost adiabatic and the system remains on the lower eigenstate $|\phi_1\rangle$ as predicted by the adiabatic theorem. As we increase the velocity (Fig. 7.9b, c) $|\psi_1(t)\rangle$ becomes less able to adapt itself to follow the lower energy state, retaining more of

Fig. 7.10 The value of the projection $|\langle \phi_1(R)\psi_1(t)\rangle|^2$ as a function of velocity from simulations using a toy model of an avoided eigenvalue crossing. This projection measures the extent to which the evolving state can adapt to follow the lower eigenvalue; in effect a measure of the adiabaticity of the evolution



its initial character $|1\rangle$ and acquiring a significant projection into the higher eigenstate $|\phi_2\rangle$. At very high velocities (Fig. 7.9d) we approach the *sudden approximation* and $|\psi_1(t)\rangle$ remains 'locked-in' to the basis state $|1\rangle$ switching its character to that of the higher eigenstate $|\phi_2\rangle$. Figure 7.10 shows the extent to which the system is able to remain on the lower eigenstate as a function of the velocity ν .

7.2.3 Achieving Adiabatic Evolution by Altering the Electron–Ion Mass Ratio

At times in our work it will be useful to compare the evolution of a system of ions and electrons with the corresponding adiabatic evolution for the same set of initial conditions. We would therefore like to have a simple means of determining this adiabatic evolution. The most straight forward approach, guided by the adiabatic theorem, would be to repeatedly diagonalize the electronic Hamiltonian \hat{H} and reconstruct the electronic density matrix from the instantaneous energy eigenstates in the adiabatic form.

$$\hat{\rho}^{Ad} = \sum_{i} |\phi_{i}(\mathbf{R})\rangle o_{i}\langle \phi_{i}(\mathbf{R})|, \qquad (7.10)$$

where $\{o_i\}$ are the (fixed) initial occupations of the initial eigenstates. This will give us the adiabatic evolution, in which no electronic excitations occur and the forces experienced by the ions are those consistent with keeping the electrons in their ground state. Unfortunately, diagonalization of the Hamiltonian is a computationally costly operation that scales as the third power of the number of atomic orbitals in the tight-binding model. For systems of thousands of atoms it would be impossible to diagonalize the Hamiltonian sufficiently frequently to obtain the adiabatic evolution over a useful time period.

Instead we have found it useful to exploit a numerical trick to find the adiabatic evolution. We can understand the basis of this trick by noting that the Born-Oppenheimer approximation essentially exploits the large difference in mass between the ions and electrons: the much lighter electrons, under certain conditions, such as not too fast movement of the ions, can be regarded as responding instantaneously to changes in the ion positions. If we undertake a simulation in which we artificially reduce the electron mass then the electrons will evolve more quickly and the evolving wavefunctions will follow the instantaneous eigenstates more closely. To see how this works, we recall that our electronic density matrix is evolved according to the quantum Liouville equation,

$$\frac{\mathrm{d}}{\mathrm{d}t}\hat{\rho}(t) = -\frac{\mathrm{i}}{\hbar}[\hat{H}(\mathbf{R};t),\hat{\rho}(t)]. \tag{7.11}$$

In a numerical integration of this equation, \hbar appears as a parameter that scales the size of the changes made to the density matrix at each time step. If we reduce the value of \hbar these changes become larger and the electronic evolution is accelerated. Reducing \hbar is, in fact, equivalent to reducing the electron mass. This is because in our model's description of the electrons, \hbar also appears *implicitly* in the hopping integrals between tight-binding orbitals. If we hold these (the off-diagonal elements of the electronic Hamiltonian in the atomic orbital basis) fixed then we are effectively maintaining a constant value for the quotient $\hbar^2/m_{\rm e}$ (cf. the expression for the free-electron band structure $E_{\rm free}(k)=\hbar^2k^2/2m_{\rm e}$). If at the same time we reduce the value of \hbar in the integration of the Liouville equation then we are implicitly reducing the electron mass.

Figure 7.11 shows the results of simulations using a simple Fortran 90 code to implement the integration of the quantum Liouville equation in a 500 atom chain of our tight-binding model, in which one atom is forced to oscillate parallel to the chain and the other atoms are held fixed. The figure shows the electronic energy (which will be strictly periodic in the adiabatic case) as a function of oscillator cycles at different rates of evolution (different values of \hbar or, equivalently, of

Fig. 7.11 A plot of the electronic energy in a 500 atom tight-binding chain with one atom forced to oscillate sinusoidally at 1 PHz. The evolution is shown for a variety of values of \hbar and for the adiabatic case calculated by direct diagonalization of the Hamiltonian

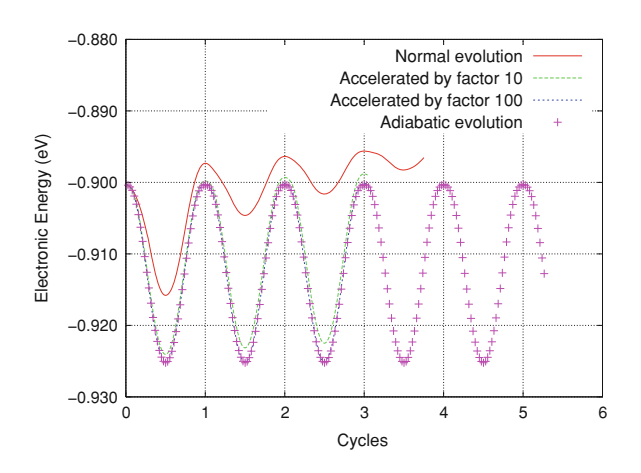
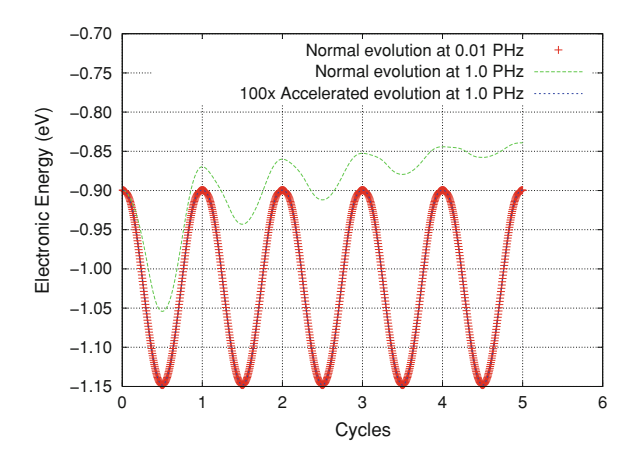


Fig. 7.12 A plot of the electronic energy in a 500 atom tight-binding chain with one atom forced to oscillate sinusoidally. Decreasing the frequency of the oscillation by a factor of 100 is equivalent to increasing the value of \hbar in the Liouville equation (accelerating the electronic evolution) by a factor of 100



electron mass). As the value of \hbar is decreased the evolution of the electronic system approaches the adiabatic value and the heating clearly evident in the normal evolution is eliminated. Reducing \hbar by a factor of 100, i.e. reducing the electron mass by a factor of 10^4 , appears to be sufficient to achieve convergence in this simple system.

In fact, for practical purposes it proves easier to increase the ion mass, rather than to decrease the electron mass (i.e. than to change \hbar). This has the effect of scaling the speed of the ions whilst leaving the magnitude of the forces they experience unchanged (except for those parts of the forces due to non-adiabatic effects, of course!). Thinking in terms of excitations as the electronic system passes through avoided eigenvalue crossings, we see that slowing the evolution of the ions reduces the rate at which avoided crossings are traversed, making it more likely that the evolving wavefunctions will follow the instantaneous energy eigenstates. Figure 7.12 demonstrates the exact equivalence between slowing the evolution of the Hamiltonian (by reducing the oscillator frequency in this example of a forced oscillator in a tight-binding chain) and increasing the rate of electronic evolution.

Clearly, slowing the ionic motion means that our simulations will run proportionately more slowly, but if we had taken the alternative route of speeding up the electronic evolution then we would have had to use a smaller time-step to maintain a valid evolution and the increase in computational time would have been the same. This increase in computational time is significant, but for larger systems it will be much more efficient than direct diagonalization of the electronic Hamiltonian. For even the largest systems, we can achieve some reduction in non-adiabatic effects by scaling the ionic mass.

7.2.3.1 Some Cascade Simulations at High Ion Mass

We will now examine the effect of increasing the ion mass on some simple dynamical simulations using the *spICED* code. In Figs. 7.13 and 7.14 we show the

Fig. 7.13 The evolution of the irreversible energy transfer early on in a *spICED* simulation of a replacement collision sequence in a 240 atom super-cell. Convergence is achieved for an ion mass increase of 1,000 ×

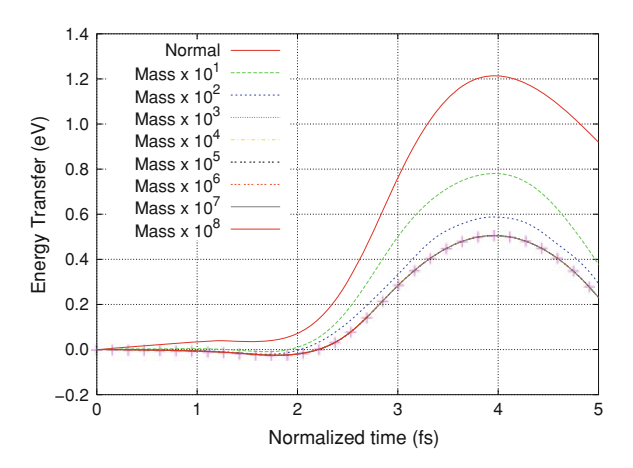
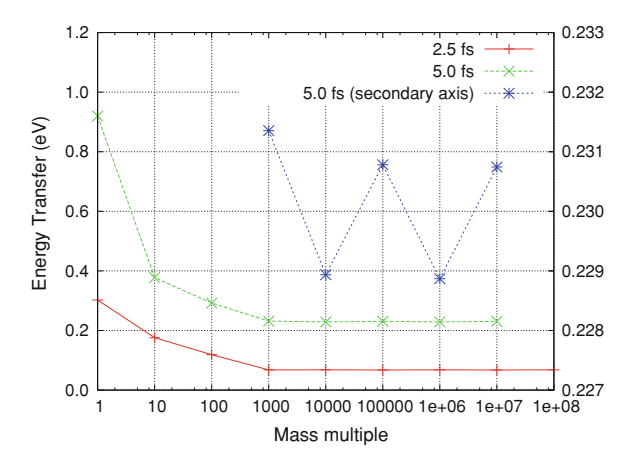


Fig. 7.14 As for Fig. 7.13 except that the energy transfer at two times is shown as a function of ion mass multiple



irreversible energy transfer into the electronic system during the first 5 fs of a 500 eV replacement collision sequence in the [5] direction in a 240 atom super-cell of our tight-binding model. The figures show that the evolution of the energy transfer is converged for a mass increase of 1,000 \times , corresponding to a penalty in simulation time of $10\sqrt{10} \approx 36$.

Notice that the energy transfer does not converge to zero as we would expect. This effect is due to a subtlety of the evolution that we will return to below, but for now we note that the expected behaviour can be achieved with a careful choice of the band-filling parameter for our tight-binding model (see Sect. 5.1 for an explanation of this parameter). Figure 7.15 shows the energy transfer in similar simulations of an RCS with just such a careful choice of the band-filling. We see that for a mass multiple of $10^4 \times$ the evolution converges to the adiabatic result of zero energy transfer.

Fig. 7.15 The evolution of the irreversible energy transfer in RCS simulations with a carefully chosen bandfilling parameter. The expected convergence to the adiabatic result is now observed

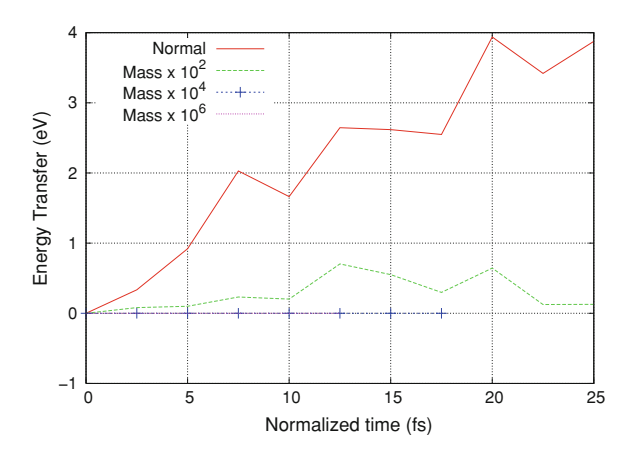
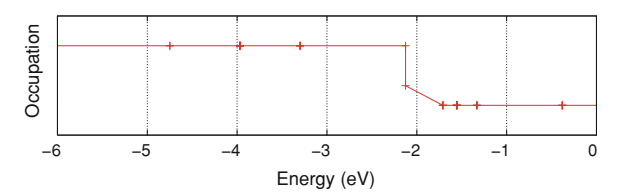


Fig. 7.16 The initial occupations of the eigenstates in the simulations illustrated in Figs. 7.13 and 7.14. At the Fermi level, just below – 2 eV, we have two nearly degenerate states with different occupations



So why do we see convergence to the adiabatic evolution only with certain choices of band filling? The answer lies in the interaction of nearly degenerate states early in the simulation. As we saw in Sect. 7.2.2, the concept of adiabaticity is not really an absolute one: adiabaticity will be achieved to a greater or lesser extent depending on the rate of change of the Hamiltonian compared with energy level spacings in the electronic system. Excitations between closely spaced energy levels will remain likely even for very slow evolution, whereas systems with wider energy spacings will behave more adiabatically. It is for this reason that semi-conductor and insulator systems are more obvious candidates for treatment within the Born-Oppenheimer approximation.

Figure 7.16 shows the initial eigenvalue spectrum and its occupation at 0 K in the simulations showing imperfect convergence to adiabaticity in Figs. 7.13 and 7.14. We can see that at the Fermi level we have one fully filled energy level and one partially filled level that are very close together in energy. The partial filling of the highest occupied level is a result of the standard choice for our band-filling parameter. Note that the failure to converge to adiabaticity is not a result of this partial occupation, rather it is due to incomplete occupation of one of a pair of nearly degenerate states; the same result would occur if one state were completely filled and the other completely empty. Figure 7.17 shows the occupation of the

Fig. 7.17 The eigenstate occupations after 25 fs of RCS simulation with different ion masses. Even with a very slow evolution, the interaction of the two nearly degenerate states at the Fermi level produces an electronic excitation. The initial values and occupations of the eigenvalues are shown in green for comparison

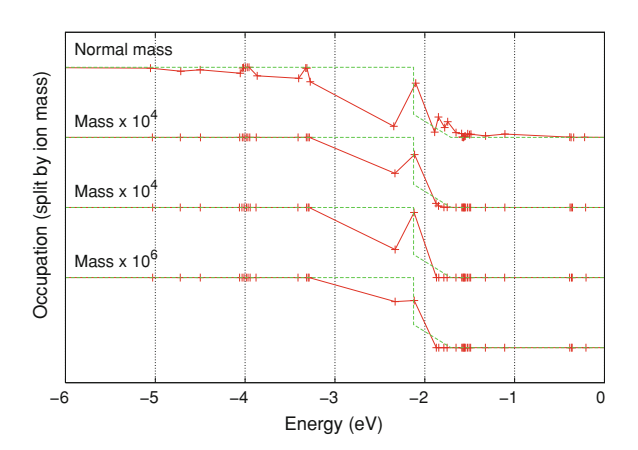
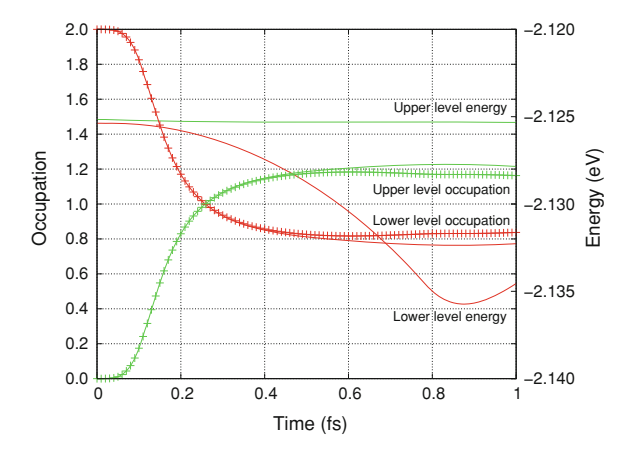


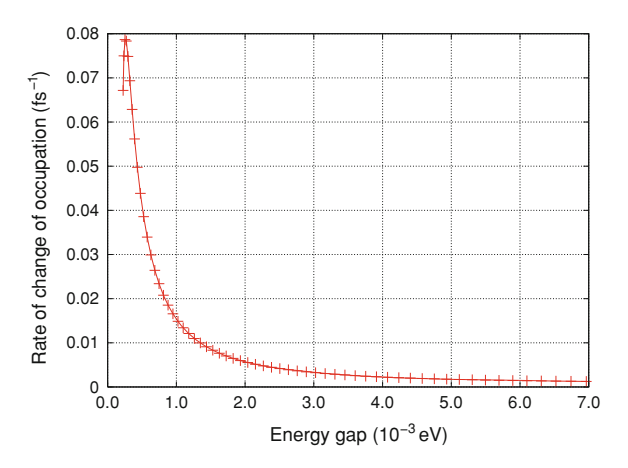
Fig. 7.18 The evolution of the energies (right hand axis) and occupations of the two nearly degenerate eigenstates at the Fermi level in our RCS simulations. In the case of the occupations, the solid lines show data in the case of evolution at normal mass and the crosses show the evolution with $10^6 \times \text{normal}$ mass



instantaneous energy eigenstates after 25 fs of evolution. Even for a mass multiple of 10⁶, slowing the ionic evolution by a factor of 1,000, we can see that for the initially nearly degenerate states, the occupations evolve from one completely filled and one partially filled level to being two partially filled levels.

Figure 7.18 shows the eigenstate energies and the evolution of their occupations in the case of very high ion mass (\times 10⁶) and for the normal ion mass. There is a significant transfer of occupation (electron-hole excitation) between these closely spaced levels even in the case of very slow evolution. Only once the eigenvalues are separated by around 3×10^{-3} eV does the slowed evolution diverge from the normal evolution and become effectively adiabatic. Figure 7.19 shows the rate of transfer of occupation as a function of the changing eigenvalue spacing during the simulation. The convergence to adiabaticity shown in Fig. 7.15 is achieved by adjusting the band-filling parameter to place the Fermi level in the gap around -2 eV so that both of the nearly degenerate levels are completely filled and are well separated from the nearest unfilled eigenstate.

Fig. 7.19 The rate of transfer of occupation between the two initially nearly degenerate eigenstates as a function of their evolving separation



What the above discussion shows is that adiabatic evolution is in general difficult to attain, but that in specific cases it may be possible with computationally achievable increases in ion mass. In general, any increase in ion mass will at least act to move us towards adiabaticity to some extent. We should also bear in mind that increasing our system size will shrink the average eigenvalue spacing proportionately and will thus make the adiabatic evolution harder to achieve.

7.2.4 The Irreversible Energy Transfer

An important quantity for measuring the effect of electron–ion interactions in our simulations will be the irreversible energy transfer $\Delta E(t)$. This energy transfer will be equal to the work done by the non-adiabatic forces and so corresponds to the effects of electronic stopping power in the theories considered in Sect. 3.2. We introduced a simple definition of $\Delta E(t)$ when we discussed the single oscillating ion in Chap. 6. For a cascade simulation, when the ionic configuration is not periodic in time, we would like a more general expression.

Our fundamental definition of irreversible energy transfer will be that it is the difference between the electronic energy embodied in the evolved density matrix in our simulations and the density matrix that we would have if the ions had traversed *the same paths* infinitely slowly. We denote this latter adiabatic density matrix $\rho^{Ad}(t)$ and it will take the same form discussed in Sect. 7.2.3,

$$\hat{\rho}^{Ad} = \sum_{i} |\phi_{i}(\mathbf{R})\rangle o_{i}\langle \phi_{i}(\mathbf{R})|, \tag{7.10}$$

diagonal in the instantaneous eigenstate basis with fixed occupations. The irreversible energy transfer is thus defined,

$$\Delta E(t) \equiv \text{Tr} \left[(\hat{\rho}(t) - \hat{\rho}^{\text{Ad}}(\mathbf{R}; t)) \hat{H}(\mathbf{R}; t) \right]. \tag{7.12}$$

In terms of the evolved Ehrenfest wavefunctions (see Eq. 7.3 in Sect. 7.2.1) and the instantaneous eigenstates, this is

$$\Delta E(t) = \sum_{ij} \left\{ \left| \left\langle \phi_i \middle| \psi_j(t) \right\rangle \right|^2 o_j - o_i \delta_{ij} \right\} \varepsilon_i. \tag{7.13}$$

For complete clarity we point out that $\hat{\rho}^{Ad}$ is not the same thing as the density matrix that results from adiabatic *evolution* (e.g. in the infinite ion mass limit), because this latter evolution would involve different forces and so different ion paths from those in our finite rate Ehrenfest dynamics simulations used to calculate $\hat{\rho}^{Ad}$. Nor is $\hat{\rho}^{Ad}$ the same as the canonical density matrix,

$$\hat{\rho}^{\mathrm{Can}}(\mathbf{R};t,T_{\mathrm{e}}(t=0)) = \sum_{i} |\phi_{i}(\mathbf{R};t)\rangle f(\varepsilon_{i}(\mathbf{R};t);T_{\mathrm{e}}(t=0))\langle \phi_{i}(\mathbf{R};t)|,$$

(7.14) in which the occupations change to maintain a constant electronic temperature (although $\hat{\rho}^{\text{Can}}(\mathbf{R};t,T_{\text{e}}(t=0))=\hat{\rho}^{\text{Ad}}$ when $T_{\text{e}}(t=0)=0$ and assuming that the non-crossing rule holds).

7.3 Conclusions

We have considered various aspects of the simulation of radiation damage collision cascades using time-dependent tight-binding in Ehrenfest dynamics. We outlined our approach to initializing the combined electron—ion system to some chosen temperature and examined some typical features of the ionic evolution in a cascade simulation.

We then considered the evolution of the electronic system in detail, from several different viewpoints. We presented the results of a toy model of an avoided eigenvalue crossing to illuminate some aspects of non-adiabaticity and explored a way to obtain the adiabatic evolution.

Finally, we gave a general expression for the non-adiabatic energy transfer from ions to electrons, a quantity of high importance in the results discussed in the following chapters.

References

- Sutton, A.P., Chen, J.: Long-range finnis-sinclair potentials. Philos. Mag. Lett. 61(3), 139–146 (1990)
- Alden Mead, C.: The "noncrossing" rule for electronic potential energy surfaces: the role of time-reversal invariance. J. Chem. Phys. 70(5), 2276–2283 (1979)
- 3. Kato, T: On the adiabatic theorem of quantum mechanics. J. Phys. Soc. Jpn **5**(6), 435–439 (1950)
- 4. Messiah, A.: Quantum Mechanics, pp. 747-750. Dover Publications, Inc., Mineola (1999)
- Duvenbeck, A., Sroubek, Z., Wucher, A.: Electronic excitation in atomic collision cascades. Nucl. Instrum. Methods Phys. Res. B Beam Interact. Mater. At. 228(1–4), 325–329 (2005)

Chapter 8 The Nature of the Electronic Excitations

Summary: In this chapter we examine the nature of the electronic excitations stimulated during collision cascades. We find that these excitations are well-characterized by an elevated electronic pseudo-temperature and develop a simple temperature fitting algorithm. We explain the emergence of a pseudo-temperature despite the absence of thermalizing electron–electron interactions or a correct treatment of the electron–phonon interaction in our Ehrenfest dynamics by considering the spectrum of frequencies in the ionic motion in a typical cascade. Identifying an inconsistency between a rising electronic temperature and the fixed entropy of the electronic density matrix, we briefly consider an alternative definition of the electronic entropy.

If we wish to understand the effect of electrons on ion dynamics then we need to understand how electronic excitations affect the electronic force. As we will discuss in more detail in Chap. 9 these effects can be divided into two types: short term effects due to the finite response time of the electrons to ionic motion and longer term effects due to the accumulation of excitations in the system. To properly understand the second of these effects, we need to study the nature of the electronic excitations stimulated by the ionic system. As we shall see, in the case of collision cascades these excitations take a particularly simple form, a result of significance for anyone attempting to account for such excitations in a classical simulation framework.

8.1 Patterns of Excitation in Collision Cascades

To gather a representative sample of excited electronic spectra we have performed a set of 44 simulations of collision cascades with a PKA energy of 2 keV. The electronic Hamiltonian does not include the charge-self-consistent terms as charge

transfer effects in low energy cascades are small. Each cascade takes place in a simulation super-cell of 2,016 atoms (9 × 7 × 8 fcc unit cells) with periodic boundary conditions and the initial PKA direction is uniformly distributed over the $4\pi/48$ steradian irreducible solid angle of the fcc unit cell (for details of the calculation of the directions see reference [1]). Prior to the knock-on event the simulation cells are thermalized to an ionic temperature of 300 K with 1 ps of classical MD and 100 fs of quasi-Born–Oppenheimer dynamics, as described in Sect. 7.1.1. The electronic density operator is initialized at an electronic temperature of 300 K and the simulations are allowed to evolve under Ehrenfest dynamics for 225 fs, by which time around 45 eV, or 22 meV per electron, is transferred irreversibly into the electronic system. Every 10 fs the electronic Hamiltonian $\hat{H}(\mathbf{R};t)$ is diagonalized to obtain the electronic eigenstates $\{|\phi_i(\mathbf{R};t)\rangle\}$ with energies $\{\varepsilon_i\}$. We can then calculate an occupation of each energy eigenstate as

$$o_i(t) \equiv \langle \phi_i | \hat{\rho}(t) | \phi_i \rangle.$$
 (8.1)

A plot of such occupations after 225 fs of a representative simulation is shown in Fig. 8.1.

A striking feature of Fig. 8.1 is that the electrons appear to have a Fermi–Dirac distribution at an elevated temperature (a best-fit is shown in the figure). This is unexpected because our electronic Hamiltonian does not include the direct electron–electron interactions that could thermalize a non-equilibrium electronic

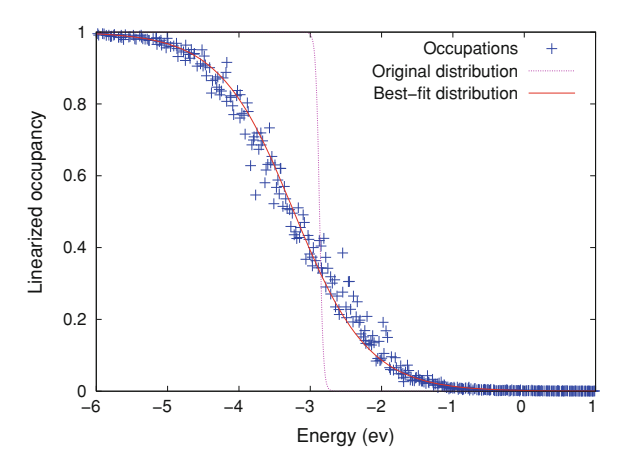


Fig. 8.1 The occupations o_i of the instantaneous eigenstates around the Fermi level as a function of eigenstate energy ε_i for a typical simulation after 225 fs. A Fermi–Dirac distribution corresponding to the original temperature of 300 K is shown, along with a Fermi–Dirac function corresponding to a temperature of 6055 K as a best-fit to the excited occupation distribution (Reprinted figure 2 with permission from Race, C.P., Mason, D.R., Sutton, A.P.: Electronic excitations and their effect on the interionic forces in simulations of radiation damage in metals. J. Phys. Condens. Matter 21(11), 115702 (2009). Copyright (2009) by the Institute of Physics Publishing Ltd.)

distribution. In a real system we would also expect the electron–ion interaction (the electron–phonon coupling) to act to thermalize the electrons, but as discussed in Sect. 4.6.2, Ehrenfest dynamics does not correctly reproduce this electron–ion interaction because it omits spontaneous phonon emission. For these reasons we will refer to the apparent electronic temperature as a *pseudo-temperature*.

8.1.1 Fitting a Pseudo-temperature

Having identified the approximately thermal nature of the excited electrons in our collision cascade simulations it will be useful to have a means of fitting a pseudotemperature to a set of eigenstate occupations. In this section we will briefly outline a simple algorithm for finding the best fit temperature. More details of the method and some of the subtleties involved can be found in Sect. 13.4.

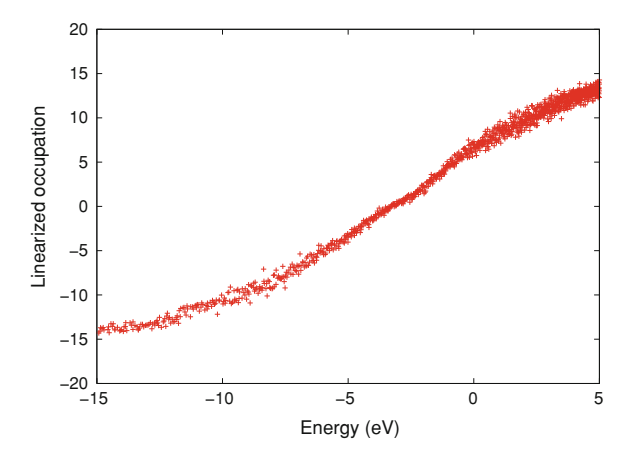
To make the fitting process as simple as possible we will consider the Fermi–Dirac distribution $f(\varepsilon; T)$ in a form in which it is linear in the energy ε ,

$$\left| \ln \left(\frac{1}{f(\varepsilon; T)} - 1 \right) \right| = \frac{1}{k_{\rm B} T} |(\varepsilon - \mu(T))|, \tag{8.2}$$

where $\mu(T)$ is the chemical potential, which will depend on the temperature T. We have taken the absolute value of both sides for numerical convenience. By applying a similar transformation to a set of eigenstate energies $\{\varepsilon_i\}$ and occupations $\{o_i\}$ we can use simple linear regression to fit $|\ln[(1/o_i)-1]|$ against $|\varepsilon_i-\mu(T)|$ to obtain an estimator for the inverse temperature 1/T. Figure 8.2 shows transformed data from a sample simulation.

Two particular difficulties arise in the fitting process. First, because the chemical potential used in the transformation of the occupation data is itself a function of temperature, our algorithm must incorporate a self-consistency loop.

Fig. 8.2 The linearized form of the occupations o_i of the instantaneous eigenstates as a function of eigenstate energy ε_i for a typical simulation after 225 fs

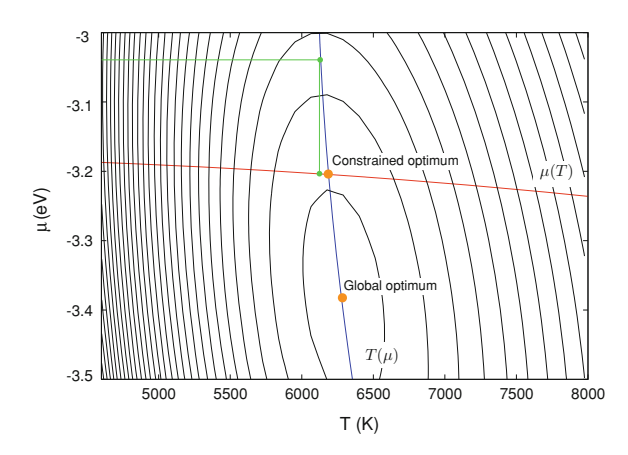


We begin by calculating an initial best-fit temperature $T_1(\mu_0)$ using an initial estimate of the chemical potential μ_0 . We can then calculate a revised estimate $\mu_1(T_1)$ based on the requirement of fixed electron number and use this to calculate a new best-fit temperature $T_2(\mu_1)$. This procedure is repeated until consecutive estimates of the temperature are in agreement to within a single degree. In practice, because μ varies only slowly with temperature the loop tends to converge within three iterations (see Fig. 8.3).

The second difficulty is caused by high frequencies present in the characteristic spectrum of hopping integral variations early in the cascade. These are due to fast moving ions in the brief period when the initial PKA energy is shared between only a few ions. These high frequencies can stimulate excitations across the full electronic band width which appear as a deviation from linearity at high and low energies that persists throughout the simulation, even when many lower energy excitations have given rise to a well-defined pseudo-temperature closer to the Fermi level. These features are visible in the sample data shown in Fig. 8.2 and are discussed in more detail in Sect. 13.4.1. To prevent these unrepresentative early excitations from corrupting the temperature estimate we choose to fit only against those data which fall within an energy window around the Fermi level.

The final temperature fitting algorithm works as follows. We begin by finding a best-fit temperature (with a self-consistent value for $\mu(T)$) to those data that lie within an initial energy window $|\varepsilon_i - \mu(T)| < \varepsilon_{\max}$. A value of $\varepsilon_{\max} = 0.2\,\mathrm{eV}$ tends to include enough data to achieve a good fit. Next, we gradually increase the value of ε_{\max} , repeatedly finding a new best-fit temperature. This process continues while ever ε_{\max} is such that $|f(\varepsilon_{\max};T) - 0.5| < O_{\max}$ where O_{\max} is a bound on the eigenstate occupations chosen to include as many data as possible without introducing the corrupting influence of high energy excitations from the early stages of the cascade. A good value seems to be $O_{\max} = 0.49$. Figure 8.4 shows the result of the fitting process for the data shown in Fig. 8.2. Having calculated a temperature for a range of values of ε_{\max} , we select the result with the highest value of the R^2 goodness-of-fit measure. Figure 8.5 shows the R^2 values achieved for our set of forty-four 2 keV cascade simulations as a function of simulation time. Typically

Fig. 8.3 The R^2 goodness-of-fit landscape for a sample dataset. Also shown is $\mu(T)$ subject to the constraint of fixed electron number and the best fit temperature as a function of μ . The intersection of the *two lines* indicates the constrained optimum fit and the *green lines* show how a single iteration of the self-consistency loop from an initial guess for μ arrives at a near optimum constrained fit



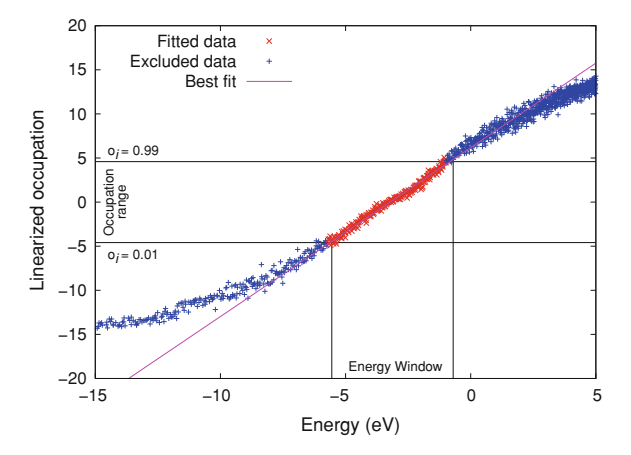


Fig. 8.4 The linearized form of the occupations o_i of the instantaneous eigenstates as a function of eigenstate energy ε_i for a typical simulation after 225 fs. The best fit is achieved by exploiting the maximum fitting window in this case. Excluded data points are shown in *blue* and the 228 included data points in *red*. Also shown is a best-fit temperature line with $T=6055\pm48~\rm K$, μ ($T=-3.226~\rm eV$ (Reprinted figure A.1 with permission from Race, C.P., Mason, D.R., Sutton, A.P.: Electronic excitations and their effect on the interionic forces in simulations of radiation damage in metals. J. Phys. Condens. Matter **21**(11), 115702 (2009). Copyright (2009) by the Institute of Physics Publishing Ltd.)

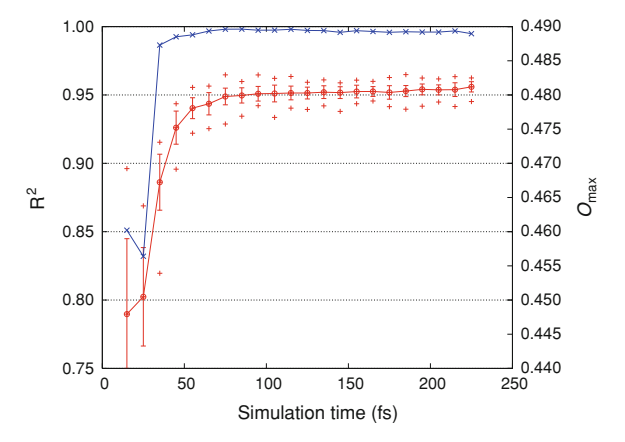


Fig. 8.5 The R^2 fitting measure for the temperature fitting algorithm for a set of forty-four 2 keV cascade simulations as a function of simulation time. *Red circles* show the mean of the distribution of R^2 across all simulations at a particular time. The *error bars* show the standard deviation and the *red vertical crosses* indicate the maximum and minimum R^2 within the set of simulations. The *blue diagonal crosses* show how the value of the parameter O_{max} for the optimum fit varies with time (Reprinted figure A.2 with permission from Race, C.P., Mason, D.R., Sutton, A.P.: Electronic excitations and their effect on the interionic forces in simulations of radiation damage in metals. J. Phys. Condens. Matter **21**(11), 115702 (2009). Copyright (2009) by the Institute of Physics Publishing Ltd.)

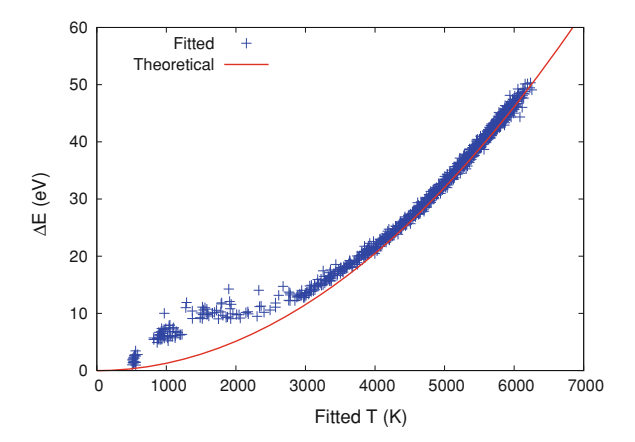


Fig. 8.6 A plot of the irreversible energy transfer into the electronic system against the best-fit temperature using our fitting algorithm. Data are shown at 10 fs intervals over 200 fs for each of forty-four 2 keV cascade simulations. The *red line* shows the predictions of the Sommerfeld model for the electronic heat capacity as discussed in the text (Reprinted figure 3 with permission from Race, C.P., Mason, D.R., Sutton, A.P.: Electronic excitations and their effect on the interionic forces in simulations of radiation damage in metals. J. Phys. Condens. Matter **21**(11), 115702 (2009). Copyright (2009) by the Institute of Physics Publishing Ltd.)

we find $0.94 \lesssim R^2 \lesssim 0.965$. Also shown is the optimum value of $O_{\rm max}$ and we can see that after about 35 fs of simulation the best fit is achieved by using the maximum fitting window. In Sect. 13.4.2 we present data that give us confidence that a window of this size is large enough to capture 98% of the changes in eigenstate occupations due to electronic excitations within the system.

In Fig. 8.6 we show a plot of the non-adiabatic energy transfer ΔE into the electronic system as a function of our fitted temperature at 10 fs for each of our forty-four 2 keV cascade simulations (a total 880 data-points). Also shown is the temperature–energy relation predicted by the Sommerfeld model for the heat capacity of a free electrons gas parameterized to match our tight-binding model (see Sect. 13.4.3 for a derivation). Except at low temperatures, the agreement between the theory and our simulation results is remarkably good. The deviation, which occurs in the fitted temperatures over the first 30–40 fs of cascade evolution is essentially the result of there being too little time for a well-defined electronic temperature to be established. Further discussion of this point can be found in Sect. 13.4.4.

8.1.2 Why do We Obtain Hot Electrons?

If the interactions in our semi-classical system are not expected to thermalize the electrons then why do we apparently obtain a well-defined temperature? Such

behaviour could also be explained if the interactions between the electrons and ions were such that the excitations generated in the electronic system were thermal *in the first instance*, rather than being non-equilibrium excitations that were subsequently thermalized. We can imagine that something like a Fermi–Dirac distribution would arise if our initial occupation distribution (a sharply defined, almost step-like distribution) were to evolve as if it were diffusing down the 'concentration gradient'. Such a diffusive evolution is plausible if the excitation of the electrons is the result of many 'jumps' in energy, all small on the scale of the width of the Fermi–Dirac distribution.

Imagine an initial occupation distribution $f(\varepsilon)$ evolving in time as a result of many small jumps of energy $\hbar\omega$ and subject to Pauli exclusion. The rate of change of the occupation distribution will be given by,

$$\frac{\mathrm{d}f(\varepsilon)}{\mathrm{d}t} \propto [1 - f(\varepsilon)][f(\varepsilon + \hbar\omega) + f(\varepsilon - \hbar\omega)]
- f(\varepsilon)\{[1 - f(\varepsilon + \hbar\omega)] + [1 - f(\varepsilon - \hbar\omega)]\},$$
(8.3)

where the first term corresponds to transitions into the state at energy ε from states $\hbar\omega$ either side and the second term corresponds to transitions out. Cancellation gives

$$\frac{\mathrm{d}f(\varepsilon)}{\mathrm{d}t} \propto [f(\varepsilon + \hbar\omega) - f(\varepsilon)] - [f(\varepsilon) - f(\varepsilon - \hbar\omega)]. \tag{8.4}$$

If the characteristic frequency ω is small enough that the jumps are small on the scale of variation of $f(\varepsilon)$ then we can write

$$\frac{\mathrm{df}(\varepsilon)}{\mathrm{d}t} \propto \hbar\omega \left[\frac{\mathrm{df}}{\mathrm{d}\varepsilon} \bigg|_{\varepsilon + \hbar\omega/2} - \frac{\mathrm{df}}{\mathrm{d}\varepsilon} \bigg|_{\varepsilon - \hbar\omega/2} \right],\tag{8.5}$$

and

$$\frac{\mathrm{df}(\varepsilon)}{\mathrm{d}t} \propto (\hbar\omega)^2 \frac{\mathrm{d}^2 \mathrm{f}}{\mathrm{d}\varepsilon^2} \bigg|_{\varepsilon}.$$
 (8.6)

The evolution of $f(\varepsilon)$ is thus governed by a one-dimensional diffusion equation in energy space.

In our cascade simulations the diffusional 'jumps' correspond to the electronhole excitations stimulated by the motion of the ions in our cascade. The size of the jumps will be determined by the characteristic frequencies of the changes in the hopping integrals in the electronic Hamiltonian. We might expect that a cascade would contain some very high frequencies: a 2 keV PKA, with velocity $v_{\rm max}=780~{\rm \AA~ps^{-1}}$, passing a nearest neighbour at an impact parameter of half the close-packed distance, $b_{\rm min}=1.28~{\rm \AA}$, will have a characteristic frequency,

$$\omega = 2\pi \frac{v_{\text{max}}}{h_{\text{min}}} = 3.8 \,\text{PHz},\tag{8.7}$$

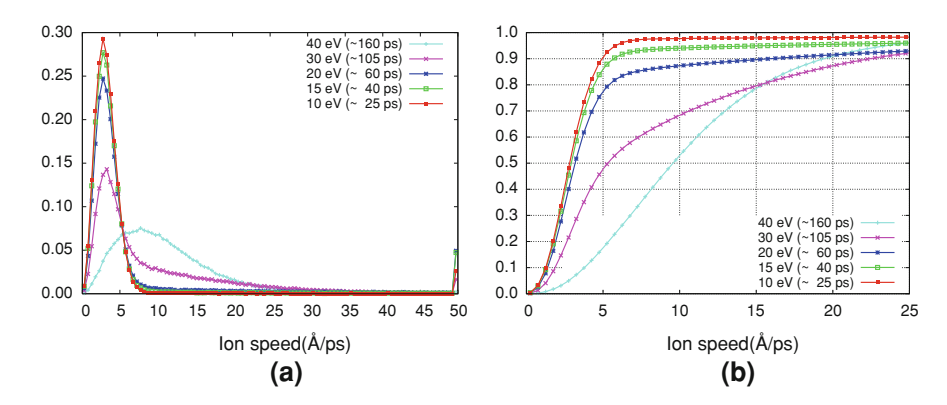


Fig. 8.7 Distribution of ion speeds at various stages in a set of forty-four 2 keV cascades simulations: **a** histogram, **b** ascending cumulative distribution. To gather statistics, the correspondence between different simulations has been made on the basis of the irreversible energy transfer to the electrons during the cascade (ΔE is indicated in the key). An indication of the approximate time at which each energy transfer occurs is also given in the key

corresponding to an energy of around 2.5 eV, certainly not small on the scale of the width of our initial Fermi–Dirac distribution. However, the initial PKA kinetic energy is rapidly shared amongst a large number of ions in the collision cascade and so a more typical ion velocity would be $\lesssim 20\,\mathrm{\AA\,ps^{-1}}$, as we can see from Fig. 8.7. This corresponds to excitations of frequencies $\lesssim 0.1\,\mathrm{PHz}$ and energies $\lesssim 0.06\,\mathrm{eV}$, making a diffusional evolution more plausible.

So far, all we have done is argue that it is plausible that the evolution of the electronic occupation function in a collision cascade will take the form of a one-dimensional diffusion in energy space. This will only give apparent heating of the electrons if diffusional evolution takes the occupation function from a lower temperature Fermi–Dirac distribution into a higher temperature one. Starting with the Fermi–Dirac distribution $f(\varepsilon) = [1 + \mathrm{e}^{\varepsilon/k_\mathrm{B}T}]^{-1}$, where we have assumed the chemical potential is zero, we can compare the rate of change with increasing temperature,

$$\frac{\mathrm{df}(\varepsilon)}{\mathrm{d}t} = \frac{\mathrm{e}^{\varepsilon/\mathrm{kT}}}{(1 + \mathrm{e}^{\varepsilon/kT})^2} \frac{\varepsilon}{kT^2}.$$
 (8.8)

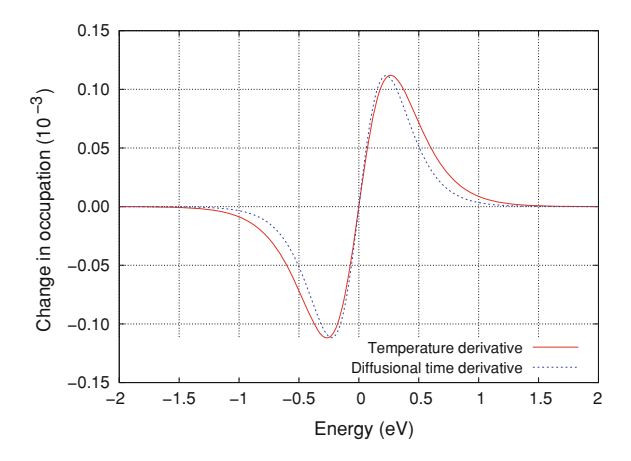
with the rate of change under the diffusion equation,

$$\frac{\mathrm{df}}{\mathrm{d}t} = \eta \frac{\mathrm{d}^{2} f}{\mathrm{d}\varepsilon^{2}}$$

$$= \frac{\eta}{(kT)^{2}} \frac{\mathrm{e}^{\varepsilon/\mathrm{kT}} (\mathrm{e}^{\varepsilon/\mathrm{kT}} - 1)}{(\mathrm{e}^{\varepsilon/\mathrm{kT}} + 1)^{3}}$$

$$= \frac{\eta}{2(kT)^{2}} \frac{\sinh(\varepsilon/\mathrm{kT})}{(\cosh(\varepsilon/\mathrm{kT}) + 1)^{2}},$$
(8.9)

Fig. 8.8 A comparison of the temperature derivative of the Fermi-Dirac function and its time evolution under the diffusion equation. The effective diffusion coefficient is chosen freely to allow comparison of the shape of the curves



where η is some diffusion coefficient. A comparison of the shapes of these two curves is shown in Fig. 8.8 where they can be seen to be very similar.

We can take the analysis a little further if we return to Eq. 8.4 but do not make the approximation of small ω . Then we have,

$$\frac{\mathrm{d}f(\varepsilon)}{\mathrm{d}t} \propto \left[f(\varepsilon + \hbar\omega) - f(\varepsilon) \right] - \left[f(\varepsilon) - f(\varepsilon - \hbar\omega) \right] \\ \propto \frac{\sinh(\varepsilon/\mathrm{kT})}{\cosh(\varepsilon/\mathrm{kT}) + 1} - \frac{\sinh(\varepsilon/\mathrm{kT})}{\cosh(\varepsilon/\mathrm{kT}) + \cosh(\hbar\omega/\mathrm{kT})}. \tag{8.10}$$

Note that in the case of low frequencies $\cosh(\hbar\omega/k_{\rm B}T)\approx 1$ and this becomes

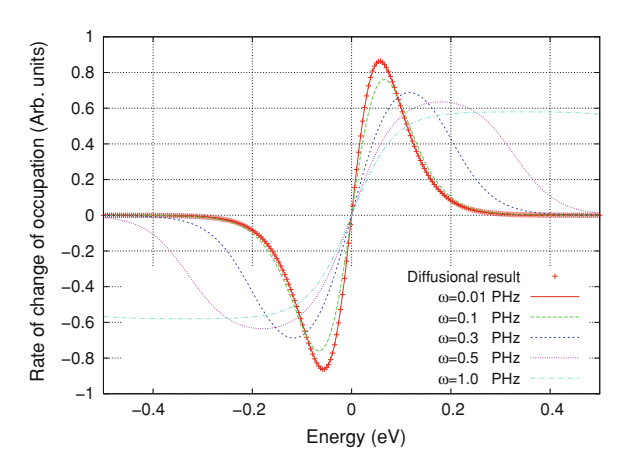
$$\frac{\mathrm{df}(\varepsilon)}{\mathrm{d}t} \propto \frac{1}{2(kT)^2} \frac{\sinh(\varepsilon/kT)}{\left[\cosh(\varepsilon/kT) + 1\right]^2},\tag{8.11}$$

which has the same form as the diffusional result (8.9) as expected. In Fig. 8.9 we compare the exact expression for the effect of finite energy jumps of $\hbar\omega$ (8.10) with the diffusional result (8.9). We can see that at the typical cascade frequency of \lesssim 0.1 PHz the effect of discrete jumps is very similar to a diffusive evolution of the Fermi–Dirac distribution. This in turn (as shown in Fig. 8.8) gives an evolution close to that corresponding to a rise in temperature and we can see how an apparently thermal excited electronic system can arise in cascade simulations where no obvious thermalization mechanism exists.

8.1.3 The Importance of the Result

In the preceding sections we presented results that show that in our Ehrenfest dynamics cascade simulations the electrons are excited in such a way that they appear to acquire an elevated temperature. We also showed that this can be

Fig. 8.9 The time derivative of the occupation function as given by (8.10) for a selection of frequencies. The plots have been given an arbitrary vertical scaling to allow comparison of their shapes and the result from the diffusion equation (8.9) is indicated for comparison



understood, in the absence of any obvious thermalizing mechanism, to be the result of the cumulative effect of many single-particle excitations, small on the scale of the width of the Fermi–Dirac distribution. However, in real metallic systems, both the direct electron–electron interactions and the electron–ion interactions will act to thermalize a non-equilibrium excited electronic system. It thus seems that our result may be peculiar to the (in this respect defective) Ehrenfest dynamics in our simulations and so of limited importance.

To see why our result might have broader significance, we will consider a particular situation in which it might be useful. The work of Duffy et al. [3–5]

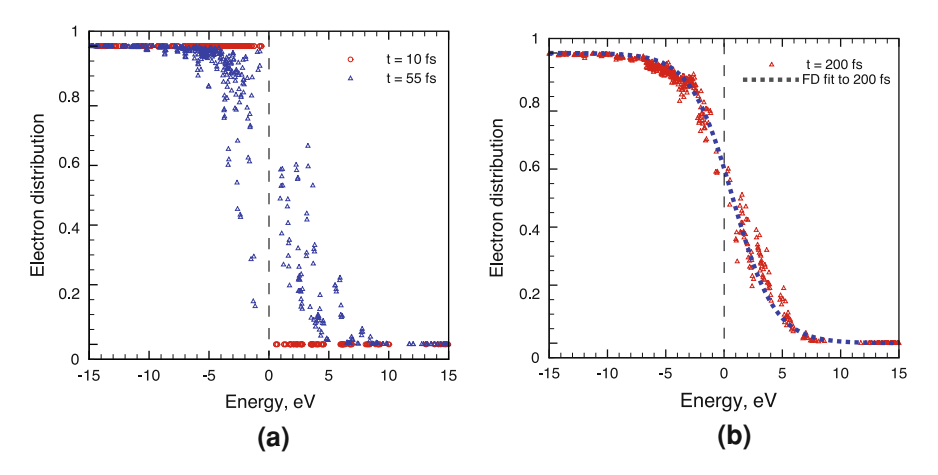


Fig. 8.10 Data from semi-classical DFT simulations of femtosecond laser experiments on a graphene bilayer. **a** The electronic occupation function for a double layer of graphene before and after excitation by a 45 fs laser pulse. The electronic system is driven far from equilibrium. **b** The electronic occupation function after 200 fs of simulation under semi-classical dynamics. A best-fit Fermi-Dirac distribution with a temperature of 20 880 K is shown (Reprinted figures 1 and 3 with permission from Lin, Z., Allen, R.E.: Ultrafast equilibration of excited electrons in dynamical simulations. J. Phys. Condens. Matter. **21**(48), 485503, (2009). Copyright (2009) by the Institute of Physics Publishing Ltd.)

discussed in Sect. 3.4.2.2 can be viewed as an early step in attempting to incorporate the effects of electronic excitations into classical MD simulations of radiation damage phenomena. One of the key underlying assumptions of their model is the existence of a well-defined electronic temperature throughout a radiation damage event.

Furthermore, one deficiency of the current model of Duffy et al. is that no account is taken in the classical potentials of the effect of the cumulative excitation of the electronic system. As the electrons are excited by the ionic motion, the bonds between atoms will weaken. We have investigated just this effect using our Ehrenfest dynamics model (the results are presented in Chap. 9), but for now we will note that in theory it could be accommodated in a classical simulation scheme via an excitation-dependent potential.

In general such a potential would be difficult to formulate, but matters are simplified significantly if we can assume that the electrons always have a well-defined temperature. The potential can then be defined as a function of temperature and the simulation need only keep track of the electronic temperature in order to describe the degree of excitation. Khakshouri et al. [6] have produced just such a potential for tungsten for use in the model of Duffy et al. [3–5].

The validity of the assumption of a well-defined electronic temperature is then key. Femtosecond laser experiments by Del Fatti et al. [7] suggest that electron-electron interaction time-scales are of the order of a few hundred femtoseconds (they find time-scales of 350 fs in silver and 500 fs in gold). This is certainly not short on the time-scale of a typical collision cascade, in which the displacement phase is over within several picoseconds. What is more, the time-scale of the electron-phonon interaction is of a similar order of magnitude (Qiu and Tien [8] use experimental data to find values of 650 fs in copper and only 64 fs in vanadium). We might thus expect the ionic motion to be driving the electronic system away from equilibrium at least as fast as the electron-electron interaction can act to re-establish a well-defined temperature. The fact that the ionic motion actually tends to excite the electronic system through a series of increasing temperatures, as revealed by our simulations, is thus critically important in validating the simplifying assumption of a well-defined electronic temperature in work such as that described in reference [6].

8.1.4 Thermalization or Thermal Excitation?

In the foregoing discussion we have made a distinction between *thermalization* of the electronic system, which we take to mean the action of mechanisms of electron–electron and electron–ion interaction to produce an equilibrium electronic distribution in a real metal and the processes taking place in our Ehrenfest simulations of collision cascades which give rise to an approximately thermal distribution as a direct result of the pattern of excitations stimulated by the ionic motion. In this latter case, since it is the interaction with the ions that yields a well-

defined electronic temperature, we might be tempted to regard our findings as evidence of thermalization by the electron-ion interaction.

In a recent paper [9], Lin and Allen draw just such a conclusion from semiclassical simulations of femtosecond laser experiments with a DFT model of the electronic system. They simulate the effect of a 45 fs laser pulse on the electrons of a 224 atom model of a graphene bilayer with four orbitals per atom. Figure 8.10a shows the initial 300 K electronic occupation function and the effect of excitation by the laser pulse. The ions are also given an initial temperature of 300 K. After 200 fs of the simulation the electrons appear to have a well-defined temperature (see Fig. 8.10b) and Lin and Allen attribute this result to thermalization by the motion of the ions via the electron—ion interaction.

A comparison with our cascade simulations is instructive. In the case of a collision cascade we start off with a well-defined low electronic temperature. This is a highly ordered state of the electronic system and so the effect of any set of excitations will tend to drive the electronic system to a higher entropy state. When these excitations are all small, their cumulative statistical effect is such that those higher entropy states are approximately the maximum entropy equilibrium states and the electrons appear to acquire an elevated temperature. In the case of Lin and Allen's simulations, the electrons are excited far from equilibrium by the laser pulse and so the above argument seems like it should not apply. However, a closer look at Fig. 8.10a reveals that, though the laser pulse generates disorder in the electronic occupations, this disorder is highly localized in energy space and superimposed upon an underlying occupation distribution that remains highly ordered. The ionic motion appears to thermalize the electrons only once the cumulative effect of many excitations has generated a high enough pseudo-temperature to swallow the initial disruption to the occupancy function.

The important point is that Ehrenfest dynamics does not treat the electron–ion interaction correctly because it ignores spontaneous phonon emission. As shown by le Page et al. [10] and discussed in Sect. 4.6.2, this should not cause significant problems when treating systems in which energy transfer is predominantly from hot ions to cool electrons. However, when spontaneous phonon emission is a significant effect we should be careful about drawing conclusions from Ehrenfest dynamics simulations. Such simulations will certainly not give equilibration between ions and electrons and will not give a correct treatment of the electron–ion interaction whenever the electrons are hotter than or at a similar temperature to the ions.

To emphasise this point we have carried out a series of very simple numerical simulations within a toy model. In each case we start with a model electronic occupation function in a set of states evenly distributed between 0 eV and 1,000 eV and implement a series of random jumps of size 10 eV, obeying Pauli exclusion. We are thus implementing the simple diffusional model for the effect of the ionic motion on the electronic system. Figure 8.11a shows the effect of random jumps on an initially cold occupation distribution. The jumps take the system through a series of increasing pseudo-temperatures. In Fig. 8.11b we have chosen an initial occupation distribution that mimics the effect of laser heating in the

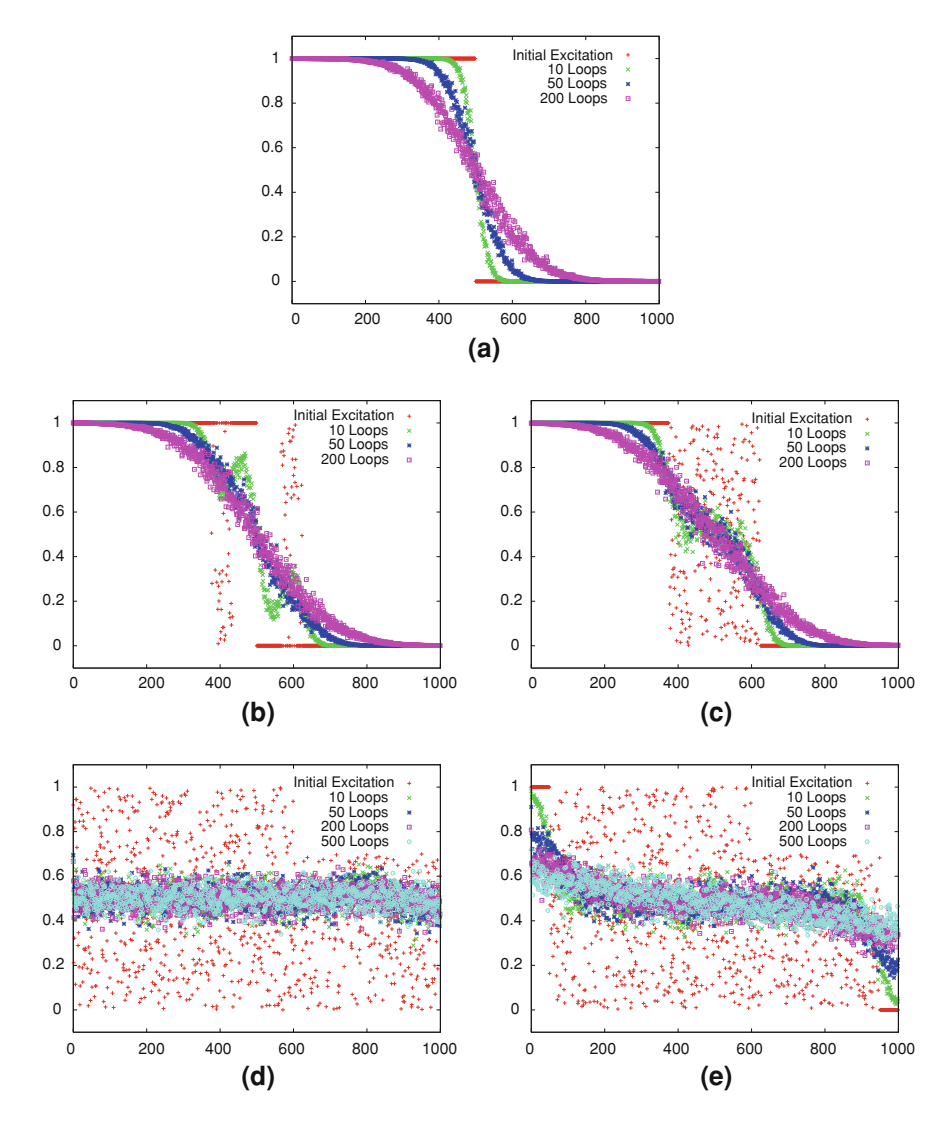


Fig. 8.11 The results of numerical simulations of a diffusive excitation model. In each case the initial occupation function is shown along with the occupations after a series of small random jumps of 1/100th the total width of the distribution. The simulations are implemented in loops of 1,000 jumps and the number of loops corresponding to each distribution is indicated in the key. **a** Heating of an initially cold electronic system. **b** An initial excitation pattern designed to mirror the effect of laser heating in the simulations of Lin and Allen [9]. **c** A more extreme, but still localized initial excitation. **d** An initial infinite temperature distribution. **e** A very broad excitation (see main text for further discussion of these results)

simulations of Lin and Allen [9]. After 50 loops of 1,000 jumps each the disorder in the initial excitation spectrum is swallowed by the appearance of a sufficiently high pseudo-temperature. When more disorder is introduced in the initial

excitations, but still confined to a narrow range of energies, as shown in Fig. 8.11c we still see a pseudo-temperature emerging, but only after a longer time. When the initial excitations span the whole band width, as shown in Fig. 8.11d, the diffusional model cannot yield thermalization. The long-term steady state is the same as that given by Ehrenfest dynamics (when sufficient ionic energy is present) and the system fluctuates around an infinite temperature. Similar behaviour is seen in Fig. 8.11e when excitations are introduced over a very broad energy range.

What the above results show is that even a very simple model of the electronic excitation process, and one which most definitely does not incorporate a thermalization process or the possibility of a finite temperature long-term steady state, can still act to produce an apparently well-defined electronic temperature even in an initially excited system. We should thus be very careful when referring to 'thermalization' processes that there is a genuine approach to some sort of equilibrium. In particular, quantitative conclusions that rely on the flawed representation of the electron—ion interaction in Ehrenfest dynamics can be questionable.

8.2 Electronic Entropy in Ehrenfest Simulations

In discussing the appearance of an elevated pseudo-temperature in our cascade simulations we remarked that the excitations stimulated by the motion of the ions drove the electronic system from an initially ordered low temperature state towards a more disordered state with an elevated pseudo-temperature. Unfortunately, the corresponding notion of increasing electronic entropy is inconsistent with the fact that the electronic density matrix undergoes unitary evolution under the quantum Liouville equation and so its entropy remains fixed.

If we initialize our density matrix according to Fermi–Dirac occupations $\{f_i(\varepsilon_i(\mathbf{R};t=0))\}$ chosen based on the initial energy eigenvalues $\{\varepsilon_i\}$ of the electronic Hamiltonian then we can write

$$\hat{\rho}(t=0) = \sum_{i} f_i(\varepsilon_i(\mathbf{R}; t=0)) |\phi_i(\mathbf{R}; t=0)\rangle \langle \phi_i(\mathbf{R}; t=0)|,$$
 (8.12)

where $\{|\phi_i(\mathbf{R};t=0)\}$ are the initial eigenstates of the electronic Hamiltonian. In the wavefunction view of Ehrenfest dynamics (see Sect. 7.2.1) in which the initial eigenstate $|\phi_i(\mathbf{R};t=0)\rangle$ evolves into a state $|\psi_i(t)\rangle$ at time t under the action of the electronic Hamiltonian, then the density matrix can always be written

$$\hat{\rho}(t) = \sum_{i} f_i(\varepsilon_i(\mathbf{R}; t=0)) |\psi_i(t)\rangle \langle \psi_i(t)|. \tag{8.13}$$

In other words the density matrix is diagonal in the basis of Ehrenfest wavefunctions evolved from the initial energy eigenstates. Its eigenvalues $\{\lambda_i\}$ are fixed at the values

$$\lambda_i = f_i(\varepsilon_i(\mathbf{R}; t = 0)) = \langle \psi_i(t) | \hat{\rho}(t) | \psi_i(t) \rangle. \tag{8.14}$$

8.2.1 Two Definitions of Electronic Entropy

A natural definition of the electronic entropy is

$$S(\hat{\rho}) = -k_{\rm B} \sum_{i} (\lambda_i \ln \lambda_i + (1 - \lambda_i) \ln(1 - \lambda_i)), \tag{8.15}$$

which, because of the unitary evolution of $\hat{\rho}(t)$, remains constant.

However, simulation results like those presented in Fig. 8.1 show a relationship between the eigenstate occupations o_i and their energies ε_i that is highly suggestive of some process of heating of the electronic system. This is inconsistent with an isentropic unitary evolution and motivates us to define an alternative pseudo-entropy

$$\tilde{S}(\hat{\rho}) \equiv -k_{\rm B} \sum_{i} (o_i \ln o_i + (1 - o_i) \ln(1 - o_i)), \tag{8.16}$$

where o_i is the occupation of the instantaneous eigenstate $|\phi_i\rangle$ of the evolving Hamiltonian: $o_i(t) \equiv \langle \phi_i | \hat{\rho}(t) | \phi_i \rangle$. If we choose to write the density matrix in the basis of instantaneous energy eigenstates,

$$\hat{\rho} = \sum_{ii} |\phi_i(\mathbf{R}; t)\rangle \,\rho_{ij}(t) \,\langle \phi_j(\mathbf{R}; t)|, \qquad \rho_{ij}(t) \equiv \langle \phi_i(\mathbf{R}; t)|\hat{\rho}|\phi_j(\mathbf{R}; t)\rangle, \quad (8.17)$$

then we can introduce a new truncated density matrix

$$\hat{\rho}^{\text{Diag}} \equiv \sum_{i} |\phi_{i}(\mathbf{R};t)\rangle \, \rho_{ii}(t) \, \langle \phi_{i}(\mathbf{R};t)|. \tag{8.18}$$

The natural entropy of this new density matrix will be equal to the pseudo-entropy of the full density matrix,

$$\tilde{S}(\hat{\rho}) = S(\hat{\rho}^{\text{Diag}}). \tag{8.19}$$

This is an attractive property of \tilde{S} since the truncation of the density matrix defined above preserves both the particle number and the electronic energy of the full density matrix:

$$\operatorname{Tr}(\hat{\rho}) = \operatorname{Tr}(\hat{\rho}^{\operatorname{Diag}}), \qquad \operatorname{Tr}(\hat{\rho}\hat{H}) = \operatorname{Tr}(\hat{\rho}^{\operatorname{Diag}}\hat{H}).$$
 (8.20)

 \tilde{S} has two further desirable properties for a density matrix:

- 1. It tends to increase with time (see Sect. 13.1.12).
- 2. It is extensive (additive) if we consider the extension of our system to be via the introduction of multiple equivalent copies of the original evolving system.

8.2.2 Reconciling the Two Entropies

We now have two, apparently very different, definitions of the entropy of our electronic system: S which is fixed throughout our simulations and \tilde{S} which increases. As we noted above $\tilde{S}(\hat{\rho}) = S(\hat{\rho}^{\text{Diag}})$ and so understanding the relationship between the two entropies will require an understanding of the meaning of the off-diagonal elements of the density matrix in the eigenstate basis. Given that $S(\hat{\rho}) \leq \tilde{S}(\hat{\rho})$ we might say that these off-diagonal elements have an 'ordering' effect on the system; they contain information that tends to lower the entropy. Since the diagonal density matrix contains all the information about the energy and number of the electrons, the information in the off-diagonal terms must concern the dynamics, past and present, of the electron system. Our full density matrix has a 'memory' extending all the way back to t=0, keeping track of the correlations between the instantaneous eigenstates. This long memory is a consequence of the (fully coherent) unitary evolution of our closed electronic system embodied in the quantum Liouville equation.

Landau and Lifshitz [11] point out that the concept of entropy only makes sense when considered as an average over some finite time interval. Entropy is an equilibrium property and so can only be well-defined over a period of time that is long compared with the relaxation time of the system under study, but short when compared with the time-scale of its interactions with any environment. This directs us to consider a time-averaged density matrix

$$\bar{\rho}(t; \Delta t) \equiv \frac{1}{\Delta t} \int_{t_{-}}^{t} \hat{\rho}(s) ds. \tag{8.21}$$

Our two definitions of the entropy might be reconciled if

$$\lim_{\Delta t \to \infty} S(\bar{\rho}(t; \Delta t)) = \tilde{S}(\hat{\rho}(t)) = S(\hat{\rho}^{\text{Diag}}(t)), \tag{8.22}$$

or if, more strongly,

$$\lim_{\Delta t \to \infty} \bar{\rho}(t; \Delta t) = \hat{\rho}^{\text{Diag}}(t). \tag{8.23}$$

We will now consider a thought experiment that gives us some confidence that the above limits make sense.

8.2.3 A Thought Experiment

Imagine that we initialize a density matrix at time t_0 and allow it to evolve under a time varying Hamiltonian $\hat{H}(t)$ up to a time t_1 . We then suddenly freeze the Hamiltonian and carry out a further evolution to time t under the time-invariant

Hamiltonian $\hat{H}(t_1)$. The time evolution operator under this constant Hamiltonian is simply

$$\hat{U}(t;t_1) = e^{-i\hat{\mathbf{H}}(t_1)[t-t_1]/\hbar}, \tag{8.24}$$

and so we can write down the elements of the density matrix $\hat{\rho}(t)$ in the instantaneous eigenstate basis:

$$\hat{\rho}(t \ge t_1) = \sum_{ij} e^{-i(\varepsilon_i - \varepsilon_j)(t - t_1)/\hbar} |\phi_i(t_1)\rangle \, \rho_{ij}(t_1) \, \langle \phi_j(t_1)|. \tag{8.25}$$

We can see that the diagonal elements (eigenstate occupancies) remain fixed whilst the off-diagonal elements have a fixed amplitude and an oscillating phase. If we now form the time-averaged density matrix $\bar{\rho}(t; \Delta t = t - t_1)$, it will have off-diagonal elements

$$\bar{\rho}_{ij} = \left(\frac{1}{t - t_1} \int_{t_1}^{t} e^{-i(\varepsilon_i - \varepsilon_j)(t - t_1)/\hbar} \right) \rho_{ij}(t_1), \tag{8.26}$$

which clearly decay with time.

It is important to note that the decay in the off-diagonal elements is entirely due to the effect of averaging over a larger and larger time window. In the picture in which the non-adiabatic energy transfer to the electrons is due to the inability of the density matrix to keep up with the changing Hamiltonian, one might think that stopping the Hamiltonian would give the electrons chance to 'catch up'. We can see from the above discussion that this is not the case; the density matrix elements continue to oscillate with fixed amplitudes in perpetuity. The density matrix is thus periodic in time, with some (likely large) period determined by the mixture of eigenvalue separations in the energy spectrum.

8.3 Conclusions

We have exploited the information about the electronic system available within our semi-classical simulations to study the nature of the electronic excitations stimulated by the motion of the ions in low energy collision cascades. We have found that these excitations are well-characterized by an increasing pseudo-temperature (Sect. 8.1.) and have developed an algorithm to fit such temperatures (Sect. 8.1.1). The emergence of a pseudo-temperature can be explained using a diffusive picture of excitation within the occupation distribution (Sect. 8.1.2).

That the excited electrons in a collision cascade can be described using an elevated temperature is of significant importance to anyone attempting to develop an excitation-dependent classical potential for use in radiation damage simulations (Sect. 8.1.3). If the excitations generated by the ionic motion in the cascades were not nearly thermal in the first instance then the relative time-scales for

electron-electron and electron-phonon interaction suggest that the electrons would tend to acquire a thermal distribution, complicating any efforts to build an excitation-dependent potential.

In Ehrenfest dynamics the electronic entropy is fixed, which seems to be inconsistent with the notion of an increasing electronic temperature. However, by noting that the historical "memory" of the system evolution is contained in the off-diagonal elements of the density matrix in the instantaneous energy eigenstate basis and defining an alternative entropy based only on the diagonal elements we obtain a more consistent picture.

References

- le Page, J.: The transfer of energy between electrons and ions in solids. PhD thesis, University of London (2008)
- Race, C.P., Mason, D.R., Sutton, A.P.: Electronic excitations and their effect on the interionic forces in simulations of radiation damage in metals. J. Phys. Condens. Matter 21(11), 115702 (2009)
- 3. Duffy, D.M., Rutherford, A.M.: Including the effects of electronic stopping and electron—ion interactions in radiation damage simulations. J. Phys. Condens. Matter 19(1), 016207 (2007)
- 4. Duffy, D.M., Itoh, N., Rutherford, A.M., Stoneham, A.M.: Making tracks in metals. J. Phys. Condens. Matter **20**(8), 082201 (2008)
- Rutherford, A.M., Duffy, D.M.: The effect of electron-ion interactions on radiation damage simulations. J. Phys. Condens. Matter 19(49), 496201 (2007)
- Khakshouri, S., Alfe, D., Duffy, D.M.: Development of an electron-temperature dependent interatomic potential for molecular dynamics simulation of tungsten under electronic excitation. Phys. Rev. B (Condens. Matter Mater. Phys.) 78(22), 224304 (2008)
- Del Fatti, N., Voisin, C., Achermann, M., Tzortzakis, S., Christofilos, D., Vallée, F.: Nonequilibrium electron dynamics in noble metals. Phys. Rev. B 61(24), 16956–16966 (2000)
- 8. Qiu, T.Q., Tien, C.L.: Short-pulse laser heating on metals. Int. J. Heat Mass Transf. 35(3), 719–726 (1992)
- 9. Lin, Z., Allen, R.E.: Ultrafast equilibration of excited electrons in dynamical simulations. J. Phys. Condens. Matter. **21**(48), 485503 (6pp), 2009
- 10. le Page, J., Mason, D.R., Foulkes, W.M.C.: The Ehrenfest approximation for electrons coupled to a phonon system. J. Phys. Condens. Matter **20**(12), 125212 (2008)
- 11. Landau, L.D., Lifshitz, E.M.: Statistical Physics (Part 1), p. 27. Elsevier, Amsterdam (2005)

Chapter 9 The Electronic Forces

Summary: In this chapter we will begin a detailed analysis of the electronic forces acting on ions during collision cascades. We will first break out the non-adiabatic aspects of the force into components due to the accumulation of excitations in the electronic system and components due to the finite response time of the electrons to motion of the ions. We then focus our attention in this chapter on the first of these (the latter will be considered in detail in Chap. 11). We find that the reduction in the magnitude of the attractive electronic forces between ions can be significant at high electronic temperatures, ~ 10000 K. We analyse the effect of high electronic temperatures on the lengths of replacement collision sequences and consider the effect of bond-weakening in terms of the implied volume strain on electronically hot regions of the target material.

The primary purpose of simulations of radiation damage is to determine and understand the damage caused to the target material. Essentially, this damage is fully determined by knowledge of the ionic positions at the conclusion of the radiation damage event. When we consider the effect of electronic excitations on radiation damage we are really asking how the electrons affect the positions of the ions, or, in other words, we wish to know how electronic excitations affect the forces on the ions.

In this chapter we will consider the electronic force on the ions in our Ehrenfest simulations in detail. We will develop a way of breaking down this force into more easily understandable components and present the results of simulations that answer some key questions about the behaviour of the forces in radiation damage events.

9.1 Understanding the Electronic Force

Classical molecular dynamics can successfully incorporate much of the effect of the electrons on the forces felt by the ions: a well designed classical potential should capture the electronic bonding forces between ions under the assumption that the electrons remain in their ground state (i.e. the Born–Oppenheimer approximation is made). But, because such potentials treat the ions as quasistatic, they fail to include potentially important non-adiabatic effects. These will be of two main types:

- 1. The finite response time of the electronic system to changes in the electronic Hamiltonian (i.e. to the positions of the ions) will give rise to non-adiabatic forces. These forces should depend only on the relatively recent history of the cascade evolution. The drag forces included in the simulation frameworks [1–4] discussed in Sect. 3.4.2 are an attempt to incorporate the effects of these non-adiabatic forces.
- 2. Over the course of a cascade evolution, the ions will do work against the non-adiabatic forces discussed above. This work will manifest itself as excitations in the electronic subsystem. As these excitations accumulate the electrons will gradually heat up (with a well-defined pseudo-temperature as we saw in Chap. 8) and the bonding forces between ions will weaken. Temperature dependent classical potentials (as discussed in Sect. 8.1.3) are an attempt to incorporate this effect.

We would like to make the above distinction more concrete and so we begin by considering the Hellmann–Feynman force (4.129) for our non-charge-self-consistent model given in Sect. 4.5.2,

$$\mathbf{F}_{e} = -\text{Tr}(\hat{\rho}\nabla\hat{H}). \tag{9.1}$$

If we choose to work in the basis of instantaneous eigenstates of \hat{H} , denoted $\{|\phi_i(\mathbf{R};t)\rangle\}$ with eigenvalues $\{\varepsilon_i(\mathbf{R};t)\}$ (from which we will from now on omit the dependence on the ionic coordinates \mathbf{R} and the parametric dependence on time, t, then the Hamiltonian takes a particularly simple form,

$$\hat{H} = \sum_{i,i} \varepsilon_i \delta_{ij} |\phi_i\rangle \langle \phi_i|. \tag{9.2}$$

We can write the density matrix as

$$\hat{\rho} = \sum_{i,j} |\phi_i\rangle \rho_{ij} \langle \phi_j|, \quad \rho_{ij} \equiv \langle \phi_i|\hat{\rho}|\phi_j\rangle, \tag{9.3}$$

and the Hellmann-Feynman force is written (see Sect. 13.1.13),

$$\mathbf{F}_{e} = -\sum_{i} \rho_{ii} \nabla \varepsilon_{i} - \sum_{i, i \neq i} (\varepsilon_{i} - \varepsilon_{j}) \rho_{ij} \langle \phi_{j} | \nabla \phi_{i} \rangle. \tag{9.4}$$

The first term in (9.4) represents motion on a collection of potential energy surfaces defined by the instantaneous eigenvalues $\{\varepsilon_i\}$ occupied according to the diagonal elements $\{\rho_{ii}\}$. The second term gives the effect of non-adiabaticity. The factors $\langle \phi_j | \nabla \phi_i \rangle$ are often referred to as the *non-adiabatic coupling vectors* [5] and are frequently denoted \mathbf{d}_{ij} . Note, however, that there is nothing *inherently* non-adiabatic about these quantities; they are entirely determined by the positions of the ions and the non-adiabaticity is introduced by the finite response time of the matrix elements ρ_{ij} to changes in \hat{H} . The vectors \mathbf{d}_{ij} do, however, give the direction of the non-adiabatic forces.

We can carry this analysis further by splitting out the density matrix into its adiabatic form and a component due to the accumulated excitations. Under the assumption that the ions have traversed their paths infinitely slowly, the density matrix takes the adiabatic form (see Sect. 7.2.3, Eq. 7.10),

$$\hat{\rho}^{\mathrm{Ad}} = \sum_{i} |\phi_{i}\rangle f_{i}(\varepsilon(t=0); T_{\mathrm{e}}(t=0))\langle \phi_{i}|, \tag{9.5}$$

where $\{f_i(\varepsilon(t=0); T_{\rm e}(t=0))\}$ are the initial occupations of the instantaneous eigenstates, which we have assumed to be a Fermi-Dirac distribution at an initial temperature $T_{\rm e}(t=0)$. As we saw in Sect. 8.1, the electronic excitations occurring during a collision cascade are close to thermal, and so we introduce a third density matrix,

$$\hat{\rho}^T \equiv \sum_{i} |\phi_i\rangle f_i(\varepsilon(t); T_{\rm e}(t))\langle\phi_i| \tag{9.6}$$

where the occupations $\{f_i(\varepsilon(t); T_e(t))\}$ are distributed according to a Fermi–Dirac distribution at a best-fit pseudo-temperature $T_e(t)$. By also defining a truncated density matrix that omits the off-diagonal elements,

$$\hat{\rho}^{\text{Diag}} \equiv \sum_{i} |\phi_{i}\rangle \rho_{ii}\langle \phi_{i}|. \tag{9.7}$$

we can now express the full density matrix as,

$$\hat{\rho} = \hat{\rho}^{Ad} + (\hat{\rho}^T - \hat{\rho}^{Ad}) + (\hat{\rho}^{Diag} - \hat{\rho}^T) + (\hat{\rho} - \hat{\rho}^{Diag}). \tag{9.8}$$

The first term is then the unexcited density matrix, the second term represents a set of thermal excitations, and the third term gives 'corrections' to those thermal excitations. The fourth term contains all the dynamical information concerning correlation between and the rate of change of occupation of the eigenstates. Combining this splitting of the density matrix with the force expression (9.4) allows us to further split out the electronic force,

$$\mathbf{F}_e = \mathbf{f}_1 + \mathbf{f}_2 + \mathbf{f}_3 + \mathbf{f}_4 \tag{9.9}$$

¹ This density matrix also appears in Eq. 8.18 in our discussion of electronic entropy.

where.

$$\mathbf{f}_1 = -\sum_{i} f_i(\varepsilon(t=0); T(t=0)) \nabla \varepsilon_i, \tag{9.10}$$

$$\mathbf{f}_2 = -\sum_{i} [f_i(\varepsilon(t); T(t)) - f_i(\varepsilon(t=0); T(t=0))] \nabla \varepsilon_i, \tag{9.11}$$

$$\mathbf{f}_{3} = -\sum_{i} [\rho_{ii} - f_{i}(\varepsilon(t); T(t))] \nabla \varepsilon_{i}, \tag{9.12}$$

$$\mathbf{f}_4 = -\sum_{i,j \neq i} (\varepsilon_i - \varepsilon_j) \rho_{ij} \langle \phi_j | \nabla \phi_i \rangle. \tag{9.13}$$

We will now consider each contribution in turn:

 \mathbf{f}_1 , the adiabatic force: This force is analogous to the one captured by the potentials used in classical MD simulations. It represents motion on a mixture of adiabatic potential energy surfaces in which the occupations are fixed in time. This force is fully conservative.

 \mathbf{f}_2 , the force due to thermal excitations: This force represents motion on a mixture of adiabatic potential energy surfaces with occupations that vary according to a time-dependent pseudo-temperature. It is conservative provided the additional variable T(t) is also taken into account. The results presented in Sect. 8.1 suggest that \mathbf{f}_2 should capture most of the effect of cumulative excitations on the electronic force. Temperature dependent classical potentials correspond to the combination $\mathbf{f}_1 + \mathbf{f}_2$

 \mathbf{f}_3 , the force due to athermal excitations: This force represents a correction to the force $\mathbf{f}_1 + \mathbf{f}_2$ required to fully capture the effect of cumulative excitations. The results of Sect. 8.1 suggest that it should be small in comparison to \mathbf{f}_2 . This force is also conservative in the sense that it does not generate excitations in the electronic system. It is conservative if the occupations $\{\rho_{ii}\}$ are taken into account.

 \mathbf{f}_4 , the non-adiabatic force: \mathbf{f}_4 is the force against which the ions do work to generate the excitations that give rise to the forces \mathbf{f}_2 and \mathbf{f}_3 (see Sect. 11.2.1 for further discussion of this point). In contrast to the other three components, it is not immediately obvious that \mathbf{f}_4 is real. Sect. 13.1.14 shows that \mathbf{f}_4 is indeed real, as required. In the adiabatic limit, \mathbf{f}_4 will tend to zero because $\hat{\rho}$ will become diagonal in the instantaneous eigenstate basis.

We can easily calculate the above components of the electronic force within our simulations provided that we have access to the instantaneous eigenstates of the electronic Hamiltonian. The *spICED* software incorporates a facility to output such force information and in the rest of this chapter we will consider the results of simulations designed to investigate the behaviour of the various components.

9.2 The Effect of Electronic Excitations on the 'Conservative' Force

As we have discussed above, we expect that the accumulation of excitations in the electronic subsystem during the course of a collision cascade will act to weaken the bonding forces between ions. It would be useful to have information on the size of this effect as a measure of the scale of one source of error in the Born–Oppenheimer approximation assumed to hold in classical molecular dynamics. Such information would also help determine the need for excitation- (or electronic temperature-) dependent potentials in classical simulations.

To address the above issues we have run a set of forty-four cascade simulations in a $9 \times 7 \times 8$ fcc unit-cell block of our tight-binding metal with periodic boundary conditions. 2 keV of kinetic energy is given to a PKA in directions distributed evenly over the irreducible 1/48th of the fcc unit cell. More details of these simulations can be found in Sect. 8.1. The *spICED* software gives us access to each of the force components \mathbf{f}_1 - \mathbf{f}_4 on a per atom basis whenever a direct diagonalization of the electronic Hamiltonian is performed. In these simulations we have obtained the force information every 10 fs over the 225 fs duration of each simulation. To help analyse the large volume of data generated in the simulations we have aggregated the information on the forces in a double histogram for each simulation and for each data output step. Every pair of ions I, J is assigned to a histogram bin according to the distance $|\mathbf{R}_{IJ}| = |\mathbf{R}_J - \mathbf{R}_I|$ and the bond order $\rho_{IJ} + \rho_{JI}$ between the atoms. Because the electronic Hamiltonian is a simple function of ion–ion separation, we can then calculate the average electronic force for each bin in the two-dimensional histogram:

$$|\mathbf{F}_{II}| = \frac{\mathrm{d}\gamma(\mathrm{R})}{\mathrm{d}R}\bigg|_{|\mathbf{R}_{II}|} (\rho_{II} + \rho_{II}),\tag{9.14}$$

where $\gamma(R)$ is the hopping integral between ions at separation R. The binning process is repeated for both the full density matrix $\hat{\rho}(t)$ and the adiabatic density matrix $\hat{\rho}^{Ad}$. This gives information about the distribution over pairs of atoms in the simulations of the forces ${}^2\mathbf{F}_e = \mathbf{f}_1 + \mathbf{f}_2 + \mathbf{f}_3 + \mathbf{f}_4$ and \mathbf{f}_1 .

Figure 9.1 illustrates the sort of information that we can extract from our double histogram data. The surface plot shows the frequency data for the histogram for the full evolved density matrix minus that for the adiabatic density matrix. It thus provides a view of the average change in bond strength at a given separation (shown in the right-hand vertical panel of Fig. 9.1) and allows us to

At the time that the simulations documented in this section were carried out, *spICED* was not able to directly output data associated with the thermal density matrix $\hat{\rho}^T$ or with the diagonal density matrix $\hat{\rho}^{\text{Diag}}$ and so these matrices had to be calculated off-line. This facility was added at a later date.

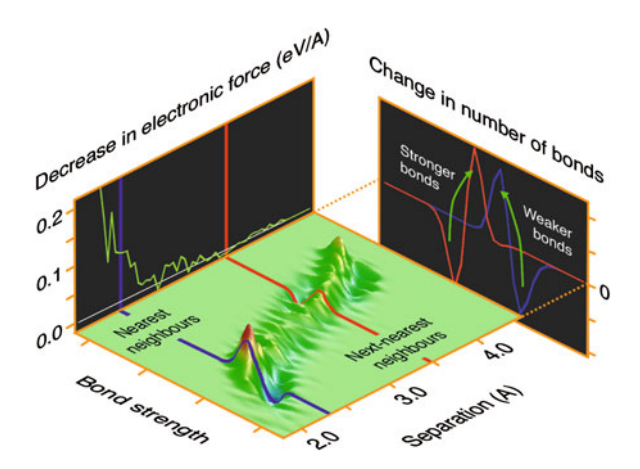


Fig. 9.1 A sample of the data resulting from the double histogram binning process discussed in the text. Each ion pair in our simulations is assigned to a bin based on the separation of the ions and the bond-order between them. The surface shows the difference in the frequencies for the histogram constructed using the full evolved density matrix and that constructed using the adiabatic density matrix constructed from the instantaneous eigenstates of the Hamiltonian. The *blue line* indicates the nearest-neighbour separation in the perfect lattice, the *red line* the next-nearest-neighbour separation. By averaging over the bond-order bins we can calculate the average change due to non-adiabatic effects in the attractive electronic force as a function of separation (rear *vertical panel*). We can also examine the shift in the bond-order distribution at a given separation (*right-hand vertical panel*)

calculate the change in the average electronic bonding force as a function of separation (the left-hand vertical panel in Fig. 9.1).

If we average our double histogram data over the bond-order bins then we can obtain the average attractive electronic force as a function of inter-ionic separation. In Fig. 9.2 we show the average excited force $\langle \mathbf{F}_e \rangle$ averaged over all the simulations at the point, towards the end of our simulations, when the irreversible energy transfer into the electrons is $\Delta E \approx 43$ eV (around 0.02 eV per electron). We also show the percentage reduction in this bonding force in comparison with the mean adiabatic force $\langle \mathbf{f}_1 \rangle$, i.e. the quantity $(\langle \mathbf{f}_1 \rangle - \langle \mathbf{F}_e \rangle)/\langle \mathbf{f}_1 \rangle$. The excitations clearly cause a weakening of the inter-ionic bonds, but the effect is only around 0.4% at this level of excitation.

In fact, Fig. 9.2 does not show the exact comparison that we require: rather we would like to exclude the non-adiabatic force $\langle \mathbf{f}_4 \rangle$ from the comparison. However, we can also obtain force data corresponding to the density matrices $\hat{\rho}^T$ and $\hat{\rho}^{\text{Diag}}$ and hence obtain the force curves for the average forces $\langle |\mathbf{f}_1 + \mathbf{f}_2| \rangle$ and $\langle |\mathbf{f}_1 + \mathbf{f}_2 + \mathbf{f}_3| \rangle$ respectively. Figure 9.3 shows the absolute contribution to the reduction in the bonding force when each additional force component \mathbf{f}_2 , \mathbf{f}_3 and \mathbf{f}_4

³ Calculation of these additional density matrices had to be performed separately at the time that this analysis was undertaken (see previous footnote).

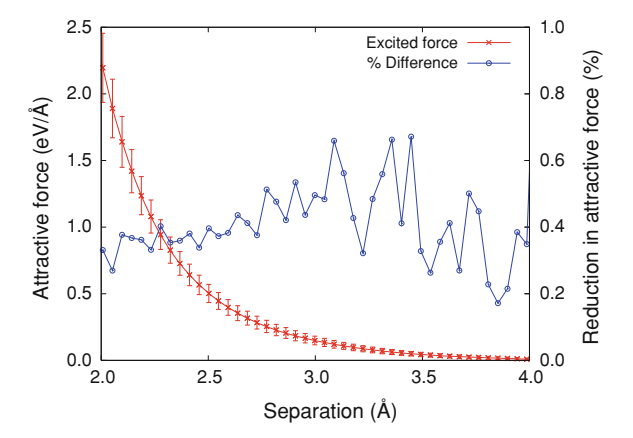


Fig. 9.2 The strength of the attractive electronic force between ion pairs as a function of the interionic separation. The data are shown for the full density matrix $\hat{\rho}$ corresponding to $\langle |\mathbf{f}_1|+\mathbf{f}_2+\mathbf{f}_3+\mathbf{f}_4| \rangle$ (crosses). The force curve for the adiabatic density operator $\hat{\rho}^{\mathrm{Ad}}$ corresponding to $\langle |\mathbf{f}_1| \rangle$ would be indistinguishable at this scale. Variations in the local atomic environments give a spread in the bond orders between ion pairs with a given separation and the error bars show the standard deviation of the corresponding spread in the force. The right-hand vertical axis shows the percentage difference between the expectations of the two forces (circles). (Reprinted figure 1 with permission from Race, C.P., Mason, D.R., Sutton, A.P.: Electronic excitations and their effect on the interionic forces in simulations of radiation damage in metals. J. Phys. Condens. Matter 21(11), 115702 (2009). Copyright (2009) by the Institute of Physics Publishing Ltd.)

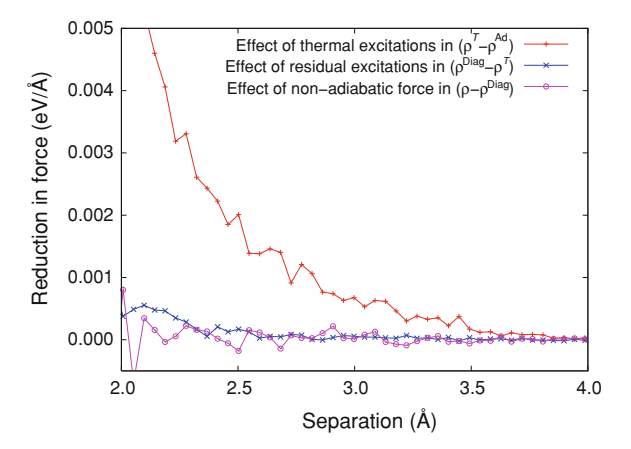


Fig. 9.3 The reduction in the mean attractive electronic force as a function of pairwise separation when various components of the electronic force are ignored: The effect of thermal excitations, $\langle |\mathbf{f}_1 + \mathbf{f}_2| \rangle - \langle |\mathbf{f}_1| \rangle$ (vertical crosses), the effect of excitations not captured by the thermal model, $\langle |\mathbf{f}_1 + \mathbf{f}_2 + \mathbf{f}_3| \rangle - \langle |\mathbf{f}_1 + \mathbf{f}_2| \rangle$ (diagonal crosses) and the effect of the non-adiabatic forces, $\langle |\mathbf{f}_1 + \mathbf{f}_2 + \mathbf{f}_3| + \mathbf{f}_4| \rangle - \langle |\mathbf{f}_1 + \mathbf{f}_2 + \mathbf{f}_3| \rangle$ (circles). (Reprinted figure 4 with permission from Race, C.P., Mason, D.R., Sutton, A.P.: Electronic excitations and their effect on the interionic forces in simulations of radiation damage in metals. J. Phys. Condens. Matter **21**(11), 115702 (2009). Copyright (2009) by the Institute of Physics Publishing Ltd.)

is taken into account. It is clear that the reduction in force is dominated by the effect of the changing occupation of the instantaneous eigenstates. The non-adiabatic forces make very little contribution and, in fact, the thermal model for the electronic excitations is so good that the residual excitations in $\hat{\rho}^{\text{Diag}} - \hat{\rho}^T$ also have little further effect on the average bonding force.

We need to be careful in interpreting the small effect of the non-adiabatic force \mathbf{f}_4 on the bonding forces. In fact this force has a similar magnitude to the force \mathbf{f}_2 that dominates the reduction in bonding. However, unlike \mathbf{f}_2 , the direction of \mathbf{f}_4 has no strong correlation with the direction of the bonds and so has a reduced effect in the aggregate averages presented above.

Whilst the reduction in the bonding forces observed in our simulations and plotted in Fig. 9.2 is only small, we should bear in mind that the 2 keV PKA energy in our cascade simulations is relatively small. Because of the computational complexity of Ehrenfest dynamics it is not possible to undertake large numbers of simulations in the larger simulation cells required to contain more energetic cascades. However, because a thermal model for the electronic excitations captures the majority of their effect on the bonding forces we can explore the higher degrees of excitation by simply elevating the electronic temperature in our system. We have adopted three methods of extrapolating our results to higher excitation energies:

- 1. We have taken the atomic positions from the end of our 2 keV cascade simulations and generated force histograms corresponding to density matrices with a range of elevated temperatures. For these calculations the simulations have simply served as a means of generating a representative set of distorted atomic configurations. Figure 9.4a and b shows the effect of elevated electronic temperature on the average forces between ions at two typical inter-atomic separations.
- 2. By extracting information from our tight-binding model of the bond-orders between nearest and next-nearest neighbours in a perfect fcc lattice as a

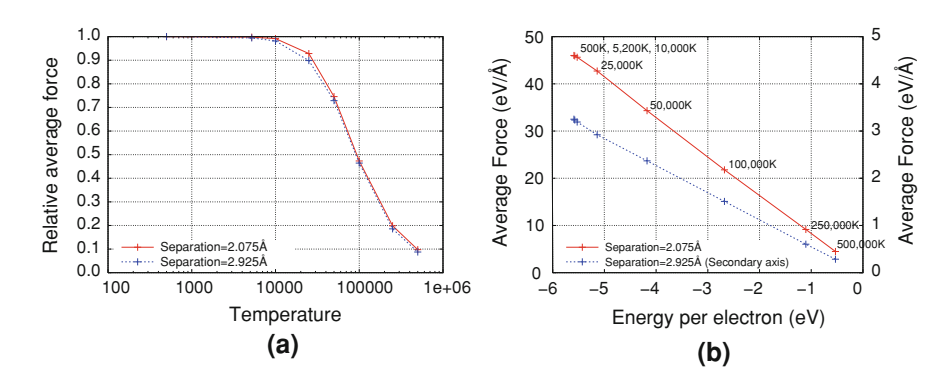


Fig. 9.4 The effect of increasing the electronic temperature on the average attractive force between ions in a lattice distorted by the evolution of a cascade. The forces are shown at two representative inter-ionic separations. **a** The relative strength of the attractive force shown as a function of electronic temperature. **b** The absolute size of the attractive force shown as a function of the electronic energy per electron

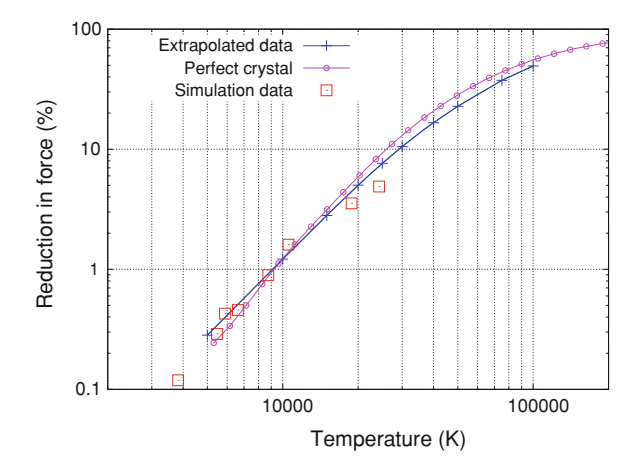


Fig. 9.5 The results of three methods of extrapolation of the effect of electronic excitation on the attractive electronic force: (1) Imposing the electronic temperature on ionic configurations taken from our 2 keV simulations (*crosses*). (2) Calculations from data for the effect of electronic temperature on the bond orders in a perfect crystal (*circles*). (3) Results from higher energy cascade simulations up to 50 keV (*boxes*). (Reprinted figure 5 with permission from Race, C.P., Mason, D.R., Sutton, A.P.: Electronic excitations and their effect on the interionic forces in simulations of radiation damage in metals. J. Phys. Condens. Matter **21**(11), 115702 (2009). Copyright (2009) by the Institute of Physics Publishing Ltd.)

function of electronic temperature we can calculate the corresponding percentage reduction in force.

3. We have run further sets of cascade simulations in 2016 atom simulation cells at PKA energies of 1, 5, 10, 20 and 50 keV. Although the higher energy cascades will rapidly cross the simulation cell boundaries, they provide a means of injecting larger amounts of energy into the electronic system within a dynamically distorted ionic system. By fitting temperatures to the resulting excited eigenvalue occupation spectra and calculating the average forces from our double histogram output we obtain a third measure of the reduction in attractive electronic force as a function of electronic temperature.

The results of these various approaches to extrapolating our data are combined in Fig. 9.5 and all tell a similar story. They suggest significant reduction of order 10% in the strength of the attractive electronic force for electronic temperatures above 3×10^4 K.

9.2.1 The Importance of the Reduction in the Attractive Electronic Force

The practical importance of the results presented above depends on the sorts of electronic temperatures likely to be generated in real radiation damage events.

Real events will involve higher PKA energies, but they will also take place in open systems, in contrast to our small, closed simulation cells.

The model of Duffy et al. [4, 6] makes predictions about the evolution of the spatial distribution of the electronic temperature in collision cascades. They find [6] maximum electronic temperatures of up to 7000 K in 10 keV collision cascades in iron, although their results are highly sensitive to the choice of value for the electron-phonon coupling (something very much open to debate as we saw in Sect. 3.3.4). At these temperatures, reductions in bonding forces of $\sim 0.5\%$ are possible.

9.2.1.1 The Effective Strain Due to Electronic Heating

We have seen that the effect of a collision cascade is to heat the electrons in the cascade region and that this heating can lead to significantly weakened bonds. In turn, the weakened bonds will imply an increase in the equilibrium lattice constant for the material in the electronically hot region. However, because the surrounding material will prevent the expansion of this region, it will be placed under an effective strain. Because the electronic thermal conductivity is relatively high, the region in which the electrons are heated will generally extend significantly beyond the borders of the ionic disruption caused by the cascade. We therefore suggest that a reasonable model for the effect of electronic heating would be a strained spherical inclusion within the surrounding material. This spherical inclusion will exert an outward pressure on its host medium. Whilst this pressure will be relatively short lived, it may persist for long enough to cause an outward propagating elastic wave, which might then influence the evolution of the pre-existing defect distribution in the material surrounding a cascade. In this section we will briefly present some preliminary calculations designed to investigate the above phenomenon.

We must begin by estimating the effective strain of an electronically hot inclusion. By extracting data from *spICED* for a perfect lattice at a range of electronic temperatures we can obtain the nearest- and next-nearest-neighbour bond-orders as a function of electronic temperature. A cubic spline fit to these data is shown in Fig. 9.6. The decrease in bond-orders with increasing temperature implies an increase in the equilibrium lattice parameter. Within our tight-binding model we can find the new equilibrium lattice parameter by minimising the binding energy per atom given by Eq. 5.10

$$\frac{E_{\rm B}}{N_{\rm a}} = \frac{\epsilon}{2} \sum_{J \neq I} \left(\frac{a_{\rm f}}{|\mathbf{R}_{IJ}|} \right)^p - \epsilon c \sum_{J \neq I} \rho_{IJ} \left(\frac{a_{\rm f}}{|\vec{R}_{IJ}|} \right)^q, \tag{5.10}$$

with decreased bond-orders. This task is made more difficult because at finite electronic temperature the bond-orders also vary with lattice constant. However, because of the power-law scaling of the hopping integrals in our model, we can exploit an exact equivalence between the effects of volume and electronic temperature changes to obtain a minimization condition that is a simple function of the bond order variations with temperature.

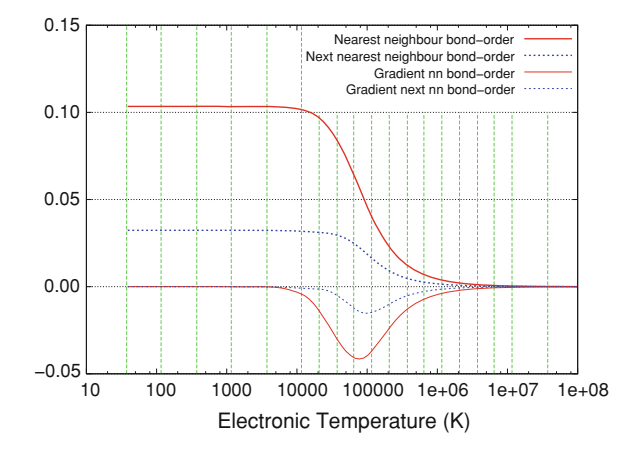
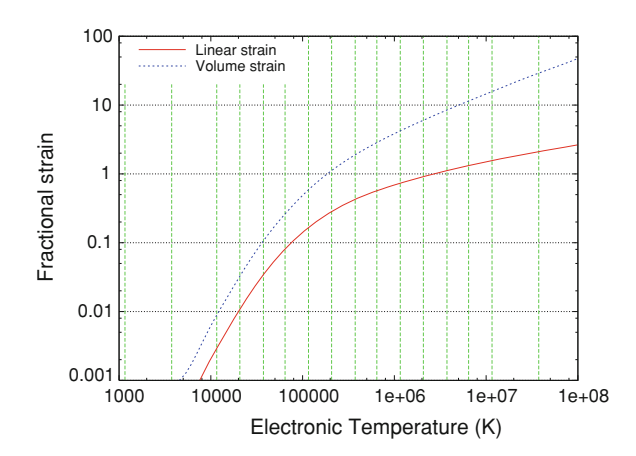


Fig. 9.6 The variation with electronic temperature of the ground state bond-orders in our tight-binding model. Data were obtained at the temperatures indicated by the *green lines* and the *solid red* and *blue lines* show the results of a cubic spline fit to these data

Fig. 9.7 The temperature dependence of the effective volume strain on a heated region of our tight-binding model calculated using the method described in Sect. 13.5



Details of the analysis are given in Sect. 13.5 and the effect of electronic heating on the implied strain is shown in Fig. 9.7. Electronic temperatures of 10000 K, then, imply volume strains of $\sim 1\%$ on the heated region. Such strains could have a significant effect on the evolution of the damage distribution if they persist for long enough to give rise to an outward propagating elastic wave.

9.2.2 Replacement Collision Sequences

Having established that the accumulation of electronic excitations generated by a cascade can cause significant weakening of the bonding forces between ions we will now examine how these changes affect cascade evolution. A key mechanism

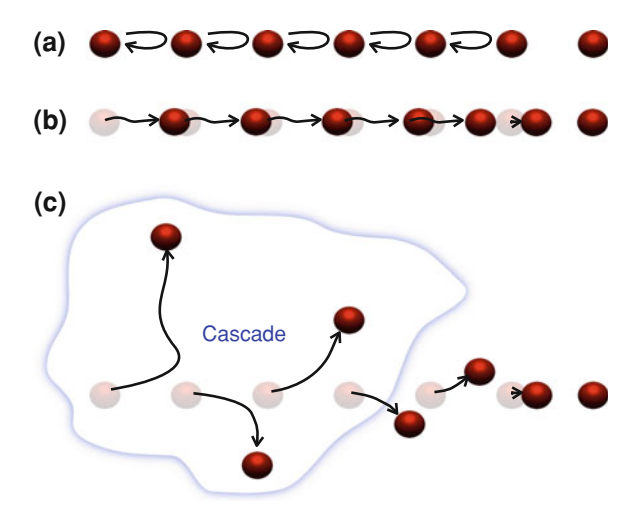


Fig. 9.8 A schematic representation of the different modes of behaviour exhibited when the kinetic energy of an ion is directed along a close-packed row in the crystal lattice. At the lowest energies a phonon propagates along the *row* and each atom returns to its equilibrium position. At higher energies it is possible for each atom to displace the next in the row and replace it at its lattice site: an RCS forms. At higher energies still, small misalignments due to thermal vibration of the ions prevent an RCS from forming and a collision cascade forms. If sufficient energy is dissipated by this cascade an RCS may then emerge along a close-packed row leading out of the cascade region

of damage creation is the replacement collision sequence (RCS) introduced in Sect. 2.2. A sequence of collisions proceeding along a close-packed line of ions in a lattice is able to carry a resulting interstitial atom a long way from the corresponding vacancy, increasing the probability that the defects will fail to annihilate and will form part of the residual damage distribution.

The phenomenon of replacement collision sequences has been extensively explored via classical simulations [7, 8] and it is well established that there is an upper kinetic energy threshold, beyond which a replacement collision sequence will not form and a lower threshold, below which a phonon-like behaviour is observed. Three modes of behaviour are shown schematically in Fig. 9.8 and can be observed in our simulation data in Fig. 9.9. The lattice temperature has a strong effect on the stability of an RCS: at elevated temperatures the ions are not generally well aligned, making it more difficult for an RCS to progress.

We have investigated the effect of *electronic* temperature on the formation of replacement collision sequences. This is something that cannot be established using classical simulations and will be a useful test of the importance of accumulated electronic excitations in affecting the ionic dynamics in collision cascades. We have run 1029 separate simulations of replacement collision sequences in which a PKA is given kinetic energy ranging from 10 to 100 eV in a [9] close-packed direction. The simulations take place in a 1120 atom lattice of our model metal with periodic

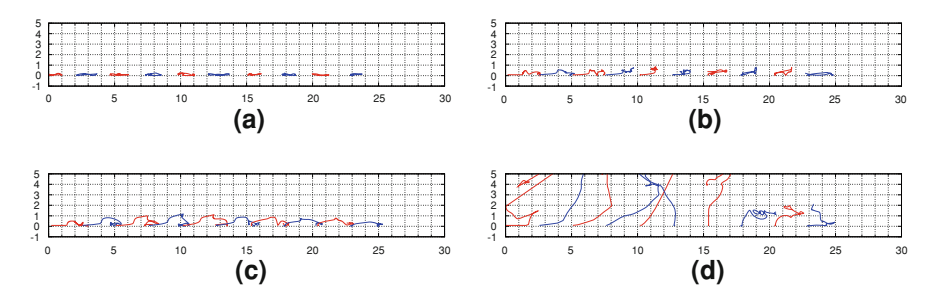


Fig. 9.9 Sample data showing the paths taken by ten ions along a close-packed row during the course of an RCS simulation. The PKA is at the *left* and the *horizontal axis* shows the position of the ions parallel to the close-packed direction. The *vertical axis* indicates the distance of the ions from the close-packed line in a perpendicular direction. Data for four different PKA energies are shown. **a** At 10 eV all the ions return to their original lattice sites. No RCS is initiated and a phonon can be seen propagating along the close-packed row. **b** At 50 eV the first four ions move on to the next lattice site in the row as part of an RCS. After this, sufficient kinetic energy has been dissipated and the energy transferred to the fifth ion is below the displacement threshold energy. The remaining atoms take part in a phonon-like behaviour, returning to their original lattice sites. **c** At 100 eV there is sufficient energy to continue the RCS for the full length of the ten ion row. **d** At 2000 eV an RCS cannot form and the PKA initiates a small collision cascade. However, once the majority of the initial kinetic energy has been redistributed an RCS or a phonon can be seen emerging towards the end of the close-packed row

boundary conditions, with a lattice temperature of 300 K established via 1 ps of classical molecular dynamics and 100 fs of thermalized Ehrenfest dynamics as described in Sect. 7.1.1. The electronic temperature of the simulations is chosen to be one of the values 1×10^3 , 10×10^3 , 20×10^3 , 50×10^3 and 100×10^3 K. The simulations are run for between 300 and 500 fs depending on the PKA energy

To characterise the behaviour of the RCS in each simulation we classify each of ten atoms along a close-packed line, including the PKA, as having either returned to their lattice site, moved to the next lattice site along the line or left the close-packed row entirely by the end of the simulation. An ion is associated with a particular site along the close-packed row if it lies within half the close-packed separation (1.27 Å in copper). Figures 9.10 and 9.11 show the percentage of the ten ions in the close-packed row included in the RCS at each energy for each electronic temperature.

From Figs. 9.10 and 9.11 we can see that the displacement threshold energy for our model metal lies somewhere between 20 and 30 eV. For PKA energies below this threshold the PKA always returns to its original lattice site and no RCS is initiated. As the PKA energy is increased, the replacement collision sequences lengthen, apparently reaching a plateau by 80 eV. As for the question that the simulations are designed to address, whether the electronic excitations have a significant effect on RCS behaviour, we can see that only at very high electronic temperatures is the length of the RCS affected.

As the electronic temperature is increased the attractive bonding forces are weakened and the repulsive inter-ionic forces become more significant.

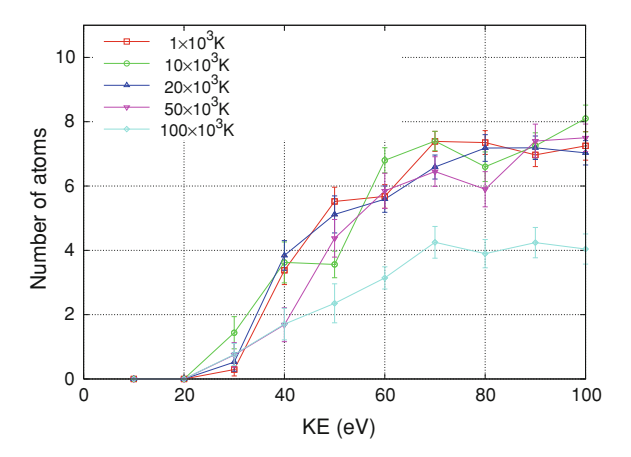


Fig. 9.10 The number of ions displaced to the next lattice site along a close-packed row of 10 atoms as a function of PKA energy in simulations of replacement collision sequences. Data are presented for a variety of electronic temperatures. The data points indicate mean averages taken across all simulations (approximately 20 for each point) at a given energy and temperature. The *error bars* indicate the standard error in this estimate of the mean. The *lines* are to guide the eye. In effect, the figure shows the average length of the RCS as a function of energy and temperature

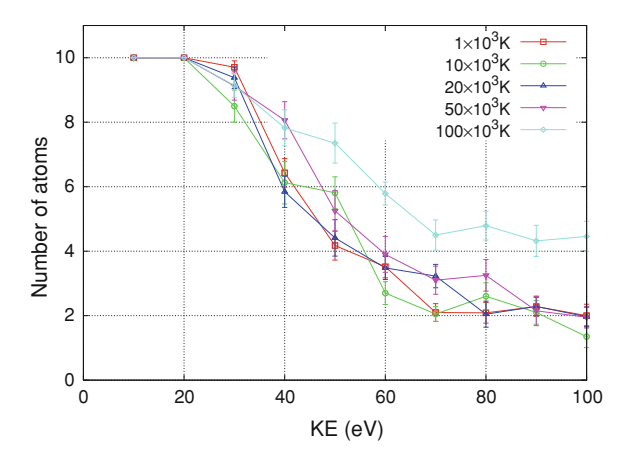


Fig. 9.11 The number of ions returning to their original lattice site along a close-packed row of 10 atoms as a function of PKA energy in simulations of replacement collision sequences. Data are presented for a variety of electronic temperatures. The data points indicate mean averages taken across all simulations (approximately 20 for each point) at a given energy and temperature. The *error bars* indicate the standard error in this estimate of the mean. The *lines* are to guide the eye

This makes the inter-ionic collisions 'harder' and the replacement collision sequences are more likely to be broken. We can just discern the onset of this effect at 50×10^3 K and by 100×10^3 K it significantly reduces RCS length. These temperatures are ludicrously high; way beyond anything likely to be seen in a collision cascade, and so we can reasonably conclude that our results

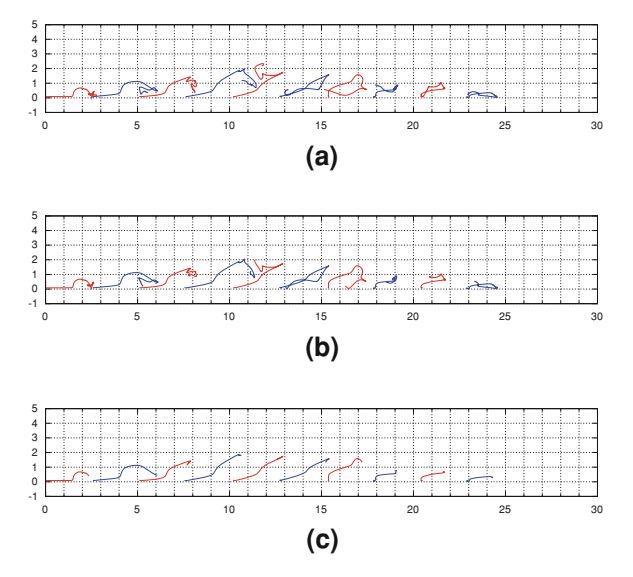


Fig. 9.12 A plot of the ion paths in an RCS with a PKA energy of 200 eV. The data are plotted as described in Fig. 9.9. The different plots show simulations with equivalent starting conditions but different values for the ion masses: **a** Normal ion mass. **b** Ten times normal ion mass. **c** One hundred times normal ion mass

indicate that accumulated excitations should not significantly affect RCS length. Certainly the electronic temperature is a much less significant factor than the ionic temperature.

9.2.2.1 Does the Non-adiabatic Force Have an Effect on RCS Dynamics?

We might also consider the other potential effect of electronic excitations on RCS dynamics: does the non-adiabatic force \mathbf{f}_4 (defined in Eq. 9.13), which arises because of the finite response time of the electrons to changes in the electronic Hamiltonian, affect the evolution of a replacement collision sequence? We do not expect it to do so, because an RCS is an inherently low speed phenomenon, which will not form much above 100 eV in typical metals. We have confirmed this expectation using the method outlined in Sect. 7.2.3 and running equivalent simulations with increased ionic mass to slow down the development of the cascade and eliminate most of whatever non-adiabatic force is present. The results of such simulations are shown in Figs. 9.12 and 9.13 where we show the evolving position of the tenth atom in a replacement collision sequence. We can see that $|\mathbf{f}_4|$ must be very small indeed for the ion dynamics at different ion masses to mirror one another so closely even at the end of the simulation. In Chaps. 10 and 11 we discuss some work in which the non-adiabatic force does play an important role.

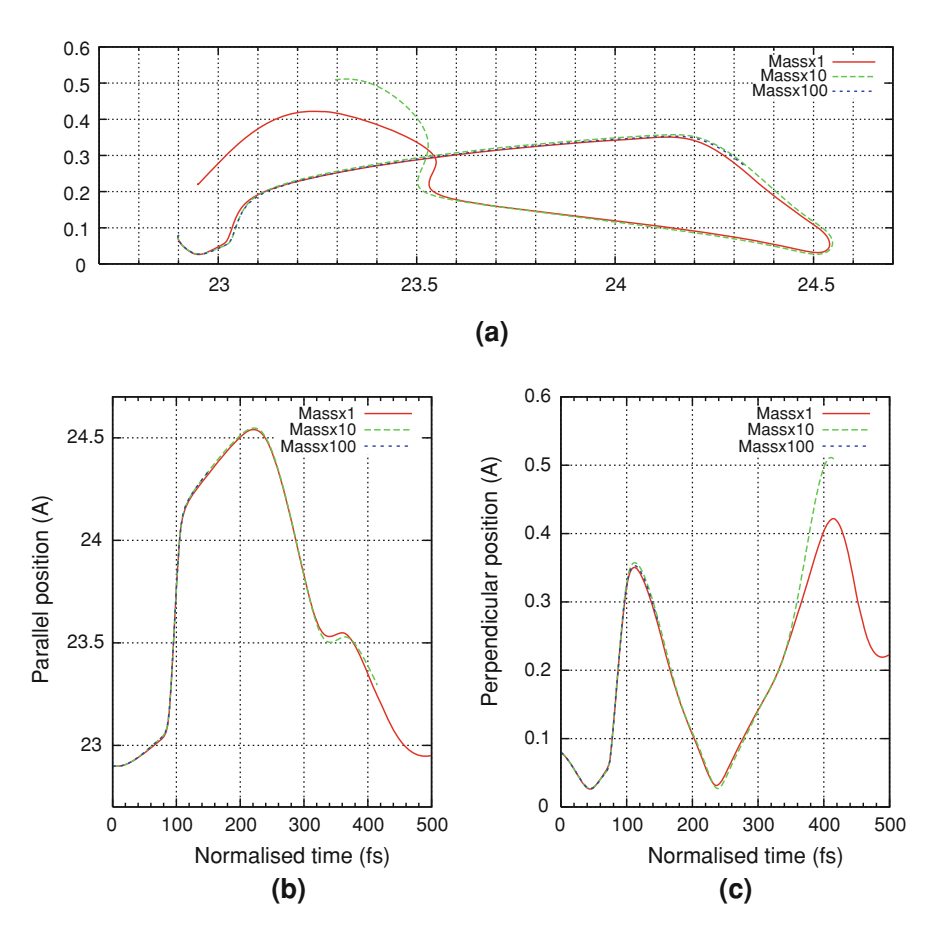


Fig. 9.13 Detail of the evolution of the position of the tenth ion in the RCS shown in Fig. 9.12: **a** The ion path. **b** The ion position parallel to the close-packed RCS direction. **c** The ion position perpendicular to the close-packed direction

9.3 Conclusions

In this chapter we began a detailed analysis of the electronic forces on ions in collision cascades that we will conclude in Chap. 11. We analysed the electronic (Hellmann–Feynman) force in the basis of instantaneous eigenstates of the electronic Hamiltonian and split the force into four components (Sect. 9.1). We then focussed our attention on the bond-weakening effects of accumulating electronic excitations on the conservative forces on the ions (Sect. 9.2). At levels of electronic excitation corresponding to temperatures of $\sim 10000~\rm K$ there was significant weakening of these forces ($\sim 1\%$) and a thermal model of these excitations was able to capture 95% of this weakening. Calculations of the effective volume strain in our tight-binding model as a function of electronic excitation suggest significant

9.3 Conclusions 187

strains, perhaps high enough to influence defect dynamics (Sect. 9.2.1.1). Simulations of replacement collision sequences at a range of electronic temperatures suggest that their lengths should not be significantly reduced at temperatures below $\sim 50000 \text{ K}$ (Sect. 9.2.2).

References

- 1. Gao, F., Bacon, D.J., Flewitt, P.E.J., Lewis, T.A.: The effects of electron-phonon coupling on defect production by displacement cascades in α -iron. Model. Simul. Mater. Sci. Eng. $\mathbf{6}(5)$, 543–556 (1998)
- Nordlund, K., Wei, L., Zhong, Y., Averback, R.S.: Role of electron-phonon coupling on collision cascade development in Ni, Pd, and Pt. Phys. Rev. B 57(22), R13965–R13968 (1998)
- Caro, A., Victoria, M.: Ion-electron interaction in molecular-dynamics cascades. Phys. Rev. A 40(5), 2287–2291 (1989)
- 4. Duffy, D.M., Rutherford, A.M.: Including the effects of electronic stopping and electron-ion interactions in radiation damage simulations. J. Phys.: Condens. Matter 19(1), 016207 (2007)
- 5. Tully, J.C.: Molecular dynamics with electronic transitions. J. Chem. Phys. **93**(2), 1061–1071 (1990)
- Rutherford, A.M., Duffy, D.M.: The effect of electron-ion interactions on radiation damage simulations. J. Phys.: Condens. Matter 19(49), 496201 (2007)
- Becquart, C.S., Souidi, A., Hou, M.: Replacement collision and focuson sequences revisited by full molecular dynamics and its binary collision approximation. Philos. Mag. 85(4), 409– 415 (2005)
- Foreman, A.J.E., English, C.A., Phythian, W.J.: Molecular dynamics calculations of displacement threshold energies and replacement collision sequences in copper using a many-body potential. Philos. Mag. A 66(5), 655–669 (1992)
- Duvenbeck, A., Sroubek, Z., Wucher, A.: Electronic excitation in atomic collision cascades. Nucl. Instrum. Methods Phys. Res. Sect. B 228(1-4), 325-329 (2005)
- Race, C.P., Mason, D.R., Sutton, A.P.: Electronic excitations and their effect on the interionic forces in simulations of radiation damage in metals. J. Phys.: Condens. Matter 21(11), 115702 (2009)

Chapter 10 Channelling Ions

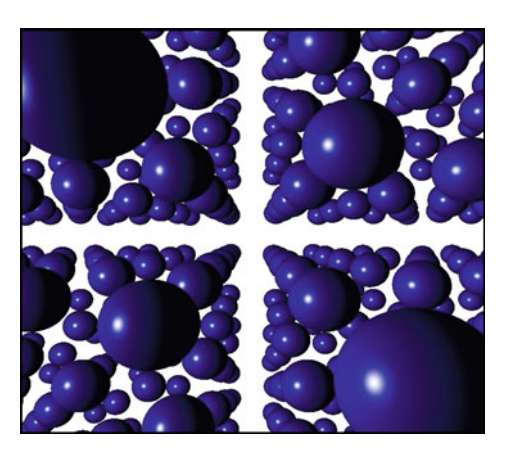
Summary: In this chapter we examine the results of simulations of ion channelling at kinetic energies of up to 1.3 MeV in our tight-binding model metal. Our explicit treatment of both the ionic positions and of the electronic system allows new features to emerge that are not predicted by simpler models employing a spatially invariant stopping medium. So, whilst we find that at velocities of less than 6 Å fs^{-1} the stopping power is proportional to velocity, we also find a suppression of the stopping power at higher speeds. This suppression is significant and becomes very large when high values of the on-site charge self consistency parameter U are employed. We also find a resonant enhancement of the steady state average charge on the channelling ion over a well-defined range of velocities. We explain all of our results within a tight-binding picture of bonds between neighbouring atoms and using perturbation theory analysis.

Attribution: The large scale simulations of ion channelling used to map out the stopping power and charge behaviour were performed by D. R. Mason.

The simulations that we have discussed so far in this thesis have all been confined to relatively low energies. The computational complexity of our simulation method is the key reason behind this: higher energy processes would tend to need a large simulation cell and a smaller time-step and would quickly get beyond the reach of our resources. However, the phenomenon of ion channelling (see Sect. 2.1) *does* lend itself to smaller scale simulations. A swift ion passing down an open channel in a crystalline material (see Fig. 10.1) loses very little energy to the surrounding ions and so there is little disruption of the simulation cell. This means that not only can the cell be kept relatively small, but also the evolution of the ionic system retains a high symmetry, reducing the need to gather statistical results by running multiple simulations with similar initial conditions.

In this chapter we will describe some results of Ehrenfest dynamics simulations of the channelling of ions in our model metal with energies of up to 1.3 MeV. The key quantities of interest are the steady state charge and stopping power of the

Fig. 10.1 A schematic illustration of a [100] channel in a face-centred cubic lattice



channelling ion. We will see that both quantities display an unexpected resonant behaviour and we will explain this behaviour using time-dependent perturbation theory.

10.1 Semi-Classical Simulations of Ion Channelling

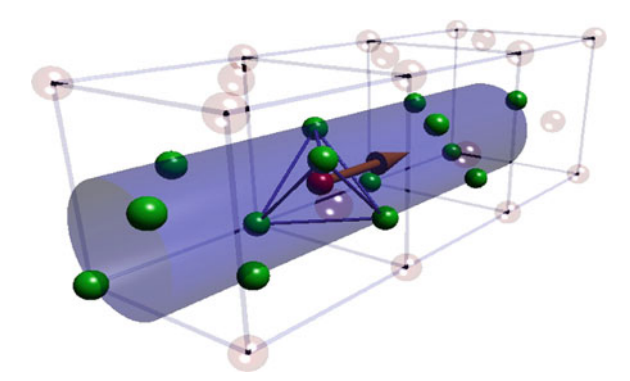
10.1.1 The Simulation Set-Up

Our simulations were performed in a $7 \times 9 \times 32$ unit cell block (8064 atoms with periodic boundary conditions) of our tight-binding model metal with all the ions held rigidly fixed at their perfect fcc lattice sites. An additional ion was introduced at a tetrahedral interstitial site (no relaxation of the surrounding ions was permitted) and given some initial kinetic energy in the long [100] direction. This initial set-up is illustrated in Fig. 10.2. Simulations were performed at kinetic energies from 1 keV up to 1334 keV. The ions were held fixed to simplify the cascade dynamics so that our chosen output variables could be more easily calculated; there would have been no great increase in computational cost if we had allowed all the ions to move. The approximation of a fixed lattice is physically reasonable (certainly at the higher velocities) because the fast ion interacts only fleetingly with the ions forming the channel wall and so imparts only a small impulse to them.

At the high velocities used in our channelling simulations, it becomes possible for ions to come into unusually close proximity with one another and so the possibility of large charge transfers arises. To improve the modelling of such charge transfers, the charge self-consistent form of our tight-binding model

¹ These simulations were carried out by D. R. Mason. Some smaller scale channelling simulations, discussed later, were carried out by the present author.

Fig. 10.2 A schematic illustration of the fcc lattice in the vicinity of a [100] ion channel. The channelling ion is shown (in *red*) with its velocity indicated by an (*orange*) *arrow*. A cage of four atoms around a tetrahedral interstitial site is also indicated



(see Sect. 5.1) was used in these simulations. In this model the basic electronic Hamiltonian (5.1),

$$\hat{H} = \sum_{IJ} |\mathbf{R}_I\rangle \gamma(|\mathbf{R}_{IJ}|)\langle \mathbf{R}_J|, \qquad (10.1)$$

is augmented with charge self-consistent terms (5.7),

$$\hat{H}^{SC} = \hat{H} + \sum_{I} |\mathbf{R}_{I}\rangle \left(Uq_{I} + \sum_{J} z_{IJ}q_{J}\right) \langle \mathbf{R}_{I}|,$$
 (10.2)

where,

$$z_{IJ} = \frac{e^2}{4\pi\epsilon_0} \left(|\mathbf{R}_{IJ}|^2 + \left[\frac{e^2}{4\pi\epsilon_0 V} \right]^2 \right)^{-1/2}, \tag{10.3}$$

As we will see when we examine the simulation results, such terms can have a significant effect on the system behaviour. The electronic density matrix was constructed with an initial electronic temperature of $T_{\rm e}=1000~{\rm K},$

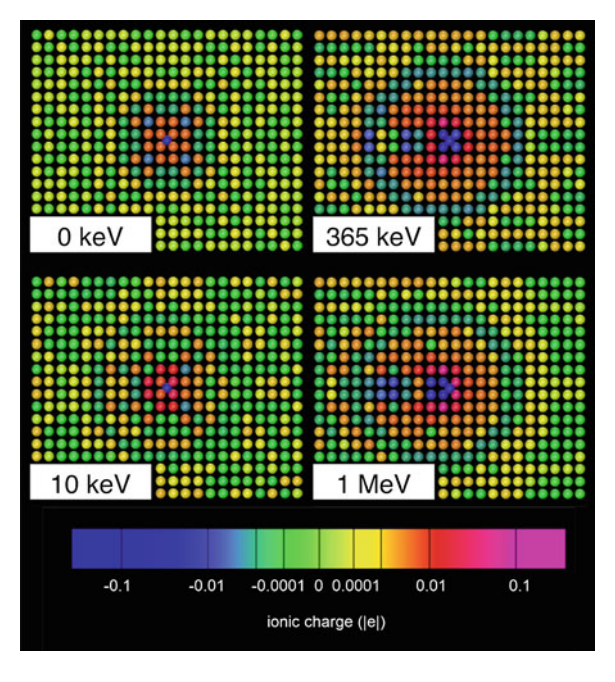
$$\hat{\rho} = \sum_{i} |\phi_{i}\rangle f(\varepsilon_{i}; T_{e}, \mu)\langle \phi_{i}|, \qquad (10.4)$$

where $\{|\phi_i\rangle\}$ are the eigenstates of the initial self-consistent Hamiltonian.

10.1.2 The Evolution of a Channelling Simulation

At the beginning of the simulations the channelling ion (effectively an unrelaxed tetrahedral interstitial defect) has a significant negative charge. This is because the bonds between the channelling ion and its nearest neighbours are unusually short. These short bonds, and their unusually large hopping integrals, give rise to a low energy bonding state, highly localized on the channelling ion. Occupation of this bonding state leads to an excess of electronic charge on the channelling ion.

Fig. 10.3 Snapshots of the ionic charge distribution in the steady state for channelling ions at a sample of kinetic energies. The various features of the plots are discussed in the main text (image created by D. R. Mason)



As the projectile ion moves down the channel, its charge, the electronic energy and the electrostatic energy all oscillate with the frequency at which the ion passes between equivalent lattice positions. Over the first 4-6 fs of a simulation transient behaviour is observed, but after this period a steady state emerges. The charge on the ion continues to oscillate, but it does so about a well-defined mean value. The rate of energy loss with distance (the stopping power) also stabilizes to a steady average. Figure 10.3 shows the distribution of electronic charge in the steady state at a sample of ion velocities. The negative charge on the channelling ion is clearly visible in all cases, as is a sphere of compensating positively charged ions surrounding it (a screening effect). At higher ion velocities we can see the finite response time of the electronic system manifest in a lagging of this screening cloud, which is now centred some way behind the projectile. This response is analogous to the stopping mechanism in the Lindhard dielectric stopping theory of slow particles (see Sect. 3.2.5.2) and we shall return to this point later. At the highest velocities a streak of negative charge can be seen behind the channelling ion; the localized charge is unable to "keep up" with the ion and slowly decaying localized states are left behind.

10.1.3 Challenges in Simulating Ion Channelling

Ehrenfest simulations of ion channelling represent a considerable challenge. In order to get well-converged results it is necessary to use simulation cells no smaller than those employed in the simulations described above. Lateral

dimensions of around 8 unit cells are needed to give good convergence of the Hartree energy of the system. The long dimension is dictated by the need to achieve a steady state behaviour before the ion crosses the boundary of the periodic simulation cell. This requirement is not an obvious one: with all the other atoms held fixed, why not allow the channelling ion to pass back through the same region of lattice? One might think that the relevant time-scale for the interaction of the channelling ion with its own past effects would be set by the time taken for a disturbance in the electronic system to travel the width of the cell. However, such disturbances do not seem to have a significant effect on the stability of our results. What matters more are the slowly decaying states shed by the fastest channelling ions; when such ions are allowed to wrap around the periodic boundaries they experience significant disruption due to these larger disturbances in their own wake.

This need for a large simulation cell places a severe restriction on the sophistication of the electronic model that can be used. Anything much more complicated than the simple single *s*-band tight-binding model employed here could put well-converged channelling simulations beyond reach. A more realistic model, from the point of view of accuracy of electronic structure, could be achieved in a time-dependent density functional theory approach. Pruneda et al. [1] have carried out TD-DFT simulations of ion channelling in the insulator LiF. They were restricted to 100 atom cells by the computational complexity of their method and so their channelling ion wraps the simulation cell boundary multiple times. Whether this wrapping has any adverse effect on their results is difficult to tell because their simulation cell is so small that the stopping power that they measure is not converged with cell size within the range of sizes they were able to simulate. We have discussed these results in more detail in Sect. 3.5.

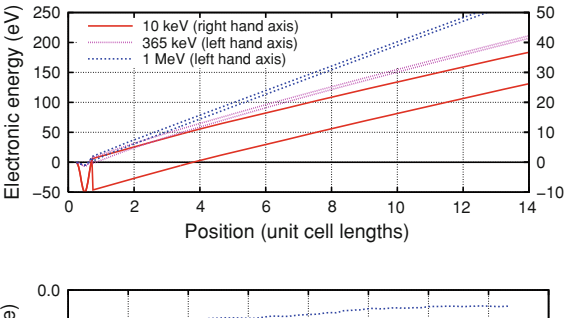
Because calculation of the instantaneous energy eigenstates requires direct diagonalization of the electronic Hamiltonian, which is prohibitively time consuming for simulation cells as large as ours at the best of times and made considerably more so by the effects of charge self-consistency, it would in general be difficult to monitor the irreversible energy transfer from the channelling ions to the electronic system. However, because we hold all the other ions fixed, the ionic configuration is strictly periodic in time and so the adiabatic electronic density matrix will be so also. Hence, by monitoring the *total* electronic energy or, alternatively, the ionic kinetic energy, at equivalent points along the channelling path, we can easily determine the non-adiabatic energy transfer.

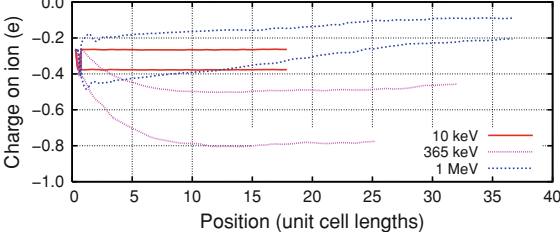
10.2 Steady State Charge

10.2.1 Results for a Non-Self-Consistent Model

In this section we will present the results of our channelling simulations. Before we do so, it is worth considering how these results have been extracted. Simulation data are output at regular, but discrete, intervals and, since our calculations rely on

Fig. 10.4 Examples of the envelopes of spline fits to the variation in energy and charge of a channelling ion with position. Sample data are shown at three representative kinetic energies (data fitted by D. R. Mason)





using the periodicity in the ionic configuration, we must be able to compare values in equivalent atomic environments. To facilitate this the raw data were spline fitted to extract the envelopes of the periodic variation in our variables of interest. From these fits, the amplitudes of oscillation and mean values of the variables are determined. Figure 10.4 shows examples of the data and the fitted envelopes.

Figure 10.5 shows the variation of the steady state charge on the channelling ion as a function of the initial velocity for a non-self-consistent electronic Hamiltonian (we will consider the effect of the self-consistent terms later, but the results show similar behaviour to the non-self-consistent case). At low velocities the electronic charge remains close to its value in the stationary unrelaxed tetrahedral interstitial case. At high velocities electrons are shed by the ion: they are unable to keep up with the ion and so are stripped away with increasing velocity. At intermediate velocities we see an unexpected feature. With relatively rapid onset, which looks much like a resonance, the negative electronic charge experiences a significant enhancement. It is this feature that we now seek to explain.

Our explanation begins with the local density of states on the channelling ion. The full density of states is defined,

$$D(\varepsilon) = \frac{1}{N_{\rm a}} \sum_{i} \delta(\varepsilon - \varepsilon_i), \tag{10.5}$$

for a system with eigenstates $\{|\phi_i\rangle\}$ of energy $\{\varepsilon_i\}$. Then, if $|\alpha_c\rangle$ is the tight-binding orbital on our channelling ion, we can write the local density of states as,

² This fitting and data extraction was carried out by D. R. Mason.

Fig. 10.5 The mean steady state charge on a channelling ion as a function of its initial velocity (data provided by D. R. Mason)

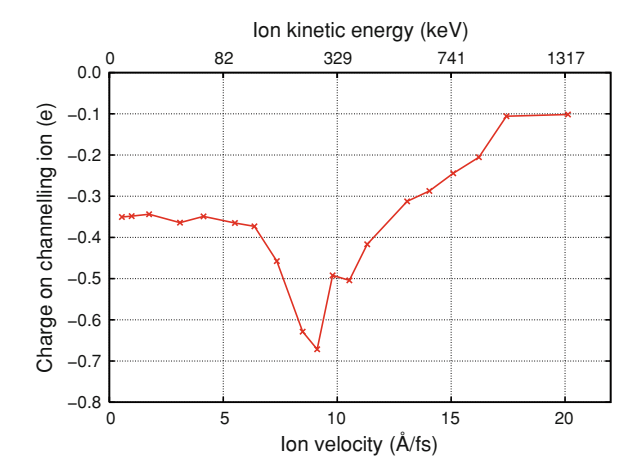
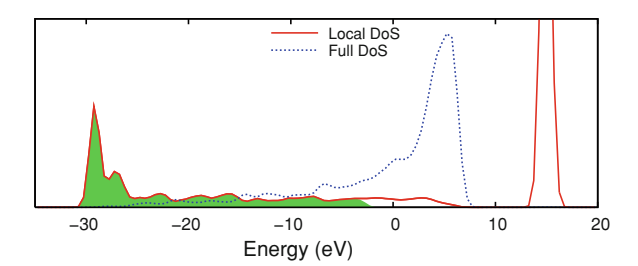


Fig. 10.6 The full density of states for our perfect lattice plus channelling ion and the local density of states on the channelling ion when at a tetrahedral interstitial position

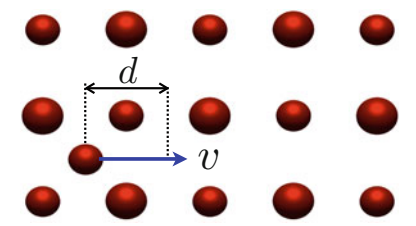


$$D_{\alpha_c}(\varepsilon) = \sum_i |\langle \alpha_c | \phi_i \rangle|^2 \delta(\varepsilon - \varepsilon_i). \tag{10.6}$$

Figure 10.6 shows a histogram of the local density of states on the channelling ion (at a tetrahedral interstitial position) along with the full density of states for comparison. There are several key features to consider in the local density of states. First, there is a group of low energy states at the bottom of the band with a large projection onto the channelling ion. These are the bonding states that we mentioned earlier and whose occupation accounts for the negative charge on the channelling ion whilst stationary at an interstitial position. Second, at high energy, above the top of the bulk density of states, there is a single excited state, highly localized on the channelling ion (in Fig. 10.6 this state is broadened into a peak by the Gaussian binning process used to construct the histogram). This state is antibonding in character and is initially unoccupied.

The form of the local density of states on the channelling ion provides us with everything we need to explain the resonance feature in Fig. 10.5. We begin by considering the effect of the motion of the channelling ion on the electronic Hamiltonian. We can regard this as providing a periodic perturbation to the electronic system whose dominant frequency will be determined by the rate at which the ion moves between equivalent positions in the lattice. If the distance

Fig. 10.7 A schematic illustration of how the channelling velocity v and the periodicity of the lattice determine the dominant frequency Ω_v in the perturbation due to the channelling ion



separating such points is d = 1.805 Å as shown in Fig. 10.7 and the ion moves with speed v, then this dominant frequency will be,

$$\Omega_{\nu} = \frac{2\pi\nu}{d}.\tag{10.7}$$

The effect of the perturbation will be to stimulate electron-hole excitations in the electronic system of corresponding energy $\hbar\Omega_{\nu}$. At low channelling velocities, only transitions close to the Fermi level will be stimulated. Such transitions are between occupied and unoccupied states with similar (relatively low) projections onto the channelling ion orbital and therefore have no effect on the ion charge. At higher speeds transitions become possible between occupied states close to the Fermi level and the unoccupied anti-bonding state at high energy. Such excitations take electrons from states with a low projection onto the channelling ion into the highly localized state. They thus have the effect of increasing the negative electronic charge on the channelling ion. In Fig. 10.8 the charge localizing transitions are indicated and labelled (A).

Our explanation suggests that the velocity at which the charge feature appears should be related to the distance above the Fermi level of the high energy defect state, an energy that we will denote $\Delta \varepsilon_a$, by the relation

$$v_{\text{onset}} = \frac{\Delta \varepsilon_{\text{a}} d}{2\pi \hbar}.$$
 (10.8)

From our density of states we have $\Delta \varepsilon_a = 17.8 \,\text{eV}$, so that $v_{\text{onset}} = 7.8 \,\text{Å fs}^{-1}$. In Fig. 10.9 we show once more the charge as a function of channelling speed, this time marking the predicted speed for this onset of the charge enhancement feature.

Thus far, our explanation of the charge feature suggests that its onset should occur sharply at ν_{onset} . This is not the case for our results and the reason lies in the fact that as the ion moves down the channel its atomic environment varies. Hence the local density of states changes with ion position and, importantly, the position of the localized anti-bonding state will oscillate with angular frequency Ω_{ν} . This variation in the position of the defect state, and hence of the energy $\Delta \epsilon_a$ has the effect of smearing out the onset of the resonance.

A similar explanation to the one advanced above accounts for the finite width of the charge enhancement feature. At a second critical velocity $v_{\rm off}\approx 10.2\,{\rm \AA\,fs^{-1}}$ (also marked in Fig. 10.9), transitions from occupied states into the localized anti-

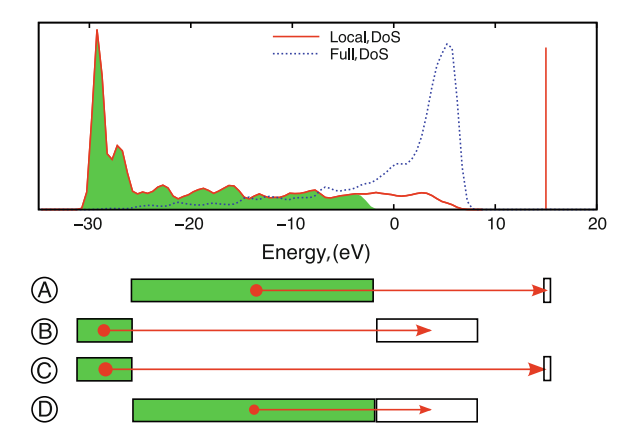
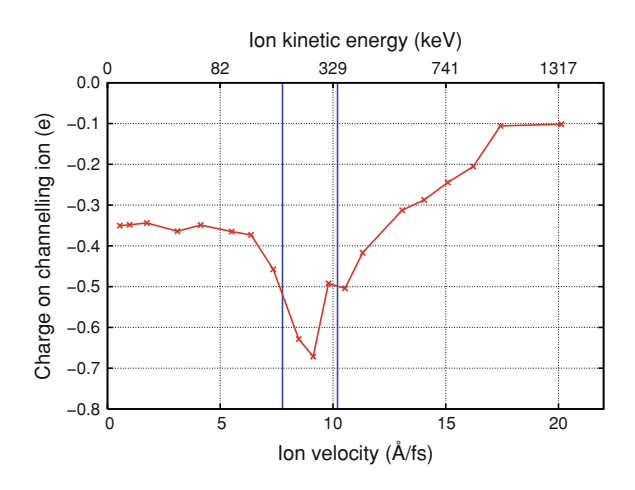


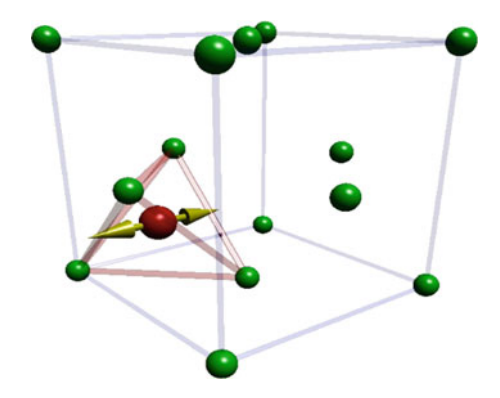
Fig. 10.8 The density of states for our tight-binding model (*dashed (blue) line*) and the local density of states on the channelling ion (*solid (red) line*). In the latter case, highly localized defect states are apparent at the bottom of the band and above the top of the band. The initially occupied states are shown *shaded (green)* and the Fermi level is at -2.83 eV. At the bottom of the figure, four types of transition are indicated schematically. Transitions of type (A), from occupied bulk states into the defect state, will localize charge on the channelling ion. Those of type (B) will delocalize charge. Transitions of type (C), from the low energy defect states into the high energy defect state, will have a small charge localizing effect and those of type (D), between delocalized bulk states, should have little effect on charge

Fig. 10.9 The data of Fig. 10.5, but showing the velocities at which charge localizing (type (A)) and charge delocalizing (type (B)) transitions are predicted to become possible. These velocities are 7.8 and 10.2 Å respectively



bonding state will no longer be possible. The only transitions stimulated by the channelling ion will be from the localized bonding states at the bottom of the band into unoccupied states above the Fermi level. These transitions, being from localized states to states with a much smaller projection onto the channelling ion, will therefore tend to pump electrons off the channelling ion, reducing its net negative charge. Transitions of this type are marked (B) in Fig. 10.8.

Fig. 10.10 A schematic illustration of the set-up for our oscillating interstitial calculation. One fcc unit cell of the lattice is shown with the interstitial atom shown in *red*. The (*yellow*) *arrows* indicate the oscillation of the



10.2.2 A Perturbation Theory Analysis

Nothing in the foregoing explanation of the charge feature makes reference to the ballistic motion of the channelling ion through the lattice. Indeed, the explanation relies explicitly on the periodicity in time of the atomic environment of the ion. This suggests that the charge feature should be present whenever we have localized defect states of the kind in the channelling simulations and when the correct frequencies are present in the variation of the electronic Hamiltonian. To verify our explanation and to allow us to explore the response of the system more deeply, we will undertake a time-dependent perturbation theory analysis of the analogue system of an oscillating unrelaxed tetrahedral interstitial atom (see Fig. 10.10 for a schematic illustration).

We consider a block of perfect lattice of our tight-binding model with an additional ion at a tetrahedral interstitial position. This ion is forced to undergo small amplitude oscillations at a fixed frequency Ω in the [100] direction. This defines a periodic perturbation $\hat{V}(t)$ to the electronic Hamiltonian \hat{H} of the perfect lattice plus tetrahedral interstitial ion.

$$\hat{V}(t) = \hat{V}^0 \sin \Omega t \qquad \hat{V}^0 = \nabla_{\mathbf{R}_c} \hat{H} \cdot \mathbf{A}, \tag{10.9}$$

where \mathbf{R}_c is the position of the oscillating ion relative to the tetrahedral site and \mathbf{A} gives the direction and amplitude of the oscillation.

The analysis follows in a similar way to that given for the single oscillating atom and discussed in Chap. 6. Full details of the derivation of the following formulae can be found in Sect. 13.2. The key result is an approximate expression for $\Delta q_{\rm c}$, the change in the number of electrons on the oscillating interstitial atom as a result of the action of the perturbation,

$$\Delta q_{c}approx \frac{1}{2\hbar^{2}} \sum_{i,j} s(i,j;\Omega,t) f(\varepsilon_{i}) (1 - f(\varepsilon_{j})) \Big\{ |\langle \alpha_{c} | \phi_{j} \rangle|^{2} - |\langle \alpha_{c} | \phi_{i} \rangle|^{2} \Big\} |\langle \phi_{j} | \hat{V} | \phi_{i} \rangle|^{2}.$$

$$(10.10)$$

 \hat{V} is the perturbation: the change in the non-self-consistent electronic Hamiltonian due to moving the interstitial atom away from its tetrahedral position and $s(i, j; \Omega, t)$ is the usual time-dependence for a sinusoidal perturbation,

$$s(i,j;\Omega,t) \xrightarrow{t\to\infty} 2\pi t \left\{ \delta[(\varepsilon_i - \varepsilon_i)/\hbar - \Omega] - \delta[(\varepsilon_i - \varepsilon_i)/\hbar + \Omega] \right\}. \tag{10.11}$$

The δ -function terms correspond to transitions of $\hbar\Omega$ upward and downward in energy. We see that the charge transfer is given by a sum over all possible transitions in the system between states i and j, restricted by exclusion and weighted by the matrix elements of the perturbation \hat{V} . The term in braces gives the change in charge associated with each transition. The level of approximation involved in (10.10) is greater than that in the corresponding expression for the non-adiabatic energy transfer considered in Chap. 6: in (10.10) we have neglected the effect of (albeit oscillatory) off-diagonal terms in the density matrix that do not come into the energy transfer expression. This issue is discussed in detail in Sect. 13.2.2.3.

Figure 10.11 shows the results of calculating Δq_c for a 3600 + 1 atom system using (10.10) along with the data from the Ehrenfest channelling simulations. The correspondence between channelling velocity and the frequency of the perturbation is made using (10.7) and the onset and shape of the charge localization feature clearly agree well. The effects of the two types of excitation (A) and (B), discussed above and indicated schematically in Fig. 10.8 are shown separately in Fig. 10.11, confirming the details of our explanation. The agreement between perturbation theory and simulation is less good above 25 eV: an

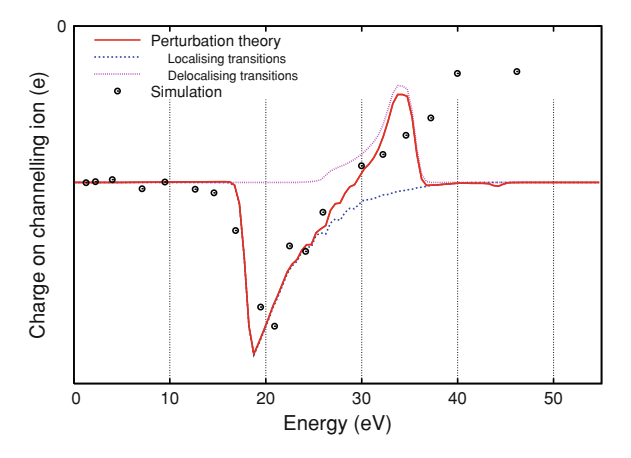


Fig. 10.11 Results of a simple perturbative calculation (*solid* (*red*) *line*) of the charge on an oscillating interstitial atom (described in the main text) compared to the steady state charge found in a non-self-consistent channelling simulation (U = V = 0) (*black circles*). The onset and width of the charge enhancement feature are correctly reproduced. The (*blue*) *short dashed* and the (*purple*) *dotted line* show the contributions from the two types of transitions illustrated in Fig. 10.8. The vertical scale is arbitrary as the FGR calculation does not yield a steady state

oscillating interstitial becomes an increasingly poor analogue of a channelling ion at high velocities, when the localized electrons are actually left behind in the wake of the moving ion.

We should note that the vertical scale of the perturbation theory and simulation results in Fig. 10.11 is chosen independently and arbitrarily. This is because no steady state exists in the perturbation theory view. In contrast, the large variation of the hopping integrals between the channelling ion and its nearest-neighbours means that the variation of the electronic Hamiltonian in the case of the simulations lies far beyond the perturbative regime. Excitations occur at a high rate and a steady state is established fairly rapidly. In the case of the resonance, this steady state arises when the occupations of the eigenstates are such that there is a balance in transitions up and down in energy between the high energy localized state and those lying $\hbar\Omega_{\nu}$ below it.

10.2.2.1 A More Detailed Look at the Perturbation Theory Expression

To get a better understanding of the behaviour of the charge on our oscillating interstitial atom, and so on our channelling ion, we will now examine the various terms in Eq. 10.10 in more detail. Figure 10.12 shows plots of the factors contributing to Δq_c . The left hand panels (a, c, e, and g) show the average values of the contributions to (10.10), i.e. the number of transitions, the effects of quantum mechanical exclusion, the coupling due to the perturbation and the charge difference between states, as a function of the energy of transitions. The right hand panels (b, d, f, and h) show the effect of adding in these terms cumulatively to arrive at the full expression for the charge enhancement (10.10). In each panel, three particular energies are indicated by vertical lines. These are (in order, from low to high energy),

- 1. The separation of the anti-bonding defect state from the Fermi level. This is the minimum energy for charge localizing transitions of type (A) in Fig. 10.8.
- 2. The separation of the Fermi level from the top of the bonding state. Above this energy, charge delocalising transitions of type (B) in Fig. 10.8 become possible.
- 3. The separation of the anti-bonding state from the top of the bonding states. At this energy transitions of type (C) become possible.

 In addition to marking these particular energies, each panel contains plots for the four classes of transition shown in Fig. 10.8 (though not all are visible in every panel). These are:

Orange: Charge localizing transitions of type (A).

Blue: Charge delocalizing transitions of type (B).

Purple: Transitions of type (C) with a small charge localizing effect.

Light blue: Transitions of type (D) with no significant effect on the charge on the channelling ion.

The red lines in each case plot the total effect of all transitions.

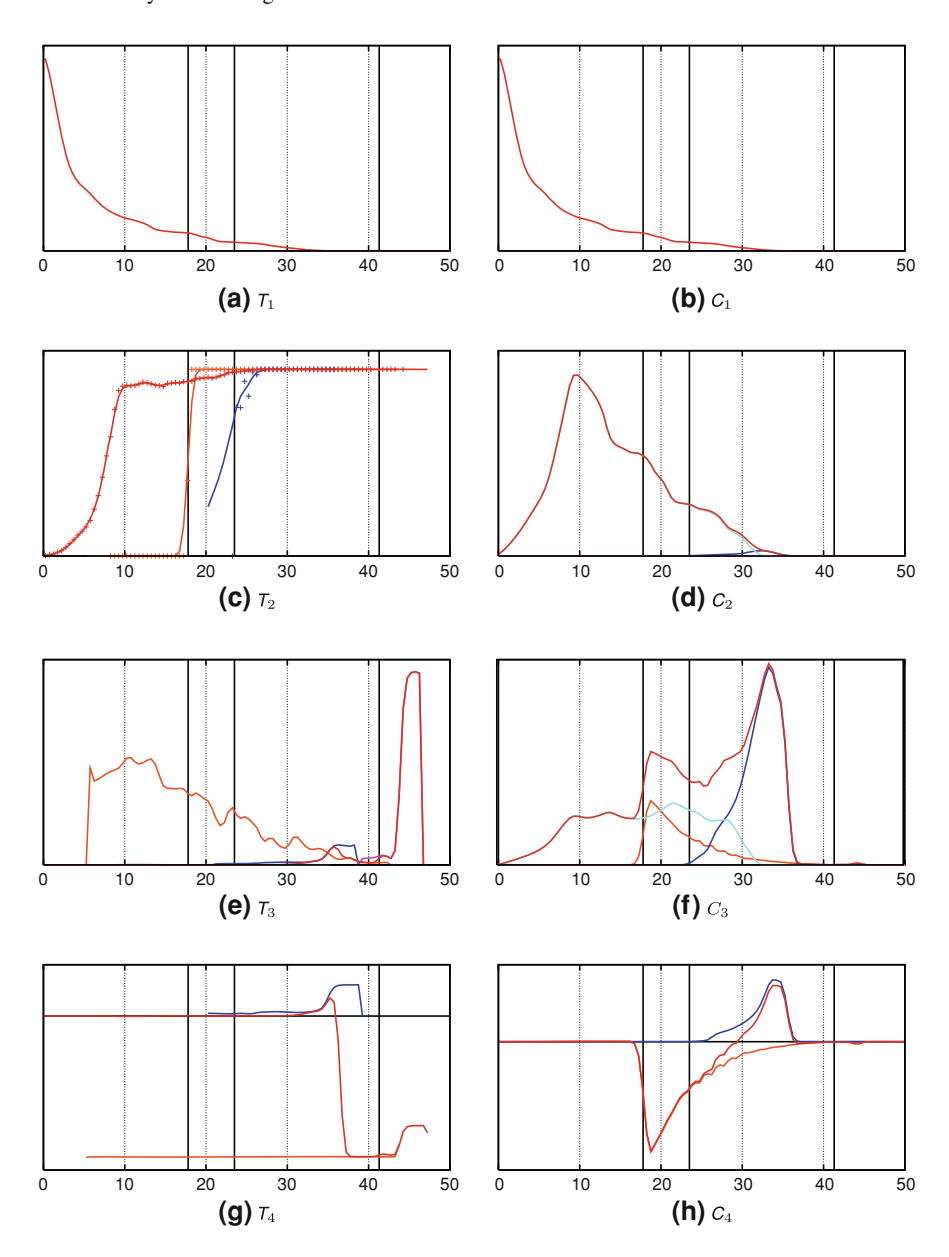


Fig. 10.12 The behaviour of various terms in the expression for the excess charge on an oscillating interstitial (10.10). The details of the figures are discussed in the text. The *lines* represent a histogram with Gaussian smoothing. Points, where present, give the results with simple, unsmoothed binning. The horizontal axis shows the energy of transitions $\varepsilon = \hbar \Omega$

We will now treat each panel in turn:

(a) and (b): The density of transitions, effectively a histogram of the energy differences between all pairs of states in the system. We define it as,

$$T_1(\hbar\Omega) = C_1(\hbar\Omega) \equiv \frac{1}{N_{\rm a}^2} \sum_{ij} \delta(\varepsilon_j - \varepsilon_i - \hbar\Omega) \stackrel{N_{\rm a} \to \infty}{\longrightarrow} \int {\rm d}\varepsilon D(\varepsilon) D(\varepsilon + \hbar\Omega), \quad (10.12)$$

where $D(\varepsilon)$ is the density of states of the lattice plus oscillator, and note that it is dominated by the large number of low energy transitions within the peak of the density of states.

(c): The average occupation factor:

$$T_{2}(\hbar\Omega) \equiv \frac{1}{T_{1}} \frac{1}{N_{a}^{2}} \sum_{ij} f(\varepsilon_{j}) (1 - f(\varepsilon_{i})) \delta(\varepsilon_{j} - \varepsilon_{i} - \hbar\Omega)$$

$$\stackrel{N_{a} \to \infty}{\longrightarrow} \frac{1}{T_{1}} \int d\varepsilon D(\varepsilon) D(\varepsilon + \hbar\Omega) f(\varepsilon) (1 - f(\varepsilon + \hbar\Omega)).$$
(10.13)

Note that the orange and blue lines for transitions of type (A) and (B) show the expected behaviour, becoming active at the energies indicated by the vertical lines (defined above).

(d): The density of allowed transitions,

$$C_{2}(\hbar\Omega) \equiv \frac{1}{N_{a}^{2}} \sum_{ij} f(\varepsilon_{j}) (1 - f(\varepsilon_{i})) \delta(\varepsilon_{j} - \varepsilon_{i} - \hbar\Omega)$$

$$\stackrel{N_{a} \to \infty}{\longrightarrow} \int d\varepsilon D(\varepsilon) D(\varepsilon + \hbar\Omega) f(\varepsilon) (1 - f(\varepsilon + \hbar\Omega)).$$
(10.14)

Here the large central peak, consisting mostly of transitions from unoccupied to unoccupied states, is suppressed.

(e): The average coupling factor:

$$T_3(\hbar\Omega) \equiv \frac{1}{T_1} \frac{1}{N_a^2} \sum_{ii} |\langle \phi_i | \hat{V} | \phi_j \rangle|^2 \delta(\varepsilon_j - \varepsilon_i - \hbar\Omega). \tag{10.15}$$

The perturbation due to the oscillating ion is only strong between pairs of states in which at least one has a strong projection onto the channelling ion. Transitions into the anti-bonding state (orange line, type (A)) and out of the bonding state (blue line, type (B)) are relatively strongly coupled. The right most peak is due to transitions of type (C) from the bonding to the anti-bonding state (purple line). The coupling between other pairs of states (type (D)), neither of which is localized on the oscillator, is too weak to show up on this scale. Note that overall, the average coupling strength for all transition types (shown in red) is dominated at lower energies ($\lesssim 30\,\text{eV}$) by the large number of these weakly coupled transitions between delocalized states.

(f): The density of coupled, allowed transitions,

$$C_3(\hbar\Omega) \equiv \frac{1}{N_a^2} \sum_{ij} f(\varepsilon_i) (1 - f(\varepsilon_i)) |\langle \phi_i | \hat{V} | \phi_j \rangle|^2 \delta(\varepsilon_i - \varepsilon_i - \hbar\Omega). \tag{10.16}$$

We can understand the behaviour of C_3 with reference to T_3 , noting that C_3 now takes into account the underlying density of transitions at each energy and the effects of exclusion. The peak in T_3 above 40 eV is now suppressed, since transitions of type (C) are small in number. Transitions of type (D) dominate C_3 at low energies, but the relatively high average coupling for the relatively rare transitions of types (A) and (B) still gives them a significant contribution.

(g): The average charge transfer:

$$T_4(\hbar\Omega) \equiv \frac{1}{T_1} \frac{1}{N_a^2} \sum_{ij} (q_j - q_i) \delta(\varepsilon_j - \varepsilon_i - \hbar\omega). \tag{10.17}$$

Again, only transitions of types (A), (B) and (C) show up with any significance, and again, as an average across all transitions, their effects are dwarfed by the large number of transitions of type (D). Only at the highest energies, where no type (D) transitions are possible, do we see a large charge transfer on average. (h): The charge transfer spectrum,

$$C_4(\hbar\Omega) \equiv \frac{1}{N_a^2} \sum_{ii} f(\varepsilon_i) (1 - f(\varepsilon_i)) |\langle \phi_i | \hat{V} | \phi_j \rangle|^2 (q_j - q_i) \delta(\varepsilon_j - \varepsilon_i - \hbar\Omega). \quad (10.18)$$

Now adding into T_4 the effects of transition density, exclusion and coupling strength, the full picture emerges, with the overall charge transfer behaviour dominated by transitions of types (A) and (B). A tiny enhancement in negative charge due to transitions of type (C) is just visible at around 43 eV.

10.2.2.2 A Toy Model

To highlight the important features of our perturbation theory expression for the charge transfer we will briefly consider a toy model of our oscillator system. We imagine a system with a rectangular density of states as shown in Fig. 10.13a. The system consists of a set of N delocalized bulk states lying between energies ε_b and ε_t and two groups of localized states. At high energy, between ε_A and $\varepsilon_A + \Delta \varepsilon_A$, we have one set of initially unoccupied states highly localized on our channelling ion. At low energy, between $\varepsilon_B - \Delta \varepsilon_B$ and ε_B we have a second set of localized states, initially occupied and responsible for the initial negative charge on the channelling ion. We denote the Fermi level by ε_F . The density of states for our system can thus be written,

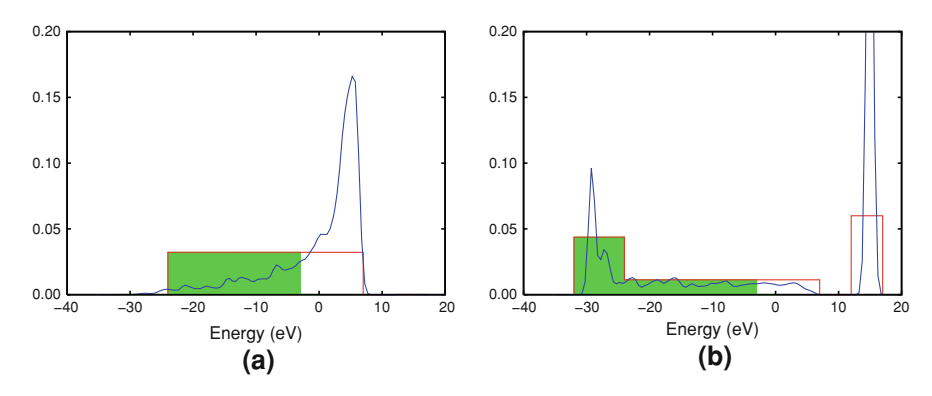


Fig. 10.13 a The density of states and b the local density of states on the channelling ion for our toy model compared with those for our tight-binding model

$$D(\varepsilon) = [H(\varepsilon - \varepsilon_{\rm B} + \Delta \varepsilon_{\rm B}) - H(\varepsilon - \varepsilon_{\rm B})] \frac{1}{\Delta \varepsilon_{\rm B}} + [H(\varepsilon - \varepsilon_{\rm A}) - H(\varepsilon - \varepsilon_{\rm A} - \Delta \varepsilon_{\rm A})] \frac{1}{\Delta \varepsilon_{\rm A}} + [H(\varepsilon - \varepsilon_{\rm b}) - H(\varepsilon - \varepsilon_{\rm t})] \left(\frac{N-2}{\varepsilon_{\rm t} - \varepsilon_{\rm b}}\right),$$

$$(10.19)$$

where H is the Heaviside step function,

$$H(\varepsilon) = 0, \quad \varepsilon < 0$$

= 1, $\varepsilon \ge 0$, (10.20)

and we have assumed that each of the groups of localized states has unit total weight. If we define the total projection of the low energy localized states onto the channelling ion as $a_{\rm B}$ and that of the high energy localized states as $a_{\rm A}$, then we obtain for the local density of states on the channelling ion (illustrated in Fig. 10.13b),

$$\begin{split} D_{c}(\varepsilon) &= \left[H(\varepsilon - \varepsilon_{B} + \Delta \varepsilon_{B}) - H(\varepsilon - \varepsilon_{B}) \right] \frac{a_{B}}{\Delta \varepsilon_{B}} + \left[H(\varepsilon - \varepsilon_{A}) - H(\varepsilon - \varepsilon_{A} - \Delta \varepsilon_{A}) \right] \frac{a_{A}}{\Delta \varepsilon_{A}} \\ &+ \left[H(\varepsilon - \varepsilon_{b}) - H(\varepsilon - \varepsilon_{t}) \right] a_{i} \left(\frac{N-2}{\varepsilon_{t} - \varepsilon_{b}} \right), \end{split}$$

$$(10.21)$$

where

$$a_i = \frac{1 - (a_A + a_B)}{N - 2}. (10.22)$$

is the projection of a general bulk state onto the channelling ion. We now wish to calculate the steady state charge in our toy model as a function of the perturbation frequency Ω ,

$$\Delta q_{\rm c} = \frac{\pi t}{\hbar^2} \iint \mathrm{d}\varepsilon \, \mathrm{d}\varepsilon' D(\varepsilon) D(\varepsilon') f(\varepsilon) [1 - f(\varepsilon')] \Delta q_{\varepsilon \to \varepsilon'} |V|_{\varepsilon \to \varepsilon'}^2 \delta((\varepsilon' - \varepsilon)/\hbar - \Omega), \tag{10.23}$$

where $\Delta q_{\varepsilon \to \varepsilon'}$ is the change in charge associated with a transition between states at ε and $|V|_{\varepsilon \to \varepsilon'}^2$ is the square of the coupling matrix element.

Only three types of transition will result in a change in charge on the channelling ion in our model:

1. For transitions of type (A), $\Delta q_{\varepsilon \to \varepsilon'} = a_{\rm A} - a_i$ and we will write the coupling as $|V|^2_{i \to {\rm A}}$. Then the contribution to the change in charge will be,

$$\Delta q_{1} = A_{1} \times \begin{cases} \epsilon_{F} + \hbar\Omega - \epsilon_{A} & \text{if } \epsilon_{A} - \epsilon_{F} < \hbar\Omega < \epsilon_{A} + \Delta\epsilon_{A} - \epsilon_{F} \\ \Delta\epsilon_{A} & \text{if } \epsilon_{A} + \Delta\epsilon_{A} - \epsilon_{F} < \hbar\Omega < \epsilon_{A} - \epsilon_{B} \\ \epsilon_{A} + \Delta\epsilon_{A} - \hbar\Omega - \epsilon_{B} & \text{if } \epsilon_{A} - \epsilon_{B} < \hbar\Omega < \epsilon_{A} + \Delta\epsilon_{A} - \epsilon_{B} \\ 0 & \text{otherwise} \end{cases}$$
(10.24)

where,

$$A_{1} = \frac{\pi t}{\hbar} \frac{1}{\Lambda \epsilon_{\text{A}}} \frac{N-2}{\epsilon_{t} - \epsilon_{\text{b}}} (a_{\text{A}} - a_{i}) |V|_{i \to \text{A}}^{2}.$$
 (10.25)

2. For transitions of type (B), $\Delta q_{\varepsilon \to \varepsilon'} = a_i - a_B$ and we will write the coupling as $|V|^2_B \to i$. Then the contribution to the change in charge will be,

$$\Delta q_{2} = A_{2} \times \begin{cases} \varepsilon - \varepsilon_{F} + \hbar \Omega & \text{if } \varepsilon_{F} - \varepsilon_{B} < \hbar \Omega < \varepsilon_{F} - (\varepsilon_{B} - \Delta \varepsilon_{B}) \\ \Delta \varepsilon_{B} & \text{if } \varepsilon_{F} - (\varepsilon_{B} - \Delta \varepsilon_{B}) < \hbar \Omega < \varepsilon - \varepsilon_{B} \\ \varepsilon - \hbar \Omega - \varepsilon_{B} + \Delta \varepsilon_{B} & \text{if } \varepsilon_{t} - \varepsilon < \hbar \Omega < \varepsilon_{t} - (\varepsilon - \Delta \varepsilon_{B}) \\ 0 & \text{otherwise} \end{cases}$$
(10.26)

where,

$$A_2 = \frac{\pi t}{\hbar} \frac{1}{\Delta \varepsilon_{\rm B}} \frac{N - 2}{\varepsilon_{\rm t} - \varepsilon_{\rm b}} (a_i - a_{\rm B}) |V|_{{\rm B} \to i}^2.$$
 (10.27)

3. For transitions of type (c), $\Delta q_{\varepsilon \to \varepsilon'} = a_A - a_B$ and we will write the coupling as $|V|^2_B \to A$. Then the contribution to the change in charge will be,

where.

$$A_3 = \frac{\pi t e}{\hbar^2} \frac{1}{\Delta \varepsilon_{\rm A} \Delta \varepsilon_{\rm B}} (a_{\rm A} - a_{\rm B}) |V|_{\rm B \to A}^2. \tag{10.29}$$

We now pick parameters to correspond to our tight-binding model as illustrated in Fig. 10.13a, b:

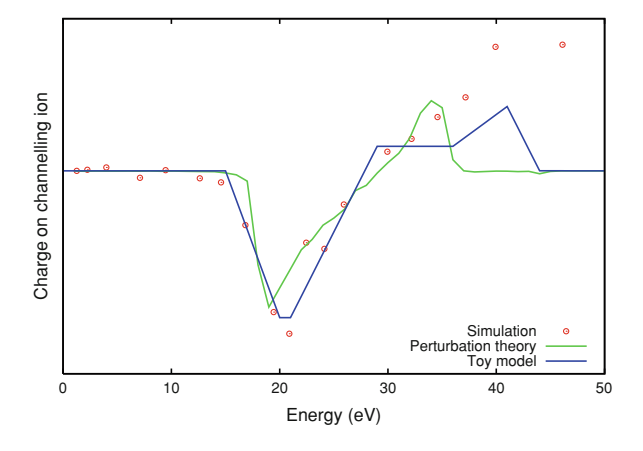
$$\begin{aligned}
\varepsilon_{\text{B}} &= -24 \, \text{eV} \\
\Delta \varepsilon_{\text{B}} &= 8 \, \text{eV} \\
\varepsilon_{\text{F}} &= -3 \, \text{eV} \\
\varepsilon_{\text{t}} &= 7 \, \text{eV} \\
\varepsilon_{\text{B}} &= 12 \, \text{eV} \\
\Delta \varepsilon_{\text{B}} &= 5 \, \text{eV} \\
a_{\text{A}} &= 0.3 \\
a_{\text{B}} &= 0.35 \\
a_{\text{i}} &= 3.51 \times 10^{-4}.
\end{aligned}$$

where the width $\Delta \epsilon_A$ of the high energy localized states represents a statistical spread due to the periodic variation in the local atomic environment of the channelling ion. With these parameters we obtain the results shown in Fig. 10.14 in which we see that the features of our simple model are sufficient to reproduce the pattern of behaviour in the channelling simulations.

10.2.3 The Effect of Channelling Direction

One way that we can seek more supporting evidence for our explanation of the charge accumulation feature is to vary the channelling geometry. In Fig. 10.15 we

Fig. 10.14 Steady state charge predicted by the toy model described in the text and compared with results from our simulations and our perturbation theory analysis. The vertical scaling is arbitrary



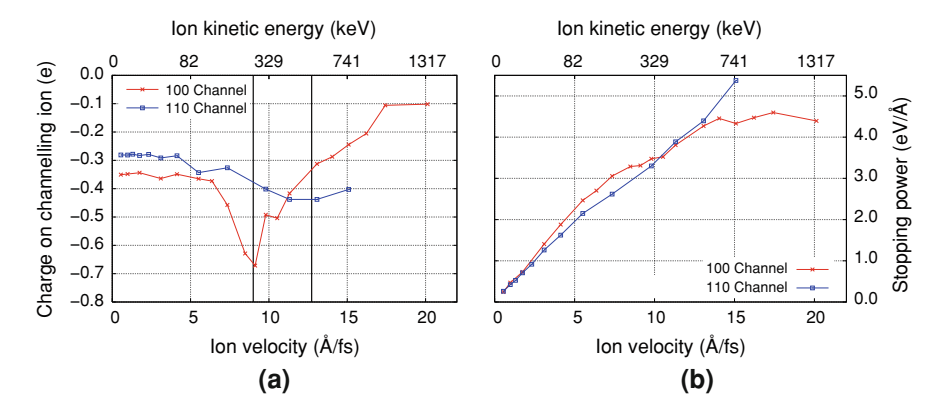


Fig. 10.15 a The steady state charge and b stopping power for two different channels. In the *left-hand panel* the two *vertical lines* are marked at velocities that differ by a factor of $\sqrt{2}$ equal to the ratio of the periodic repeat distances along the two channels (data provided by D. R. Mason)

show the results of channelling simulations with U=V=0 for an ion moving down a channel in the [110] direction. We compare the steady state charge and stopping power as a function of velocity with the equivalent simulations for the [100] channel. Given our explanation for the behaviour of the data in the [100] channel we expect to see the charge response in the [110] channel at velocities a factor of $\sqrt{2}$ higher, since the periodic repeat distance of the atomic environment of the projectile is $a/\sqrt{2}$ in the latter case, compared to a/2 in the former. Lines are marked in Fig. 10.15 at two velocities differing by this factor of $\sqrt{2}$ to aid in reading the plots and suggest that the behaviour is as expected. The geometry of the [110] channel is such that the variation in the nearest-neighbour hopping integrals to the channelling ion is larger and so we should expect to see a less well defined resonance. This too is confirmed by the data in Fig. 10.15.

10.2.4 The Effect of Charge Self-Consistency Parameters U and V

So far we have been considering only the case of the charge on our channelling ion in the case of a non-charge-self-consistent model (i.e. the parameters in the charge self-consistent Hamiltonian (10.2) and (10.3) are U = 0 and V = 0). In this section we will examine and explain the effect of adding in a non-zero energy associated with charge localization. In Fig. 10.16 we see the effect of increasing V first to its most realistic value of V = 7 and then to a high exploratory value of V = 50. In neither case do we see much effect on the charge response. Introducing an energy penalty for localizing charge simply reduces the magnitude of the charge response, as we might expect, though not dramatically.

Fig. 10.16 The mean steady state charge on a channelling ion as a function of its initial velocity for a variety of values of the inter-site charge self-consistency parameter *V* (data provided by D. R. Mason)

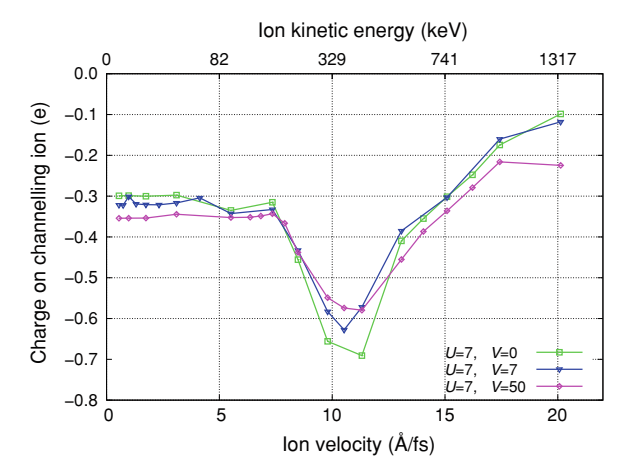
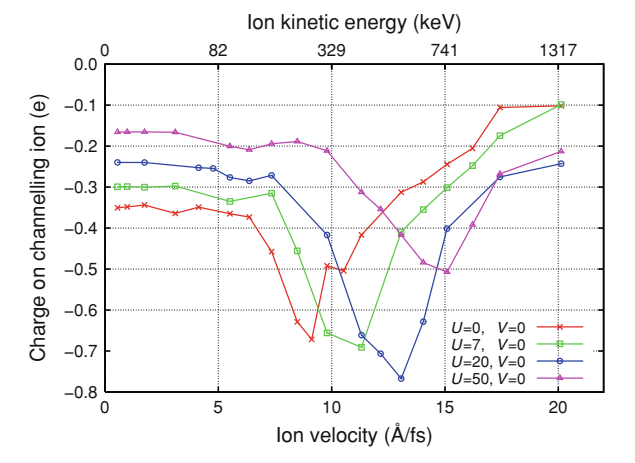


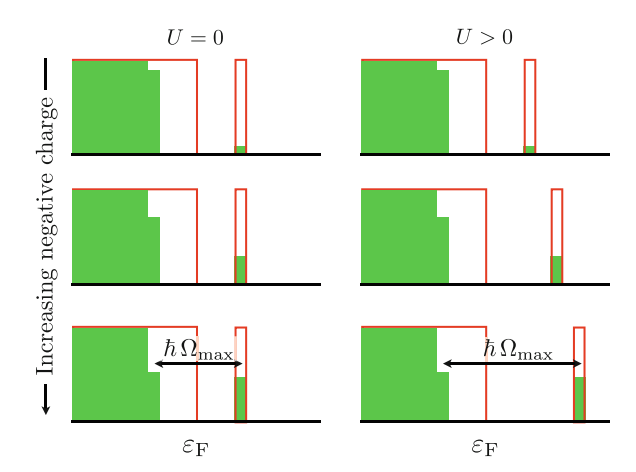
Fig. 10.17 The mean steady state charge on a channelling ion as a function of its initial velocity for a variety of values of the on-site charge self-consistency parameter *U* (data provided by D. R. Mason)



In Fig. 10.17 we show the effect of increasing U, first to its realistic value of U = 7 and then to two exploratory values of U = 20 and U = 50. Various strong features are apparent:

1. The steady state negative charge at low velocity (essentially the value for a stationary tetrahedral interstitial) is reduced with increasing *U*. This is exactly what we would expect given that we are imposing an energy penalty for charge localization. An alternative interpretation would be to consider the low energy localized states on the channelling ion. These are fully occupied and are responsible for the excess electronic charge in the quasi-static case. At zero *U* these states form a resonance right at the bottom of the band of our tight-binding model. The effect of a finite *U* is to increase the energy of these states and bring them further into the band, reducing the strength of the resonance and making the states less highly localized, pushing charge off the channelling ion.

Fig. 10.18 A schematic view of the change in the position of the high energy defect state as it becomes occupied in the case where U > 0. The diagrams show the local density of states with occupied states indicated by (green) shading. The separation of the defect state from the Fermi level is increased for higher U, increasing the velocity at which the maximum charge response occurs



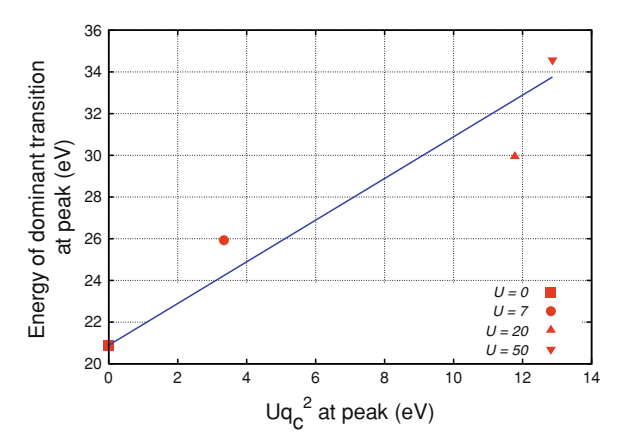
2. The position of the charge resonance moves upwards in velocity with increasing U. As the localized high energy defect state becomes occupied its energy will increase if U > 0. Hence the minimum velocity at which electrons can be excited from the Fermi level into the localized state increases as the state becomes occupied and the position of the maximum will depend on U. This process is illustrated schematically in Fig. 10.18. If we assume the high energy defect state is entirely localized on the channelling ion, then given the form of the charge self-consistent energy in our model we would expect the velocity at which the maximum charge enhancement occurs, v_{max} , to be related to the maximum charge enhancement Δq_{max} by,

$$\hbar\Omega_{\rm max} = \frac{2\pi\hbar v_{\rm max}}{D} = Uq_{\rm max}^2 + \langle \Delta \varepsilon_0 \rangle, \tag{10.30}$$

where $\langle \Delta \varepsilon_0 \rangle$ is the separation of the high energy defect state from the Fermi level in the case of U=0 (or, equivalently, in the uncharged state) as an average over the varying local environment of the channelling ion. The data from our simulations can be seen in Fig. 10.19 to adhere to this relationship.

3. The depth of the charge response, measured as the difference between the charge at low velocity and that at maximum response, first increases with increasing U and then decreases again. This behaviour is once again due to the dependence of the position of the high energy defect state on its occupation (i.e. on the charge on the channelling ion) that exists at finite U. The steady state of our system arises when excitations into and out of the high energy defect state become equally likely, which will occur when the defect state and those a distance $\hbar\Omega_v$ below it are equally occupied. Because the energy of the defect state fluctuates with the local atomic environment it receives electrons excited from states in a finite range of energy below the Fermi level. If there is additional variation in the energy of the defect state with its charge, because of a finite U, then the electrons excited into the defect state will come from a broader range of states below the Fermi level and so the balance in

Fig. 10.19 The relationship between the position of the maximum charge response and its magnitude as the onsite charge self-consistency parameter U is varied



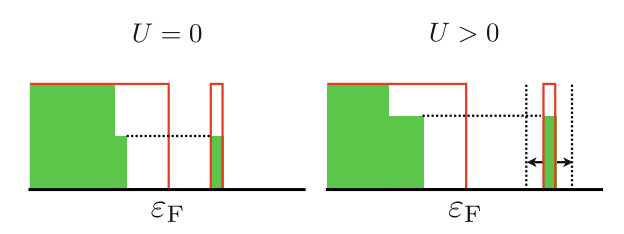


Fig. 10.20 A schematic view of the states contributing electrons to the high energy defect state in the steady state. For U > 0, fluctuation in the energy of the defect state with its occupation means that excitations from a broader range of states below the Fermi level are possible

occupations will occur at a higher occupation of the defect state. This situation is illustrated schematically in Fig. 10.20.

10.3 Electronic Stopping Power for a Channelling Ion

10.3.1 Results

In addition to recording the steady state charge on the channelling ion we also have data on the irreversible energy transfer into the electronic system as the channelling ion moves down the channel. This energy transfer corresponds to the electronic stopping power of our tight-binding model for the channelling ion. Figure 10.21 shows how the steady state stopping power varies with the initial channelling ion velocity. Figures 10.22 and 10.23 show the effect of the charge self-consistency parameters V and U respectively on the variation of the stopping power. The following patterns emerge in the data:

Fig. 10.21 The steady state stopping power acting on our channelling ion as a function of its initial velocity for the case of no charge self-consistency (U = V = 0) (data provided by D. R. Mason)

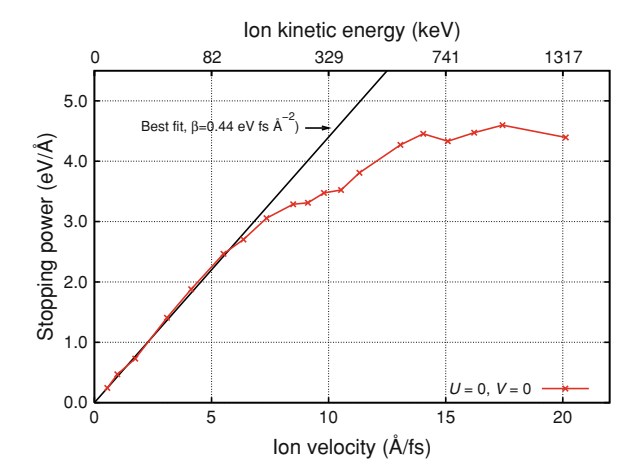
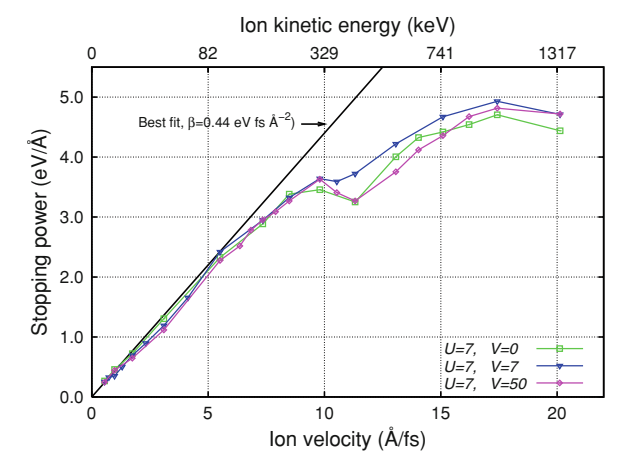
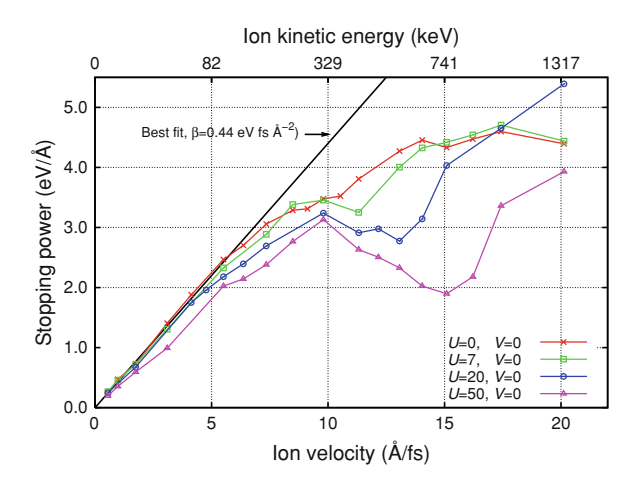


Fig. 10.22 The variation of the behaviour of the steady state stopping power acting on our channelling ion with different values for the intersite charge self-consistency parameter *V* (data provided by D. R. Mason)



- 1. The stopping power at low velocities increases approximately linearly with velocity in accordance with theories of the stopping of slow particles (see Sect. 3.2.5). The best-fit effective damping coefficient is $\beta = (dE/dx)/v = 0.44 \pm 0.01 \text{ eV Å}^{-2}$ fs for U = 0.
- 2. The inter-site charge self-consistency parameter V has no significant effect on the stopping power (see Fig. 10.22).
- 3. When U = V = 0 the stopping power curve exhibits a pronounced 'knee' at around the velocity corresponding to the resonant charge accumulation phenomenon (compare Fig. 10.21 with Fig. 10.5).
- 4. When U > 0 this knee becomes a significant dip in the stopping power over the range of velocities in which we see the charge resonance (compare Fig. 10.23 with Fig. 10.17). In particular, we would like to explain the last two of these features.

Fig. 10.23 The variation of the behaviour of the steady state stopping power acting on our channelling ion with different values for the onsite charge self-consistency parameter U (data provided by D. R. Mason)



10.3.2 The Origin of the Stopping Power: A Tight-Binding Perspective

Before we attempt to explain the behaviour of the stopping power in our simulations data, we will consider how the stopping power arises within a tight-binding model of the electronic structure. All the forces on our ions can be attributed to bonds between ion pairs. The expression for the Hellmann-Feynman force,

$$\mathbf{F}_{\mathrm{e}} = -2\mathrm{Tr}\{\hat{\rho}\nabla_{\mathbf{R}}\hat{H}\},\tag{10.31}$$

gives for the force acting on the ion at \mathbf{R}_a due to the ion at \mathbf{R}_b ,

$$\mathbf{F}_{ab} = -2(\rho_{ba}\nabla_{\mathbf{R}_a}H_{ab} + \rho_{ab}\nabla_{\mathbf{R}_a}H_{ba})$$

$$= -2[2\Re{\{\rho_{ba}\}}]\gamma'(|\mathbf{R}_{ab}|)\frac{\mathbf{R}_{ab}}{|\mathbf{R}_{ab}|},$$
(10.32)

where $\rho_{ab} = \langle \mathbf{R}_a | \hat{\rho} | \mathbf{R}_b \rangle$, $H_{ab} = \langle \mathbf{R}_a | \hat{H} | \mathbf{R}_b \rangle$, $\mathbf{R}_{ab} = \mathbf{R}_b - \mathbf{R}_a$, $\gamma'(R) = \mathrm{d}\gamma(R)/\mathrm{d}R$ and $\gamma(R)$ is our hopping integral. So the force acting on an ion due to each neighbour will be a product of the bond-order $2\Re\{\rho_{ba}\}$ and the gradient of the hopping integral.

Now let us consider our channelling ion moving past an ion in the channel wall as illustrated schematically in Fig. 10.24a. As the two ions get closer together the hopping integral becomes more negative, becoming a minimum at the point of closest approach (see Fig. 10.24b), and so its gradient behaves as in Fig. 10.24c. Now, as the ions move closer together, an increasingly strong bond forms between them and the bond-order increases. If the channelling ion were moving infinitely slowly, the bond-order would become a maximum at the point of closest approach, but if the ion is moving with finite velocity, the electronic response will lag behind

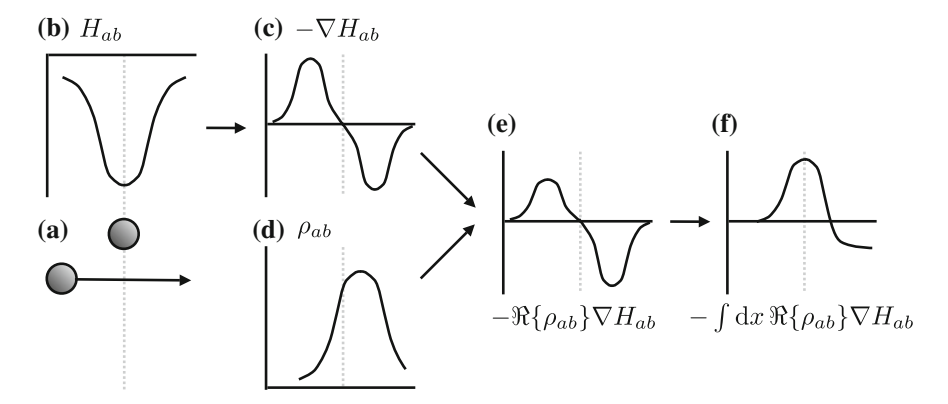


Fig. 10.24 A schematic view of the mechanism of stopping in ion channelling. **a** the channelling ion passing a nearest-neighbour, with the point of closest approach indicated by a *grey dashed line*. **b** the variation of the hopping integral between the channelling ion and its nearest neighbour, which shows a minimum at the point of closest approach. **c** the negative of the gradient of this hopping integral. **d** the variation of the corresponding bond-order. Because of the finite response time of the electronic system, the maximum of the bond-order occurs only after the channelling ion has passed the point of closest approach. **e** the component of the bond force parallel to the direction of motion of the channelling ion and **f** the cumulative work done by this force as the ion passes its neighbour. It is this work that corresponds to the stopping power

this adiabatic response. Hence, at finite channelling velocity we will see the bond-order form a maximum only *after* the channelling ion has passed the point of closest approach (see Fig. 10.24d). If we now consider the variation of the force due to this lagged bonding response (see Fig. 10.24e) and the work done by it on the channelling ion (see Fig. 10.24f) then we can see that the asymmetry of the bond-order about the point of closest approach is what gives rise to the stopping power. At higher and higher channelling velocities, the lag in the bonding response will get larger and larger, increasing the net work done by the asymmetric force and implying a larger stopping power.

10.3.2.1 Bond-Orders in Channelling Simulations

In order to explain the features in our stopping power data we have performed some additional channelling simulations and extracted information about the bond-orders between the channelling ion and its neighbours. These simulations used smaller (2016 ion) simulation cells than those used to obtain the main stopping power and charge data and a less sophisticated method of identifying the steady state was employed. To give confidence that the data from these smaller simulations will be valid (at least for analysis purposes), Fig. 10.25a, b compare the charge and stopping power results for the two sets of simulations with different cell sizes. Figure 10.26a, b shows examples of the raw data and a fitted trend line (calculated as a moving average over two periods of the channelling environment)

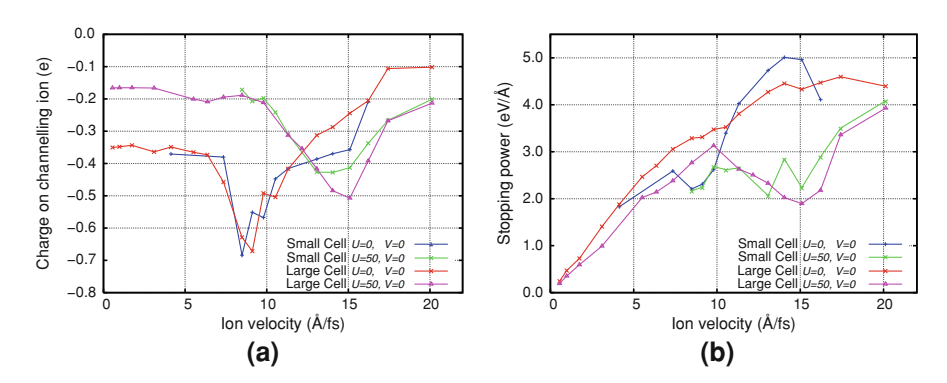


Fig. 10.25 A comparison of, **a** the steady state charge on a channelling ion and **b** the stopping power, as a function of speed between the original large simulation cell (8064 atoms) and results obtained with a smaller simulation cell (2016 atoms) and a simpler fitting process. The smaller cell results show the same behavioural trends as those from the larger cell

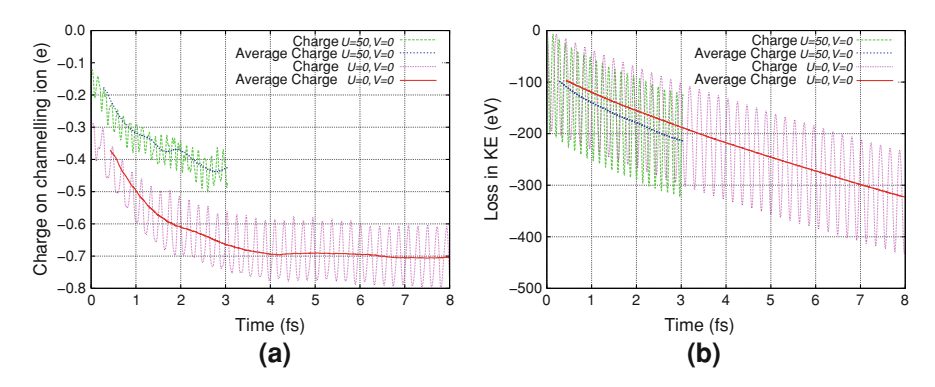


Fig. 10.26 Examples of the results of the moving average fitting process used to extract information from small cell simulations of ion channelling. The U=0 data are for 237 keV and the U=50 data are for 562 keV, within the charge resonance in each case. Shown are **a** ion charge and **b** loss in ion kinetic energy

for the charge and loss in kinetic energy (corresponding to stopping power) in sample simulations in the smaller cells. The data fitting methodology is sufficiently stable and the overall trends in the results sufficiently similar to those derived from the larger simulations for us to be able to use the bond-order data from the smaller simulations in our analysis.

10.3.3 The 'Knee' in the Stopping Power for U = V = 0

We now return to explain the behaviour of the stopping power in our simulations, making use of the data from the simulations described above. First we consider the

'knee' that appears in the stopping power at the charge resonance when U = V = 0. This can be explained if we consider the nature of the localized states on the channelling ion.

Because the channelling ion comes into unusually close proximity with its neighbours in the channel wall, it interacts very strongly with them and forms highly localized states. The lower energy localized states will be strongly bonding in character (occupation of them will make a large positive contribution to the bond-order) and the higher energy states will be strongly anti-bonding in character (making a large negative contribution to the bond-order). We can see this more clearly if we note that the magnitude of the hopping integrals between the channelling ion and its neighbours are unusually large and so we can imagine an extreme case in which the channelling ion and its neighbouring ion are effectively decoupled from the rest of the lattice. This situation gives rise to a pair of states, one bonding, one anti-bonding as the ions form a dimer. In our simulations the situation is less extreme, but of similar character.

Now, when the high-energy defect state becomes occupied as we enter the resonance feature and electrons are pumped onto the channelling ion, the bond-orders between the channelling ion and its neighbours will be reduced. The asymmetry in the bond-force due to the lag in the response of the density matrix will remain the same, but the absolute size of the forces will be reduced due to the lower bond-order. Hence the net work done by the force on the ion and so the stopping power will be reduced.

Data from our small-scale channelling simulations support the above interpretation. In Fig. 10.27a we show how the bond-order between the channelling ion and a series of its neighbours at equivalent points along its trajectory is reduced as the high energy defect state (the anti-bonding state) becomes occupied. Note also the clear lag in the bond-order relative to the point of closest approach, marked by a

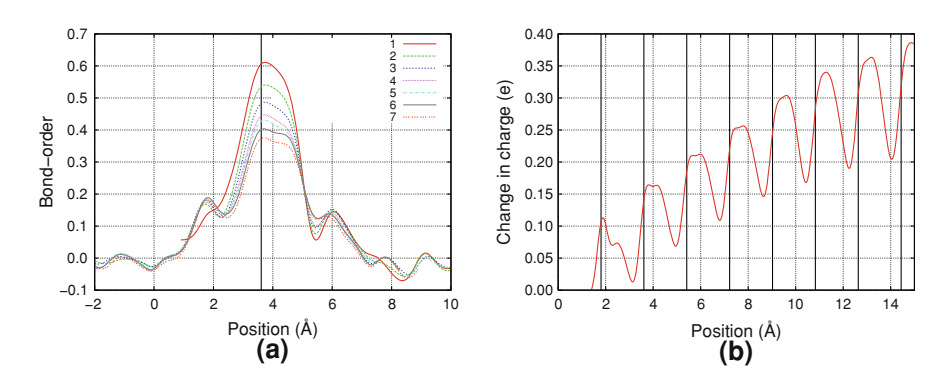
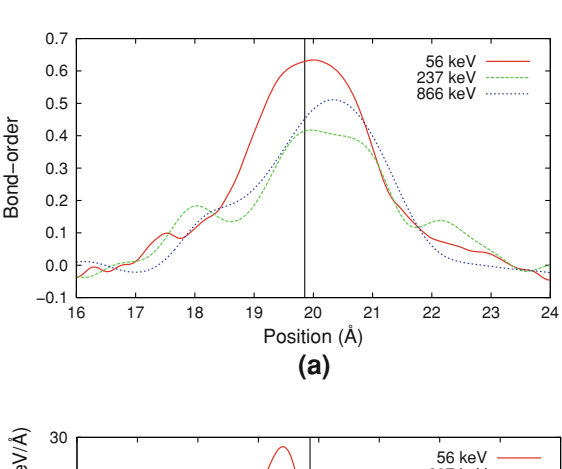


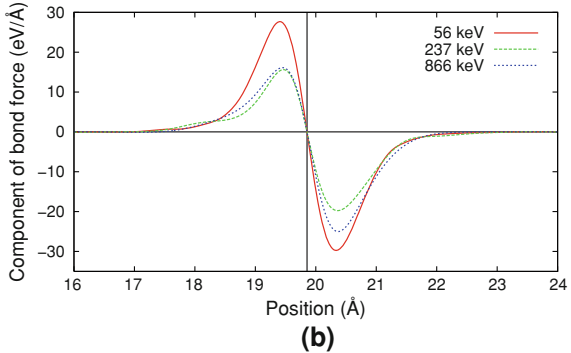
Fig. 10.27 a The bond-order between the channelling ion and a nearest-neighbour at a saddle point as a function of the channelling ion position. The bond-order is shown for a series of equivalent neighbours along the ion path (shifted by an appropriate multiple of lattice vectors so that they coincide). The results displayed correspond to the maximum charge response for a non-self-consistent simulation (U=0) at 237 keV. **b** The variation of the charge on the channelling ion as a function of its position in the same simulations. The saddle points are marked by *vertical lines*

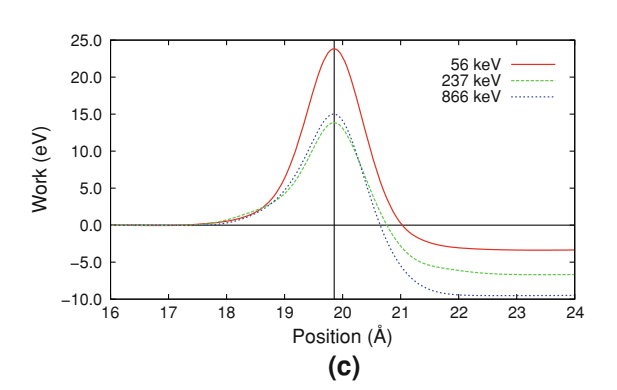
vertical line. Figure 10.27b shows the increasing excess of electrons on the channelling ion, resulting from occupation of the anti-bonding state, for comparison.

In Fig. 10.28a we show the variation of the bond-order as the channelling ion passes a nearest-neighbour (the point of closest approach is marked by a vertical line) after the steady state has been established. Data are shown for a simulation below the charge resonance, at the peak charge response and at a high velocity beyond the resonance. We can see that the bond-order is significantly suppressed

Fig. 10.28 The evolution of a the nearest-neighbour bondorder, b the projection of the bond force onto the ion velocity, and c the work done by that force, around a saddle point in the channelling ion path. Data are shown for simulations with U=0 at a velocity below the charge resonance (56 keV), at the resonance (237 keV) and beyond the resonance 866 keV







at the peak charge response, recovering at the higher velocity. Note also that the higher the velocity, the greater the lag in the bonding response; it is this increasing lag that gives an increasing stopping power even as the bond-order decreases into the charge resonance. Also shown are the component along the velocity of the force between the channelling ion and its neighbour (Fig. 10.28b) and the work done by this force (Fig. 10.28c).

One final feature remains to be explained: in Fig. 10.25a we see that the enhancement of the charge on the channelling ion has a well-defined finite width. In contrast, the bond-orders in Fig. 10.28a are reduced at the onset of the charge enhancement but recover only slightly at the highest velocities. To explain this we recall that the finite width of the charge feature is defined by the velocity at which charge delocalizing transitions (of type (B) in Fig. 10.8) become active. Whilst these transitions act in *opposition* to those charge localizing transitions of type (A) in respect of the charge on the channelling ion, they have *the same* effect on the stopping power. Transitions of type (B) involve excitations out of the localized low energy defect state and into delocalized states above the Fermi level. Because the low energy defect state is *bonding* in character, the effect of transitions of type (B), like those of type (A) is to reduce the bond-orders between the channelling ion and its neighbours (though the effect of type (B) transitions is less strong than those of type (A), because the low energy defect state is less localized than the high energy defect state).

10.3.4 Effect of Onsite Charge Self-Consistency

Now we will consider the effect of the on-site charge self-consistency parameter U on the variation of stopping power with channelling ion velocity, as depicted in Fig. 10.23. The main feature that we wish to explain is the large drop in stopping power coincident with the charge accumulation feature that occurs in the case of large U. This is different in character to the 'knee' in the stopping power in the case of U = 0, in that it has a finite width.

Once again, since the forces in our tight-binding model can always be written in terms of products of bond-orders and gradients of hopping integrals, an analysis of the bond-orders from our small-scale channelling simulations should be informative. Figure 10.29a shows the bond-orders between the channelling ion and a series of equivalent nearest neighbours along the channel as the steady state charge is approached for a simulation at the maximum in the charge resonance for U=50. Comparing this with Fig. 10.27a, we can see that the suppression of the bond-orders when the high energy defect state becomes occupied is much more dramatic at high U.

In Fig. 10.30a we show the variation of the bond-order as the channelling ion passes a nearest-neighbour in the steady state. Once again data are shown for a simulation below the charge resonance, at the peak charge response and at a high velocity beyond the resonance, and as in the U=0 case there is a significant suppression of the bond-order at the resonance. In contrast with the U=0 case,

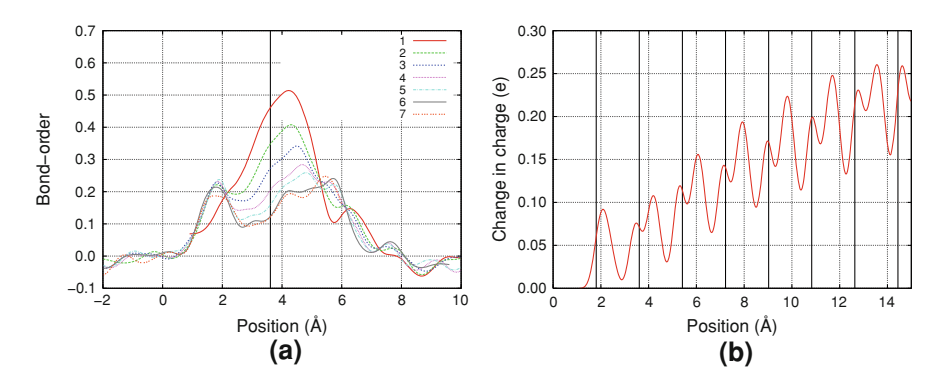


Fig. 10.29 a The bond-order between the channelling ion and a nearest neighbour at a saddle point as a function of the channelling ion position. The bond order is shown for a series of equivalent neighbours along the ion path (shifted by an appropriate multiple of lattice vectors so that they coincide). The results displayed correspond to the maximum charge response for a charge self-consistent simulation (U=50) at 749 keV. **b** The variation of the charge on the channelling ion as a function of its position in the same simulations. The saddle points are marked by *vertical lines*

however (see Fig. 10.28a) the recovery of the bond-order at velocities beyond the charge feature is much more complete. This suggests that some extra mechanism is leading to an extra suppression of the bond-orders over a finite range of velocities, in addition to that proposed to explain the stopping power 'knee' at U = 0. Figure 10.30b, c shows the component of the force acting on the ion parallel to its velocity and the work done by that force respectively.

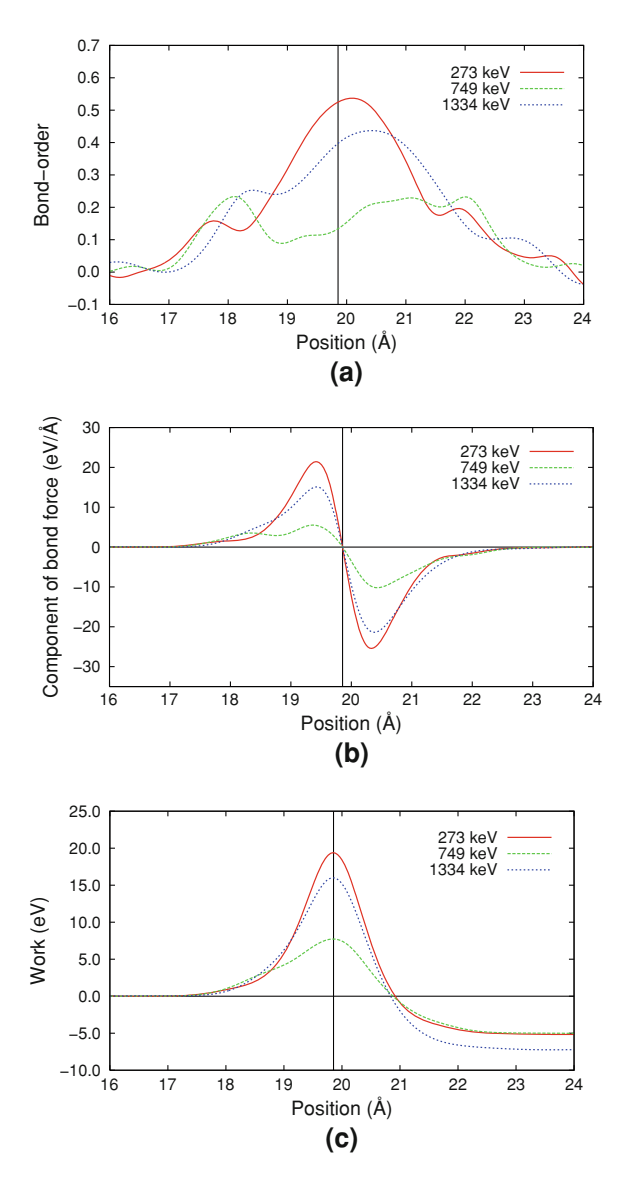
In Fig. 10.31 we have aggregated information about the nearest-neighbour bond-orders in our simulations, to highlight the effect of velocity and of U on the stopping power via the mechanisms discussed above. At the charge resonance we can see that the maximum value of the bond-orders is suppressed and much more strongly so in the case where U=50. In both cases we see the underlying mechanism for the increase in stopping power with velocity: the position of the maximum bond-order relative to the point of closest approach shows an increasing lag with increasing velocity, giving a greater asymmetry in the bonding force and increasing the net work done by the atom against this force in passing its neighbour.

10.3.4.1 A *U*-Dependent Mechanism for Suppressing the Bond-Orders

To see how a large U could affect the bond-orders we will consider a simple model system as an analogue of our channelling ion. We define a Hamiltonian \hat{H}^0 to represent the channelling system before any charge has been excited into the high-energy defect state,

$$\hat{H}^{0} = \sum_{I,J \neq I} |I\rangle \gamma \langle J| + |\mathbf{n}\rangle \Gamma \langle \mathbf{c}| + |\mathbf{c}\rangle \Gamma \langle \mathbf{n}| + |\mathbf{c}\rangle U(q^{0})^{2} \langle \mathbf{c}|, \qquad (10.33)$$

Fig. 10.30 The evolution of a the nearest-neighbour bondorder, b the projection of the bond force onto the ion velocity, and c the work done by that force, around a saddle point in the channelling ion path. Data are shown for simulations with U = 50 at a velocity below the charge resonance (273 keV), at the resonance (749 keV) and beyond the resonance 1334 keV



where $|I\rangle$, $|J\rangle$ are the atomic orbitals on the ions of the lattice, $|c\rangle$ is the orbital on the channelling ion and $|n\rangle$ is the orbital on the nearest-neighbour of the channelling ion (we represent only one neighbour explicitly, though in reality there will be several near-neighbours). γ is the hopping integral in the lattice and Γ is the much larger hopping integral between the channelling ion and its neighbour. q^0 is the quasistatic excess charge on the channelling ion. We will denote the eigenstates of this Hamiltonian by $\{|\phi_i\rangle\}$ except that we consider two special states, $|\phi_B\rangle$ and $|\phi_A\rangle$, the bonding and anti-bonding localized defect states respectively.

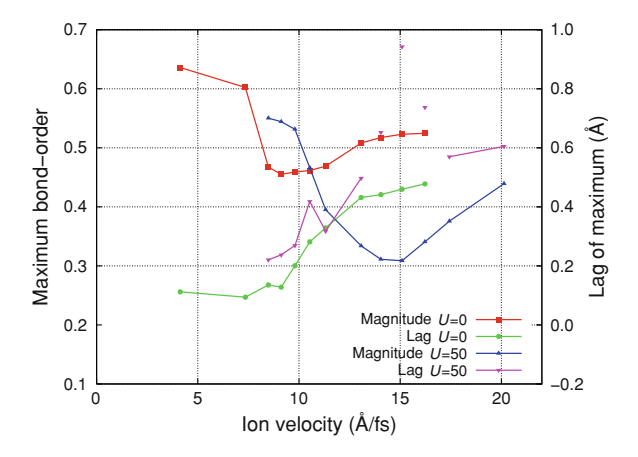


Fig. 10.31 An analysis of the behaviour of the bond-order between a channelling ion and its nearest neighbour at a saddle point in the channel in the steady state. Data are shown as a function of velocity for U = 0 and U = 50. On the left-hand axis we plot the maximum value of the bond-order. On the right-hand axis we show the position of this maximum relative to the point of close approach (the 'lag'). Lines are to guide the eye and we omit the guideline for part of the lag data for U = 50 where the bond-order is so heavily suppressed that the position of its maximum is ill-defined

These states appear in our model because $\Gamma \gg \gamma$. Initially we assume that the bonding state $|\phi_{\rm B}\rangle$ is fully occupied, some lowest lying fraction of the states $\{|\phi_i\rangle\}$ are occupied and the anti-bonding state $|\phi_{\rm A}\rangle$ is unoccupied.

Now we consider what happens at the resonance. First we assume δq electrons are excited from states $\{|\phi_i\rangle\}$ into the anti-bonding state $|\phi_A\rangle$. This has the effect of localizing charge on the channelling ion, which, because of the finite U, increases the onsite term in the Hamiltonian and gives us an effective perturbation,

$$\hat{V} = |\mathbf{c}\rangle\Delta\langle\mathbf{c}|, \qquad \Delta = U[q^2 - (q^0)^2]$$
 (10.34)

where q is the new charge on the channelling ion. We are going to ignore the subtlety that arises because this perturbation will then affect the projections of the eigenstates onto the channelling ion which will in turn affect the charge, requiring a self-consistent solution and instead claim that the new charge q is the one resulting from a self-consistent solution (we are about to make harsher approximations than this, in any case).

Now we will assume that $q-q^0$ is sufficiently small that \hat{V} can be treated perturbatively. The essence of our model is that the additional onsite energy on the channelling ion will now cause a 'mixing' of the eigenstates of \hat{H} . From time-independent perturbation theory we can say that the bonding state will become

$$|\phi_{\rm B}'\rangle = |\phi_{\rm B}\rangle + \sum_{i} \frac{\langle \phi_{i} | c \rangle \Delta \langle c | \phi_{\rm B} \rangle}{\varepsilon_{\rm B} - \varepsilon_{i}} |\phi_{i}\rangle + \frac{\langle \phi_{\rm A} | c \rangle \Delta \langle c | \phi_{\rm B} \rangle}{\varepsilon_{\rm B} - \varepsilon_{\rm A}} |\phi_{\rm A}\rangle. \tag{10.35}$$

Now we will assume that since only the bonding and anti-bonding states have a significant projection onto the channelling ion we can write the perturbed bonding state as,

$$|\phi_{\rm B}'\rangle \approx |\phi_{\rm B}\rangle + \frac{\langle \phi_{\rm A}|c\rangle \Delta \langle c|\phi_{\rm B}\rangle}{\varepsilon_{\rm R} - \varepsilon_{\rm A}} |\phi_{\rm A}\rangle,$$
 (10.36)

and by similar reasoning, the perturbed anti-bonding state as,

$$|\phi_{\rm A}'\rangle \approx |\phi_{\rm A}\rangle + \frac{\langle \phi_{\rm B}|c\rangle \Delta \langle c|\phi_{\rm A}\rangle}{\varepsilon_{\rm A} - \varepsilon_{\rm B}} |\phi_{\rm B}\rangle.$$
 (10.37)

The onsite perturbation due to the localization of charge on the channelling ion thus mixes the bonding and anti-bonding states together. This will cause a change in the bond-order between the channelling ion and its neighbour given by,

$$\Delta \rho_{\rm cn} = 2 \left| \frac{\langle \phi | \mathbf{c} \rangle \Delta \langle \mathbf{c} | \phi \rangle}{\varepsilon_{\rm A} - \varepsilon_{\rm B}} \right|^2 (\langle \mathbf{c} | \phi_{\rm A} \rangle 2 \langle \phi | \mathbf{n} \rangle + \langle \mathbf{c} | \phi \rangle \delta q \langle \phi_{\rm B} | \mathbf{n} \rangle), \tag{10.38}$$

where we have assumed for notational simplicity that the eigenstates are real. Since ϕ_A is strongly anti-bonding we can write $\langle c|\phi_A\rangle\langle\phi_A|n\rangle=-0.5$ and since ϕ_B is strongly bonding, $\langle c|\phi_B\rangle\langle\phi_B|n\rangle=0.5$. Hence we have a change in bond-order,

$$\Delta \rho_{\rm cn} = \left| \frac{\langle \phi_{\rm B} | {\rm c} \rangle \Delta \langle {\rm c} | \phi_{\rm A} \rangle}{\varepsilon_{\rm A} - \varepsilon_{\rm B}} \right|^2 (\delta q - 2), \tag{10.39}$$

a negative change as required.

10.4 Conclusions

We have undertaken simulations of ion channelling in our simple tight-binding model metal to investigate the non-adiabatic electronic effects. We found that at lower velocities ($v \lesssim 6 \, \text{Å fs}^{-1}$) the stopping power (the non-adiabatic electronic force) on the channelling ion is roughly proportional to velocity in accordance with theories of slow ion stopping.

We also examined the steady state average charge on the channelling ion and found a resonant enhancement of the negative charge over a finite range of velocities. We attributed this enhancement to the velocity-dependent excitation of electrons into a high energy defect state localized on the channelling ion. First order time-dependent perturbation theory verifies our explanation (Sect. 10.2.2) and a simple toy model demonstrates that the features of the resonance are dependent on a few well-defined characteristics of the local density of states on the channelling ion (Sect. 10.2.2.2). We were able to extend our explanation of the resonance to explain the changes in the size and position of the charge enhancement with variation of the charge self-consistency parameters U and V (Sect. 10.2.4).

When we examined the stopping power at higher velocities, we found a 'knee' in the linear relationship when U = 0. This 'knee' coincides with the onset of the charge resonance and we explained its existence by noting that the high energy

defect state that is occupied over the width of the resonance is anti-bonding in character and so suppresses the bond-orders (Sect. 10.3.3). This accounts for the reduction in stopping at higher velocities given the nature of the stopping mechanism within the tight-binding approximation (Sect. 10.3.2).

At high U we found a significant trough in the stopping power over the width of the charge resonance (Sect. 10.3.4) and we attributed this to a further suppression of the bond-orders between the channelling ion and its neighbours due to the action of the significant onsite energy that arises when the negative charge on the channelling ion is enhanced. This onsite addition to the Hamiltonian causes a mixing of the defect states localized on the channelling ion, reducing the bonding character of the fully occupied lower energy state and hence reducing the bond orders (Sect. 10.3.4.1).

How significant are our results? What we have found are some interesting effects at low channelling velocity. The emergence of these effects in a simulation requires both an explicit treatment of the ionic positions (so that the extreme nature and periodic variation of the local environment of the channelling ion is captured) and a quantum mechanical model of the electrons (so that the required features of the local density of states are present) and so our time-dependent tight-binding approach is one of the few ways currently available to explore such phenomena. We are, however, using only a simple model metal and so we must question the transferability of our results to real materials. Calculations using the density functional theory code VASP [2] carried out by D. R. Mason for unrelaxed tetrahedral defects in a number of transition metals suggest that the required localized defect states might exist. The position of such states relative to the Fermi level would then determine whether we would expect to see a resonant enhancement or depletion of the number of electrons on a channelling ion and over what velocity range it would occur.

Certainly ion channelling is an important mechanism in radiation damage both where it is undesirable (such as in nuclear reactor environments) and where it is intended (such as in processes of materials modification by ion implantation). Our results suggest that any simple damping model of the stopping power acting on a channelling ion will tend to over-estimate the stopping over a range of velocities when resonant charge effects are possible. Any simulations making use of such a damping model will then tend to under-estimate the range of such ions. Whether such mis-estimation is of consequence will, of course, depend on the magnitude of the phenomenon and the sensitivity to error in the application of the model.

References

- Pruneda, J.M., Sanchez-Portal, D., Arnau, A., Juaristi J.I., Artacho E.: Electronic stopping power in lif from first principles. Phys. Rev. Lett. 99(23), 235501 (2007)
- Kresse, G., Hafner, J.: Ab initio molecular dynamics for liquid metals. Phys. Rev. B 47, 558– 561 (1993)

Chapter 11 The Electronic Drag Force

Summary: In this chapter we return to our study of non-adiabatic effects on the forces in collision cascades. In this case we examine the behaviour of the nonadiabatic force on the moving ions. Various attempts have been made to capture the effects of such forces in classical MD simulations by adding a drag force to the ionic dynamics. Our time-dependent tight-binding simulations give us direct access to information about these forces and so we use a set of cascade simulations to assess the validity of simple drag models. By considering the origin of the nonadiabatic force within a tight-binding picture we are able to propose a new classical model for the non-adiabatic force; one which can be easily incorporated within a classical MD scheme at near zero computational cost. We evaluate the performance of our model using simulation data and find that it is a significant improvement over simple damping models. In particular, it is able to replicate the non-adiabatic energy loss from ions at the individual ion level and over times that are short on the time-scale of individual collision events, and able to capture the variation of the individual cartesian components of the non-adiabatic force. This should be contrasted with the simple damping models, which can only replicate the average energy loss at the level of a whole cascade and over much longer time-scales, and which are explicitly constrained to apply forces in opposition to the ionic velocities.

Attribution: The simulations discussed in Sect. 11.1.1 undertaken by J. le Page and analysed by J. le Page and D. R. Mason in collaboration with the present author.

At the beginning of Chap. 9 we identified two possible effects of electronic excitations on the forces between the ions. The second effect, the tendency of accumulated excitations to weaken the bonding-forces between the ions, we dealt with in that chapter. Now we will consider the first identified effect: that of the finite response time of the electronic system to changes in the electronic Hamiltonian (i.e. in response to the movement of the ions). We will refer to the corresponding forces on the ions as *non-adiabatic forces*.

Attempts to capture within classical MD simulations the effect of the retarded response of the electrons rely on the introduction of additional forces. Such models were discussed in the introductory review in Sects. 3.4.2.1 and 3.4.2.2, but in general the non-adiabatic force on the *I*th ion can be written

$$\mathbf{F}_I' = -\beta_I \dot{\mathbf{R}}_I + \boldsymbol{\eta}_I(t), \tag{11.1}$$

where $\dot{\mathbf{R}}_I = \mathrm{d}\mathbf{R}_I/\mathrm{d}t$ is the velocity of the *I*th ion. The term $\eta_I(t)$, if present, normally takes the form of a stochastic force [1], which may be dependent on some local measure of electronic excitation [2, 3], and is designed to represent the return of energy from ions to electrons. The first term, $-\beta_I \dot{\mathbf{R}}_I$, represents a drag force on the ions. This force is explicitly opposed to the velocity of the ions. Furthermore, though we have indicated that the damping coefficient β_I may vary from ion to ion, it is normally taken to be a constant [4–7] or at most to have a dependence on some measure of the local electron density [1].

11.1 Is a Simple Drag Model Good Enough?

The choice of a simple drag force to represent the non-adiabatic electronic force on the ions essentially derives from the theory of the stopping of slow particles (see Sect. 3.2.5). Such theories predict that the rate of energy loss of slow particles moving through some stopping medium will be proportional to the square of the velocity, consistent with a force on the particles proportional to and directly opposed to their velocities. These stopping power theories are strongly supported by the available experimental data, but we must bear in mind the nature of those data. Experimentalists only have access to fairly high level information about the development of cascade events and so the experimental validation of any model for the non-adiabatic forces will be very much on an *average* basis, commonly as an average over the path of an individual ion down an ion channel or through many collisions in a damage cascade. Experiment can give us no microscopic details of the behaviour of the non-adiabatic force.

If we look again at the results of our simulations of a single-oscillating ion in our tight-binding metal (see Fig. 6.4), we see that the rate of energy transfer to the electrons (here expressed as an effective damping coefficient consistent with the simple classical models) is strongly dependent on the position and direction of the oscillator. We therefore expect that the non-adiabatic force will, in detail, have a complex structure, dependent on velocity and local atomic environment.

11.1.1 An Investigation of Damping Models for Total Energy Loss in Collision Cascades

Our framework for time-dependent tight-binding simulations gives us the opportunity of examining the non-adiabatic force in detail and of assessing the validity

of simple damping models from a theoretical perspective. Before we undertake a more detailed analysis we will briefly discuss the results of some simulations undertaken by J. le Page and analysed by J. le Page and D. R. Mason in collaboration with the present author. More details can be found in [8, 9].

A set of 240 cascades in 2,016 atom zero-temperature super-cells with PKA velocities in 24 different directions for each of ten PKA kinetic energies evenly distributed between 100 eV and 1 keV were simulated for 200 fs and the non-adiabatic energy transfer, which we will denote $\Delta E_{\rm Ehr}(t)$, recorded every 5 fs. By taking the histories of the ion positions and velocities, we are able to calculate the energy transfer,

$$\Delta E_{\text{model}}(t) = \sum_{I} \int_{0}^{t} dt' \, \beta_{I}(t') |\dot{\mathbf{R}}_{I}(t')|^{2}$$
(11.2)

that would have been predicted by various classical models for β_I in the literature for each cascade *if the ions had followed the same trajectories*. The final qualification is important, because, of course, any force model that differed even slightly from the Ehrenfest forces within our simulations would give rise to a different set of ion trajectories. By comparing $\Delta E_{\rm Ehr}(t)$ and $\Delta E_{\rm model}(t)$ we can obtain a measure of the plausibility of the various models that we test.

We have chosen to test three models:

- 1. A simple damping constant applied to all ions at all velocities, $\beta_I(t) = \beta$, equivalent to the zero electronic temperature limit of the model due to Finnis et al. [10] and applied in [11] for example.
- 2. A simple damping constant applied only to ions with a kinetic energy greater than 10 eV:

$$\beta_I(t) = \beta \qquad \frac{1}{2} M_I |\dot{\mathbf{R}}_I|^2 \ge 10 \,\text{eV}$$

$$= 0 \qquad \text{otherwise.}$$
(11.3)

Nordlund et al. [5] have implemented a scheme of this kind. No thorough justification for the cut-off is given in the literature, but it is generally understood to ensure that the damping force does not cool the ions to 0 K.

3. A model in which the damping coefficient is a function of the local electron density within an embedded atom model. This model was proposed by Caro and Victoria [1] and made use of, for example, in [12].

Figure 11.1 shows our results at two PKA energies for the energy transfer in the three classical models compared to that in our Ehrenfest simulations as a function of time. If a model perfectly replicated the effect of the non-adiabatic force in our simulations all the data-points would lie on a line of gradient 1. Models 1 and 3 perform well, but the data for model 2 clearly show that the cut-off in the application of the damping force is not helpful; our simulations suggest significant energy transfer from ions with kinetic energies below 10 eV.

Our simulation data allow us to calculate the best-fit damping coefficients within each of the models under test, corresponding to the non-adiabatic force in

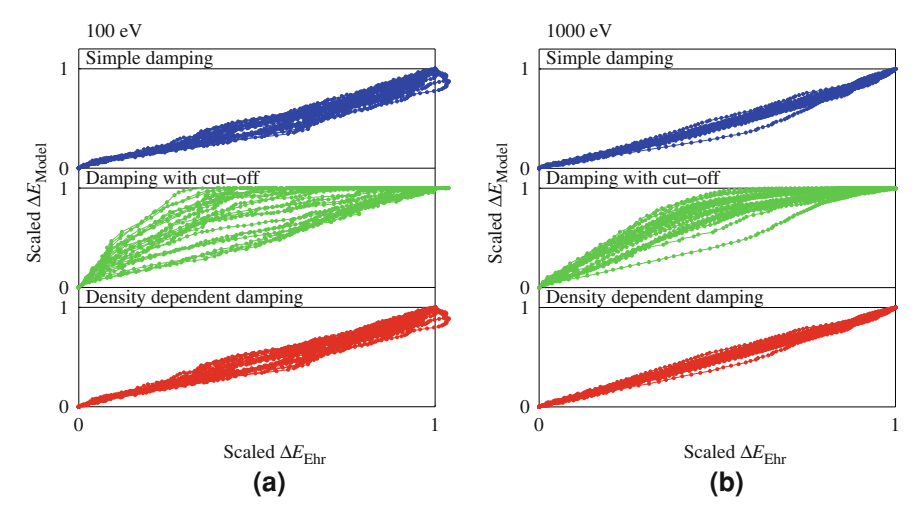


Fig. 11.1 Scatter plots of the irreversible energy transfer calculated by three different classical models against the energy transfer found in simulations with Ehrenfest dynamics. **a** Data for all 24 initial PKA directions for a kinetic energy of 100 eV. **b** The same for initial kinetic energy 1,000 eV. The data are scaled by the energy transfer found by each method at 200 fs, so that a perfect match between a classical method and the Ehrenfest results would appear as a straight line of gradient 1. Models 1 (simple damping—*top panels*) and 3 (density-dependent damping—*bottom panels*) are closest to linear, indicating that they best reproduce the Ehrenfest energy transfer. Model 2 (damping with cut-off—*middle panels*) fails to capture the energy loss from slow moving ions

our time-dependent tight-binding simulations. Figure 11.2a shows the average damping coefficient at each PKA energy with the standard deviation across the different PKA directions indicated by the error bars. We note the following:

- 1. The absolute values of the damping coefficient should not be compared between models, because of the different nature of each model.
- 2. At each energy we have treated the simulations in which the PKA initial velocity is directed along the close-packed (110) direction separately. As the computed damping coefficients for model 1 show, the energy transfer to electrons when the ions form a replacement collision sequence (RCS) is enhanced by a factor of between 2 and 3. The density dependent damping (model 3) does a much better job of capturing this difference automatically. Note that the apparent good performance of the damping model with a cut-off (model 2) in this respect is simply fortuitous: because the model ignores the energy transfer from slower ions, the average damping coefficient is pushed up closer to the value required to capture the energy transfer from an RCS.
- 3. The damping coefficient does not vary much as a function of PKA energy. This might be taken as an indication that the damping coefficient has at most a weak dependence on particle velocity (the models assume velocity independence),

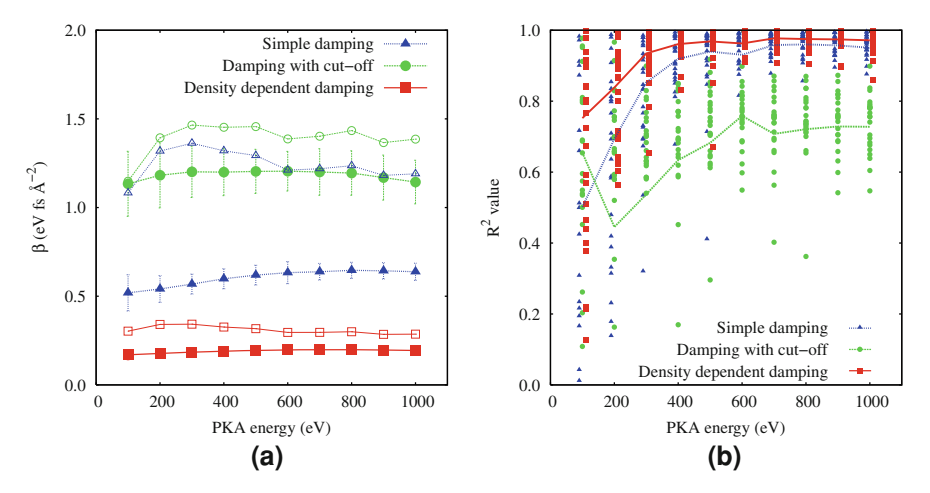


Fig. 11.2 a The damping coefficient as a function of PKA energy calculated for each of the three classical models under test. The *larger solid symbols* are an average across all PKA directions except for the $\langle 110 \rangle$ direction. Best-fit damping coefficients for the simulations in the $\langle 110 \rangle$ direction are shown by *smaller open symbols*. *Lines* are included as a guide for the eye. **b** R^2 measures of goodness of fit for the three classical models under test. Each data-point represents one cascade simulation. The lines join the averages of the R^2 values for each model at each PKA energy (simulations in the $\langle 110 \rangle$ directions are excluded) and provide a guide for the eye

but we must remember that the initial PKA energy is rapidly distributed amongst many ions in a cascade and so the moving ions in a cascade may have similar velocity distributions at all PKA energies explored.

In Fig. 11.2b we have applied the mean best-fit damping coefficient to the data from each simulation to calculate the R^2 goodness of fit statistics for each of the models. Each data-point represents a single simulation. Once again, we see that our results do not justify the use of a kinetic energy cut-off in the application of the damping (model 2 shows the least good fit) and that they indicate that a density dependence (model 3) improves the fit.

11.2 The Microscopic Behaviour of the Non-Adiabatic Force

11.2.1 The Non-Adiabatic Force in Ehrenfest Dynamics

The results above suggest that simple damping models can do a good job of capturing the irreversible energy transfer from ions to electrons over the course of a collision cascade. This energy transfer is equal to the work done by the non-adiabatic forces and so we can reasonably conclude that a simple damping is a valid model for the *average* non-adiabatic force as an *average* over all atoms and over the duration of a cascade. This validation of the models on

average reflects the extent to which stopping power theories are validated by experimental data.

But with our Ehrenfest dynamics simulations we can go further. In Chap. 9 we took the electronic force,

$$\mathbf{F}_{e} = -\text{Tr}(\hat{\rho}\nabla_{\mathbf{R}}\hat{H}),\tag{11.4}$$

where $\mathbf{R} = \{\mathbf{R}_I\}$ represents the position coordinates of all the ions, and wrote it in the basis of instantaneous eigenstates $\{|\phi_i\rangle\}$ of the electronic Hamiltonian, with energies $\{\varepsilon_i\}$, to obtain (9.4),

$$\mathbf{F}_{e} = -\sum_{i} \rho_{ii} \nabla_{\mathbf{R}} \varepsilon_{i} - \sum_{i,j \neq i} (\varepsilon_{i} - \varepsilon_{j}) \, \rho_{ij} \langle \phi_{j} | \nabla_{\mathbf{R}} \phi_{i} \rangle. \tag{9.4}$$

 $\rho_{ij} = \langle \phi_i | \hat{\rho}(t) | \phi_j \rangle$ and we have split out the forces due to the diagonal and off-diagonal elements of the density matrix. The rate at which work is done on the electrons by this force as a result of the ionic motion is,

$$\frac{\mathrm{dW}}{\mathrm{d}t} = -\mathbf{F}_{\mathrm{e}} \cdot \dot{\mathbf{R}}
= \sum_{i} \rho_{ii} (\nabla_{\mathbf{R}} \varepsilon_{i} \cdot \dot{\mathbf{R}}) + \sum_{i, j \neq i} (\varepsilon_{i} - \varepsilon_{j}) \rho_{ij} \langle \phi_{j} | \nabla_{\mathbf{R}} \phi_{i} \rangle \cdot \dot{\mathbf{R}},$$
(11.5)

where $\dot{\mathbf{R}} = d\mathbf{R}/dt$. Since,

$$\nabla_{\mathbf{R}}\varepsilon_i \cdot \dot{\mathbf{R}} = \frac{\mathrm{d}\varepsilon_i}{\mathrm{d}t},\tag{11.6}$$

and,

$$|\nabla_{\mathbf{R}}\phi_i\rangle \cdot \dot{\mathbf{R}} = \frac{\mathrm{d}}{\mathrm{d}t}|\phi_i\rangle \tag{11.7}$$

this power into the electrons can be rewritten,

$$\frac{\mathrm{dW}}{\mathrm{d}t} = \sum_{i} \rho_{ii} \frac{\mathrm{d}\varepsilon_{i}}{\mathrm{d}t} + \sum_{i,i \neq i} (\varepsilon_{i} - \varepsilon_{j}) \, \rho_{ij} \langle \phi_{j} | \left(\frac{\mathrm{d}}{\mathrm{d}t} | \phi_{i} \rangle \right). \tag{11.8}$$

In Sect. 13.1.15 we show that we can rewrite the second term to give a final expression for the power,

$$\frac{\mathrm{dW}}{\mathrm{d}t} = \sum_{i} \rho_{ii} \frac{\mathrm{d}\varepsilon_{i}}{\mathrm{d}t} + \sum_{i} \frac{\mathrm{d}\rho_{ii}}{\mathrm{d}t} \varepsilon_{i}. \tag{11.9}$$

This result makes clear the origins of the two terms in the expression for \mathbf{F}_{e} above. The first term represents the forces due to motion on a collection of adiabatic energy surfaces defined by the instantaneous eigenvalues $\{\varepsilon_{i}(\mathbf{R})\}$ weighted by the diagonal elements of the density matrix in the instantaneous eigenstate basis, ρ_{ii} . The non-adiabatic force in the second term is what gives rise to the

irreversible transfer of energy into the electrons. It is the work done by this term that appears in excitations, manifest in the instantaneous eigenstate basis as changes in the diagonal elements of the density matrix.

11.2.2 The Character of the Non-Adiabatic Force

The latest version of our simulation software splCED is able to output the non-adiabatic force, which we will henceforth denote \mathbf{F}^{NAd} ,

$$\mathbf{F}^{\text{NAd}} = -\sum_{i,j \neq i} (\varepsilon_i - \varepsilon_j) \, \rho_{ij} \langle \phi_j | \nabla_{\mathbf{R}} \phi_i \rangle, \tag{11.10}$$

on a per ion basis. Obtaining data on $\mathbf{F}^{\mathrm{NAd}}$ can be computationally costly, because it requires a direct diagonalization of the electronic Hamiltonian (an N^3 operation), but it is possible to get such data with reasonable frequency for small simulation cells. Much of the remaining analysis in this chapter is based on data obtained from a set of 24 cascade simulations carried out in 2,016 atom super-cells, with a 1 keV PKA given an initial velocity in 24 evenly distributed directions. The simulations were carried out in a perfect static lattice in order to isolate the effects of energy transfer from cascade atoms from the excitations due to the thermal motion of ions outside the cascade. At the chosen system size, it is possible to obtain the non-adiabatic force every 0.05 fs for \sim 25 fs of simulation time in 72 h on a single processor. Even this short simulation time is enough to generate a statistically valid sample of collision events and ion trajectories over our set of cascade simulations.

But first, as a simple demonstration of the behaviour of the non-adiabatic force, we will examine data from a set of 24 cascade simulations with 1 keV PKA energies running for 200 fs. Considering each ion in each simulation once every femtosecond to provide a separate data-point, we can bin the data according to the ion kinetic energy and the cosine of the angle between the non-adiabatic force on the ion and its velocity, i.e.

$$\cos \theta = \frac{\mathbf{F}^{\text{NAd}} \cdot \dot{\mathbf{R}}}{|\mathbf{F}^{\text{NAd}}||\dot{\mathbf{R}}|}.$$
 (11.11)

Figure 11.3a shows this information. We can see that at higher kinetic energies the non-adiabatic force has a tendency to oppose the velocity, but that there is certainly a significant variation in the direction and the correlation between the directions is all but gone for ions below 10 eV. For comparison, Fig. 11.3b shows the same plot but for the *adiabatic force* (i.e. that force that the ions would experience if they traversed their paths infinitely slowly). The fact that strong correlation also exists between the direction of this force and the velocity suggests that even such correlation that we do see for the non-adiabatic force may be a consequence of the pattern of ionic motion in a collision cascade rather than because of some fundamental physical reason for the non-adiabatic force to oppose the velocity.

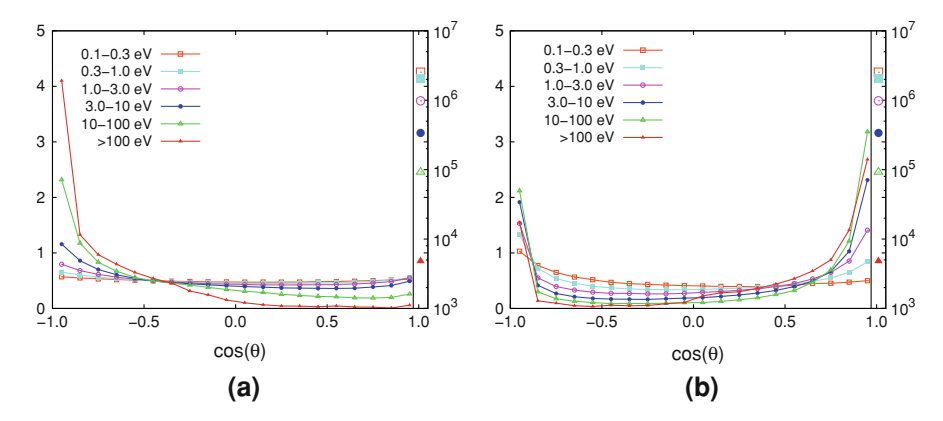


Fig. 11.3 Histogram data for the angle between electronic forces on the ions and their velocities. Data are broken out by ion kinetic energy. Shown are data for **a** the non-adiabatic force and **b** the adiabatic force, as discussed in the text. The *symbols* against the right-hand axis indicate the number of data-points in each line in the plots

11.3 An Improved Model of the Non-Adiabatic Force

The above discussions clearly show that the non-adiabatic force acting on an ion does not, in general, directly oppose its motion. This suggests that it might be possible to find a classical model for the non-adiabatic force that improves on the simple damping models examined in Sect. 11.1.1. At a minimum, we might hope for a model that improves the predictions of the irreversible energy transfer from ions to electrons. But we might also hope to capture some detail of the direction and magnitude of the non-adiabatic force at the atomic level and on the time-scale of individual inter-atomic interactions within the cascade. Our aim should not be to reproduce the Ehrenfest trajectories *exactly*, since that would be to focus incorrectly on the microscopic details of our simulations, but we should be concerned to ensure that any model of the non-adiabatic force reproduces the correct statistical behaviour of a cascade. As such, a model that correctly captured some details of the Ehrenfest non-adiabatic force might do a better job by, for example, ensuring that the relative rates of energy loss from different modes of ionic motion (such as replacement collision sequences as compared to glancing collisions) were correctly captured.

In this section we will take our expression (11.10) for the non-adiabatic force and derive a new classical model that we hope will improve upon a simple damping coefficient.¹

¹ A derivation of this model is given in [13].

11.3.1 A "Non-Adiabatic Bond Model"

The central concept of our proposed model is that the non-adiabatic force on an ion arises because of a lag in the bonding response of electrons to ionic motion. When two ions move into close proximity it takes a finite time for a bond to form. We discussed just this phenomenon when we considered the stopping force on a channelling ion in Sect. 10.3.2. Our derivation of our model will include some "arm-waving" arguments, but we hope that it remains plausible and, in any case, we will test it against data from our Ehrenfest dynamics simulations.

We start with the non-adiabatic force

$$\mathbf{F}^{\text{NAd}} = -\sum_{i,j \neq i} \langle \phi_i | \hat{\rho} | \phi_j \rangle (\varepsilon_i - \varepsilon_j) \langle \phi_j | \nabla_{\mathbf{R}} \phi_i \rangle, \tag{11.10}$$

and write it (see Sect. 13.1.16)

$$\mathbf{F}^{\text{NAd}} = -\sum_{i,j \neq i} \langle \phi_i | \hat{\rho} | \phi_j \rangle \langle \phi_j | \nabla_{\mathbf{R}} \hat{H} | \phi_i \rangle. \tag{11.12}$$

Recall that \mathbf{R} denotes the collective position coordinates of all the ions in the system and we write the coordinates of the Ith ion as \mathbf{R}_I . For clarity we will now consider the non-adiabatic force on the zeroth ion at position \mathbf{R}_0 . We write this force,

$$\mathbf{f}_{0} = -\sum_{i,j\neq i} \langle \phi_{i} | \hat{\rho} | \phi_{j} \rangle \langle \phi_{j} | \nabla_{\mathbf{R}_{0}} \hat{H} | \phi_{i} \rangle. \tag{11.13}$$

To obtain a force model suitable for inclusion in a classical MD simulation we must tackle two major issues with the above expression for the non-adiabatic force. The first is that it is non-local in time: the off-diagonal elements of the density matrix, evolving under Hamiltonian dynamics, retain a long-term "memory" of the entire evolution of the system. However, we might reasonably expect that the contributions to the off-diagonal elements from different segments of the evolution would not add constructively to the non-adiabatic force at a future time. We are thus motivated to introduce a correlation time-scale τ , over which the history of the system contributes to the non-adiabatic force.²

So we will now assume that the information in the off-diagonal elements in the density matrix relevant to calculation of the non-adiabatic force builds up over a time τ , and so to calculate the force at time t we assume that we can make use of a diagonal density matrix at an earlier time

² In any case we might also regard the long-term memory as a spurious result of the fact that our electronic system is closed in a quantum mechanical sense. In reality there would be some decoherence time-scale, which would also limit the build up of historical information in the density matrix.

$$\hat{\rho}(t-\tau) = \sum_{k} |\phi_k\rangle o_k\langle \phi_k| \tag{11.14}$$

for some set of occupations $\{o_k\}$. We then write $\mathbf{f}_0(t)$ as a Taylor series expansion

$$\mathbf{f}_{0}(t) = \mathbf{f}_{0}(t - \tau) + \frac{d\mathbf{f}_{0}}{dt} \bigg|_{t = \tau} \tau + O(\tau^{2}), \tag{11.15}$$

where $\mathbf{f}_0(t-\tau)$ will be zero given the assumed form for $\hat{\rho}(t-\tau)$. Now, the total time derivative can be written

$$\frac{\mathrm{d}\mathbf{f}_0}{\mathrm{d}t} = \frac{\mathrm{d}\mathbf{f}_0}{\mathrm{d}t} + \nabla_{\mathbf{R}}\mathbf{f}_0 \cdot \dot{\mathbf{R}}, \qquad \dot{\mathbf{R}} = \frac{\mathrm{d}\mathbf{R}}{\mathrm{d}t}, \tag{11.16}$$

and from Eq. 11.13 we obtain,

$$\frac{d\mathbf{f}_{0}}{dt} = -\sum_{i,j\neq i} \left\langle \phi_{i} \left| \frac{d\hat{\rho}}{dt} \right| \phi_{j} \right\rangle \left\langle \phi_{j} | \nabla_{\mathbf{R}_{0}} \hat{H} | \phi_{i} \right\rangle
- \sum_{i,j\neq i} \dot{\mathbf{R}} \cdot \nabla_{\mathbf{R}} \left(\left\langle \phi_{i} | \hat{\rho} | \phi_{j} \right\rangle \right) \left\langle \phi_{j} | \nabla_{\mathbf{R}_{0}} \hat{H} | \phi_{i} \right\rangle
- \sum_{i,j\neq i} \left\langle \phi_{i} | \hat{\rho} | \phi_{j} \right\rangle \dot{\mathbf{R}} \cdot \nabla_{\mathbf{R}} \left(\left\langle \phi_{j} | \nabla_{\mathbf{R}_{0}} \hat{H} | \phi_{i} \right\rangle \right).$$
(11.17)

For diagonal $\hat{\rho}(t-\tau)$, this gives (see Sect. 13.1.17)

$$\mathbf{f}_{0}(t) = \tau \sum_{i,j \neq i} \frac{o_{j} - o_{i}}{\varepsilon_{i} - \varepsilon_{j}} \left(\langle \phi_{i} | \nabla_{\mathbf{R}} \hat{H} | \phi_{j} \rangle \cdot \dot{\mathbf{R}} \right) \langle \phi_{j} | \nabla_{\mathbf{R}_{0}} \hat{H} | \phi_{i} \rangle. \tag{11.18}$$

We now have a time-local force, but the second major issue has become apparent. In the first matrix element in Eq. 11.18 the gradient is taken with respect to the position of all atoms in the system and so our force is not spatially local. This reflects the non-local nature of the density matrix. However, if our correlation time τ is small compared to a typical electron hopping time $\hbar/\langle H \rangle$, where $\langle H \rangle$ is some typical value for the hopping integral in our tight-binding model, then we can hope that a spatially local form of Eq. 11.18 will capture the majority of the non-adiabatic force.

We will now attempt to rewrite the factors in $\nabla_{\mathbf{R}}\hat{H}$ and $\nabla_{\mathbf{R}_0}\hat{H}$ in the basis of local orbitals $\{|\mathbf{R}_I\rangle\}$ where $|\mathbf{R}_I\rangle$ is the orbital on the ion at position \mathbf{R}_I . For the second factor we write

$$\langle \phi_j | \nabla_{\mathbf{R}_0} \hat{H} | \phi_i \rangle = \sum_{II} \langle \phi_j | \mathbf{R}_I \rangle \langle \mathbf{R}_I | \nabla_{\mathbf{R}_0} \hat{H} | \mathbf{R}_J \rangle \langle \mathbf{R}_J | \phi_i \rangle. \tag{11.19}$$

Because only elements of \hat{H} involving $|\mathbf{R}_0\rangle$ depend on \mathbf{R}_0 , this becomes

$$\langle \phi_{j} | \nabla_{\mathbf{R}_{0}} \hat{H} | \phi_{i} \rangle = \sum_{I \in \mathbf{n}_{0}} \langle \phi_{j} | \mathbf{R}_{I} \rangle \langle \mathbf{R}_{I} | \nabla_{\mathbf{R}_{0}} \hat{H} | \mathbf{R}_{0} \rangle \langle \mathbf{R}_{0} | \phi_{i} \rangle$$

$$+ \sum_{J \in \mathbf{n}_{a}} \langle \phi_{j} | \mathbf{R}_{0} \rangle \langle \mathbf{R}_{0} | \nabla_{\mathbf{R}_{0}} \hat{H} | \mathbf{R}_{J} \rangle \langle \mathbf{R}_{J} | \phi_{i} \rangle$$

$$= \sum_{I \in \mathbf{n}_{0}} \nabla_{\mathbf{R}_{0I}} \gamma(\mathbf{R}_{0I}) \{ \langle \phi_{j} | \mathbf{R}_{I} \rangle \langle \mathbf{R}_{0} | \phi_{i} \rangle + \langle \phi_{j} | \mathbf{R}_{0} \rangle \langle \mathbf{R}_{I} | \phi_{i} \rangle \},$$
(11.20)

where n_0 is the set of neighbours of the ion at \mathbf{R}_0 and $\gamma(\mathbf{R}_{0I})$ is the hopping integral between the orbitals $|\mathbf{R}_0\rangle$ and $|\mathbf{R}_I\rangle$, written as a function of their relative positions, $\mathbf{R}_{0I} = \mathbf{R}_I - \mathbf{R}_0$. This second factor, then, is explicitly local and involves a sum over all the bonds between the ion at \mathbf{R}_0 and it neighbours.

For the first factor we write

$$\langle \phi_{i} | \nabla_{\mathbf{R}} \hat{H} | \phi_{j} \rangle \cdot \mathbf{R} = \sum_{IJ} \left(\langle \phi_{i} | \mathbf{R}_{I} \rangle \langle \mathbf{R}_{I} | \nabla_{\mathbf{R}} \hat{H} | \mathbf{R}_{J} \rangle \langle \mathbf{R}_{J} | \phi_{j} \rangle \right) \cdot \dot{\mathbf{R}}$$

$$= \sum_{IJ} \sum_{K} \left(\langle \phi_{i} | \mathbf{R}_{I} \rangle \langle \mathbf{R}_{I} | \nabla_{\mathbf{R}_{K}} \hat{H} | \mathbf{R}_{J} \rangle \langle \mathbf{R}_{J} | \phi_{j} \rangle \right) \cdot \dot{\mathbf{R}}_{K}$$

$$= \sum_{I,J \in \mathbf{n}_{I}} \left\{ \langle \phi_{i} | \mathbf{R}_{I} \rangle \langle \mathbf{R}_{I} | \nabla_{\mathbf{R}_{J}} \hat{H} | \mathbf{R}_{J} \rangle \langle \mathbf{R}_{J} | \phi_{j} \rangle \cdot \dot{\mathbf{R}}_{J} \right\}$$

$$+ \langle \phi_{i} | \mathbf{R}_{I} \rangle \langle \mathbf{R}_{I} | \nabla_{\mathbf{R}_{I}} \hat{H} | \mathbf{R}_{J} \rangle \langle \mathbf{R}_{J} | \phi_{j} \rangle \cdot \dot{\mathbf{R}}_{I} \right\}$$

$$= \sum_{I,J \in \mathbf{n}_{I}} \langle \phi_{i} | \mathbf{R}_{I} \rangle \left\{ \nabla_{\mathbf{R}_{J}} \gamma (\mathbf{R}_{IJ}) \cdot \dot{\mathbf{R}}_{J} + \nabla_{\mathbf{R}_{I}} \gamma (\mathbf{R}_{IJ}) \cdot \dot{\mathbf{R}}_{I} \right\} \langle \mathbf{R}_{J} | \phi_{j} \rangle$$

$$= \sum_{I,J \in \mathbf{n}_{I}} \langle \phi_{i} | \mathbf{R}_{I} \rangle \nabla_{\mathbf{R}_{IJ}} \gamma (\mathbf{R}_{IJ}) \cdot \dot{\mathbf{R}}_{IJ} \langle \mathbf{R}_{J} | \phi_{j} \rangle,$$

$$(11.21)$$

where we have used $\nabla_{\mathbf{R}_J} \gamma(\mathbf{R}_{IJ}) = -\nabla_{\mathbf{R}_J} \gamma(\mathbf{R}_{IJ})$. This factor, reflecting the non-adiabaticity in the density matrix, takes the form of a sum over *all* the bonds in the system. Now we will make our assumption of spatial locality and state that with each term in the sum in Eq. 11.20 we will associate a single term from the double sum in Eq. 11.21. We are then assuming that the non-adiabaticity in the density matrix corresponding to each bond depends only on the rate of change *of that same bond*. To obtain a final expression for the non-adiabatic force we now make the following assumptions:

- 1. The eigenstates involved in the excitations corresponding to the work done by the non-adiabatic force are delocalized and have no particularly strong projection onto any ion. We will thus absorb all factors like $\langle \mathbf{R}_I | \phi_i \rangle$ into a constant of proportionality.
- 2. The state of the electronic system is well-characterized by a low temperature so that $o_i = 1$ if $\varepsilon_i < \varepsilon_F$, for some Fermi energy ε_F , and $o_i = 0$ otherwise.
- 3. The non-adiabatic forces will be dominated by pairs of states close to the Fermi level because of the factor of $1/(\varepsilon_i \varepsilon_j)$. We will choose to write $\varepsilon_i \varepsilon_j = \Delta$, some characteristic eigenvalue spacing.

4. The correlation time τ will be proportional to the local density of states, which in turn is inversely proportional to a typical eigenvalue spacing. We choose to write $\tau \approx 1/\Delta$.

Our expression for the force becomes

$$\mathbf{f}_0 \approx \frac{\chi}{\Delta^2} \sum_{I \in \mathbf{n}_0} \left(\nabla_{\mathbf{R}_{0I}} \gamma(\mathbf{R}_{0I}) \cdot \dot{\mathbf{R}}_{0I} \right) \nabla_{\mathbf{R}_{0I}} \gamma(\mathbf{R}_{0I}), \tag{11.22}$$

where χ is a constant of proportionality. In our tight-binding model the hopping integrals between our *s*-like orbitals are a function of the inter-ionic separation only and so we can write

$$\mathbf{f}_0 \approx \frac{\chi}{\Delta^2} \sum_{I \in \mathbf{n}_0} \left| \gamma'(|\mathbf{R}_{0I}|) \right|^2 \frac{\mathbf{R}_{0I} \cdot \dot{\mathbf{R}}_{0I}}{\left| \mathbf{R}_{0I} \right|^2} \mathbf{R}_{0I}, \tag{11.23}$$

where

$$\gamma'(R) = \frac{\mathrm{d}\gamma(R)}{\mathrm{d}R}.\tag{11.24}$$

If we choose to make a second moment approximation so that

$$\Delta^2 = \sum_{J \in \mathbf{n}_0} \left[\gamma(|\mathbf{R}_{0J}|) \right]^2, \tag{11.25}$$

then we obtain a final model for the non-adiabatic force,

$$\mathbf{f}_{0} \approx \chi \left(\frac{1}{\sum_{J \in \mathbf{n}_{0}} [\gamma(|\mathbf{R}_{0J}|)]^{2}} \right) \sum_{I \in \mathbf{n}_{0}} |\gamma'(|\mathbf{R}_{0I}|)|^{2} \frac{\mathbf{R}_{0I} \cdot \dot{\mathbf{R}}_{0I}}{|\mathbf{R}_{0I}|^{2}} \mathbf{R}_{0I}.$$
(11.26)

This model has several appealing characteristics:

- It is local and could be calculated within a classical simulation with very little cost and no change in the scaling of the simulation time with system size.
- It has intuitive appeal in that it takes the form of a sum over the bonds on a given atom with each bond having a "non-adiabaticity" related to its instantaneous rate of change.
- It bears a clear relationship to the underlying tight-binding model, the effects of whose semi-classical evolution it is intended to mimic. The lack of rigour with which we derived this correspondence not withstanding, this means that a more *quantitatively* accurate model could in principle be derived from a more sophisticated tight-binding model. Of course, we have made no effort to determine a value for the constant χ, but if we desired a quantitatively accurate model this constant could be fitted to some high level experimental measure of the non-adiabatic energy loss, much as the damping coefficients in existing simple drag models are.

• The force given by our model is not in general opposed to the direction of motion of the ion. There is at least some hope, then, that it might reproduce some important detail within the behaviour of the "true" non-adiabatic force.

11.3.2 The Performance of Our Proposed Model

In this section we will present the results of some simulations designed to evaluate the performance of our proposed model for the non-adiabatic force (11.26). We have run 24 cascade simulations for approximately 25 fs, calculating the eigenspectrum and the non-adiabatic force every 0.05 fs. The PKA energy is 1 keV in every simulation and the PKA direction is distributed evenly over the irreducible 1/48th fraction of the fcc unit cell. The simulations take place in an initially perfect super-cell of 2,016 atoms ($9 \times 7 \times 8$ unit cells) with periodic boundary conditions with zero initial ionic kinetic energy. We choose this static lattice condition to eliminate the effects of thermal ions from our results. Figure 11.3 suggests a different behaviour for the lowest energy ions and we would like to investigate them separately.

11.3.2.1 The Irreversible Energy Transfer

Our analysis of the results of these simulations will be the analogue of that discussed in Sect. 11.1.1 where we evaluated some existing classical damping models from the literature. Now, however, we have access to detailed information about the non-adiabatic force and so our data-points for a statistical analysis will be individual atom trajectories rather than whole simulations.

We begin by calculating the work done by the non-adiabatic force in the Ehrenfest simulation over the course of the simulation for each atom individually. We call this $\Delta E_{\rm Ehr}$. We also calculate the work done by the non-adiabatic forces predicted by our proposed model and a simple drag along *the same atomic trajectories*. We will denote these by:

- $\Delta E_{\rm model}$: Our proposed non-adiabatic bond model for the non-adiabatic force in Eq. 11.26.
- ΔE_{drag} : A simple drag model in which a constant drag coefficient is applied to all moving ions. To calculate this we integrate the kinetic energy of each ion along its path so that our force model in the following analysis is effectively,

$$f_0 = -\frac{1}{2}\beta_{\rm drag}M_I\dot{R}_0. \tag{11.27}$$

Considering only those ions whose maximum kinetic energy exceeds 1 eV during the simulation (again to focus on non-adiabatic effects on cascade atoms),

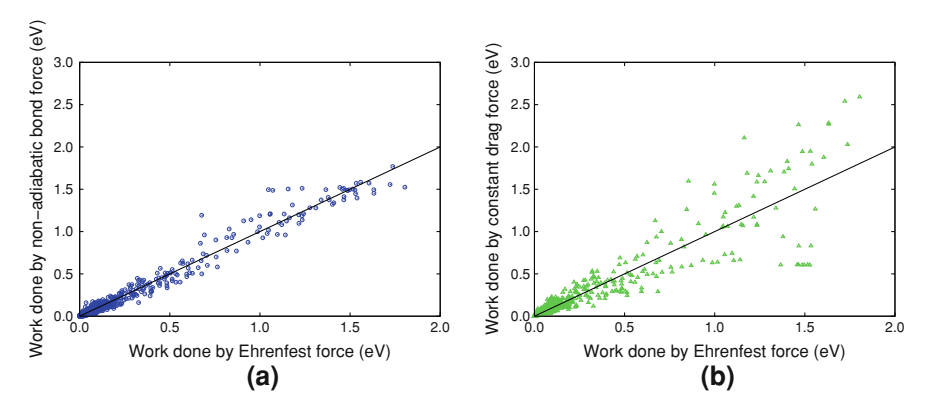


Fig. 11.4 Scatter plots of the work done by the non-adiabatic force calculated for each model, scaled by a best-fit damping coefficient, against the work done by the non-adiabatic force in our Ehrenfest simulations: **a** The non-adiabatic bond model of Eq. 11.26. **b** A simple constant drag coefficient. In each case *each data-point* represents the work done over 25 fs of the trajectory of each of 831 atoms drawn from our 24 cascade simulations

we carry out a linear regression analysis to calculate the constant of proportionality for each model. We find³:

Damping constant	Value	R^2 goodness of fit
$\chi/(eV \text{ Å ps}^{-1})$	14.81 ± 0.07	0.9806
$\beta_{\rm drag}/({\rm ps}^{-1})$	0.246 ± 0.003	0.8790

Comparison of the fitted values of the constants of proportionality is uninformative, but we will use them to scale the data in the analysis that follows. Figure 11.4 shows the fitted data for the 831 atom trajectories from our 24 simulations for each model scaled by the best-fit damping constant. Our newly proposed model is a significant improvement over a constant drag model.

11.3.2.2 The Non-Adiabatic Force

A potentially attractive feature of our non-adiabatic bond model is that it predicts not just the magnitude of a drag force, but also a direction for a much more richly structured non-adiabatic force. What we would like to know is how well the predicted force matches that found in our Ehrenfest simulations, given the many approximations introduced in order to arrive at a tractable model. In Fig. 11.5 we show detailed information for two atoms involved in a glancing collision at the

Note that the equivalent value of β_{drag} from the analysis in Sect. 11.1.1 is 0.386 \pm 0.002 ps⁻¹.

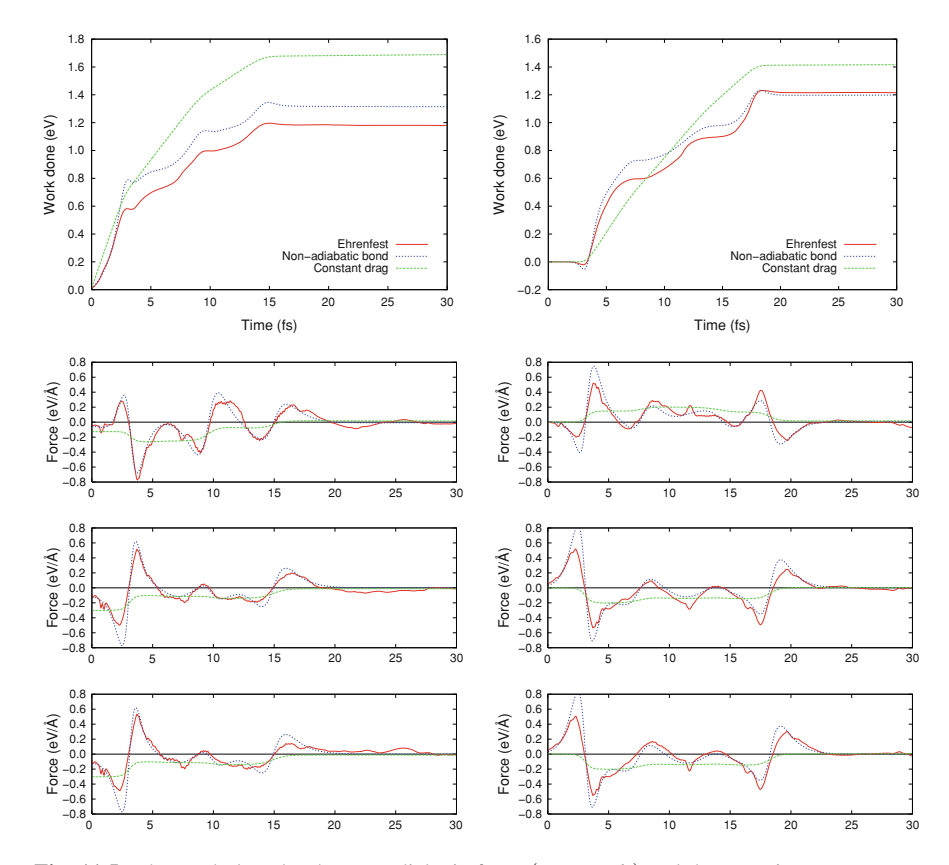


Fig. 11.5 The work done by the non-adiabatic force (*top panels*) and the cartesian components of the non-adiabatic force (*lower triplets of panels*) for our Ehrenfest simulations and for the models under test. The *left hand set of panels* are for the PKA in a typical simulation and the *right hand set* for the first atom with which it collides (in a glancing collision)

start of one of our simulations. The detailed shape of the evolving work done by the non-adiabatic bond force closely follows that of the Ehrenfest simulation force, although the absolute level does not match perfectly (as we would expect from the scatter in Fig. 11.4a). Also shown in Fig. 11.5 are the cartesian components of the non-adiabatic forces and there is once again a remarkably good match in the detail of the non-adiabatic bond model and the simulation results.

In Fig. 11.6 we show the work done by the forces on the primary knock-on atom and the first ion with which it collides in a simulation in which the PKA kinetic energy is directed along a close-packed line of ions, initiating a replacement collision sequence (RCS). We recall from Sect. 11.1.1 that the simple drag models coped particularly badly in the case of an RCS. In contrast, the more sophisticated form of our non-adiabatic bond model seems to do a much better job of capturing the enhanced energy transfer. It again captures much of the detail in the variation of the force in the Ehrenfest simulation.

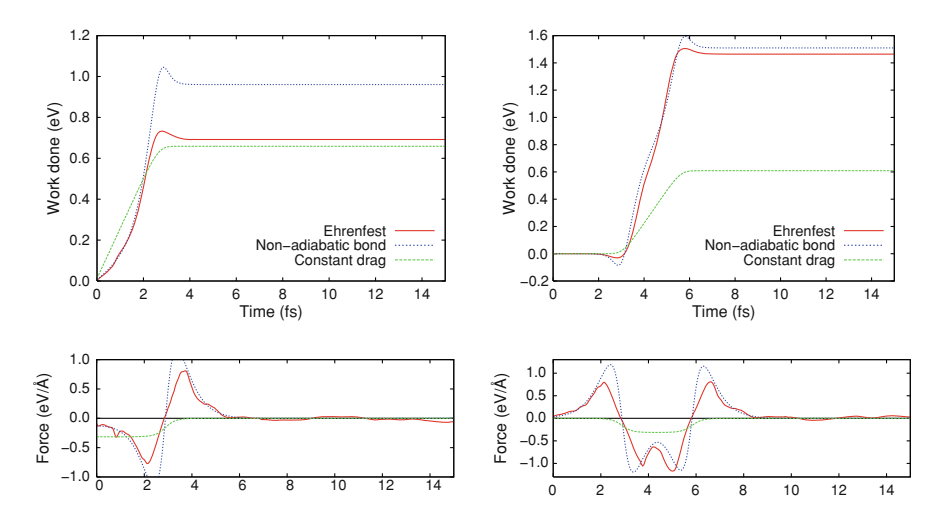


Fig. 11.6 The work done by the non-adiabatic force (*top panels*) and the cartesian components of the non-adiabatic force (*lower panels*) for our Ehrenfest simulations and for the models under test. The *left hand set of panels* are for the PKA in a simulation of a replacement collision sequence and the *right hand set* for the first atom with which it collides (in a head-on collision)

Figure 11.7 shows data for some more atoms. The right hand sequence show the work done and the non-adiabatic force for the next atom displaced in the RCS simulation considered in Fig. 11.6. The non-adiabatic bond model continues to perform well in reproducing the simulation data. The left hand sequence of panels in Fig. 11.7 shows data for an ion displaced later in the cascade of Fig. 11.5. Again, the non-adabatic bond model gives satisfactory results, but we can see new features emerging in the simulation data. The variation of the components of the non-adiabatic force has become much more "noisy", showing fluctuations on a time-scale that is short compared to that of the collision. We speculate that these fluctuations are due to non-local non-adiabatic features in the density matrix in our simulations. Variation of the off-diagonal elements of the density matrix in the energy eigenstate basis due to variation of bond lengths other than the one under consideration was explicitly excluded in our non-adiabatic bond model when we made our localizing assumption to obtain Eq. 11.22. In theory, a less local formulation of the model is possible, in which the non-adiabaticity of the density matrix is allowed to depend on the motion of more than a pair of ions at a time. There would be an increased computational cost to such a model, but it might not be prohibitive if the summations remained reasonably local and an efficient neighbour-list were available.

As an alternative view of the behaviour of the different force models, Figs. 11.8 and 11.9 show snapshots of the evolving positions and forces on the ions considered in Figs. 11.5 and 11.6 respectively.

Figure 11.10 shows histogram data for the angles between the non-adiabatic forces predicted by our proposed models and those found in our Ehrenfest

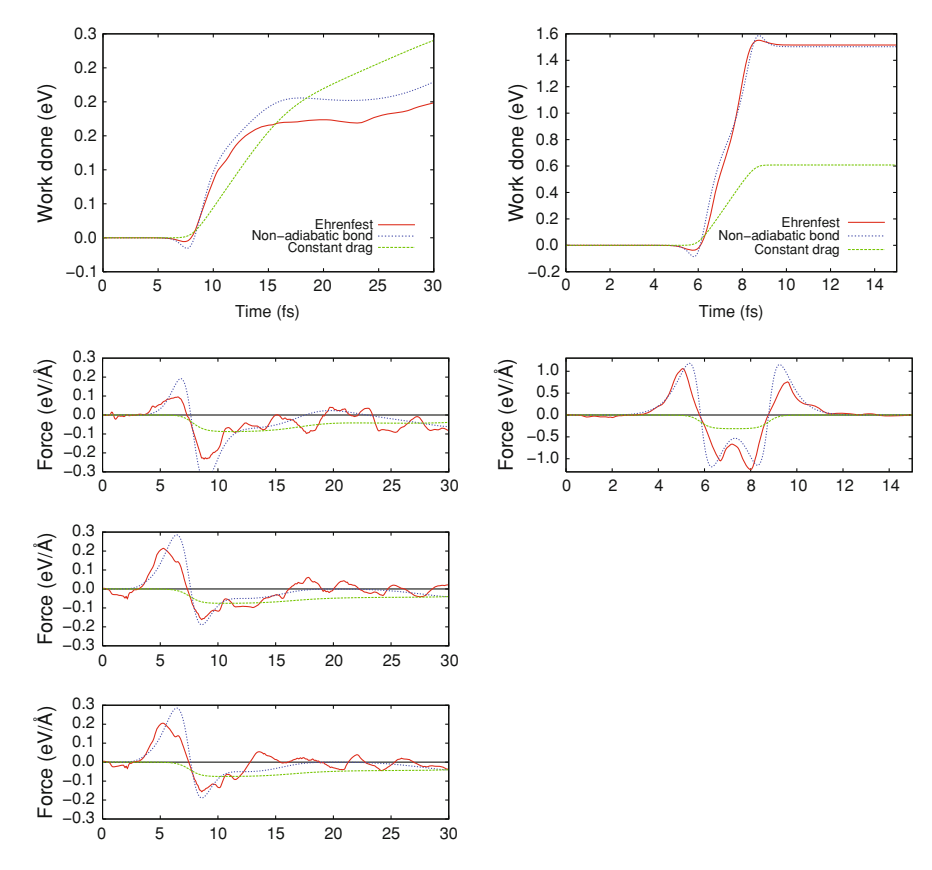


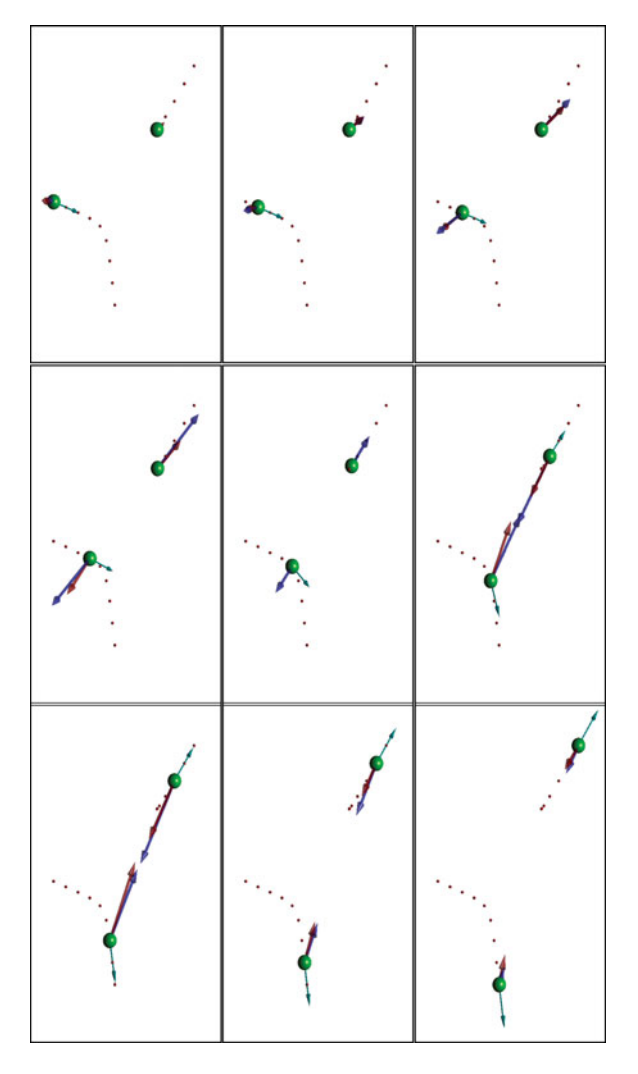
Fig. 11.7 The work done by the non-adiabatic force (*top panels*) and the cartesian components of the non-adiabatic force (*lower panels*) for our Ehrenfest simulations and for the models under test. The *left hand set of panels* are for an atom involved later on in the cascade simulation considered in Fig. 11.5 and the *right hand set* for the third atom in the RCS considered in Fig. 11.6

simulations. We can see that the non-adiabatic bond model considerably improves the prediction of the direction of the non-adiabatic force over the drag model (in which the non-adiabatic force is constrained to oppose the ion velocity).

11.3.2.3 Model Performance at the Cascade Level

As a final piece of analysis of our simulation data-set we will calculate the total work done by the non-adiabatic force on all atoms for each of our 24 simulations. This gives us data that are directly comparable to those used in the analysis in Sect. 11.1.1 and in [8, 9]. In the earlier analysis we found that even a simple damping did a good job of reproducing the total irreversible energy transfer (equivalent to the work done by the non-adiabatic force) over the course

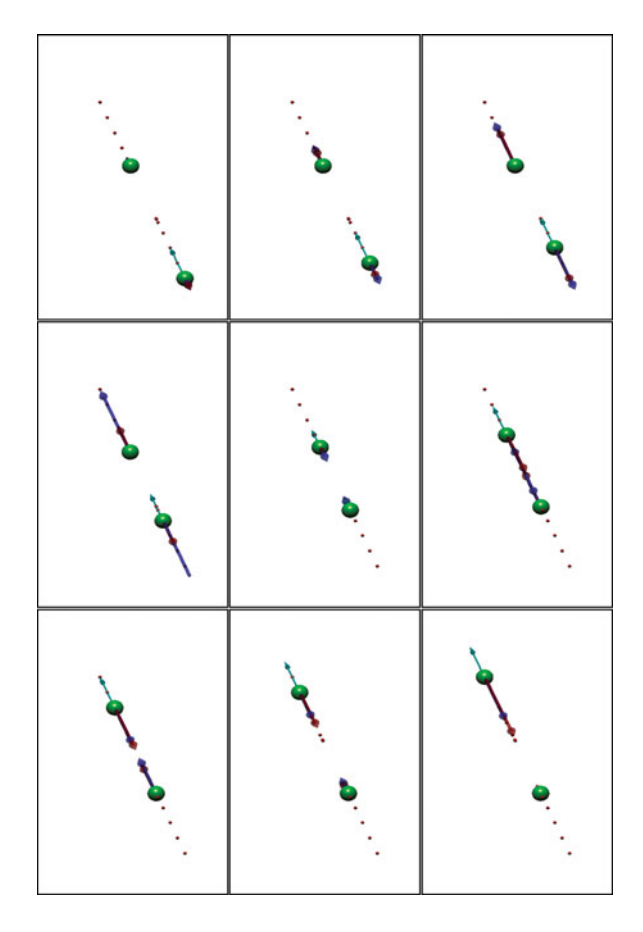
Fig. 11.8 Graphical depiction of the evolution of the ion positions of the PKA and its target atom in a glancing collision and the non-adiabatic forces as also shown in Fig. 11.5. Snapshots are taken at 0.5 fs intervals. The light blue arrow indicates the velocity and the small red dots show the past and future positions of the participating ions. The red arrow shows the magnitude and direction of the non-adiabatic force from the Ehrenfest simulations and the dark blue arrow shows the non-adiabatic bond model force. The scaling of the magnitudes of both forces is the same



of 200 fs of cascade evolution at a range of PKA energies in the same 24 directions used for the above analysis and in the same simulation cell with the same initial conditions.

Figure 11.11 compares the irreversible energy transfer calculated by our non-adiabatic bond model and using a simple damping with the results of the Ehrenfest simulations using *spICED*. Each data-point represents a single simulation. Our proposed models does a good job of capturing the variation exhibited by the simulation data. What is interesting is that the energy transfer in the simple drag model (essentially the integral of the ionic kinetic energy) shows hardly any variation between simulations. This should not be particularly surprising, since over the 25 fs of our simulations there is very little variation in the total ionic kinetic energy, but it appears to contradict the conclusions of the earlier analysis of

Fig. 11.9 As for Fig. 11.8, but for the PKA and first target atom in the RCS also illustrated in Fig. 11.5



Sect. 11.1.1. In fact, these earlier simulations showed very similar behaviour and the spread in the simulated irreversible energy transfer for simulations at a PKA energy of 1 keV is similar in both sets of simulations. The apparent usefulness of a constant damping coefficient emerges in the earlier analysis when data from a range of PKA energies are considered, but it should not be so surprising that the Ehrenfest energy transfer should scale with the total excess kinetic energy introduced to initiate the cascade.

11.4 Conclusions

In this chapter we have used our semi-classical simulation framework to test various models for the non-adiabatic force acting on ions in collision cascades. In Sect. 11.1 we examined data from our simulations and found that the non-adiabatic force predicted by Ehrenfest dynamics has a complex dependence on local atomic environment and on ion velocity.

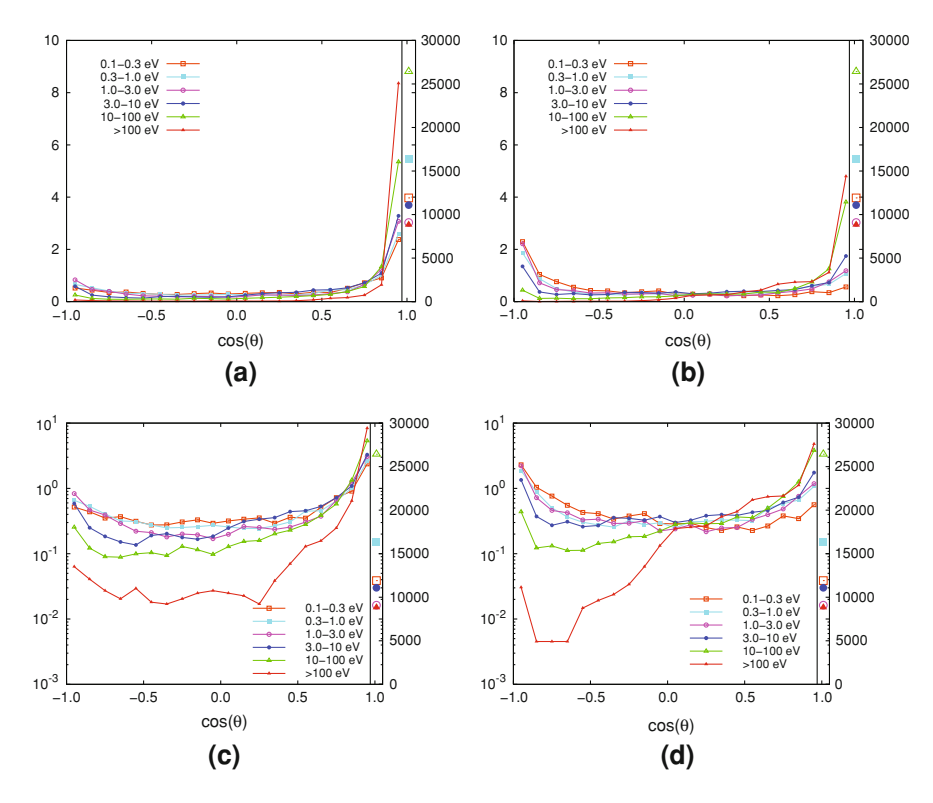


Fig. 11.10 Histograms of the angle between the non-adiabatic force in our Ehrenfest simulations and those predicted by our force models, split by ion kinetic energy. The *left-hand panels* (**a** and **c**) are for the non-adiabatic bond model. The *right-hand panels* (**b** and **d**) are for the simple drag model. The *lower panels* show the same data as the *upper panels*, but on a log scale. The *symbols* against the right hand axis indicate the number of data-points in each line of the plots

The effect of the non-adiabatic force in removing energy from the ionic subsystem during radiation damage cascades is believed to have a potentially important effect on the final damage yield. Several classical MD models in the literature (discussed in Sects. 3.4.2.1 and 3.4.2.2) attempt to capture such effects by adding a drag force to the ions, opposed to their motion and proportional to their velocities. The choice of a drag force is often justified by reference to various theoretical models for the stopping force experienced by slow light ions (see Sect. 3.2.5 for a discussion), which predict just such a drag force. Such justification is, however, spurious.

The stopping power theories are derived in very particular, highly idealized scenarios. The models of Firsov [14] and Lindhard and Scharff [15] (see Sect. 3.2.5.1) consider isolated binary collisions in a simple classical model and predict that the non-adiabatic force between atoms during a collision will be proportional to the relative velocity of the two atoms. Other models, such as that of Lindhard [16] (see Sect. 3.2.5.2) consider the effects of an electron gas and so

11.4 Conclusions 243

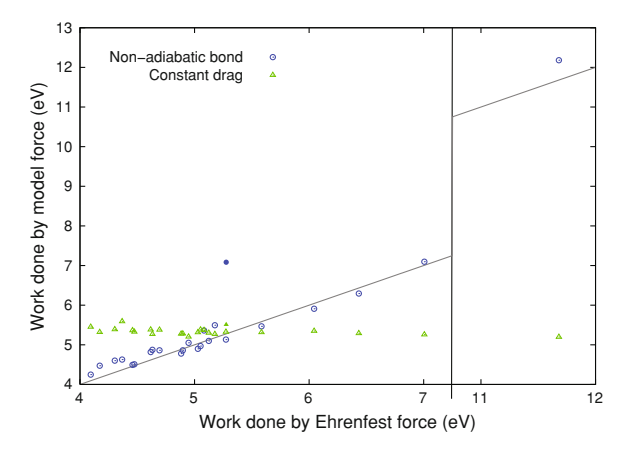


Fig. 11.11 Comparison of the work done by the non-adiabatic forces on *all* the atoms in our cascade simulations. Our force models are compared with the forces from the Ehrenfest simulations and *each data-point* represents a single simulations. The *rightmost points* (note the split axis) are for the RCS in the $\langle 110 \rangle$ direction. Data for a second replacement collision sequence initiated by a PKA fired in a $\langle 100 \rangle$ direction are indicated by *filled symbols*

explicitly treat a homogeneous medium. Such simple models are clearly at odds with the complex many-atom interactions occurring in a typical cascade, in which the non-adiabatic force is a result neither of isolated inelastic collisions nor of an interaction with a homogeneous medium. Additionally, whilst the concept of a drag force proportional to velocity is supported by experimental data, such verification only really exists for ions moving at velocities approaching 10^6 m s⁻¹. In the case of a copper ion this corresponds to a kinetic energy of ~ 0.3 MeV, which should be compared to cascade PKA energies of $\lesssim 10 \, \text{keV}$.

So to claim that the use of a drag force in a classical MD simulation is motivated by stopping power models is to take those models beyond the limits of their underlying assumptions and to apply them in a situation in which no experimental verification is possible. The use of such drag forces is perhaps better to be regarded as a simple means of extracting energy from the ions in a cascade in such a way that the energy is preferentially removed from the most energetic ions. The value of the drag coefficient is then determined by the need to remove energy from the cascade at the correct rate *on average*. In Sect. 11.1.1 we evaluated some of the drag models made use of in the literature on just such a basis.

Because we can obtain detailed information about the adiabatic force on a per atom basis from our semi-classical simulations, we were motivated in Sect. 11.3 to attempt to find an improved model for the non-adiabatic force. Such a model, we hoped, would be able to better reproduce the details of the non-adiabatic force, in particular its direction. Our hope is that such a model will then act to extract energy from the ionic motion in a more correct way, overcoming problems in simpler models such as the significant under-damping of RCSs.

We proposed a model, the non-adiabatic bond model, based on the reasoning that the non-adiabatic forces in collision cascades arise because of a lagged response of the electrons in forming and breaking bonds between ions. This picture is not only consistent with our tight-binding simulation framework, but also has intuitive appeal and results in a model with the local character necessary for implementation in a classical molecular dynamics code. Testing our model, we found that it significantly out-performed simple drag models of the adiabatic force and was able to closely replicate the direction of the non-adiabatic force from our Ehrenfest simulations (and hence the individual cartesian components).

References

- Caro, A., Victoria, M.: Ion–electron interaction in molecular-dynamics cascades. Phys. Rev. A 40(5), 2287–2291 (1989)
- Duffy, D.M., Rutherford, A.M.: Including the effects of electronic stopping and electron—ion interactions in radiation damage simulations. J. Phys. Condens. Matter 19(1), 016207 (2007)
- Rutherford, A.M., Duffy, D.M.: The effect of electron-ion interactions on radiation damage simulations. J. Phys. Condens. Matter 19(49), 496201 (2007)
- 4. Gao, F., Bacon, D.J., Flewitt, P.E.J., Lewis, T.A.: The effects of electron–phonon coupling on defect production by displacement cascades in α -iron. Model. Simul. Mater. Sci. Eng. $\mathbf{6}(5)$, 543–556 (1998)
- Nordlund, K., Wei, L., Zhong, Y., Averback, R.S.: Role of electron-phonon coupling on collision cascade development in Ni, Pd, and Pt. Phys. Rev. B 57(22), R13965–R13968 (1998)
- Kapinos, V.G., Bacon, D.J.: Influence of ion-electron interaction on the formation mechanism of depleted zones in displacement cascades in metals. Phys. Rev. B 50(18), 13194–13203 (1994)
- Kapinos, V.G., Bacon, D.J.: Effect of melting and electron-phonon coupling on the collapse of depleted zones in copper, nickel, and α-iron. Phys. Rev. B 53(13), 8287–8295 (1996)
- 8. le Page, J., Mason, D.R., Race, C.P., Foulkes, W.M.C.: How good is damped molecular dynamics as a method to simulate radiation damage in metals? New J. Phys. **11**(1), 013004 (2009)
- Race, C.P., Mason, D.R., le Page, J., Finnis, M.W., Foulkes, W.M.C., Sutton, A.P.: Aiding the design of radiation resistant materials with multiphysics simulations of damage processes. In: Neugebauer, J., Asta, M., Umantsev, A.. (eds.) Multiphysics Modeling in Materials Design (Materials Research Society Symposium Proceedings), vol. 1229E, Warrendale, PA, USA, 2010. Mater. Res. Soc.
- Finnis, M.W., Agnew, P., Foreman, A.J.E.: Thermal excitation of electrons in energetic displacement cascades. Phys. Rev. B 44(2), 567–574 (1991)
- 11. Gao, F., Bacon, D.J., Flewitt, P.E.J., Lewis, T.A.: The effects of electron–phonon coupling on defect production by displacement cascades in α -iron. Model. Simul. Mater. Sci. Eng. 6(5), 543–556 (1998)
- Prönnecke, S., Caro, A., Victoria, M., Diaz de la Rubia, T., Guinan, M.W.: The effect of electronic energy loss on the dynamics of thermal spikes in Cu. J. Mater. Res. 6(3), 483–491 (1991)
- 13. Race, C.P., Mason, D.R., Sutton, A.P.: An improved model of interatomic forces for large simulations of metals containing excited electrons. New J. Phys. 12, 93049 (2010)

References 245

14. Firsov, O.B.: A quantitative interpretation of the mean electronic excitation energy in atomic collisions. Sov. Phys. JETP **36**, 1076 (1959)

- Lindhard, J., Scharff, M.: Energy dissipation by ions in the kev region. Phys. Rev. 124(1), 128–130 (1961)
- Lindhard, J.: On the properties of a gas of charged particles. Matematisk Fysiske Meddelelser
 Kongelige Danske Videnskabernes Selskab 28(8), 1–57 (1954)

Chapter 12 Concluding Remarks

12.1 Our Aims

As we discussed in our introduction in Chap. 1, an understanding of radiation damage is important to technological progress in many diverse areas as well as being of intrinsic scientific interest. Non-adiabatic effects, in which energy exchange between the ionic and electronic subsystems is significant, are widely acknowledged to have an important influence on the evolution of damage distributions (in Chap. 2 we drew attention to some of those effects in a typical collision cascade). But, our review of the treatment of energy exchange processes in the radiation damage literature in Chap. 3 served to highlight a significant gap: theories of the effects of electronic excitations on ion dynamics deal only with highly idealized situations, such a binary collisions or homogeneous electronic systems, and predict a simple electronic drag force opposing the ionic velocity. Attempts to incorporate non-adiabatic effects in dynamic simulations of radiation damage have adopted these theoretical models, often on spurious grounds, by adding a drag term to the equations of motion of classical ions.

The work documented in this thesis aims to go beyond earlier, simple treatments of non-adiabatic effects in radiation damage simulations. By adopting a simple time-dependent tight-binding model, evolving under Ehrenfest dynamics, we have perhaps the simplest possible simulation framework that incorporates both an explicit set of classical ions and an explicit model of quantum mechanical electrons. The theory behind this model was introduced in Chap. 4 (in particular in Sect. 4.5) and the model itself in Chap. 5. We discussed how Ehrenfest dynamics is able to give a good account of electron—ion energy exchange processes in a typical radiation damage scenario and in Chap. 6 we established the suitability of our simulation framework for the simulation of radiation damage events. We thus have a means of exploring the effect of non-adiabatic processes on the evolution of radiation damage in metals by direct simulation.

12.2 Our Results

In Chap. 6 our preliminary investigation of the energy transfer to the electrons from a single oscillating ion in a sample of perfect metallic crystal of our tight-binding model showed a rich structure. When analysed in terms of an oscillator damping force, analogous to stopping power theories in common usage, we found that such a force would need to be dependent on the direction and frequency of oscillation, on the local atomic environment and on the electronic temperature in order to correctly capture the energy transfer predicted by our semi-classical simulations. These preliminary results suggested the importance of a more indepth analysis of non-adiabatic processes in radiation damage.

Chapter 7 illuminated some important features of the evolution of a semiclassical system during a radiation damage collision cascade, and Chaps. 8–11 contain details of the results of our investigations. The key results of our work are given in the following sections.

12.2.1 The Nature of the Electronic Excitations

In Chap. 8 we used the results from a set of cascade simulations to investigate the nature of the electronic excitations stimulated by the ionic motion. We found that the electronic system tended to evolve through a series of very nearly thermal distributions at a gradually increasing temperature. We remarked that such a behaviour should not necessarily be expected, because our system dynamics does not include the thermalizing effects of direct electron–electron interactions or a correct treatment of the full electron–phonon interaction. Instead, we explained the emergence of a well-defined electronic pseudo-temperature by considering the characteristic frequencies of the ionic motion and noting that these would stimulate electronic excitations of energies small on the scale of the width of the Fermi surface. The statistical effect of many of these small excitations is to give rise to an almost thermal eigenstate occupation distribution.

We considered the importance of the existence of a well-defined electronic pseudo-temperature throughout a cascade. In particular, we noted that a useful way of accounting for the effect of electronic excitations on the forces within a classical molecular dynamics (MD) simulation would be to make use of an electronic excitation dependent potential. The development of such a potential would be considerably simplified if the electronic excitations could be assumed to be thermal. However, a comparison of typical time-scales for electron-electron and electron-phonon interaction processes (discussed in Sect. 8.1.3) does not suggest that such an assumption would generally be valid. Demonstrating that the electronic excitations in a cascade are in the first instance (almost) thermal, and therefore require very little thermalization, is thus a necessary step in the justification of the use of an electronic temperature dependent potential to capture the effect of accumulating excitations.

12.2 Our Results 249

We discussed a number of details of the excitation spectrum and some corresponding subtleties in the development of a simple temperature fitting algorithm (treated in more detail in Sect. 13.4). We also briefly considered two alternative definitions of the electronic entropy and suggested that by neglecting the off-diagonal elements of the density matrix in the instantaneous energy eigenstate basis it might be possible to define an entropy consistent with the apparently rising electronic pseudo-temperature despite our electronic system being closed (in the quantum mechanical sense) and so evolving without a change in entropy.

12.2.2 The Effect of Electronic Excitations on the Conservative Forces

In Chap. 9 we began a detailed analysis of the non-adiabatic effects on the electronic forces in collision cascades. We identified two key effects of non-adiabaticity: the accumulation of electronic excitations resulting in weakening of the electronic bonds between ions and the non-adiabatic forces arising from the finite response time of the electrons to changes in the electronic Hamiltonian. We focused first on the effect of accumulating excitations (the latter point to be addressed in Chap. 11).

By running a set of low energy collision cascade simulations we found that the electronic bonds would be significantly weakened (by $\sim\!1\%$) at high degrees of electronic excitation (equivalent to a pseudo-temperature of $\sim\!10,\!000$ K). We pointed to evidence from augmented classical MD simulations [1] that such temperatures might well occur in collision cascades, depending on the strength of the electron–phonon interaction (a quantity poorly determined both theoretically and experimentally). We found that the bond-weakening effect was almost completely (94%) accounted for by a thermal model of the electronic excitations, consistent with our previous identification of a well-defined electronic pseudo-temperature.

We also considered the implications of the weakened bonds for a region of lattice bathed in hot electrons. Such a region would be under an effective compressive strain and we undertook a brief analysis of this strain, noting that if it persisted for long enough it might give rise to an outward propagating elastic wave, which might influence defect dynamics in the surrounding material.

Finally, we examined the results of a large number of simulations of replacement collision sequences (RCS) in lattices at different electronic temperatures. The RCS is an important mechanism of damage production and so any change on electronic excitation to the ability of an RCS to propagate might be significant. We found no significant effects below electronic temperatures of $\sim 50,000$ K, and at higher temperatures the weakened electronic bonds (and so 'harder' inter-ionic interactions) make an RCS less likely to propagate.

12.2.3 Non-Adiabatic Effects on Channelling Ions

In Chap. 10, by simulating the passage of fast ions down open channels in relatively large cells of our tight-binding model we were able to investigate the effects of electronic excitations on various aspects of the channelling process. Our key simulation results were the behaviour of the steady state ion charge and the steady state electronic stopping power as a function of initial ion velocity and the charge-self-consistency parameters in our model.

First, we found an enhancement of the negative electronic charge on the channelling ion over a range of velocities. We attributed this behaviour to the resonant occupation of a defect state, highly localized on the channelling ion, whenever the frequency corresponding to the rate at which the ion moved between equivalent points in the periodic lattice matched a possible excitation from an occupied bulk state into the defect state. We verified this explanation using time-dependent perturbation theory and by considering a simple toy model.

The variation of the width, depth and position of the resonant charge enhancement with changes to the self-consistency parameters U and V was explained within the same conceptual framework.

When we examined the steady state stopping power we found that at low velocities it was roughly proportional to the ion speed as predicted by simple stopping power theories. However, we found that at higher speeds, in the case when U=V=0, there was a 'knee' in the increase of the stopping power with increasing velocity corresponding to the resonant charge feature. Having explored the mechanism of electronic stopping from a time-dependent tight-binding perspective, we attributed the reduction of the stopping power below the linear trend to the occupation of the defect state. This state will be strongly anti-bonding in character and so its occupation will weaken all the bonding forces on the channelling ion. Since the stopping power results from an asymmetry in these bonding forces, it too will be reduced.

We also found that at high values of the on-site charge self-consistency parameter U, the 'knee' in the stopping power became a pronounced dip, extending over the range of velocities corresponding to the resonant charge enhancement. We explained this behaviour by noting that occupation of the high energy defect state and the accompanying localization of charge would give rise to a significant on-site perturbation to the electronic Hamiltonian on the channelling ion. This perturbation would have the effect of mixing together the bonding and anti-bonding defect states (which both have large projections onto the atomic orbital on the channelling ion) thereby reducing the bonding character of the fully occupied low energy defect state. This, in turn, reduces all the bonding forces acting on the channelling ion and suppresses the stopping force.

12.2 Our Results 251

12.2.4 The Non-Adiabatic Force in Collision Cascades

In Chap. 11 we returned to our study of the effects of electronic excitations on the electronic forces in radiation damage collision cascades. In this case we examined the effects of the finite response time of the electronic density matrix to changes in the electronic Hamiltonian (i.e. to changes in the ionic positions). We identified a non-adiabatic force corresponding to this lagged response and showed that it is the work done by this force that is manifest as excitations in the electronic system.

By running a set of short cascade simulations, gathering data on the excitation spectrum with high frequency, we were able to calculate the non-adiabatic force acting on each atom throughout the cascades. A preliminary examination of the direction of this force showed that it is not, in general, opposed to the ionic motion, contradicting the application of simple electronic stopping power theory in augmented classical MD simulations. We were thus motivated to attempt to develop an improved classical model of the quantum mechanical non-adiabatic electronic force.

By beginning with an expression for the non-adiabatic force in the basis of instantaneous eigenstates of the electronic Hamiltonian (as one part of the Hellmann–Feynman force) we derived a spatially and temporally localized form, written entirely in terms of quantities readily accessible within a classical MD simulation. In deriving our simplified form we were guided by a conceptual picture of the stopping force as arising from the lagged response of bond-orders between neighbouring atoms to changes in the corresponding bond lengths.

We tested our new model on data from our set of cascade simulations and found that it significantly outperformed a simple drag model in capturing the energy loss due to the non-adiabatic force at an individual atom level. More than this, we found that our new model did a remarkably good job of capturing the variation in the individual Cartesian components of the non-adiabatic force and was thus reproducing much of the microscopic detail in the direction and strength of the force in the semi-classical simulations. Finally, we repeated a simple analysis of the total work done by the non-adiabatic force as an average over all the atoms in a given cascade. On the short time-scales of our data-set we found that a simple damping force captures none of the significant variation of the effect of the non-adiabatic force with initial PKA direction. In contrast, our new model does a very good job of reproducing the variation.

12.3 Possible Directions for Further Research

In the work documented in this thesis we have established the value of using semiclassical time-dependent tight-binding simulations under Ehrenfest dynamics for the study of radiation damage phenomena. We have seen that with currently available computational resources it is possible to reach simulation time- and length-scales necessary for the simulation of small, low energy collision cascades and of ion channelling. We have witnessed the emergence of new phenomena in our simulation results and seen how the wealth of information about the semi-classical system available to us illuminates the physics behind these phenomena.

However, as discussed in Sect. 4.1, the method of choice for simulating radiation damage on more realistic time- and length-scales will continue to be classical molecular dynamics for some years to come. Only classical MD can cope with the millions of atoms and hundreds of picoseconds of evolution necessary to probe the residual defect distribution arising from collision cascades. For this reason, we have viewed our work as part of a multi-scale materials modelling chain, and have aimed to use our simulation results to inform the building of better forms of augmented classical MD models.

Our simulation results make it clear that there is much more to the non-adiabatic effects of electron—ion energy exchange on the ion dynamics than can be captured by a simple drag force. In fact, the simplifying assumptions used in the theories that predict such forces mean that their application in an augmented MD model should only ever be regarded as an attempt to effect the correct energy loss rate from the ions on an average basis across the whole cascade and over times of hundreds of femtoseconds. The fact that the drag forces are, however, applied at the microscopic level might cause us concern: are we over- or under-damping certain modes of ionic motion and could this have significant consequences for the predicted damage?

Two obvious ways of improving classical molecular dynamics models suggest themselves and our work has something to say about both of them. First, the accumulation of electronic excitations and the implied gradual weakening of the inter-ionic bonding interactions might be taken into account using an excitation-dependent potential. We have seen that such a potential could reasonably make the assumption of a well-defined electronic temperature. We have also seen that it should not capture any significant effects at electronic temperatures less than around 10 000 K. Such temperatures may well arise in some high energy cascades and are likely to exist around the paths of channelling ions. Only by applying such potentials can their implications for damage production be explored.

Second, the use of a more valid model of the non-adiabatic force in classical MD is desirable. We have used our semi-classical simulation framework to suggest just such a model; one that captures much of the microscopic behaviour of the non-adiabatic force. An obvious next step would be to incorporate our new force model in a classical MD code to assess its impact on the production of damage in cascades.

A third improvement to classical MD would be the correct treatment of the return of energy from hot electrons to cooler ions. This phenomenon is particularly important in the later stages of cascade evolution and defect recovery. We have been unable to say anything on this issue because of a fundamental failure of Ehrenfest dynamics: it does not include the effects of spontaneous phonon emission. To explore these effects we would have to reintroduce some quantum mechanical features of the ions. A productive line for future research in this

direction might be to apply the correlated electron ion dynamics (CEID) formalism of Horsfield et al. [2, 3].

References

- Rutherford, A.M., Duffy, D.M.: The effect of electron-ion interactions on radiation damage simulations. J. Phys. Condens. Matter 19(49), 496201 (2007)
- Horsfield, A.P., Bowler, D.R., Fisher, A.J., Todorov, T.N., Sanchez, C.G.: Correlated electronion dynamics: the excitation of atomic motion by energetic electrons. J. Phys. Condens. Matter 17, 4793–4812 (2005)
- 3. Horsfield, A.P., Bowler, D.R., Fisher, A.J., Todorov, T.N., Sanchez, C.: Beyond Ehrenfest: correlated non-adiabatic molecular dynamics. J. Phys. Condens. Matter 16(46), 8251–8266 (2004)

Chapter 13 Appendices

13.1 Appendix A: Selected proofs

13.1.1 Proof of Equation (4.10)-(i)

We wish to prove that the expectation of an observable \hat{A} for a state $|\Phi(t)\rangle$ evolving under a Hamiltonian \hat{H} changes with time according to

$$i\hbar \frac{d}{dt} \langle \Phi(t) | \hat{A} | \Phi(t) \rangle = \langle \Phi(t) | [\hat{A}, \hat{H}] | \Phi(t) \rangle.$$
 (A.1)

We write

$$\frac{\mathrm{d}}{\mathrm{d}t} \langle \Phi(t) | \hat{A} | \Phi(t) \rangle = \left(\frac{\mathrm{d}}{\mathrm{d}t} \langle \Phi(t) | \right) \hat{A} | \Phi(t) \rangle + \langle \Phi(t) | \hat{A} \left(\frac{\mathrm{d}}{\mathrm{d}t} | \Phi(t) \rangle \right). \tag{A.2}$$

From the time-dependent Schrödinger equation we have,

$$i\hbar \frac{d}{dt}|\Phi\rangle = \hat{H}|\Phi\rangle,$$
 (A.3)

$$-i\hbar \frac{\mathrm{d}}{\mathrm{d}t} \langle \Phi | = \langle \Phi | \hat{H}, \tag{A.4}$$

since \hat{H} is Hermitian $(\hat{H}^{\dagger} = \hat{H})$, and so the result Sect. 13.1.1 is proved. Note that as always we are working in the Schrödinger picture. In the Heisenberg picture, in which the state vectors are stationary and the observables evolve, Eq. A.1 becomes the Heisenberg equation of motion.

13.1.2 Proof of Equation (4.10)-(ii)

We wish to prove that for a function $F(\hat{\mathbf{P}})$ that can be expanded in powers of a momentum operator $\hat{\mathbf{P}}$, then if \hat{R}_{η} is the η th cartesian component of the corresponding position operator, we can write

$$[\hat{R}_{\eta}, F(\hat{\mathbf{P}})] = i\hbar \frac{\partial F}{\partial \hat{P}_{\eta}}, \tag{A.5}$$

where \hat{P}_n is the η th cartesian component of $\hat{\mathbf{P}}$. We write,

$$F(\hat{\mathbf{P}}) = \sum_{i} a_{j}(\hat{\mathbf{P}})^{j},\tag{A.6}$$

for some set of coefficients $\{a_i\}_{i=0}^{\infty}$ so that,

$$[\hat{R}_{\eta}, F] = \sum_{j} a_{j} [\hat{R}_{\eta}, (\hat{\mathbf{P}})^{j}]. \tag{A.7}$$

Using the identity $[\hat{A}, \hat{B}\hat{C}] = [\hat{A}, \hat{B}]\hat{C} + \hat{B}[\hat{A}, \hat{C}]$ this becomes,

$$[\hat{R}_{\eta}, F] = \sum_{j} a_{j} \left\{ [\hat{R}_{\eta}, \hat{\mathbf{P}}] (\hat{\mathbf{P}})^{j-1} + \hat{\mathbf{P}} [\hat{R}_{\eta}, (\hat{\mathbf{P}})^{j-1}] \right\}$$

$$= \sum_{j} a_{j} \left\{ i\hbar (\hat{\mathbf{P}})^{j-1} \boldsymbol{\eta} + \hat{\mathbf{P}} [\hat{R}_{\eta}, (\hat{\mathbf{P}})^{j-1}] \right\},$$
(A.8)

where we have used the commutation relations $[\hat{R}_{\eta}, \hat{P}_{\mu}] = i\hbar \delta_{\eta\mu}$ and η is the unit vector in the η th cartesian direction. Repeating the above step j times for the jth component in the expansion of F gives,

$$[\hat{R}_{\eta}, F] = i\hbar \sum_{j} a_{j} j(\hat{\mathbf{P}})^{j-1} \boldsymbol{\eta}, \tag{A.9}$$

proving (A.5)

13.1.3 Proof of Equation (4.12)

If we follow the procedure in Sect. 13.1.2, but consider instead a function $G(\mathbf{R})$ expandable in powers of a position operator $\hat{\mathbf{R}}$, then use of the commutation relations $[\hat{P}_{\eta}, \hat{R}_{\mu}] = -i\hbar \delta_{\eta\mu}$ leads to the required result

$$[\hat{P}_{\eta}, G(\hat{\mathbf{R}})] = -i\hbar \frac{\partial G}{\partial \hat{R}_{\eta}}, \tag{A.10}$$

13.1.4 Proof of Equation (4.28)

We want to prove that for an arbitrary electronic operator $\hat{A}(\{\hat{\mathbf{r}}_i\}, \{\hat{\mathbf{p}}_i\})$ the expectation values satisfy

$$\langle \Phi(t)|\hat{A}|\Phi(t)\rangle = \langle \Psi^I(t)|\hat{A}|\Psi^I(t)\rangle,$$
 (A.11)

with $|\Phi(t)\rangle$ defined as in Sect. 4.2 and $|\Psi^I(t)\rangle$ defined as in Sect. 4.2.1 such that it satisfies (4.25). Hence we have by definition:

$$\langle \Phi(t_0)|\hat{A}|\Phi(t_0)\rangle = \langle \Psi^I(t_0)|\hat{A}|\Psi^I(t_0)\rangle.$$
 (A.12)

We follow Todorov [1] by splitting the time interval t_0 to t into $N \to \infty$ time steps and define $t_n = t_0 + n\delta t$, n = 0, 1, 2, ..., N, $\delta t = (t - t_0)/N$, so that $\langle \Phi(t)|\hat{A}|\Phi(t)\rangle = \langle \Phi(t_N)|\hat{A}|\Phi(t_N)\rangle$. From the TDSE (4.1) we have

$$|\Phi(t_N)\rangle = |\Phi(t_{N-1})\rangle \left(1 + \frac{\delta t}{i\hbar}\hat{H}\right),$$
 (A.13)

$$\langle \Phi(t_N)| = \langle \Phi(t_{N-1})| \left(1 - \frac{\delta t}{i\hbar} \hat{H}\right),$$
 (A.14)

so that,

$$\langle \Phi(t_N)|\hat{A}|\Phi(t_N)\rangle = \langle \Phi(t_{N-1})|\left(\hat{A} + [\hat{A},\hat{H}]\frac{\delta t}{i\hbar} + O(\delta t^2)\right)|\Phi(t_{N-1})\rangle. \tag{A.15}$$

Because \hat{A} is an electronic operator and all the position and momentum operators of the electrons commute with those of the nuclei we have $[\hat{A}, \hat{V}_{nn}] = 0$, $[\hat{A}, \hat{T}_n] = 0$ and so,

$$\langle \Phi(t_N) | \hat{A} | \Phi(t_N) \rangle = \langle \Phi(t_{N-1}) | \left(\hat{A} + [\hat{A}, \hat{T}_e + \hat{V}_{ee} + \hat{V}_{ne}] \frac{\delta t}{i\hbar} + O(\delta t^2) \right) | \Phi(t_{N-1}) \rangle, \tag{A.16}$$

to first order in δt . We can then use the assumption (4.13) that the nuclear wavefunctions are highly spatially confined, to write

$$\langle \Phi(t_{N-1}) | [\hat{A}, \hat{V}_{ne}(\{\hat{\mathbf{R}}_I\}, \{\hat{\mathbf{r}}_i\})] | \Phi(t_{N-1}) \rangle = \langle \Phi(t_{N-1}) | [\hat{A}, \hat{V}'_{ne}(\{\mathbf{R}_I(t_{N-1})\}, \{\hat{\mathbf{r}}_i\})] | \Phi(t_{N-1}) \rangle, \tag{A.17}$$

where the correct time must be specified for the classical ionic coordinates.

$$\langle \Phi(t_N) | \hat{A} | \Phi(t_N) \rangle = \langle \Phi(t_{N-1}) | \left(\hat{A} + [\hat{A}, \hat{H}_e(t_{N-1})] \frac{\delta t}{i\hbar} \right) | \Phi(t_{N-1}) \rangle. \tag{A.18}$$

Now by defining $\hat{A}_N = \hat{A}$ and $\hat{A}_{N-1} = \hat{A}_N + [\hat{A}_N, \hat{H}_e(t_{N-1})]\delta t/i\hbar$ we have,

$$\langle \Phi(t_N) | \hat{A}_N | \Phi(t_N) \rangle = \langle \Phi(t_{N-1}) | \hat{A}_{N-1} | \Phi(t_{N-1}) \rangle. \tag{A.19}$$

Iterating backwards gives,

$$\langle \Phi(t_N) | \hat{A}_N | \Phi(t_N) \rangle = \langle \Phi(t_0) | \hat{A}_0 | \Phi(t_0) \rangle$$

= $\langle \Psi''(t_0) | \hat{A}_0 | \Psi''(t_0) \rangle$, (A.20)

by the definition of $|\Psi'^{I}(t_0)\rangle$. We can also consider,

$$\langle \Psi^{I}(t_{N})|\hat{A}|\Psi^{I}(t_{N})\rangle = \langle \Psi^{I}(t_{N-1})|\left(\hat{A}+[\hat{A},\hat{H}_{e}(t_{N-1})]\frac{\delta t}{i\hbar}\right)|\Psi^{I}(t_{N-1})\rangle, \quad (A.21)$$

since

$$i\hbar \frac{d}{dt} |\psi^I(t)\rangle = \hat{H}_e(t) |\psi^I(t)\rangle,$$
 (A.22)

which on iteration gives,

$$\langle \Psi^{I}(t_{N})|\hat{A}_{N}|\Psi^{I}(t_{N})\rangle = \langle \Psi^{I}(t_{0})|\hat{A}_{0}|\Psi^{I}(t_{0})\rangle, \tag{A.23}$$

thereby proving the result (4.28)

13.1.5 Proof of Equation (4.85)

We need to calculate

$$E_{\rm H}[\rho] - \int d\mathbf{r} \rho(\mathbf{r}) V_{\rm H}[\rho^{\rm in}](\mathbf{r}), \tag{A.24}$$

for $\rho = \rho^{\rm in} + \delta \rho$. Now,

$$E_{H}[\rho^{in} + \delta\rho] = E_{H}[\rho^{in}] + \int d\mathbf{r} \frac{\delta E_{H}}{\delta\rho} \Big|_{\rho^{in}(\mathbf{r})} \delta\rho(\mathbf{r})$$

$$+ \frac{1}{2} \iint d\mathbf{r} d\mathbf{r}' \frac{\delta^{2} E_{H}[\rho]}{\delta\rho(\mathbf{r}')\delta\rho(\mathbf{r})} \Big|_{\rho^{in}(\mathbf{r}')} \delta\rho(\mathbf{r}') \delta\rho(\mathbf{r})$$

$$= E_{H}[\rho^{in}] + \frac{1}{2} \iint d\mathbf{r} d\mathbf{r}' \frac{\delta\rho(\mathbf{r})\rho^{in}(\mathbf{r}')}{|\mathbf{r} - \mathbf{r}'|}$$

$$+ \frac{1}{2} \iint d\mathbf{r} d\mathbf{r}' \frac{\delta\rho(\mathbf{r}')\rho^{in}(\mathbf{r})}{|\mathbf{r} - \mathbf{r}'|} + \frac{1}{2} \iint d\mathbf{r} d\mathbf{r}' \frac{\delta\rho(\mathbf{r})\delta\rho(\mathbf{r}')}{|\mathbf{r} - \mathbf{r}'|}$$

$$= E_{H}[\rho^{in}] + \int d\mathbf{r} \delta\rho(\mathbf{r}) V_{H}[\rho^{in}](\mathbf{r}) + \frac{1}{2} \iint d\mathbf{r} d\mathbf{r}' \frac{\delta\rho(\mathbf{r})\delta\rho(\mathbf{r}')}{|\mathbf{r} - \mathbf{r}'|},$$
(A.25)

but,

$$E_{\rm H}[\rho^{\rm in}] = \frac{1}{2} \int d\mathbf{r} \rho^{\rm in}(\mathbf{r}) V_{\rm H}[\rho^{\rm in}](\mathbf{r}), \tag{A.26}$$

so.

$$E_{\rm H}[\rho^{\rm in} + \delta \rho] = \int d\mathbf{r}(\rho^{\rm in} + \delta \rho) V_{\rm H}[\rho^{\rm in}](\mathbf{r}) - E_{\rm H}[\rho^{\rm in}] + \frac{1}{2} \iint d\mathbf{r} d\mathbf{r}' \frac{\delta \rho(\mathbf{r}) \delta \rho(\mathbf{r}')}{|\mathbf{r} - \mathbf{r}'|}, \tag{A.27}$$

and hence,

$$E_{\rm H}[\rho] - \int d\mathbf{r} \rho(\mathbf{r}) V_{\rm H}[\rho^{\rm in}](\mathbf{r}) = -E_{\rm H}[\rho^{\rm in}] + \frac{1}{2} \iint d\mathbf{r} d\mathbf{r}' \frac{\delta \rho(\mathbf{r}) \delta \rho(\mathbf{r}')}{|\mathbf{r} - \mathbf{r}'|}. \tag{A.28}$$

13.1.6 Proof of Equation (4.86)

We need to calculate

$$E_{\rm XC}[\rho] - \int d\mathbf{r} \rho(\mathbf{r}) V_{\rm XC}[\rho^{\rm in}](\mathbf{r}), \tag{A.29}$$

for $\rho = \rho^{\text{in}} + \delta \rho$. We write,

$$\begin{split} E_{\mathrm{XC}}[\rho^{\mathrm{in}} + \delta \rho] &= E_{\mathrm{XC}}[\rho^{\mathrm{in}}] + \int d\mathbf{r} \frac{\delta E_{\mathrm{XC}}}{\delta \rho} \Big|_{\rho^{\mathrm{in}}(\mathbf{r})} \delta \rho(\mathbf{r}) + \frac{1}{2} \iint d\mathbf{r} d\mathbf{r}' \frac{\delta^{2} E_{\mathrm{XC}}[\rho]}{\delta \rho(\mathbf{r}') \delta \rho(\mathbf{r})} \Big|_{\rho^{\mathrm{in}}(\mathbf{r}')} \\ &= E_{\mathrm{XC}}[\rho^{\mathrm{in}}] + \int d\mathbf{r} V_{\mathrm{XC}}[\rho^{\mathrm{in}}] \delta \rho(\mathbf{r}) \\ &+ \frac{1}{2} \iint d\mathbf{r} d\mathbf{r}' \frac{\delta^{2} E_{\mathrm{XC}}[\rho]}{\delta \rho(\mathbf{r}') \delta \rho(\mathbf{r})} \Big|_{\rho^{\mathrm{in}}(\mathbf{r}')} \delta \rho(\mathbf{r}') \delta \rho(\mathbf{r}) \\ &= E_{\mathrm{XC}}[\rho^{\mathrm{in}}] + \int d\mathbf{r} V_{\mathrm{XC}}[\rho^{\mathrm{in}}] \rho(\mathbf{r}) - \int d\mathbf{r} V_{\mathrm{XC}}[\rho^{\mathrm{in}}] \rho^{\mathrm{in}}(\mathbf{r}) \\ &+ \frac{1}{2} \iint d\mathbf{r} d\mathbf{r}' \frac{\delta^{2} E_{\mathrm{XC}}[\rho]}{\delta \rho(\mathbf{r}') \delta \rho(\mathbf{r})} \Big|_{\rho^{\mathrm{in}}(\mathbf{r}')} \delta \rho(\mathbf{r}') \delta \rho(\mathbf{r}), \end{split} \tag{A.30}$$

and so,

$$E_{\text{XC}}[\rho] - \int d\mathbf{r} \rho(\mathbf{r}) V_{\text{XC}}[\rho^{\text{in}}](\mathbf{r}) = E_{\text{XC}}[\rho^{\text{in}}] - \int d\mathbf{r} V_{\text{XC}}[\rho^{\text{in}}] \rho^{\text{in}}(\mathbf{r})$$

$$+ \frac{1}{2} \iint d\mathbf{r} d\mathbf{r}' \frac{\delta^2 E_{\text{XC}}[\rho]}{\delta \rho(\mathbf{r}') \delta \rho(\mathbf{r})} \Big|_{\rho^{\text{in}}(\mathbf{r}')} \delta \rho(\mathbf{r}') \delta \rho(\mathbf{r}),$$
(A.31)

13.1.7 Proof of Equation (4.102)

We want to show that if we assume the local density approximation for the exchange-correlation functional and that $V_{\text{LDA}}[\rho]$ is linear in $\rho(\mathbf{r})$ and we write the density as a sum of atom-centred contributions $\rho(\mathbf{r}) = \sum_{I} \rho_{I}(\mathbf{r})$ then the external potential in the Kohn–Sham equations can be written as a sum of atomic contributions,

$$V_{\text{ext}}^{\text{KS}}[\rho] = \sum_{I} V_{\text{ext},I}^{\text{KS}}[\rho_I(\mathbf{r})]. \tag{4.102}$$

Now,

$$V_{\text{avt}}^{\text{KS}}[\rho](\mathbf{r}) = V_{\text{ne}}(\mathbf{r}) + V_{\text{n}}[\rho](\mathbf{r}) + V_{\text{XC}}[\rho](\mathbf{r}). \tag{A.32}$$

Taking each term in turn we have,

$$V_{\text{ne}}(\mathbf{r}) = -\sum_{I} \frac{Z_{I}}{|\mathbf{r} - \mathbf{R}_{I}|},\tag{A.33}$$

which can clearly be written as a sum over atom-centred terms.

$$V_{\rm H}[\rho](\mathbf{r}) = \int d\mathbf{r}' \frac{\rho(\mathbf{r}')}{|\mathbf{r} - \mathbf{r}'|} = \sum_{I} \int d\mathbf{r}' \frac{\rho_{I}(\mathbf{r}')}{|\mathbf{r} - \mathbf{r}'|}, \tag{A.34}$$

again a sum of atom-centred contributions.

For the final term, we are assuming the local density approximation,

$$E_{\rm XC}[\rho](\mathbf{r}) = \int d\mathbf{r}' V_{\rm LDA}[\rho(\mathbf{r}')]\rho(\mathbf{r}'). \tag{A.35}$$

If we further assume that $V_{\rm LDA}$ is linear in $\rho(\mathbf{r})$, i.e. $V_{\rm LDA} = C\rho(\mathbf{r})$ for some constant C, then,

$$V_{\rm XC}[\rho](\mathbf{r}) \equiv \frac{\delta E_{\rm XC}}{\delta \rho} = C \rho(\mathbf{r}) = \sum_{I} C \rho_{I}(\mathbf{r}). \tag{A.36}$$

Again a sum of atom-centred contributions, this proves (4.102) and we have

$$V_{\text{ext}}^{\text{KS}}[\rho] = \sum_{I} V_{\text{ext},I}^{\text{KS}}[\rho_{I}(\mathbf{r})], \qquad V_{\text{ext},I}^{\text{KS}} = \frac{-Z_{I}}{|\mathbf{r} - \mathbf{R}_{I}|} + \int d\mathbf{r}' \frac{\rho_{I}(\mathbf{r}')}{|\mathbf{r} - \mathbf{r}'|} + C\rho_{I}(\mathbf{r}).$$
(A.37)

The error in this form due to the approximations made to $V_{\rm XC}$ will be [2],

$$\sum_{I} V_{\rm XC}[\rho_I] - V_{\rm XC} \left[\rho = \sum_{I} \rho_I \right]. \tag{A.38}$$

13.1.8 Proof of Equation (4.131)

$$i\hbar \frac{d}{dt} |\psi_i(t)\rangle = \hat{H}^{TB} |\psi_I\rangle + \frac{1}{2o_i} \sum_I \frac{\partial}{\partial a_{iI}^*} \mathcal{E}[\rho - \rho^0] |\mathbf{R}_I\rangle$$
 (4.131)

We start with Eq. 4.128

$$2i\hbar o_i \frac{\mathrm{d}}{\mathrm{d}t} a_{iI} = 2o_i \sum_{I} a_{iJ} \langle \mathbf{R}_J | \hat{H}^{\mathrm{TB}} | \mathbf{R}_I \rangle | + \frac{\hat{o}}{\hat{o} a_{iI}^*} \mathcal{E}[\rho - \rho^0](\mathbf{R}). \tag{4.128}$$

Now,

$$i\hbar \frac{\mathrm{d}}{\mathrm{d}t} |\psi_{i}(t)\rangle = i\hbar \sum_{I} \dot{a}_{iI} |\mathbf{R}_{I}\rangle$$

$$= \sum_{I} \left(\sum_{I} a_{iJ} \langle \mathbf{R}_{J} | \hat{H}^{\mathrm{TB}} |\mathbf{R}_{I}\rangle + \frac{1}{2o_{i}} \frac{\partial}{\partial a_{iI}^{*}} \mathcal{E}[\rho - \rho_{0}] \right) |\mathbf{R}_{I}\rangle. \tag{A.39}$$

by the symmetry of \hat{H}^{TB} and the completeness of the local basis, $\sum_{I} |\mathbf{R}_{I}\rangle \langle \mathbf{R}_{I}| = \hat{1}$, we have,

$$i\hbar \frac{\mathrm{d}}{\mathrm{d}t} |\psi_i(t)\rangle = \sum_I a_{iJ} \hat{H}^{\mathrm{TB}} |\mathbf{R}_J\rangle + \frac{1}{2o_i} \sum_I \frac{\partial}{\partial a_{iI}^*} \mathcal{E}[\rho - \rho_0] |\mathbf{R}_I\rangle, \tag{A.40}$$

but,

$$\sum_{I} a_{iJ} |\mathbf{R}_{J}\rangle = |\psi_{i}\rangle \tag{A.41}$$

and so the result is proved.

13.1.9 Proof of Equation (4.135)

We wish to show that,

$$\frac{1}{2o_i} \sum_{I} \frac{\partial}{\partial a_{iI}^*} \mathcal{E}[\rho - \rho^0] |\mathbf{R}_I\rangle = \hat{V}^{\text{SC}} |\psi_i\rangle, \tag{A.42}$$

where,

$$\hat{V}^{\text{SC}} = \sum_{IK} |\mathbf{R}_I\rangle \left(U_I \Delta q_I + \sum_{J \neq I} U_{IJ}(\mathbf{R}) \Delta q_J \right) \delta_{IK} \langle \mathbf{R}_K |. \tag{A.43}$$

Now,

$$\frac{\partial \mathcal{E}}{\partial a_{il}^*} = \sum_{L} \frac{\partial \mathcal{E}}{\partial \Delta q_L} \frac{\partial \Delta q_L}{\partial a_{il}^*},\tag{A.44}$$

and

$$\mathcal{E} = \frac{1}{2} \sum_{K} U_K \Delta q_K^2 + \frac{1}{2} \sum_{K,J \neq K} U_{KJ}(\mathbf{R}) \Delta q_K \Delta q_J, \tag{A.45}$$

so,

$$\frac{\partial \mathcal{E}}{\partial \Delta q_L} = U_L \Delta q_L + \frac{1}{2} \left(\sum_{J \neq L} U_{LJ}(\mathbf{R}) \Delta q_J + \sum_{K \neq L} U_{KL}(\mathbf{R}) \Delta q_K \right),$$

$$= U_L \Delta q_L + \sum_{J \neq L} U_{LJ}(\mathbf{R}) \Delta q_J,$$
(A.46)

where we have used the fact that $U_{IJ} = U_{JI}$. Given the definition of Δq_L ,

$$\Delta q_L = 2\sum_{j} o_j a_{jL}^* a_{jL} - q_0, \tag{A.47}$$

$$\frac{\partial \Delta q_L}{\partial a_{il}^*} = 2o_i a_{iL} \delta_{IL}. \tag{A.48}$$

So we have for the left-hand side of (A.42),

$$\frac{1}{2o_{i}} \sum_{I} \frac{\partial}{\partial a_{iI}^{*}} \mathcal{E}[\rho - \rho^{0}] |\mathbf{R}_{I}\rangle = \sum_{IL} a_{iL} \delta_{IL} \left(U_{L} \Delta q_{L} + \sum_{J \neq L} U_{LJ} \Delta q_{J} \right) |\mathbf{R}_{I}\rangle
= \sum_{I} a_{iI} \left(U_{I} \Delta q_{I} + \sum_{J \neq I} U_{IJ} \Delta q_{J} \right) |\mathbf{R}_{I}\rangle.$$
(A.49)

And for the right-hand side of (A.42),

$$\hat{V}^{\text{SC}}|\psi_{i}\rangle, = \sum_{IK} |\mathbf{R}_{I}\rangle \left(U_{I}\Delta q_{I} + \sum_{J\neq I} U_{IJ}\Delta q_{J} \right) \delta_{IK}\langle \mathbf{R}_{K}| \left(\sum_{L} a_{iL} |\mathbf{R}_{L}\rangle \right)
= \sum_{I} a_{iI} \left(U_{I}\Delta q_{I} + \sum_{J\neq I} U_{IJ}\Delta q_{J} \right) |\mathbf{R}_{I}\rangle,$$
(A.50)

since $\langle \mathbf{R}_K | \mathbf{R}_L \rangle = \delta_{KL}$, proving the result.

13.1.10 Proof of Equation (4.137)

We wish to show that the quantum Liouville equation for the evolution of the density matrix,

$$i\hbar \frac{d}{dt}\hat{\rho} = [\hat{H}^{TB}, \hat{\rho}] \tag{4.137}$$

is equivalent to the time-dependent Schrödinger equation

$$i\hbar \frac{d}{dt} |\psi_i\rangle = \hat{H}^{TB\prime} |\psi_i\rangle.$$
 (A.51)

Because \hat{H}^{TB} and \hat{V}^{SC} are Hermitian we have,

$$-i\hbar \frac{\mathrm{d}}{\mathrm{d}t} \langle \psi_i | = \langle \psi_i | \hat{H}^{\mathrm{TB}\prime}. \tag{A.52}$$

Hence,

$$i\hbar \frac{d}{dt}\hat{\rho}(t) = i\hbar \frac{d}{dt} \left(\sum_{i} o_{i} |\psi_{i}\rangle \langle \psi_{i}| \right)$$

$$= i\hbar \sum_{i} o_{i} \left\{ \left(\frac{d}{dt} |\psi_{i}\rangle \right) \langle \psi_{i}| + |\psi_{i}\rangle \left(\frac{d}{dt} \langle \psi_{i}| \right) \right\}$$

$$= \sum_{i} o_{i} (\hat{H}^{TB}|\psi_{i}\rangle \langle \psi_{i}| - |\psi_{i}\rangle \langle \psi_{i}| \hat{H}^{TB})$$

$$= \hat{H}^{TB}|\hat{\rho} - \hat{\rho}\hat{H}^{TB}|$$

$$= [\hat{H}^{TB}|, \hat{\rho}|.$$
(A.53)

13.1.11 Proof of Equation (4.141): The Conservation of Total Energy

We wish to show that our time-dependent tight-binding dynamics preserves the total energy of the semi-classical system:

$$\frac{d}{dt} \left(E^{TB'} + \sum_{I} \frac{1}{2} M_{I} \dot{\mathbf{R}}^{2} \right) = 0. \tag{4.141}$$

Writing

$$\frac{\mathrm{d}}{\mathrm{d}t} = \frac{\hat{o}}{\hat{o}t} + \dot{\mathbf{R}} \cdot \nabla_{\mathbf{R}},\tag{A.54}$$

we must then consider,

$$2\operatorname{Tr}\left\{\frac{\partial\hat{\rho}}{\partial t}\hat{H}^{\mathrm{TB}}\right\} + 2\operatorname{Tr}\left\{\hat{\rho}\nabla_{\mathbf{R}}\hat{H}^{\mathrm{TB}}\right\} \cdot \dot{\mathbf{R}} + \frac{\partial\mathcal{E}}{\partial t} + \dot{\mathbf{R}} \cdot \nabla_{\mathbf{R}}\mathcal{E} + \dot{\mathbf{R}} \cdot \nabla_{\mathbf{R}}V_{\mathrm{rep}} + \frac{\partial}{\partial t}\left\{\sum_{I}\frac{1}{2}M_{I}\dot{\mathbf{R}}^{2}\right\}. \tag{A.55}$$

Using the quantum Liouville equation (4.140), the first term becomes,

$$2\operatorname{Tr}\left\{\frac{\partial\hat{\rho}}{\partial t}\hat{H}^{\mathrm{TB}}\right\} = -\frac{2\mathrm{i}}{\hbar}\operatorname{Tr}\left\{\left[\hat{H}^{\mathrm{TB}} + \hat{V}^{\mathrm{SC}}, \hat{\rho}\right]\hat{H}^{\mathrm{TB}}\right\}$$

$$= -\frac{2\mathrm{i}}{\hbar}\left(\operatorname{Tr}\left\{\left[\hat{H}^{\mathrm{TB}}, \hat{\rho}\right]\hat{H}^{\mathrm{TB}}\right\} + \operatorname{Tr}\left\{\left[\hat{V}^{\mathrm{SC}}, \hat{\rho}\right]\hat{H}^{\mathrm{TB}}\right\}\right).$$
(A.56)

In general Tr([A,B]A) = 0 and so we are left with a total time derivative of the system energy,

$$-\frac{2\mathbf{i}}{\hbar} \text{Tr} \left\{ [\hat{V}^{\text{SC}}, \hat{\rho}] \hat{H}^{\text{TB}} \right\} + 2 \text{Tr} \left\{ \hat{\rho} \nabla_{\mathbf{R}} \hat{H}^{\text{TB}} \right\} \cdot \dot{\mathbf{R}} + \frac{\partial \mathcal{E}}{\partial t} + \dot{\mathbf{R}} \cdot \nabla_{\mathbf{R}} \mathcal{E} + \dot{\mathbf{R}} \cdot \nabla_{\mathbf{R}} V_{\text{rep}} + \frac{\partial}{\partial t} \left\{ \sum_{I} \frac{1}{2} M_{I} \dot{\mathbf{R}}^{2} \right\}.$$
(A.57)

Now,

$$\frac{\partial}{\partial t} \left(\sum_{I} \frac{1}{2} M_{I} \dot{\mathbf{R}}_{I}^{2} \right) = \sum_{I} M_{I} \dot{\mathbf{R}}_{I} \cdot \ddot{\mathbf{R}}_{I}, \tag{A.58}$$

which from (4.139) becomes

$$\sum_{I} M_{I} \dot{\mathbf{R}}_{I} \cdot \ddot{\mathbf{R}}_{I} = \dot{\mathbf{R}}_{I} \cdot \sum_{I} \left\{ -2 \operatorname{Tr} \left(\hat{\rho} \nabla_{\mathbf{R}_{I}} \hat{H}^{TB} \right) - \nabla_{\mathbf{R}_{I}} \mathcal{E} [\rho - \rho^{0}](\mathbf{R}) - \nabla_{\mathbf{R}_{I}} V_{\text{rep}}(\mathbf{R}) \right\}. \tag{A.59}$$

Thus the 6th term in (A.57) cancels the 2nd, 4th and 5th terms and we are left with a total energy derivative,

$$-\frac{2\mathrm{i}}{\hbar}\mathrm{Tr}\{\hat{V}^{\mathrm{SC}}\hat{\rho}\hat{H}^{\mathrm{TB}}\} + \frac{2\mathrm{i}}{\hbar}\mathrm{Tr}\{\hat{\rho}\hat{V}^{\mathrm{SC}}\hat{H}^{\mathrm{TB}}\} + \frac{\partial\mathcal{E}}{\partial t}.\tag{A.60}$$

Now,

$$\frac{\partial \mathcal{E}}{\partial t} = \sum_{iI} \frac{\partial \mathcal{E}}{\partial a_{iI}} \dot{a}_{iI} + \sum_{iI} \frac{\partial \mathcal{E}}{\partial a_{iI}^*} \dot{a}_{iI}^*, \tag{A.61}$$

since a_{iI} and a_{iI}^* must be treated independently. From (4.124) we have,

$$\sum_{iI} \frac{\partial \mathcal{E}}{\partial a_{iI}} \dot{a}_{iI} = \sum_{iI} \frac{\partial \mathcal{E}}{\partial a_{iI}} \left\{ -\frac{\mathrm{i}}{\hbar} \sum_{J} a_{iJ} \langle \mathbf{R}_{J} | \hat{H}^{\mathrm{TB}} | \mathbf{R}_{I} \rangle - \frac{\mathrm{i}}{2\hbar o_{i}} \frac{\partial \mathcal{E}}{\partial a_{iI}^{*}} \right\}, \tag{A.62}$$

and from (4.123) we have,

$$\sum_{il} \frac{\partial \mathcal{E}}{\partial a_{il}^*} \dot{a}_{il}^* = \sum_{il} \frac{\partial \mathcal{E}}{\partial a_{il}^*} \left\{ \frac{i}{\hbar} \sum_{J} a_{iJ}^* \langle \mathbf{R}_J | \hat{H}^{TB} | \mathbf{R}_I \rangle + \frac{i}{2\hbar o_i} \frac{\partial \mathcal{E}}{\partial a_{iI}} \right\}, \tag{A.63}$$

and so

$$\frac{\partial \mathcal{E}}{\partial t} = \frac{i}{\hbar} \sum_{iIJ} \left\{ \frac{\partial \mathcal{E}}{\partial a_{iI}^*} a_{iJ}^* \langle \mathbf{R}_J | \hat{H}^{TB} | \mathbf{R}_I \rangle - \frac{\partial \mathcal{E}}{\partial a_{iI}} a_{iJ} \langle \mathbf{R}_J | \hat{H}^{TB} | \mathbf{R}_I \rangle \right\}, \tag{A.64}$$

We can also write,

$$\hat{V}^{\text{SC}}\hat{\rho} = \sum_{i} o_{i} \hat{V}^{\text{SC}} |\psi_{i}\rangle \langle \psi_{i}|
= \frac{1}{2} \sum_{iI} \frac{\partial \mathcal{E}}{\partial a_{iI}^{*}} |\mathbf{R}_{I}\rangle \langle \psi_{i}|
= \frac{1}{2} \sum_{iI} \frac{\partial \mathcal{E}}{\partial a_{iI}^{*}} a_{iJ}^{*} |\mathbf{R}_{I}\rangle \langle \mathbf{R}_{J}|,$$
(A.65)

where to get the final line we used the result proved in Sect. 13.1.9. Hence,

$$\operatorname{Tr}\{\hat{V}^{\text{SC}}\hat{\rho}\hat{H}^{\text{TB}}\} = \frac{1}{2} \sum_{iII} \frac{\partial \mathcal{E}}{\partial a_{iI}^*} a_{iJ}^* \langle \mathbf{R}_J | \hat{H}^{\text{TB}} | \mathbf{R}_I \rangle. \tag{A.66}$$

We also have,

$$\hat{\rho}\hat{V}^{\text{SC}} = \sum_{i} o_{i} |\psi_{i}\rangle\langle\psi_{i}|\hat{V}^{\text{SC}}$$

$$= \frac{1}{2} \sum_{iI} |\psi_{i}\rangle\langle\mathbf{R}_{I}| \frac{\partial \mathcal{E}}{\partial a_{iI}}$$

$$= \frac{1}{2} \sum_{iII} \frac{\partial \mathcal{E}}{\partial a_{iI}} a_{iJ} |\mathbf{R}_{J}\rangle\langle\mathbf{R}_{I}|,$$
(A.67)

where we have used the result proved in Sect. 13.1.9 and the fact that \hat{V}^{SC} is hermitian. Hence,

$$\operatorname{Tr}\left\{\hat{\rho}\hat{V}^{\text{SC}}\hat{H}^{\text{TB}}\right\} = \frac{1}{2}\sum_{iII}\frac{\partial \mathcal{E}}{\partial a_{iI}}a_{iJ}\langle\mathbf{R}_{J}|\hat{H}^{\text{TB}}|\mathbf{R}_{I}\rangle. \tag{A.68}$$

From Eqs. A.64, A.66 and A.68 we can see that,

$$-\frac{2\mathrm{i}}{\hbar} \left(\mathrm{Tr} \left\{ \hat{V}^{\mathrm{SC}} \hat{\rho} \hat{H}^{\mathrm{TB}} \right\} - \mathrm{Tr} \left\{ \hat{\rho} \hat{V}^{\mathrm{SC}} \hat{H}^{\mathrm{TB}} \right\} \right) + \frac{\partial \mathcal{E}}{\partial t} = 0, \tag{A.69}$$

proving that the total system energy is conserved by our dynamics.

13.1.12 Proof of Increase of Pseudo-Entropy (8.16)

We wish to show that our pseudo-entropy

$$\tilde{S}(\hat{\rho}) \equiv -k_{\rm B} \sum_{i} (o_i \ln o_i + (1 - o_i) \ln(1 - o_i)),$$
 (8.16)

will tend to increase with time. Taking the time derivative we have

$$\frac{1}{k_{\rm B}}\frac{\mathrm{d}}{\mathrm{d}t}\tilde{S}(\hat{\rho}) = -\sum_{i}\dot{o}_{i}(\ln o_{i} - \ln(1 - o_{i})). \tag{A.70}$$

If we assume that excitations from state i to state j take place at an underlying rate w_{ij} , where $w_{ji} = w_{ij}$, then, given the constraints of exclusion,

$$\dot{o}_i = \sum_i w_{ji} (o_j - o_i). \tag{A.71}$$

Hence we have,

$$\frac{1}{k_{\rm B}} \frac{\rm d}{{\rm d}t} \tilde{S}(\hat{\rho}) = -\sum_{ij} w_{ji} (o_j - o_i) (\ln o_i - \ln(1 - o_i))$$

$$= \frac{1}{2} \sum_{ij} w_{ji} (o_i - o_j) \left[\ln \left(\frac{o_i}{1 - o_i} \right) - \ln \left(\frac{o_j}{1 - o_j} \right) \right]$$

$$= \frac{1}{2} \sum_{ij} w_{ji} (o_i - o_j) \ln \left(\frac{o_i / o_j - o_i}{1 - o_i} \right)$$
(A.72)

where to get the second line we paired terms in i, j and j, i. All of the terms in the double sum, whether $o_i > o_j$ or $o_j > o_i$ must be greater than or equal to zero and so our pseudo-entropy must increase with time.

13.1.13 **Proof of Equation** (9.4)

We wish to show that we can write the electronic (Hellmann-Feynman) force on the ions in our simulations can be written

$$\mathbf{F}_{e} = -\sum_{i} \rho_{ii} \nabla \varepsilon_{i} - \sum_{i,j \neq i} (\varepsilon_{i} - \varepsilon_{j}) \rho_{ij} \langle \phi_{j} | \nabla \phi_{i} \rangle. \tag{9.4}$$

where $\{|\phi_i\rangle\}$ are the instantaneous eigenstates of the non-self-consistent Hamiltonian \hat{H} with eigenvalues $\{\varepsilon_i\}$. We start with the general expression for the Hellmann–Feynman force,

$$\mathbf{F}_{e} = -\text{Tr}\{\hat{\rho}\nabla_{\mathbf{R}}\hat{H}\},\tag{A.73}$$

and write it in the eigenstate basis,

$$\mathbf{F}_{e} = -\sum_{ij} \langle \phi_{i} | \hat{\rho} | \phi_{j} \rangle \langle \phi_{j} | \nabla_{\mathbf{R}} \hat{H} | \phi_{i} \rangle. \tag{A.74}$$

We then split out the contribution from the diagonal elements of $\hat{\rho}$,

$$\mathbf{F}_{\mathrm{e}} = -\sum_{i} \rho_{ii} \langle \phi_{i} | \nabla_{\mathbf{R}} \hat{H} | \phi_{i} \rangle - \sum_{i,j \neq i} \rho_{ij} \langle \phi_{j} | \nabla_{\mathbf{R}} \hat{H} | \phi_{i} \rangle, \tag{A.75}$$

where we have written $\rho_{ij} = \langle \phi_i | \hat{\rho} | \phi_j \rangle$. Next we consider,

$$\nabla_{\mathbf{R}} (\langle \phi_j | \hat{H} | \phi_i \rangle) = \langle \nabla_{\mathbf{R}} \phi_j | \hat{H} | \phi_i \rangle + \langle \phi_j | \hat{H} | \nabla_{\mathbf{R}} \phi_i \rangle + \langle \phi_j | \nabla_{\mathbf{R}} \hat{H} | \phi_i \rangle$$

$$= \varepsilon_i \langle \nabla_{\mathbf{R}} \phi_i | \phi_i \rangle + \varepsilon_j \langle \phi_i | \nabla_{\mathbf{R}} \phi_i \rangle + \langle \phi_j | \nabla_{\mathbf{R}} \hat{H} | \phi_i \rangle, \tag{A.76}$$

but since the orthonormality of the eigenstates must be preserved,

$$\nabla_{\mathbf{R}}(\langle \phi_i | \phi_i \rangle) = \langle \nabla_{\mathbf{R}} \phi_i | \phi_i \rangle + \langle \phi_i | \nabla_{\mathbf{R}} \phi_i \rangle = 0, \tag{A.77}$$

and so

$$\nabla_{\mathbf{R}}(\langle \phi_i | \hat{H} | \phi_i \rangle) = (\varepsilon_j - \varepsilon_i) \langle \phi_i | \nabla_{\mathbf{R}} \phi_i \rangle + \langle \phi_i | \nabla_{\mathbf{R}} \hat{H} | \phi_i \rangle. \tag{A.78}$$

For i = j we have,

$$\langle \phi_i | \nabla_{\mathbf{R}} \hat{H} | \phi_i \rangle = \nabla_{\mathbf{R}} \left(\langle \phi_i | \hat{H} | \phi_i \rangle \right) = \nabla_{\mathbf{R}} \varepsilon_i. \tag{A.79}$$

For $i \neq j$ we have,

$$\nabla_{\mathbf{R}}(\langle \phi_i | \hat{H} | \phi_i \rangle) = 0 \tag{A.80}$$

since \hat{H} is diagonal and so,

$$\langle \phi_i | \nabla_{\mathbf{R}} \hat{H} | \phi_i \rangle = (\varepsilon_i - \varepsilon_i) \langle \phi_i | \nabla_{\mathbf{R}} \phi_i \rangle, \tag{A.81}$$

and our result is proved.

13.1.14 Proof that $Im\{f_4\} = 0$

We wish to show that the force

$$\mathbf{f}_4 = -\sum_{i,j \neq i} (\varepsilon_i - \varepsilon_j) \rho_{ij} \langle \phi_j | \nabla \phi_i \rangle, \tag{9.13}$$

is real. We begin by considering the pair of terms in i, j and j, i:

$$\mathbf{f}_{4} = -\frac{1}{2} \sum_{i \neq i} \left\{ (\varepsilon_{i} - \varepsilon_{j}) \rho_{ij} \langle \phi_{j} | \nabla \phi_{i} \rangle + (\varepsilon_{j} - \varepsilon_{i}) \rho_{ji} \langle \phi_{i} | \nabla \phi_{j} \rangle \right\}, \tag{A.82}$$

where the factor of 1/2 corrects for the double-counting. Now we note that $\nabla_{\mathbf{R}}(\langle \phi_i | \phi_i \rangle) = 0$ and so $\langle \nabla_{\mathbf{R}} \phi_i | \phi_i \rangle = -\langle \phi_i | \nabla_{\mathbf{R}} \phi_i \rangle$. Hence,

$$\langle \phi_i | \nabla_{\mathbf{R}} \phi_j \rangle = (\langle \nabla_{\mathbf{R}} \phi_j | \phi_i \rangle)^* = (\langle \phi_j | \nabla_{\mathbf{R}} \phi_i \rangle)^*. \tag{A.83}$$

The density matrix is anti-Hermitian, $\rho_{ij}^* = -\rho_{ji}$ so,

$$\mathbf{f}_{4} = -\frac{1}{2} \sum_{i,j \neq i} (\varepsilon_{i} - \varepsilon_{j}) \left[\rho_{ij} \langle \phi_{j} | \nabla_{\mathbf{R}} \phi_{i} \rangle + \rho_{ij}^{*} (\langle \phi_{j} | \nabla_{\mathbf{R}} \phi_{i} \rangle)^{*} \right]$$

$$= -\sum_{i,j \neq i} (\varepsilon_{i} - \varepsilon_{j}) \Re \left\{ \rho_{ij} \langle \phi_{j} | \nabla_{\mathbf{R}} \phi_{i} \rangle \right\},$$
(A.84)

as required.

13.1.15 Proof of Equation (11.9)

We wish to show that we can write

$$\sum_{i,j\neq i} (\varepsilon_i - \varepsilon_j) \rho_{ij} \langle \phi_j | \left(\frac{\mathrm{d}}{\mathrm{d}t} | \phi_i \rangle \right) = \sum_i \frac{\mathrm{d}\rho_{ii}}{\mathrm{d}t} \varepsilon_i. \tag{A.85}$$

We begin by considering

$$\frac{\mathrm{d}\rho_{ii}}{\mathrm{d}t} = \frac{\mathrm{d}}{\mathrm{d}t} \langle \phi_i | \hat{\rho} | \phi_i \rangle
= \left(\frac{\mathrm{d}}{\mathrm{d}t} \langle \phi_i | \right) \hat{\rho} | \phi_i \rangle + \langle \phi_i | \left(\frac{\mathrm{d}}{\mathrm{d}t} \hat{\rho} \right) | \phi_i \rangle + \langle \phi_i | \hat{\rho} \left(\frac{\mathrm{d}}{\mathrm{d}t} | \phi_i \rangle \right).$$
(A.86)

The quantum Liouville equation gives us the evolution of $\hat{\rho}$,

$$i\hbar \frac{\mathrm{d}\hat{p}}{\mathrm{d}t} = [\hat{H}, \hat{\rho}] = \sum_{ii} |\phi_i\rangle (\varepsilon_i - \varepsilon_j) \rho_{ij} \langle \phi_j|, \tag{A.87}$$

and so,

$$\langle \phi_i | \left(\frac{\mathrm{d}}{\mathrm{d}t} \hat{\rho} \right) | \phi_i \rangle = 0.$$
 (A.88)

Hence, exploiting the completeness of the eigenstate basis, $\sum_{j} |\phi_{j}\rangle\langle\phi_{j}|$, we can write,

$$\frac{\mathrm{d}\rho_{ii}}{\mathrm{d}t} = \sum_{j} \left(\frac{\mathrm{d}}{\mathrm{d}t} \langle \phi_{i} | \right) |\phi_{j}\rangle \rho_{ji} + \langle \phi_{j} | \left(\frac{\mathrm{d}}{\mathrm{d}t} |\phi_{i}\rangle \right) \rho_{ij}
= \sum_{j} \langle \phi_{j} | \left(\frac{\mathrm{d}}{\mathrm{d}t} |\phi_{i}\rangle \right) \rho_{ij} - \langle \phi_{i} | \left(\frac{\mathrm{d}}{\mathrm{d}t} |\phi_{j}\rangle \right) \rho_{ji}.$$
(A.89)

To obtain the second line we used d $\langle \phi_i | \phi_i \rangle / dt$. Now,

$$\sum_{i} \frac{\mathrm{d}\rho_{ii}}{\mathrm{d}t} \varepsilon_{i} = \sum_{ij} \left\{ \langle \phi_{j} | \left(\frac{\mathrm{d}}{\mathrm{d}t} | \phi_{i} \rangle \right) \rho_{ij} - \langle \phi_{i} | \left(\frac{\mathrm{d}}{\mathrm{d}t} | \phi_{j} \rangle \right) \rho_{ji} \right\} \varepsilon_{i} \\
= \sum_{ij} \left\{ \langle \phi_{j} | \left(\frac{\mathrm{d}}{\mathrm{d}t} | \phi_{i} \rangle \right) \rho_{ij} \varepsilon_{i} - \langle \phi_{j} | \left(\frac{\mathrm{d}}{\mathrm{d}t} | \phi_{i} \rangle \right) \rho_{ij} \varepsilon_{j} \right\}, \tag{A.90}$$

proving the result.

13.1.16 Proof of Equation (11.12)

We wish to show,

$$\sum_{i,j\neq i} \langle \phi_i | \hat{\rho} | \phi_j \rangle (\varepsilon_i - \varepsilon_j) \langle \phi_j | \nabla_{\mathbf{R}} \phi_i \rangle = \sum_{i,j\neq i} \langle \phi_i | \hat{\rho} | \phi_j \rangle \langle \phi_j | \nabla_{\mathbf{R}} \hat{H} | \phi_i \rangle. \tag{A.91}$$

For a small change $\delta \mathbf{R}$ in \mathbf{R} , first order perturbation theory gives us the change in an eigenstate,

$$\nabla_{\mathbf{R}} |\phi_i\rangle \cdot \delta \mathbf{R} = \sum_{k} \frac{\langle \phi_k | \nabla_{\mathbf{R}} \hat{H} \cdot \delta \mathbf{R} | \phi_i \rangle}{\varepsilon_i - \varepsilon_k} |\phi_k\rangle, \tag{A.92}$$

and so

$$\langle \phi_j | \nabla_{\mathbf{R}} | \phi_i \rangle = \frac{\langle \phi_j | \nabla_{\mathbf{R}} \hat{H} \cdot \delta \mathbf{R} | \phi_i \rangle}{\varepsilon_i - \varepsilon_j}, \tag{A.93}$$

since $\delta \mathbf{R}$ is arbitrary, proving the result.

13.1.17 Proof of Equation (11.18)

We wish to show that

$$\frac{\mathrm{d}\mathbf{f}_{0}}{\mathrm{d}t} = -\sum_{i,j\neq i} \langle \phi_{i} | \frac{\mathrm{d}\hat{\rho}}{\mathrm{d}t} | \phi_{j} \rangle \langle \phi_{j} | \nabla_{\mathbf{R}_{0}} \hat{H} | \phi_{i} \rangle
- \sum_{i,j\neq i} \dot{\mathbf{R}} \cdot \nabla_{\mathbf{R}} (\langle \phi_{i} | \hat{\rho} | \phi_{j} \rangle) \langle \phi_{j} | \nabla_{\mathbf{R}_{0}} \hat{H} | \phi_{i} \rangle
- \sum_{i,j\neq i} \langle \phi_{i} | \hat{\rho} | \phi_{j} \rangle \dot{\mathbf{R}} \cdot \nabla_{\mathbf{R}} (\langle \phi_{j} | \nabla_{\mathbf{R}_{0}} \hat{H} | \phi_{i} \rangle),$$
(A.94)

can be rewritten,

$$\frac{\mathrm{d}\mathbf{f}_{0}(t)}{\mathrm{d}t} = \sum_{i,j\neq i} \frac{o_{j} - o_{i}}{\varepsilon_{i} - \varepsilon_{j}} \left(\langle \phi_{i} | \nabla_{\mathbf{R}} \hat{H} | \phi_{j} \rangle \cdot \dot{\mathbf{R}} \right) \langle \phi_{j} | \nabla_{\mathbf{R}_{0}} \hat{H} | \phi_{i} \rangle. \tag{A.95}$$

We have three terms to deal with, which we will take in turn. First,

$$\frac{\mathrm{d}}{\mathrm{d}t}\rho_{ij} = -\frac{\mathrm{i}}{\hbar}\langle\phi_{i}|[\hat{H},\hat{\rho}]|\phi_{j}\rangle
= -\frac{\mathrm{i}}{\hbar}\sum_{k} \left\{ \langle\phi_{i}|\hat{H}|\phi_{k}\rangle\langle\phi_{k}|\hat{\rho}|\phi_{j}\rangle - \langle\phi_{i}|\hat{\rho}|\phi_{k}\rangle\langle\phi_{k}|\hat{H}|\phi_{j}\rangle \right\},$$
(A.96)

by the completeness relation $\sum_{k} |\phi_{k}\rangle \langle \phi_{k}| = \hat{1}$. Now, $\langle \phi_{i}|\hat{H}|\phi_{i}\rangle = \varepsilon_{i}\delta_{ij}$, so,

$$\frac{\mathrm{d}}{\mathrm{d}t}\rho_{ij} = -\frac{\mathrm{i}}{\hbar}(\varepsilon_i - \varepsilon_j)\langle\phi_i|\hat{\rho}|\phi_j\rangle. \tag{A.97}$$

Second, we consider,

$$\nabla_{\mathbf{R}}\rho_{ii} \cdot \dot{\mathbf{R}} = \left(\langle \nabla_{\mathbf{R}}\phi_i | \hat{\rho} | \phi_i \rangle + \langle \phi_i | \hat{\rho} | \nabla_{\mathbf{R}}\phi_i \rangle \right) \cdot \mathbf{R}. \tag{A.98}$$

From first order perturbation theory,

$$\nabla_{\mathbf{R}}|\phi_{j}\rangle\cdot\dot{\mathbf{R}}\delta t = \sum_{k} \frac{\langle\phi_{k}|\nabla_{\mathbf{R}}\hat{H}\cdot\dot{\mathbf{R}}\delta t|\phi_{j}\rangle}{\varepsilon_{j} - \varepsilon_{k}}|\phi_{k}\rangle, \tag{A.99}$$

we obtain,

$$\nabla_{\mathbf{R}}\rho_{ij} \cdot \dot{\mathbf{R}} = \sum_{k} \left\{ \frac{\langle \phi_{i} | \nabla_{\mathbf{R}} \hat{H} | \phi_{k} \rangle \cdot \dot{\mathbf{R}}}{\varepsilon_{k} - \varepsilon_{i}} \langle \phi_{k} | \hat{\rho} | \phi_{j} \rangle + \frac{\langle \phi_{k} | \nabla_{\mathbf{R}} \hat{H} | \phi_{j} \rangle \cdot \dot{\mathbf{R}}}{\varepsilon_{j} - \varepsilon_{k}} \langle \phi_{i} | \hat{\rho} | \phi_{k} \rangle \right\}$$
(A.100)

And third we must consider,

$$\nabla_{\mathbf{R}} (\langle \phi_{j} | \nabla_{\mathbf{R}_{0}} \hat{H} | \phi_{i} \rangle) \cdot \mathbf{R} = (\langle \nabla_{\mathbf{R}} \phi_{j} | \nabla_{\mathbf{R}_{0}} \hat{H} | \phi_{i} \rangle + \langle \phi_{j} | \nabla_{\mathbf{R}_{0}} \hat{H} | \nabla_{\mathbf{R}} \phi_{i} \rangle + \langle \phi_{j} | \nabla_{\mathbf{R}} \phi_{i} \rangle + \langle \phi_{j} | \nabla_{\mathbf{R}} (\nabla_{\mathbf{R}_{0}} \hat{H}) | \phi_{i} \rangle) \cdot \dot{\mathbf{R}}$$

$$= \sum_{k} \left\{ \frac{\langle \phi_{j} | \nabla_{\mathbf{R}} \hat{H} | \phi_{k} \rangle \cdot \dot{\mathbf{R}}}{\varepsilon_{k} - \varepsilon_{j}} \langle \phi_{k} | \nabla_{\mathbf{R}_{0}} \hat{H} | \phi_{i} \rangle + \frac{\langle \phi_{k} | \nabla_{\mathbf{R}} \hat{H} | \phi_{i} \rangle \cdot \dot{\mathbf{R}}}{\varepsilon_{i} - \varepsilon_{k}} \langle \phi_{j} | \nabla_{\mathbf{R}_{0}} \hat{H} | \phi_{k} \rangle \right\}$$

$$+ \langle \phi_{i} | \nabla_{\mathbf{R}} (\nabla_{\mathbf{R}_{i}} \hat{H}) | \phi_{i} \rangle \cdot \dot{\mathbf{R}}. \tag{A.102}$$

With these three terms rewritten as above we have

$$\begin{split} \frac{\mathrm{d}\mathbf{f}_{0}}{\mathrm{d}t} &= \sum_{i,j\neq i} \frac{\mathrm{i}}{\hbar} (\varepsilon_{i} - \varepsilon_{j}) \langle \phi_{i} | \hat{\rho} | \phi_{j} \rangle \langle \phi_{j} | \nabla_{\mathbf{R}_{0}} \hat{H} | \phi_{i} \rangle \\ &- \sum_{i,j\neq i} \sum_{k} \left\{ \frac{\langle \phi_{i} | \nabla_{\mathbf{R}} \hat{H} | \phi_{k} \rangle \cdot \dot{\mathbf{R}}}{\varepsilon_{i} - \varepsilon_{k}} \langle \phi_{k} | \hat{\rho} | \phi_{j} \rangle \\ &+ \frac{\langle \phi_{k} | \nabla_{\mathbf{R}} \hat{H} | \phi_{j} \rangle \cdot \dot{\mathbf{R}}}{\varepsilon_{j} - \varepsilon_{k}} \langle \phi_{i} | \hat{\rho} | \phi_{k} \rangle \right\} \langle \phi_{j} | \nabla_{\mathbf{R}_{0}} \hat{H} | \phi_{i} \rangle \\ &- \sum_{i,j\neq i} \langle \phi_{i} | \hat{\rho} | \phi_{j} \rangle \left[\sum_{k} \left\{ \frac{\langle \phi_{j} | \nabla_{\mathbf{R}} \hat{H} | \phi_{k} \rangle \cdot \dot{\mathbf{R}}}{\varepsilon_{k} - \varepsilon_{j}} \langle \phi_{k} | \nabla_{\mathbf{R}_{0}} \hat{H} | \phi_{i} \rangle \right. \\ &+ \frac{\langle \phi_{k} | \nabla_{\mathbf{R}} \hat{H} | \phi_{i} \rangle \cdot \dot{\mathbf{R}}}{\varepsilon_{i} - \varepsilon_{k}} \langle \phi_{j} | \nabla_{\mathbf{R}_{0}} \hat{H} | \phi_{k} \rangle \right\} + \langle \phi_{j} | \dot{\mathbf{R}} \cdot \nabla_{\mathbf{R}} (\nabla_{\mathbf{R}_{0}} \hat{H}) | \phi_{i} \rangle \right], \quad (A.103) \end{split}$$

Now, the first and last terms including a summation $\sum_{i,j \neq i}$ are zero because of the condition $j \neq i$. This leaves,

$$\frac{\mathrm{d}\mathbf{f}_{0}}{\mathrm{d}t} = -\sum_{i,j\neq i} \left\{ \frac{\langle \phi_{i} | \nabla_{\mathbf{R}} \hat{H} | \phi_{j} \rangle \cdot \dot{\mathbf{R}}}{\varepsilon_{j} - \varepsilon_{i}} o_{j} + \frac{\langle \phi_{i} | \nabla_{\mathbf{R}} \hat{H} | \phi_{j} \rangle \cdot \dot{\mathbf{R}}}{\varepsilon_{j} - \varepsilon_{i}} o_{i} \right\} \langle \phi_{j} | \nabla_{\mathbf{R}_{0}} \hat{H} | \phi_{i} \rangle
= \sum_{i,j\neq i} \frac{o_{j} - o_{i}}{\varepsilon_{i} - \varepsilon_{j}} (\langle \phi_{i} | \nabla_{\mathbf{R}} \hat{H} | \phi_{j} \rangle \cdot \dot{\mathbf{R}}) \langle \phi_{j} | \nabla_{\mathbf{R}_{0}} \hat{H} | \phi_{i} \rangle.$$
(A.104)

13.2 Appendix B: Perturbation Theory

In this appendix we will derive some useful results in time-dependent perturbation theory. We will begin with a fairly general presentation of the theory, before going on to consider the effect of a sinusoidal perturbation on an electronic system represented by a single particle density matrix. We will then specialize even further to derive an analytical expression for the effect of a single oscillating ion in our single *s*-band tight-binding model. In a further section we derive basic results for a quantum mechanical oscillator.

Our approach to time-dependent perturbation theory will consider the effect of adding a time-dependent perturbation $\hat{V}(t)$ to a time-independent Hamiltonian \hat{H}^0 on the evolution of a quantum mechanical system. We will work in terms of *time evolution operators*, $\hat{U}(t;t_0)$, whose action is to carry a state of our system at time t_0 , $|\psi(t_0)\rangle$, over into an evolved state at time t, $|\psi(t)\rangle$ [3, pp. 69–71],

$$\hat{U}(t;t_0)|\psi(t_0)\rangle = |\psi(t)\rangle. \tag{B.1}$$

We will work in the basis of eigenstates, $\{|\phi_i\rangle\}$ of \hat{H}^0 with eigenvalues $\{\varepsilon_i\}$,

$$\hat{H}^0|\phi_i\rangle = \varepsilon_i|\phi_i\rangle. \tag{B.2}$$

We can define an evolution operator for the unperturbed system, \hat{U}^0 , by its action on an eigenstate,

$$\hat{U}^{0}(t)|\phi_{i}\rangle = e^{-\frac{i}{\hbar}\varepsilon_{i}t}|\phi_{i}\rangle, \tag{B.3}$$

where from now on we will assume, without loss of generality, that $t_0 = 0$ and leave it implicit in our notation for time evolution operators. $\hat{U}^0(t)$ satisfies,

$$i\hbar \frac{\mathrm{d}}{\mathrm{d}t}\hat{U}^0(t) = \hat{H}^0\hat{U}^0(t). \tag{B.4}$$

Our notation here will be the one that we have been using for our independent electron system. The derivation is, though, more general.

We will want to compare this evolution operator with the one that gives the evolution of the system under the full perturbed Hamiltonian $\hat{H}(t) = \hat{H}^0 + \hat{V}(t)$. This evolution operator, $\hat{U}(t)$, will satisfy,

$$i\hbar \frac{d}{dt}\hat{U}(t) = \hat{H}(t)\hat{U}(t). \tag{B.5}$$

We now use the effect of $\hat{U}(t)$ on the eigenstates of \hat{H}^0 to define a set of evolving wavefunctions $\{|\psi_i(t)\rangle\}$:

$$|\psi_i(t)\rangle = \hat{U}(t)|\phi_i\rangle.$$
 (B.6)

Our perturbation theory is fundamentally about comparing the evolution given by $\hat{U}(t)$ with that given by $\hat{U}^0(t)$. So an important object will be the projection of an eigenstate evolved under the perturbed Hamiltonian onto one evolved under the Hamiltonian \hat{H}^0 :

$$\langle \phi_i | \hat{U}^0(t)^{\dagger} | \psi_i(t) \rangle = \langle \phi_i | \hat{U}^{0\dagger}(t) \hat{U}(t) | \phi_i \rangle. \tag{B.7}$$

From now on, to aid readability, we will leave the time dependence of \hat{U}^0 , \hat{U} and \hat{H} implicit.

We now define an evolution operator,

$$\hat{U}' = \hat{U}^{0\dagger} \hat{U} \tag{B.8}$$

whose effect on the eigenstates will be small if the perturbation $\hat{V}(t)$ is small compared with \hat{H}^0 . We differentiate \hat{U}' :

$$\frac{\mathrm{d}}{\mathrm{d}t}\hat{U}' = \left(\frac{\mathrm{d}}{\mathrm{d}t}\hat{U}^{0\dagger}\right)\hat{U} + \hat{U}^{0\dagger}\left(\frac{\mathrm{d}}{\mathrm{d}t}\hat{U}\right),\tag{B.9}$$

which from (B.4) and (B.5) becomes,

$$\frac{\mathrm{d}}{\mathrm{d}t}\hat{U}' = -\frac{\mathrm{i}}{\hbar} \left(-\hat{U}^{0\dagger}\hat{H}^0\hat{U} + \hat{U}^{0\dagger}\hat{H}\hat{U} \right)
= -\frac{\mathrm{i}}{\hbar}\hat{U}^{0\dagger} \left(\hat{H} - \hat{H}^0 \right) \hat{U}.$$
(B.10)

Now $\hat{H} - \hat{H}^0 = \hat{V}$, and $\hat{U}' = \hat{U}^{0\dagger} \hat{U} \Rightarrow \hat{U} = \hat{U}^0 \hat{U}'$, since \hat{U}^0 is unitary,so,

$$\frac{\mathrm{d}}{\mathrm{d}t}\hat{U}' = -\frac{\mathrm{i}}{\hbar}(\hat{U}^{0\dagger}\hat{V}\hat{U}^0)\hat{U}'. \tag{B.11}$$

We now integrate this expression to obtain,

$$\hat{U}'(t) - \hat{U}'(0) = -\frac{i}{\hbar} \int_{0}^{t} dt' (\hat{U}^{0\dagger} \hat{V}(t') \hat{U}^{0}) \hat{U}'.$$
 (B.12)

Since $\hat{U}'(0) = \hat{1}$, the identity operator,

$$\hat{U}'(t) = \hat{1} + \left(-\frac{i}{\hbar}\right) \int_{0}^{t} dt' \left(\hat{U}^{0\dagger}(t')\hat{V}(t')\hat{U}^{0}(t')\right)
+ \left(-\frac{i}{\hbar}\right)^{2} \int_{0}^{t} dt' \left(\hat{U}^{0\dagger}(t')\hat{V}(t')\hat{U}^{0}(t')\right) \int_{0}^{t'} dt'' \left(\hat{U}^{0\dagger}(t'')\hat{V}(t'')\hat{U}^{0}(t'')\right) \hat{U}'.$$
(B.13)

We can repeat the above process of expanding $\hat{U}'(t)$ to obtain the *Dyson series*,

$$\begin{split} \hat{U}'(t) &= \hat{1} + \left(-\frac{i}{\hbar} \right) \int_{0}^{t} dt' e^{\frac{i}{\hbar} \hat{H}^{0} t'} \hat{V}(t') e^{-\frac{i}{\hbar} \hat{H}^{0} t'} \\ &+ \left(-\frac{i}{\hbar} \right)^{2} \int_{0}^{t} dt' e^{\frac{i}{\hbar} \hat{H}^{0} t'} \hat{V}(t') e^{-\frac{i}{\hbar} \hat{H}^{0} t'} \int_{0}^{t'} dt'' e^{\frac{i}{\hbar} \hat{H}^{0} t''} \hat{V}(t'') e^{-\frac{i}{\hbar} \hat{H}^{0} t''} \hat{V}(t'') e^{-\frac{i}{\hbar} \hat{H}^{0} t''} \hat{V}(t'') e^{-\frac{i}{\hbar} \hat{H}^{0} t''} + \cdots, \end{split}$$

$$(B.14)$$

where we have used the fact that,

$$\hat{U}^0(t) = e^{-\frac{i}{\hbar}\hat{H}^0t}.$$
 (B.15)

13.2.1 A Periodic Perturbation

We will now consider the case of a perturbation that varies sinusoidally in time, with angular frequency Ω :

$$\hat{V}(t) = \hat{V}^0 \sin \Omega t, \tag{B.16}$$

and derive expressions for the terms of the Dyson series (B.14). We will write the matrix elements of \hat{U}' as an expansion,

$$\langle \phi_i | \hat{U}' | \phi_i \rangle = \langle \phi_i | (\hat{U}'^{(0)} + \hat{U}'^{(1)} + \hat{U}'^{(2)} + \cdots) | \phi_i \rangle,$$
 (B.17)

where the terms $\hat{U}^{\prime(i)}$ correspond to the terms in (B.14). Immediately we can see that the zeroth order term will be,

$$\langle \phi_i | \hat{U}'^{(0)} | \phi_j \rangle = \langle \phi_i | \phi_j \rangle = \delta_{ij},$$
 (B.18)

by the orthonormality of the eigenstates. For the first order term,

$$\begin{split} \langle \phi_{i} | \hat{U}^{\prime(1)} | \phi_{j} \rangle &= -\frac{\mathrm{i}}{\hbar} \int_{0}^{t} \mathrm{d}t' \langle \phi_{i} | \mathrm{e}^{\frac{\mathrm{i}}{\hbar} \hat{H}^{0} t'} \hat{V}^{0} \mathrm{e}^{-\frac{\mathrm{i}}{\hbar} \hat{H}^{0} t'} | \phi_{j} \rangle \mathrm{sin} \Omega t' \\ &= -\frac{\mathrm{i}}{\hbar} \langle \phi_{i} | \hat{V}^{0} | \phi_{j} \rangle \int_{0}^{t} \mathrm{d}t' \mathrm{e}^{\frac{\mathrm{i}}{\hbar} (\hat{e}_{i} - \hat{e}_{j}) t'} \mathrm{sin} \Omega t'. \end{split} \tag{B.19}$$

Writing $\varepsilon_i - \varepsilon_j = \hbar \omega_{ji}$, we have,

$$\begin{split} \langle \phi_{i} | \hat{U}'^{(1)} | \phi_{j} \rangle &= -\frac{\mathrm{i}}{\hbar} \langle \phi_{i} | \hat{V}^{0} | \phi_{j} \rangle \int_{0}^{t} \mathrm{d}t' \mathrm{e}^{\mathrm{i}\omega_{ji}t'} \mathrm{sin}\Omega t' \\ &= -\frac{1}{2\hbar} \langle \phi_{i} | \hat{V}^{0} | \phi_{j} \rangle \int_{0}^{t} \mathrm{d}t' \left(\mathrm{e}^{\mathrm{i}(\Omega + \omega_{ji})t'} - \mathrm{e}^{\mathrm{i}(\Omega - \omega_{ji})t'} \right) \\ &= \frac{\mathrm{i}}{2\hbar} \langle \phi_{i} | \hat{V}^{0} | \phi_{j} \rangle \left\{ \frac{\mathrm{e}^{\mathrm{i}(\Omega + \omega_{ji})t'}}{\Omega + \omega_{ji}} \right]_{0}^{t} - \left[\frac{\mathrm{e}^{\mathrm{i}(\Omega - \omega_{ji})t'}}{\Omega - \omega_{ji}} \right]_{0}^{t} \right\} \\ &= -\frac{1}{2\hbar} \langle \phi_{i} | \hat{V}^{0} | \phi_{j} \rangle \left\{ \frac{\mathrm{e}^{\mathrm{i}(\Omega + \omega_{ji})t} - 1}{\Omega + \omega_{ji}} - \frac{\mathrm{e}^{\mathrm{i}(\Omega - \omega_{ji})t} - 1}{\Omega - \omega_{ji}} \right\} \\ &= \frac{1}{2\hbar} \langle \phi_{i} | \hat{V}^{0} | \phi_{j} \rangle \left\{ \frac{\mathrm{e}^{\mathrm{i}(\Omega - \omega_{ji})t/2} (1/2\mathrm{i}) \left(\mathrm{e}^{\mathrm{i}(\Omega - \omega_{ji})t/2} - \mathrm{e}^{-\mathrm{i}(\Omega - \omega_{ji})t/2} \right)}{\frac{1}{2} (\Omega - \omega_{ji})} \right\} \\ &= \frac{t}{2\hbar} \langle \phi_{i} | \hat{V}^{0} | \phi_{j} \rangle \left\{ \mathrm{e}^{\mathrm{i}(\Omega - \omega_{ji})t/2} \mathrm{sinc} \left[(\Omega - \omega_{ji})t/2 \right] - \mathrm{e}^{\mathrm{i}(\Omega + \omega_{ji})t/2} \mathrm{sinc} \left[(\Omega + \omega_{ji})t/2 \right] \right\}, \end{split}$$

$$(B.20)$$

where, $\sin c(x) = \sin(x)/x$.

All of the results that we make use of in this thesis require only the terms of the Dyson series up to first order in \hat{V}^0 . We will therefore simply quote the second order terms without giving a derivation.

$$\langle \phi_{i} | \hat{U}^{\prime(2)} | \phi_{j} \rangle = -\frac{1}{\hbar^{2}} \sum_{k} \langle \phi_{i} | \hat{V}^{0} | \phi_{k} \rangle \langle \phi_{k} | \hat{V}^{0\dagger} | \phi_{j} \rangle$$

$$\times [I(1,1) + I(-1,1) + I(1,-1) + I(-1,-1)], \qquad (B.21)$$

where

$$I(\nu,\mu) \equiv \frac{1}{2i} \frac{\mu}{\omega_{jk} + \Omega} \left\{ \frac{e^{i(\omega_{ki} + \mu\Omega)t/2} \sin[(\omega_{ki} + \mu\Omega)t/2]}{\omega_{ki} + \mu\Omega} - \frac{e^{i[\omega_{ji} + (\nu + \mu)\Omega]t/2} \sin\{[\omega_{ji} + (\nu + \mu)\Omega]t/2\}}{\omega_{ji} + (\nu + \mu)\Omega} \right\}.$$
(B.22)

Later we will return to consider the behaviour of the term $\langle \phi_i | \hat{U}'^{(1)} | \phi_i \rangle$ in more detail.

13.2.2 The Effect of a Sinusoidal Perturbation on an Electronic System

To make use of the above theory, we need to develop expressions for some quantities of interest in terms of the matrix elements $\langle \phi_i | \hat{U}' | \phi_j \rangle$. To make our discussion more concrete, we will focus on the effects of a sinusoidal perturbation on a single-particle density matrix $\hat{\rho}(t)$, representing an electronic system. We will consider two density matrices, $\hat{\rho}^0(t)$ and $\hat{\rho}(t)$ chosen to be initially equal at time t=0 and diagonal in the basis of eigenstates of \hat{H}^0 , now defined as an operator acting only on the Hilbert space of the electrons,

$$\hat{\rho}^{0}(t=0) = \hat{\rho}(t=0) = \sum_{i} |\phi_{i}\rangle o_{i}\langle \phi_{i}|. \tag{B.23}$$

 $\{o_i\}$ is the set of initial occupations restricted to be between 0 and 1. $\hat{\rho}^0(t)$ is defined as that density matrix evolving from $\hat{\rho}^0(0)$ under the unperturbed Hamiltonian \hat{H}^0 , which we can write,

$$\hat{\rho}^{0}(t) = \hat{U}^{0}(t)\hat{\rho}(0)\hat{U}^{0\dagger}(t) = \sum_{i} \hat{U}^{0}(t)|\phi_{i}\rangle o_{i}\langle\phi_{i}|\hat{U}^{0\dagger}(t) = \sum_{i}|\phi_{i}\rangle o_{i}\langle\phi_{i}|, \quad (B.24)$$

i.e. independent of time.

 $\hat{\rho}(t)$ is the density matrix evolved under the perturbed Hamiltonian $\hat{H}(t)$,

$$\hat{\rho}(t) = \hat{U}(t)\hat{\rho}(0)\hat{U}^{\dagger}(t) = \sum_{k} \hat{U}(t)|\phi_{k}\rangle o_{k}\langle\phi_{k}|\hat{U}^{\dagger}(t). \tag{B.25}$$

For $t \neq 0$, $\hat{\rho}(t)$ will, in general, have non-zero off-diagonal terms and so we must consider the general matrix element,

$$\begin{split} \langle \phi_{i} | \hat{\rho}(t) | \phi_{j} \rangle &= \sum_{k} \langle \phi_{i} | \hat{U} | \phi_{k} \rangle o_{k} \langle \phi_{k} | \hat{U}^{\dagger} | \phi_{j} \rangle \\ &= \sum_{k} \langle \phi_{i} | e^{i\varepsilon_{i}t/\hbar} \hat{U} | \phi_{k} \rangle o_{k} \langle \phi_{k} | \hat{U}^{\dagger} e^{-i\varepsilon_{j}t/\hbar} | \phi_{j} \rangle e^{i(\varepsilon_{j} - \varepsilon_{i})t/\hbar} \\ &= \sum_{k} \langle \phi_{i} | \hat{U}^{0\dagger} \hat{U} | \phi_{k} \rangle o_{k} \langle \phi_{k} | \hat{U}^{\dagger} \hat{U}^{0} | \phi_{j} \rangle e^{i(\varepsilon_{j} - \varepsilon_{i})t/\hbar} \\ &= \sum_{k} \langle \phi_{i} | \hat{U}'^{\dagger} | \phi_{k} \rangle o_{k} \langle \phi_{k} | \hat{U}' | \phi_{j} \rangle e^{i(\varepsilon_{j} - \varepsilon_{i})t/\hbar} \end{split} \tag{B.26}$$

13.2.2.1 The Irreversible Energy Transfer

In Sect. 7.2.4 we define the irreversible energy transfer into the electronic system in a radiation damage event as the excess energy in the electrons compared with the adiabatic evolution. This precise definition is examined in more detail in

Sect. 7.2.4, but here we consider a parallel definition of $\Delta E(t)$. For our current purposes, the energy transfer will be defined as the excess energy in $\hat{\rho}(t)$ as a result of the action of the perturbation $\hat{V}(t)$, when compared with that in $\hat{\rho}^0$. Hence,

$$\Delta E(t) = 2\text{Tr}(\hat{\rho}(t)\hat{H}(t)) - 2\text{Tr}(\hat{\rho}^0\hat{H}^0), \tag{B.27}$$

Where the factor of two accounts for spin degeneracy (i.e. double occupancy of each electronic eigenstate). From (B.24) we have

$$\operatorname{Tr}(\hat{\rho}^{0}\hat{H}^{0}) = \sum_{j} \langle \phi_{j} | \sum_{i} |\phi_{i}\rangle o_{i} \langle \phi_{i} | \hat{H}^{0} | \phi_{j}\rangle$$

$$= \sum_{j} \langle \phi_{j} | \sum_{i} |\phi_{i}\rangle o_{i} \langle \phi_{i} | \phi_{j}\rangle \varepsilon_{j}$$

$$= \sum_{i} o_{i}\varepsilon_{i},$$
(B.28)

and,

$$\operatorname{Tr}(\hat{\rho}\hat{H}) = \operatorname{Tr}(\hat{\rho}\hat{H}^{0}) + \operatorname{Tr}(\hat{\rho}\hat{V})$$

$$= \sum_{i} \varepsilon_{i} \langle \phi_{i} | \hat{\rho} | \phi_{i} \rangle + \operatorname{Tr}(\hat{\rho}\hat{V}). \tag{B.29}$$

In general the second term,

$$\operatorname{Tr}(\hat{\rho}\hat{V}) = \sum_{ij} \langle \phi_i | \hat{\rho} | \phi_j \rangle \langle \phi_j | \hat{V} | \phi_i \rangle, \tag{B.30}$$

is complicated, but for a sinusoidal perturbation it will return periodically to zero and so we can choose to ignore it. Using (B.26) to rewrite the diagonal elements of $\hat{\rho}$, we have,

$$\Delta E(t) = 2\sum_{ii} \varepsilon_i o_i |\langle \phi_i | \hat{U}' | \phi_j \rangle|^2 - 2\sum_i \varepsilon_i o_i + 2 \text{Tr}(\hat{\rho} \hat{V}).$$
 (B.31)

Because \hat{U} is unitary,

$$\langle \phi_i | \hat{U}' \hat{U}'^{\dagger} | \phi_k \rangle = \langle \phi_i | \hat{1} | \phi_k \rangle = \delta_{ik},$$
 (B.32)

and so by the completeness of $\{|\phi_i\rangle\}$

$$\sum_{i} \langle \phi_{i} | \hat{U}' | \phi_{j} \rangle \langle \phi_{j} | \hat{U}'^{\dagger} | \phi_{k} \rangle = \langle \phi_{i} | \hat{1} | \phi_{k} \rangle = \delta_{ik}, \tag{B.33}$$

and,

$$\sum_{i} |\langle \phi_i | \hat{U}' | \phi_j \rangle|^2 = 1, \tag{B.34}$$

Hence we can write,

$$\Delta E(t) = 2\sum_{ij} (o_j - o_i)\varepsilon_i |\langle \phi_i | \hat{U}' | \phi_j \rangle|^2 + 2\text{Tr}(\hat{\rho}\hat{V}). \tag{B.35}$$

13.2.2.2 Charge Transfer

We will now consider how the electronic charge on an ion is affected by our perturbation. We will denote the number of electrons on the α th ion, i.e. the occupation of the local orbital $|\mathbf{R}_{\alpha}\rangle$ on the ion at \mathbf{R}_{α} in our single s-band tight-binding model, as q_{α} . The *excess* electronic charge generated by the perturbation will be given by,

$$\Delta q_{\alpha} = 2\langle \alpha | (\rho(\hat{t}) - \rho^{0}(\hat{t})) | \alpha \rangle, \tag{B.36}$$

where the factor of two accounts for spin degeneracy. Unlike the case of $\Delta E(t)$, in which, by ignoring the contribution form $\mathrm{Tr}(\hat{\rho}\hat{V})$, we could focus on the diagonal elements of $\hat{\rho}$ in the eigenstate basis, here the off-diagonal elements contribute to Δq_{α} . Substituting for $\hat{\rho}$ and $\hat{\rho}^0$ we have,

$$\Delta q_{\alpha} = 2 \sum_{ijk} \langle \mathbf{R}_{\alpha} | \phi_{i} \rangle \langle \phi_{i} | \hat{U}' | \phi_{k} \rangle o_{k} \langle \phi_{k} | \hat{U}'^{\dagger} | \phi_{j} \rangle \langle \phi_{j} | \mathbf{R}_{\alpha} \rangle e^{i(\varepsilon_{j} - \varepsilon_{i})t/\hbar}$$

$$- 2 \sum_{i} \langle \mathbf{R}_{\alpha} | \phi_{i} \rangle o_{i} \langle \phi_{i} | \mathbf{R}_{\alpha} \rangle.$$
(B.37)

Using the identity $\sum_{j} |\langle \phi_{i} | \hat{U}' | \phi_{j} \rangle|^{2} = 1$ we have,

$$\Delta q_{\alpha} = 2 \sum_{ik} |\langle \mathbf{R}_{\alpha} | \phi_{i} \rangle|^{2} |\langle \phi_{i} | \hat{U}' | \phi_{k} \rangle|^{2} (o_{k} - o_{i}) 2 \sum_{ik} \langle \mathbf{R}_{\alpha} | \phi_{i} \rangle \langle \phi_{i} | \hat{U}' | \phi_{k} \rangle o_{k} \langle \phi_{k} | \hat{U}'^{\dagger} | \phi_{j} \rangle \langle \phi_{j} | \mathbf{R}_{\alpha} \rangle e^{i(\varepsilon_{j} - \varepsilon_{i})t/\hbar}.$$
(B.38)

Now, the terms in the second summation, arising from the off-diagonal elements of $\hat{\rho}(t)$ have significant magnitude. However, we can show (see Sect. 13.2.2.3) that their contribution is strictly oscillatory and so we can write, from (B.37),

$$\Delta q_{\alpha} \approx 2 \sum_{ik} |\langle \mathbf{R}_{\alpha} | \phi_i \rangle|^2 |\langle \phi_i | \hat{U}' | \phi_k \rangle|^2 o_k - 2 \sum_i |\langle \mathbf{R}_{\alpha} | \phi_i \rangle|^2 o_i, \tag{B.39}$$

and from (B.38),

$$\Delta q_{\alpha} \approx 2 \sum_{i} |\langle \phi_{i} | \hat{U}' | \phi_{k} \rangle|^{2} (o_{k} - o_{i}) |\langle \mathbf{R}_{\alpha} | \phi_{i} \rangle|^{2}.$$
 (B.40)

13.2.2.3 First-Order Perturbation Theory Approximations

We will now derive approximate expressions for $\Delta E(t)$ and $\Delta q_{\alpha}(t)$ to first-order in the expansion of the time evolution operator $\hat{U}'(t)$. We need to deal with quantities like,

$$\langle \phi_i | \hat{U}' | \phi_k \rangle \langle \phi_k | \hat{U}'^{\dagger} | \phi_i \rangle.$$
 (B.41)

To second order in the perturbation \hat{V} , these are,

$$\langle \phi_{i}|\hat{U}'|\phi_{k}\rangle\langle \phi_{k}|\hat{U}'^{\dagger}|\phi_{j}\rangle = \langle \phi_{i}|\hat{U}'^{(0)}|\phi_{k}\rangle\langle \phi_{k}|\hat{U}'^{(0)\dagger}|\phi_{j}\rangle$$

$$+ \langle \phi_{i}|\hat{U}'^{(0)}|\phi_{k}\rangle\langle \phi_{k}|\hat{U}'^{(1)\dagger}|\phi_{j}\rangle$$

$$+ \langle \phi_{i}|\hat{U}'^{(1)}|\phi_{k}\rangle\langle \phi_{k}|\hat{U}'^{(0)\dagger}|\phi_{j}\rangle$$

$$+ \langle \phi_{i}|\hat{U}'^{(0)}|\phi_{k}\rangle\langle \phi_{k}|\hat{U}'^{(2)\dagger}|\phi_{j}\rangle$$

$$+ \langle \phi_{i}|\hat{U}'^{(2)}|\phi_{k}\rangle\langle \phi_{k}|\hat{U}'^{(0)\dagger}|\phi_{j}\rangle$$

$$+ \langle \phi_{i}|\hat{U}'^{(1)}|\phi_{k}\rangle\langle \phi_{k}|\hat{U}'^{(0)\dagger}|\phi_{j}\rangle .$$

$$(B.42)$$

Given that $\langle \phi_i | \hat{U}'^{(0)} | \phi_k \rangle = \delta_{ik}$, this becomes,

$$\begin{split} \langle \phi_{i} | \hat{U}' | \phi_{k} \rangle \langle \phi_{k} | \hat{U}'^{\dagger} | \phi_{j} \rangle &= \delta_{ik} \delta_{kj} + \delta_{ik} 2 \Re \left\{ \langle \phi_{i} | \hat{U}'^{(1)} | \phi_{j} \rangle \right\} + \delta_{ik} 2 \Re \left\{ \langle \phi_{i} | \hat{U}'^{(2)} | \phi_{j} \rangle \right\} \\ &+ \langle \phi_{i} | \hat{U}'^{(1)} | \phi_{k} \rangle \langle \phi_{k} | \hat{U}'^{(1)\dagger} | \phi_{j} \rangle. \end{split} \tag{B.43}$$

For the energy transfer $\Delta E(t)$ and for our approximations (B.39) and (B.40) to $\Delta q_{\alpha}(t)$ we need only the diagonal elements of $\hat{\rho}(t)$ and so we can focus on,

$$\begin{aligned} |\langle \phi_i | \hat{U}' | \phi_k \rangle|^2 &= \delta_{ik} + \delta_{ik} 2\Re \left\{ \langle \phi_i | \hat{U}'^{(1)\dagger} | \phi_i \rangle \right\} + \delta_{ik} 2\Re \left\{ \langle \phi_i | \hat{U}'^{(2)\dagger} | \phi_i \rangle \right\} \\ &+ |\langle \phi_i | \hat{U}'^{(1)} | \phi_k \rangle|^2. \end{aligned} \tag{B.44}$$

Expressions like (B.35) and (B.40) both contain factors of $(o_k - o_i)$ and so we can ignore terms involving factors of δ_{ki} and we need only go to first order in the expansion of \hat{U}' to capture all terms up to second order in \hat{V} . If we let a_i stand for ε_i in (B.35) and $|\langle \mathbf{R}_{\alpha} | \phi_i \rangle|^2$ in (B.40) then we can write

$$\sum_{ij} (o_j - o_i) a_i |\langle \phi_i | \hat{U}' | \phi_k \rangle|^2 \approx \sum_{ij} (o_j - o_i) a_i |\langle \phi_i | (\hat{U}'^{(0)} + \hat{U}'^{(1)}) | \phi_j \rangle|^2.$$
 (B.45)

The Time Dependence of the Energy and Charge Transfer

The time dependence of the energy and charge transfer as expressed in (B.45) is all contained in the squared matrix elements $|\langle \phi_i | (\hat{U}'^{(1)}) | \phi_j \rangle|^2$. Using (B.20) we can write these as,

$$\begin{split} |\langle \phi_i | (\hat{U}'^{(1)}) | \phi_j \rangle|^2 &= \frac{t^2}{4\hbar^2} |\langle \phi_i | \hat{V}^0 | \phi_j \rangle|^2 \left\{ \operatorname{sinc}^2 \left[(\Omega - \omega_{ji}) t / 2 \right] + \operatorname{sinc}^2 \left[(\Omega + \omega_{ji}) t / 2 \right] \right. \\ &\left. - \operatorname{sinc} \left[(\Omega - \omega_{ji}) t / 2 \right] \operatorname{sinc} \left[(\Omega + \omega_{ji}) t / 2 \right] (e^{i\Omega t} + e^{-i\Omega t}) \right\}. \end{split}$$

$$(B.46)$$

We can regard $|\langle \phi_i|(\hat{U}'^{(1)})|\phi_j\rangle|^2$ as a measure of the extent to which an eigenstate $|\phi_i\rangle$ has "evolved into" the eigenstate $|\phi_i\rangle$ by time t. Probabilistically speaking we would say that $|\langle \phi_i|(\hat{U}'^{(1)})|\phi_j\rangle|^2$ gives the probability that the system has undergone a transition from state $|\phi_j\rangle$ to state $|\phi_i\rangle$ as a result of the action of the perturbation $\hat{V}(t)$. Before we consider (B.46) further we will introduce some simplifying notation and write

$$V_{ii}^{0} = \langle \phi_i | \hat{V}^0 | \phi_i \rangle, \tag{B.47}$$

and

$$s(\varepsilon, \Omega; t) \equiv t^{2} \left(\operatorname{sinc}^{2} [(\varepsilon/\hbar - \Omega)t/2] + \operatorname{sinc}^{2} [(\varepsilon/\hbar + \Omega)t/2] - \operatorname{sinc} [(\varepsilon/\hbar - \Omega)t/2] \operatorname{sinc} [(\varepsilon/\hbar + \Omega)t/2] (e^{i\Omega t} + e^{-i\Omega t}) \right).$$
(B.48)

We thus write,

$$|\langle \phi_i | (\hat{U}'^{(1)}) | \phi_j \rangle|^2 = \frac{1}{4\hbar^2} |V_{ij}^0|^2 s(\hbar \omega_{ji}, \Omega; t).$$
 (B.49)

All the time dependence in the matrix elements $\langle \phi_i | (\hat{U}'^{(1)}) | \phi_j \rangle$ is contained within the function $s(\varepsilon, \Omega; t)$. We will often be interested in the behaviour of the energy and charge transfer at long times when we will make use of the limit,

$$\lim_{t \to \infty} s(\varepsilon, \Omega; t) = 2\pi t [\delta(\varepsilon/\hbar - \Omega) + \delta(\varepsilon/\hbar + \Omega)]$$
 (B.50)

$$=2\pi\hbar t[\delta(\varepsilon-\hbar\Omega)+\delta(\varepsilon+\hbar\Omega)], \tag{B.51}$$

where we have used the identity $\lim_{t\to\infty} [t \operatorname{sinc}^2(ut)] = \pi \delta(u)$

Interpreting the Perturbation Theory Expressions

To help us understand the physics captured in our first-order time-dependent perturbation theory expressions for the energy and charge transfer we will first write them in a more intuitive form. We start with the energy transfer expression (B.35), but ignore the term $2\text{Tr}(\hat{\rho}\hat{V})$,

$$\Delta E(t) = 2\sum_{ii} (o_j - o_i)\varepsilon_i |\langle \phi_i | \hat{U}' | \phi_j \rangle|^2.$$
 (B.52)

To first order this is,

$$\Delta E(t) = \frac{1}{2\hbar^2} \sum_{ij} (o_j - o_i) \varepsilon_i |V_{ij}^0|^2 s(\varepsilon_i - \varepsilon_j, \Omega; t)$$

$$= \frac{1}{2\hbar^2} \sum_{ij} \left[o_j (1 - o_i) - o_i (1 - o_j) \right] \varepsilon_i |V_{ij}^0|^2 s(\varepsilon_i - \varepsilon_j, \Omega; t).$$
(B.53)

Now, since $s(\varepsilon,\Omega;t)=s(-\varepsilon,\Omega;t)$ and $|V_{ij}^0|^2=|V_{ji}^0|^2$ we can swap summation indices on half the terms to write

$$\Delta E(t) = \frac{1}{2\hbar^2} \sum_{ij} o_i (1 - o_j) (\varepsilon_j - \varepsilon_i) |V_{ij}^0|^2 s(\varepsilon_i - \varepsilon_j, \Omega; t).$$
 (B.54)

We can now interpret Eq. B.54 as representing a sum over all possible transitions $|\phi_i\rangle \rightarrow |\phi_j\rangle$ in our system. The factor of $o_i(1-o_j)$ accounts for the effects of quantum mechanical exclusion, the matrix element $|V_{ij}^0|^2$ determines the strength of the coupling of a given pair of states by our perturbation and the function $s(\varepsilon_i - \varepsilon_j, \Omega; t)$ can be regarded as determining a time-dependent sampling of the possible transitions.

The equivalent expression for the charge transfer making the same assumptions as in Eq. B.40 is,

$$\Delta q_{\alpha}(t) = -\frac{e}{2\hbar^{2}} \sum_{ij} o_{i} (1 - o_{j}) \left[|\langle \mathbf{R}_{\alpha} | \phi_{j} \rangle|^{2} - |\langle \mathbf{R}_{\alpha} | \phi_{i} \rangle|^{2} \right] |V_{ij}^{0}|^{2} s(\varepsilon_{i} - \varepsilon_{j}, \Omega; t).$$
(B.55)

Can We Neglect the Off-Diagonal Elements of $\hat{\rho}$ in our Expression for Δq_{α} ?

We would now like to show that our simple expression (B.40) for the charge transfer is a valid approximation. In (B.40) we neglected the contribution of elements $\langle \phi_i | \hat{U}' | \phi_k \rangle \langle \phi_k | \hat{U}'^\dagger | \phi_j \rangle$ for $i \neq j$. These terms are certainly not zero, but we might hope that they are oscillatory and so will not contribute to the average charge transfer. Because in our consideration of the importance of the second-order terms $\hat{U}'^{(2)}$ above we considered only the diagonal elements of $\hat{\rho}$, we must show oscillatory behaviour up to second order. To simplify the notation we will define,

$$\hat{\Delta U}' \equiv \hat{U}'^{(1)} + \hat{U}'^{(2)} + \cdots,$$
 (B.56)

and write the contribution to the charge transfer of the off-diagonal elements of the density matrix as $\Delta q_{\alpha}^{\text{OD}}$. We have,

$$\begin{split} \Delta q_{\alpha}^{\text{OD}} &= \sum_{ik,j\neq i} \langle \mathbf{R}_{\alpha} | \phi_{i} \rangle \langle \phi_{j} | \mathbf{R}_{\alpha} \rangle f_{k} \mathrm{e}^{\mathrm{i}\omega_{ij}t} \Big\{ \langle \phi_{i} | \hat{U}'^{(0)} | \phi_{k} \rangle \langle \phi_{k} | \hat{U}'^{(0)\dagger} | \phi_{j} \rangle \\ &+ \langle \phi_{i} | \hat{U}'^{(0)} | \phi_{k} \rangle \langle \phi_{k} | \hat{\Delta U}'^{\dagger} | \phi_{j} \rangle + \langle \phi_{i} | \hat{\Delta U}' | \phi_{k} \rangle \langle \phi_{k} | \hat{U}'^{(0)\dagger} | \phi_{j} \rangle \\ &+ \langle \phi_{i} | \hat{\Delta U}' | \phi_{k} \rangle \langle \phi_{k} | \hat{\Delta U}'^{\dagger} | \phi_{j} \rangle \Big\}, \end{split} \tag{B.57}$$

$$\Delta q_{\alpha}^{\text{OD}} = \sum_{ik,j\neq i} \langle \mathbf{R}_{\alpha} | \phi_{i} \rangle \langle \phi_{j} | \mathbf{R}_{\alpha} \rangle f_{k} e^{i\omega_{ij}t} \Big\{ \delta_{ik} \delta_{jk} + \delta_{ik} \langle \phi_{k} | \hat{\Delta U}^{\prime\dagger} | \phi_{j} \rangle \\
+ \delta_{jk} \langle \phi_{i} | \hat{\Delta U}^{\prime} | \phi_{k} \rangle + \langle \phi_{i} | \hat{\Delta U}^{\prime} | \phi_{k} \rangle \langle \phi_{k} | \hat{\Delta U}^{\prime\dagger} | \phi_{j} \rangle \Big\},$$
(B.58)

$$\Delta q_{\alpha}^{\text{OD}} = \sum_{i,j\neq i} \langle \mathbf{R}_{\alpha} | \phi_{i} \rangle \langle \phi_{j} | \mathbf{R}_{\alpha} \rangle e^{i\omega_{ij}t} \left\{ f_{i} \langle \phi_{i} | \hat{U}'^{\dagger} | \phi_{j} \rangle + f_{j} \langle \phi_{i} | \hat{U}' | \phi_{j} \rangle \right\}
+ \sum_{ik} \langle \mathbf{R}_{\alpha} | \phi_{i} \rangle \langle \phi_{j} | \mathbf{R}_{\alpha} \rangle f_{k} e^{i\omega_{ij}t} \langle \phi_{i} | \hat{\Delta U}' | \phi_{k} \rangle \langle \phi_{k} | \hat{\Delta U}'^{\dagger} | \phi_{j} \rangle,$$
(B.59)

since, $\Delta \hat{U}' = \hat{U}'$ for $i \neq j$.

We will now take the two summations in the above expression separately. In the case of the first, consideration of the sum of the term in i, j and its twin in j, i shows that the contribution is real, as we would hope. Furthermore, we are left only with the problem of determining the time dependence of $\langle \phi_i | \hat{U}^{\prime \dagger} | \phi_j \rangle$ for $i \neq j$. The first order contribution (B.20) contains only terms like $t \sin(\omega t)$ for some frequency ω . In the long time limit $t \sin(\omega t) \rightarrow \pi \delta(\omega)$, such terms have only a zeroth-order time dependence and are oscillatory. The same is true for the second order terms of form (B.21).

We now need to consider the second summation term,

$$T \equiv \sum_{ik,j \neq i} \langle \mathbf{R}_{\alpha} | \phi_i \rangle \langle \phi_j | \mathbf{R}_{\alpha} \rangle f_k e^{i\omega_{ij}t} \langle \phi_i | \hat{\Delta U}' | \phi_k \rangle \langle \phi_k | \hat{\Delta U}'^{\dagger} | \phi_j \rangle, \tag{B.60}$$

in which we need only expand $\hat{\Delta U}'$ up to the first order term. We will write this out explicitly,

$$T = \sum_{ik,j\neq i} \langle \mathbf{R}_{\alpha} | \phi_{i} \rangle \langle \phi_{j} | \mathbf{R}_{\alpha} \rangle f_{k} e^{i\omega_{ij}t} \frac{t^{2}}{4\hbar^{2}} \langle \phi_{i} | \hat{V} | \phi_{k} \rangle \langle \phi_{k} | \hat{V} | \phi_{j} \rangle$$

$$\times \left\{ e^{i(\omega_{ki} - \Omega)t/2} \operatorname{sinc}[(\omega_{ki} - \Omega)t/2] - e^{i(\omega_{ki} + \Omega)t/2} \operatorname{sinc}[(\omega_{ki} + \Omega)t/2] \right\}$$

$$\times \left\{ e^{-i(\omega_{kj} - \Omega)t/2} \operatorname{sinc}[(\omega_{kj} - \Omega)t/2] - e^{-i(\omega_{kj} + \Omega)t/2} \operatorname{sinc}[(\omega_{kj} + \Omega)t/2] \right\},$$
(B.61)

$$T = \sum_{ik,j\neq i} \langle \mathbf{R}_{\alpha} | \phi_{i} \rangle \langle \phi_{j} | \mathbf{R}_{\alpha} \rangle f_{k} e^{i\omega_{ij}t} \frac{t^{2}}{4\hbar^{2}} \langle \phi_{i} | \hat{V} | \phi_{k} \rangle \langle \phi_{k} | \hat{V} | \phi_{j} \rangle$$

$$\times \left\{ e^{i(\omega_{ji})t/2} \operatorname{sinc}[(\omega_{ki} - \Omega)t/2] \operatorname{sinc}[(\omega_{kj} - \Omega)t/2] + e^{i(\omega_{ji})t/2} \operatorname{sinc}[(\omega_{ki} + \Omega)t/2] \operatorname{sinc}[(\omega_{kj} + \Omega)t/2] - e^{i(\omega_{ji} + 2\Omega)t/2} \operatorname{sinc}[(\omega_{ki} + \Omega)t/2] \operatorname{sinc}[(\omega_{kj} - \Omega)t/2] - e^{i(\omega_{ji} - 2\Omega)t/2} \operatorname{sinc}[(\omega_{ki} - \Omega)t/2] \operatorname{sinc}[(\omega_{kj} + \Omega)t/2] \right\}.$$
(B.62)

In the long time limit this becomes,

$$T = \sum_{ik,j\neq i} \langle \mathbf{R}_{\alpha} | \phi_{i} \rangle \langle \phi_{j} | \mathbf{R}_{\alpha} \rangle f_{k} e^{i\omega_{ij}t/2} \frac{\pi^{2}}{4\hbar^{2}} \langle \phi_{i} | \hat{V} | \phi_{k} \rangle \langle \phi_{k} | \hat{V} | \phi_{j} \rangle$$

$$\times \left\{ \left[\delta(\omega_{ki} - \Omega)\delta(\omega_{kj} - \Omega) + \delta(\omega_{ki} + \Omega)\delta(\omega_{kj} + \Omega) \right] - \left[e^{i\Omega t} \delta(\omega_{ki} + \Omega)\delta(\omega_{kj} - \Omega) + e^{-i\Omega t} \delta(\omega_{ki} - \Omega)\delta(\omega_{kj} + \Omega) \right] \right\}.$$
(B.63)

Again, pairing terms in i, j and j, i shows that the contribution is real. The terms in the second square brackets involving factors of $e^{\pm i\Omega t}$ will again give an oscillatory contribution. The term in the first square brackets is only non-zero in the case of degeneracy $\varepsilon_i = \varepsilon_j$ and gives a constant contribution. However, even in an infinite system this term along with the others in the second summation in (B.59) will be small compared to those in the first summation (the latter are proportional to the density of states cubed, the former to the density of states squared).

Some Numerical Results

As a check on the above algebraic argument, we have made some direct calculations of the behaviour of the off-diagonal terms in the energy transfer. FGR calculations were carried out for a small ($5 \times 6 \times 7$ unit cells) block of our tight-binding model with a single oscillating tetrahedral interstitial (we must consider a system with some sort of defect in order to obtain a non-zero charge transfer). The results are shown in Figs. B.1, B.2 and B.3. All the data only include terms from the expansion of \hat{U}' up to first-order and comparison is made between the expression including off-diagonal elements of $\hat{\rho}$ and the approximate expression (B.40).

13.2.3 A Quantum Mechanical Oscillator

To help illuminate our discussion of the behaviour of the electron-ion energy exchange in Sect. 4.6.2 we will now undertake a perturbation theory analysis of a simple quantum mechanical oscillator.

Fig. B.1 The charge transfer after 5 fs as a function of oscillator frequency Ω

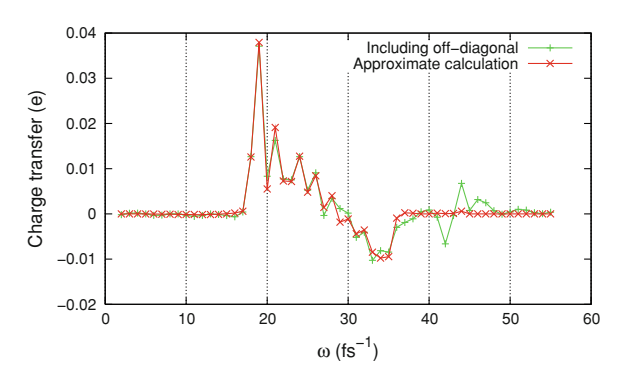


Fig. B.2 The charge transfer as a function of time for an oscillator frequency $\Omega = 20 \, \text{rad fs}^{-1}$

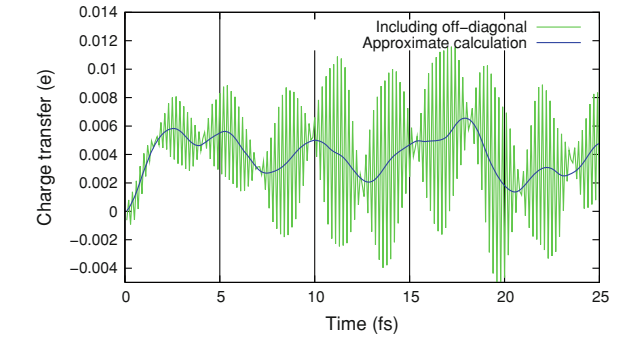
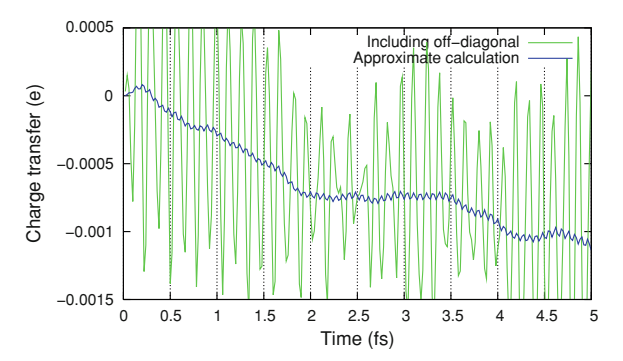


Fig. B.3 The charge transfer as a function of time for an oscillator frequency $\Omega = 30 \ \text{rad fs}^{-1}$



We consider a combined system of an electronic system described by a Hamiltonian \hat{H}_e , acting on a Hilbert space \mathcal{W}_e , with eigenstates $\{|\phi_i\rangle\}$ of energies $\{\varepsilon_i\}$ and a single quantum mechanical oscillator described by a Hamiltonian \hat{H}_n , acting on a Hilbert space \mathcal{W}_n , with eigenstates $\{|N\rangle\}$ of energies $\{U_N=(N+\frac{1}{2})\hbar\Omega\}$ where Ω is the oscillator frequency. The Hamiltonian for the combined system will be $\hat{H}=\hat{H}_e+\hat{H}_n$ with eigenstates in the product space $\mathcal{W}=\mathcal{W}_e\otimes\mathcal{W}_n$:

$$|\phi_i N\rangle = |\phi_i\rangle \otimes |N\rangle. \tag{B.64}$$

We then introduce a perturbative coupling between the oscillator and the electronic system

$$\hat{V} = \frac{\partial \hat{H}_{e}}{\partial x} \hat{x} \tag{B.65}$$

where \hat{x} is the position operator of the oscillator and x is a parameter of the electronic Hamiltonian corresponding to the oscillator position.

If we assume that our system is initially in the state $|\phi_i N\rangle$ with energy $\varepsilon_i + U_N$ then the energy transferred from the oscillator to the electrons will be given by

$$\Delta E_{\rm QM} = 2\sum_{iM} (\varepsilon_i - \varepsilon_i) |\langle \phi_i N | \hat{U}'^{(1)} | \phi_j M \rangle|^2. \tag{B.66}$$

From (B.19) we have

$$\langle \phi_i N | \hat{U}^{\prime(1)} | \phi_j M \rangle = -\frac{i}{\hbar} \left\langle \phi_i \left| \frac{\partial \hat{H}_e}{\partial x} \right| \phi_j \right\rangle \langle N | \hat{x} | M \rangle \int_0^t dt' e^{i\omega_{iN,jM}t'}, \tag{B.67}$$

where $\hbar\omega_{iN,jM} = (\varepsilon_j - \varepsilon_i) - (U_M - U_N)$. Using the standard results for a quantum mechanical oscillator of mass m [3, pp. 89–97]:

$$\hat{x} = \sqrt{\frac{\hbar}{2m\Omega}} (\hat{a}^{\dagger} + \hat{a}), \tag{B.68}$$

$$\hat{a}^{\dagger}|N\rangle = \sqrt{N+1}|N+1\rangle, \qquad \hat{a}|N\rangle = \sqrt{N}|N-1\rangle,$$
 (B.69)

we obtain

$$\langle \phi_{i} N | \hat{U}^{\prime(1)} | \phi_{j} M \rangle = -\frac{t}{2\hbar} \sqrt{\frac{\hbar}{2m\Omega}} \langle \phi_{i} | \frac{\partial \hat{H}_{e}}{\partial x} | \phi_{j} \rangle e^{i\omega_{iN,jM}t/2}$$

$$\times \operatorname{sinc}(\omega_{iN,jM}t/2) (\sqrt{N+1}\delta_{M,N+1} + \sqrt{N+1}\delta_{M,N+1}),$$
(B.70)

by the orthonormality of the oscillator eigenstates. The δ -functions constrain the change in the energy of the electronic system to be $\pm\hbar\Omega$ and so select two terms in the sum over $|M\rangle$ for each electronic eigenstate $|\phi_j\rangle$. In the long time limit (see Eq. B.50) this gives an energy transfer,

$$\Delta E_{\rm QM} = \frac{\pi t}{2m\Omega} \sum_{j} (\varepsilon_{j} - \varepsilon_{i}) \left| \left\langle \phi_{i} \left| \frac{\partial \hat{H}_{e}}{\partial x} \right| \phi_{j} \right\rangle \right|^{2} \left\{ (N+1)\delta(\varepsilon_{i} - \varepsilon_{j} - \hbar\Omega) + N\delta(\varepsilon_{i} - \varepsilon_{j} + \hbar\Omega) \right\}.$$
(B.71)

If we compare the equivalent expression for a classical oscillator $\hat{V} = \hat{V}^0 \sin(\Omega t)$,

$$\Delta E_{\text{CI}} = \frac{\pi t}{N\hbar} \sum_{j} (\varepsilon_{j} - \varepsilon_{i}) |\langle \phi_{i} | \hat{V}^{0} | \phi_{j} \rangle|^{2} \{ N \delta(\varepsilon_{i} - \varepsilon_{j} - \hbar \Omega) + N \delta(\varepsilon_{i} - \varepsilon_{j} + \hbar \Omega) \},$$
(B.72)

then we can see that the quantum mechanical nature of our oscillator changes the prefactor $N \rightarrow N+1$ in the term corresponding to de-excitation of the electronic system (i.e. to the emission of phonons). This change corresponds to the effect of spontaneous phonon emission. If we identify the oscillator occupation number N with an ionic "temperature" then we can see that the difference between the quantum mechanical and the semi-classical treatments will be insignificant when N is large. In our radiation damage simulations the ionic system is initially highly excited and so a semi-classical treatment, neglecting spontaneous phonon emission, should be valid.

13.3 Appendix C: The Coupling Matrix for a Single Oscillating Ion

In this appendix we consider the effect of $V_{\bf kk'}^0$ in suppressing low energy transitions in more detail. Equation 6.37,

$$V_{\mathbf{k}\mathbf{k}'}^{0} = \frac{2\mathbf{i}}{N_{\mathbf{a}}} \sin(\Omega t) e^{\mathbf{i}(\mathbf{k}' - \mathbf{k}) \cdot \mathbf{R}_{0}} \sum_{b} \sum_{a} \left(\frac{\mathbf{A} \cdot \mathbf{d}_{a}^{b}}{|\mathbf{d}_{a}^{b}|} \frac{\mathrm{d}\gamma(\mathbf{R})}{\mathrm{d}R} |_{R = |\mathbf{d}_{a}^{b}|} \right) \times \left\{ \sin(\mathbf{k} \cdot \mathbf{d}_{a}^{b}) - \sin(\mathbf{k}' \cdot \mathbf{d}_{a}^{b}) \right\}.$$
(6.37)

gives some insight into this behaviour. Each pair of atoms symmetric about the oscillating atom site acts to couple together pairs of states $|\mathbf{k}\rangle$ and $|\mathbf{k}'\rangle$ with a strength which depends on the change in the phase difference of the states across the pair of atoms as given by the term $\sin(\mathbf{k}\cdot\mathbf{d}_a^b) - \sin(\mathbf{k}'\cdot\mathbf{d}_a^b)$. States which have very large changes in phase difference across a given pair of atoms will be strongly coupled by that pair. Hence we can see that states at the top of the band, where phase changes only slowly with position (or equivalently with \mathbf{k}) will be relatively weakly coupled.

The equivalence of changing an atom's position and changing the wave vector suggests a more physical interpretation of the coupling matrix. If we simplify our tight-binding model to include only nearest-neighbour interactions then we can rewrite the coupling matrix as,

$$|V_{\mathbf{k}\mathbf{k}'}^{0}|^{2} = \sum_{\eta} \left(\frac{2R_{\eta}}{N_{a}}\right)^{2} \left(\frac{\hbar}{\sqrt{2}a}\right)^{2} \left(\frac{\gamma'}{\gamma}\right)^{2} \left|\left(v_{g}(\mathbf{k}') - v_{g}(\mathbf{k})\right)\right|_{\eta}^{2}$$
 (C.1)

where we have written the group velocity of an electron in state $|\mathbf{k}\rangle$ as,

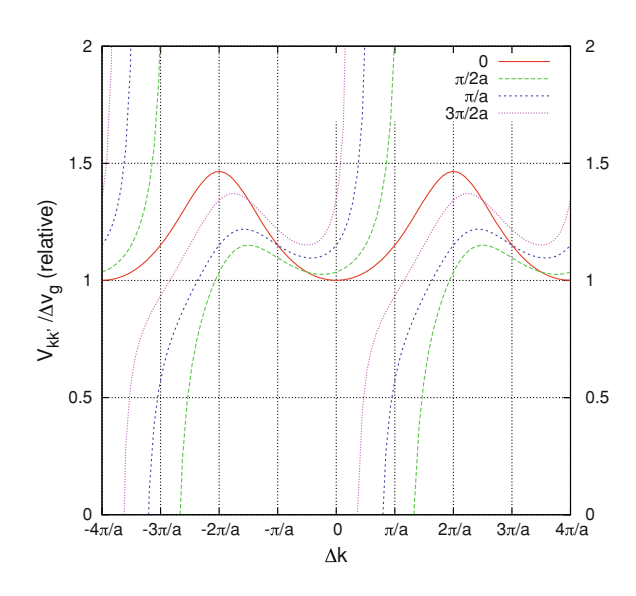
$$v_g(\mathbf{k}) = \frac{1}{\hbar} \nabla_{\mathbf{k}} E_{\mathbf{k}} \tag{C.2}$$

We can see that the effect of the perturbation is to couple pairs of states with a strength proportional to the square of the change in group velocity. It is not possible to rewrite the coupling matrix in terms of the change in electron group velocity when we include more than one neighbour shell in the Hamiltonian, but the situation is not drastically changed. Figure C.1 shows the ratio of the coupling matrix to the change in group velocity for our original Hamiltonian for a variety of initial states $|\mathbf{k}_i\rangle$ and changes in the wave vector $\Delta \mathbf{k}$ along the line $\Gamma \to X$ in k-space. There is only moderate variation in this ratio for most values of Δk with divergence only when $\nu_g(\mathbf{k}') - \nu_g(\mathbf{k})$ goes to zero (see Fig. C.2).

 $q(\varepsilon;T_{\rm e})$ depends on $V_{\bf k}^{\bf k}$ ' through the function $\tilde{V}(e,e+\varepsilon)$ which additionally includes the effect of the density of states at $E_{\bf k}$ and $E_{\bf k'}$. It is the combined effect of the coupling matrix and the density of states that gives the correct form of $q(\varepsilon;T_{\rm e})$ for frequency independent damping at high temperature. Figure C.3 illustrates the point. Figure C.3a shows part of the band structure with four examples of low energy electronic transitions. Each of these transitions is also marked on a contour plot of the coupling matrix (Fig. C.3b) and the function $|\tilde{V}(e,e+\varepsilon)|^2$ (Fig. C.3c) and we will consider each in turn:

1. Transitions between states at the top of the band with small $|\Delta \mathbf{v}_g|$ are weakly coupled but large in number because of the strongly peaked density of states. Hence they are strongly weighted by $\tilde{V}(e, e + \varepsilon)$.

Fig. C.1 The ratio of the coupling matrix to the change in group velocity for our original Hamiltonian for a variety of initial states $|\mathbf{k}_i\rangle$ (indicated in the key) and changes in the wave vector $\Delta \mathbf{k}$ along the line $\Gamma \rightarrow X$ in k-space



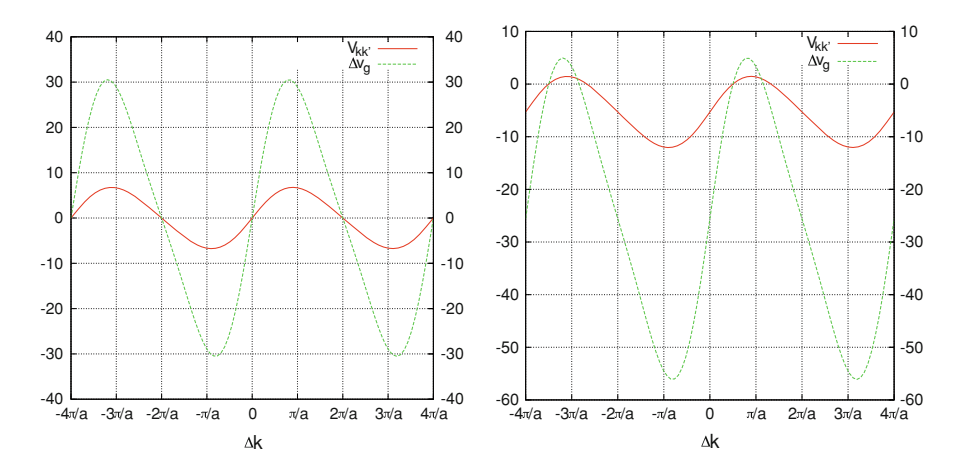


Fig. C.2 The coupling matrix and the change in group velocity as a function of the change in wave vector $\Delta \mathbf{k}$ along the line $\Gamma \to X$ in k-space for initial states $|\mathbf{k}_i\rangle = 0$ (left plot) and $|\mathbf{k}_i\rangle = \pi/2$ (right plot)

- 2. Transitions of large $|\Delta \mathbf{v}_g|$ across the middle of the band are very strongly coupled but are between states in the tail of the density of states and so are moderately weighted by $\tilde{V}(e, e + \varepsilon)$.
- 3. These transitions are large in number but very weakly coupled and are moderately weighted by $\tilde{V}(e, e + \varepsilon)$.

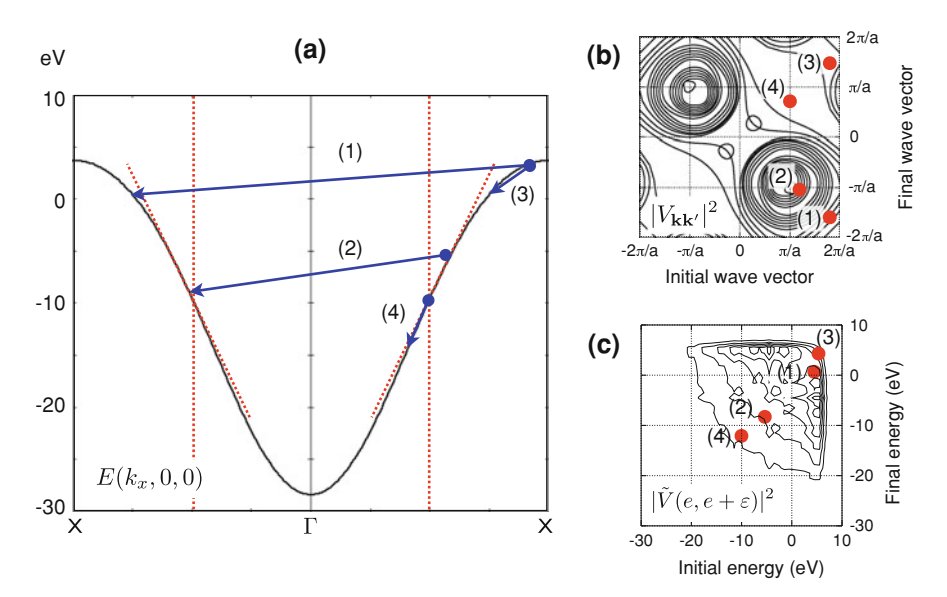


Fig. C.3 Examples of low energy transitions shown against (a) the band structure; (b) the coupling matrix $\langle \mathbf{k} | \hat{V}^0 | \mathbf{k}' \rangle$ and (c) the function $|\tilde{V}(e, e + \varepsilon)|^2$. See main text for details

4. Transitions of small $|\Delta \mathbf{v}_g|$ around the middle of the band are few in number and weakly coupled and so are weakly weighted by $\tilde{V}(e, e + \varepsilon)$.

13.4 Appendix D: Some Features of the Electronic Excitation Spectrum in Collision Cascades

13.4.1 Anomalous Excitations Early in the Cascade

In Sect. 8.1.1 we saw that there appears to be a larger degree of excitation out of the lowest energy states and into the highest energy states than we would expect given that the ionic motion in our cascade simulations contains only relatively low frequencies. These anomalous excitations might originate from errors in the RK4 integrator or from high frequencies in the initial ionic motion at the start of the cascade. By running a few 2 keV cascade simulations with diagonalization of the Hamiltonian and calculation of the excitation spectrum every femtosecond, we can shed some light on this issue. Figure D.1 shows the occupancy distribution over two 3 fs periods during the thermalization stage of a sample simulation. In each case the earliest sample corresponds to the point at which the density matrix is returned to its ground state (see Sect. 7.1.1 for an explanation of our thermalization scheme). The tails in this case are therefore characteristic of the numerical precision of the simulation. One femtosecond later the tails have changed, but change no further over the next femtosecond. We might reasonably ascribe this change, then, to the integrator rather than any actual excitation.

Figure D.2 shows what happens once the PKA is in motion. In Fig. D.2a and enlarged in Fig. D.2b we can see that in the first femtosecond the behaviour is as in the thermalization phase. Over the next few femtoseconds we can see the effect of

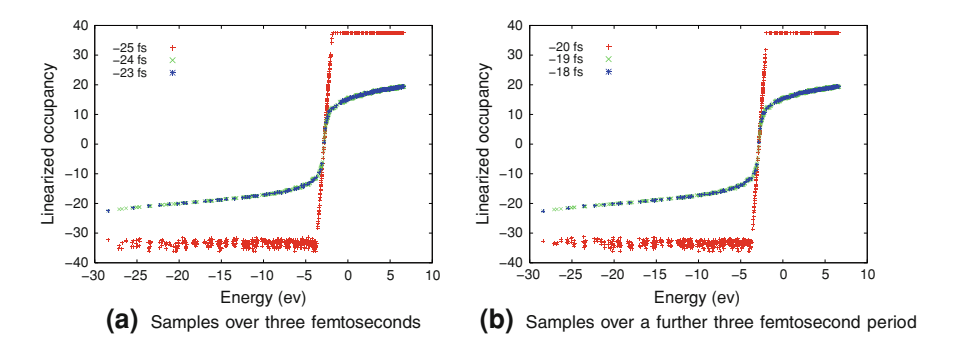


Fig. D.1 The linearized occupation distribution at various times during the thermalization phase of a sample simulation. The negative times are relative to the point at which the cascade is initiated by imparting 2 keV to the PKA. **a** Samples over 3 fs. **b** Samples over a further 3 fs period

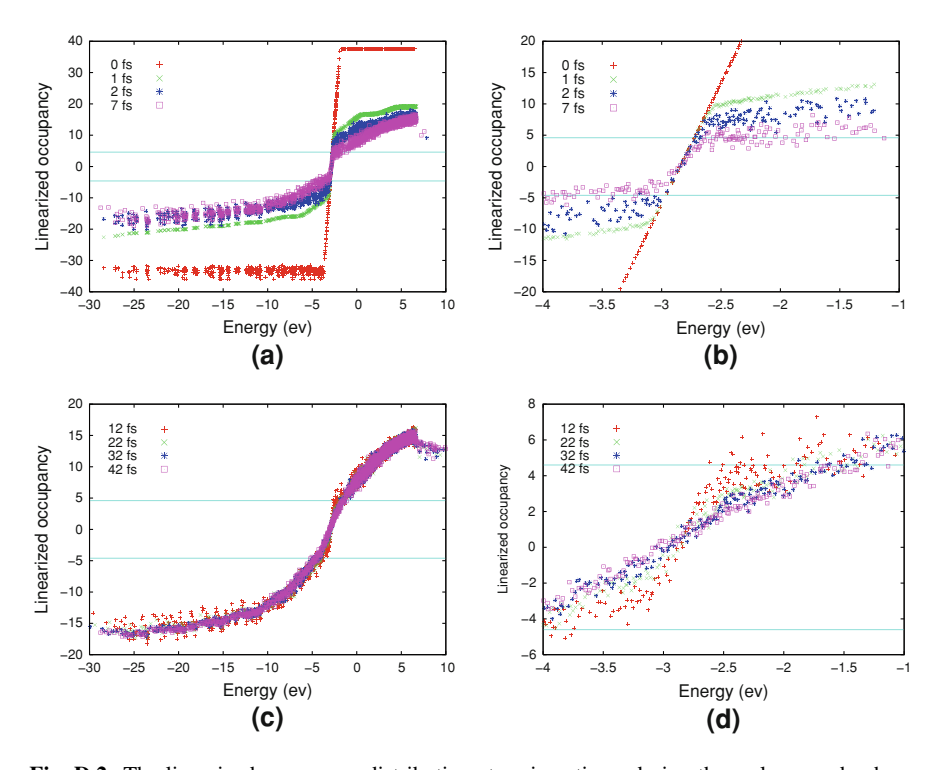


Fig. D.2 The linearized occupancy distribution at various times during the early cascade phase of a sample simulation. The *horizontal lines* indicate occupancies of 0.01 and 0.99, the bounds of our maximum fitting window. The interpretation of these figures is to be found in the *main text*

excitations appear. In Fig. D.2c we can see the effect of excitations on the tails is largely established after only 12 fs. Subsequent excitations appear only to affect the central thermal portion of the distribution (shown enlarged in Fig. D.2d).

We might reasonably conclude, therefore, that both suggested mechanisms are at work in generating the anomalous tails of the occupation distribution.

13.4.2 The Width of the Temperature Fitting Window

Given that there is some excitation of electrons occurring outside our maximum chosen fitting window, we should be concerned to ensure that the portion of the excitation spectrum to which we fit a pseudo-temperature contains the majority of the effect of electronic excitations. We can use data from the simulations introduced in Sect. 13.4.1 in which we obtain the excitation spectrum every femto-second to study how the change in occupation and total electronic energy is distributed across the eigenspectrum. We calculate for each eigenstate at each

timestep the following quantities, where t_i is the time of the *i*th timestep, o_j is the occupation of the *j*th eigenstate and ε_i is its energy:

• The absolute instantaneous change in occupation over the last femtosecond

$$|o_i(t_i) - o_i(t_{i-1})|.$$
 (D.1)

• The absolute total change in occupation over the course of the simulation

$$|o_i(t_i) - o_i(t_0)|. \tag{D.2}$$

• The instantaneous change in energy over the last femtosecond²

$$\left(\varepsilon_j(t_i) - \mu_0\right) \left(o_j(t_i) - o_j(t_{i-1})\right),\tag{D.3}$$

where $\mu_0 = 2.83$ eV is a rough estimate of the chemical potential over the course of the simulation (it does not change much on the scale of the energy range we are examining).

• The total change in energy over the course of the simulation

$$\left(\varepsilon_i(t_i) - \mu_0\right) \left(o_i(t_i) - o_i(t_0)\right). \tag{D.4}$$

Figure D.3 shows the cumulative excitation (in terms of occupation and energy) as we sweep up the energy scale. The effect of electronic excitation is mostly confined to a narrow energy range of a few eV and we see that an occupation range from 0.01 to 0.99 will accommodate 98% of the effect of excitations in terms of the changes in occupation and 87% of the irreversible energy transfer after 49 fs.

13.4.3 The Sommerfeld Expression for the Heat Capacity of Our Model

The Sommerfeld expansion [4] allows us to write an integral of some function $H(\varepsilon)$ of electronic energy and the Fermi-Dirac distribution $f(\varepsilon)$ as an expansion in even powers of temperature. To second order the expansion is,

$$\int_{-\infty}^{\infty} H(\varepsilon)f(\varepsilon)d\varepsilon \approx \int_{-\infty}^{\mu} H(\varepsilon)d\varepsilon + \frac{\pi^2}{6}(k_{\rm B}T)^2 H'(\varepsilon). \tag{D.5}$$

² This is not very well defined because the eigenstate energies move around and so we have chosen to use the *current* energy of the eigenstate as the reference.

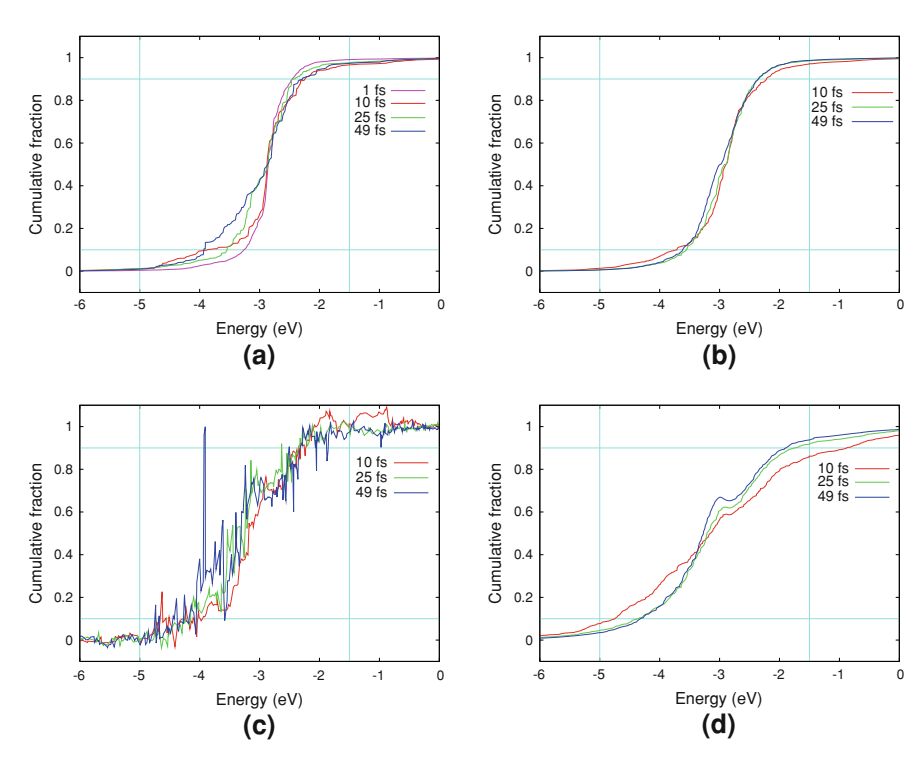


Fig. D.3 The fraction of the total excitation in the occupation spectrum shown cumulatively for all eigenstates up to the energy indicated and at various times in a typical simulation. The *left-hand panels* show data for only those changes in occupation taking place over the most recent femtosecond of cascade evolution, the *right-hand panels* show data for all excitations up to the indicated time. The *upper panels* show the change in occupation and the *lower panels* show the irreversible energy transfer attributable to the changes in occupation. The *horizontal lines* mark the region containing 80% of the excitation. The *vertical lines* show energy bounds roughly corresponding to an occupation range from 0.01 to 0.99 at 49 fs (i.e. the bounds of our maximum fitting window)

We can thus write the electronic energy as,

$$E = \int_{-\infty}^{\infty} \varepsilon g(\varepsilon) f(\varepsilon) d\varepsilon \approx \int_{-\infty}^{\mu} \varepsilon g(\varepsilon) d\varepsilon + \frac{\pi^2}{6} (k_{\rm B} T)^2 (\mu g'(\mu) + g(\mu))$$
 (D.6)

where $g(\varepsilon)$ is the density of states. μ will differ from the Fermi energy $E_{\rm F}$ by terms of order T^2 so we can write,

$$E \approx \int_{-\infty}^{E_{\rm F}} \varepsilon g(\varepsilon) d\varepsilon + E_{\rm F}(\mu - E_{\rm F}) g(E_{\rm F}) + \frac{\pi^2}{6} (k_{\rm B}T)^2 E_{\rm F} g'(E_{\rm F}) + \frac{\pi^2}{6} (k_{\rm B}T)^2 g(E_{\rm F}). \tag{D.7}$$

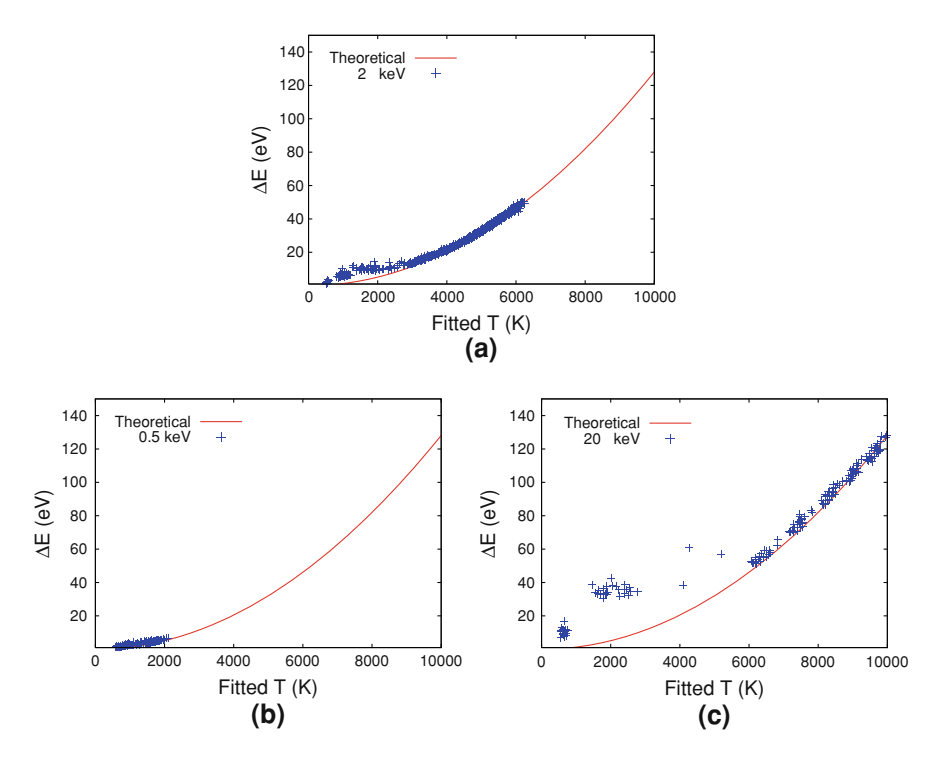


Fig. D.4 A plot of the irreversible energy transfer into the electronic system against the best-fit temperature using our fitting algorithm. Data are shown at 10 fs intervals over 200 fs for sets of cascade simulations with PKA energies of (**a**) 2 keV, (**b**) 0.5 keV, and 20 keV. The *red line* shows the predictions of the Sommerfeld model for the electronic heat capacity as discussed in the *text*

The number of electrons is constrained to N and so,

$$N = \int_{-\infty}^{\infty} g(\varepsilon) f(\varepsilon) d\varepsilon \approx \int_{-\infty}^{E_{\rm F}} g(\varepsilon) d\varepsilon + (\mu - E_{\rm F}) g(E_{\rm F}) + \frac{\pi^2}{6} (k_{\rm B} T)^2 g'(E_{\rm F}), \quad (D.8)$$

giving,

$$\mu = E_{\rm F} - \frac{\pi^2}{6} (k_{\rm B} T)^2 \frac{g'(E_{\rm F})}{g(E_{\rm F})}.$$
 (D.9)

This form for the chemical potential gives cancellation of the second and third terms in the expression for E and we have,

$$E \approx \int_{-\infty}^{E_{\rm F}} \varepsilon g(\varepsilon) d\varepsilon + \frac{\pi^2}{6} (k_{\rm B} T)^2 g(E_{\rm F}). \tag{D.10}$$

Hence the heat capacity (dE/dT) is simply,

$$c = \frac{\pi^2}{3} k_{\rm B}^2 T g(E_{\rm F}). \tag{D.11}$$

Using the values for our simple tight-biding model ($E_F = -2.83 \text{ eV}$, $g(E_F) = 0.026 \text{ eV}^{-1}$) gives a formula for the electronic energy,

$$E = E_0 + \gamma T^2$$
, $\gamma = 6.35 \times 10^{-10} \,\text{eV} \,\text{K}^{-2}$. (D.12)

13.4.4 Behaviour of the Fitted Temperature Early in the Cascade

In Fig. D.2 in chapter 8 we noted that at low temperatures, corresponding to early times in our 2 keV cascade simulations, the fitted temperature deviated significantly from the theoretical predictions of the Sommerfeld model (this figure is reproduced in Fig. D.4a for convenience). Given our explanation for the appearance of a well-defined electronic temperature (see Sect. 8.1.2) we can see that this deviation could be due to the fact that early in a cascade only a small number of individual electronic excitations will have occurred and so a new elevated temperature will not have been established by the statistical mechanism that we propose. This explanation is supported by the data in Fig. D.4b, c showing fitted temperature data for simulations of 0.5 keV and 20 keV cascade simulations respectively. In the case of the lower energy cascades (Fig. D.4b), we can see that it is perfectly possible to establish a well-defined thermal excitation distribution at lower temperatures, provided enough excitations have occurred (i.e. provided that the cascade has evolved for long enough. Conversely, for the higher energy cascades (Fig. D.4c) significant excitation of the electronic system occurs before a well-defined temperature is established. The relatively high energy transfer ΔE early in the cascade is the result of only a small number of high energy excitations due to the rapidly moving ions at this high PKA energy.

13.5 Appendix E: The Strain on an Inclusion due to Electronic Heating

The effect of increasing the electronic temperature of a block of our tight-binding model will be to reduce the bonding interactions between the ions and therefore increase the equilibrium lattice parameter. For a volume constrained portion of material this will imply a volume strain and hence a pressure on the surface of the portion.

The lattice parameter of a tight-binding slab with an elevated electronic temperature will be determined (as in the zero temperature case) by minimisation of the cohesive energy E_c (the binding energy per atom),

$$E_{\rm c} = \frac{\epsilon}{2} \sum_{J \neq I} \left(\frac{a}{R_{II}} \right)^p - \epsilon c \sum_{J \neq I} \rho_{II} \left(\frac{a}{R_{II}} \right)^q. \tag{E.1}$$

 E_c is easily minimised at T=0 as the elements of the density matrix ρ_{JI} are independent of volume scaling. Heating the electrons weakens the bonds and will cause thermal expansion of the crystal. We allow for this by introducing a linear strain e and writing,

$$R_{II} = xR_{II}^{(0)} \tag{E.2}$$

where x = 1 + e. Now we write,

$$E_c = \frac{\epsilon}{2} \sum_{J \neq I} \left(\frac{a}{R_{JI}^{(0)}} \right)^p \left(\frac{1}{x} \right)^p - \epsilon c \sum_{J \neq I} \rho_{JI} \left(\frac{a}{R_{JI}^{(0)}} \right)^q \left(\frac{1}{x} \right)^q, \tag{E.3}$$

$$E_c = \frac{\epsilon}{2} s \left(\frac{1}{x}\right)^p - \epsilon c \sigma(T) \left(\frac{1}{x}\right)^q \tag{E.4}$$

where

$$s \equiv \sum_{J \neq I} \left(\frac{a}{R_{JI}^{(0)}}\right)^p,\tag{E.5}$$

and

$$\sigma(T) \equiv \sum_{J \neq I} \rho_{JI} \left(\frac{a}{R_{II}^{(0)}} \right)^{q} \tag{E.6}$$

is written as a function of temperature because the bond-order terms ρ_{II} are temperature dependent. We can easily obtain $\sigma(T)$ at a fixed lattice parameter, but we note that the density matrix at $T \neq 0$ will depend on the lattice parameter and so σ will also have a dependence on x. This makes the minimisation of E_c more complicated, but we can proceed by noting that there is an equivalence between dilating the crystal (narrowing the eigenvalue spacing) and heating the electrons (broadening the Fermi surface). Figure E.1 illustrates this equivalence.

We assume we have access to data which tells us $\sigma(T^{(0)})$ as a function of temperature $T^{(0)}$ for the undilated crystal (x=1). We expect the heated crystal to dilate so that any initial eigenvalue spacing $\Delta \varepsilon^{(0)}$ will become smaller as the hopping integrals decrease $(\Delta \varepsilon^{(0)} \to \Delta \varepsilon'$ as $x \to x'$). In particular we can see that $\Delta \varepsilon'$ is smaller on the scale of the variation of the Fermi function, $kT^{(0)}$. It is this ratio $\Delta \varepsilon'/kT^{(0)}$ on which σ depends and so we can also obtain the same value of σ by

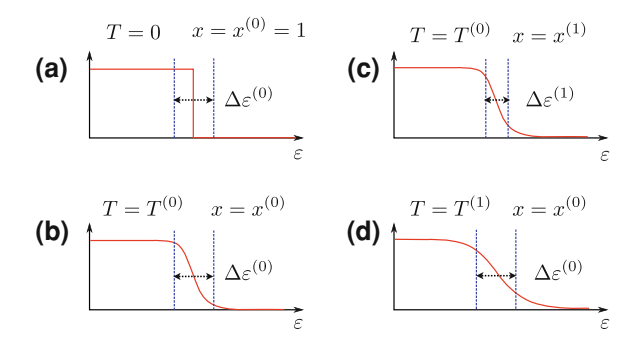


Fig. E.1 The equivalence of volume and temperature changes on the density matrix elements illustrated by a schematic diagram of the Fermi function and a typical eigenvalue spacing $\Delta \varepsilon$. a shows the cold crystal. **b** shows the crystal heated to some new temperature $T^{(0)}$ but with the same lattice parameter $T^{(0)} = 0$. **c** illustrates the effect of allowing the heated crystal to dilate to a new equilibrium lattice parameter $T^{(1)}$. **d** shows the equivalent effect form the point of view of eigenfunction occupations, brought about by a further heating of the *undilated* crystal to some temperature $T^{(1)}$

considering an unstrained crystal $x=1, \Delta \varepsilon^{(0)}$ at a new temperature T=T' such that

$$\frac{\Delta \varepsilon'}{kT(0)} = \frac{\Delta \varepsilon^{(0)}}{kT'} \Rightarrow T' = \frac{\Delta \varepsilon^{(0)}}{\Delta \varepsilon'} T^{(0)}.$$
 (E.7)

We know that the hopping integrals scale according to a power law and so

$$\Delta \varepsilon \propto \left(\frac{1}{x}\right)^q$$
. (E.8)

Hence

$$T' = x^q T^{(0)} \tag{E.9}$$

is our equivalent temperature. Making this scaling identification allows us to write

$$\sigma(T^{(0)}, x) = \sigma(T, x^{(0)}) \quad \text{if} \quad T = \left(\frac{x}{x^{(0)}}\right)^q T^{(0)}.$$
 (E.10)

Now we can return to consider,

$$E_c = \frac{\epsilon}{2} s \left(\frac{1}{x}\right)^p - \epsilon c \sigma(T) \left(\frac{1}{x}\right)^q \tag{E.11}$$

and differentiate to find the equilibrium at $x^{(1)}$, $T^{(0)}$ from

$$\frac{dE_c}{dx}\Big|_{x^{(1)},T^{(0)}} = 0.$$
 (E.12)

Now

$$\frac{dE_{c}}{dx} = -\frac{p\epsilon s}{2} \left(\frac{1}{x}\right)^{p+1} - \epsilon c \left\{\frac{d\sigma}{dx} \left(\frac{1}{x}\right)^{q} - q\sigma(x, T) \left(\frac{1}{x}\right)^{q}\right\}$$
 (E.13)

and we require

$$\frac{d\sigma}{dr}\Big|_{r^{(1)}T^{(0)}} = \frac{d\sigma}{dT}\Big|_{r^{(0)}T^{(1)}} \frac{dT}{dr}\Big|_{r^{(0)}}.$$
 (E.14)

But

$$T = x^q T^{(0)} \tag{E.15}$$

and so

$$\frac{dT}{dx} = qx^{q-1}T^{(0)}. (E.16)$$

Then

$$\frac{dE_{c}}{dx}\Big|_{x^{(1)},T^{(0)}} = -\frac{p\epsilon s}{2} \left\{ \left(\frac{1}{x}\right)^{p+1} + \frac{1}{\sigma(1,0)} \left(\frac{1}{x}\right)^{q+1} \left[\sigma(T^{(1)},x^{(0)}) - x^{q}T^{(0)} \frac{d\sigma}{dT} \Big|_{x^{(0)},T^{(1)}} \right] \right\}$$
(E.17)

So the equilibrium condition is

$$1 + \frac{x^{p-q}}{\sigma(1,0)} \left[x^q T^{(0)} \frac{d\sigma}{dT} |_{x^{(0)},T^{(1)}} - \sigma(T^{(1)},x^{(0)}) \right] = 0.$$
 (E.18)

Given data on the variation of the bond orders with temperature for the undilated crystal we can implement a cubic spline fit to $\sigma(T,x^{(0)}=1)$ (see Fig. 9.6) and hence determine the equilibrium linear and volume strain for the crystal with hot electrons from the equilibrium condition. Figure 9.7 shows the results from the fitted data.

References

- Todorov, T.N.: Time-dependent tight binding. J. Phys. Condens. Matter 13(45), 10125–10148 (2001)
- 2. Foulkes, W.M.C.: PhD thesis. Cambridge (1987)
- 3. Sakurai, J.J.: Modern Quantum Mechanics, pp. 69–71, 89–97. Addison Wesley Longman, Reading (1994)
- 4. Ashcroft, N.W., Mermin, N.D.: Solid State Physics. Thomson, Toronto (1976)

Index

A	replacement collision sequence, see
Ab-initio tight-binding, see tight-binding	replacement collision sequence
ab-initio tight-binding	sub-cascade branching, see sub-cascade
Adiabatic evolution	branching
adiabatic theorem, see adiabatic theorem	thermal spike, see thermal spike, in
in simulations, see Ehrenfest simulations,	collision cascade
electronic evolution, adiabatic	cooling phase, 12
evolution	role of electrons, 12
adiabatic theorem, 142	correlated electron-ion dynamics, 58
avoided crossing, 140	coulomb explosion, see ion channelling,
example of, 140	coulomb explosion model
toy model of, 143	
	_
n	D
B	damage recovery, 12
band-filling, see tight-binding, s-band model,	damping
band-filling	directional dependence, see single oscil-
Barkas effect, <i>see</i> electronic stopping power,	lating ion, damping, direction
models, Barkas effect	dependence of
Bethe stopping model, <i>see</i> electronic stopping	frequency dependence, <i>see</i> single oscillating in dempine frequency
power, models, Bethe	ing ion, damping, frequency dependence of
Bloch stopping model, <i>see</i> electronic stopping power, models, Bloch formula	position dependence, <i>see</i> single oscillating
Bohr stopping model, <i>see</i> electronic stopping	ion, damping, position
power, models, Bohr	dependence of
power, moders, bom	temperature dependence, <i>see</i> single oscil-
	lating ion, damping, temperature
C	dependence of
CEID, <i>see</i> correlated electron-ion dynamics	density functional theory, 76
channelling, see ion channelling	exchange-correlation potential, 80
collision cascade	Hohenberg–Kohn theorem, 76
cooling phase, see cooling phase	Kohn–Sham effective potential, 80
damage recovery, see damage recovery	Kohn–Sham equations, 80
displacement phase, see displacementphase	time-dependent, see time-dependent den-
evolution of, 9	sity functional theory
primary knock-on atom, see primary	DFT, see density functional theory
knock-on atom	displacement phase, 12
	-

300 Index

D (cont.)	electron gas stopping model, see electronic
role of electrons, 12	stopping power, models, electron
drag force, see non-adiabatic force	gas
evidence for, 41	electron-phonon coupling
model for electron-phonon coupling, see	experimental determination of, 49
electron-phonon coupling, repre-	importance of, 43
sentation of in molecular dynamics	in a thermal spike, 43
problems with, 41	models
use of in molecular	drag, see electron-phonon coupling,rep-
dynamics, 16, 51	resentation of in molecular
.,, ., .	dynamics
	Finnis et al., 45, 46
E	Flynn–Averback, see electron–phonon
effective charge, 28, 29	coupling, in a thermal spike
problems with, 40	general form, 46
Ehrenfest approximation, see Ehrenfest	Kaganov et al., 47
dynamics, equations of	two temperature, 44
Ehrenfest dynamics	regime of, 17, 18
approximations in, 74	representation of in molecular dynamics,
	46
comparison with surface hopping, see sur-	
face hopping	the importance of
energy transfer, 98	evidence for from simulation, 50
equations of, 72	theory of, 46
failure of, 98	values of, 48
of tight-binding system, see time-depen-	electronic effects
dent tight-binding, electronic	environmental dependence, 40
evolution; time-dependent tight-	models of
binding, ionic evolution	drag force, see drag force, use of in
suitability for simulating a metallic system,	molecular dynamics
97	explicit, 15
suitability for simulating radiation	implicit, 16
damage, 97	electronic entropy
wavefunction Ehrenfest, see Ehrenfestsi-	a thought experiment, 168
mulations, electronic evolution,	definitions of, 166
wavefunction picture	in Ehrenfest dynamics, 166
Ehrenfest simulations	electronic force
at high ion mass, 148	components of, 172
electronic evolution	conservative, 174
adiabatic evolution, 145	due to accumulated excitations, 174
eigenstate occupation picture, 140	non-adiabatic component, see non-adia-
eigenvalue spectrum, 140	batic force
real-space picture, 139	electronic stopping force, see electronic stop-
wavefunction picture, 139	ping power
intialization of electronic system, 138	electronic stopping power
ion channelling, 189	applications, 18
projectile charge, 193	definition, 19
stopping power, 210	dominance of at high speed, 20
ionic evolution, 137	models
irreversible energy transfer	Barkas effect, 27
definition of, 151	Bethe, 23
single oscillating ion, see single	Binary Theory, 30
oscillating ion	Bloch formula, 26
thermalization, 133	Bohr, 22
Ehrenfest theorem, 71	Darwin, 22
Ememest moorem, /1	-ui wiii,

effective charge, <i>see</i> effective charge electron gas, <i>see</i> electronic stopping power models, Fermi-Teller; electronic stopping power, models, Lindhard; electronic stopping power, models, non-linear	Finnis–Sinclair potential, 68 Firsov stopping model, <i>see</i> electronic stopping power, models, Firsov Flynn–Averback model, <i>see</i> electron–phonon coupling, in a thermal spike
empirical, see electronic stopping power, models, SRIM; electronic stopping power models, Paul and Schinner Fermi-Teller, 36 Firsov, 36 gaps in, 39 Grüner, 31 Lindhard, 33 Lindhard-Scharff, 33	H Harris–Foulkes functional, 83, see tight binding, Harris–Foulkes functional Hartree potential, 80 heat capacity electronic, see electronic temperature,heat capacity two temperature models, see electron—phonon coupling, models,
motivation for, 21 non-linear, 37, 38	two-temperature
Paul and Schinner, 35 screening corrections, 27 shell corrections, 27 Sigmund and Schinner, 30, see electronicstopping power, models, Binary Theory SRIM, 33 Unitary Convolution Approximation, 32 validity of, 23–26 projectile classification, 18 regime of, 17 Rutherford formula, 20 scaling properties, 33 electronic temperature heat capacity Sommerfeld model, 155, 289–291 pseudo-temperature, 154 thermalization, see thermalization two-temperature models, see electronic temperature models, see electronic temperature models, see electronic two-temperature models, see electronic temperature	I independent electron approximation, 75 ion channelling bond weakening model, 11 coulomb explosion model, 11 damage tracks, 11 description of, 11 Ehrenfest simulations, see Ehrenfest simulations, ion channelling energy loss mechanism, 11 experimental evidence for, 11 thermal spike model, 11 time-dependent density functional theory simulations of, see time-dependent density functional theory, simulations irreversible energy transfer, see Ehrenfest simulations, irreversible energy transfer, definition of; single oscillating ion, energy transfer
electronic, <i>see</i> electronic entropy exchange-correlation potential, <i>see</i> density functional theory, exchange-corre- lation potential	K Kohn–Sham equations, tions, <i>see</i> density functional theory, Kohn–Sham equations
F Fermi-Teller stopping model, <i>see</i> electronic stopping power, models, Fermi-Teller	L Langevin model, see molecular dynamics, electronic heat bath
finite system size effects, <i>see</i> single oscillating ion, finite system size effects; tight-binding, <i>s</i> -band model, finite system size effects	level crossing, see avoided crossing; non- crossing theorem; Ehrenfest simu- lations, electronic evolution, eigenvalue spectrum

302 Index

L (cont.)	S
Lindhard stopping model, see	self-consistent charge transfer model, see
electronic stopping power,	tight-binding, self-consistent charge
models, Lindhard	transfer model
Lindhard-Scharff stopping model, see elec-	shell correction, see electronic stopping
tronic stopping power, models,	power, models, shell correction
Lindhar-Scharff	single oscillating ion, 113–131
Liouville equation, 95, 109	damping
1 · · · · · · · · · · · · · · · · · · ·	behaviour of, 116
	definition of, 115
M	direction dependence of, 118
molecular dynamics	frequency dependence of, 117
augmented models, 16, 51–58	position dependence of, 118
electronic heat bath	temperature dependence of, 117
Caro–Victoria model, 54	energy transfer, 120
inhomogeneous, 55	finite system size effects, 123
simulations, 51	oscillator coupling matrix, 123
time-dependent density	perturbation theory analysis, 118
functional theory, 58	transition spectrum
with drag force, 51	sparseness of, 124
	transition spectrum density, 120
	software, see spICED
N	Sommerfeld model, see heat capacity, elec-
non-adiabatic force	tronic, Sommerfeld model
as component of Hellmann-Feynman	sparse parallel Imperial College Ehrenfest
force, 174	Dynamics code, see spICED
improved model for, 230	spICED, 110
non-crossing theorem, 140	performance of, 110
	spontaneous phonon emission, see Ehrenfest
	dynamics, failure of
P	stopping power
PKA, see primary knock-on atom	electronic, see electronic stopping power
polarization effect, see electronic	sub-cascade branching, 11
stopping power, models,	importance of, 11
Barkas effect	surface hopping, 95
primary knock on atom, 9	
spectrum, 9	
projectile classification, see electronic stop-	T
ping power, projectile	TD-DFT, see time dependent density func-
classification	tional theory
quantum Liouville equation, see	thermal spike
Liouville equation	Flynn–Averback model of, 43
Elouville equation	in collision cascade, 12
	model of track damage, see ion channel-
R	ling, thermal spike model
RCS, see replacement collision sequence	thermalization
replacement collision sequence, 12	by electron—ion interaction, 163
effect of excitations on, 181	statistical explanation of, 157
	•
Runge–Gross theorem, see time-dependent	timescales for, 162
density functional theory, Runge-	tight-binding
Gross theorem	s-band model, 103–111
Rutherford scattering, see electronic	band-filling, 104
stopping power, Rutherford	density matrix, 104
formula	Ehrenfest dynamics, 109

electronic structure, 105	Tilinin s
finite band width, 123	
finite system size effects, 123	time-de
hopping integral, 108	Rung
hopping integral truncation, 108	simu
parameterization, 105	
self-consistent charge	time-de _l
transfer terms, 104	elect
ab-initio tight-binding, 81	ionic
self-consistent charge transfer model, 90	theo
self-consistent tight-binding, 89	TRIM, s
semi-empirical tight-binding, 83	
heory, 81–90	wavefur
ime-dependent tight-binding, see time-de-	
pendenttight-binding	

Tilinin stopping model, *see* electronic stopping power, models, Lindhard-Scharff time-dependent density functional theory Runge-Gross theorem, 80 simulations, *see* molecular dynamics, time-dependent density functional theory time-dependent tight-binding electronic evolution, 94 ionic evolution, 95 theory, 91–95

TRIM, *see* electronic stopping power, models, SRIM

wavefunction Ehrenfest, *see* Ehrenfest simulations, electronic evolution, wavefunction picture